Structure-Property Relationships of Tantalum Carbide Foams and Synthesis of an Interpenetrating Phase Composite

Eric J. Faierson

Dissertation submitted to the faculty of the Virginia Polytechnic Institute and State University in partial fulfillment of the requirements for the degree of

Doctor of Philosophy
Materials Science and Engineering

Kathryn V. Logan, Chair
David E. Clark
Norman E. Dowling
Richard L. Kiefer

August 4, 2011
Blacksburg, VA

Structure-Property Relationships of Tantalum Carbide Foams and Synthesis of an Interpenetrating Phase Composite

Eric J. Faierson

Abstract

Ceramic and refractory metal foams have a potential for use in extreme environments, such as in fuel elements within nuclear reactors both in space and terrestrial applications. In addition, infiltrating an open-cell ceramic foam with a continuous second phase can create an interpenetrating phase composite (IPC), consisting of a three-dimensional reinforcement structure. One aspect of investigation within this study was the influence of foam pore/strut size, foam composition, and foam density on neutronic and mechanical properties. Neutron transmission through open-cell tantalum carbide foams was measured using experimental techniques and modeled with Monte Carlo N-Particle (MCNP) transport code. Neutron transmission decreased linearly within tantalum carbide (TaC)/reticulated vitreous carbon (RVC) foams as areal TaC density increased. All MCNP modeling runs predicted slightly higher neutron transmission than what was experimentally measured, potentially indicating that the foam structure had a small influence on neutron transmission. Compressive strength and Young's moduli of tantalum carbide foams were measured for foam specimens that were exposed to thermal cycling and thermal shock, as well as for baseline specimens. Extensive micro-cracking was observed in the foams after 18 thermal cycles to 2100° C. However, thermal shock in liquid nitrogen did not produce observable micro-cracking in the TaC foams. The average strengths of baseline TaC/RVC foams ranged from 1.97 MPa - 3.82 MPa. The baseline TaC/PyC/RVC foams exhibited strengths ranging from 4.57 MPa - 12.60 MPa. The compressive strength of thermally cycled foams tended to be 1/3-1/2 that of baseline specimens.

Another aspect of this study investigated the infiltration of RVC foams with tungsten powder in an attempt to form a tungsten-ceramic foam interpenetrating phase composite (IPC). It was found that tungsten particle size influenced infiltrated densities more than foam pore size. Significantly lower infiltrated densities were obtained using sub-micron tungsten than with 5-10 micron tungsten as a result of particle agglomeration. Infiltrated 5-10 micron tungsten achieved

densities ranging from 23-25% theoretical within RVC foams, whereas sub-micron tungsten densities ranged from 11-16% theoretical. Constrained densification was observed during sintering of tungsten-infiltrated foams.

This work is dedicated to my parents and grandparents, who always supported me in my endeavors and taught me to reach for the stars.

Acknowledgements

Dr. Kathryn Logan, my advisor, for advice, guidance, and the opportunities I have had at Virginia Tech, the National Institute of Aerospace, and NASA Langley Research Center (LaRC)

Dr. David Clark, Dr. Norman Dowling, and Dr. Richard Kiefer for being on my committee, and offering advice with respect to this work

Brian Stewart for research advice throughout my graduate study

Dr. Robert Singleterry for assistance with radiation modeling

The National Institute of Aerospace for funding this work

NASA LaRC for the use of laboratory facilities

Non-destructive measurements for this study were performed on a DEPA system from Jagdish Electronics of Bangalore, India, supplied by Matrix Enterprises, their US representative

Jim Baughman and Steve McCartney for assistance and training with SEM

Mac McCord for assistance with compressive strength testing

David Berry for assistance with particle size analysis

Patricia Davis for assistance with surface area analysis

Michael Hunt, Sharon Jefferies, and Susan Holt for research advice during my graduate study

All images by author, 2011

Table of Contents

Table of Figures

Table of Tables

List of Abbreviations and Symbols

ppi	Pores per inch (commercial designation of foam pore density)
MOR	Modulus of rupture (flexural strength)
TaC	Tantalum carbide
PyC	Pyrolytic carbon
RVC	Reticulated vitreous carbon
W	Tungsten
MCNP	Monte Carlo N-Particle transport code
IPC	Interpenetrating phase composite
MeV	Megaelectron volt
CVI	Chemical vapor infiltration
DBTT	Ductile-brittle transition temperature
ρ_r	Relative density of foam (ρ/ρ_s)
ρ	Density of foam
ρ_s	Density of foam strut
t	Thickness of foam strut
l	Cell edge length of foam
C	Proportionality constant
F	Force
E	Elastic modulus
I	Area moment of inertia
σ	Compressive stress
ε	Strain
E_s	Elastic modulus of foam strut
E_f	Elastic modulus of foam
σ_{cs}	Compressive strength
σ_{mr}	Modulus of rupture (flexural strength)
σ_{diff}	Standard error of difference between two means
df	Degrees of freedom

I. Introduction

Ceramic and refractory metal foams have a potential for use in a variety of applications, one of which is in fuel elements in nuclear reactors. Of particular interest to this study is the use of foam within a nuclear propulsion reactor for space exploration applications. Nuclear propulsion can significantly increase spacecraft performance, decreasing travel time, and enabling missions to Mars and beyond. Furthermore, use of nuclear reactors on planetary surfaces would be of great benefit for permanent settlements. Influences of foam strut/pore size, foam composition, and foam density were investigated with respect to both neutronic and mechanical properties within this study. Neutron transmission in tantalum carbide foams was measured experimentally, and modeling was performed using Monte Carlo N-Particle Transport Code. Constitutive equations were used to predict mechanical properties of the foams. The compressive strength and Young's modulus of tantalum carbide foams were measured for foams exposed to thermal cycling and thermal shock, along with baseline foam specimens. Furthermore, vibration-induced tungsten powder infiltration and densification within ceramic foams was investigated for the purpose of creating an interpenetrating phase composite (IPC). The infiltrated foams were consolidated by vacuum sintering.

Objectives

1. Understand the neutronic and mechanical properties of tantalum carbide/pyrolytic carbon/reticulated vitreous carbon (TaC/PyC/RVC) foams and tantalum carbide/ reticulated vitreous carbon (TaC/RVC) foams.
    a. Understand the influence of strut/pore size, foam composition, and foam density on the neutron transmission in the foams.
    b. Understand the influence of strut/pore size, foam composition, foam density, thermal fatigue, and thermal shock on mechanical behavior of the foams.
2. Understand the influence of foam pore size and tungsten particle size/surface area on vibration-induced tungsten particle infiltration and densification within RVC foams, with the goal of forming an interpenetrating phase composite.

Justification

Ceramic foams and tungsten-cermets have potential applications in extreme environments such as nuclear propulsion systems, solar-thermal propulsion systems, and nuclear reactors.[1, 2] In addition, tungsten-cermets also have potential applications in rocket nozzles, hypersonic engines, and radiation shielding.[3]

Materials utilized in nuclear reactors must retain adequate performance properties under high temperatures and radiation fluences. Increasing the operating temperature of reactors provides greater energy conversion efficiency; and in the case of nuclear rockets, greater propulsion performance. Advances in foam/foam-composite research could facilitate nuclear propulsion systems enabling more rapid travel time to destinations such as Mars, and contribute to the development of high-performance nuclear power for use on planetary surfaces.

Utilizing a ceramic foam incorporating tantalum carbide (m.p. 3880° C)[4] in a nuclear thermal rocket fuel element could reduce the overall mass, increase the fuel fracture toughness, inhibit catastrophic fuel fracture from vibration fatigue, increase high temperature strength, maintain fuel integrity during gas release induced by nuclear fission, and allow higher operating temperatures to be achieved.[1] Prior studies have shown that tungsten and tungsten alloys are good candidate materials for fuel encapsulation in fast nuclear thermal propulsion reactors, and for first wall materials in fusion reactors. Tungsten has the highest melting point of all metals, 3422° C[3], and a high thermal conductivity (171 W/m·K at 300 K).[5]

It is important for the fuel element to be resistant to damage from thermal cycling if it is desired for the reactor to be able to be shut off and restarted. Multiple restarts would be of use for multiple fuel burns and in bi-modal space nuclear reactors, which can be used in both propulsion and power applications. Thermal shock resistance is also important since cryogenic hydrogen would be flowing into the reactor core. Evaluation of the neutronic properties for a potential fuel element is important since neutron absorption can result in too few neutrons to sustain nuclear fission, making reactor criticality unachievable.

Infiltrating ceramic foam with tungsten could create an interpenetrating phase composite (IPC), and is predicted to enhance the high-temperature strength and stiffness of tungsten. The tungsten- ceramic foam composite would have reduced mass, which could reduce launch costs in aerospace applications.

II. Background

Nuclear Propulsion Technologies

The future of human space exploration requires significant advances in propulsion technology and energy generation. Nuclear propulsion technologies have potential to offer significant advantages over conventional chemical propulsion technology. The velocity change that is either required or available for propulsion and orbital maneuvering of a spacecraft is referred to as ΔV. The largest ΔV that a conventional chemical rocket, utilizing hydrogen and oxygen for combustion, can provide to a spacecraft leaving Earth orbit is ~10 km/s. Nuclear thermal rockets could provide a ΔV of ~22 km/s to the same spacecraft. [6] The calculation of ΔV can be performed using Equation 1, where I_{sp}, is specific impulse, m_i is the initial mass of the vehicle, m_f, is mass after fuel burn, and g is 9.8 m/s^2. [7]

Equation 1. $$\Delta V = I_{sp} g \ln \frac{m_i}{m_f}$$

There are three basic concepts for nuclear propulsion technologies. Nuclear thermal propulsion (NTP) uses heat generated by nuclear reactions to heat a propellant. Nuclear electric propulsion (NEP) converts heat from nuclear reactions into electricity, which is used to create electromagnetic fields in order to direct and propel ionized gas in a plasma rocket. [8] A third type of nuclear propulsion technology utilizes electromagnetic fields to direct high energy fission fragments from a nuclear reaction out of the rocket in order to produce thrust. [9]

Nuclear Thermal Propulsion Reactors

The US Air Force began the Nuclear Engine for Rocket Vehicle Applications (NERVA) program in 1947 for use in propelling intercontinental ballistic missiles (ICBMs). NASA took over the program in 1958, in order to develop the technology for space exploration. Reactor sizes ranging from 300-200,000 MW were utilized. A total of 28 tests at full-power were conducted, for up to 30 minutes each. Restarts were also performed, resulting in a total reactor life of 90 minutes. Thrust to weight ratios between 3:1 and 4:1 were achieved, as well as specific impulse values up to 835 seconds. The majority of the tests were conducted at the Nuclear Rocket Development Station at the Nevada test site. The program ended in 1972. The NERVA reactor utilized particles of uranium carbide nuclear fuel dispersed in hexagonal graphite

elements. The NERVA reactor was a thermal reactor that utilized graphite as both a moderator and structural element. The fuel elements were protected from the hydrogen propellant with coatings of zirconium carbide or niobium carbide. [8]

Another reactor design for a nuclear rocket is the Particle-Bed Reactor (PBR), which was developed primarily by the Air Force Space Nuclear Thermal Propulsion program (SNTP). The PBR provides for a higher power density than the NERVA by both increasing the fuel surface area and the propellant temperature. Hydrogen propellant cools spherical particles of uranium carbide fuel coated with graphite and zirconium carbide. The PBR is a thermal reactor and graphite is used as the moderator. The PBR has a thrust to weight ratio of about 40:1. No full-scale engine tests were performed, but smaller tests for proof-of-concept have been conducted. The program ended in 1993. Tests on the nuclear fuel were conducted up to 3000 K, whereas NERVA fuel only reached 2650 K. [8]

The CERMET-core reactor is a third type of nuclear thermal rocket that utilizes fast neutrons (> 1 MeV) for fission, eliminating the need for a moderator. Tests have indicated that CERMET fuel is significantly more resilient than the NERVA or PBR fuel, allowing for many reactor restarts and subsequent fuel burns. Tested CERMET fuels have consisted of uranium dioxide particles dispersed in a tungsten or tungsten-rhenium matrix. [8] Tungsten CERMET nuclear fuel has a high melting point, good resistance to creep, and a high thermal conductivity. Tungsten additives such as rhenium, molybdenum, ThO_2, and GdO_3 can increase ductility, increase toughness, and/or modify the ductile-brittle transition temperature. [10] The 710 program run by General Electric in the 1960's utilized a fuel composition of 60% UO_2 and 40% tungsten, by volume, with a cladding of tungsten-rhenium. Fuel elements were tested at temperatures up to ~2500° C and cycled up to 100 times. Work performed by Argonne National Lab found that fuel loss from UO_2 could be prevented by adding gadolinia to the matrix. A potential method to increase the melting temperature limitations of UO_2 is to utilize a UO_2-Th mixture, which has a higher melting point that pure UO_2. [11]

CERMET fuels are expected to last for over 40 hours, be more compatible with hydrogen propellant, and withstand thermal cycling at high temperatures. [8] The greater compatibility

with hydrogen allows better retention of fission products and greater fuel integrity. [8, 10] Other CERMET fuel tests have been conducted at temperatures up to 1900 K for 10,000 hours. The thrust to weight ratio of the CERMET-core design is 5.3:1. [8]

The use of a fast-fission spectrum in a nuclear reactor offers many benefits over a thermal-fission spectrum. An important environmental benefit is that transuranic elements are burned up in the core, decreasing the quantity of long-lived radioactive waste. Fast reactors have a lower reactor core mass and a higher power density. In addition, fast reactors use neutron reflectors, and do not require moderator materials to reduce neutron energy. Loss or damage to the neutron reflector ensures the reactor will not go super-critical. Furthermore, melting of the reactor core leads to a negative feedback condition, forcing the reactor into a sub-critical state. [10]

Nuclear Propulsion Fuel Requirements

Materials utilized within a nuclear reactor must withstand high temperatures and high radiation flux. The combination of the two factors can lead to changes in the mechanical, thermal, chemical, physical, and nuclear properties of materials. Several types of radiation can be found within a fission nuclear reactor: neutrons, fission fragments, α-radiation, β-radiation, γ-radiation, and potentially protons. Significant changes in material properties can be induced by heavier particles such as neutrons, fission fragments, α-radiation, and protons. Interaction of a material with the heavier particles listed above can result in point, line, and plane defects within the crystal structure. Neutrons produce radiation damage by imparting momentum and energy to the nuclei of atoms. Neutron irradiation can produce vacancies, interstitials, and impurity atoms within materials. [12]

The fuel utilized in a nuclear thermal rocket determines the upper limit of propulsion performance. [13] Increasing the reactor temperature and decreasing the molecular weight of the propellant results in a higher specific impulse, other factors kept constant. [14] NTP reactors require fuel geometries with a high surface area to volume ratio in order to rapidly transfer heat to the propellant gas. [15] Uranium fuels with the highest melting points include: UO_2, UC, and UN. [13] Uranium density within the fuel element is also an important parameter for nuclear

reactors. Higher uranium densities are required in fast reactors due to lower fission cross sections for fast neutrons than thermal neutrons. [15]

The extreme conditions within the NTP reactor greatly limit operating life. Utilizing uranium fuels at temperatures between 2000-3500 K involves addressing a number of issues including: melting, chemical stability at high temperatures, evaporation, neutron spectrum of the nuclear reactor, creep at high temperatures, swelling, release of fission products, thermal shock resistance, fabrication methods, and fuel density. One of the most limiting factors of using uranium-based fuels at high temperature is fuel evaporation. Rockets utilizing NTP technology would heat hydrogen to temperatures over 3000 K. The nuclear fuel would generate heat at rates of over $20GW/m^3$, and could have temperatures over 3200 K. In order to reduce fuel loss by evaporation, encapsulation of the fuel is required. Tungsten has the lowest volatility of the refractory metals, and has been shown to be compatible with UO_2 at very high temperatures. [13, 15] In addition, the only two refractory metals that are fully compatible with uranium are tungsten and tantalum. Uranium does not bond with or dissolve in either. Uranium can attack tungsten and tantalum at high temperatures through grain boundary diffusion. [16] Large amounts of naturally occurring tungsten are not desirable in thermal reactors due to tungsten's large absorption cross-section and high resonance with thermal neutrons. However, isotopic refinement of tungsten can be performed to eliminate isotopes with high absorption cross-sections. [15]

One of the problems encountered within NTP reactor fuel is cracking from engine vibrations. Another issue is hydrogen degradation of fuels and coatings. [10] Hydrogen can cause the reduction of UO_2, forming uranium metal, which has a much lower melting point than UO_2.[15] Degradation of the nuclear fuel encapsulation materials by the propellant can result in fission products being emitted in the rocket exhaust. [10] Prior research has indicated that tungsten has the potential to contain UO_2 at temperatures near the melting point of UO_2 for short times. [15]

Utilizing UO_2 in a pure tungsten matrix causes fuel expansion at very high temperatures due to a CTE mismatch. The volume expansion eventually leads to fuel cracking. It was found that alloying tungsten with rhenium or rhenium/molybdenum can mitigate these issues. The CTE

mismatch can also be lowered by utilizing UN instead of UO_2. For temperatures above 2000 K, UN also has a higher thermal conductivity and fuel density than UO_2. [13]

Uranium carbides are another uranium-based nuclear fuel. The melting points of UC and UC_2 are 2525° C and 2480° C, respectively. Binary and ternary carbides incorporating UC with TaC, ZrC, HfC, and/or NbC have potential for use as fuels in nuclear propulsion applications. The binary and ternary carbides have higher melting points and can reduce evaporation of nuclear fuel. [14] The compositions with the highest melting points in the Ta-C, Zr-C, Hf-C, and Nb-C systems are hypo-stoichiometric with respect to carbon. A relatively small change in carbon content within the carbide can reduce the melting point 300-800 K below the composition with the highest melting point. For example, within the tantalum-carbon system, the composition $TaC_{0.89}$ has the highest melting point (4258 K). [15]

Tungsten has a very low evaporation rate, but reacts with materials containing carbon to form W_2C at significant rates. Tungsten could be used to contain a uranium carbide fuel, but temperatures would need to be maintained below 3060 K (melting point of W_2C) and operating times would be limited. However, localized melting of fuel might be able to be tolerated in some instances, presuming it does not lead to a loss of structural integrity. [15]

Table I. Melting Points of Selected High-Temperature Nuclear Fuels [15]

Fuel Composition	Melting Point (K)
W-60 vol.% UO_2	3075
UC	2805
$UC_{2\ (UC2+C\ eutectic)}$	2835
$(U_{0.1}Zr_{0.9})C_{0.96}$	3550
$(U_{0.1}Zr_{0.9})C_{0.98}$	3100

Fission products are generally contained in uranium carbide fuels by encapsulating them in graphite and applying a carbide coating, such as ZrC. [15] Research performed with ZrC coatings found that the large CTE difference between ZrC and graphite tended to induce cracking in the ZrC coating. Cracking was reduced by creating a composite with networks of (U, Zr)C in a graphite matrix, and by using graphite with a higher CTE. The fuels resisted loss of

carbon through hydrogen reactions, as well as cracking. However, significantly more testing needed to be performed. Carbide fuels are fairly stable in hydrogen, and have a much higher thermal conductivity than fuels such as UO_2. [14] However, hydrogen will still interact with carbide to some degree, which will result in changes to both composition and melting point. [15] The higher thermal conductivity reduces fuel cracking by decreasing the thermal gradient between the fuel and the propellant. [14]

Properties of Foams

Foams are three dimensional cellular materials with a relative density less than ~ 0.3, and can be classified as one of two types: open or closed cell. The relative density of a foam is determined by the ratio of the foam density to the density of the bulk material. [17-19] The cells within an open cell foam have material at the cell edges, and are open to adjacent cells at the cell faces. Therefore, they exhibit connectivity throughout their structure. Closed cell foams have material at both cell edges and cell faces, isolating each cell from adjacent cells. [17]

A variety of potential applications exist for foams including: catalyst supports, molten metal filters, biomedical devices, exhaust gas filters, thermal protection systems, composite reinforcement, space mirror supports, solid oxide fuel cell components, heat exchangers, bioreactors, radiant burners, kiln furniture, and light-weight sandwich structures. Ceramic foams tend to have a high specific strength, low density, low thermal conductivity, high thermal shock resistance, high specific surface area, high permeability, high porosity, high wear resistance, and high resistance to corrosion. [18]

The pore density within a foam is typically measured in pores per inch (ppi). [20] The ppi value of a foam is a rough estimate of pore density that is used by commercial manufacturers to differentiate foam pore sizes. The edge connectivity of a foam is determined by the number of edges that join at a vertex. [17] Typically foams have an edge connectivity of four. [19] The number of faces that join at a cell edge is referred to as the face connectivity. [17] Typically open cell foams have a cell face connectivity of three, but they can range as high as six. [19] Euler's law, shown in Equation 2, gives the relationship between the number of edges, *E*, faces, *F*, vertices, *V*, and cells, *C*, in a three- dimensional foam. [17]

Equation 2: $F - E + V - C = 1$

Thermal and mechanical properties of foams depend more on the shape of cells than the size. Isotropic properties are observed in equiaxed cell structures, while anisotropy is exhibited by elongated cells. Many cell shapes are possible since the cells have to fit together in three dimensions. However, only a few geometries have been observed. Potential cell geometries include: tetrakaidecahedron, rhombic, rhombic dodecahedron, triangular, and hexagonal prisms. Isotropic ceramic and metallic foams can be approximated to tetrakaidecahedron geometry. [18, 19] A tetrakaidecahedron is a polyhedron with eight hexagonal and six square faces. [19] A tetrakaidecahedron cell has 36 edges, 24 vertices, 14 faces, a cell volume of $11.31 \cdot L^3$, a surface area of $26.80 \cdot L^2$, and an edge length of $36 \cdot L$, where L is the average strut length of the foam. [17, 19]

Properties of a foam are dictated by properties of materials from which the foam is made, relative density of the foam, connectivity of cells (open or closed), and shape of cell faces and edges. A connected network of struts is referred to as a lattice. Due to the length scale of struts in foams, a mechanical analysis needs to be performed on the foam both as a structure and as a material. Prior research has indicated that most foams are bending-dominated structures, resulting in lower stiffness and strength than stretch-dominated lattices given the same relative density. [21, 22]

According to *Ashby* [21] and *Gibson and Ashby* [23] open-cell foam can be modeled in a simplified manner by considering it as a cubic arrangement of cells with an edge length of l and a strut thickness of t. The dimensions t and l are related to the relative density, ρ_r, of a cell by Equation 3, where C_1 is a constant of proportionality. The relative density is the ratio of the density of the foam, ρ, to the density of the strut material, ρ_s. [21, 23]

Equation 3. $\rho_r = \frac{\rho}{\rho_s} = C_1 \left(\frac{t}{l} \right)^2$

Beam theory relates the deflection of a beam, δ, to the load, F, beam length, l, elastic modulus, E, and area moment of inertia, I, by Equation 4. The area moment of inertia is proportional to t^4. [23]

Equation 4. $$\delta \propto \frac{Fl^3}{EI}$$

If a uniaxial stress is applied to the foam, the force, F, will induce cell edge bending, resulting in the linear elastic behavior of the foam being proportional to Equation 4. The force, F, is related to the compressive stress, σ, and cell edge length, l, by Equation 5. [23]

Equation 5. $$F \propto \sigma l^2$$

The elastic modulus, E_f, of the foam is given by Equation 6, where, E_s, is the elastic modulus of the strut material, and C_2 reflects the geometric constants of proportionality. [23]

Equation 6. $$E_f = \frac{C_2 I E_s}{l^4}$$

As strain increases, the applied load results in an additional moment on the cell edge, not accounted for in the above equations. The elastic modulus decreases in compression and increases in tension due to the additional moment. Therefore, instead of linear-elastic response, the response is really concave downward. [23] The elastic modulus of an open cell foam, E_f, has been found to be related to the relative density by Equation 7, where C is a constant. [22]

Equation 7. $$\frac{E_f}{E_s} = C\left(\frac{\rho}{\rho_s}\right)^2$$

A bending-dominated lattice behaves in a linear elastic manner until the elastic limit is reached. Once the elastic limit is reached, the edges of the cells yield through plastic deformation, buckling, or fracture. [21] The stress required to crush an open cell foam, σ_{cs} is given by Equation 8, where σ_{mr} is the modulus of rupture (flexural strength), and C_3 is a constant of proportionality. The lattice will continue to collapse at an approximately constant stress until opposite cell edges are brought into contact, causing a steep increase in stress. [21, 22]

Equation 8. $$\sigma_{cs} = C_3 \sigma_{mr} \left(\frac{\rho}{\rho_s} \right)^{3/2}$$

A change in the temperature of a material results in thermal stresses if the material is constrained from moving. The magnitude of the thermal stress, σ, is given by Equation 9, where α_l is the linear coefficient of thermal expansion, E is the elastic modulus, and ΔT is the change in temperature. [24]

Equation 9. $$\sigma = \alpha_l E \Delta T$$

Thermal gradients within a material can also cause thermal stresses. Induced thermal gradients within a material depend on the thermal conductivity, size, and geometry of the material, as well as the rate of temperature change. [24]

Research by *Vedula et al*., [25] utilized Equation 10 in conjunction with elastic modulus measurements to predict the extent of micro-cracking present in a foam after thermal cycling, where E is the elastic modulus after thermal cycling, E_0 is the elastic modulus prior to thermal cycling, a is the crack length along the major axis, and N is the density of microcracks per unit volume. Equation 10 is a first approximation for the elastic modulus of a material with elliptical cracks.

Equation 10. $$\frac{E}{E_0} = \frac{1}{Na^3 + 1}$$

A study by *Colombo et al.*, [22] investigated properties of silicon oxycarbide foams produced through direct foaming and pyrolysis of pre-ceramic polymers. Pycnometry was utilized to measure the volume of the foam struts. Compression testing was used to measure the crush strength of foam specimens with dimensions of 6 mm x 6 mm x 12 mm. The cross-head displacement for the tests was 0.5 mm/min.

Reticulated Vitreous Carbon Foams

A reticulated vitreous carbon (RVC) foam can be created by pyrolyzing a polymer foam. [26-29] The temperature at which the heat treatment is performed determines the properties of vitreous carbon. Research has shown that heating to 1800° C produces vitreous carbon with properties suitable in a number of applications. Vitreous carbon has a fracture behavior similar to that of glass. The theoretical density for amorphous carbon is 1.88 g/cm^3. However, typically vitreous carbon contains around 30% closed porosity, resulting in the lower values shown in Table II. The closed voids do not permit substantial gas permeability within the material. The structure of vitreous carbon consists of interlocking strands of carbon, which are randomly oriented, and twist around each other. The strands can be thought of as segments of hexagonal carbon layers of multiple sizes, with minimal ordering parallel to the layers. X-ray diffraction analysis has indicated that the average crystallite height and diameter are 50 Å and 15 Å, respectively. Vitreous carbon is resistant to graphitization due to the twisted and interlocking carbon strands and micro-porosity that comprise its microstructure, all of which inhibit crystal growth and recrystallization. [29] Vitreous carbon is isotropic, has a low density, electrical conductivity, thermal conductivity, and thermal expansion coefficient. Intercalation compounds are not formed by vitreous carbon, and it has extreme resistance to most chemical reagents. Vitreous carbon is only attacked by powerful oxidizers, some hot melts, and oxygen above 550° C. [27, 28, 30] Vitreous carbon generally has greater tensile and compressive strengths than graphite. However, the thermal conductivity is lower, and the electrical resistivity is higher. [29] Properties of vitreous carbon are shown in Table II.

Reticulated vitreous carbon (RVC) foam has a high surface area and is stable at very high temperatures (3500° C) in environments devoid of oxygen. RVC foam is a brittle material at room temperature. A linear shrinkage of approximately 30% is typical during foam production. RVC foam has a porosity volume ranging from 90% to 97% depending on the pores per inch (ppi). A 100 ppi grade of foam was determined to have a surface area of ~ 65 cm^2/cm^3. [26-28]

Chemical vapor infiltration (CVI) can be used to deposit materials with controlled thickness, composition, density, and orientation onto the RVC. In the CVI process, a precursor gas, typically metal chlorides or fluorides, flows through a heated substrate. The gas condenses on

the substrate and solidifies. Many materials can be deposited using CVI at temperatures ranging from 10-50% of their melting point. The deposition process is controlled by several variables, which include: deposition time, pressure, temperature, reactant concentration, and flow rate. CVI deposited materials exhibit higher strength and stiffness than bulk materials due to their small grain size and full density. In addition, CVI produced deposits have greater fracture toughness, thermally and mechanically, than bulk ceramics. Crack propagation is greatly inhibited by the foam strut structure. [1]

Research by *Youchison et al.*, [1] demonstrated the deposition of a ZrC-NbC-TaC coating on RVC foam. The TaC was used as a surrogate for UC. Deposition was accomplished both as separate layers and as a single layer solid solution. *DelaRosa and Tuffias* [2] performed compressive strength tests on 65 pore per inch (ppi) tantalum carbide foams. It was found foams with a TaC density of 1.52 g/cm^3 had a compressive strength of ~630 psi at 1750° C, ~530 psi at 2250° C, and ~370 psi at 2750° C. Flexural strength for 65 ppi TaC foams at room temperature was found to be ~375 psi at ~ 0.85 g/cm^3 TaC density, increasing to ~875 psi at ~1.75 g/cm^3 TaC density.

Pyrolytic carbon (PyC) is produced from thermal decompositions of gases containing carbon, such as methane, followed by deposition on a substrate. [29] PyC has a fine-grained structure and does not convert to graphite easily. [30] It is also stronger, harder, and less permeable to gases than pyrolytic graphite. [26] The mechanical properties of PyC tend to be density dependent. [31] PyC is commonly used in fissile material containment and rocket nozzle applications. [26] Properties of PyC are shown in Table II.

Table II. Properties of Pyrolytic Carbon and Vitreous Carbon [29]

	Pyrolytic Carbon	Vitreous Carbon
Density (g/cm^3)	1.5-2.0[31]	1.3-1.55
Tensile strength (kg/cm^2)	-	400-1000
Thermal conductivity (cal/cm s · K)	-	0.01-0.06
Thermal expansion ($10^{-6} \cdot K^{-1}$)	5.5[32]	2-3.5
Electrical resistivity (10^{-4} Ω·cm)	-	10-50
Gas permeability (cm^2/s)	-	10^{-6}-10^{-12}
Elastic modulus (GPa)	28[31]	24[31]
Compressive strength (MPa)	517[31]	172[31]

Research performed by *Hou et al.*, [33] showed that pyrolytic carbon formed through chemical vapor infiltration (CVI) can undergo crack deflection and partial delamination during crack growth. The deflection and delamination occurred along lamina formed during the CVI process. Crack deflection and partial delamination allowed more energy to be absorbed during loading, thus providing a higher strength. In order to attain partial delamination, a moderate interface strength is needed. If the strength is too high, debonding will not occur. If the strength is too low, complete delamination will occur at a low load.

Neutrons and Neutron Production

Neutrons are particles with no electric charge. [34] A neutron cross section represents the probability of a neutron interacting with a nucleus in a thin layer of material. The neutron cross section is expressed in barns, a unit of area. One barn is equal to 10^{-24} cm^2. The total neutron cross section, σ_t , represents the probability of any type of neutron interaction taking place. Several types of neutron-nucleus interactions are possible, the two major types being scattering and absorption. A scattering interaction results in a change in speed and direction for the neutron, but no change in the number of protons and neutrons in the nucleus. The neutron may transfer some of its energy to the nucleus, leaving it in an excited state. If the nucleus is left in an excited state, it will eventually return to its ground state through a release of radiation. Neutron absorption can cause the nucleus to fission and/or emit radiation. [35]

Two types of scattering interactions are possible, elastic and inelastic scattering. The total kinetic energy of the nucleus and the neutron does not change in an elastic scattering event. An inelastic scattering event causes the nucleus to enter an excited state, eventually resulting in the release of radiation. Since some of the neutron's energy is used to put the nucleus in an excited state, the total kinetic energy of the departing neutron and the nucleus is less than that of neutron prior to the scattering event. Inelastic scattering events result in a change in speed and direction of the neutron, just as elastic scattering events do. If insufficient energy is available to produce an excited state in the nucleus, an inelastic scattering event cannot occur. No excited states are possible in the hydrogen nucleus, therefore only elastic scattering can occur. Neutron absorption can cause rearrangement of the structure of the nucleus, resulting in the emission of gamma rays. Particles such as protons, neutrons, electrons, deuterons, and alpha particles may also be emitted. Neutron absorption may also trigger fission of the nucleus.[35]

For a thick sample, the neutron transmission can be determined by treating the sample as a series of atomic layers. Equation 11 shows the intensity of neutrons in the beam that have not interacted with the material, I, as a function of thickness, x, where I_0 is the neutron beam intensity prior to reaching the sample, σ_t is the total neutron cross section, and N is the density of atoms. [35]

Equation 11. $$I(x) = I_0 e^{-N\sigma_t x}$$

One method of neutron production utilizes beryllium in conjunction with americium-241 in order to produce neutrons. Americium-241 emits an alpha particle as shown in **Error! Reference source not found.**. Then beryllium absorbs the alpha particle and releases a neutron, which is shown in Equation 13. [34]

Equation 12. $${}^{241}_{95}Am \rightarrow {}^{237}_{93}Np + {}^{4}_{2}He$$

Equation 13. $${}^{9}Be + {}^{4}He \rightarrow {}^{12}C + n$$

Americium is an element with no stable isotopes. Successive neutron capture in plutonium-239 produces plutonium-241, which has a half-life of 14.4 years. The decay of plutonium-241 produces americium-241. Americium-241 has a half-life of 432.7 years and decays through the emission of alpha particles with an average energy of 5.465 MeV. The alpha particles are accompanied by gamma rays with energies between 26.3-158.5 keV. The most prominent one is 59.5 keV, which occurs in about 80% of the decays. When beryllium captures an alpha particle, it emits a neutron ranging in energy from 0-11 MeV. The average neutron energy is 6 MeV. Roughly one neutron is produced for every 20,000 alpha decays in an americium-beryllium radiation source. [36]

Neutron Interactions with Indium

Two stable natural isotopes of indium exist, ^{113}In (4.29%) and ^{115}In (95.71%). Equation 14 and Equation 15 show the nuclear reactions that occur when a neutron is absorbed by the indium isotopes. [37]

Equation 14. $^{113}In + n \rightarrow {}^{114}In$

Equation 15. $^{115}In + n \rightarrow {}^{116}In$

In the above equations, both of the reaction products, ^{114}In and ^{116}In are unstable. The decay characteristics of ^{114}In and ^{116}In isomers are given in Table III. [37]

Table III. Decay Characteristics of Indium Isotopes [37]

Isotope	Jπ (spin & polarity)	Half-life	Decay mode
^{114}In	1+	71.9 seconds	β- (99.5%) ε (0.5%)
^{114m}In	5+	49.51 days	IT (96.75%) E (3.25%)
^{116}In	1+	14.10 seconds	β- (99.98%) ε (0.02%)
^{116m1}In	5+	54.29 minutes	β- (100%)
^{116m2}In	8-	2.18 seconds	IT (100%)

The decay mode abbreviations used in Table III, *β*-, *ε*, and *IT*, refer to β- decay, electron capture, and isomeric transitions (typically accompanied by γ-ray emission), respectively. Equation 16

shows the nuclear reaction that occurs during β- decay. A neutron within the nucleus of an atom is converted to a proton, resulting in transmutation of the original element into the element with the next highest atomic number. An electron and electron anti-neutrino are emitted during the process. [37]

Equation 16. $n \rightarrow p + e^{-} + \bar{\nu}_e$

The nuclear reaction involving electron capture is shown in Equation 17. An electron from the atom is captured by the nucleus and combines with a proton to form a neutron. The reaction results in the transmutation of the atom into the element with the next lowest atomic number. An electron neutrino is emitted during the process. Isomeric transition involves an excited nucleus releasing one or more γ-rays in order to return to a lower energy or ground state. [37]

Equation 17. $p + e^{-} \rightarrow n + \nu_e$

Monte Carlo N-Particle (MCNP) Transport Code

Monte Carlo methods simulate the behavior of individual particles to infer the average behavior of particles in a physical system. Particle interactions are determined by randomly selecting numbers between 0 and 1 based on rules of physics and particle transport data in order to determine the type and location of interactions. Continuous- energy nuclear data obtained from the Evaluated Nuclear Data File (ENDF), Evaluated Nuclear Data Library (ENDL), and the Activation Library (ACTL) is used for modeling particle transport in MCNP. Neutron energies ranging from 10^{-11} - 20 MeV can be modeled with MCNP. An input file within MCNP consists of the title card, cells cards, surface cards, and data cards. Within MCNP, a "card" is a single line of input that can contain up to 80 characters. The cell and surface cards define the geometry of the materials, density of the material, and composition of the material. The data cards determine the particle types to be modeled, parameters of the particle source, data to be gathered from the modeling, isotopic and cross-sectional parameters of materials, and when the modeling should be terminated. [38]

Synthesis and Properties of Interpenetrating Phase Composites

Typical composite materials consist of multiple inclusions of a discrete phase embedded in an interconnected matrix phase. An interpenetrating phase composite (IPC) consists of interconnected phases forming a three-dimensional network throughout the material. [39-41] Materials with interpenetrating phase microstructure are common in biological structures such as bones and plant limbs. [41]

Interpenetrating phase composites can be beneficial in applications where multi-functional characteristics are desired, such as high mechanical strength and electrical conductivity. The influence of phase connectivity and volume fraction on transport properties in IPCs is a topic of interest for investigation. [42, 43] A study by *Wegner and Gibson* [39] showed that IPC microstructure could improve yield, thermal expansion, and elastic properties through a finite element analysis, when compared to composites incorporating discrete inclusions. It was observed that a maximal contribution of desired mechanical properties is achieved for each phase within an IPC microstructure.

Incorporating a ceramic phase within a metal can result in increased strength, hardness, resistance to wear, and stiffness, while reducing the thermal expansion coefficient. Melt infiltration is one method utilized to infiltrate a preform and create an interpenetrating phase composite. Most metal melts will not wet ceramics, requiring the use of external pressure to fill the pore space. [40] In addition, the elevated temperatures required for melt infiltration can allow the melt to penetrate grain boundaries of the preform, resulting in an interruption in the connectivity of the preform. [41] Chemical reaction synthesis is another method to create an IPC. [42] Experimental and theoretical studies have shown than an increase in reinforcement phase continuity will increase the elastic modulus of the composite. [40]

Some experiments have indicated that IPCs exhibit resistance to grain growth. A possible mechanism for this observation is that interconnected phases can potentially have shapes with a surface curvature of zero, which would give a minimal surface energy. [41] Utilizing a three-

dimensional continuous reinforcing ceramic phase in a metal matrix can increase the strength of the composite by increasing the density of dislocations and reducing the grain size. [43] Densification of a semi-porous matrix around a dense preform can create stresses induced by constrained densification, which can result in multiple local densification rates. [41] Metal matrix interpenetrating phase composites (MMIPCs) have a potential to increase thermal stability, high-temperature properties, and wear resistance over that of conventional composites. MMIPCs also have increased potential for recycling the component materials over conventional composites. MMIPCs have isotropic properties, whereas conventional reinforced composites do not. [43]

The three-dimensional reinforcement within an IPC provides resistance to crack propagation in all directions. Furthermore, if the matrix phase has a larger strain to failure than the reinforcement, the reinforcement will bridge the matrix crack, increasing the energy required for crack propagation. The area fraction of the bridging phase intercepting the crack, and the work required to fracture the bridging phase determine the energy required to propagate the crack. The phases within an IPC can constrain one another, allowing residual stresses in one phase to put the other phase in compression. Fracture toughness can be increased in brittle composites by creating a weak interface between the phases. An interface that is less than ~1/4 of the strength of the reinforcing phase can allow crack deflection along the interface, increasing the energy required to propagate the crack. [41]

Functionally graded materials can be produced by infiltrating open-cell foams with another phase. [18] In a study by *Peng et al.*, [42] an open pore alumina foam was infiltrated with a molten aluminum alloy. The alumina foam had a relative density of 5.9% and a predicted volume porosity of 95.2%. Pressure was applied during the process in order to force the aluminum alloy into the pore space of the alumina. A pressure of 65 MPa was maintained until the infiltrated metal solidified. Melt infiltration can result in the creation of defects in the foam structure and interfacial debonding due to stresses generated during the solidification process. [42] In order to mediate these issues, pressure was maintained on the specimen during the solidification of aluminum, utilizing cooling rates as low as 0.017° C/s for the temperature range between the solidus and liquidus of the aluminum alloy.

The degree of reticulation affects the permeability of a foam to melt infiltration. It also affects the connectivity of the matrix, which influences transport properties. Lastly, the degree of reticulation affects the amount of residual stress generated from differential thermal contraction during cooling. [42]

A study performed by *Zhou et al*., [43] utilized a self-propagating high-temperature synthesis (SHS) reaction to produce a porous Al_2O_3-TiC ceramic reinforcement. The interconnected open porosity was ~83% of the bulk material volume. The porous ceramics were infiltrated with aluminum and 2024 aluminum alloy. Network dislocations were observed within the composite due to CTE mismatch and a fast cooling rate. Al_2O_3-TiC infiltrated with the 2024 alloy exhibited brittle fracture, due to the low ductility of the 2024 Al alloy. Cracks that formed in the composite made from pure aluminum infiltration showed evidence of plastic deformation in front of crack tips. The aluminum deformation allowed crack bridging during fracture, resulting in an increase in fracture toughness. It was found that pure aluminum bonds well to Al_2O_3-TiC; debonding at the interface did not occur after plastic deformation. The strength of the bonding along the matrix-reinforcement interface plays a large role in determining the composite fracture behavior. An advantage of IPCs is that they can transfer stress over a much larger area of the reinforcement around the fracture surface than conventional particle and fiber composites.

A study by *Cree and Pugh* [44] investigated vacuum melt infiltration of a SiC open cell foam with an aluminum alloy, creating an IPC. The foams were produced by Ultramet® and had a pore density of 100 ppi. After processing, the lowest porosity obtained for the composite was 7%. Mechanical and thermal properties for a 12% volume fraction SiC foam-Al composite were similar to those obtained from a 50-70% SiC particulate-Al composite, indicating that continuous reinforcement was more beneficial than particle reinforcement.

Fabrication and Properties of Tungsten and Tungsten Composites

The atomic number of tungsten is 74. Tungsten has a melting point of 3422° C, an atomic weight of 186.2, and a vapor pressure of ~ $4 \cdot 10^{-12}$ Torr at 2000 K. [3, 45] Tungsten has a mechanical strength at room temperature of ~800 MPa, as well as a high elastic modulus. The

thermal expansion coefficient for tungsten at 1500° C is $7.4 \cdot 10^{-6}$ K^{-1}. [3, 46] The melting point of tungsten is not increased by forming borides or carbides. [47] Tungsten exhibits poor ductility at room temperature and reduced strength at high temperatures. [3, 46] At 2100° C the strength of tungsten is 50 MPa. [3] In prior studies, ceramic particles were added to tungsten in order to increase high-temperature strength. [3, 46]

Two challenges with utilizing tungsten are that it is brittle and is difficult to fabricate. [45] The brittle nature of tungsten at ambient temperatures is largely caused by rigid covalent interatomic bonds at the edges of the BCC lattice, which provide a low solubility for interstitial elements. Impurities accumulate at grain boundaries in the form of oxide or carbide films, and act as stress concentrators that weaken grain boundaries and cause intergranular fracture. [48, 49] Single crystal tungsten has been shown to exhibit ductility below ambient temperatures. Zone purification has also been shown to decrease the ductile-brittle transition temperature (DBTT) of tungsten. Another theory on the high DBTT of tungsten is that low dislocation mobility allows crack propagation by inhibiting the blunting of crack tips. [49]

Blaschko et al., [50] sintered pressed compacts of tungsten powders with average particle sizes of 4.05 μm, 2.15 μm, and 0.77 μm. A 0.77 μm powder compact sintered at 1500° C achieved an equivalent density to that observed in the 4.05 μm powder compact sintered at 2400° C. Table IV and Table V show density evolution with respect to temperature and time, respectively, for various particle sizes of tungsten powder. Densities of sintered tungsten in Table IV are with respect to a constant sintering time, whereas densities in Table V are with respect to a constant sintering temperature. The data points were approximated from graphs in the study by *Blaschko et al.* Neutron small angle scattering was utilized to measure the total porosity surface of the sintered compacts. Results from the study indicated that a larger porosity surface has a larger surface energy, inducing a larger driving force to reach equilibrium. Smaller pore sizes are indicated by a larger porosity surface, resulting in more paths for surface diffusion, particularly when open porosity is present. Utilizing a smaller particle size of powder will result in a higher density of grain boundaries, increasing the rate of grain boundary diffusion.

Table IV. Approximate Density of Sintered Tungsten with Respect to Sintering Temperature and Tungsten Particle Size [50]

Particle Size (μm)	Sintering Temperature and Density			
	1200° C	1800° C	1950° C	2400° C
0.77	12.0 g/cm^3	17.5 g/cm^3	17.5 g/cm^3	17.5 g/cm^3
2.15	12.0 g/cm^3	17.0 g/cm^3	18.0 g/cm^3	19.0 g/cm^3
4.05	12.0 g/cm^3	14.5 g/cm^3	15.5 g/cm^3	17.5 g/cm^3

Table V. Approximate Density of Sintered Tungsten with Respect to Sintering Time and Tungsten Particle Size[50]

Particle Size (μm)	Sintering Time (at 2100° C) and Density			
	10 minutes	60 minutes	180 minutes	1080 minutes
0.77	17.5 g/cm^3	17.5 g/cm^3	17.25 g/cm^3	17.5 g/cm^3
2.15	18.25 g/cm^3	18.5 g/cm^3	18.75 g/cm^3	19.0 g/cm^3
4.05	16.0 g/cm^3	16.5 g/cm^3	17.5 g/cm^3	18.0 g/cm^3

Transition metals can be added to tungsten for activated sintering, reducing sintering temperatures to 1200-1500° C. However, using sintering aids can alter the material properties of the sintered tungsten, such as lowering the melting point. Decreasing the particle size of tungsten has been found to reduce the sintering temperature. Tungsten powder with particle sizes ranging from 400 nm to 800 nm was sintered at 1700° C to theoretical densities of over 90%. [51] Another study by *Wang et al*. utilized 500 nm and 50 nm tungsten powders. The powders were uniaxially pressed at 240 MPa, and sintered in a hydrogen atmosphere at 1400° C. The pressed compacts were heated to their final temperature at a rate of 10° C/min, and held at their final temperature for 0, 30, and 60 minutes. A relative density of 91% was achieved in the sintered 50 nm tungsten powder held at 1400° C for 60 minutes, while a relative density of 89% was achieved in the sintered 500 nm powder at the same temperature and holding time.

Research by *Kitsunai et al.*, [52] has shown that fine TiC particles dispersed in tungsten alloys can increase the impact toughness at low temperatures. The tungsten powder that was utilized had a 99.9% purity and an average particle size of 3.6 μm. The TiC powder was 98% pure and had an average particle size of 0.57 μm. In order to achieve the increase in toughness it is important to have high relative densities in the product. Two performance issues with tungsten are that its DBTT is near room temperature, and the DBTT can be significantly increased by neutron irradiation and recrystallization. The study by *Kitsunai et al*., utilized mixtures of tungsten with 0.2-0.5 wt.% TiC. The mixtures were mechanically alloyed by ball milling in an argon atmosphere. Hot isostatic pressing (HIPing) was utilized to densify the W-TiC mixture in an argon environment at 200 MPa for 18 ks. Samples were synthesized at 1623 K and 2223 K. The as-HIPed samples were 97.5% of the theoretical density.

Powder Compaction

Particle size and shape are two important factors that determine packing density. As particle roughness increases, interparticle friction increases and fractional packing density decreases. Spherical shaped powders exhibit the highest fractional packing density. Altering the particle size distribution by incorporating particles small enough to fill voids between large particles can further increase the packing density. [53]

Three major factors that determine interparticle friction are the surface roughness, surface area, and surface chemistry of the particles. Larger surface areas have higher friction, resulting in decreased particle flow and less efficient packing. The apparent density of a powder is a measure of the density of a powder in an undisturbed state. The tap density is the highest powder density that can be achieved through vibrating a powder without applying external pressure. The apparent density of a coarse spherical particle is typically around 60% of the theoretical density. The tap density is typically around 64% of the theoretical density. [53]

Segregation occurs in powders if small particles are able to pass through voids between large particles. Particle size segregation can cause a decrease in apparent density and cause a density gradient within the powder. Exposing a dry powder to vibration can result in particle size

segregation. As the ratio of the height to the diameter of a compact increases, density gradients increase and the overall density decreases. Small particle sizes are more difficult to press than larger particles due to the higher pressures required to collapse small pores than large pores. In addition, larger particle sizes have larger dislocation slip distances resulting in a decrease in particle work hardening. [53]

Two packing states for spherical particles are random close packing, having a density ~0.64, and random loose packing, having a density less than or equal to 0.60. Research has indicated that packing density is dependent on the vibration amplitude. However, other factors are also involved that determine packing density. Research has shown that compaction from vibration has a non-linear time dependence; the rate of compaction slows down as compaction increases and time increased. During vibration, competition between void eliminating and void creating processes occurs. An optimum intensity of vibration appears to exist, which allows quick granular compaction, minimizing the extent of void creation that occurs. As intensity of vibration is increased above the optimum level, lower densities are observed in the granular media. [54]

Research by *Nowak et al.*, [54] investigated densification of spherical glass beads, which are a cohesionless granular material, with diameters of 1, 2, and 3 mm. Uniaxial vibration with a frequency of 30 Hz was utilized. Starting densities were ~0.58. After vibration densities as high as ~0.64 were achieved. It was observed that the highest densities were obtained by increasing the magnitude of acceleration, followed by decreasing it slowly to a much smaller value. The critical value of acceleration must be sufficient to eliminate low density particle arrangements that have meta-stability. It was observed that the critical acceleration value for the ratio of vibrational acceleration to gravitational acceleration was three for 10^5 total vibrations.

Contact forces between particles depend on friction, gravitation, and the external force applied, if any. As the degree of particle irregularity increases, the difference between pre-vibration density and post-vibration density increases, assuming an optimum vibration intensity. [55]

Sintering

Sintering is the process of binding particles together at high temperatures. Sintering can occur through solid-state mass transport below the melting point of the material. Liquid phases can also be incorporated in the process. Particle bonding occurs through the formation of necks between particles. During the initial stage of sintering, interparticle necks grow rapidly, and the pore structure is open. The pore structure becomes more cylindrical in geometry during the intermediate stage of sintering. Grain growth typically occurs during the latter part of the intermediate stage of sintering. The sintering rate slows and closed porosity increases. Open porosity tends to become unstable when the compact has reached ~92% theoretical density. The cylindrical pores transform to spherical pores and become isolated. Any gas that is trapped within pores inhibits complete consolidation. Therefore, to achieve complete densification, vacuum sintering is required. [53]

A sintering rate diagram for pure tungsten in a study by *Ashby* [56] indicates that for a 2 μm pure tungsten powder at a temperature of 2500° C, full density is achieved after 10^2 minutes. Whereas at a temperature of 1900° C, full density is not achieved until 10^4 minutes.

The atomic motion that facilitates the sintering process occurs in order to decrease the high surface energy of the powder. The rate of sintering increases at higher temperatures due to the dependence on the diffusion of atoms. Diffusion of atoms is thermally activated, and follows an Arrhenius relationship. [53] The influence of temperature on the diffusion coefficient can be calculated with Equation 18, where D is the diffusion rate, D_0 is the temperature-independent diffusion coefficient, Q is the activation energy for diffusion, R is the gas constant, and T is the temperature. [24]

Equation 18. $$D = D_0 e^{\left(\frac{-Q}{RT}\right)}$$

The relationship between particle size and sintering temperature is given by Equation 19. [51]

Equation 19: $$n \ln\left(\frac{d_1}{d_2}\right) = \left(\frac{1}{T_2} - \frac{1}{T_1}\right) \cdot \frac{Q}{R}$$

In the above equation, the particle sizes are given by d_1 and d_2, and the sintering temperatures by T_1 and T_2. The variable Q is the activation energy, and R is the gas constant. The mechanism of diffusion determines the constant n. For grain boundary diffusion, n is equal to 1/3; and for volume diffusion, n is equal to 1/2. The dominant densification mechanism in the sintering of tungsten powder is grain boundary diffusion. [51] The temperature-independent diffusion coefficients for surface and grain boundary diffusion in tungsten are 8.5 cm^2/s and 10 cm^2/s, respectively. The activation energies for surface and grain boundary diffusion in tungsten are 78 kcal/mol and 90.5 kcal/mol, respectively. [56] Other factors held constant, the degree of densification achieved sintering particles of size d_1 at temperature T_1 will be equal to the densification achieved sintering particles of size d_2 at temperature T_2.

The driving force for sintering is a decrease in particle surface energy. Sintering that occurs through surface transport causes neck growth by mass migration from the surface through evaporation-condensation, volume diffusion, and surface diffusion. Sintering through bulk transport induces neck growth from internal sources through grain boundary diffusion, volume diffusion, and plastic flow. Shrinkage in the sintered product occurs due to bulk transport processes. [53]

TaC and TaC Composite Fabrication and Properties

Tantalum carbide has a melting point of ~3880° C. TaC is resistant to chemical attack and oxidation, and has a high hardness. In addition, TaC has good thermal and electrical conductivity. Large deficiencies of carbon can be accommodated in the tantalum carbide lattice without changing the NaCl type structure. [4, 57] Literature values for Young's modulus of TaC range from 285-560 GPa. [58]

High strength and ductility has been observed in TaC above the DBTT at 1750° C. At a temperature of 2160° C the ultimate tensile strength of TaC was found to be 98 MPa and the specimen exhibited an elongation of 33%. TaC does not exhibit significant high-temperature creep resistance. It is believed that grain boundary sliding and dislocation glide are primary factors in the lack of high-temperature creep resistance. Performance objectives for creating a

TaC composite should involve decreasing the density, increasing creep resistance, and attaining a higher toughness at low temperatures. [59]

A study by *Santoro* [60] investigated properties of TaC filaments produced by carburizing filaments of high-purity tantalum in hydrocarbon gas. The filaments had a diameter of approximately 254 microns. The filaments had lengths of 20 or 40 cm. The modulus of rupture for a $TaC_{0.91}$ composition was found to be approximately 951 MPa. Although no $TaC_{1.0}$ compositions were tested, the trend of the curve from other compositions indicated that the $TaC_{1.0}$ composition would have a larger modulus of rupture than the $TaC_{0.91}$ composition. The bend deflection of the $TaC_{0.91}$ composition was 39.4 microns. A minimum in the modulus of rupture and bend deflection was observed near $TaC_{0.80}$. A change in color from grey to gold was observed to occur between tantalum carbide compositions $TaC_{0.80}$ and $TaC_{0.85}$. [60]

Honeycutt III et al., [61] performed research on tantalum carbide matrix composites with tungsten-rhenium fibers for use in solid propellant rocket motor nozzles. Mechanical erosion of nozzles becomes an issue when alumina powder is added to solid propellant fuels. Hot pressing was used to fabricate the composites at 2150° C with an applied pressure of 3000 psi. The composites were held at those conditions for 10 minutes. Fabrication was conducted in a vacuum of less than 30 μm. TaC matrix composites were found to resist high temperature erosion better than hafnia-tungsten or graphite composites.

Impulse Excitation

Impulse excitation is a non-destructive method to evaluate the moduli of a homogeneous and isotropic material. The resonant frequencies of a material are determined by the geometry, mass, and elastic modulus of the material. A resonant frequency is a natural vibrational frequency that occurs when the body is set into flexural, longitudinal, or torsional vibration. [62, 63]

Equation 20 describes the relationship between material properties, specimen dimensions, and natural resonant frequencies. In Equation 20, the resonant frequency is given by f_1, k_1 is the term describing the geometry for the given resonant frequency, r is the radius of the round, A is the plate constant, ρ is the density of the round, and t is the thickness of the round. [62, 63]

Equation 20. $$f_1 = \frac{k_1}{2\pi r^2}\sqrt{\frac{A}{\rho t}}$$

The plate constant A in Equation 20 is calculated by using Equation 21, where E is the Young's modulus and μ is the Poisson's ratio of the round. [62, 63]

Equation 21. $$A = \frac{Et^3}{12\left(1-\mu^2\right)}$$

The Young's modulus of a round is calculated from the measurements of the resonant frequencies of the round in flexural and anti-flexural vibration modes according to Equation 22. [62, 63]

Equation 22. $$E_x = \frac{37.6991\left(f_x^2 D^2 m\left(1-\mu^2\right)\right)}{k_x^2 t^3}$$

In Equation 22, E is the Young's modulus, the sub-script x denotes either the 1st or 2nd resonant frequency, D is the diameter of the round, m is the mass of the round, μ is the Poisson's ratio of the round, k is the term describing the geometry, and t is the thickness of the round. The average of the Young's moduli calculated from the 1st and 2nd resonant frequencies is used to determine the Young's modulus of the round. The shear modulus can be calculated from the Young's modulus and Poisson's ratio using Equation 23, where G is the shear modulus. [62, 63]

Equation 23. $$G = \frac{E}{2\left(1+\mu\right)}$$

Statistical Methods Using a T-test

An independent sample t-test can be used to compare the means of two datasets that are not dependent on each other. A t-test is used to determine if there is a statistical difference between two datasets. The equation used to calculate the t-value is shown in Equation 24. [64]

Equation 24: $$t = \frac{\bar{Y}_1 - \bar{Y}_2}{\sigma_{diff}}$$

In Equation 24, Y_1 and Y_2 are the means of two datasets and σ_{diff} is the standard error of the difference between two means. The value σ_{diff} is calculated using Equation 25:

Equation 25: $$\sigma_{diff} = \sqrt{\left(\frac{S_1^2}{n_1}\right) + \left(\frac{S_2^2}{n_2}\right)}$$

In Equation 25, S_1^2 and S_2^2 are the variances of the two datasets, and n_1 and n_2 are the number of samples in the respective dataset. The value of t is compared with a statistical table that lists values for confidence, known as α, and values for the degrees of freedom. Confidence values determine the degree of statistical certainty that a difference exists between the values of the dataset means. The total number of degrees of freedom is determined by subtracting two from the total number of samples in the two datasets. [64]

III. Experimental Approach

This section describes the experimental approach used to accomplish the objectives of this study, which included: Understanding the influence of strut/pore size, foam composition, and foam density on the neutron transmission in TaC foams, understanding the influence of strut/pore size, foam composition, foam density, thermal fatigue, and thermal shock on mechanical behavior of TaC foams, and understanding the influence of foam pore size and tungsten particle size/surface area on vibration-induced tungsten particle infiltration and densification within RVC foams, with the goal of forming an interpenetrating phase composite. A summary of the experiment matrix for this study is shown in Table VI. More detailed experiment matrices are presented in subsequent sections.

Table VI. Summary of Experiment Matrix

	Foam PPI		
Foam Type	**45**	**65**	**100**
TaC/RVC	Neutron Transmission (experiments and modeling) Mechanical Testing Thermal Treatments	Neutron Transmission (experiments and modeling) Mechanical Testing Thermal Treatments	Neutron Transmission (experiments and modeling) Mechanical Testing Thermal Treatments
TaC/PyC/RVC	Neutron Transmission (experiments and modeling) Mechanical Testing Thermal Treatments	Neutron Transmission (experiments and modeling) Mechanical Testing Thermal Treatments	Neutron Transmission (experiments and modeling) Mechanical Testing Thermal Treatments
RVC	Infiltrate with sub-micron tungsten then sinter	Infiltrate with sub-micron tungsten then sinter	Infiltrate with sub-micron tungsten then sinter
	Infiltrate with 5-10 micron tungsten then sinter	Infiltrate with 5-10 micron tungsten then sinter	Infiltrate with 5-10 micron tungsten then sinter

Two different TaC foam compositions were investigated in this study. One foam composition had a vitreous carbon core, followed by a layer of tantalum carbide formed using chemical vapor infiltration (CVI). The other foam composition had a layer of pyrolytic carbon deposited using CVI between the vitreous carbon and tantalum carbide layers. TaC was chosen for a number of reasons. The extremely high melting point of TaC facilitates its use as a high temperature coating, just like SiC in TRISO nuclear fuel particles. TaC could also be incorporated into a tri-carbide nuclear fuel. Lastly, TaC has been used in prior studies as a uranium carbide surrogate material. The pyrolytic carbon was expected to increase the strength of the foams, in part due to the presence of an additional interface within the foam strut, which would increase the energy required for crack propagation through the strut. In addition, PyC has been utilized in TRISO fuel particles to retain fission products.

A typical reaction for CVI deposition of TaC is shown in Equation 26. [2]

Equation 26. $TaCl_5 + CH_4 \rightarrow TaC + 4HCl + 1/2Cl_2$

Three open-pore TaC foam pore densities were utilized: 45, 65, and 100 pores per inch (ppi). The pore densities were chosen to allow investigation of a wide range of strut and pore sizes within this study. The TaC foam was produced by Ultramet®, a commercial supplier. The foam was fabricated into rounds, each having a 1.37" O.D (-0.05", +0.00") and a 0.25" thickness (+/- 0.025"). The macroscopic structure of a 45 ppi TaC/PyC/RVC foam is shown in Figure 1. Tantalum carbide foam manufacturing specifications provided by Ultramet® are located in Appendix A.

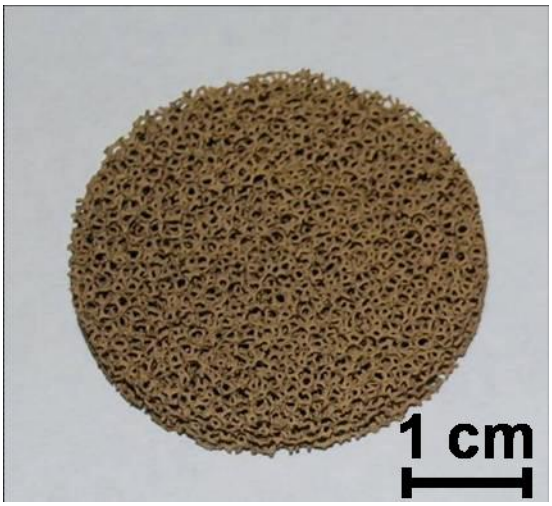

Figure 1. Image of 45 ppi TaC/PyC/RVC foam round.

Influence of Strut/Pore Size, Foam Composition, and Foam Density on the Neutronic Properties of the Foam

In this sub-section the experimental approach to understand the influence of strut/pore size, foam composition, and foam density on the neutronic properties of TaC foam is discussed. Methodology used in the volumetric and microstructural analysis of the TaC foams is described. The approach used for modeling neutron transport and experimentally measuring neutron transmission is also described.

Microstructural Analysis and Pore/Strut Size Measurements

The foam structure, strut thickness, and pore size of the foams were analyzed with a Zeiss Stemi 2000-C stereo microscope. A Canon PowerShot G10 digital camera was connected to the microscope to obtain digital images of the microstructure. After image acquisition, the images were transferred to a computer and Zeiss Axiovision v4.6 software was utilized to measure strut thickness and pore sizes of the foams. Five images were obtained from various areas of each foam specimen in order to achieve a representative sampling. Five measurements of strut thickness and pore size were made from each image, resulting in a total of 25 measurements for strut thickness and pore size for each specimen. The average and standard deviation of strut thickness and pore size were calculated for each type of foam.

Foam microstructure, morphology, and strut cross-sections were investigated using scanning electron microscopy. A Hitachi 3700SN SEM and a LEO 1550 SEM were used to perform the analyses. Image analysis software was used to determine the average thickness of the carbon and TaC layers.

Volumetric Measurement of Foams

Volumetric measurements of the foams were performed with a Quantachrome Ultrapycnometer 1000. Nitrogen gas was utilized for the analysis. The specimen chamber was pressurized to 19 psi and the sample was flow purged with nitrogen for a period of one minute prior to the start of each volume measurement. A total of 12 measurements were obtained for each piece of foam. The average and standard deviation of the last three measurements were calculated.

Neutron Transmission Measurements

Indium decay was used as a proxy measurement of neutron transmission. Indium was chosen since it undergoes beta-decay after absorption of a neutron. A Geiger-Müller probe was used to count the number of electrons emitted during the decay of a piece of indium foil. The number of electrons counted was indicative of the number of indium atoms that underwent transmutation due to absorption of a neutron. Therefore, the number of counts was proportional to the number of neutrons that passed through the foam and activated the foil. A series of five, 90 second measurements were performed to determine GM tube activation by background ionizing radiation prior to each indium foil measurement. The average and standard deviation were calculated from the background measurements, and were subtracted from each decay measurement of the indium foil.

In order to determine the neutron transmission characteristics of the tantalum carbide foam, a piece of indium foil was placed on the back of the tantalum carbide foams, and the foam/indium foil was taped to a polyethylene cylinder that surrounded an americium-beryllium neutron source. The americium-beryllium neutron source and polyethylene cylinder are shown in Figure 2.

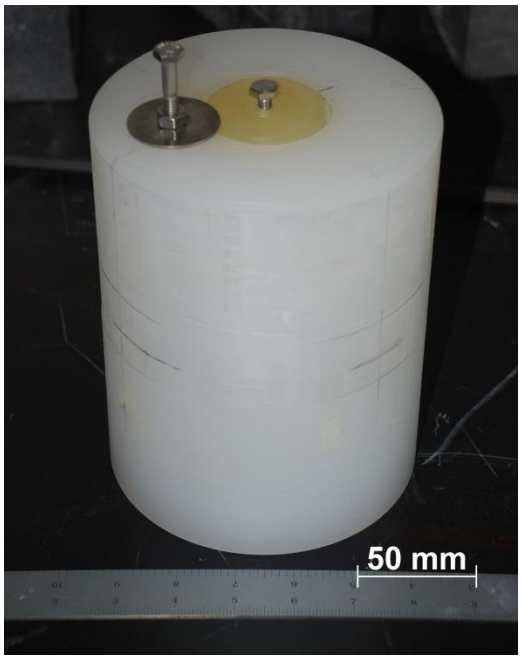

Figure 2. Image of americium-beryllium neutron source located at the center of a polyethylene neutron moderating cylinder.

The outer radius of the polyethylene cylinder was located 7.290 cm from the centerline of the neutron source. The indium foil had a 26.78 mm diameter and a 0.55 mm thickness. The volume of the foil was 0.310 cm^3 and the mass was 2.077 g. Three sets of measurements for indium foil decay were obtained from each foam round selected for neutron transmission measurements. Multiple baseline measurements were collected periodically between the neutron transmission measurements through the foams. The baseline measurements incorporated an air gap equivalent to the thickness of a foam round between the neutron source and the indium. The average and standard deviation were calculated for the baseline neutron measurements, and for each of the foam rounds. GM tube activation measurements were begun two minutes after removing the indium foil from the neutron source in order to allow time to transport the indium foil from the neutron source to the GM counter. A total of 26 measurements were performed after removal of the indium foil from the neutron source. Each measurement lasted for a period of 90 seconds and was followed by a 90 second pause prior to the start of the next measurement. Therefore, activation measurements were performed for 78.5 minutes, which is approximately 1.5 beta-decay half-lives of indium, after removal of the indium foil from the neutron source. The average background activation of the GM tube was subtracted from each of the 26 measurement averages. Each of the 26 measurements was averaged with the measurements from equivalent

time periods from the other runs for the given foam. Each value obtained was then divided by the average baseline measurement for each equivalent measurement time period, resulting in 26 ratios of neutron transmission through foam relative to baseline neutron transmission. The average and standard deviation were calculated from the 26 measurements

Table VII. Experiment Matrix for Neutron Transmission

Foam Composition	Foam Pore Size		
	45 ppi	65 ppi	100 ppi
TaC/PyC/RVC foam	2 samples- 3 measurements each sample	2 samples- 3 measurements each sample	2 samples- 3 measurements each sample
TaC/RVC foam	2 samples- 3 measurements each sample	2 samples- 3 measurements each sample	2 samples- 3 measurements each sample

In addition to the above specimens, neutron transmission was measured for two TaC foam specimens with substantially higher TaC density than those in the experimental matrix. Neutron transmission was also measured for an RVC foam round with no PyC or TaC coatings.

Modeling Neutron Transport Using MCNP

Neutron transport through the tantalum carbide foam was modeled using version 6.0 of Monte Carlo N-Particle (MCNP) transport code. In order to perform the neutron modeling, the dimensions and locations of the neutron source, polyethylene casing, foam samples, and indium foil were coded into an MCNP input file. Densities and isotopic compositions of the polyethylene, foam, and indium were also coded into the input file. The neutron spectrum of a 1Ci Americium-Beryllium neutron source, shown in Figure 3, was also coded into the file. The input file was coded to obtain tallies of neutron flux at the outer edge of the polyethylene case and at the outer edge of the foam sample. Each MCNP run simulated 10^9 neutrons. A sample input file used for neutron transport modeling with MCNP is shown in Appendix B. Neutron transmission modeling was performed for each foam round that neutron transmission was experimentally measured.

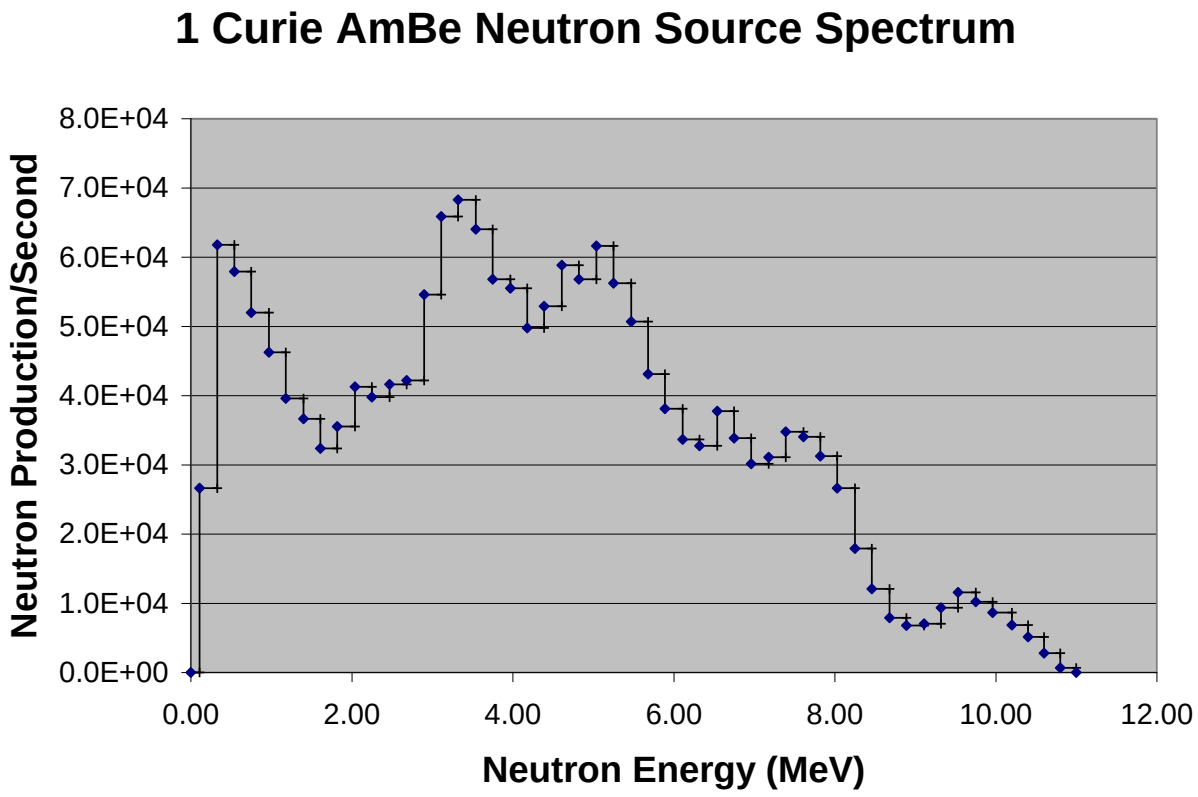

Figure 3. Graph of neutron spectrum and intensity for a 1 Ci americium-beryllium neutron source

Influence of Strut/Pore size, Foam Composition, Foam Density, Thermal Fatigue and Thermal Shock on the Mechanical Properties of the Foam

In this sub-section the experimental approach to understand the influence of strut/pore size, foam composition, foam density, thermal fatigue, and thermal shock on the mechanical properties of TaC foam is discussed. The methodology for predicting the mechanical properties of TaC foams is discussed, as are the experimental procedures used to determine the compressive strength and Young's moduli of the TaC foams. In addition, the procedures used to thermally cycle and thermally shock TaC foams are presented, as is post-thermal treatment analysis of the foams.

Prediction of Mechanical Properties of TaC Foams

Data from prior studies [60, 65, 66] of the mechanical properties of tantalum carbide and pyrolytic carbon were used in conjunction with Equation 8, obtained from *Ashby* [21] in order to calculate a range of expected compressive strengths for TaC/RVC and TaC/PyC/RVC foams.

The RVC foam component was not included in the calculations due to its negligible flexural strength (~690 kPa) [26] when compared with tantalum carbide and pyrolytic carbon.

The average relative densities for the foam specimens used in mechanical testing were calculated using Equation 3 in conjunction with measurements of strut volume, geometric volume, mass, pore size, and strut size. A modulus of rupture of 336 MPa [66] and 951 MPa [60], which were obtained from the literature, were used to calculate the minimum and maximum expected compressive strengths for TaC foams, respectively. The calculations assumed that the foam struts were composed solely of TaC. A modulus of rupture of 241 MPa [65] and 483 MPa [65] were used to calculate the minimum and maximum expected compressive strengths for PyC foams, respectively. This set of calculations assumed that the foam struts were composed solely of PyC. All the calculations used a proportionality constant of 0.2, obtained from modeling predictions by *Ashby* [21]. After the calculations above established a broad range over which the compressive strengths were expected to occur, additional calculations were made utilizing the measured cross-sectional areas for each component within the foam struts as a scaling factor for the above moduli of rupture.

It was expected that as strut thickness decreased in the foam, the strength of the foams would increase. As the strut thickness decreased, the surface area and volume of the strut would also decrease, resulting in a lower probability that pre-existing flaws of a critical size were present, following a Weibull distribution. It was also expected that the pyrolytic carbon layer would increase the strength of the foams due to the addition of interfaces that would increase the energy required for crack propagation to occur.

It was of interest to determine how accurate the composite rule of mixtures would be in predicting the Young's modulus of foam struts. Instead of using a volume fraction, the cross-sectional areas for each component within foam struts were calculated. The upper-bound limit on Young's modulus was calculated using the composite rule of mixtures. Young's modulus values of 24 GPa [31], 28 GPa [31], and 285-560 GPa [58] were used for RVC, PyC, and TaC, respectively. The wide range of values for the Young's modulus of TaC led to two calculations. One calculation was made for the minimum upper-bound limit, and one for the maximum upper-

bound limit of the Young's modulus for each foam strut. Equation 7, obtained from *Ashby* [21], was then used in conjunction with calculated relative densities to predict the minimum upper-bound and maximum upper-bound limit for the Young's modulus of each foam type. A proportionality constant of unity, as suggested by *Ashby* [21], was utilized in the calculations.

Thermo-mechanical Properties of TaC Foams

A total of 12 foam rounds, 6 rounds of TaC/PyC/RVC, and 6 rounds of TaC/RVC were used for mechanical testing. Two rounds from each of the 45, 65, and 100 ppi pore densities were selected. Six specimens were machined from each foam round for mechanical testing. The nominal dimensions of the specimens were 0.50" length, 0.25" width, and 0.25" thickness. After the samples were machined for the compressive testing, the edges of selected specimens were examined by SEM in order to characterize cross-sections of the foam struts.

Mechanical properties of twelve specimens for each foam ppi and composition were evaluated. Four of those specimens were exposed to thermal cycling. Three specimens were thermally shocked in liquid nitrogen. Five specimens were not exposed to thermal cycling or thermal shock.

Eighteen thermal cycles up to a maximum temperature of 2100° C were performed on the specimens selected for thermal cycling in an environment of argon gas (99.998%). Thermal cycling was performed in a Webb RD-G furnace. The thermal cycling temperature was dictated by the maximum temperature achievable in the furnace. The specimens were massed prior to thermal cycle 1, and after thermal cycles 1, 8, and 18. The heating curve for a pair of thermal cycling runs is shown in Figure 4. All thermal cycling runs were conducted in pairs like the ones observed in Figure 4, except for thermal cycle 1 and thermal cycle 8. As observed in Figure 4, the specimens were allowed to cool to 300° C at the end of thermal cycle *A*, prior to heating to 2100° C. After cycle *B*, the specimens were cooled to ambient temperatures.

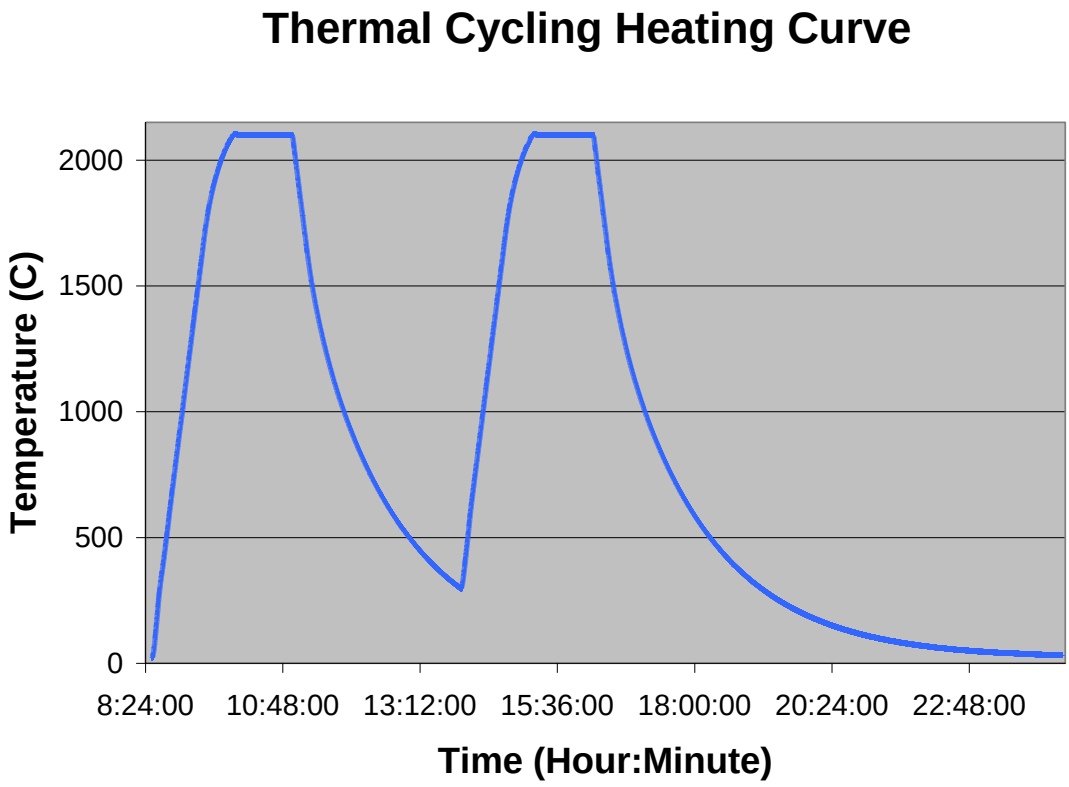

Figure 4. Heating curve for two thermal cycling runs

Specimens exposed to thermal shock were immersed in liquid nitrogen for a period of 30 seconds. The specimens were then removed and allowed to return to ambient conditions. SEM was performed on selected specimens after thermal cycling and thermal shock. Compressive testing was performed at room temperature on specimens exposed to thermal cycling, thermal shock, and baseline specimens. ASTM standard C1424 was used as a reference for conducting the testing. An Instron 4468 test machine with a 1 kN loadcell was used for compressive testing. An Epsilon Technology Corp. Model 3442-0025-005 extensometer was attached to the foam specimen using rubber bands for each test. The extensometer had a gauge length of 6.35 mm and a travel of +/-5%. In order to prevent the extensometer from being crushed during the testing, platen extensions were fabricated. A one inch length piece of steel stock with a 0.3125" x 0.3125" cross-section was attached to the center of a two inch diameter steel round with a 0.5" thickness. Two of these extensions were fabricated and mounted to the upper and lower platens on the test machine. Compressive testing was conducted with a displacement rate of 0.5 mm/min. The Young's modulus was calculated from the stress-strain curve. T-tests were

utilized to determine the statistical significance of variation in compressive strength values for samples of different pore density (ppi), composition, density, thermal cycling, and thermal shock exposure. Equation 24 and Equation 25 were used to conduct the t-tests.

Table VIII. Experiment Matrix for Compressive Strength Tests

Foam Composition	Foam Pore Size		
	45 ppi	65 ppi	100 ppi
TaC/PyC/RVC foam	2 foam rounds - 6 specimens machined from each round: 5 baseline specimens, 4 specimens exposed to thermal cycling, and 3 specimens exposed to thermal shock	2 foam rounds - 6 specimens machined from each round: 5 baseline specimens, 4 specimens exposed to thermal cycling, and 3 specimens exposed to thermal shock	2 foam rounds - 6 specimens machined from each round: 5 baseline specimens, 4 specimens exposed to thermal cycling, and 3 specimens exposed to thermal shock
TaC/RVC foam	2 foam rounds - 6 specimens machined from each round: 5 baseline specimens, 4 specimens exposed to thermal cycling, and 3 specimens exposed to thermal shock	2 foam rounds - 6 specimens machined from each round: 5 baseline specimens, 4 specimens exposed to thermal cycling, and 3 specimens exposed to thermal shock	2 foam rounds - 6 specimens machined from each round: 5 baseline specimens, 4 specimens exposed to thermal cycling, and 3 specimens exposed to thermal shock

Preliminary Research on the Formation of a Tungsten-Ceramic Foam Composite

This sub-section describes experimental methods and results of preliminary research conducted to optimize vibrational process parameters for the infiltration of ceramic foams with tungsten powder, and their subsequent consolidation. Vibrational infiltration parameters, and the infiltrated densities achieved are presented for various pore densities of foams. The process and results of consolidating the infiltrated foams through vacuum sintering are also discussed.

The high melting temperature of tungsten is prohibitive for utilizing melt infiltration for composite formation. Utilizing a powder metallurgical approach for composite synthesis could allow formation of an interpenetrating metal matrix within the pore space of TaC foam. The end

goal is to eventually infiltrate tantalum carbide foam with tungsten. However, to conserve the tantalum carbide foam while processing parameters were being evaluated, scrap pieces of SiC foam were utilized for preliminary experiments. After processing parameters had been refined to a degree, uncoated RVC foam round were used in infiltration experiments.

Mechanical and ultrasonic vibration techniques were used during preliminary experiments to infiltrate the foam with the tungsten powder. A VJ-1212 mechanical vibration platform made by the Cleveland Vibrator Company was utilized to mechanically vibrate the foam. The mechanical and ultrasonic vibration system utilized in this study was designed for sieving powders. The infiltration method used in this study was somewhat similar to sieving powders, with the exception that the sieve screen is not two dimensional with uniform mesh, rather it is a three dimensional foam with a degree of non-uniformity in the pore sizes. The other difference is that the goal was not to achieve particle size segregation. The mechanical vibration platform could be operated in two different modes: Fixed frequency vibration and variable amplitude and frequency vibration. In fixed frequency mode, vibration of the platform occurred at 3600 vibrations per minute. The amplitude of vibration (vertical displacement of platform) could be adjusted using a dial. In the variable amplitude and frequency mode, vibration frequency and amplitude were randomized, though amplitude of vibration was always very low in this randomized setting. An accelerometer was mounted on the platform to measure the mechanical vibration amplitude. The vibration of the mechanical platform was perpendicular to the foam surface.

An HK Technologies Model SLPt 40: 0.50 ultrasonic sieve was utilized during some of the vibrational infiltration experiments, and is shown in Figure 5. Ultrasonic waves were produced at a frequency of 40 kHz within the sieve ring. The ultrasonic vibrator had a variable power output, with the maximum output being 500 W. The ultrasonic ring had a 3.5” outer diameter and a 2.25” inner diameter. The upper 0.375” of the ring has an inner diameter of 3”. Ultrasonic waves can be utilized in a sieving process to reduce surface tension along the sieve mesh in order to both prevent particle blinding within the mesh and to increase the rate of particle movement through the mesh. In this study, much the same results were sought. However, it was expected that particle blinding of large particles within foam pores would only be able to be mitigated to a

certain extent due to the lower degree of translational motion available within the foam pore volume than at the surface of a sieve mesh. An image of the entire vibrational infiltration setup is shown in Figure 5.

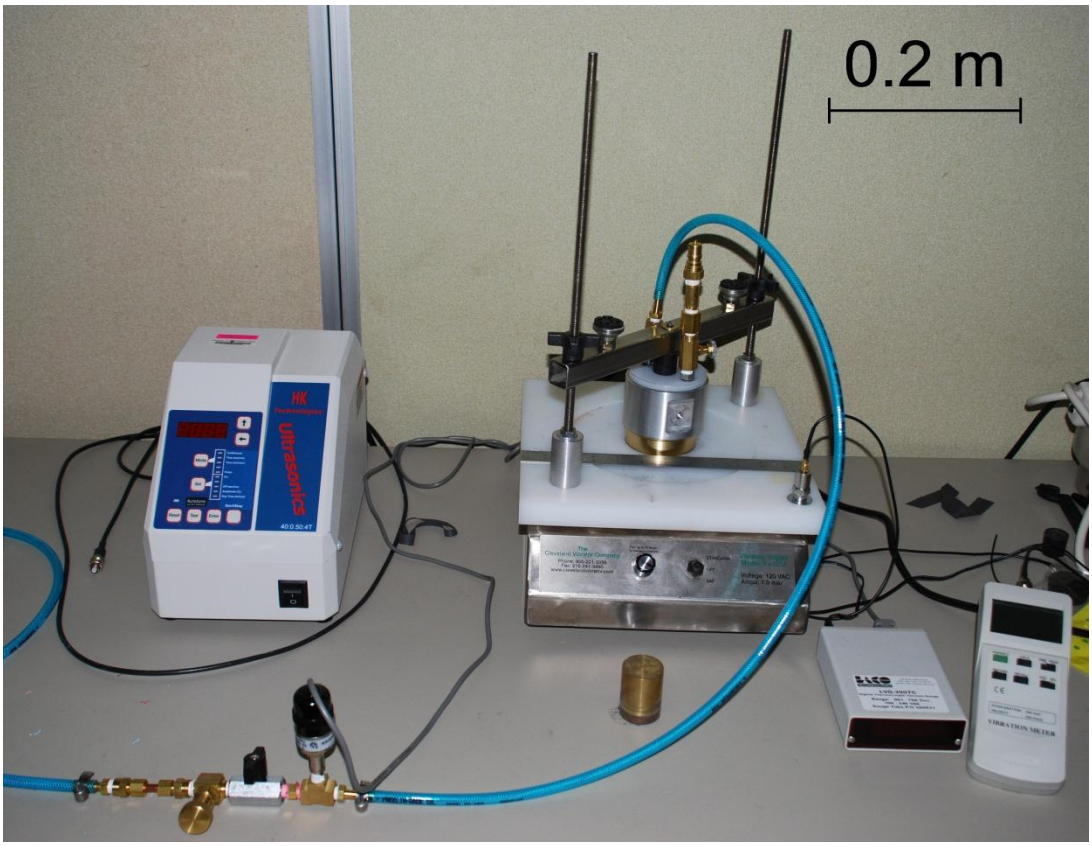

Figure 5. Image of mechanical vibration platform, vibration canister, ultrasonic generator, vacuum lines, and accelerometer.

A foam round was placed within a specially designed non-sparking brass die on the ultrasonic/mechanical vibrator. Sub-micron 99.9% tungsten powder was poured on top of the foam round within the brass die. A diagram of the infiltration setup is shown in Figure 6.

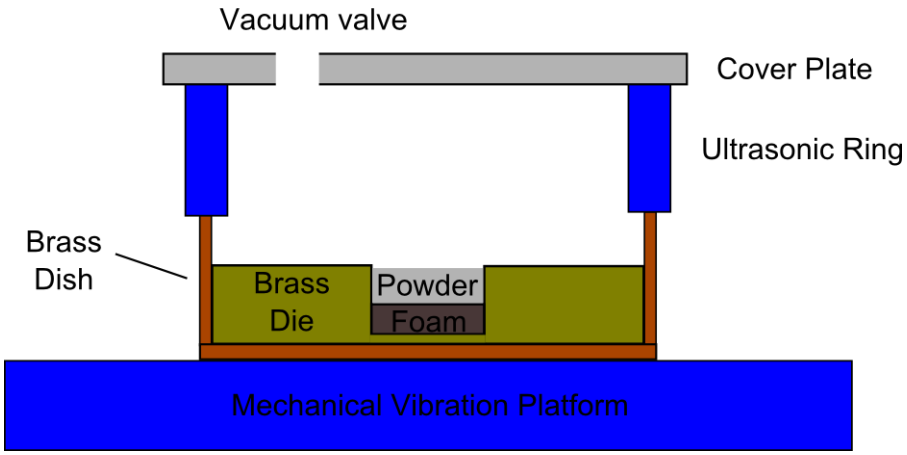

Figure 6. Foam infiltration setup

The brass dish and die had a mass of 80 g and 522 g, respectively, and are shown together in Figure 7.

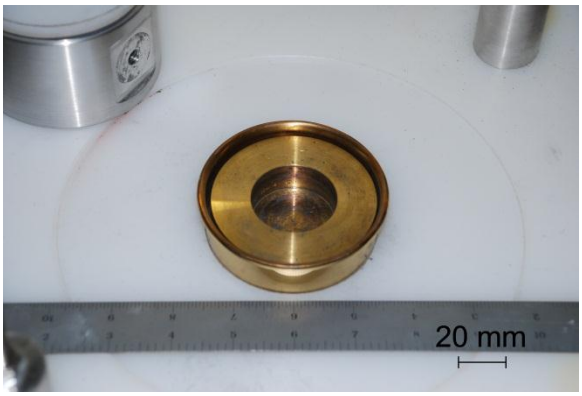

Figure 7. Image of brass dish and die.

The vibration canister, shown in Figure 8 and Figure 9, was purged with argon and mounted to the vibration platform, shown in Figure 10. In order to reduce segregation of the powders by particle size, and provide for a more thorough infiltration, the partially infiltrated foam was turned upside-down and vibrated again with 15 - 20 g of the powder on top of the foam. The procedure was repeated until less than ~0.5 g mass gain was observed for an infiltration run. Some infiltrations were conducted with a brass punch on top of the powder and foam. The brass punch has a mass of 486 g and is shown within the brass die in Figure 11. The brass punch acted as a vibrational hammer to force further infiltration of the powder within the foam. The foam was flipped for the vibration runs utilizing the brass punch as well. Further experimentation led

to the use of vacuum infiltration (evacuating the vibration canister to vacuum) and eliminating the use of argon. Evacuating the canister to a vacuum helped eliminate any influences of adsorbed water on the infiltration process.

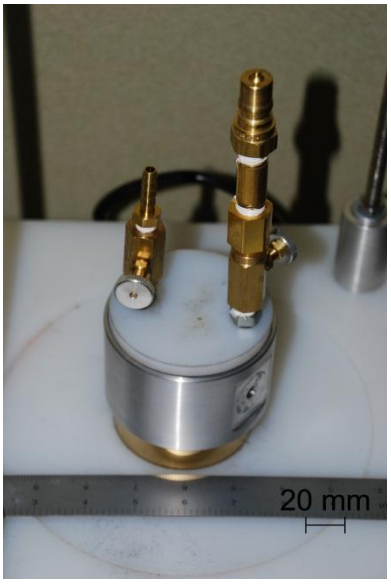

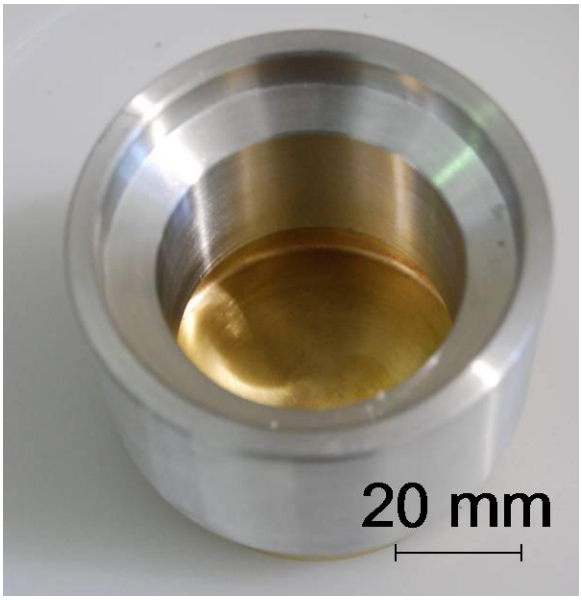

Figure 8.(left) Container for infiltrating foam under argon and vacuum.
Figure 9.(right) Container for infiltrating foam with top removed

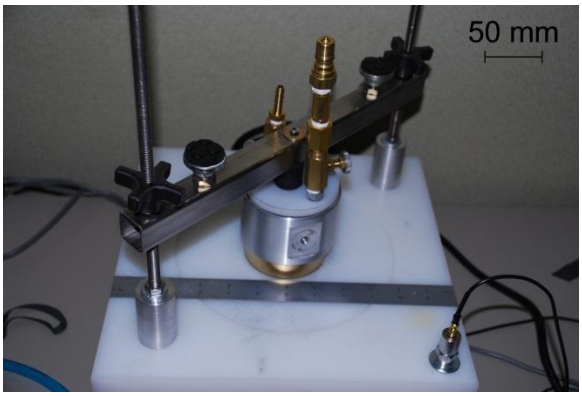

Figure 10. Vibration canister mounted to vibration platform

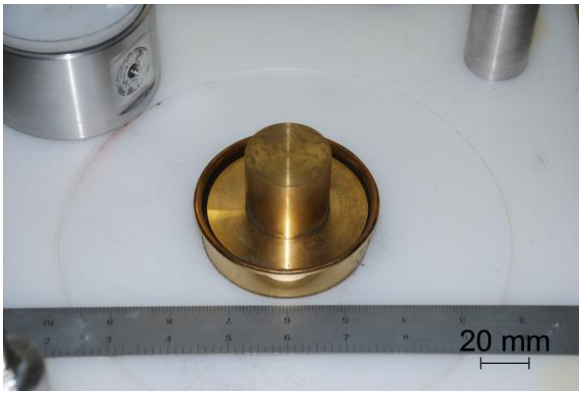

Figure 11. Image of brass punch within brass die, both of which are within the brass dish.

The influence of mechanical vibration amplitude, ultrasonic vibration power and time on the total powder infiltration of the foam was investigated. Foam infiltration was quantified by massing the foam prior to and after infiltration. Initial vibrational runs were conducted at 50% ultrasonic vibration power. The power was increased to 75% for a few runs. Mechanical vibration was conducted for periods of time ranging from 15-90 minutes, and at amplitudes ranging from 6.6-58.4 m/s^2.

The foam pieces were either in the form of squares or pie-slice-shaped segments of rounds. These shapes did not fit the shape of the containment vessel as precisely as the foam rounds. The result of the difference in shape allowed powder to be on the sides of the foam, as well as on the top of the foam during the vibration process. The parameters used for the infiltration of each sample are shown in Table IX. Within Table IX, *H* refers to the use of the brass punch as a vibrational hammer, *U* refers to the use of ultrasonic vibration, and *VAF* is variable amplitude (very low amplitudes) and frequency of vibration. The times given in Table IX refer to total vibration time, and are not necessarily individual vibration run times. The results of the foam infiltrations are shown in Table X.

Table IX. Vibration Settings for Foam Infiltration

Sample	Approximate mechanical vibration amplitude (m/s^2)
45SiC02	45 min: 12 m/s^2 - H & U
45SiC03	15 min: 7 m/s^2 - U 30 min: 13 m/s^2 - U
45SiC04	15 min: 13 m/s^2 - U 20 min: 27 m/s^2 - U 10 min: 27 m/s^2 20 min: 25 m/s^2 - H
45SiC05	30 min: VAF - U 30 min: 27 m/s^2 30 min: 25 m/s^2 - H
45SiC06	60 min: 3 m/s^2 60 min: 7 m/s^2 90 min: 27 m/s^2 30 min: 25 m/s^2 - H
65SiC01	50 min: 27 m/s^2 30 min: 25 m/s^2 - H
100SiC01	30 min: 27 m/s^2 30 min: 25 m/s^2 - H

Table X. Summary of Foam Characteristics and Results of Tungsten Infiltration

Sample	Foam volume (cm^3) (struts +porosity)	Foam start mass (g)	% Open volume	Open pore volume (cm^3)	Foam starting density (g/cm^3)	Foam end mass (g)	Mass of infiltrated tungsten (g)	Tungsten density (g/cm^3)
45SiC02	4.61	1.206	82.9%	3.82	0.262	11.833	10.627	2.78
45SiC03	4.08	1.511	75.9%	3.10	0.370	10.148	8.637	2.79
45SiC04	3.88	1.816	69.6%	2.70	0.468	12.214	10.398	3.85
65SiC01	3.06	1.680	64.3%	1.97	0.549	9.798	8.118	4.12
45SiC05	3.41	1.433	72.7%	2.48	0.420	11.534	10.101	4.07
100SiC01	2.34	0.580	83.9%	1.96	0.248	5.726	5.146	2.63
45SiC06	3.49	1.508	71.9%	2.51	0.432	11.548	10.040	4.00
65TaC	6.04	8.07	87.9%	5.31	1.377	30.042	21.968	4.14

Mechanical vibration at ~25 m/s^2 seemed to produce the best infiltration of the foams, for the parameters examined. It was found that a 15 minute vibration period induced significant compaction within the loose powder, requiring the foam to be flipped and the powder to be redistributed on top of the foam again. It was observed that mechanical vibration settings below ~6 m/s^2 produced negligible powder infiltration within the foam after both 15 and 60 minutes of vibration. Utilizing the brass punch on top of the powder, to act as a vibrational hammer increased the infiltration of the foam. Better results were achieved when the powder and foam were vibrated without the punch for several cycles, and subsequently the punch was placed on top of the powder and vibrated for several cycles. Foam infiltration tended to decrease exponentially for each subsequent vibration. The ultrasonic vibration did not seem to affect the infiltration within the experimental setup utilized. It is possible that there was insufficient ultrasonic coupling to the foam. Standard sieving mesh is physically attached to a ring at its edges. The ultrasonic ring rests on the sieve ring, allowing direct mechanical coupling between the mesh and the ultrasonic waves. The infiltration setup in this study confined the foam within the brass die. However, the foam was not attached to anything at its edges, allowing it to move

about within the circular recess of the brass container. Therefore, it may not have coupled well with the ultrasonic ring. It is possible that if a coupling method was devised between the ultrasonic ring and the foam, better infiltration results would be obtained.

Selected infiltrated foams were cross-sectioned to determine the uniformity of tungsten distribution throughout the foam thickness. Care had to be taken during this process, since the loose powder had a tendency to fall out of the pore space during the cross-sectioning. Figure 12 and Figure 13 show cross-sections of SiC foam infiltrated with sub-micron tungsten powder. The cross-sectioning process turned out particularly well in Figure 13. Fairly uniform tungsten infiltration can be observed throughout the thickness of the foam.

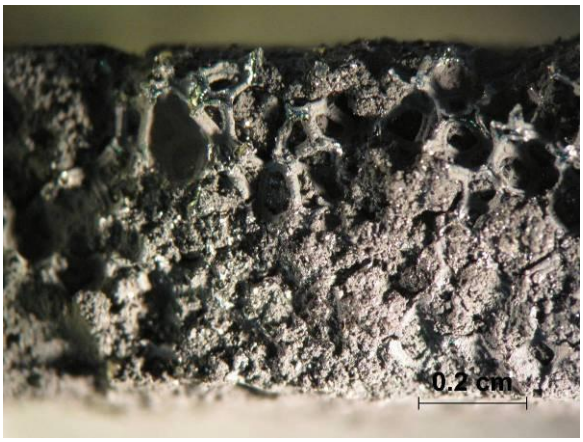

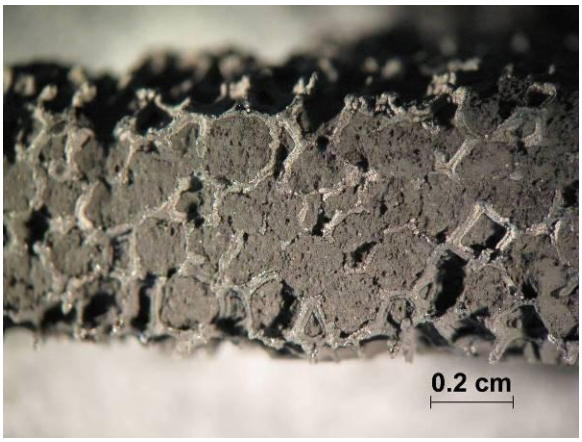

Figure 12.(left) Cross-section of 45 ppi SiC foam infiltrated with sub-micron tungsten
Figure 13.(right) Cross-section of 65 ppi SiC foam infiltrated with sub-micron tungsten

A vacuum furnace was utilized to sinter some of the infiltrated foam specimens. In the last two infiltrated samples, sintering was performed between vibrational infiltrations. A vacuum was maintained below $7x10^{-3}$ mbar during the sintering. A graph of furnace pressure for a typical sintering run is shown in Figure 19. Utilizing data from the literature, sintering temperatures between 1800-2000° C were expected to be required to achieve appreciable consolidation. Sintering on preliminary specimens was conducted at 1900° C for one hour. A heating rate of 10° C/ min. was used to heat the infiltrated foam to the final sintering temperature.

One scrap TaC round was infiltrated under vacuum and sintered between vibrational runs, which increased the overall infiltration of the foam. The highest tungsten density achieved from

vibrational foam infiltration was ~ 21% theoretical density. The infiltrated and sintered SiC and TaC foams were examined by cross-sectioning the foams and performing optical microscopy. Figure 14 and Figure 15 show cross-sections of sintered infiltrated SiC foam. Figure 16 and Figure 17 show cross-sections of sintered infiltrated TaC foam.

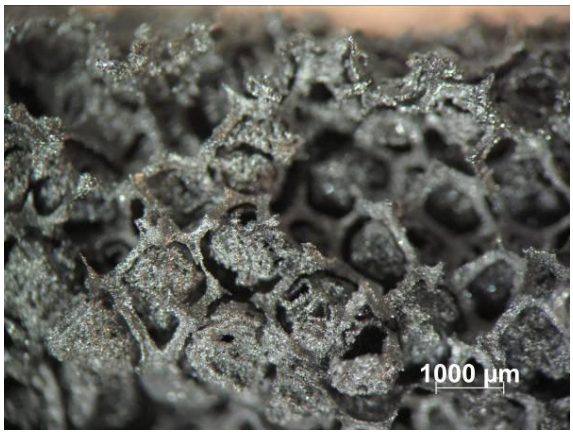

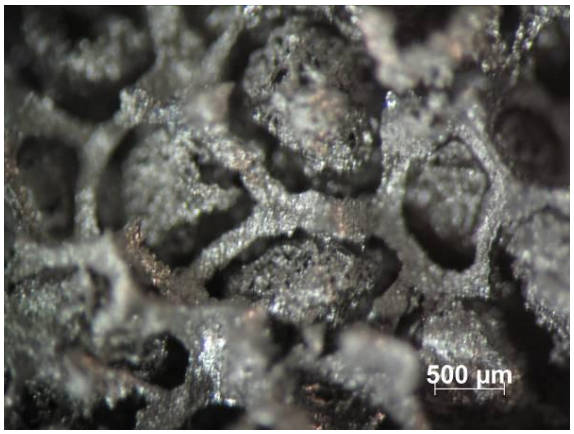

Figure 14.(left) Cross-section of infiltrated and sintered SiC foam
Figure 15.(right) Cross-section of infiltrated and sintered SiC foam

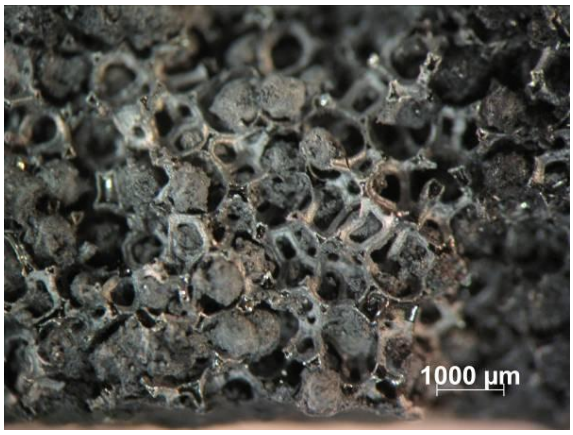

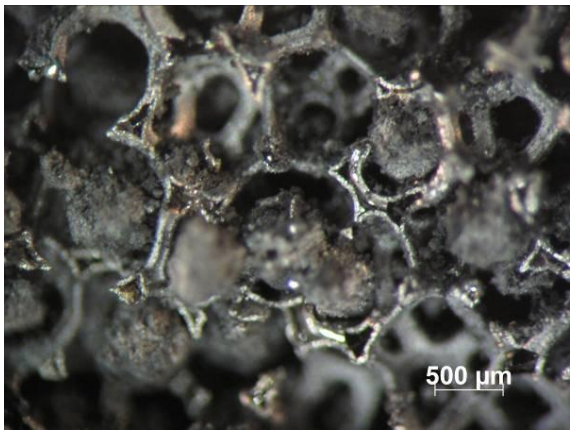

Figure 16.(left) Cross-section of infiltrated and sintered TaC foam
Figure 17.(right) Cross-section of infiltrated and sintered TaC foam

During the sintering process the sub-micron tungsten consolidated into sub-spherical-shaped particles, which occupied the open pores within the foam. The infiltrated densities were not high enough to support an interconnected network of tungsten throughout the open porosity. In addition, the high surface area of the sub-micron powder enabled more localized consolidation.

Formation of a Tungsten-Ceramic Foam Composite

This sub-section describes the experimental methodology to understand the influence of foam pore size and tungsten particle size/surface area on vibration-induced tungsten particle infiltration and densification within RVC foams, with the goal of forming an IPC. The characterization of tungsten powder through particle size analysis, surface area analysis, and scanning electron microscopy is discussed. The microstructural characterization of RVC foams is also presented. Vibrational parameters for infiltration of the RVC foams with tungsten are described, as is the process of consolidating the composite. Finally, the use of impulse excitation to non-destructively measure moduli of the composite is discussed.

Particle Size Analysis of Tungsten Powders

Particle size analysis of nominally sub-micron, and 5-10 micron tungsten powders was conducted on a Horiba LA-950 particle size analyzer. Particle size analysis was conducted using the vibrational dry feeder accessory for the LA-950. The use of vibrational feeding during particle size analysis allowed a more accurate assessment of the conditions of particles (such as agglomeration) during the vibrational infiltration of foams. Samples were selected for analysis from random areas of thoroughly mixed powder. A total of 20 analyses were performed on sub-micron tungsten powder and 13 analyses were performed on 5-10 micron tungsten powder. Scanning electron microscopy (SEM) was used to determine the sizes and shapes of the tungsten particles.

Surface Area Measurements of Tungsten Powders

The surface area of tungsten powders was determined using Brunauer, Emmett, and Teller (BET) analysis with a Quantachrome NOVA 2200 gas sorption analyzer. Specimens were vacuum degassed at 300° C for 15 hours prior to analysis. During the analysis specimens were cooled to 77.3 K using liquid nitrogen and the sorption analysis was performed using nitrogen gas. Seven adsorption points were used in the analysis.

Infiltration of RVC Foam with Tungsten Powder

It is possible that surface effects, such as agglomeration of the sub-micron tungsten powder, utilized in preliminary research, may have inhibited higher infiltration densities. It was thought that better results might be achieved using a larger particle size, such as 5-10 micron particles. Therefore, sub-micron and 5-10 micron, 99.9% tungsten powder were utilized for subsequent infiltrations. The experimental matrix for tungsten infiltration is given in Table XI.

Table XI. Experiment Matrix for RVC Foam Infiltration with Tungsten Powder

Particle Size	**Foam Pore Density**		
	45 ppi	**65 ppi**	**100 ppi**
Sub-micron tungsten	2 samples	2 samples	2 samples
5-10 micron tungsten	2 samples	2 samples	2 samples

Foam infiltrations were conducted using the equipment described in the previous section. However, ultrasonic vibration was not utilized. Foam infiltration was quantified by massing the foam prior to and after infiltration. The container holding the powder and the foam was evacuated to a vacuum of less than 2 Torr for the vibrational infiltration. For sub-micron powders, a mass of ~ 15 g of tungsten powder was placed on top of the foam. A mass of ~ 25 g of tungsten powder was used when infiltrating with 5-10 micron powders. A larger mass of tungsten was used when infiltrating with 5-10 micron tungsten due to migration of the RVC foam to the top of the tungsten during vibration. The foam migration was likely caused by the significant difference in density between the RVC foams and the SiC foams used in preliminary experiments. The recess in the brass die could not accommodate 25 g of sub-micron tungsten due to the lower tap density. Mechanical vibration was typically conducted for 10 minutes at ~ 25 m/s^2 amplitude. After 10 minutes elapsed, the foam was removed and massed. The foam was flipped upside down and another ~15 g or 25 g of powder was placed on top of the foam, depending on the nominal tungsten particle size being utilized. Vibration continued for another 10 minutes. The process was repeated until less than a ~ 0.5 g increase in infiltration was observed.

T-tests were performed to determine the statistical significance of results obtained for the influence of foam pore size and tungsten particle size on foam infiltration. Equation 24 and Equation 25 were used to perform the t-tests.

Consolidation of the Composite

The infiltrated foam was sintered in a vacuum furnace at 1950° C for 2 hours. A heating rate of 10° C/ min. was utilized. The surface and grain boundary diffusion rates for tungsten at 1950° C were calculated using Equation 18 and were found to be 1.8E-7 cm^2/s and 1.2E-8 cm^2/s, respectively. Temperature measurements were verified through correlation of a thermocouple and a pyrometer. The heating curve for the sintering process is shown in Figure 18. The vacuum furnace was evacuated to $8 \cdot 10^{-4}$ mbar prior to initiating the heating cycle. The furnace pressure during the sintering run of a selected specimen is shown in Figure 19. The peaks present in the pressure curve in Figure 19 are likely a result of outgassing from the RVC foam. A 1/8" thick piece of 99.95% tungsten was placed between the sample holder and the sample in order to minimize carbon diffusion from the sample holder into the specimen. The low strength of the sintered sub-micron infiltrated rounds prevented their removal from the tungsten spacer without damage to the round. Due to the issues with removing the sintered sub-micron infiltrated rounds from the tungsten spacer, grafoil was used in place of the tungsten round for sub-micron sintering runs. The infiltrated foam was massed after sintering.

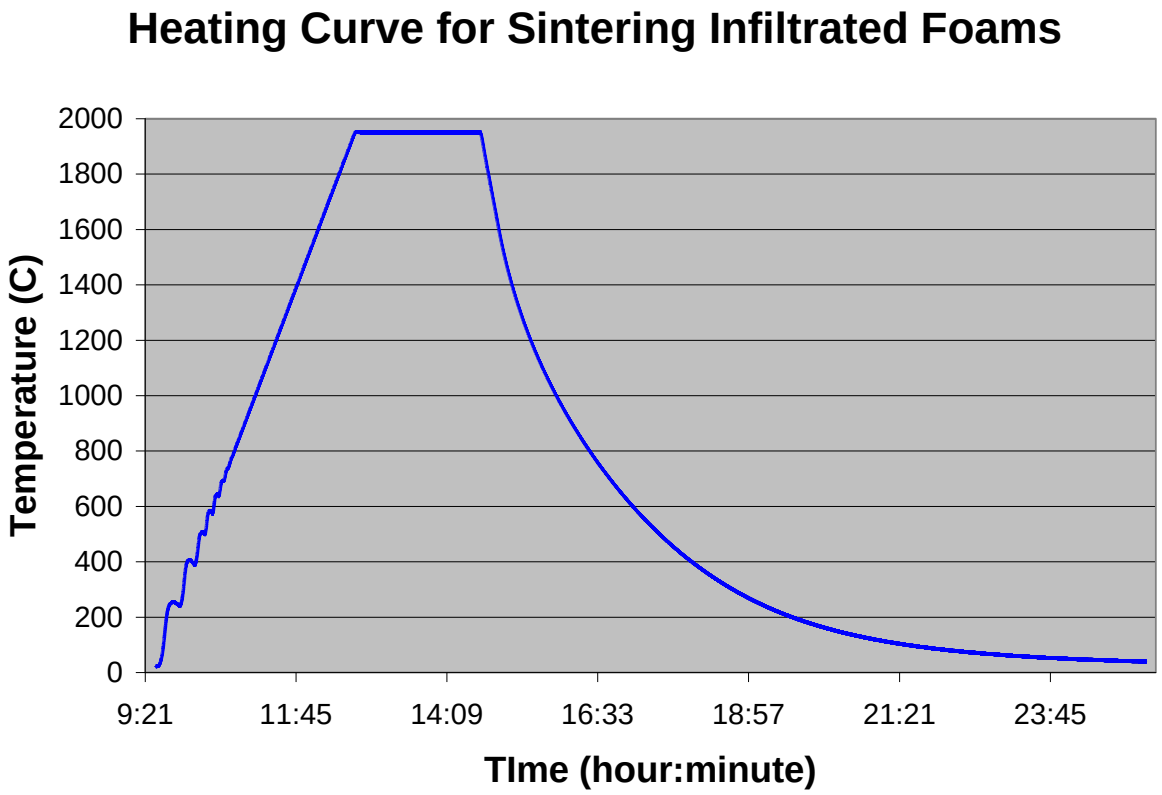

Figure 18. Heating curve for sintering infiltrated foam specimens

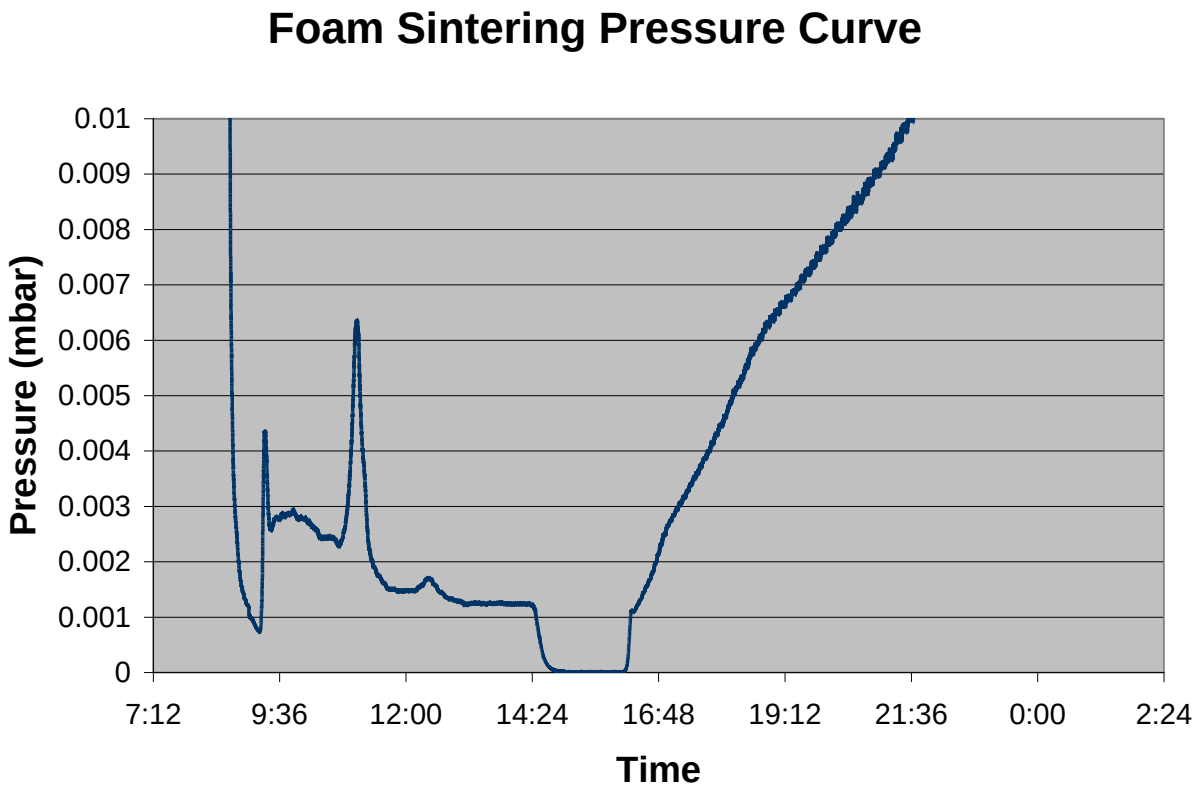

Figure 19. Vacuum furnace pressure during sintering of infiltrated foam specimens

It was of interest to determine the degree of densification within tungsten powder under similar conditions to that of the consolidation of infiltrated tungsten within RVC rounds. A mass of 35.137 g of sub-micron tungsten was placed within a graphite die with an I.D. of 1.5 inches and an O.D. of 2.5 inches. The die was lined with grafoil. The density of the loose powder within the die was 2.98 g/cm^3, which is 15.5% theoretical tungsten density. A graphite punch was placed on top of the powder within the die. No load was applied to the punch during sintering. The furnace was evacuated to 8.0E-4 mbar. A heating rate of 10° C/min was used to achieve a sintering temperature of 1850° C. The tungsten specimen was held at 1850° C for one hour. The mass of the specimen was measured after sintering, and the volume was measured through pycnometry.

Modulus Measurement Using Impulse Excitation

The moduli of foams infiltrated with 5-10 micron tungsten, and subsequently sintered, were measured using an impulse excitation technique. ASTM standards E1876 and C1259 were used as a reference for the testing procedure. Prior to measuring vibrational frequencies of the rounds, the impulse excitation system was tested on a specimen with known properties in order to ensure proper calibration of the equipment.

A steel sphere mounted on a flexible polymer rod was used to induce vibration within the infiltrated and sintered foam rounds. Vibration was induced in the round in flexural and anti-flexural modes. Ten measurements were made in each mode of vibration. In order to allow the specimen to vibrate freely in flexural and anti-flexural modes, two specimen supports were fabricated using silicone rubber. The supports used for flexural and anti-flexural vibration are shown in Figure 20 and Figure 21, respectively. A PCB model 426B03 transducer was used to measure the mechanical vibration of the composite. The transducer had a frequency response of 3.2-126000 Hz. An ICP model 480E09 sensor signal conditioner was connected to the transducer and to a Jagdish Electronics interface, which was connected to a National Instruments DAQCard-6024E PCMCIA Card. Jagdish Electronics Dynamic Elastic Properties Analyzer version 7 software was used to record the vibration induced in the composite. The software performed the fast Fourier transform on the waveform, determined the resonant frequencies, and calculated the Young's modulus, shear modulus, and Poisson's ratio of the composite.

Figure 20.(left) Image of the specimen support platform that was used for flexural vibration measurements. Figure 21.(right) Image of the specimen support platform that was used for anti-flexural vibration measurements.

The diameter and thickness of each round was measured at several points along the specimen with a digital micrometer. The average of the values was used to calculate the elastic properties of the material. The mass of each round was also measured. The infiltrated and sintered rounds did not exhibit perfect round geometry, i.e. the edges were rounded. Edge rounding and other geometric imperfections were expected to cause a small degree of error in the measurements. The sensitivity of the transducer was maximized by locating it at an anti-node relative to the specimen vibration during the excitation process. The specimen and transducer setup are shown in Figure 22 and Figure 23 for flexural and anti-flexural vibration measurements, respectively. For flexural measurements, the specimen was excited at the center of the round. In anti-flexural measurements, the specimen was excited at a point 90 degrees in rotation from the transducer, slightly in from the edge of the round.

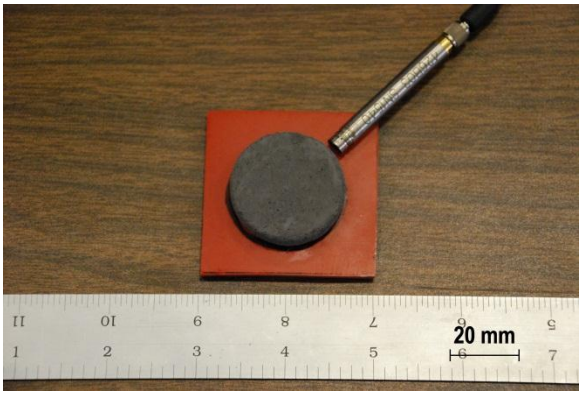

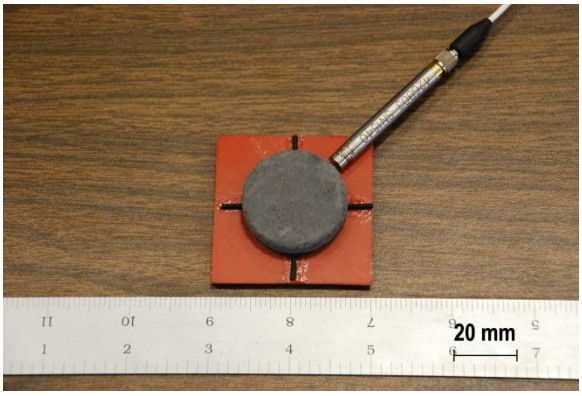

Figure 22.(left) Image of specimen test setup for flexural vibration measurements.
Figure 23.(right) Image of specimen test setup for anti-flexural vibration measurements.

IV. Results and Discussion

This section describes the results obtained to accomplish the objectives of this study, which included: Understanding the influence of strut/pore size, foam composition, and foam density on the neutron transmission in TaC foams, understanding the influence of strut/pore size, foam composition, foam density, thermal fatigue, and thermal shock on mechanical behavior of TaC foams, and understanding the influence of foam pore size and tungsten particle size/surface area on vibration-induced tungsten particle infiltration and densification within RVC foams, with the goal of forming an IPC.

Influence of Strut/Pore Size, Foam Composition, and Foam Density on the Neutronic Properties of the Foam

In this sub-section the results obtained in order to understand the influence of strut/pore size, foam composition, and foam density on the neutronic properties of TaC foam are discussed. Results from volumetric and microstructural analysis of the TaC foams are presented. In addition, the results for modeling neutron transport and experimentally measuring neutron transmission are discussed.

Microstructural Analysis and Pore/Strut Size Measurements

Optical micrographs of 45 ppi, 65 ppi, and 100 ppi TaC/PyC/RVC foams are shown in Figure 24 - Figure 29 at various magnifications. The TaC foams had a three-dimensional cell structure, with porosity that is interconnected throughout the foam. Thus, they had an open- cell structure. The TaC foams tended to exhibit cell faces with square, pentagonal, and hexagonal geometries. Adjoining cell faces form polyhedral cells with geometries similar to tetrakaidecahedrons and dodecahedrons. The coloration differences observed in the 100 ppi micrographs are due to a change in lighting conditions and camera settings. The 100 ppi images were obtained at a different time than the 45 ppi and 65 ppi images. The micrographs show that as foam pore density (ppi) increased, the pore size and strut thickness within the foam decreased.

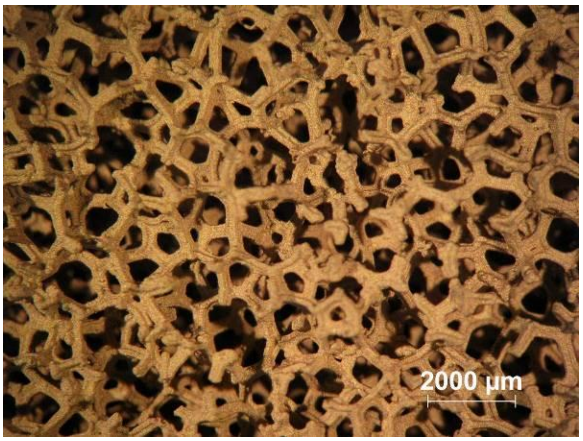

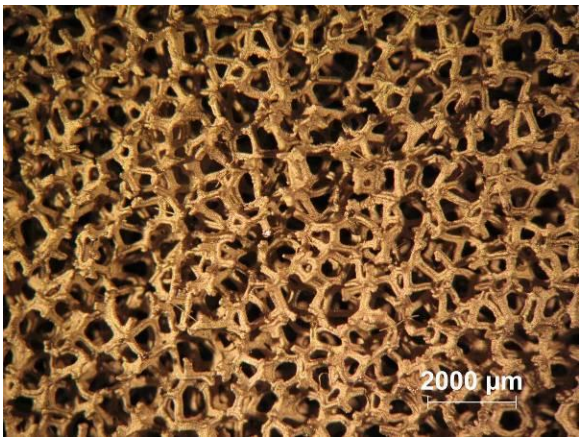

Figure 24.(left) Optical micrograph of 45 ppi TaC/PyC/RVC foam
Figure 25.(right) Optical micrograph of 65 ppi TaC/PyC/RVC foam

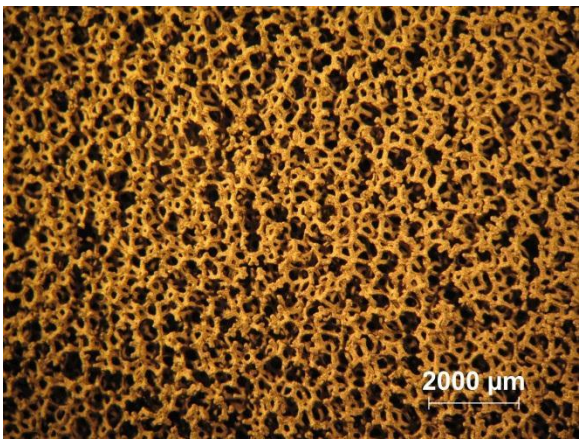

Figure 26. Optical micrograph of 100 ppi TaC/PyC/RVC foam

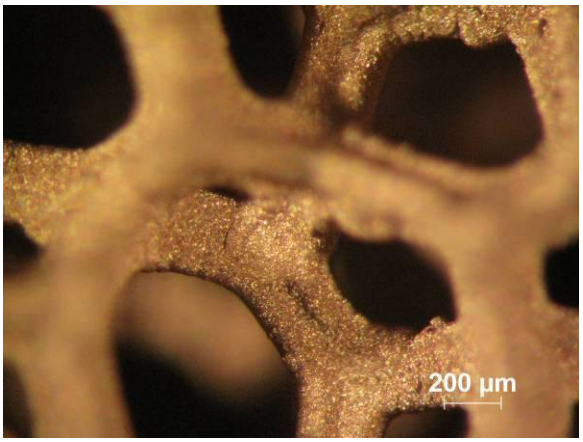

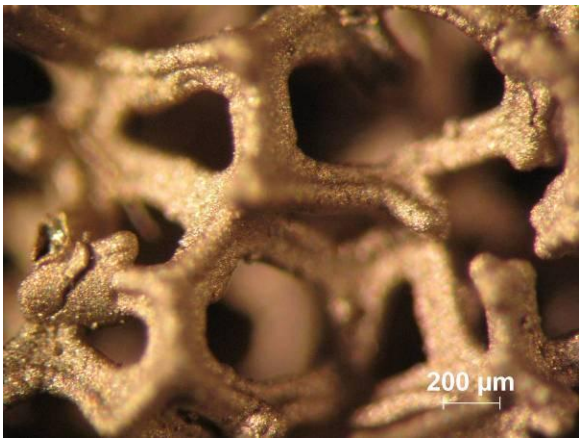

Figure 27.(left) Optical micrograph of 45 ppi TaC/PyC/RVC foam
Figure 28.(right) Optical micrograph of 65 ppi TaC/PyC/RVC foam

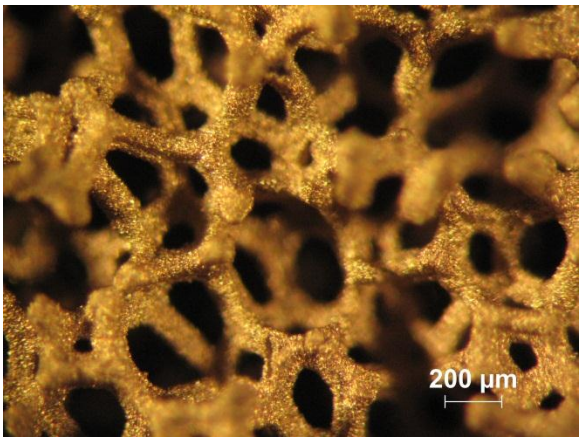

Figure 29. Optical micrograph of 100 ppi TaC/PyC/RVC foam

Measurements of average strut and pore sizes for TaC foams are shown in Table XII. The average strut thicknesses measured using optical microscopy were found to range from 256 µm - 74 µm for 45 ppi - 100 ppi TaC/RVC foams, respectively. The average strut thicknesses of TaC/PyC/RVC foams ranged from 318 µm - 142 µm for 45 ppi – 100 ppi foams. Average pore sizes for TaC/RVC foams ranged from 654 – 164 µm for 45 ppi – 100 ppi TaC/RVC foams. In TaC/PyC/RVC foams the pore sizes ranged from 546 – 198 µm for 45 - 100 ppi foams.

Table XII. Average Strut and Pore Sizes for Tantalum Carbide Foams

Foam Type	Average Strut Thickness (µm)	Standard Deviation (µm)	Average Pore Size (µm)	Standard Deviation (µm)
45 TaC/PyC/RVC	318	21	546	62
65 TaC/PyC/RVC	190	12	296	28
100 TaC/PyC/RVC Type A	142	11	198	23
100 TaC/PyC/RVC Type B	176	11	244	47
45 TaC/RVC	256	17	654	78
65 TaC/RVC	151	11	354	41
100 TaC/RVC	74	4	164	19

Figure 30 and Figure 31 show the average measured strut and pore sizes, along with standard deviations, in graphical format. As the foam pore density (ppi) increased, the strut thickness decreased and the pore size decreased.

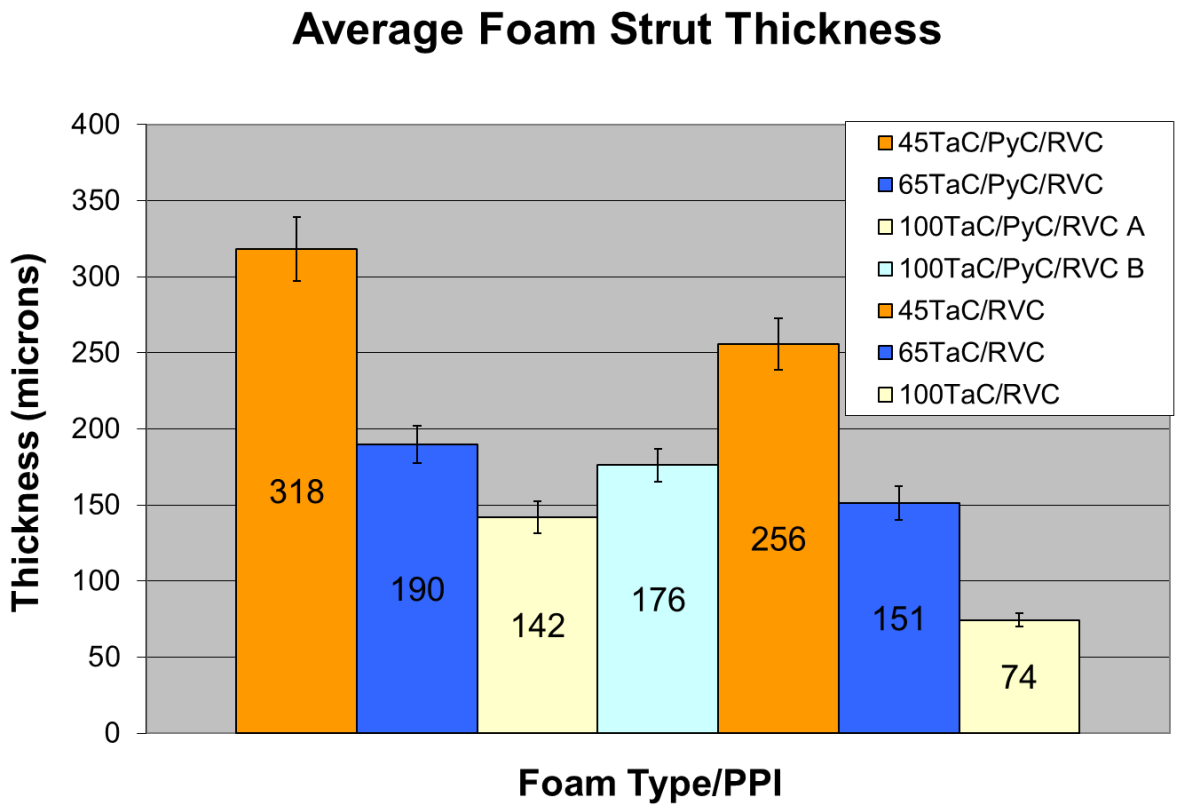

Figure 30. Chart of average measured strut thickness and standard deviation for each foam type.

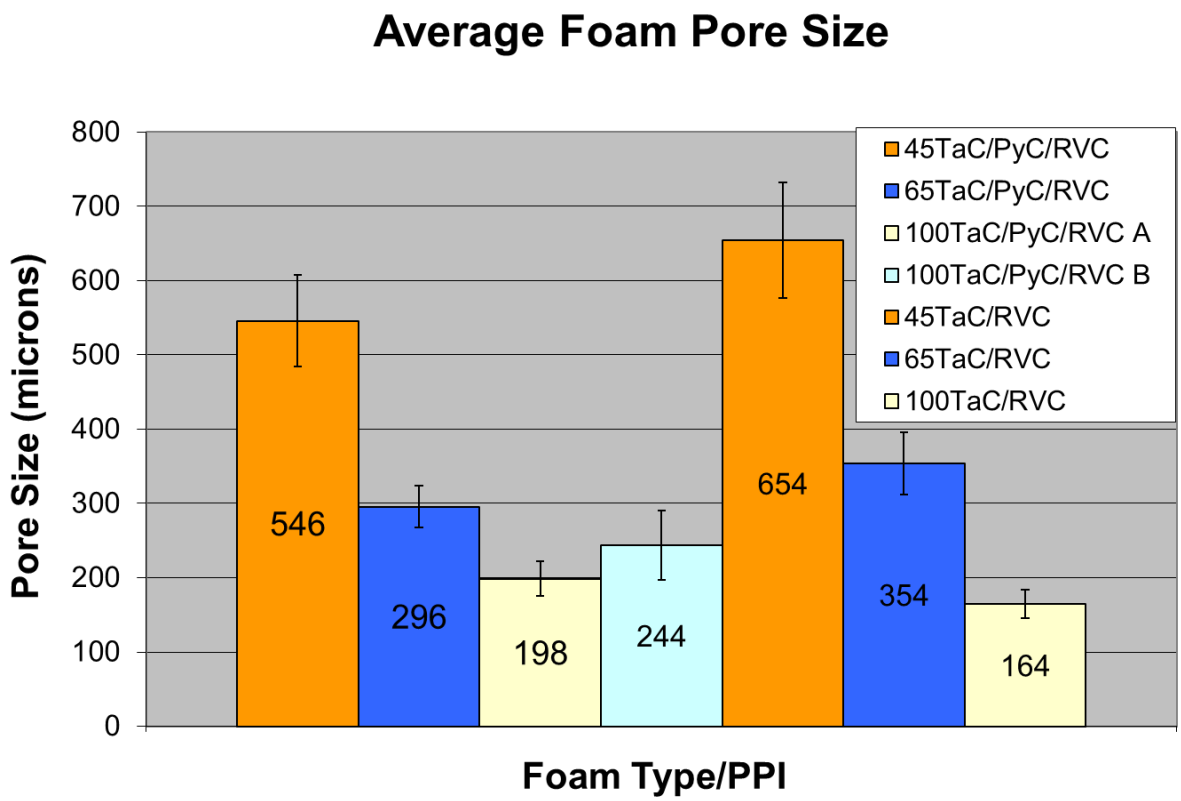

Figure 31. Chart of average measured pore size for each type of foam.

Scanning electron microscopy was utilized to examine a cross-section of a TaC/PyC/RVC foam strut shown in Figure 32. The strut core was composed of RVC. The RVC had a pyrolytic carbon coating, and the pyrolytic carbon was coated with tantalum carbide.

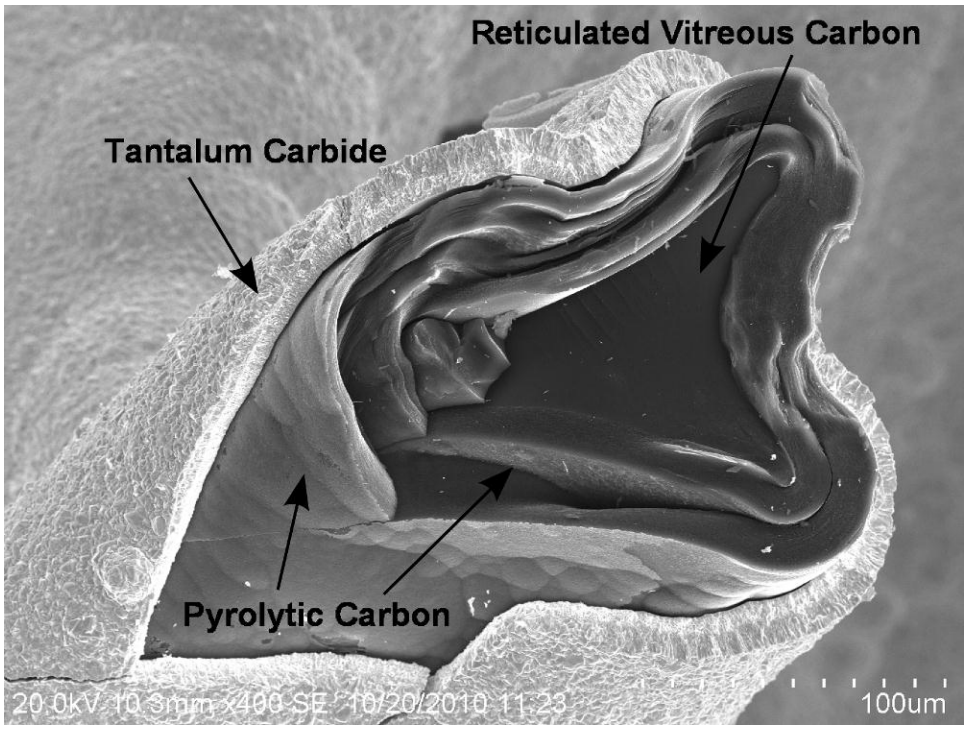

Figure 32. Scanning electron micrograph of a strut cross-section from a 65 ppi TaC/PyC/RVC foam.

Measurements were performed on SEM micrographs to determine the average thickness of the RVC core, PyC coating (when applicable), and TaC coating on the foam struts. Table XIII and Table XIV show the average coating thickness and RVC core thickness for TaC/RVC and TaC/PyC/RVC foams, respectively.

Table XIII. Thickness of Foam Strut Coatings and RVC Core for TaC/RVC Foams (microns)

	45 ppi	**65 ppi**	**100 ppi**
TaC	39 +/- 4	27 +/- 2	10 +/- 1
RVC	118 +/- 15	91 +/- 16	47 +/- 9
Strut thickness	196 +/- 23	145 +/- 20	67 +/- 11

Table XIV. Thickness of Foam Strut Coatings and RVC Core for TaC/PyC/RVC Foams (microns)

	45 ppi	65 ppi	100 ppi Type A	100 ppi Type B
TaC	40 +/- 1	30 +/- 3	14 +/- 1	18 +/- 2
PyC	44 +/- 4	10 +/- 1	7 +/- 2	24 +/- 3
RVC	130 +/- 22	77 +/- 14	45 +/- 6	52 +/- 5
Strut thickness	298 +/- 32	157 +/- 22	87 +/- 12	136 +/- 15

Micrographs of cross-sections of foam struts from 45 ppi, 65 ppi, and 100 ppi TaC/RVC foams are shown in Figure 33-Figure 35, respectively. The CVI deposition process allowed a fairly uniform coating thickness to be deposited on the RVC struts. The struts had triangular geometry with concave edges. As coating thickness increased, the vertices of the triangular strut cross-section became more rounded.

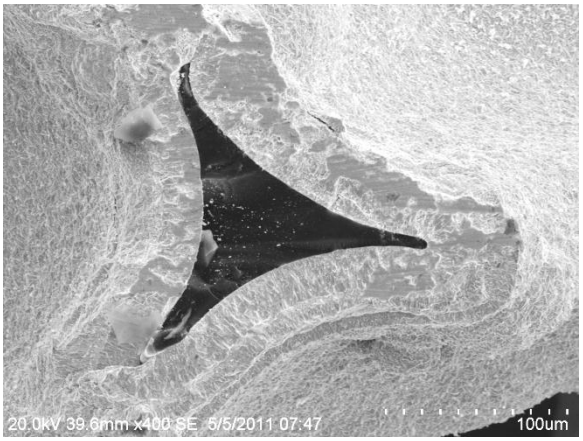

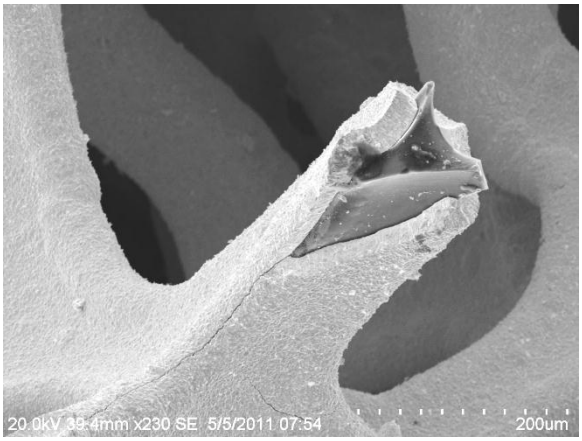

Figure 33.(left) Cross-section of a strut in a 45 ppi TaC/RVC foam
Figure 34.(right) Cross-section of a strut in a 65 ppi TaC/RVC foam

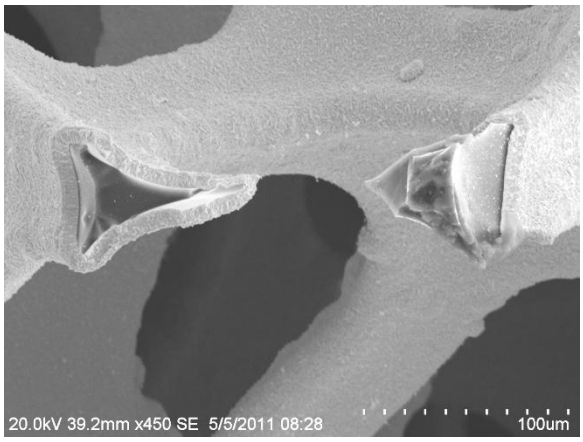

Figure 35. Cross-section of a strut in a 100 ppi TaC/RVC foam

Micrographs of cross-sections of foam struts from 45 ppi, 65 ppi, and 100 ppi TaC/PyC/RVC foams are shown in Figure 36-Figure 39, respectively.

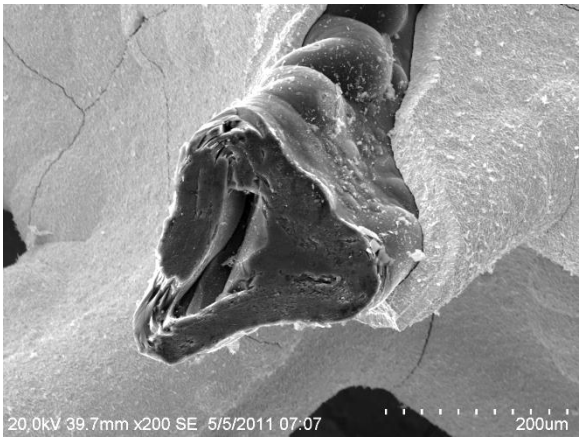

Figure 36.(left) Cross-section of a strut in a 45 ppi TaC/PyC/RVC foam
Figure 37.(right) Cross-section of a strut in a 65 ppi TaC/PyC/RVC foam

The difference in thickness of the pyrolytic carbon coating between 100 TaC/PyC/RVC Type A and Type B foams is clearly shown in Figure 38 and Figure 39.

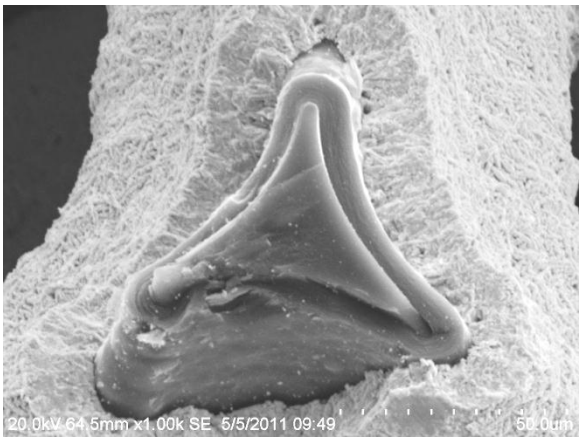

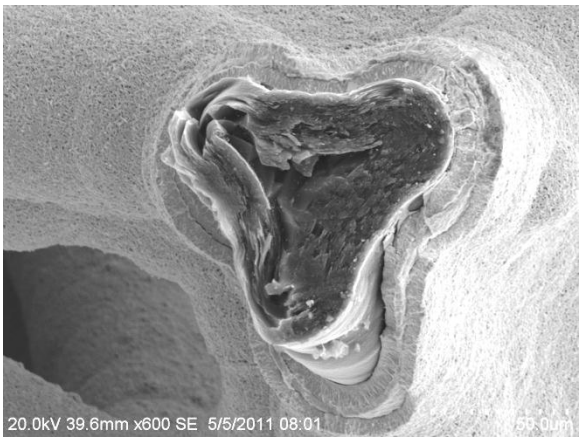

Figure 38.(left) Cross-section of a strut in a 100 ppi TaC/PyC/RVC Type A foam
Figure 39.(right) Cross-section of a strut in a 100 ppi TaC/PyC/RVC Type B foam

Volumetric Measurements of Foam

Pycnometry was used to measure the strut volume of TaC foams. The average volume for each TaC foam round, as well as the average volume for each foam type and pore density is shown in Table XV.

Table XV. Average Volumes of TaC Foams Determined through Pycnometry

Composition	PPI	Sample #	Avg (cm^3)	Std Dev (cm^3)	Group Avg (cm^3)	Std Dev (cm^3)
TaC/PyC/RVC	45	1	1.1106	0.0027	1.0901	0.0235
		3	1.1021	0.0049		
		4	1.0974	0.0012		
		5	1.1005	0.0116		
		6	1.0846	0.0008		
		7	1.0452	0.0022		
TaC/PyC/RVC	65	1	0.7543	0.0099	0.8486	0.1045
		2	0.9335	0.0034		
		3	0.8022	0.0098		
		4	0.9062	0.0098		
		5	0.9773	0.0037		

		6	0.7202	0.0068		
TaC/PyC/RVC	100 Type A	1	0.8935	0.0052	0.8894	0.0231
		2	0.8645	0.0010		
		3	0.9101	0.0034		
	100 Type B	1	1.2102	0.0165	1.2109	0.1007
		2	1.1106	0.0181		
		6	1.3119	0.0091		
TaC/RVC	45	1	0.7214	0.0063	0.6832	0.0599
		2	0.7110	0.0012		
		3	0.6677	0.0014		
		4	0.6957	0.0064		
		5	0.5700	0.0040		
		6	0.7333	0.0094		
TaC/RVC	65	2	0.6662	0.0003	0.7134	0.0659
		3	0.8097	0.0182		
		4	0.6763	0.0215		
		5	0.7014	0.0187		
TaC/RVC	100	1	0.5244	0.0019	0.5603	0.0247
		2	0.5789	0.0046		
		3	0.5645	0.0103		
		4	0.5734	0.0041		

The average strut volume for each type of TaC foam is shown graphically in Figure 40. As expected, the foams with the pyrolytic carbon coating had a larger strut volume than the TaC/RVC foams. Strut volumes for the TaC/PyC/RVC foams ranged from 0.8486 - 1.2109 cm^3, whereas strut volumes for the TaC/RVC foams ranged from 0.5603 - 0.7134 cm^3.

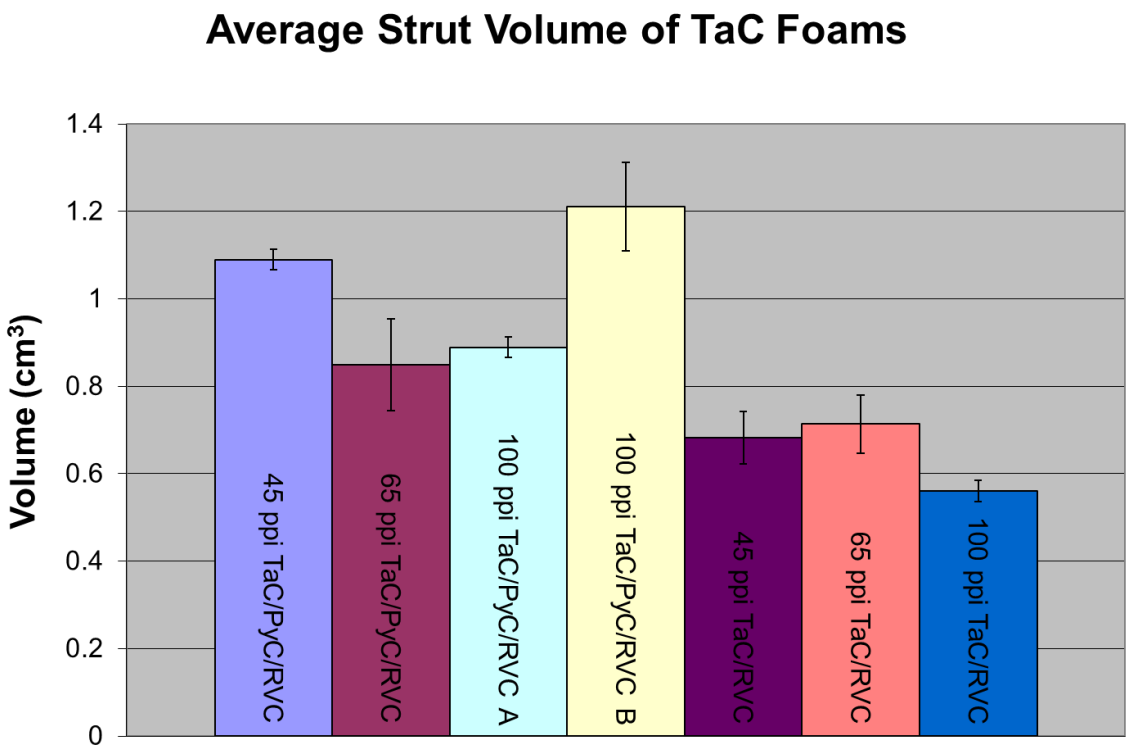

Figure 40. Average strut volume for each pore density of TaC/RVC and TaC/PyC/RVC foams

The average open porosity for each pore density of TaC/RVC and TaC/PyC/RVC foams is shown in Figure 41. Porosity ranged from 88.3% - 90.7% in TaC/RVC foams, and from 80.3 - 86.2% in TaC/PyC/RVC.

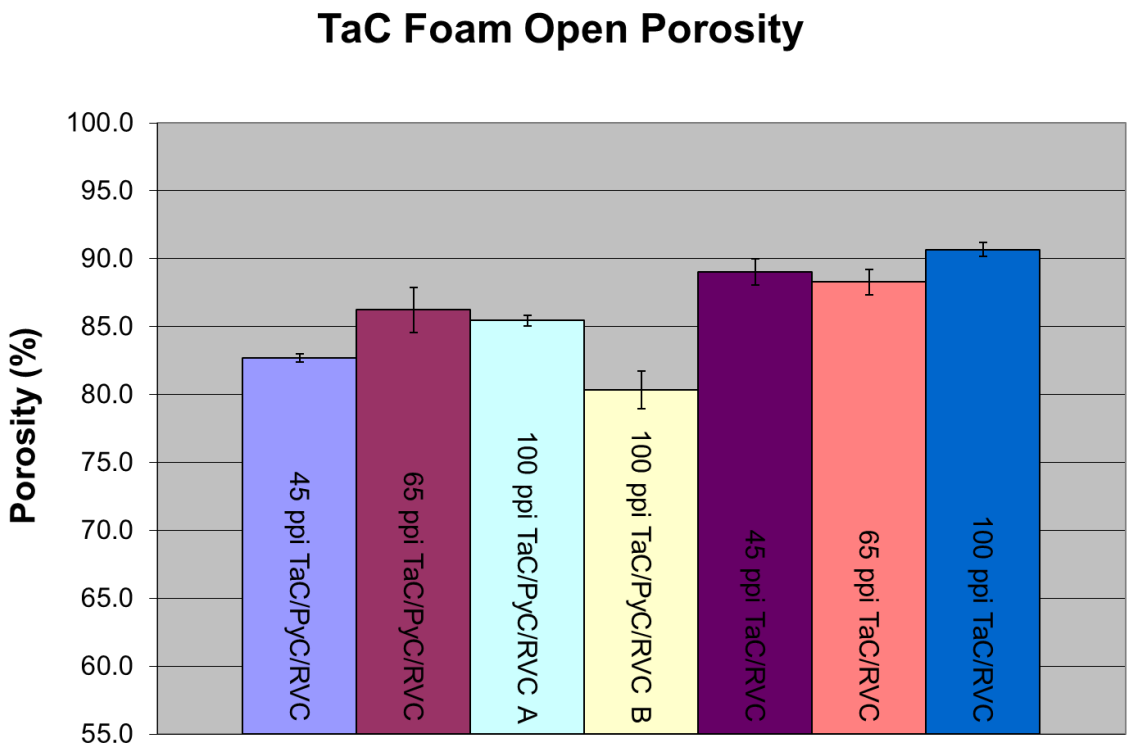

Figure 41. Average open porosity for each pore density of TaC/RVC and TaC/PyC/RVC foams.

Neutron Transmission Measurements

Figure 42 represents a compilation of averages for 26 measurements of baseline indium foil decay. Baseline indium decay refers to measurements of indium foil decay obtained after placing the indium foil ¼" from the edge of the polyethylene case on the neutron source. The ¼" gap was left to maintain the same distance between the neutron source and the indium foil for both foam and baseline measurements. Each point on the graph is representative of the number of counts during a 90 second data collection period. Between each measurement there was a 90 second pause. The observed decrease in counts with increasing time within the chart correlated well with the known half-life for beta-decay of indium, which is ~54 minutes.

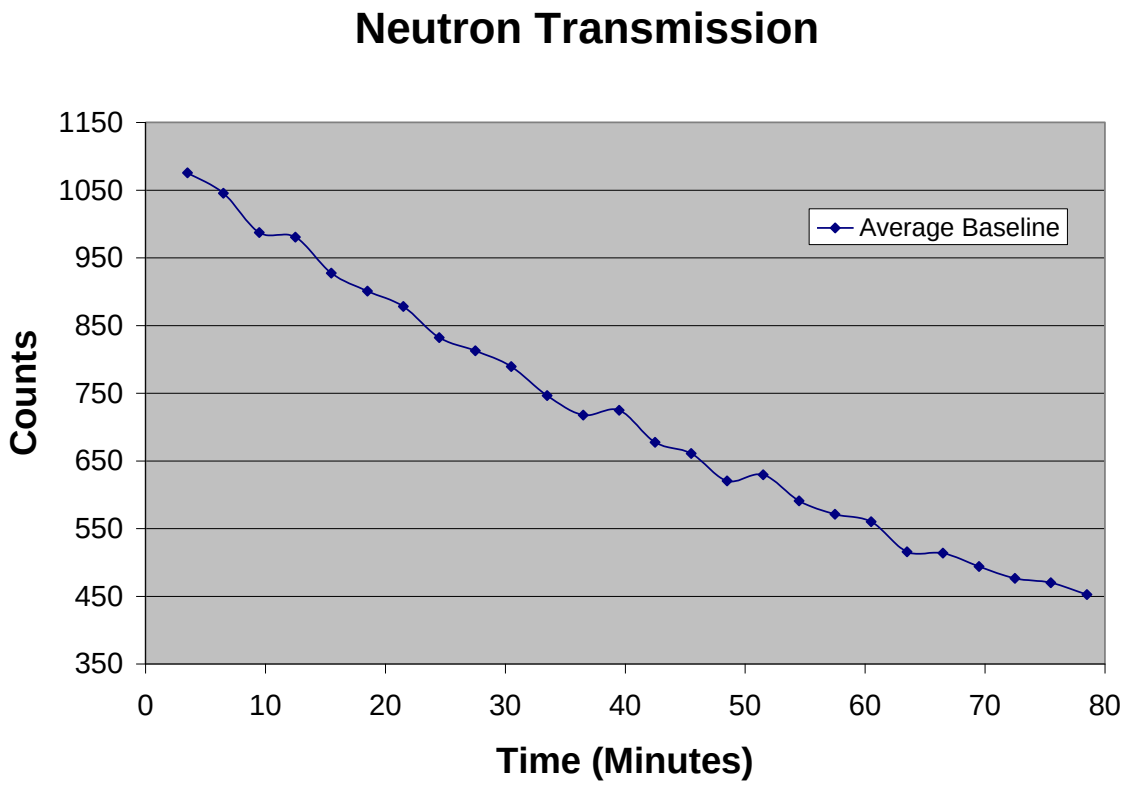

Figure 42. Graph of average baseline counts of indium foil decay vs time

The indium decay counts measured from the indium foil that was mounted to the back of a 45 ppi TaC/PyC/RVC foam round are shown in Figure 43. A total of 26 measurements were obtained, utilizing the same time periods discussed in the baseline measurements.

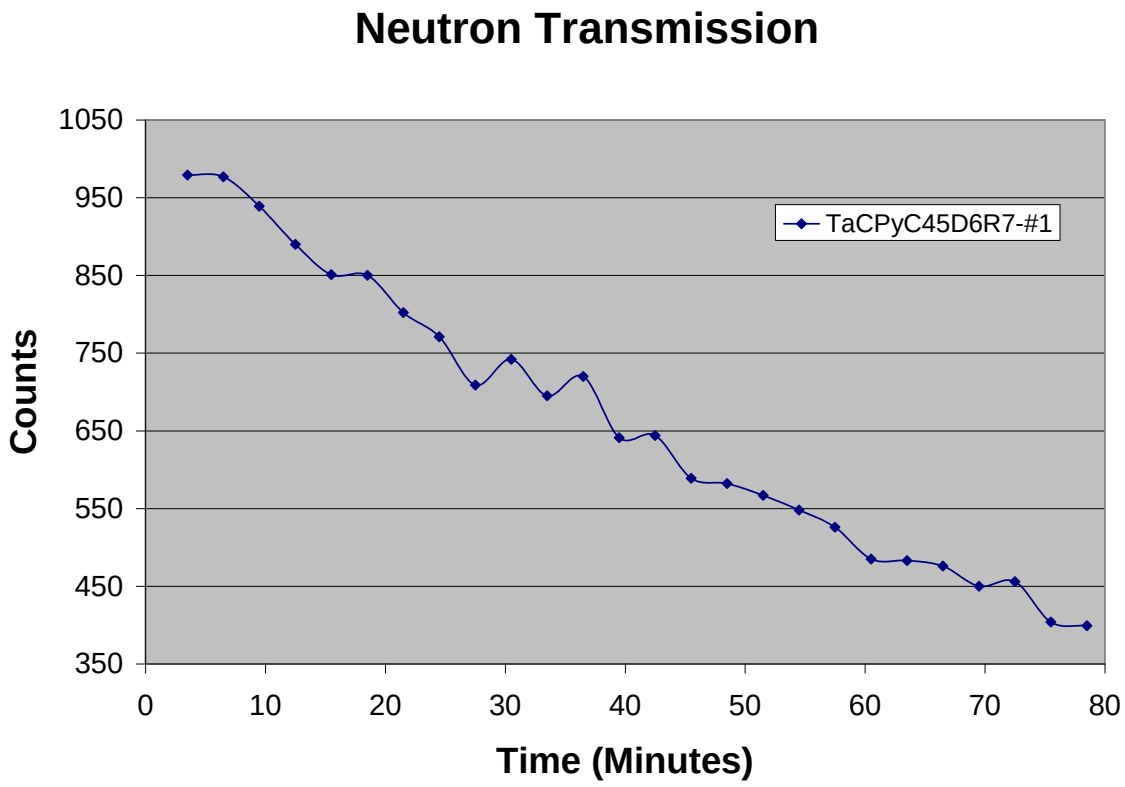

Figure 43. Graph of indium foil decay counts for 45 ppi TaC/PyC/RVC foam neutron exposure run #1 vs time

Three indium foil decay measurement runs are shown for indium foil mounted on the back of a 45 ppi TaC/PyC/RVC foam round in Figure 44. Since radioactive decay is a statistical process some variation is expected within individual measurements at a given time, as observed in the results. However, when the 26 measurements are averaged out over the three runs, as shown in Figure 45, a relatively small standard deviation (~ +/- 2-3%) was obtained for all foam and baseline indium decay measurements.

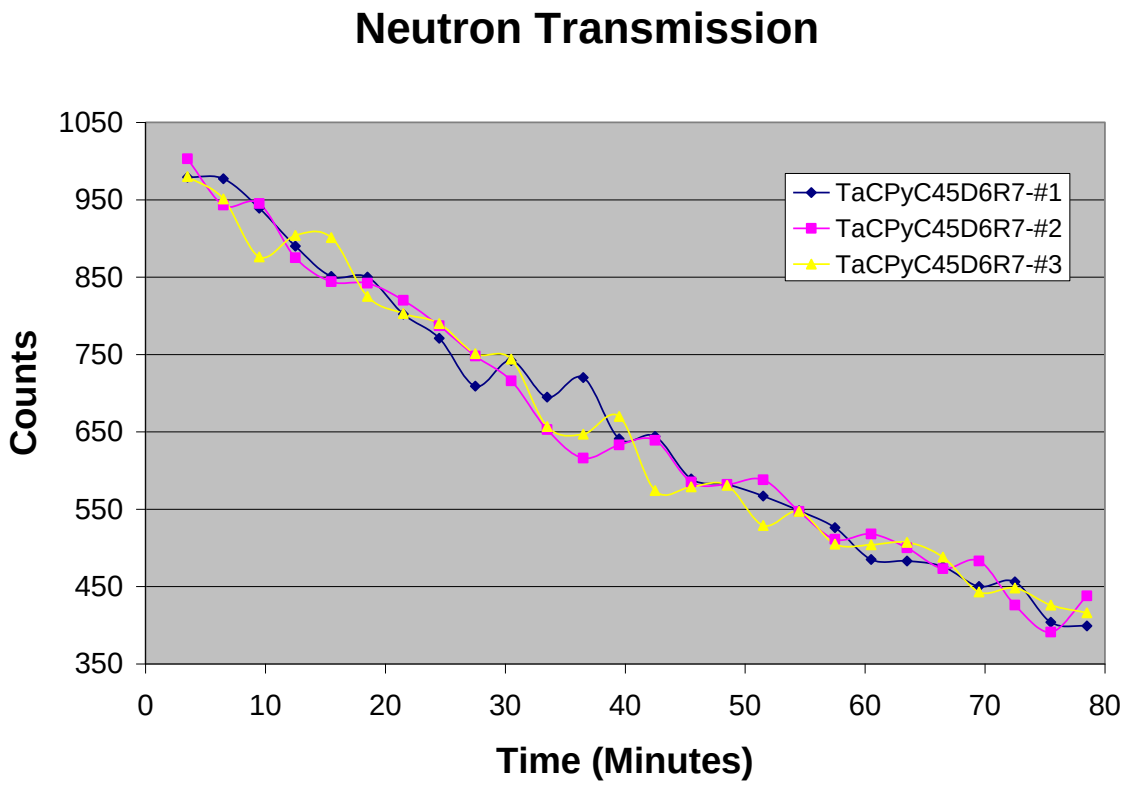

Figure 44. Graph of indium foil decay counts for 45 ppi TaC/PyC/RVC foam neutron exposure runs #1-3 vs time

The average indium decay for each of the 26 radioactive decay measurements from the three runs for indium foil mounted on the back of a piece of 45ppi TaC/PyC/RVC foam and indium foil in baseline measurements is shown in Figure 45.

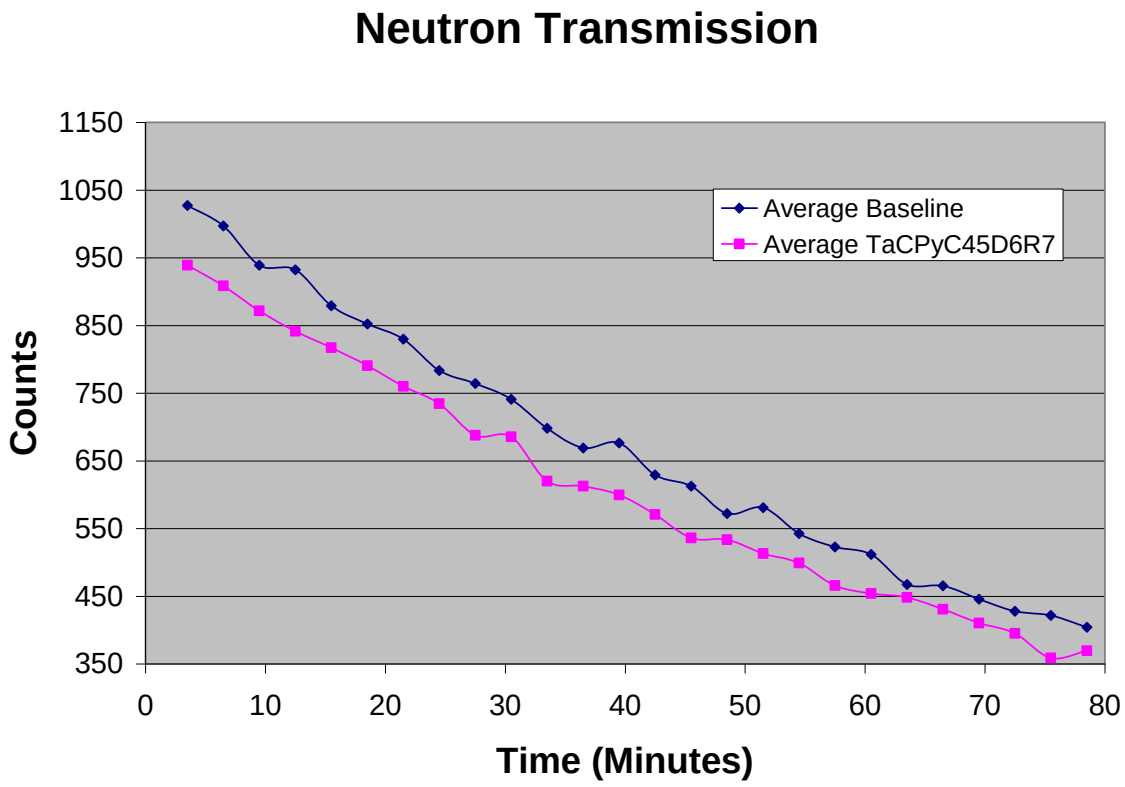

Figure 45. Graph of average baseline counts of indium foil and average indium foil counts from 45 ppi TaC/PyC/RVC foam neutron exposures vs time

Figure 44 and Figure 45 are graphs of measurements made for one of the TaC foam specimens. Graphs of the measurements performed on the other TaC specimens can be found in Appendix C. The ratio of the indium foil decay mounted behind a foam specimen to that of the baseline for each of the 26 measurement periods was calculated, and the average was determined. The average ratio was then plotted against the areal density of TaC for each TaC/RVC round in Figure 46. Only TaC/RVC rounds were utilized in the graph since they had approximately the same mass of carbon in the struts, whereas the TaC/PyC/RVC rounds did not. The data point at 0 g/cm^2 TaC areal density represents neutron transmission for an RVC round with no TaC coating. Data for TaC/PyC/RVC rounds are incorporated with the data generated using MCNP for neutron transport modeling. The results are discussed in the next section.

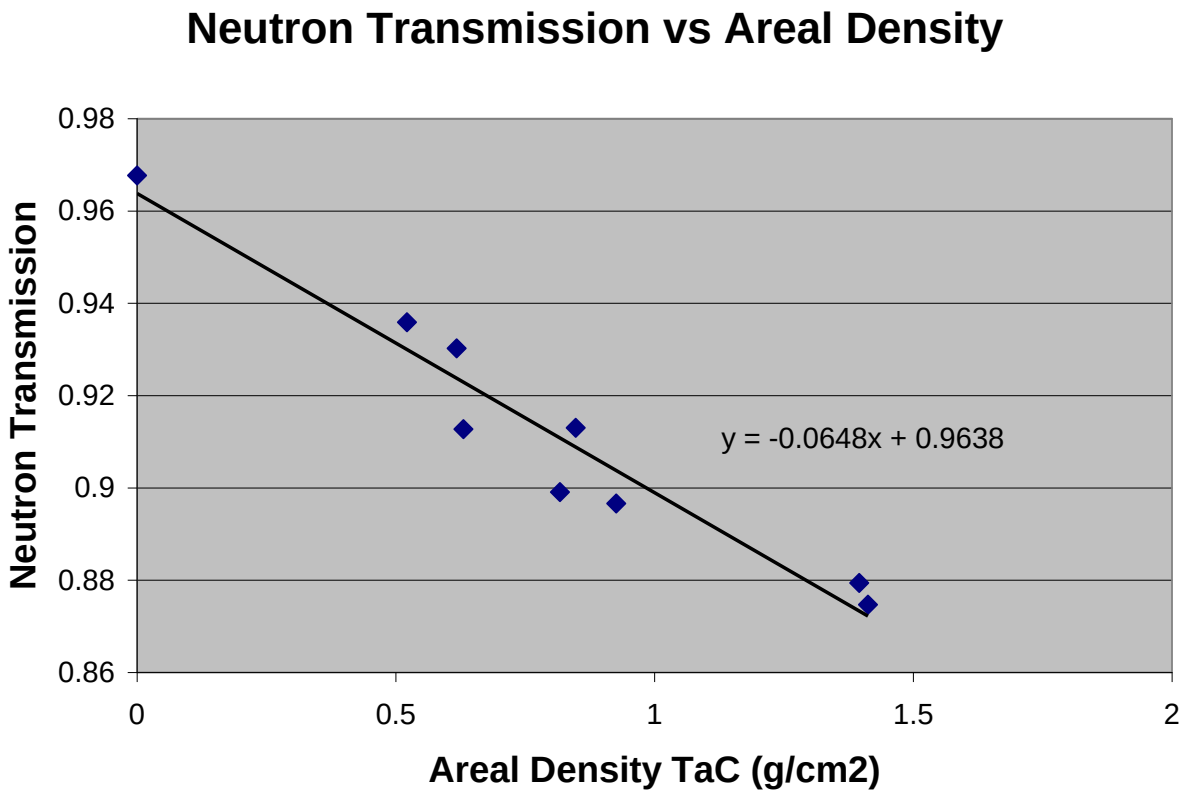

Figure 46. Graph of neutron transmission vs areal density of TaC for TaC/RVC foams

Data from Figure 46 indicated that there was a linear relationship between neutron transmission and density of TaC given by Equation 27, where x is the areal density (g/cm^2) of TaC and y is the relative neutron transmission through the foam using an AmBe neutron source. Data also indicated that there was no measurable dependence of foam strut/pore size on neutron transmission using the experimental setup in this study.

Equation 27. $y = -0.0648x + 0.9638$

Modeling Neutron Transport Using MCNP

Within this section results of neutron transport modeling through TaC foams utilizing MCNP software will be discussed. Results from modeling runs will be compared to the corresponding experimental neutron transmission measurements performed on the foams.

Neutron transmission data from experimentally measured and modeled TaC/RVC foams are shown in Figure 47. The red bars represent experimentally obtained data, while the blue bars represent MCNP modeling data. The neutron transmission ratio for each specimen is relative to baseline neutron transmission. The error bars on the experimental data represent +/- 1 standard deviation from the mean. The neutron transmission data from modeling within Figure 47 is with respect to the portion of the neutron spectrum that would induce beta-decay within indium. It does not reflect transmission for the entire neutron spectrum. The relative error on the MCNP modeling was negligible.

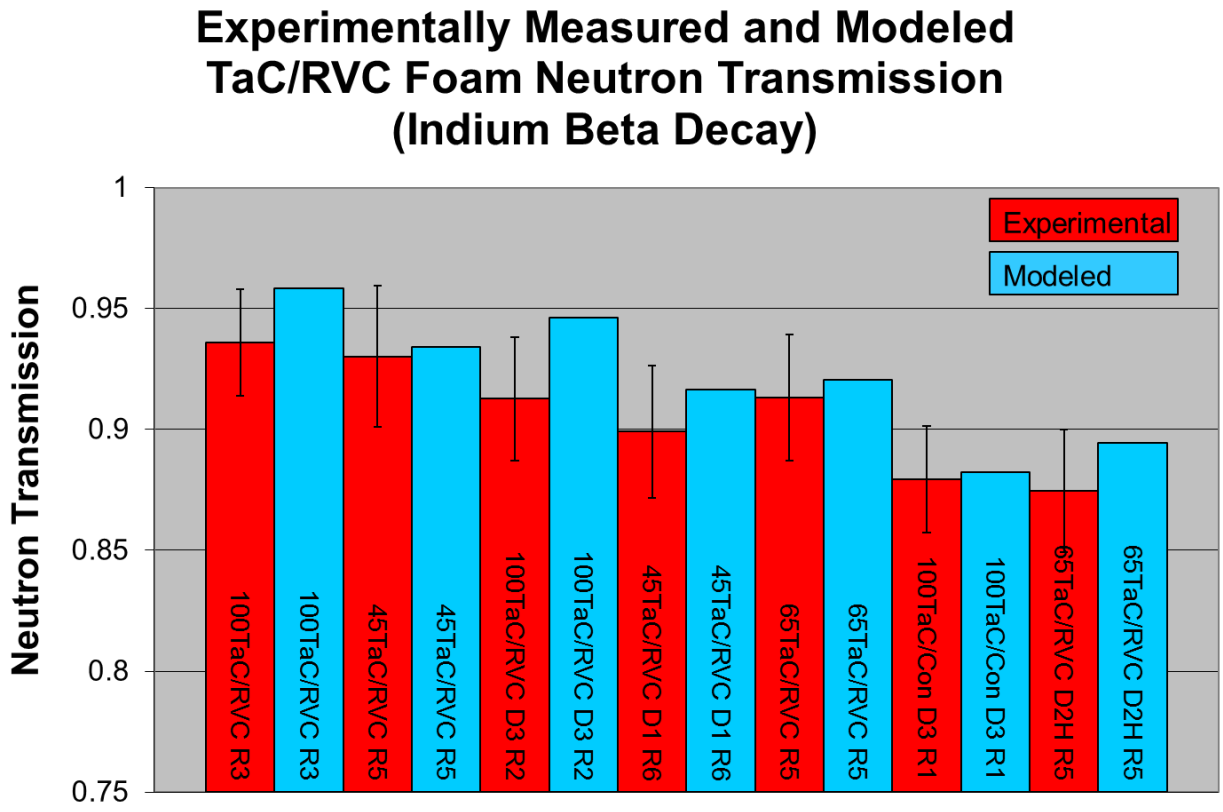

Figure 47. Neutron transmission data for experimentally measured and modeled TaC/RVC foams.

The results from the MCNP modeling runs for the TaC/RVC foams were typically within one standard deviation from the average experimental measurements. MCNP modeling always predicted greater neutron transmission than what was experimentally measured.

Ratios of modeled foam neutron transmission to modeled baseline measurements were plotted against TaC areal density of foams in Figure 48. The same graph was generated for experimental measurements in Figure 46.

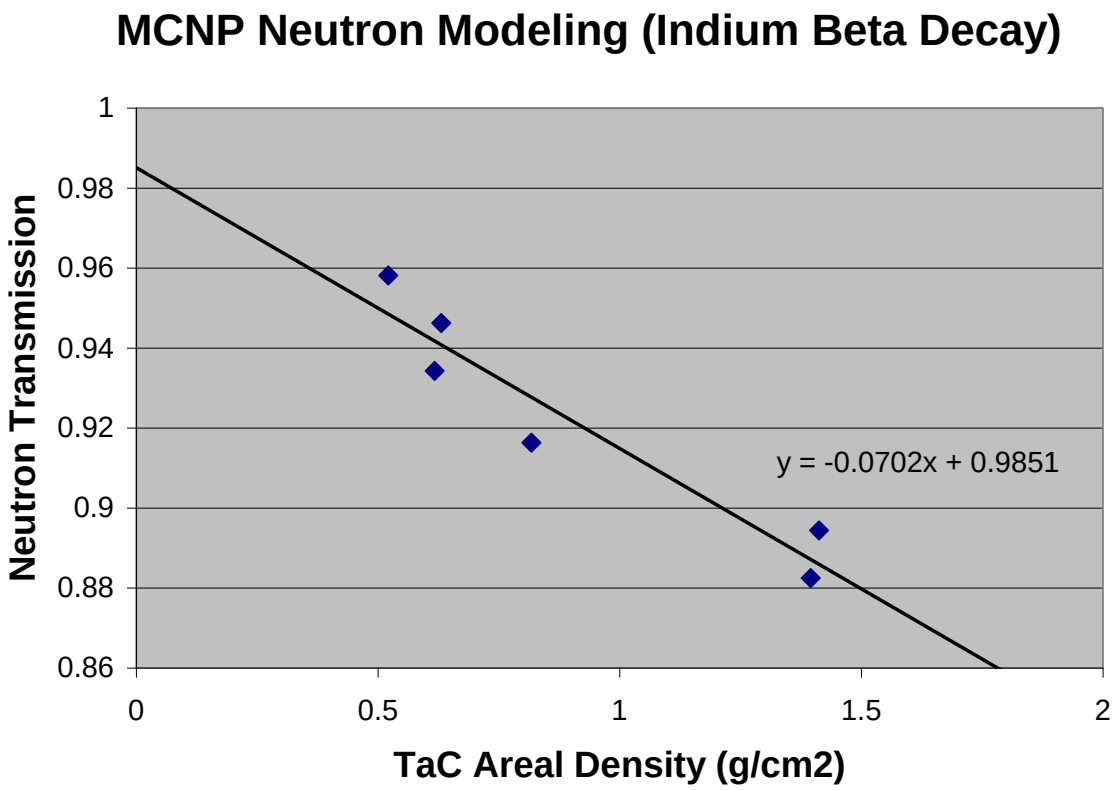

Figure 48. Graph of neutron transmission data derived from MCNP modeling of TaC/RVC foams

Data from Figure 48 indicate that there was a linear relationship between neutron transmission and density of TaC given by Equation 28, where x is the areal density (g/cm^2) of TaC and y is the relative neutron transmission through the foam determined through MCNP modeling.

Equation 28. $y = -0.0702x + 0.9851$

Neutron transmission data from experimentally measured and modeled TaC/PyC/RVC foams are shown in Figure 49. The red bars represent experimentally obtained data, while the blue bars represent MCNP modeling data. The error bars on the experimental data represent +/- 1 standard deviation from the mean. The neutron transmission data from modeling within Figure 49 is with respect to the portion of the neutron spectrum that would induce beta-decay within indium. It

does not reflect transmission for the entire neutron spectrum. The relative error on the MCNP modeling was negligible.

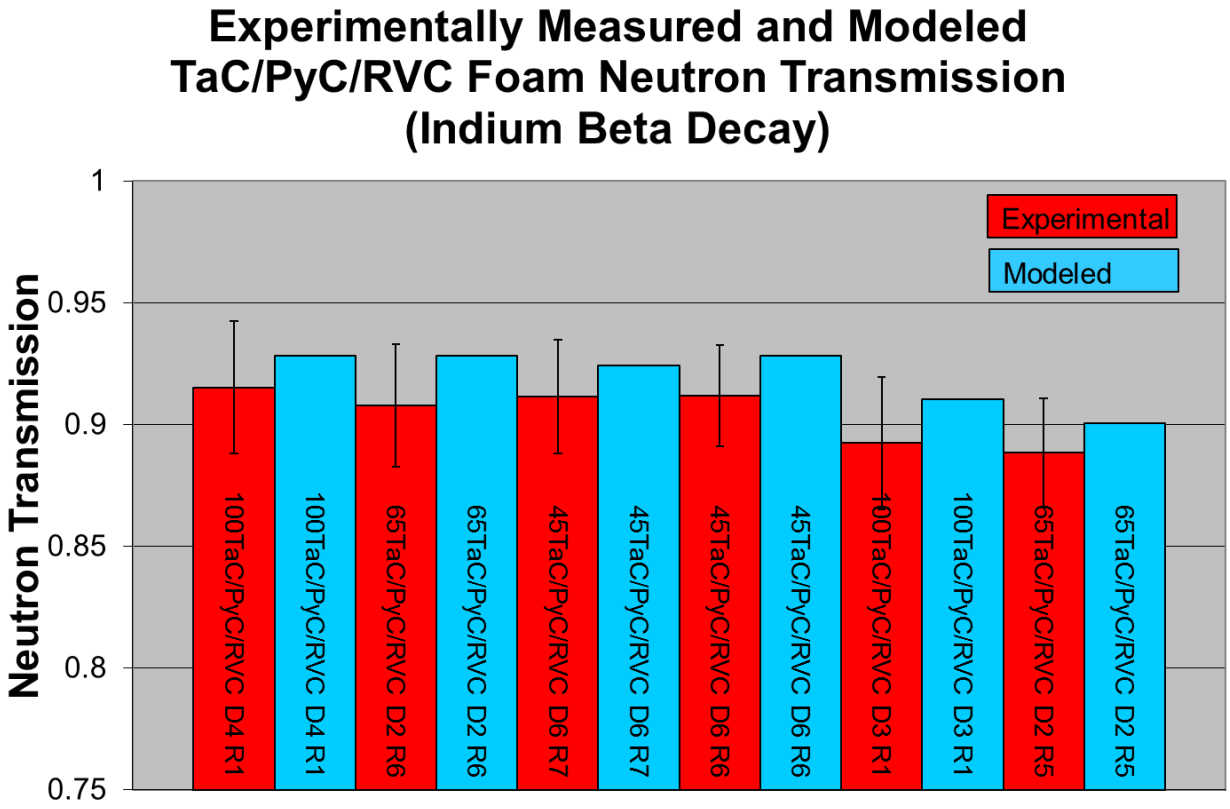

Figure 49. Neutron transmission data for experimentally measured and modeled TaC/PyC/RVC foams

The results from the MCNP modeling runs for the TaC/PyC/RVC foams were typically within one standard deviation from the average experimental measurements. As with the TaC/RVC foams, MCNP modeling always predicted greater neutron transmission than what was experimentally measured. The larger neutron transmission predicted by MCNP could indicate that the foam structure inhibited neutron transmission slightly. However, a higher resolution of neutron transmission measurements would be necessary to draw definite conclusions on whether the structure of foam influences neutron transmission with respect to a bulk specimen.

MCNP modeled neutron transmission for a selected TaC foam sample is compared to that of the baseline neutron energy spectrum emitted by an AmBe neutron source encased in polyethylene in Figure 50 and Figure 51. The selected TaC foam sample had the highest TaC areal density of

any of the specimens, and thus will represent one of the largest decreases in neutron transmission observed for any of the foam specimens. The baseline neutron spectrum outside the polyethylene is shown in blue and the neutron transmission through a selected TaC foam specimen is shown in green. The x-axes of the graphs are plotted with a log scale. The graphs indicate that neutron transmission through the TaC foam was reduced the most at neutron energies between 1E-08 – 1E-07 MeV and 3-10 MeV. There was also reduction of neutron transmission in the vicinity of 1E-05 MeV. Graphs of MCNP modeled neutron spectrums for other specimens can be found in Appendix C.

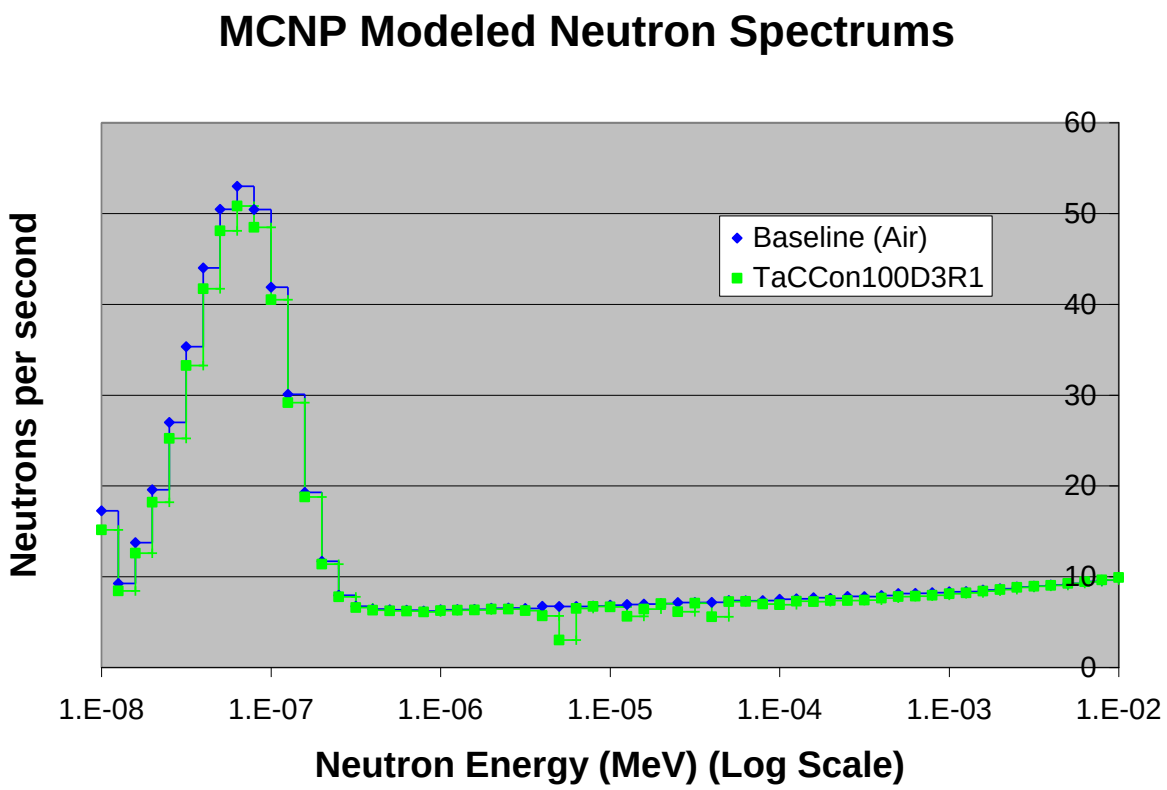

Figure 50. MCNP modeled neutron transmission over the lower portion of the neutron spectrum generated by the AmBe neutron source encased in a polyethylene cylinder.

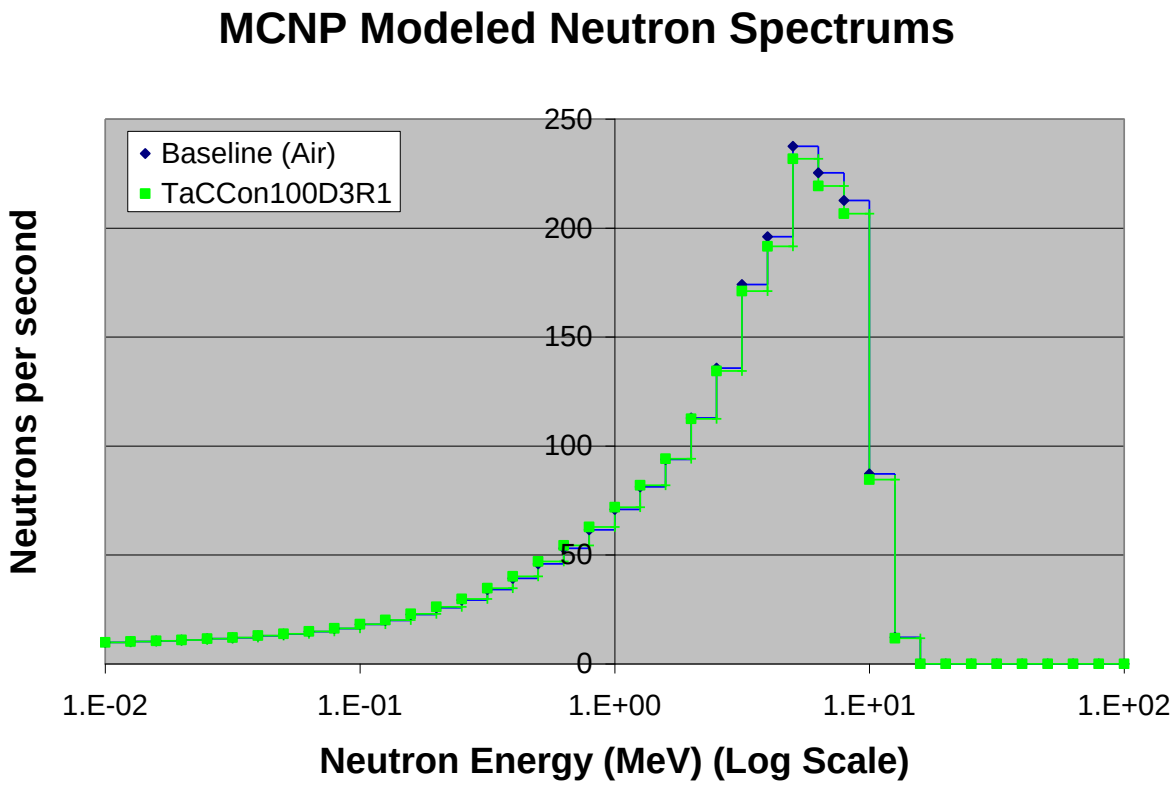

Figure 51. MCNP modeled neutron transmission over the upper portion of the neutron spectrum generated by the AmBe neutron source encased in a polyethylene cylinder.

Influence of Strut/Pore Size, Foam Composition, Foam Density, Thermal Fatigue, and Thermal Shock on the Mechanical Properties of the Foam

In this sub-section the results obtained to understand the influence of strut/pore size, foam composition, foam density, thermal fatigue, and thermal shock on the mechanical properties of TaC foam are discussed. The results of calculations using constitutive equations to predict the mechanical properties of TaC foam are presented. The results from measurements of compressive strength and Young's moduli of TaC foams are also discussed. In addition, the effects of thermal cycling and thermal shock on the microstructural integrity and compressive strength of TaC foams are presented.

Prediction of Mechanical Properties of TaC Foams

Data obtained from dimensional measurements, mass measurements, and pycnometry were used in conjunction with Equation 3 to determine the average relative densities and proportionality

constants for the seven TaC foam types investigated in this study. The results of the calculations are shown in Table XVI.

Table XVI. Relative Density and Calculated Proportionality Constant for TaC Foams

Foam Type	Relative density, ρ_r (%)	Std Dev	Proportionality Constant, C	Std Dev
45 TaC/PyC/RVC	17.3	0.30	2.54	0.04
65 TaC/PyC/RVC	13.8	1.68	2.08	0.25
100 TaC/PyC/RVC A	14.6	0.39	2.66	0.07
100 TaC/PyC/RVC B	19.7	1.38	2.83	0.20
45 TaC/RVC	11.0	0.97	3.13	0.28
65 TaC/RVC	11.7	0.93	2.31	0.18
100 TaC/RVC	9.3	0.51	1.73	0.09

The predicted minimum and maximum compressive strengths for foams composed of pure TaC and pure PyC were calculated using Equation 8 and are shown in Table XVII.

Table XVII. Predicted Upper and Lower Bounds for Compressive Strength of TaC Foams

Foam Type	Average Relative Density	TaC σ_{cs} Minimum (MPa)	TaC σ_{cs} Maximum (MPa)	PyC σ_{cs} Minimum (MPa)	PyC σ_{cs} Maximum (MPa)
45 TaC/PyC/RVC	0.176	4.96	14.04	3.56	7.13
65 TaC/PyC/RVC	0.149	3.87	10.95	2.78	5.56
100 TaC/PyC/RVC A	0.149	3.88	10.98	2.78	5.58
100 TaC/PyC/RVC B	0.210	6.48	18.33	4.65	9.31
45 TaC/RVC	0.113	2.56	7.24	1.83	3.68
65 TaC/RVC	0.111	2.49	7.06	1.79	3.59
100 TaC/RVC	0.091	1.86	5.26	1.33	2.67

Data from Table XVII predict that 100 TaC/PyC/RVC Type B foam will have the highest compressive strength, while 100 TaC/RVC foam will have the lowest. The above calculations are based on the model by *Ashby* [21], which predicts that the relative density of a foam is the primary factor in determining the strength of the foam. The Ashby model deals with single component foams. With the multi-component foams in this study, in addition to the relative

density, it is predicted that the cross-sectional area fraction of PyC and TaC within the struts, coupled with the strut size for each foam type, will determine the strength of the foam.

Since the foams investigated within this study are neither pure TaC or pure PyC, it was expected that the measured compressive strength of the foams would be a combination of the predicted strengths of pure TaC and pure PyC foams. Cross-sectional area fractions of foam struts were used in calculations to estimate modulus of rupture (MOR). The results of calculations for cross-sectional areas and area fractions for foam struts are shown in Table XVIII. The MOR was then used to predict a range of compressive strengths for TaC foams using Equation 8. The results are shown in Table XIX.

Table XVIII. Cross-sectional Areas of Foam Struts

Foam Type	Strut X-sectional Area (μm^2)	RVC Area (μm^2)	PyC Area (μm^2)	TaC Area (μm^2)	RVC Area Ratio	PyC Area Ratio	TaC Area Ratio
45 TaC/PyC/RVC	44402	8450	15312	20640	0.19	0.34	0.46
65 TaC/PyC/RVC	12324.5	2964.5	1740	7620	0.24	0.14	0.62
100 TaC/PyC/RVC A	3784.5	1012.5	728	2044	0.27	0.19	0.54
100 TaC/PyC/RVC B	9248	1352	3648	4248	0.15	0.39	0.46
45 TaC/RVC	19208	6962	-	12246	0.36	-	0.64
65 TaC/RVC	10512.5	4140.5	-	6372	0.39	-	0.61
100 TaC/RVC	2244.5	1104.5	-	1140	0.49	-	0.51

Table XIX. Predicted Minimum and Maximum Modulus of Rupture (MOR) of Foam Struts and Compressive Strength of TaC Foams

Foam Type	Average Relative Density	Minimum Strut MOR (MPa)	Maximum Strut MOR (MPa)	Minimum Strength (MPa)	Maximum Strength (MPa)
45 TaC/PyC/RVC	0.176	239	609	3.53	8.99
65 TaC/PyC/RVC	0.149	242	656	2.78	7.56
100 TaC/PyC/RVC A	0.149	228	607	2.63	7.00
100 TaC/PyC/RVC B	0.210	249	627	4.81	12.09
45 TaC/RVC	0.113	214	606	1.63	4.61
65 TaC/RVC	0.111	204	576	1.51	4.28
100 TaC/RVC	0.091	171	483	0.94	2.67

Foam strut cross-sectional area fractions were used to make predictions for the Young's modulus of foam struts and foams using Equation 7. The Young's modulus predictions are shown in Table XX, where E_s represents the Young's modulus of a strut, and E_f represents the Young's modulus of the foam.

Table XX. Estimated Upper Limits on Young's Modulus of Foam Struts and Foams

Foam Type	Lower-Upperbound E_s (Gpa)	Upper-Upperbound E_s (Gpa)	Lower-Upperbound E_f (Gpa)	Upper-Upperbound E_f (Gpa)
45 TaC/PyC/RVC	147	275	4.5	8.5
65 TaC/PyC/RVC	186	356	4.1	7.9
100 TaC/PyC/RVC A	166	314	3.7	7.0
100 TaC/PyC/RVC B	145	272	6.4	12.0
45 TaC/RVC	190	366	2.4	4.7
65 TaC/RVC	182	349	2.3	4.3
100 TaC/RVC	157	296	1.3	2.5

The calculations from Table XX predicted that foams with a PyC layer would have a higher Young's modulus than TaC/RVC foams. The calculations predicted that 100 TaC/PyC/RVC B foams would have the highest Young's modulus, which would not exceed 12 GPa. The lowest predicted Young's modulus was for 100 TaC/RVC foams, which would not exceed 2.5 GPa.

Thermo-mechanical Properties of TaC Foams

Selected micrographs from baseline and thermally cycled specimens are discussed subsequently to illustrate common micro-cracking features observed among various foam specimens. Extensive micrographs for each foam pore density and foam composition showing the microstructures of both baseline and thermally cycled TaC specimens can be found in Appendix D.

Figure 52 and Figure 53 are micrographs of baseline and thermally cycled 45 ppi TaC/PyC/RVC foam specimens, respectively. Extensive microcracking was observed in all the thermally cycled

45 ppi TaC/PyC/RVC specimens. Micro-cracking tended to be concentrated around the vertices of foam cells (intersections of foam struts).

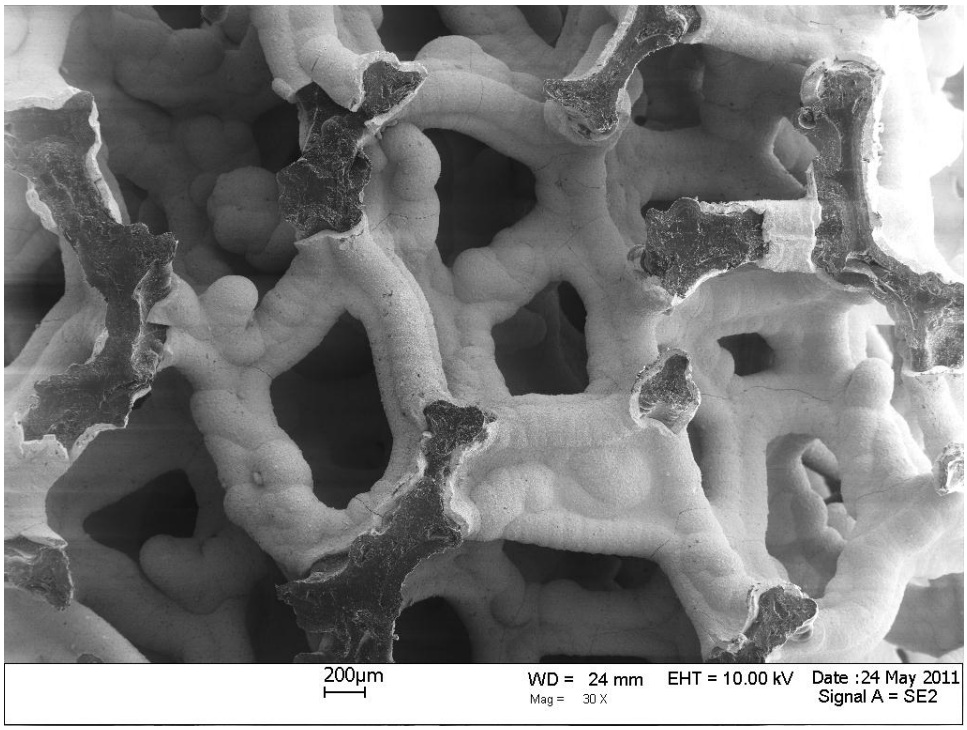

Figure 52. SEM micrograph of the microstructure of a baseline 45 ppi TaC/PyC/RVC foam specimen.

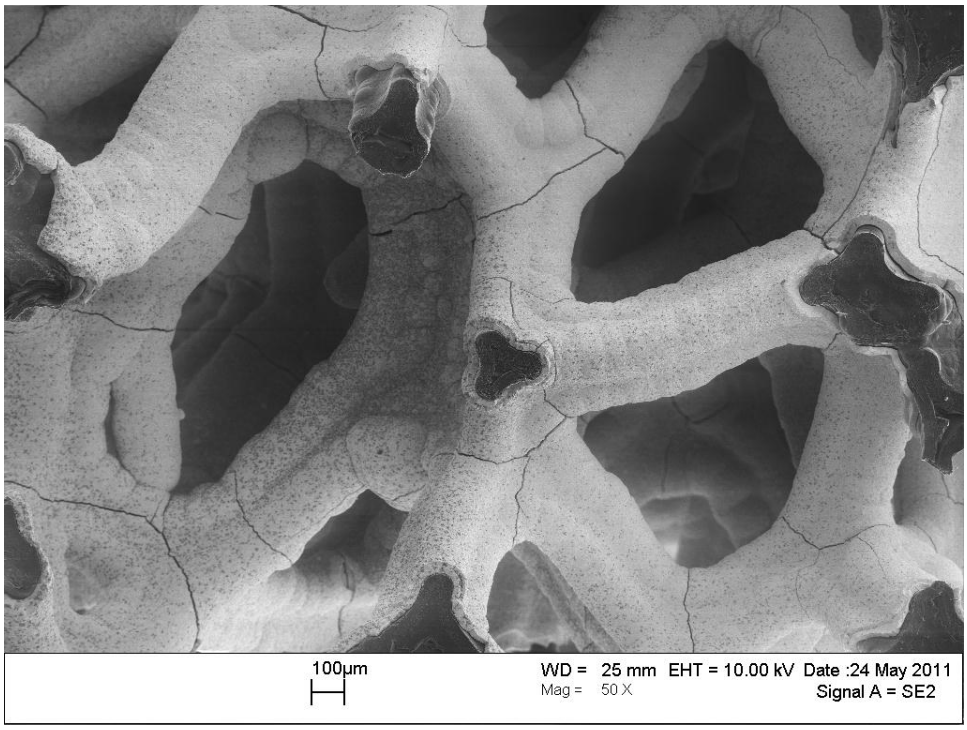

Figure 53. SEM micrograph of the microstructure of a 45 ppi TaC/PyC/RVC foam specimen after thermal cycling.

Figure 54 and Figure 55 show the microstructure of baseline and thermally cycled 65 ppi TaC/PyC/RVC foam specimens, respectively. As with the 45 ppi specimens, extensive microcracking was observed in the 65 ppi thermally cycled specimens. The micro-cracks in the 65 ppi TaC/PyC/RVC foams tended to run axially along the struts and appeared to propagate from the end points on the triangular struts.

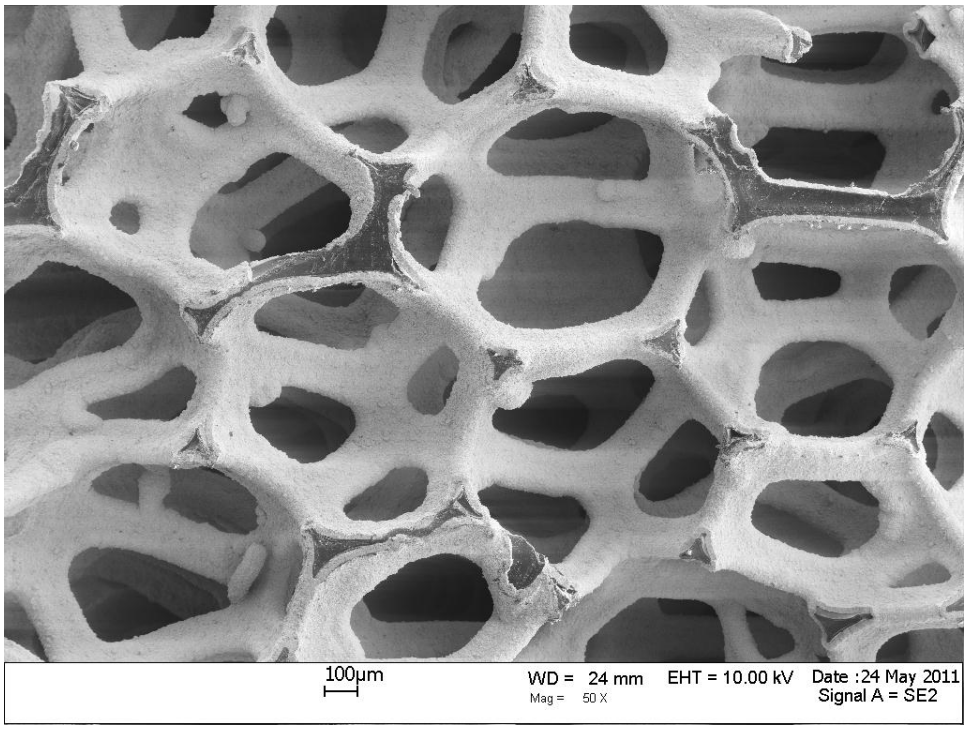

Figure 54. SEM micrograph of the microstructure of a baseline 65 ppi TaC/PyC/RVC foam specimen.

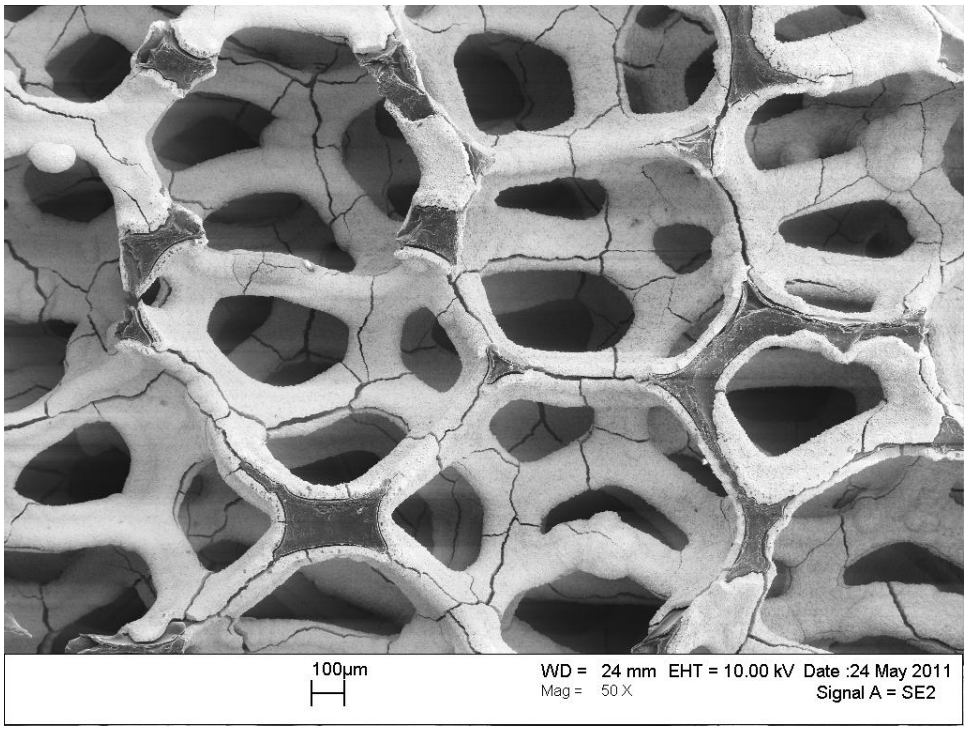

Figure 55. SEM micrograph of the microstructure of a 65 ppi TaC/PyC/RVC foam specimen after thermal cycling.

Figure 56 and Figure 57 show baseline and thermally cycled strut cross-sections of 65 ppi TaC/PyC/RVC foams, while Figure 58 and Figure 59 show baseline and thermally cycled strut cross-sections of 100 ppi foams, respectively. Within all pore densities of TaC/PyC/RVC foams it was common to observe debonding between the TaC/PyC interface after thermal cycling. No significant debonding was observed along the PyC/RVC interface.

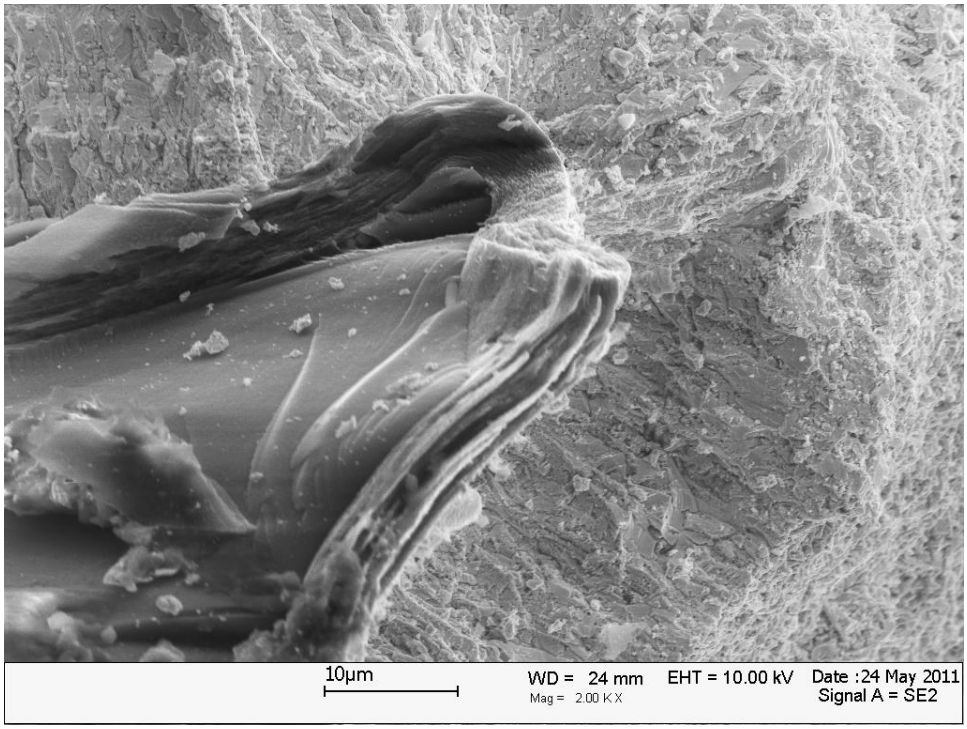

Figure 56. SEM micrograph of the cross-section of a baseline 65 ppi TaC/PyC/RVC foam strut.

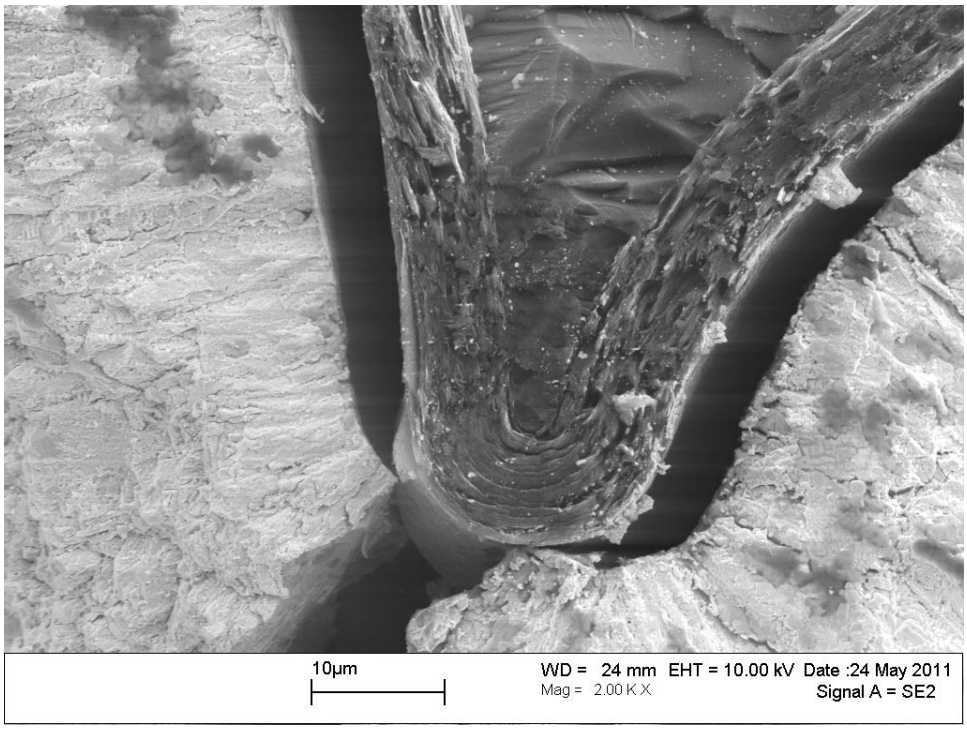

Figure 57. SEM micrograph of the cross-section of a 65 ppi TaC/PyC/RVC foam strut after thermal cycling.

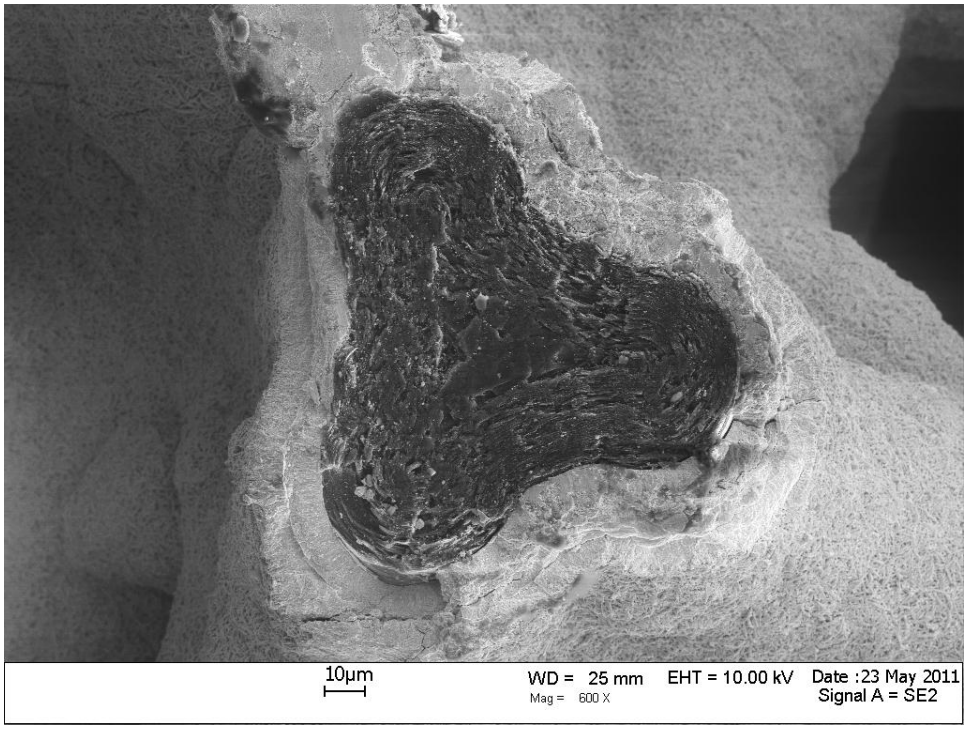

Figure 58. SEM micrograph of a cross-section of a baseline 100 ppi TaC/PyC/RVC foam strut.

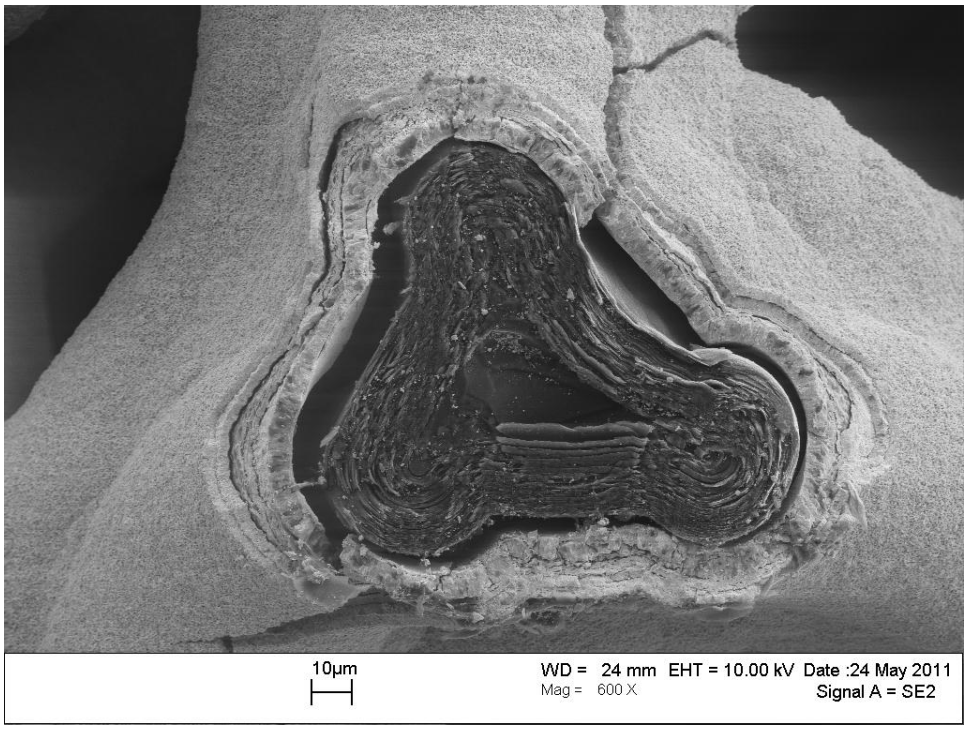

Figure 59. SEM micrograph of the cross-section of a 100 ppi TaC/PyC/RVC foam strut after thermal cycling.

Figure 60 and Figure 61 show cross-sections of 65 ppi TaC/RVC foam struts for both baseline and thermally cycled specimens, respectively. Debonding was observed along the TaC/RVC interface in many areas of thermally cycled TaC/RVC specimens. However, the degree of debonding was less severe than that of TaC/PyC/RVC specimens. The extent of micro-cracking following thermal cycling was less in TaC/RVC foams than in TaC/PyC/RVC foams. The thickness of the micro-cracks present in all pore densities of TaC/RVC foam after thermal cycling tended to be less than the thickness of micro-cracks present in TaC/PyC/RVC foams.

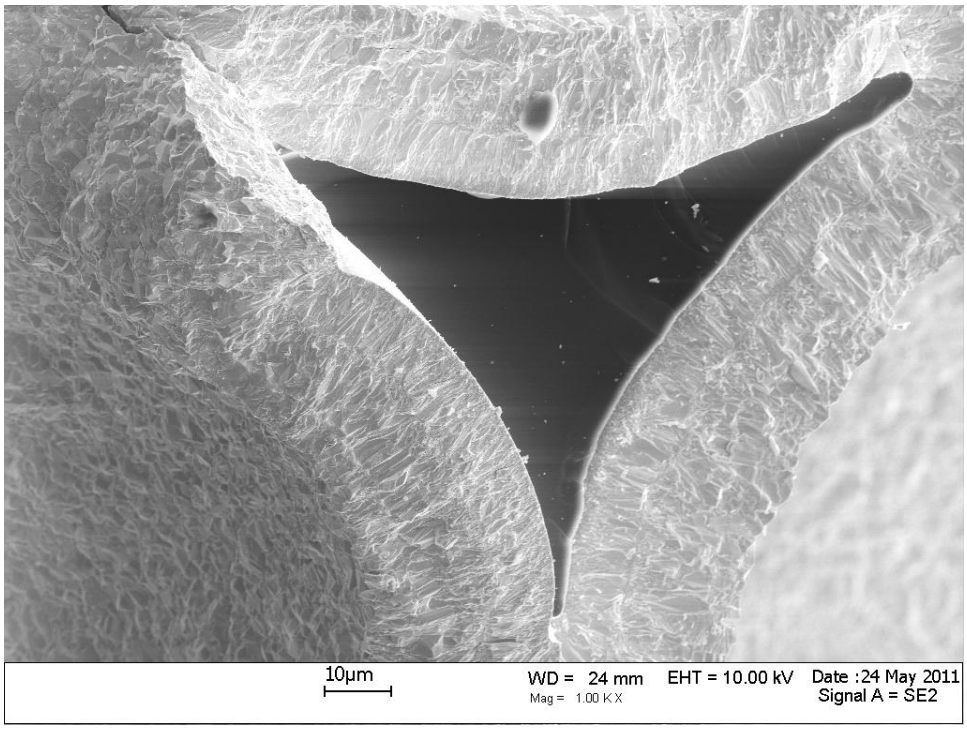

Figure 60. SEM micrograph of the cross-section of a baseline 65 ppi TaC/RVC foam strut.

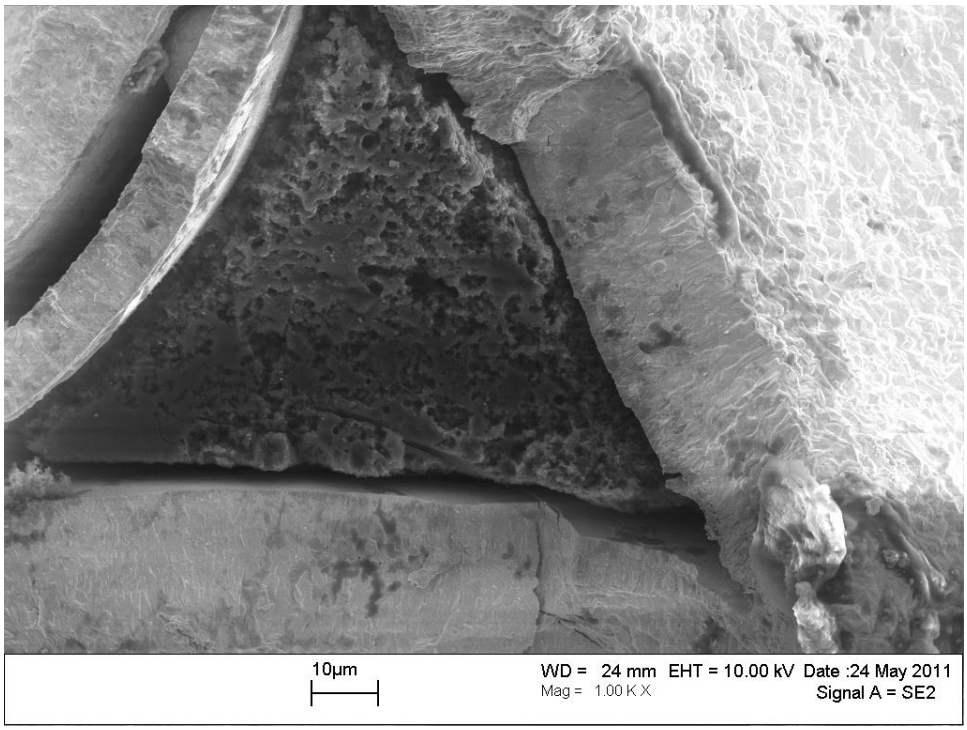

Figure 61. SEM micrograph of the cross-section of a 65 ppi TaC/RVC foam strut after thermal cycling.

Figure 62 and Figure 63 show the microstructure of baseline and thermally cycled 100 ppi TaC/RVC foams, respectively. The 100 ppi TaC/RVC foams appeared to have less micro-cracking after thermal cycling than the other pore densities of TaC/RVC, and the least of any of the TaC/PyC/RVC foams.

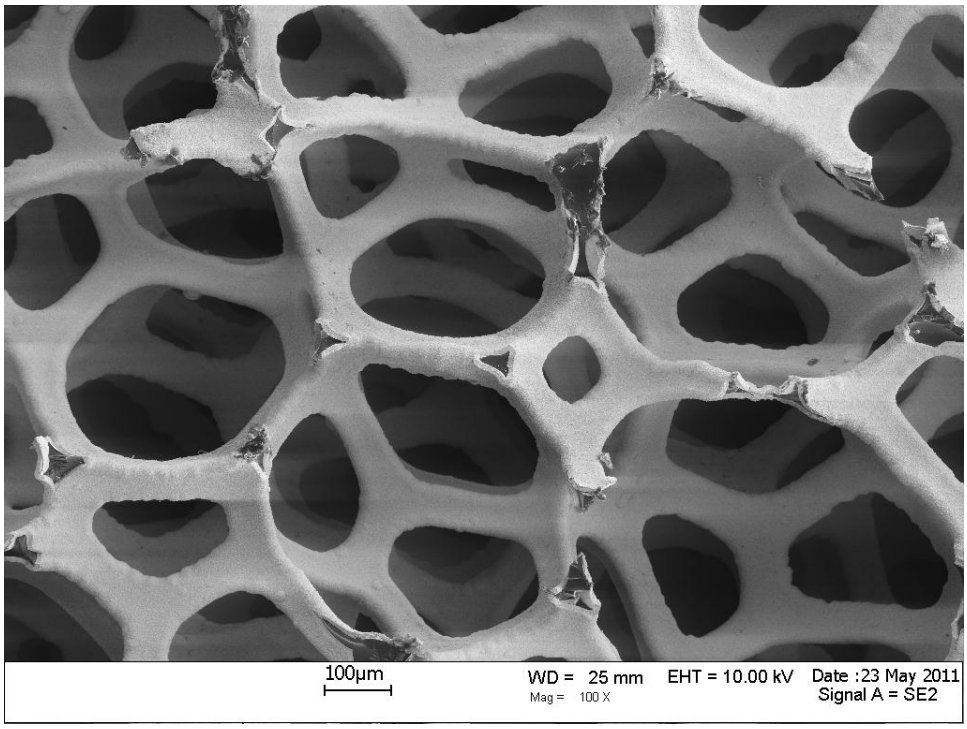

Figure 62. SEM micrograph of the microstructure of a baseline 100 ppi TaC/RVC foam specimen.

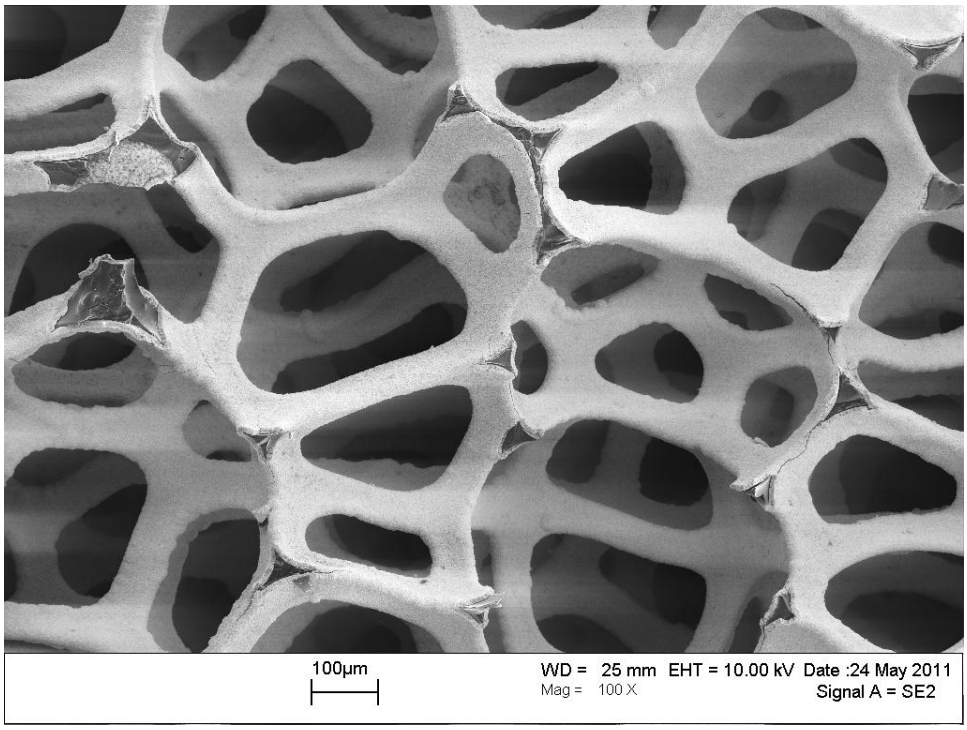

Figure 63. SEM micrograph of the microstructure of a 100 ppi TaC/RVC foam specimen after thermal cycling.

Figure 64 and Figure 65 show cross-sections of foam struts for baseline and thermally cycled 100 ppi TaC/RVC foams. The propagation of cracks from the points at the edges of the triangular cross-section of the foam strut can be observed in Figure 65. The axial crack propagation shown in Figure 65 tended to be present in 65 ppi and 100 ppi TaC/RVC and TaC/PyC/RVC foams, but was not as prevalent in the 45 ppi foams, particularly in the TaC/PyC/RVC.

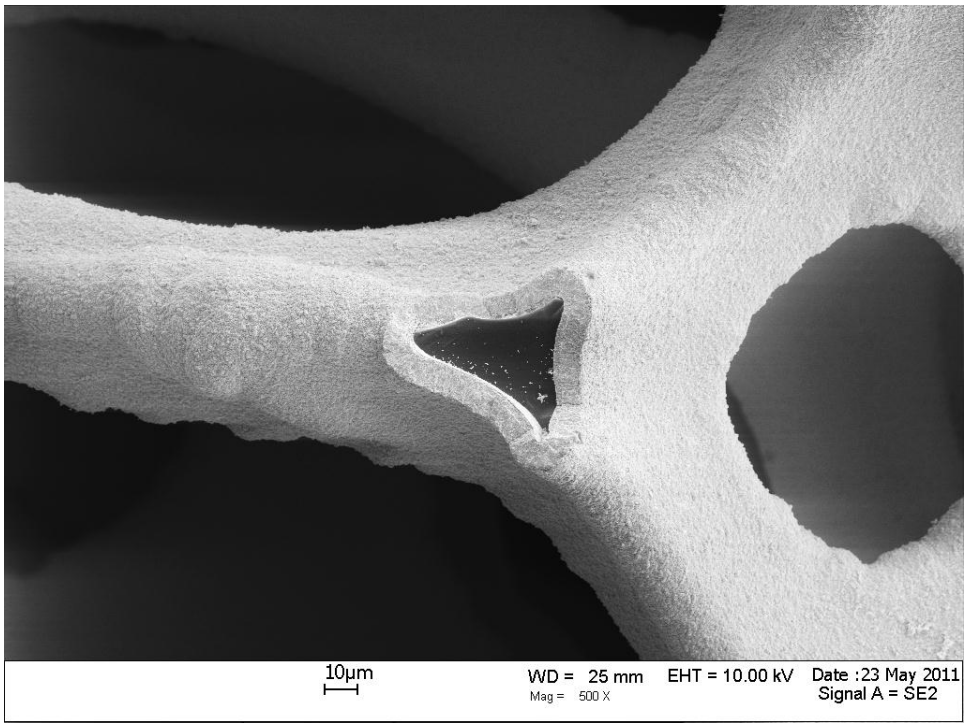

Figure 64. SEM micrograph of the cross-section of a baseline 100 ppi TaC/RVC foam strut.

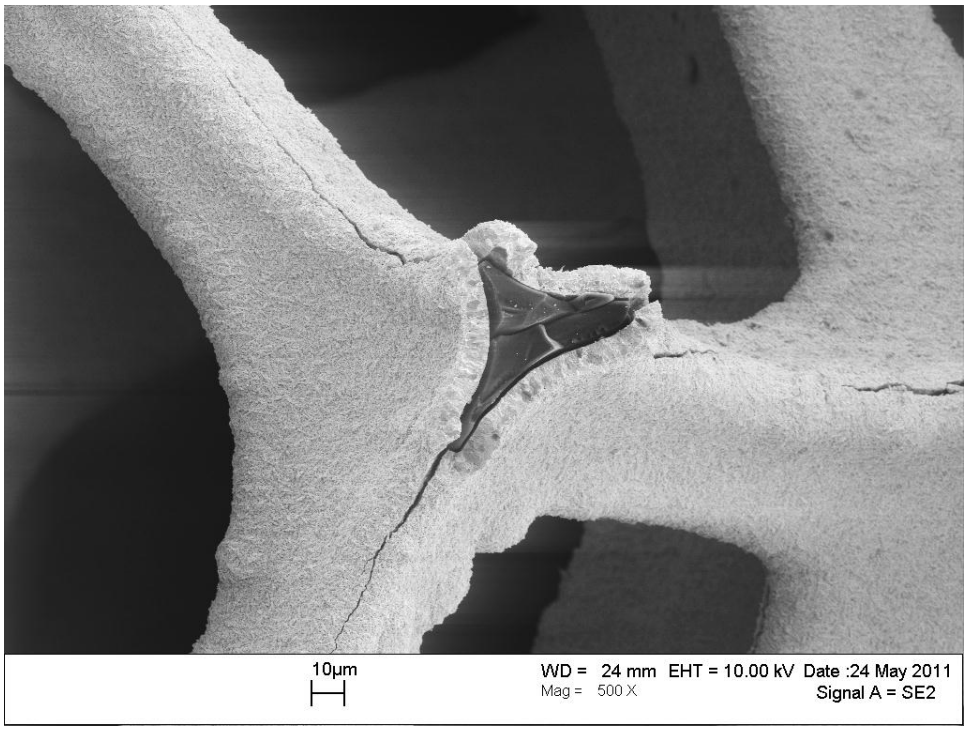

Figure 65. SEM micrograph of the cross-section of a 100 ppi TaC/RVC foam strut after thermal cycling.

Measurements of the change in mass of TaC specimens exposed to thermal cycling are shown in Appendix E. A decrease of a few thousandths of a gram was observed in most specimens. Microstructural analysis of TaC/PyC/RVC and TaC/RVC foam specimens exposed to thermal shock did not reveal any observable micro-cracking or changes in microstructure. Since no differences in the microstructure of thermally shocked foams were observed from baseline microstructures, no micrographs of the thermally shocked foams are presented.

The compressive strength of baseline, thermally cycled, and thermally shocked TaC/PyC/RVC and TaC/RVC foams are shown in Figure 66. The ordering of the TaC foams in the legend from top to bottom correspond to the bars in the graph from left to right. The prefix number for each specimen represents the pore density, while the suffix *TC* represents samples that were thermally cycled, and the suffix *TS* represents samples that were thermally shocked. No suffix indicates baseline specimens. The error bars represent +/- 1 standard deviation from the mean.

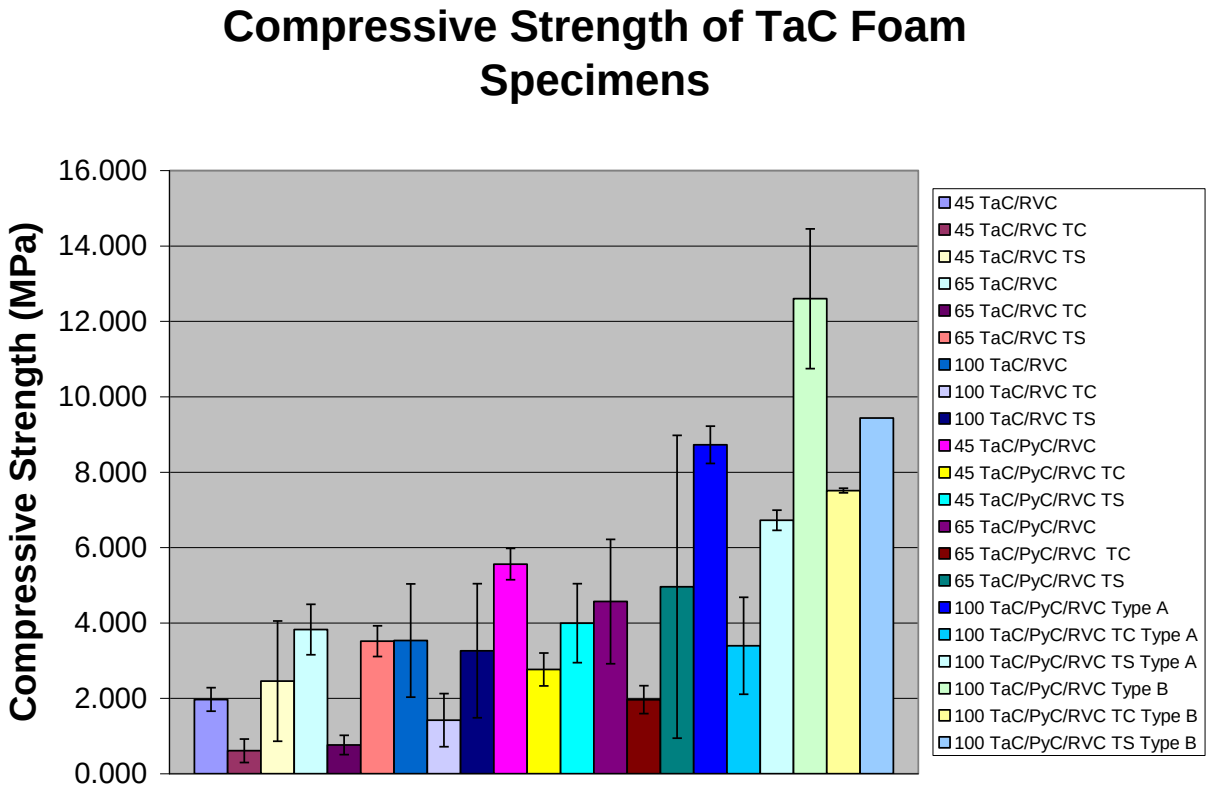

Figure 66. Compressive strength of baseline, thermally cycled (TC), and thermally shocked (TS) foams.

The compressive strength of the TaC foams generally increased with a decrease in foam strut thickness for both TaC/RVC and TaC/PyC/RVC foams. The exception to this was the 65 ppi pore density for both foam compositions. In the TaC/RVC foams, the 65 ppi foams had an average strength that was slightly higher than the 100 ppi foams. The average strength of the 65 ppi TaC/PyC/RVC foams was lower than the strength of the 45 ppi foams. The higher strength is likely the result of the lower probability of an existing flaw being present of a critical size to facilitate crack propagation within the smaller strut.

The PyC coating in TaC/PyC/RVC foams was observed to increase strength over baseline, thermally cycled, and thermally shocked TaC/RVC foams with the same pore density. The thicker PyC coating present on the 100 ppi TaC/PyC/RVC Type B foams increased the strength when compared with the 100 ppi Type A foams with a thinner PyC coating. The laminar structure of the PyC layer, shown in Figure 67, is thought to have increased the energy required to propagate a crack through the foam strut, thereby increasing the strength of the foam.

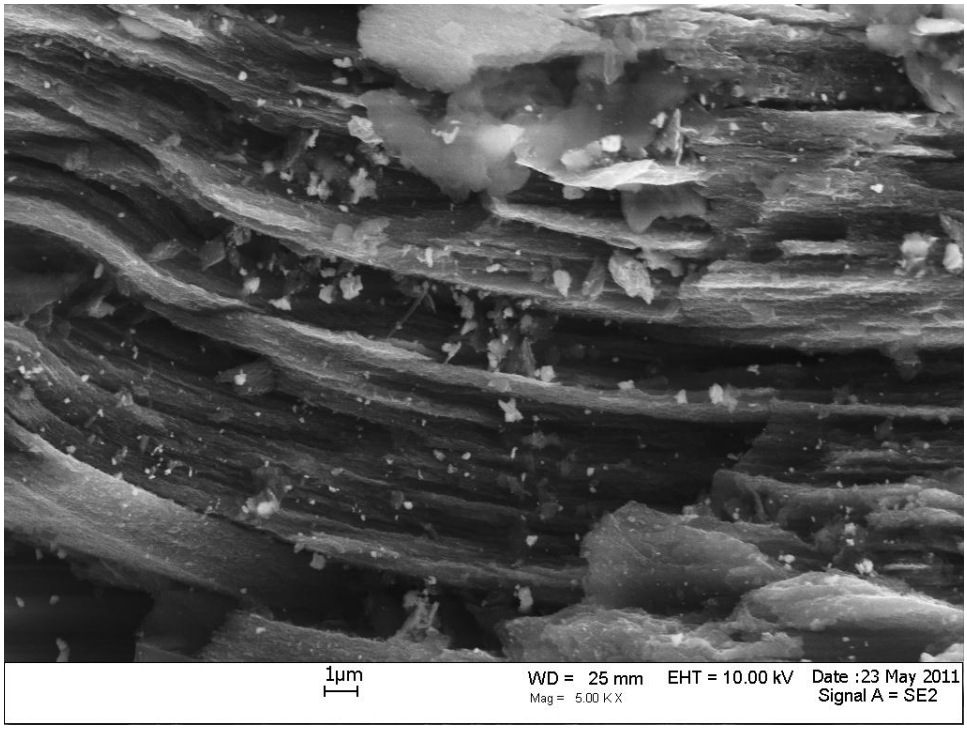

Figure 67. SEM micrograph of a cross-section of the PyC coating in a 100 ppi TaC/PyC/RVC foam strut.

Thermally shocked TaC/RVC and TaC/PyC/RVC foams had significantly higher compressive strengths than thermally cycled foams. Thermally shocked foams typically had strengths within one standard deviation of the mean baseline foam strength. The main exception was thermally shocked 100 ppi TaC/PyC/RVC foams, which had strengths below one standard deviation from the mean baseline strength. However, it is worth noting that the dataset for thermally shocked 100 ppi Type B foams only consisted of one specimen.

T-tests were performed on compressive strength datasets using Equation 24 and Equation 25. The parameters and results of the t-tests are shown numerically in Table XXI-Table XXV. The column, *df*, refers to degrees of freedom. Figure 68-Figure 72 show the results of t-tests performed on compressive strength datasets in a graphical format. The suffixes *TC* and *TS* refer to thermal cycling and thermal shock, respectively. The suffixes *A* and *B* are used only with the 100 ppi TaC/PyC/RVC foams and denote the type of 100 ppi foam being analyzed. When the suffix is enclosed in parentheses, the suffix applies to both datasets. If there are no parentheses the suffix only applies to the dataset that it immediately follows.

Table XXI and Figure 68 show the results of t-tests performed to determine the statistical significance of differences in compressive strength observed between TaC/RVC and TaC/PyC/RVC foams with the same nominal pore density (ppi).

Table XXI. Table of t-test Parameters for Compressive Strength Comparison of TaC/RVC and TaC/PyC/RVC foams.

Datasets	σ_{diff}	t	df	Confidence (%)
45 RVC - 45 PyC	0.250	14.385	7	99.95
65 RVC - 65 PyC	0.810	0.916	7	75
100 RVC - 100 PyC	0.757	6.856	5	99.9
100 RVC - 100 PyC B	1.263	7.178	6	99.95
45 RVC - 45 PyC (TC)	0.268	8.034	6	99.95
65 RVC - 65 PyC (TC)	0.260	4.613	4	99.5
100 RVC - 100 PyC A (TC)	0.977	2.020	4	90
100 RVC - 100 PyC B (TC)	0.356	17.116	4	99.95
45 RVC - 45 PyC (TS)	1.103	1.396	4	85
65 RVC - 65 PyC (TS)	2.330	0.620	4	50
100 RVC - 100 PyC A (TS)	1.043	3.316	3	97.5
100 RVC - 100 PyC B (TS)	1.026	6.018	2	97.5

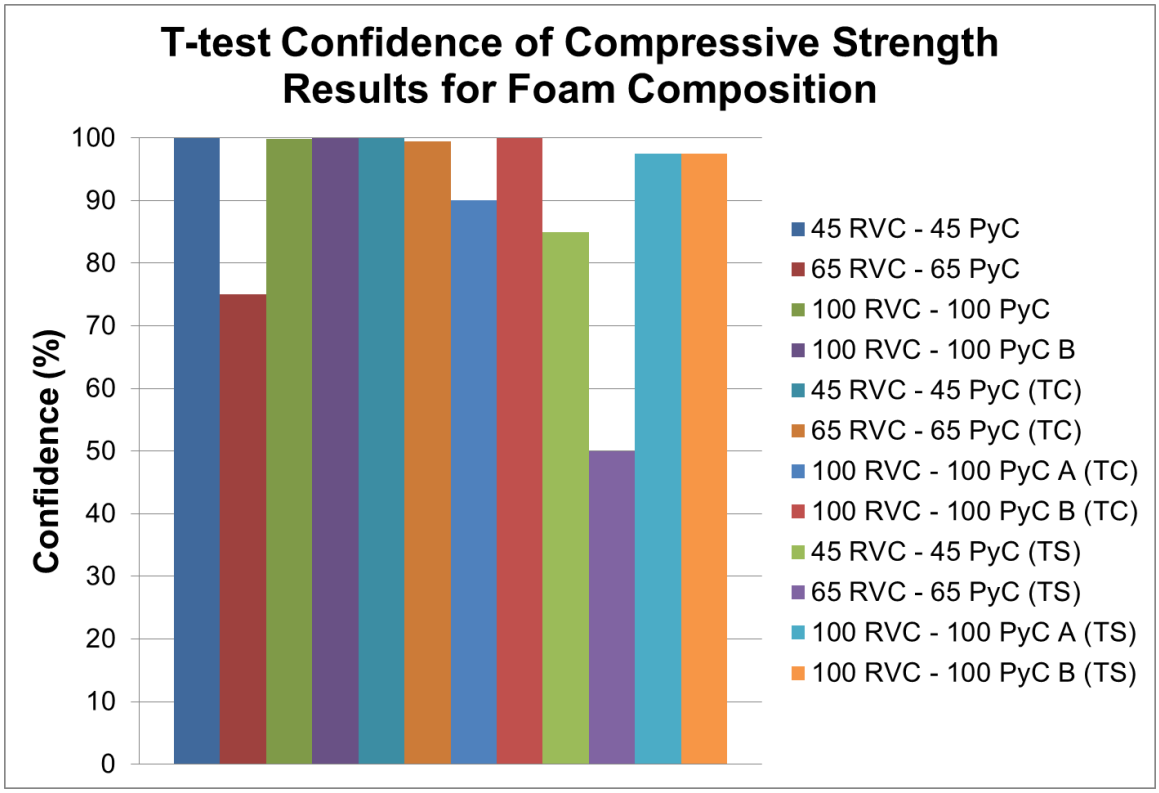

Figure 68. Chart of t-test confidence of compressive strength results for TaC/RVC and TaC/PyC/RVC foams.

Within Table XXI and Figure 68, statistical confidences of at least 90% were observed for all dataset comparisons except baseline 65 ppi foams, thermally shocked 45 ppi foams, and thermally shocked 65 ppi foams. The results indicate that there is over a 90% probability that the presence of a pyrolytic carbon layer in TaC/PyC/RVC foams increased the compressive strength over TaC/RVC foams in nine of the twelve datasets.

Table XXII and Figure 69 show the results of t-tests performed to determine the statistical significance of differences in compressive strength observed within TaC/RVC foams of different strut/pore sizes.

Table XXII. Table of t-test Parameters for Compressive Strength Comparison of TaC/RVC Foam Strut/Pore Size

Datasets	σ_{diff}	t	df	Confidence (%)
45 ppi - 65 ppi	0.362	5.125	7	99.9
45 ppi - 100 ppi	0.685	2.278	8	95
65 ppi - 100 ppi	0.750	-0.390	7	50
45 ppi - 65 ppi (TC)	0.216	0.716	5	50
45 ppi - 100 ppi (TC)	0.386	2.100	6	95
65 ppi - 100 ppi (TC)	0.383	1.714	5	90
45 ppi - 65 ppi (TS)	0.951	1.114	4	80
45 ppi - 100 ppi (TS)	1.379	0.584	4	50
65 ppi - 100 ppi (TS)	1.053	-0.241	4	50

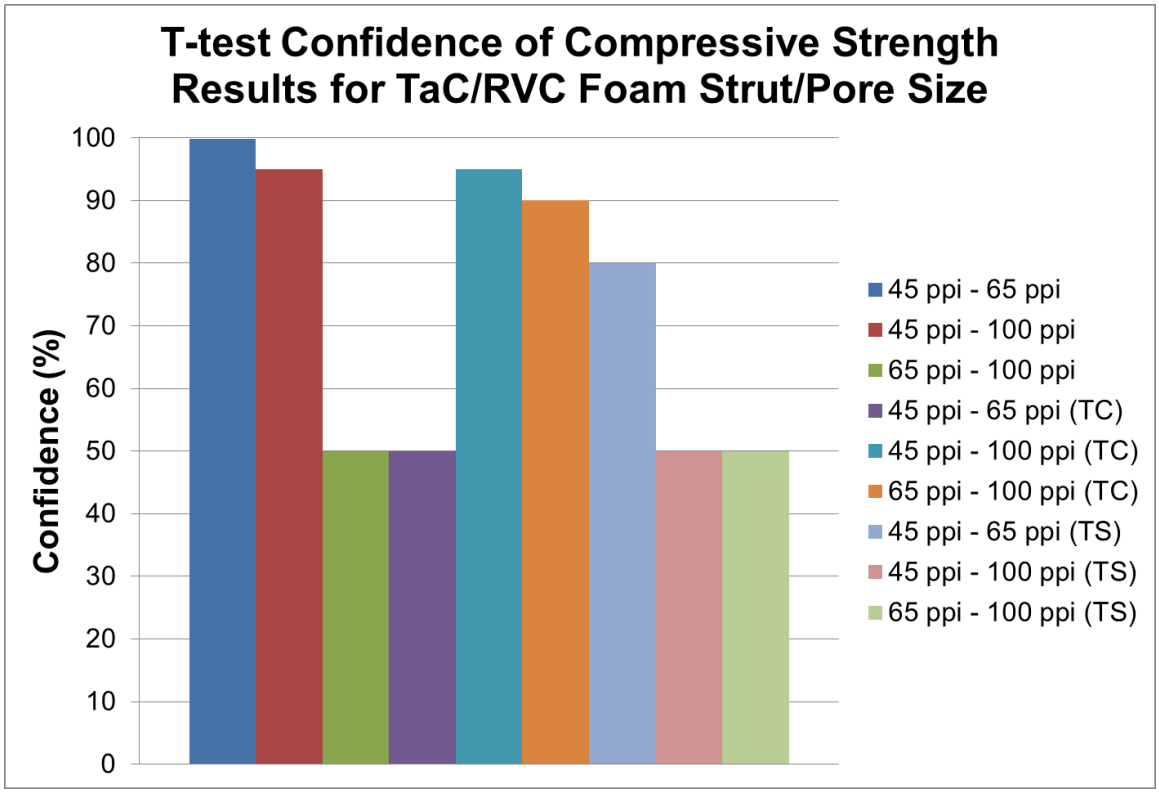

Figure 69. Chart of t-test confidence of compressive strength results for TaC/RVC foam strut/pore size.

Within Table XXII and Figure 69 statistical confidences of at least 90% were observed in comparisons of baseline 45 ppi - 65 ppi and 45 ppi - 100 ppi TaC/RVC foams, as well as thermally cycled 45 ppi - 100 ppi and 65 ppi - 100 ppi TaC/RVC foams. The results indicate that there is over a 90% probability that foam strut/pore size influences the compressive strength for four of the nine TaC/RVC foam datasets.

Table XXIII and Figure 70 show the results of t-tests performed to determine the statistical significance of differences in compressive strength observed within TaC/PyC/RVC foams of different strut/pore sizes.

Table XXIII. Table of t-test Parameters for Compressive Strength Comparison of TaC/PyC/RVC Foam Strut/Pore Size

Datasets	σ_{diff}	t	df	Confidence (%)
45 ppi - 65 ppi	0.766	-1.296	7	85
45 ppi - 100 ppi A	0.408	7.761	4	99.9
65 ppi - 100 ppi A	0.817	-5.089	5	99.5
45 ppi - 100 ppi B	1.090	-6.457	5	99.9
65 ppi - 100 ppi B	1.300	-6.179	6	99.95
45 ppi - 65 ppi (TC)	0.305	-2.627	5	97.5
45 ppi - 100 ppi A (TC)	0.936	-0.671	4	50
65 ppi - 100 ppi A (TC)	0.935	-1.529	3	85
45 ppi - 100 ppi B (TC)	0.222	-21.343	4	99.95
65 ppi - 100 ppi B (TC)	0.218	-25.480	3	99.95
45 ppi - 65 ppi (TS)	2.396	-0.403	4	50
45 ppi - 100 ppi A (TS)	0.634	-4.300	3	97.5
65 ppi - 100 ppi A (TS)	2.325	-0.757	3	50
45 ppi - 100 ppi B (TS)	0.605	-8.989	2	99
65 ppi - 100 ppi B (TS)	2.318	-1.931	2	90

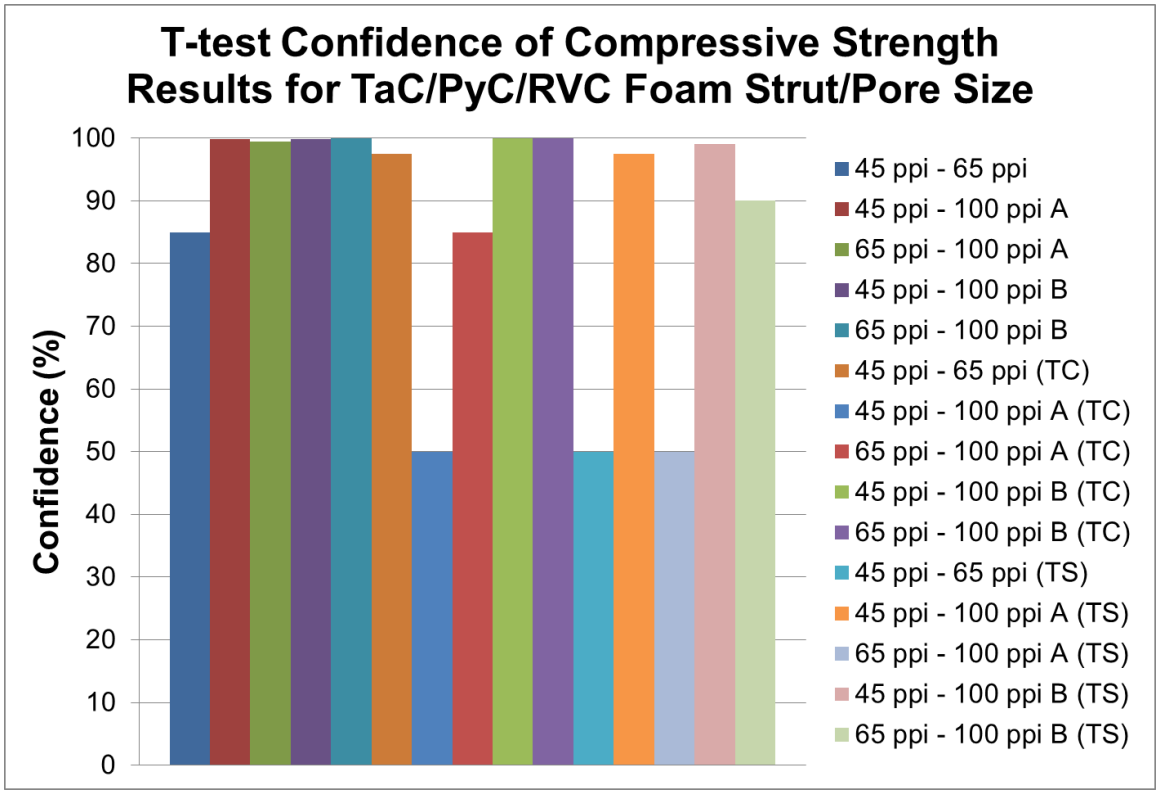

Figure 70. Chart of t-test confidence of compressive strength results for TaC/PyC/RVC foam strut/pore size.

Within Table XXIII and Figure 70 statistical confidences of at least 85% were observed in all comparisons of compressive strength datasets for TaC/PyC/RVC foams except for thermally cycled 65 ppi – 100 ppi A, thermally shocked 45 ppi – 65 ppi, and thermally shocked 65 ppi – 100 ppi A datasets. The results indicate that for the vast majority of TaC/PyC/RVC foam datasets, there is at least an 85% probability that foam strut/pore size influenced the compressive strength of the foam in 12 of the 15 TaC/PyC/RVC datasets.

Table XXIV and Figure 71 show the results of t-tests performed to determine the statistical significance of differences in compressive strength observed within baseline TaC/RVC foams and those exposed to thermal cycling and thermal shock.

Table XXIV. Table of t-test Parameters for Compressive Strength Comparison of TaC/RVC Foams Exposed to Thermal Cycling and Thermal Shock

Datasets	σ_{diff}	t	df	Confidence (%)
45 ppi - 45 ppi TC	0.209	-6.508	7	99.95
45 ppi TC - 45 ppi TS	0.935	1.975	5	90
45 ppi - 45 ppi TS	0.932	-0.521	6	50
65 ppi - 65 ppi TC	0.366	8.368	5	99.95
65 ppi TC - 65 ppi TS	0.278	-9.902	4	99.95
65 ppi - 65 ppi TS	0.408	-0.758	5	50
100 ppi - 100 ppi TC	0.758	2.783	7	97.5
100 ppi TC - 100 ppi TS	1.085	-1.696	5	90
100 ppi - 100 ppi TS	1.226	-0.220	6	50

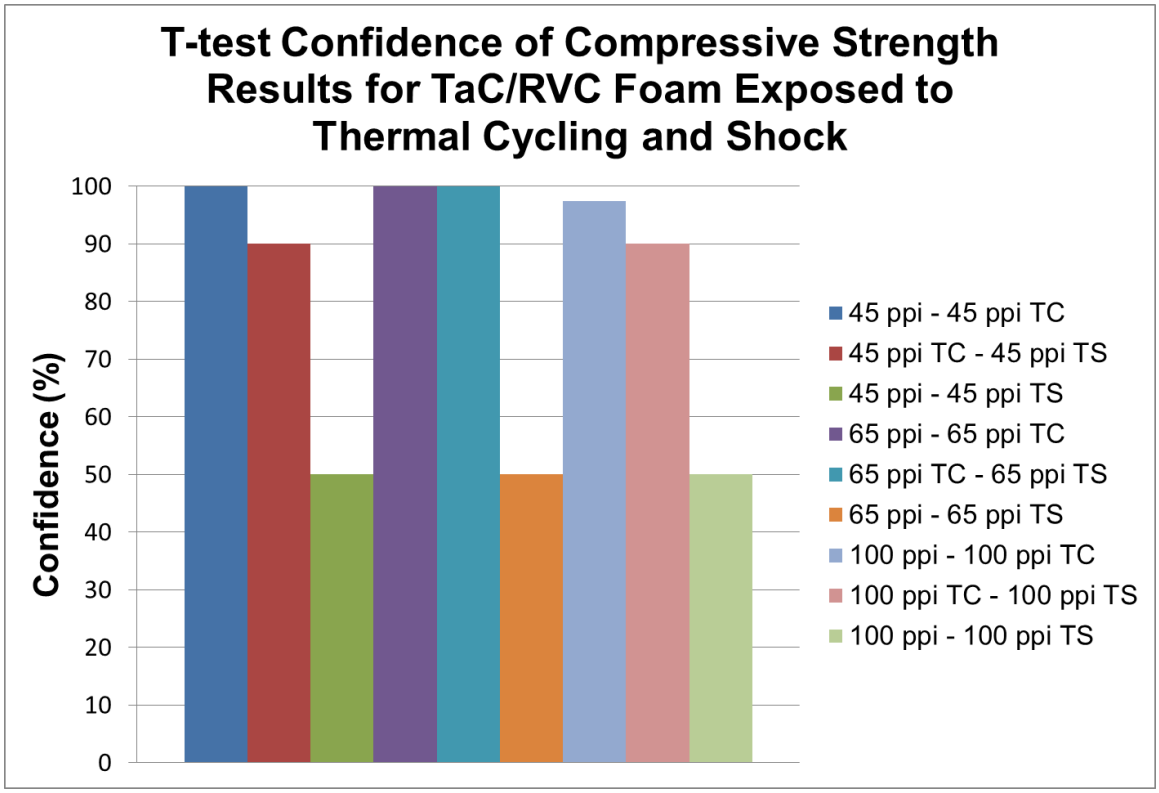

Figure 71. Chart of t-test confidence of compressive strength results for TaC/RVC foams exposed to thermal cycling and thermal shock.

Within Table XXIV and Figure 71 statistical confidences of at least 90% were observed in all TaC/RVC foam dataset comparisons except for 45 ppi – 45 ppi TS, 65 ppi – 65 ppi TS, and 100 ppi – 100 ppi TS. The results indicate that there is at least a 90% probability that thermal cycling decreased the mechanical strength when compared with baseline foams and thermally shocked foams of the same pore density in six of the nine datasets. The results also indicate that there is a

low probability that thermal shock influenced the mechanical strength of the foams when compared with baseline specimens of the same pore density.

Table XXV and Figure 72 show the results of t-tests performed to determine the statistical significance of differences in compressive strength observed within baseline TaC/PyC/RVC foams and those exposed to thermal cycling and thermal shock.

Table XXV. Table of t-test Parameters for Compressive Strength Comparison of TaC/PyC/RVC Foams Exposed to Thermal Cycling and Thermal Shock

Datasets	σ_{diff}	t	df	Confidence (%)
45 ppi - 45 ppi TC	0.301	9.281	6	99.95
45 ppi TC - 45 ppi TS	0.644	-1.908	5	90
45 ppi - 45 ppi TS	0.640	-2.447	5	95
65 ppi - 65 ppi TC	0.768	3.388	6	99
65 ppi TC - 65 ppi TS	0.644	-1.908	4	90
65 ppi - 65 ppi TS	2.432	-0.162	6	50
100 ppi A - 100 ppi A TC	0.976	5.463	2	97.5
100 ppi A TC - 100 ppi A TS	0.930	-3.578	2	95
100 ppi A - 100 ppi A TS	0.399	-5.024	2	97.5
100 ppi B - 100 ppi B TC	1.071	4.751	3	99
100 ppi B TC - 100 ppi B TS	0.043	-45.330	1	99
100 ppi B - 100 ppi B TS	1.070	-2.955	2	95

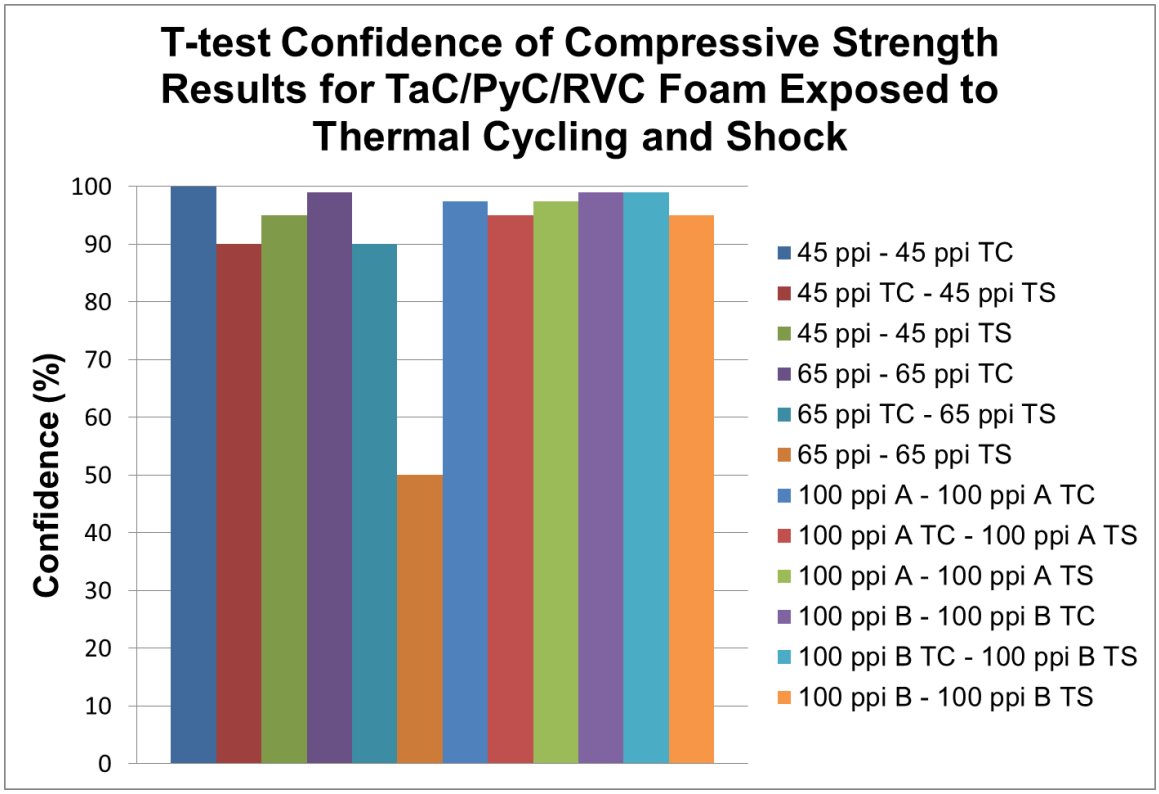

Figure 72. Chart of t-test confidence of compressive strength results for TaC/PyC/RVC foams exposed to thermal cycling and thermal shock.

Within Table XXV and Figure 72 statistical confidences of at least 90% were observed in all comparisons of TaC/PyC/RVC foam datasets except for 65 ppi – 65 ppi TS. The results indicate that within TaC/PyC/RVC foams there is at least a 90% probability that thermal cycling and thermal shock influenced mechanical strength of the foams when compared to baseline specimens of the same pore density within 11 of the 12 datasets.

In order to determine the influence of PyC and TaC coating thickness on compressive strength of the foams, the respective data were plotted in Figure 73. Each pore density of TaC/PyC/RVC consists of two points located at the same compressive strength on the chart. The point that represents the TaC coating thickness is red, while the point that represents the PyC coating thickness is green. Each pore density of TaC/RVC foams consists of one point, which is blue and represents the TaC coating thickness.

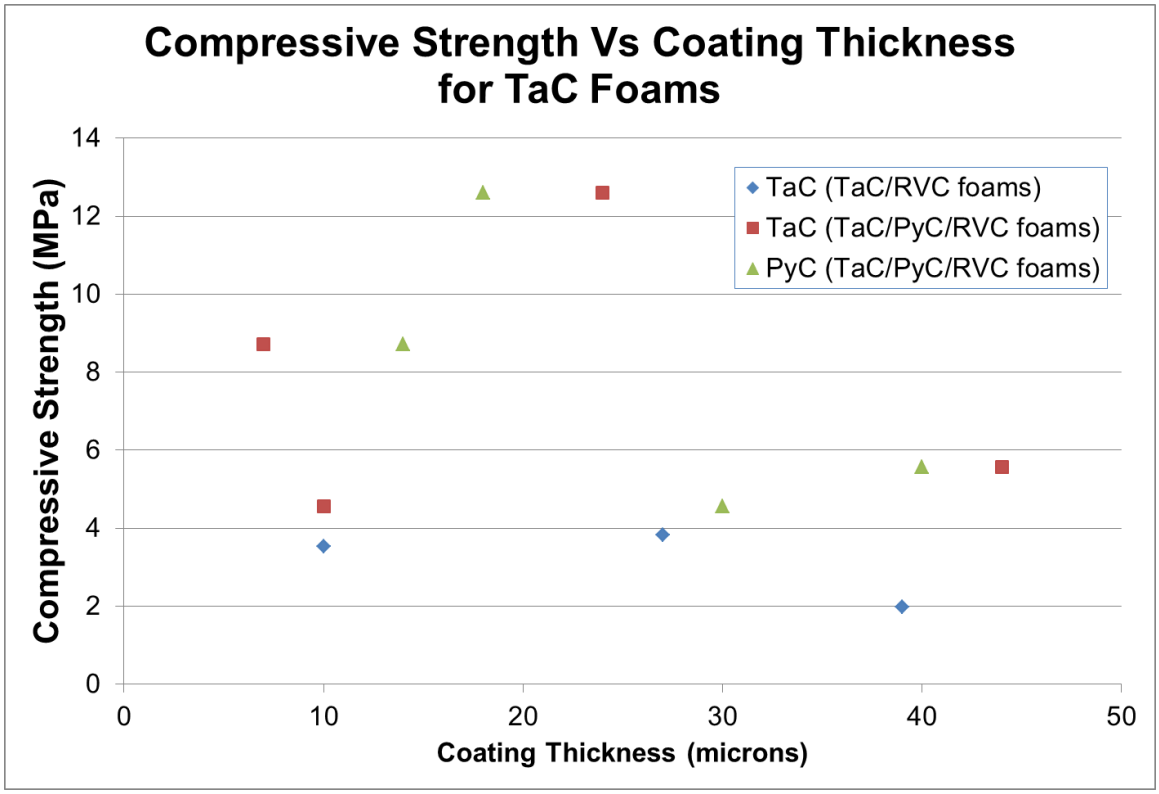

Figure 73. Compressive strength vs coating thickness for TaC foams.

Data from Figure 73 indicate that TaC coatings of ~25 microns and PyC coatings between 15-20 microns yielded the highest compressive strengths. As TaC and PyC coatings increased beyond those thicknesses the compressive strength decreased, potentially due to the increased probability of a flaw existing of critical size to allow crack propagation. It was also noted that as coating thicknesses decreased below 20 microns, the compressive strength decreased.

The experimentally measured compressive strengths of TaC foams are compared with a predicted range of values in Table XXVI. The modulus of rupture was calculated for each foam type using Equation 8 with a proportionality constant of 0.2.

Table XXVI. Predicted and Experimental Compressive Strengths of TaC Foams and Calculated Modulus of Rupture

	Predicted				Experimental	
Foam Type	**TaC σ_{cs} Min (MPa)**	**TaC σ_{cs} Max (MPa)**	**PyC σ_{cs} Min (MPa)**	**PyC σ_{cs} Max (MPa)**	**σ_{cs} (MPa)**	**Calculated MOR (MPa)**
45 TaC/PyC/RVC	4.96	14.04	3.56	7.13	5.56	377
65 TaC/PyC/RVC	3.87	10.95	2.78	5.56	4.57	396
100 TaC/PyC/RVC A	3.88	10.98	2.78	5.58	8.72	756
100 TaC/PyC/RVC B	6.48	18.33	4.65	9.31	12.60	654
45 TaC/RVC	2.56	7.24	1.83	3.68	1.97	259
65 TaC/RVC	2.49	7.06	1.79	3.59	3.82	515
100 TaC/RVC	1.86	5.26	1.33	2.67	3.53	639

Data from Table XXVI indicate the experimental results for 45 and 65 ppi TaC/PyC/RVC foams fell in between the minimum pure TaC strut strength predictions and the maximum pure PyC strut strength predictions. The strengths of the 100 ppi TaC/PyC/RVC foams were in between the maximum pure TaC strut strength predictions and the maximum pure PyC strut strength predictions. With the exception of the 45 ppi TaC/RVC foams, TaC/RVC foam strength was between the minimum and maximum pure TaC strut strength prediction.

In Table XXVII the predictions made for compressive strength of TaC foams incorporating cross-sectional area fractions of foams struts using Equation 8 are compared with measured values. The experimental MOR was calculated using Equation 8 and the experimentally measured compressive strength.

Table XXVII. Comparison of Predicted Compressive Strengths Using Cross-sectional Areas of Struts and Experimentally Measured Compressive Strengths

	Predicted				Experimental	
Foam Type	**Min. Strut MOR (MPa)**	**Max. Strut MOR (MPa)**	**Min. Strength (MPa)**	**Max. Strength (MPa)**	**Compressive Strength (MPa)**	**Calculated MOR (MPa)**
45 TaC/PyC/RVC	239	609	3.53	8.99	5.56	377
65 TaC/PyC/RVC	242	656	2.78	7.56	4.57	396
100 TaC/PyC/RVC A	228	607	2.63	7.00	8.72	756
100 TaC/PyC/RVC B	249	627	4.81	12.09	12.60	654
45 TaC/RVC	214	606	1.63	4.61	1.97	259
65 TaC/RVC	204	576	1.51	4.28	3.82	515
100 TaC/RVC	171	483	0.94	2.67	3.53	639

The data within Table XXVII indicate a good correlation between experimentally measured and predicted foam compressive strength. The experimentally measured compressive strengths of all foam types except 100 ppi TaC/RVC and TaC/PyC/RVC foams fell within the predicted strength range. All 100 ppi foams exhibited higher compressive strengths than the maximum strength predicted. The results indicate that strut cross-sectional area fractions can be used to calculate a composite strut modulus of rupture, which can be used in Equation 7 to estimate the compressive strength of the foam.

Prior studies have indicated that the relative density of foams is an important factor in compressive strength. Figure 74 and Figure 75 show the compressive strength vs TaC relative density for TaC/RVC and TaC/PyC/RVC foams, respectively.

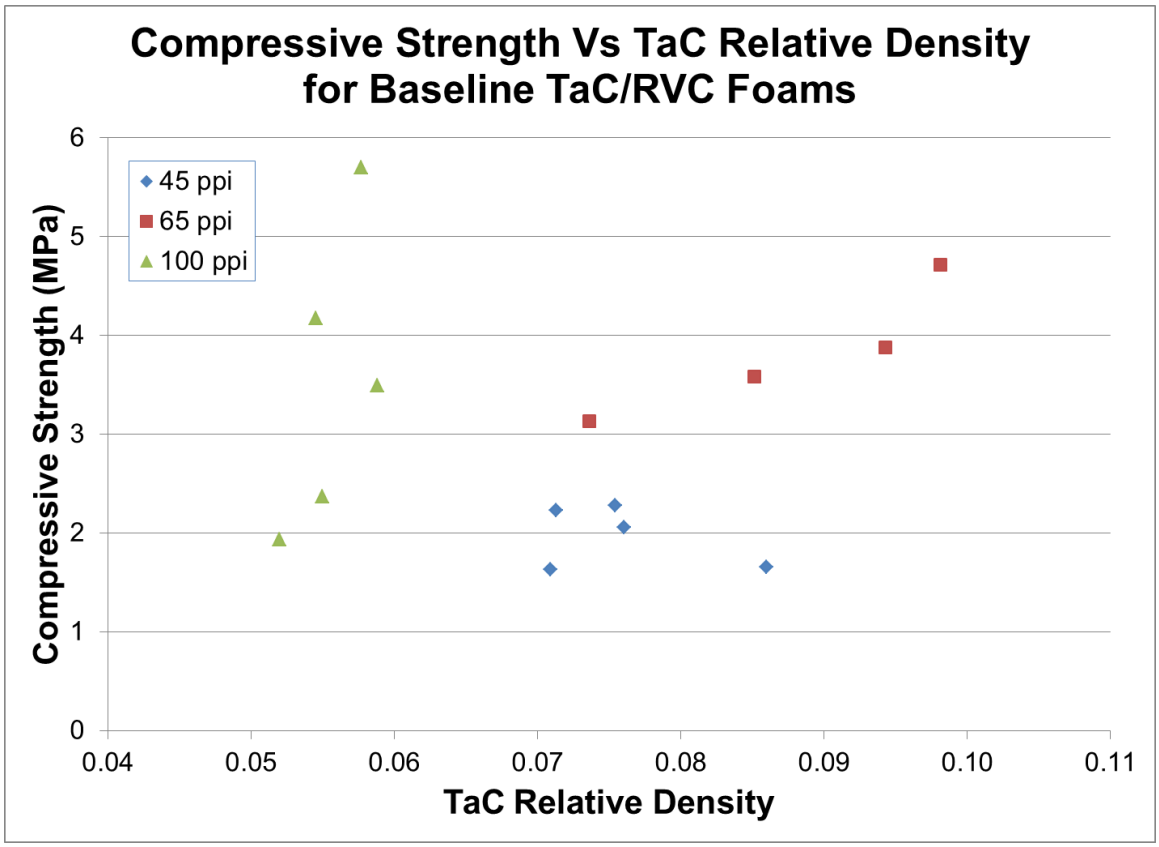

Figure 74. Graph of compressive strength vs TaC relative density for baseline TaC/RVC foams.

The data from Figure 74 indicate that within TaC/RVC foams, compressive strength tended to increase with TaC relative density. The strength increase was most predominant in 100 ppi foams.

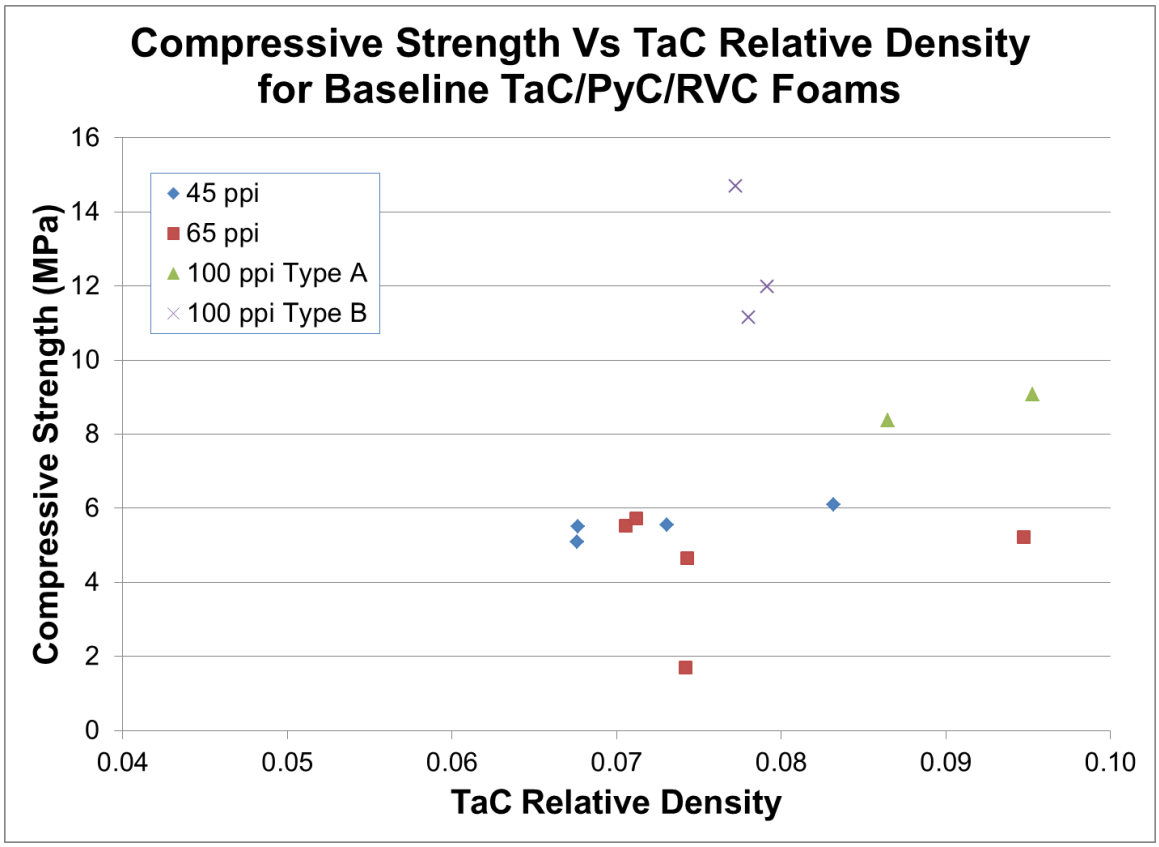

Figure 75. Graph of compressive strength vs TaC relative density for baseline TaC/PyC/RVC foams.

The increase in strength with TaC relative density is not as clear in Figure 75, which shows data from TaC/PyC/RVC foams. It is likely that lack of clear trends are a result of the PyC coating, which increased the strength, but is not included in the TaC relative density calculation.

The average Young's moduli of TaC foams are shown in Figure 78. The error bars represent +/- 1 standard deviation from the mean. Many of the stress-strain curves for TaC foams exhibited concave downward behavior, following a brief linear regime shortly after load application, as shown in Figure 76. Some foams exhibited mainly linear behavior as shown in Figure 77. Although the stress was plotted on the positive y-axis, the stress on each specimen was compressive. In some of the stress-strain curves, such as Figure 77, strain reversal was observed shortly after initial loading. It is thought that the small specimen size coupled with the structure of the foam could have created localized tension on one side of the specimen and compression on the opposite side for a short period of time during initial loading. After the initial period of

positive strain, the strain would always become negative. Stress-strain curves for all the TaC foams are located in Appendix F.

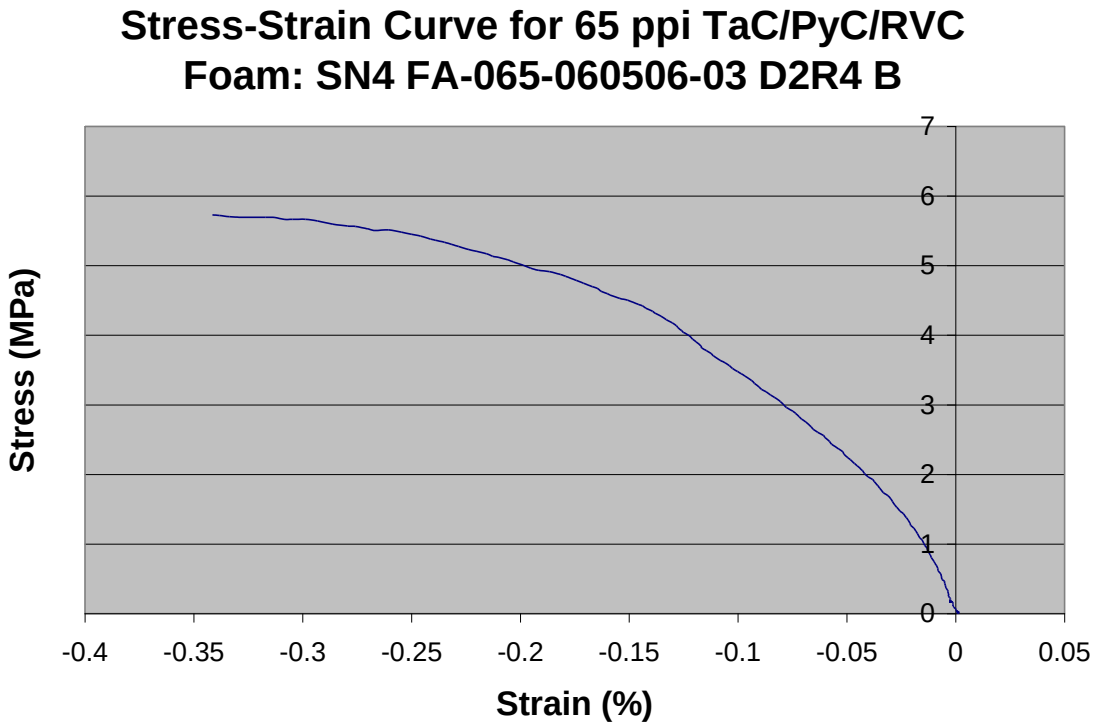

Figure 76. Stress-strain curve for a baseline specimen of 65 ppi TaC/PyC/RVC foam.

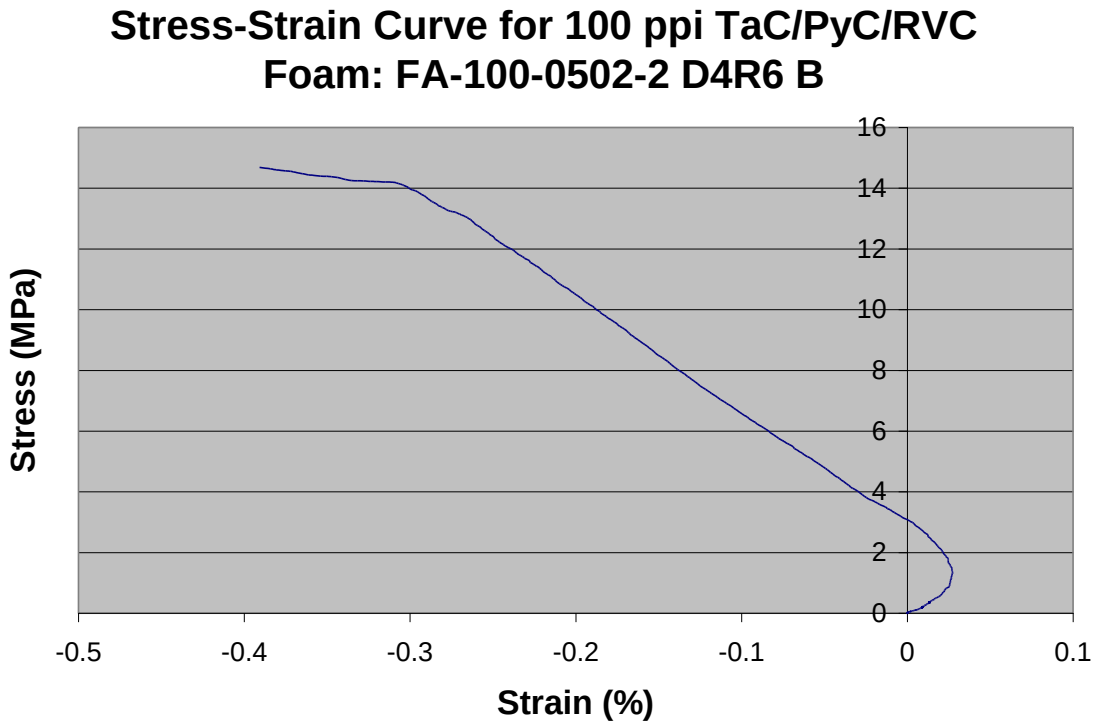

Figure 77. Stress-strain curve for a baseline specimen of 100 ppi TaC/PyC/RVC foam.

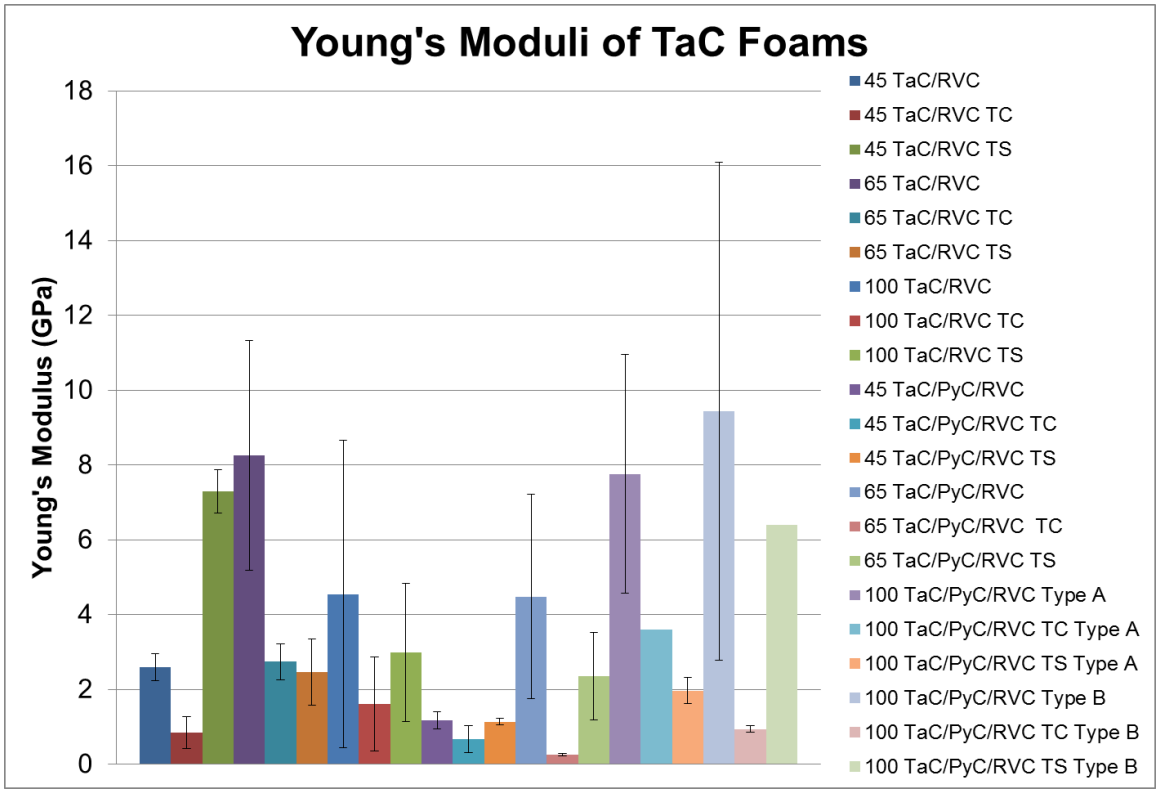

Figure 78. Graph of Young's moduli for TaC foams

The standard deviations of Young's moduli for baseline TaC foam specimens were quite large. It is possible that the porosity within the foam structure caused poor extensometer blade contact on some of the specimens. As strut thickness decreased within TaC/PyC/RVC baseline foams the average Young's modulus increased, ranging from approximately 1-9 GPa. The 45 ppi and 100 ppi type A thermally cycled TaC/PyC/RVC foams followed the same trend, but the 65 ppi and 100 ppi type B foams exhibited significantly lower Young's moduli. Within the TaC/RVC baseline foams, the 65 ppi foams exhibited the highest Young's modulus, followed by the 100 ppi and 45 ppi foams. Young's moduli of baseline TaC/RVC foams ranged from approximately 2.5-8 GPa. The thermally cycled TaC/RVC foams followed the same trend. Results of Young's moduli predictions are compared with experimental measurements in Table XXVIII.

Table XXVIII. Comparison of Predicted and Experimentally Measured Young's Moduli

Foam Type	Min. Upper-bound E_s (GPa)	Max. Upper-bound E_s (GPa)	Min. Upper-bound E_f (GPa)	Max. Upper-bound E_f (GPa)	Experimental E_f (GPa)
45 TaC/PyC/RVC	147	275	4.5	8.5	1.17
65 TaC/PyC/RVC	186	356	4.1	7.9	4.48
100 TaC/PyC/RVC A	166	314	3.7	7.0	7.76
100 TaC/PyC/RVC B	145	272	6.4	12.0	9.44
45 TaC/RVC	190	366	2.4	4.7	2.59
65 TaC/RVC	182	349	2.3	4.3	8.27
100 TaC/RVC	157	296	1.3	2.5	4.55

All experimental Young's modulus measurements were within or above the predicted Young's modulus range except for 45 TaC/PyC/RVC foams. Micro-cracks were observed in baseline 45 TaC/PyC/RVC foams, which likely resulted in a reduced Young's modulus. The Young's moduli of 65 ppi and 100 ppi TaC/RVC were twice that of the maximum predicted.

Young's moduli from baseline and thermally cycled samples were used in conjunction with Equation 10 to estimate the extent of micro-cracking induced by thermal cycling in a semi-quantitative manner. The results of the calculations are presented graphically in Figure 79.

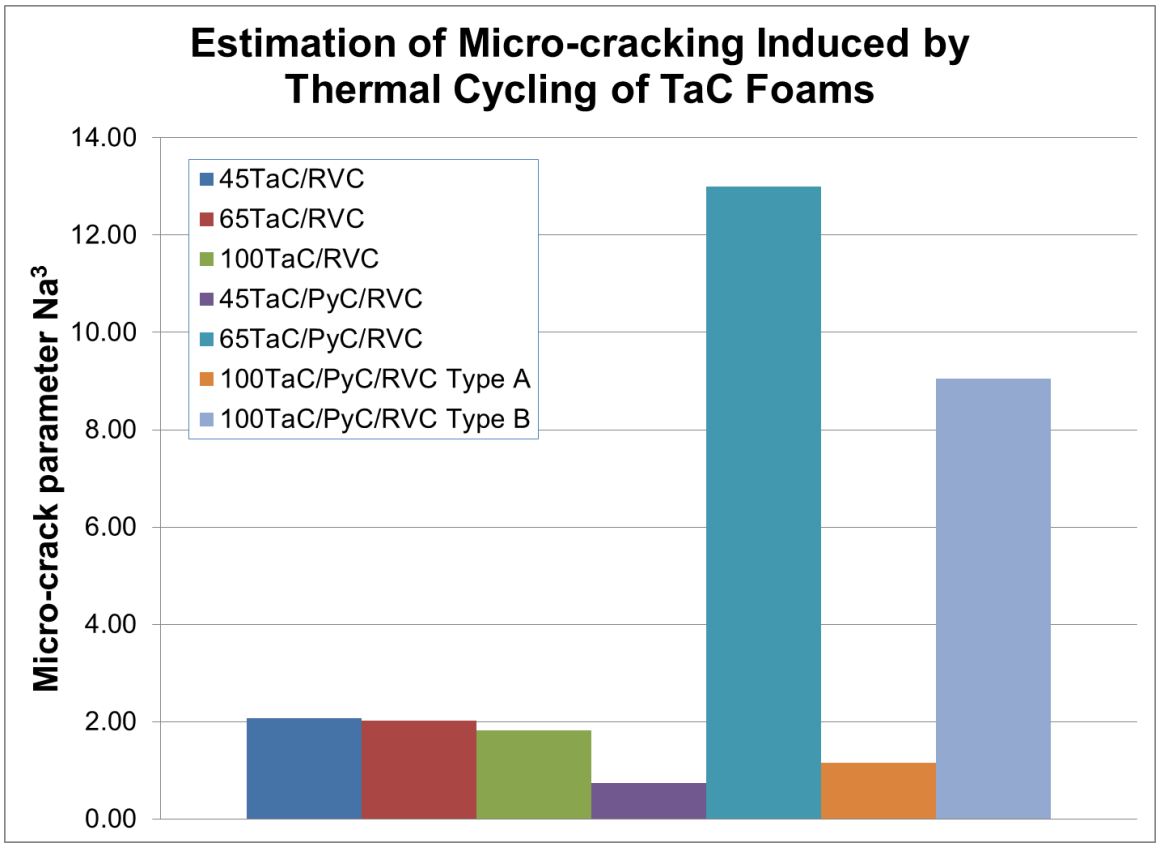

Figure 79. Graph of calculated micro-cracking parameter Na^3 for TaC foams.

Significantly more micro-cracking was predicted to be present in the 65 ppi TaC/PyC/RVC and 100 ppi TaC/PyC/RVC Type B foams than other types of foams. The results from compressive strength tests do not correlate with the significantly larger quantities of predicted micro-cracks in 65 and 100 ppi Type B TaC/PyC/RVC foams.

Formation of a Tungsten- Ceramic Foam Composite

This sub-section describes the results obtained to understand the influence of foam pore size and tungsten particle size on vibration-induced tungsten particle infiltration and densification within RVC foams. The results of characterization of tungsten powder through particle size analysis, surface area analysis, and scanning electron microscopy are discussed. Micrographs of the microstructure of the RVC foams are presented, along with measurements of strut and pore sizes for each foam pore density. Infiltrated RVC foam densities and results of consolidation of the composite are discussed. Finally, the results of moduli measurement of tungsten-foam composites using impulse excitation are presented.

Particle Size Analysis of Tungsten Powders

The flow of tungsten particles was significantly different for the sub-micron and 5-10 micron powders. The sub-micron powder tended to agglomerate, whereas the 5-10 micron powder flowed very smoothly. Data from the particle size analysis supported significant agglomeration of sub-micron tungsten particles. A total of 20 analyses were performed on the sub-micron powder. Thirteen of the analyses yielded a bi-modal particle distribution that had peaks of ~ 10 and ~ 100 microns. The particle size distribution obtained from the 13 analyses was averaged and the results are shown in Figure 80. Seven of the analyses had a bi-modal particle distribution that had peaks of ~ 100 microns and ~ 1000 microns. The average particle size distribution obtained from the seven analyses was averaged and the results are shown in Figure 81.

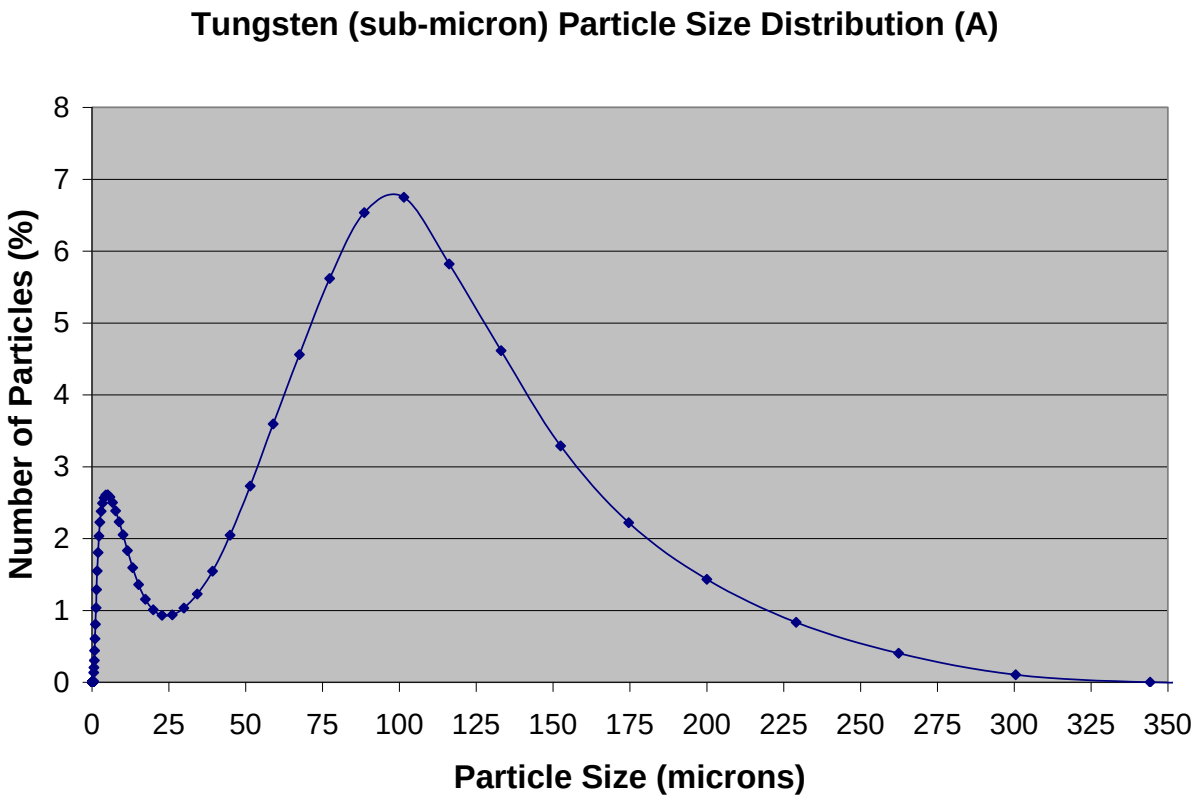

Figure 80. Chart of particle size distribution A for sub-micron tungsten powder

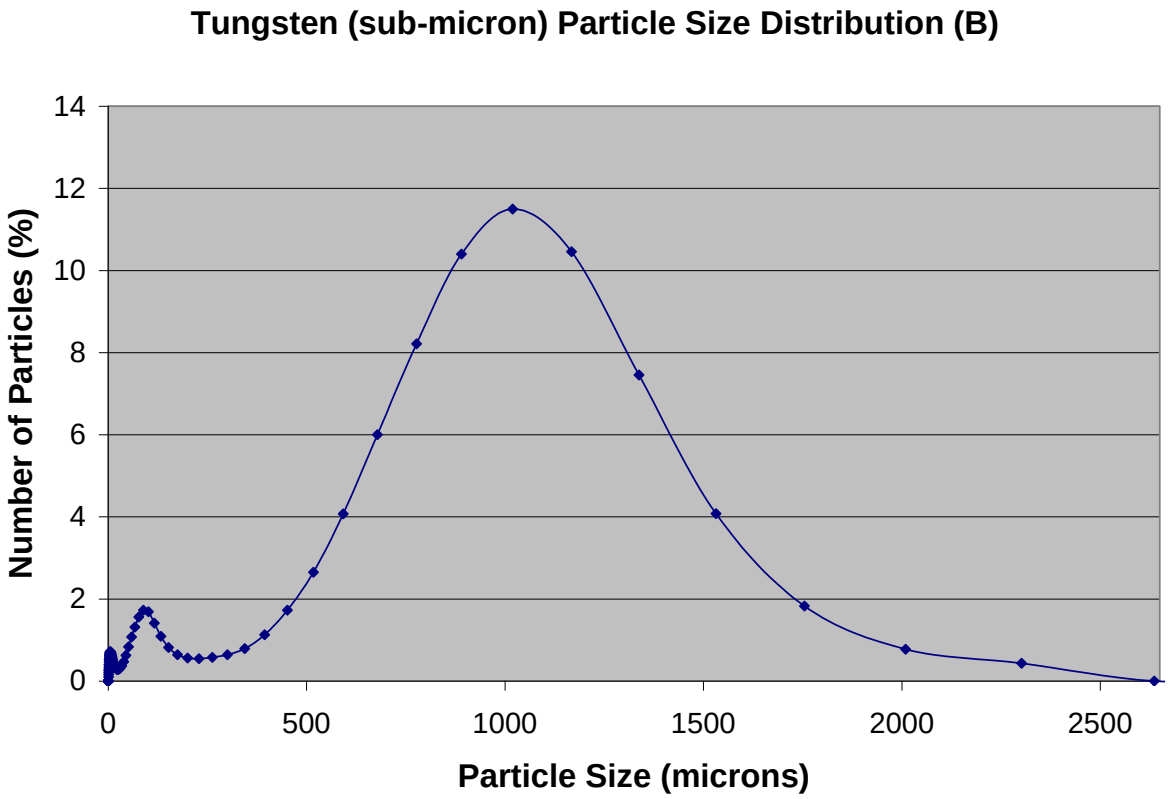

Figure 81. Chart of particle size distribution B for sub-micron tungsten powder

Analysis of the 5-10 micron yielded one peak slightly larger than 10 microns. Measurements performed on the 5-10 micron powder exhibited excellent repeatability. The particle size distribution obtained from 13 analyses was averaged and the results are shown in Figure 82.

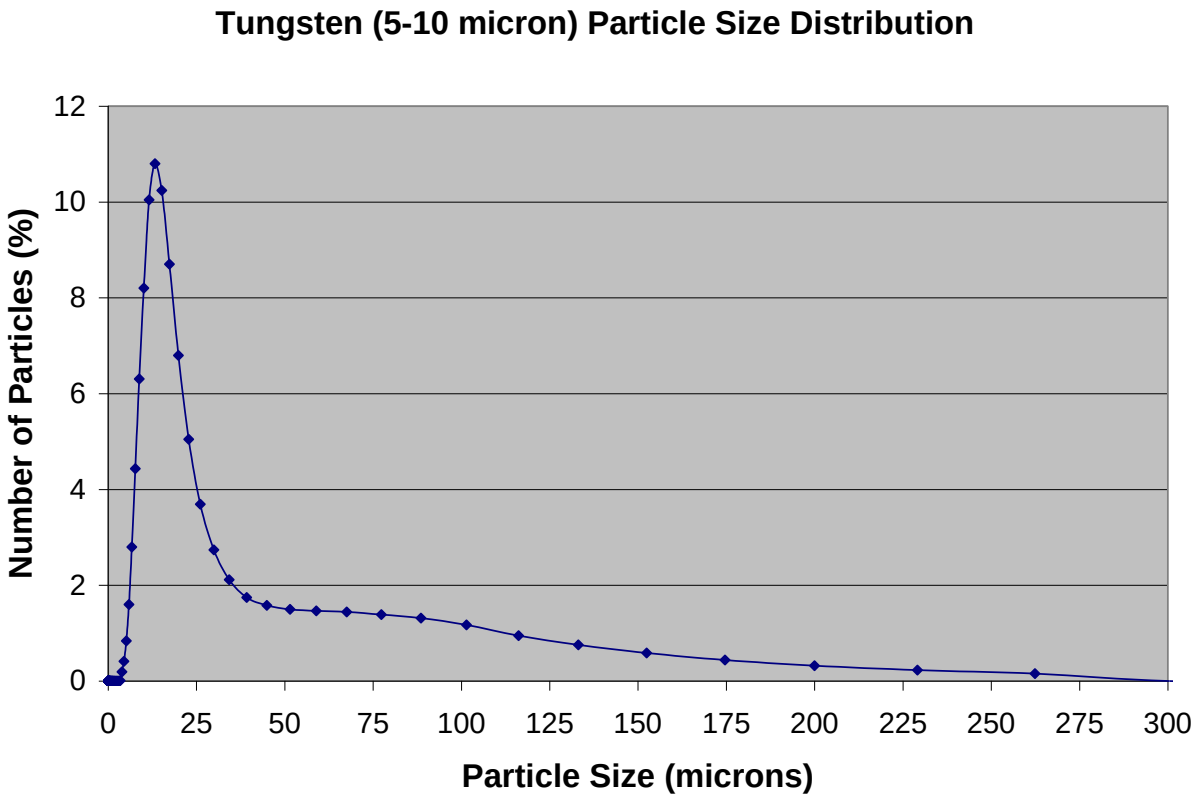

Figure 82. Chart of particle size distribution for 5-10 micron tungsten powder

Surface Area Analysis of Tungsten Powders

Multi-point BET graphs for sub-micron and 5-10 micron tungsten powders are shown in Figure 83 and Figure 84, respectively. The seven adsorption points in each graph exhibited negligible deviation from a linear trend.

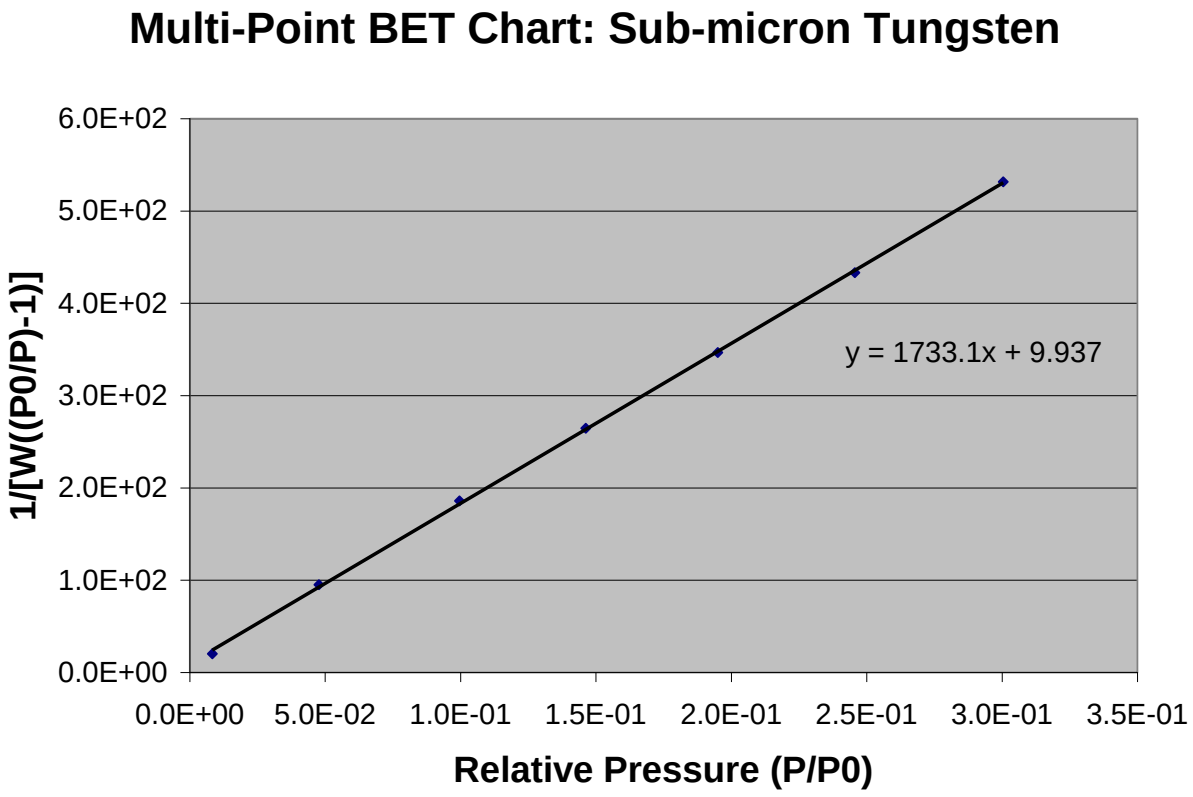

Figure 83. Multi-point BET chart for sub-micron tungsten powder

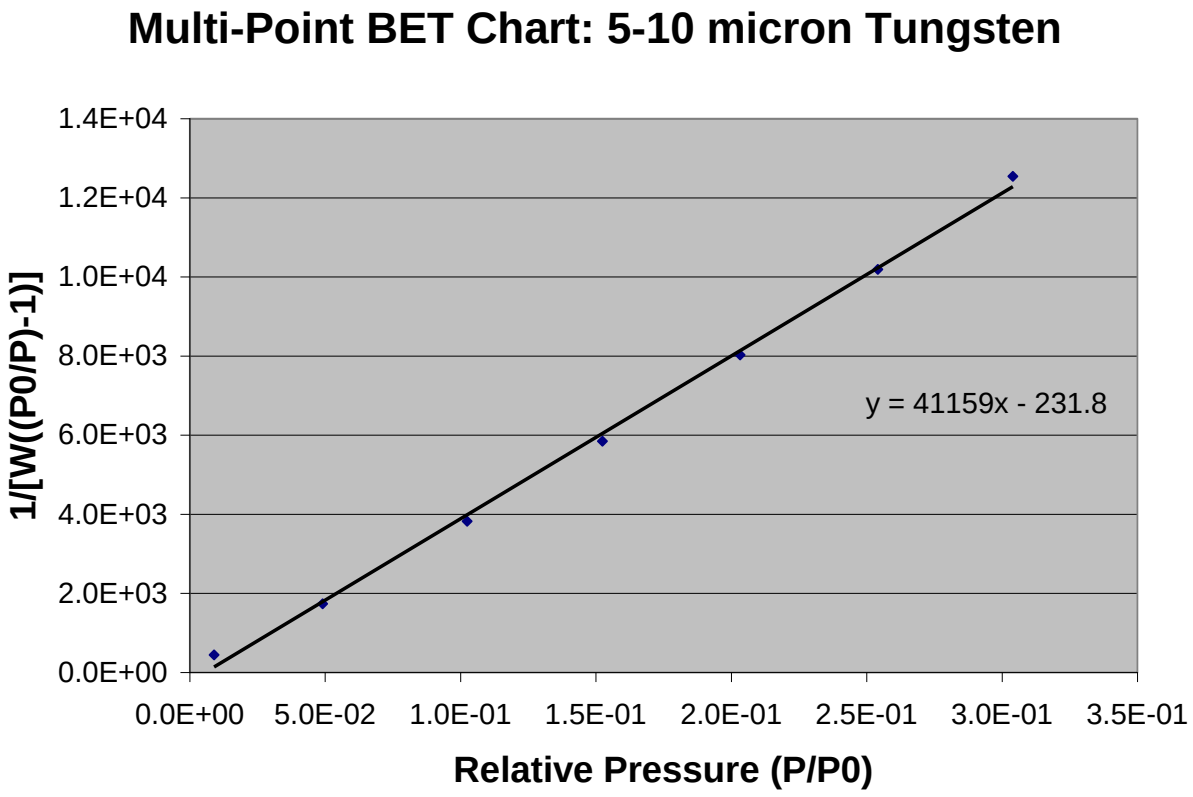

Figure 84. Multi-point BET chart for 5-10 micron tungsten powder

Table XXIX summarizes the results from BET analysis of sub-micron and 5-10 micron tungsten powders. The sub-micron powder had a surface area of 1.998 m^2/g, while the 5-10 micron powder had a surface area of 0.085 m^2/g. As expected, the surface area of sub-micron tungsten powder was significantly larger than that of the 5-10 micron powder. The larger surface area facilitated agglomeration of particles by inter-particle forces.

Table XXIX. Results of BET Analysis of Tungsten Powders

	Sub-micron Tungsten	**5-10 micron Tungsten**
Slope	1733.114	41158.926
Intercept	9.937	-231.8
Correlation coefficient (r)	0.999887	0.998988
Constant (C)	175.411	-176.549
Surface Area (m^2/g)	1.998	0.085

Characterization of Reticulated Vitreous Carbon Foam

Prior to infiltration, images of RVC foams were obtained using a camera, and the microstructure of the RVC foams was characterized using SEM. Figure 85-Figure 87 show images of 45 ppi, 65 ppi, and 100 ppi RVC foams, respectively.

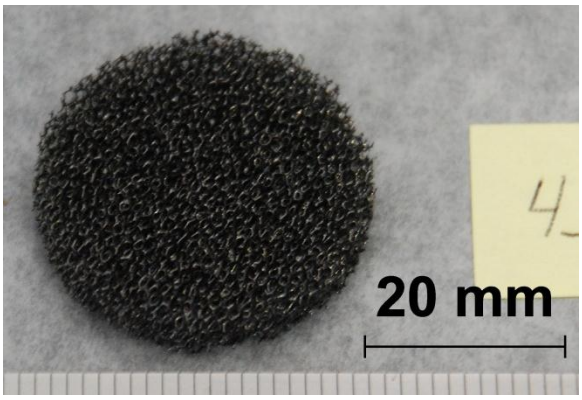

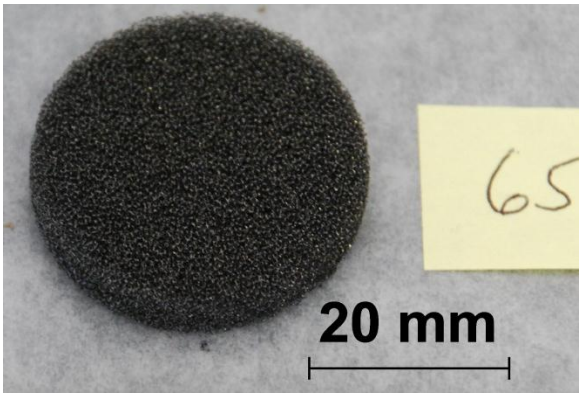

Figure 85. (left) Image of 45 ppi RVC foam.
Figure 86. (right) Image of 65 ppi RVC foam.

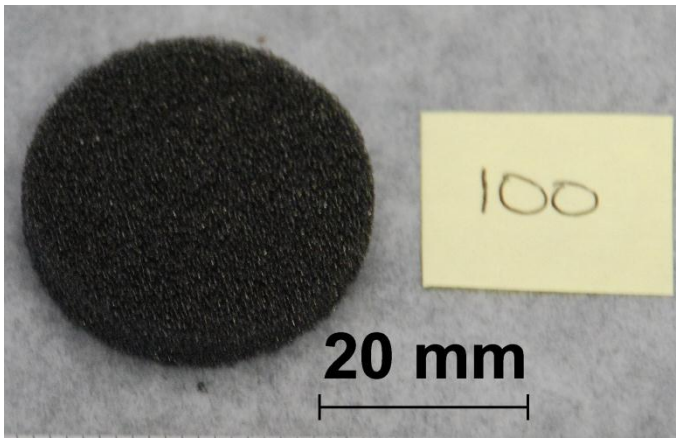

Figure 87. Image of 100 ppi RVC foam.

SEM micrographs of 45, 65, and 100 ppi RVC foams are shown in Figure 88-Figure 90, respectively. The cross-section of an RVC foam strut is shown in Figure 91.

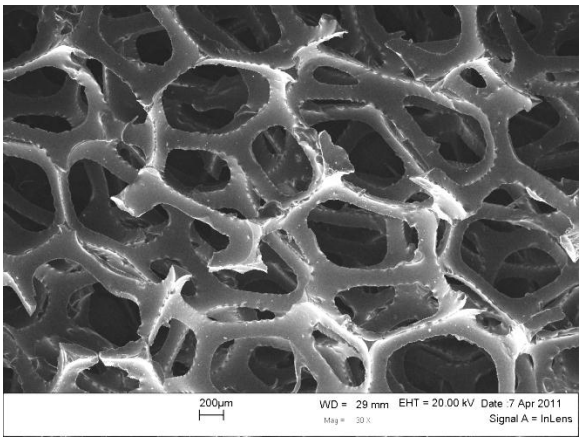

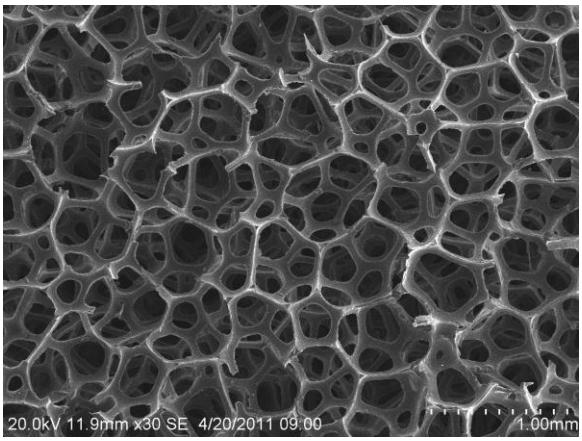

Figure 88.(left) SEM micrograph of 45 ppi RVC foam
Figure 89.(right) SEM micrograph of 65 ppi RVC foam

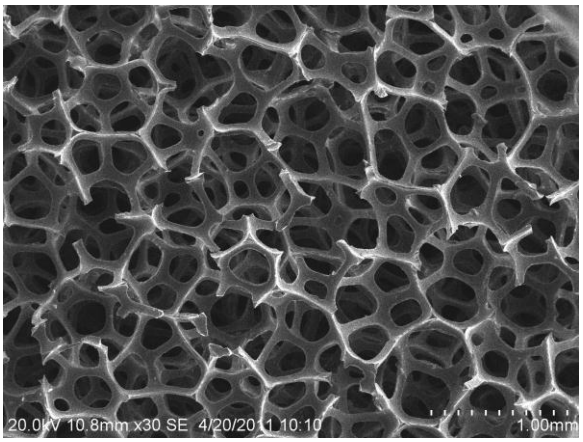

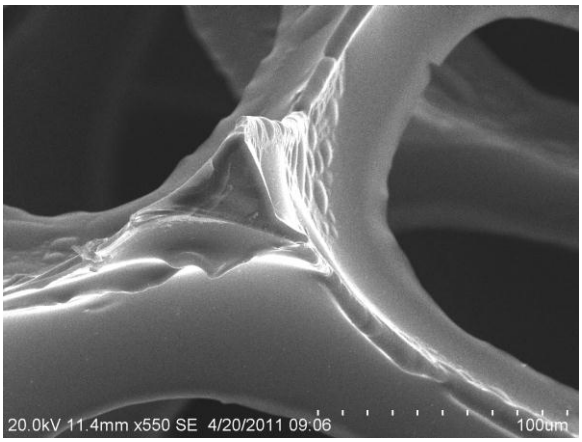

Figure 90.(left) SEM micrograph of 100 ppi RVC foam
Figure 91.(right) SEM micrograph of a 65 ppi RVC foam strut

The RVC foams had a three-dimensional cell structure, with porosity that is interconnected throughout the foam, thus they had an open- cell structure. The RVC foams tended to exhibit cell faces with square, pentagonal, and hexagonal geometries. Adjoining cell faces formed polyhedral cells with geometries similar to tetrakaidecahedrons and dodecahedrons. The above micrographs show that as foam pore density (ppi) increased, the pore size and strut thickness within the foam decreased. The RVC foam struts exhibited triangular cross-sectional geometry.

The average strut and pore size measurements for various pore densities of RVC foams are shown in Table XXX. Average strut thickness ranged from 146-67 µm for 45-100 ppi RVC foams, respectively. Average pore sizes ranged from 633-205 µm, respectively. Graphical

representations of the average strut and pore sizes are shown in Figure 92 and Figure 93, respectively.

Table XXX. Average Strut and Pore Sizes for RVC Foams

Foam Type	Average Strut Thickness (µm)	Standard Deviation (µm)	Average Pore Size (µm)	Standard Deviation (µm)
45 ppi RVC	146	9	633	93
65 ppi RVC	89	7	282	36
100 ppi RVC	67	6	205	37

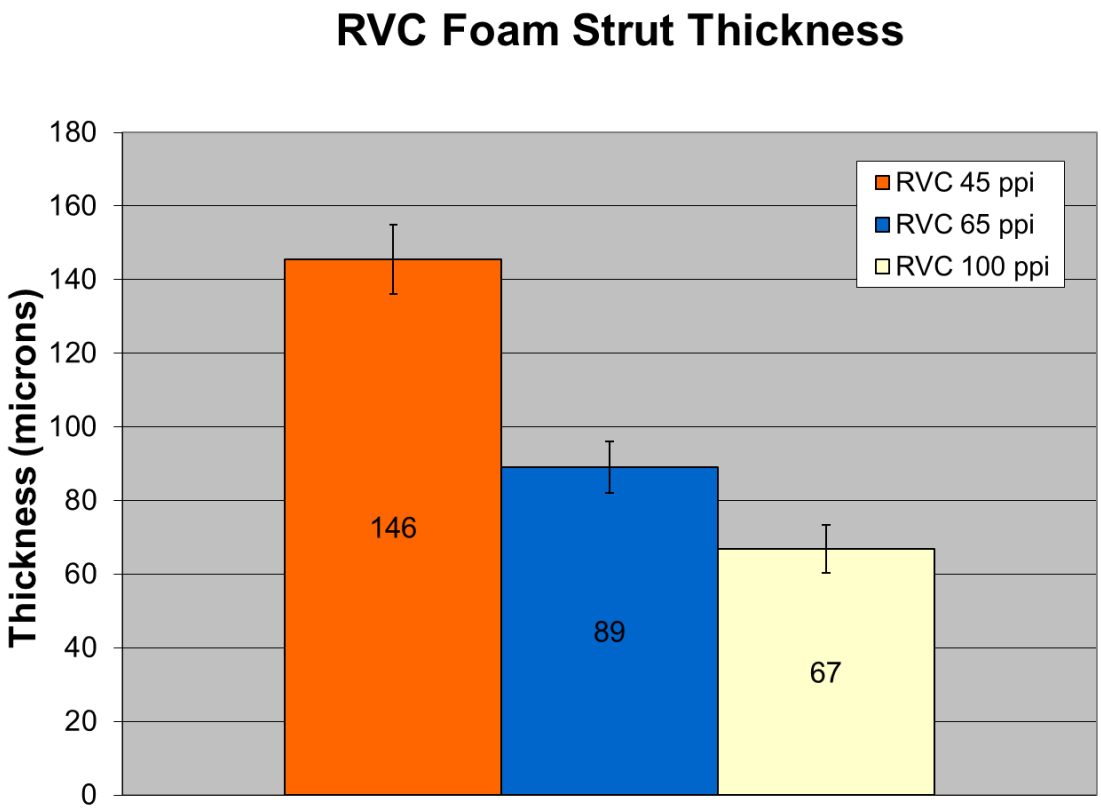

Figure 92. Chart of average strut thicknesses of RVC foams

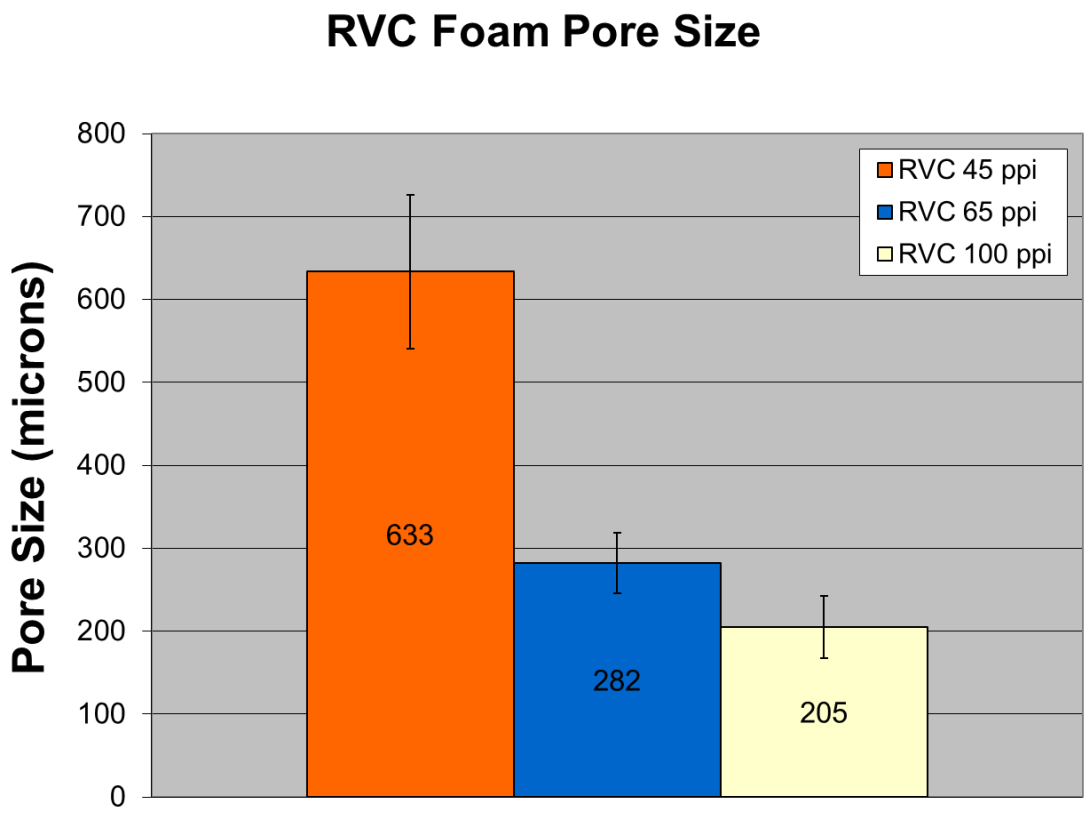

Figure 93. Chart of average pore sizes for RVC foams

Infiltration of Foam with Tungsten Powder

SEM micrographs showing particle size and morphology of sub-micron tungsten particles are shown in Figure 94-Figure 95. The particles tended to be agglomerated, and were sub-rounded with sizes ranging between 200 nm and 500 nm.

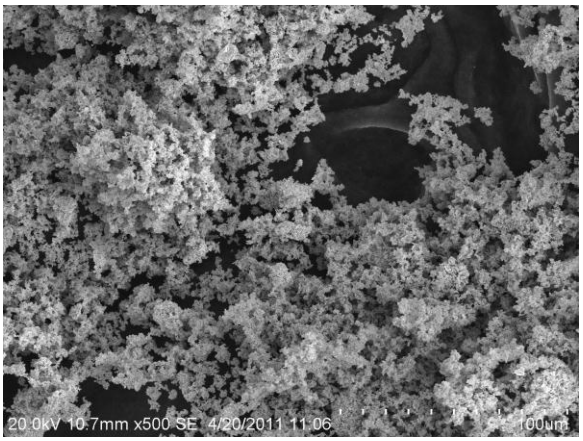

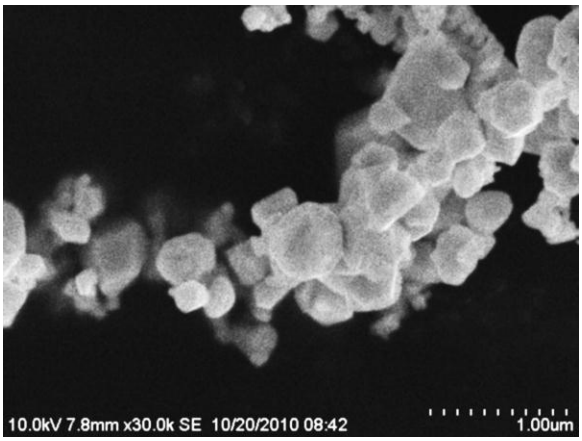

Figure 94.(left) Scanning electron micrograph of sub-micron tungsten particles
Figure 95.(right) Scanning electron micrograph of sub-micron tungsten particles

Figure 96-Figure 97 show particle size and morphology of nominally 5-10 micron tungsten particles. Significantly less agglomeration was observed in the 5-10 micron tungsten particles than in the sub-micron particles. Particles tended to be sub-rounded and 1-10 microns in diameter.

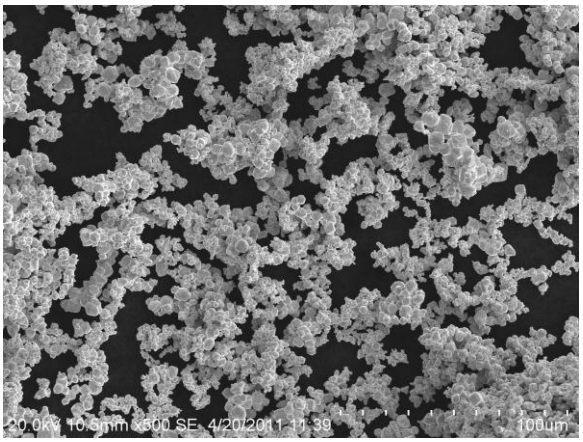

Figure 96. Scanning electron micrograph of 5-10 micron tungsten particles
Figure 97. Scanning electron micrograph of 5-10 micron tungsten particles

The vibrational densification of the two particle size distributions of tungsten powder was measured with no RVC foam present in the brass recess. A total of 39.362 g of sub-micron tungsten powder was found to fit within the brass recess used for foam infiltration. The apparent density was 2.2 g/cm^3, which is 11% of the theoretical density of tungsten. After vibrating the powder at 23-25 m/s^2 for 10 minutes, the tap density was measured to be 3.6 g/cm^3. No

measurable change in tap density was observed after two additional 10 minute vibration periods at 23-25 m/s^2.

The brass recess was able to accommodate 59.680 g of 5-10 micron tungsten powder, resulting in an apparent density of 3.3 g/cm^3. The powder was vibrated for 10 minutes at 23-25 m/s^2. The tap density was found to be 5.5 g/cm^3, 29% the theoretical density of tungsten. The powder was vibrated for two additional 10 minute periods at 23-25 m/s^2. No measurable change in tap density was observed. The brass recess was filled with 59.680 g of 5-10 micron tungsten powder again, and vibrated for 10 minutes at 23-25 m/s^2. The tap density was again found to be 5.5 g/cm^3. The powder was then vibrated for two additional 10 minute periods at 38-42 m/s^2 and 14.4-14.7 m/s^2. No measurable change in tap density was observed from either vibration period.

The first vibrational infiltration attempt using 15 g of 5-10 micron tungsten powder at an acceleration of 23-25 m/s^2 resulted in migration of the RVC foam to the top of the powder and very low infiltration of the foam. It is suspected that the significantly lower density of the RVC foams compared to the SiC foams was responsible. As a result, the quantity of 5-10 micron tungsten was increased to 25 g, and the acceleration was decreased to 13.4-13.7 m/s^2 in an effort to restrict migration of the RVC foam during vibration. The increase in powder mass and decrease in acceleration was successful in preventing migration of the RVC foam and allowing infiltration of the foam with the tungsten powder. After two vibration runs at the lower acceleration, the acceleration was increased to 23-25 m/s^2, which proved to be the most effective parameters for the infiltration of RVC foam.

Figure 98 and Figure 99 are graphs of tungsten infiltration in 65 ppi RVC foams vs time for 5-10 micron tungsten and sub-micron tungsten, respectively. Table XXXI and Table XXXII show the vibrational infiltration parameters that were used with 5-10 micron tungsten and sub-micron tungsten, respectively. Within the infiltrations tables, *tungsten mass* refers to the quantity of tungsten placed on top of the foam round prior to each infiltration run, *infiltrated mass* refers to the net infiltrated foam mass from time zero, and *infiltration rate* refers to the rate of infiltration for the given vibrational infiltration time period. Tables and graphs of infiltration parameters and results for all foam rounds are located in Appendix G.

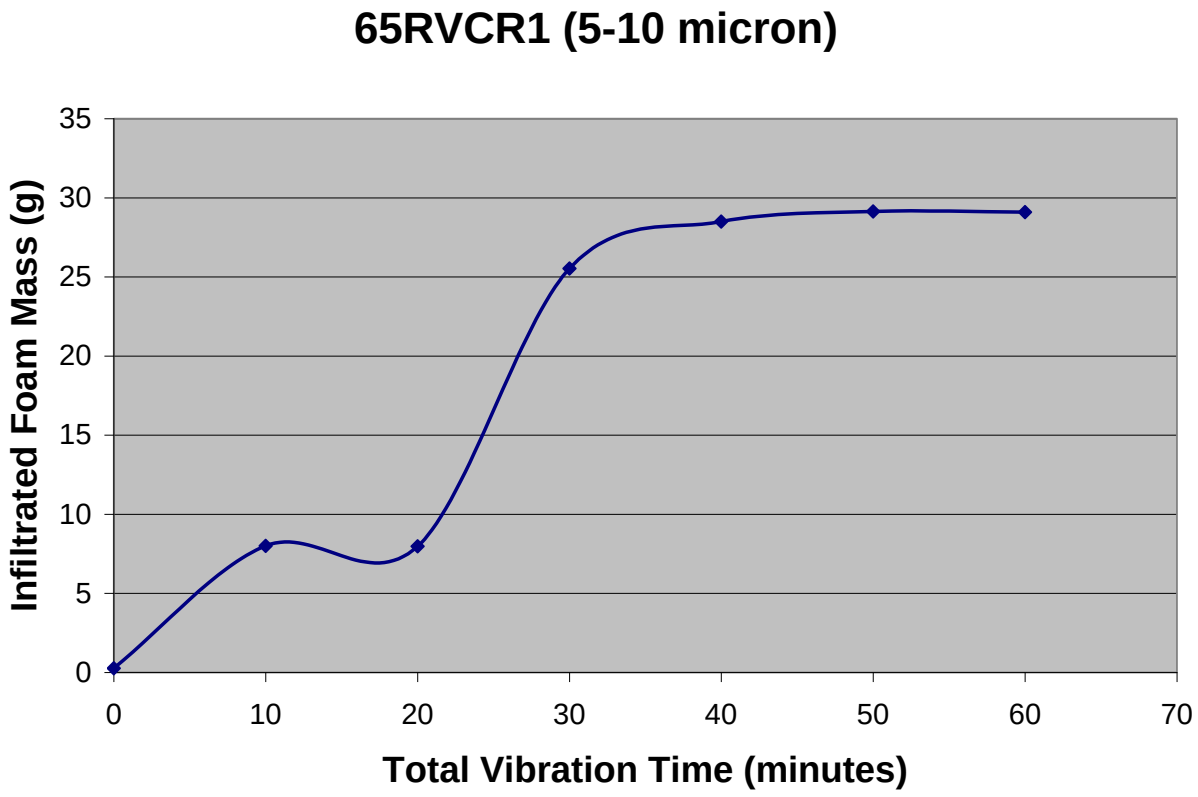

Figure 98. Graph of 5-10 micron tungsten infiltration within RVC 65 ppi foam round 1.

Table XXXI. Table of 5-10 Micron Tungsten Infiltration Parameters and Measurements for RVC 65 ppi Foam Round 1

Net vibration time (min)	Vibration run time (min)	Acceleration min (m/s^2)	Acceleration max (m/s^2)	Tungsten mass (g)	Infiltrated mass (g)	Infiltration rate (g/min)
0	-	-	-	-	0.261	-
10	10	13.2	13.4	25.048	8.001	0.774
20	10	13.2	13.5	25.067	7.97	-0.003
30	10	23	25	25.085	25.535	1.757
40	10	23	25	25.092	28.492	0.296
50	10	23	25	25.046	29.136	0.064
60	10	23	25	25.038	29.096	-0.004

The data from Figure 98 and Table XXXI show that after the initial 10 minutes of infiltration at 13 m/s^2, tungsten was actually lost from the round by continuing at that rate of vibration. The

greatest infiltration rate was achieved with an acceleration of 23-25 m/s^2 between 20-30 minutes of net vibration. The infiltration plateaued after 40 minutes of vibration, at 29 g net infiltrated foam mass.

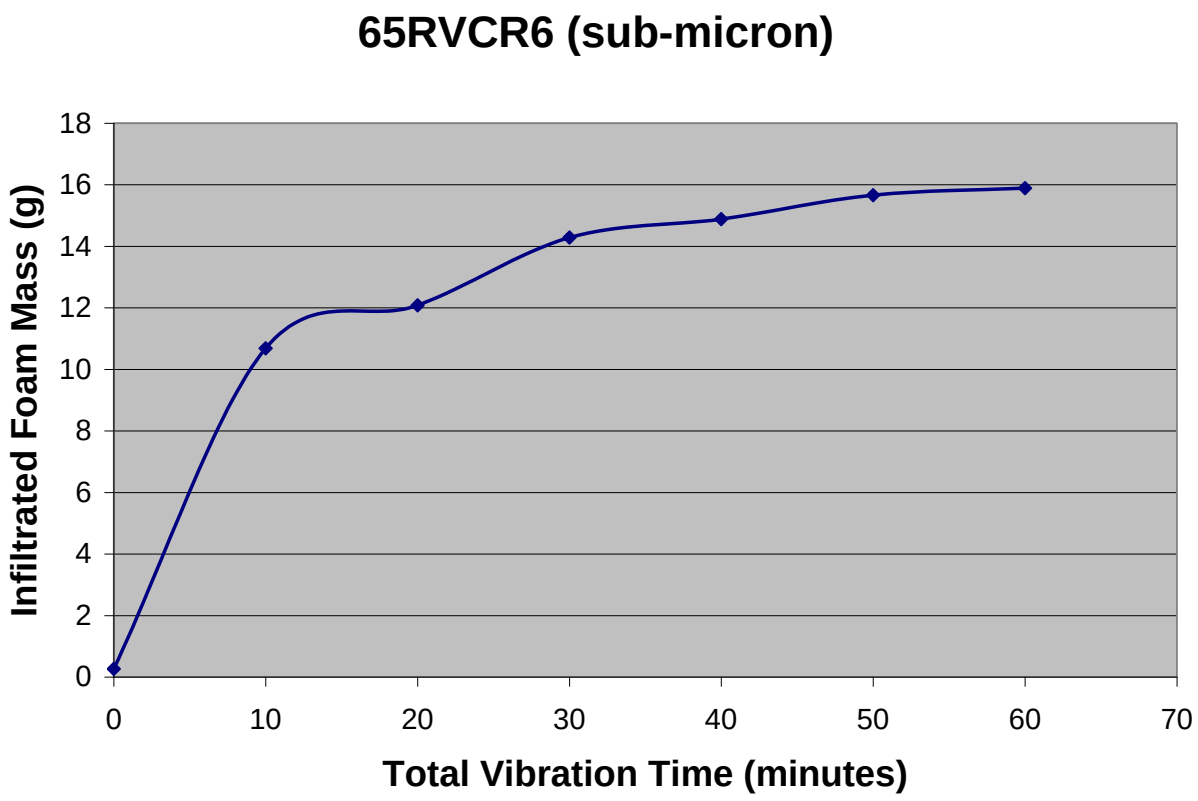

Figure 99. Graph of Sub-micron tungsten infiltration within RVC 65 ppi foam round 6.

Table XXXII. Table of Sub-micron Tungsten Infiltration Parameters and Measurements for RVC 65 ppi Foam Round 6

Net vibration time (min)	Vibration run time (min)	Acceleration min (m/s^2)	Acceleration max (m/s^2)	Tungsten mass (g)	Infiltrated mass (g)	Infiltration rate (g/min)
0	-	-	-	-	0.261	-
10	10	23	25	15.022	10.685	1.042
20	10	23	25	15.015	12.079	0.139
30	10	23	25	15.008	14.284	0.221
40	10	23	25	15.031	14.881	0.060
50	10	23	25	15.069	15.663	0.078
60	10	23	25	15.035	15.888	0.023

Data from Figure 99 and Table XXXII show that sub-micron tungsten powder exhibited significantly lower infiltration than 5-10 micron tungsten. After the initial rapid infiltration between 0 and 10 minutes, the infiltration rate slowed considerably. Infiltration eventually reached a plateau around 50 minutes just under 16 g net infiltrated foam mass.

Figure 100 shows a graph of average tungsten density versus foam pore density for RVC foams that were vibrationally infiltrated with sub-micron and 5-10 micron tungsten powder. The cyan bars represent samples infiltrated with 5-10 micron tungsten and the orange bars represent samples infiltrated with sub-micron tungsten. The data in Figure 100 indicate that the infiltrated tungsten density of RVC foams is significantly more dependent on the particle size of tungsten than on the foam pore size. Data points were plotted for the infiltrated densities of 45, 65, and 100 ppi RVC foams, and for the density of vibrated tungsten with no foam present, shown at 0 ppi.

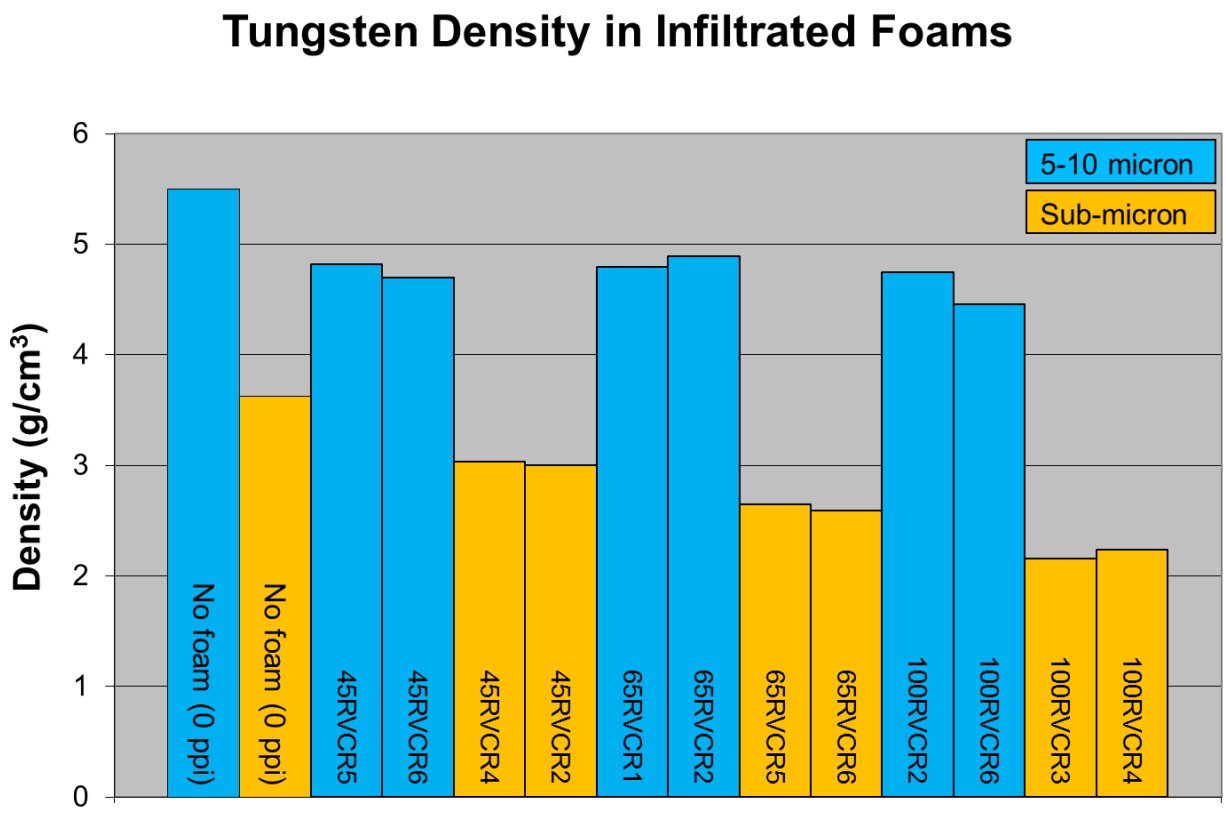

Figure 100. Graph of infiltrated tungsten density vs RVC foam ppi

As the foam pore density increased, the infiltrated tungsten density that was achieved using sub-micron tungsten was observed to decrease. The infiltrated 45 ppi RVC foams exhibited an average tap density that was 84% that of baseline (0 ppi) vibrated sub-micron tungsten powder. The tap density of infiltrated 65 ppi and 100 ppi RVC foams decreased to 73% and 62%, respectively.

As observed with the sub-micron tungsten powder, an increase in foam pore density resulted in a decrease in the infiltrated tungsten density achieved with the 5-10 micron tungsten powder. However, an exception occurred with the 45 ppi and 65 ppi data points, where the 65 ppi infiltrated density is higher than that of the 45 ppi. The lower density achieved in the 45 ppi RVC foam may have been a result of the larger pore size, allowing 5-10 micron tungsten powder to fall out of the porosity. Agglomeration of the sub-micron powder may have prevented the powder from falling out, and is likely the reason why the same effect was not observed with the infiltration of the sub-micron tungsten powder. Table XXXIII shows the maximum mass attained during the infiltration of RVC foams and the mass at the end of the infiltration process. The data indicate that if vibration is continued after a given point, a net loss of infiltrated powder can occur within the porosity, resulting in a decrease in infiltrated density.

Table XXXIII. Maximum Mass and End Mass for Infiltrated RVC Foams

Sample	Tungsten Particle Size	Max. Mass (g)	End Mass (g)
45RVCR1	5-10 micron	28.105	26.387
45RVCR5	5-10 micron	29.319	29.319
45RVCR6	5-10micron	28.453	28.453
65RVCR1	5-10 micron	29.136	29.096
65RVCR2	5-10 micron	29.841	29.824
100RVCR2	5-10 micron	28.975	28.975
100RVCR6	5-10 micron	27.335	26.917
45RVCR4	sub-micron	18.546	17.491
45RVCR2	sub-micron	18.447	18.447
65RVCR5	sub-micron	16.232	16.232
65RVCR6	sub-micron	15.888	15.888
100RVCR3	sub-micron	13.354	13.354
100RVCR4	sub-micron	13.831	13.831

Foams infiltrated with 5-10 micron powder exhibited less pronounced variation in infiltrated density with pore size. The infiltrated 65 ppi RVC foams averaged 89% of the tap density of 5-10 micron powder, while the 45 ppi and 100 ppi foams averaged 87% and 85%, respectively. Significantly higher tap densities were obtained infiltrating foams with 5-10 micron tungsten powder than with sub-micron tungsten powder. The higher tap densities obtained in 5-10 micron tungsten infiltrations were likely the result of the lower baseline (0 ppi) tap density of sub-micron tungsten powders induced by the high surface areas of the particles, and the agglomeration of sub-micron particles. Particle agglomeration would have made the effective particle size larger, as was observed in the particle size analysis. The larger effective particle size would have made it more difficult for groups of agglomerated particles to pass through the foam cells, reducing the infiltrated density achieved.

T-tests were conducted on the results from infiltration of RVC foams with tungsten powder using Equation 24 and Equation 25. The parameters and results of the t-tests are listed in Table XXXIV. The suffixes *SM* and *M* refer to sub-micron and 5-10 micron tungsten powders, respectively.

Table XXXIV. T-test Parameters and Confidence for Foam Infiltration Data

Type	Datasets	σ_{diff}	t	df	Confidence (%)
5-10 micron	45 ppi - 65 ppi	0.506	-1.736	3	90
	65 ppi - 100 ppi	0.908	1.518	2	85
	45 ppi - 100 ppi	0.914	0.548	3	50
sub-micron	45 ppi - 65 ppi	0.181	13.363	2	99.5
	65 ppi - 100 ppi	0.284	8.842	2	99
	45 ppi - 100 ppi	0.234	21.054	2	99.5
particle size	45 ppi SM - 45 ppi M	0.370	27.399	3	99.95
	65 ppi SM - 65 ppi M	0.389	34.507	2	99.95
	100 ppi SM - 100 ppi M	0.868	16.780	2	99.5

Figure 101 shows the t-test confidence results for the influence of foam pore/strut size on the infiltration of 5-10 micron tungsten powder in graphical format.

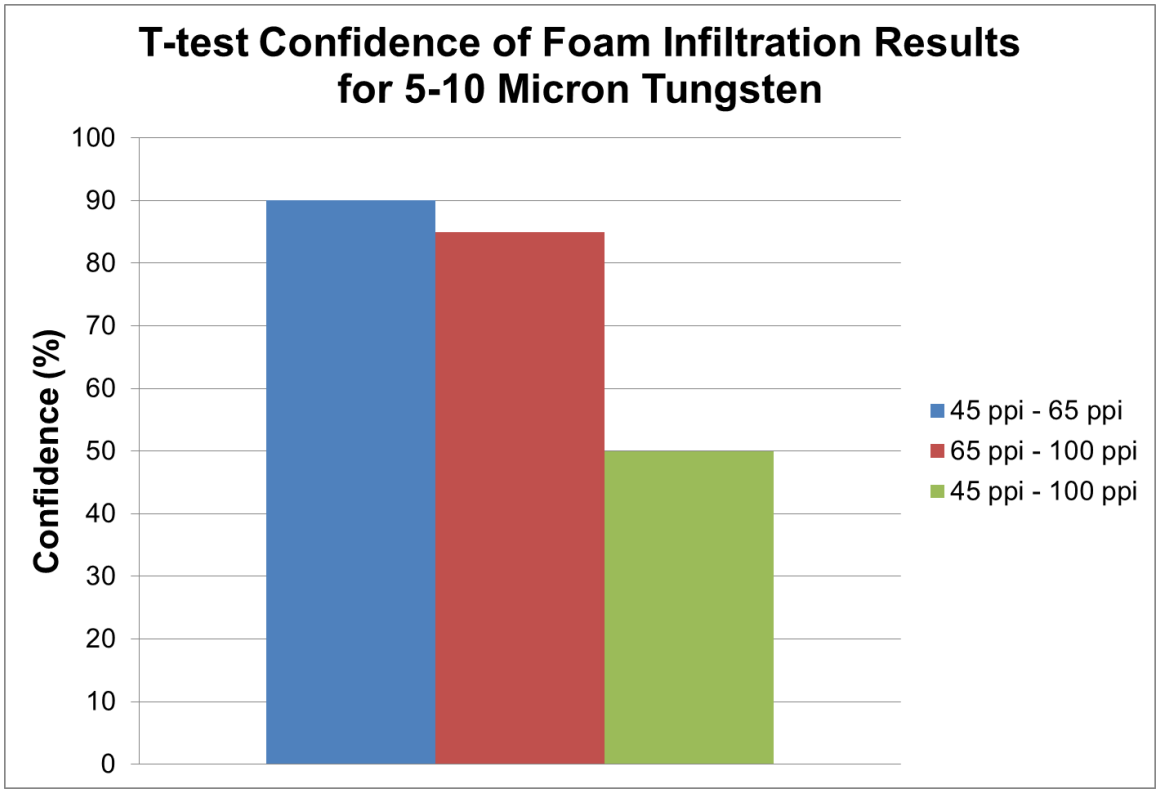

Figure 101. T-test confidence of foam infiltration results for 5-10 micron tungsten.

The statistical analysis shown in Table XXXIV and Figure 101 indicate that at least an 85% probability exists that 5-10 micron tungsten powder can infiltrate 65 ppi RVC foams to a higher density than 45 ppi and 100 ppi foams. It is surmised that 45 ppi RVC foams exhibit lower

infiltration since the larger pores can allow some of the infiltrated powder to leave the pore space during the infiltration process. The smaller pore size of the 100 ppi RVC foam likely inhibits infiltration of some particles, resulting in a lower infiltration.

Figure 102 shows the t-test confidence results for the influence of foam pore/strut size on the infiltration of sub-micron tungsten powder in graphical format.

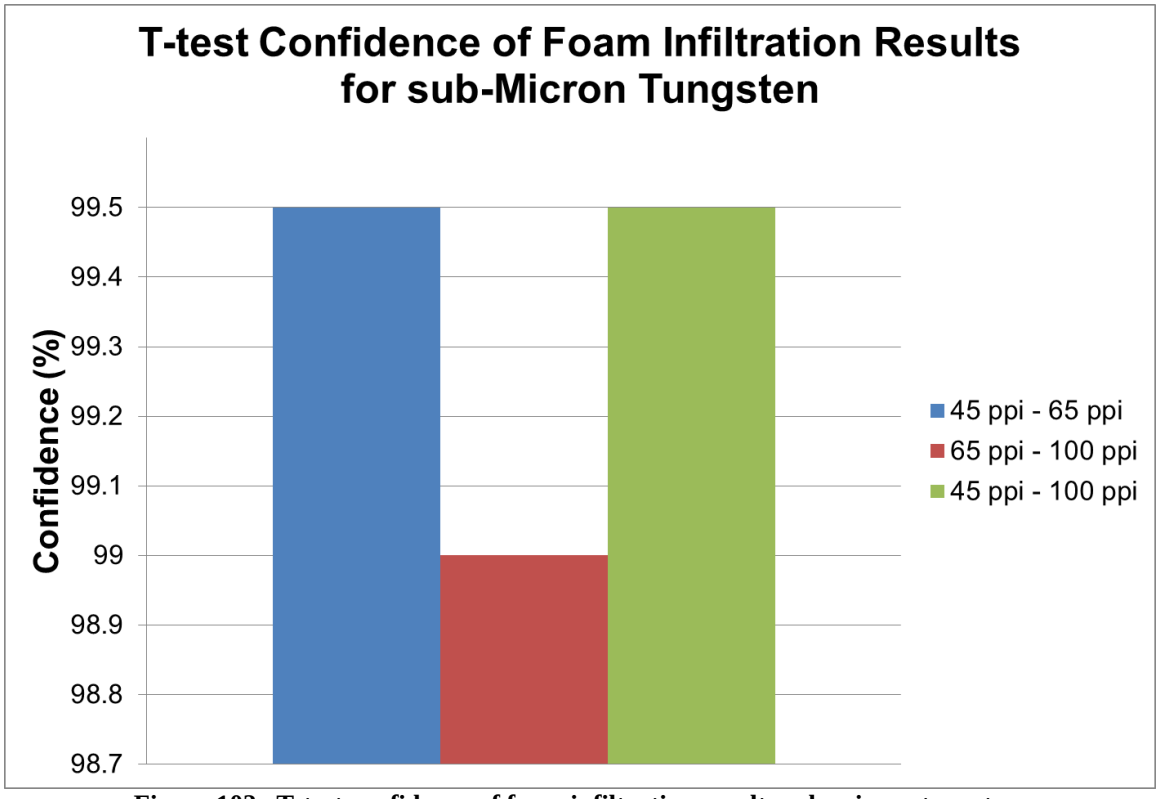

Figure 102. T-test confidence of foam infiltration results sub-micron tungsten.

The statistical analysis shown in Table XXXIV and Figure 102 indicate that there is at least a 99% probability that the pore size of RVC foam influences the infiltration of sub-micron tungsten powder for all datasets comparisons. The large apparent particle size of the agglomerated sub-micron tungsten produces a greater influence on infiltration than RVC foam pore size. Furthermore, due to the agglomeration of the sub-micron particles, infiltrated particles are less likely to fall out of the 45 ppi foam during subsequent vibrations.

Figure 103 shows the t-test confidence results for the influence of tungsten particle size on the infiltration of RVC foams in graphical format.

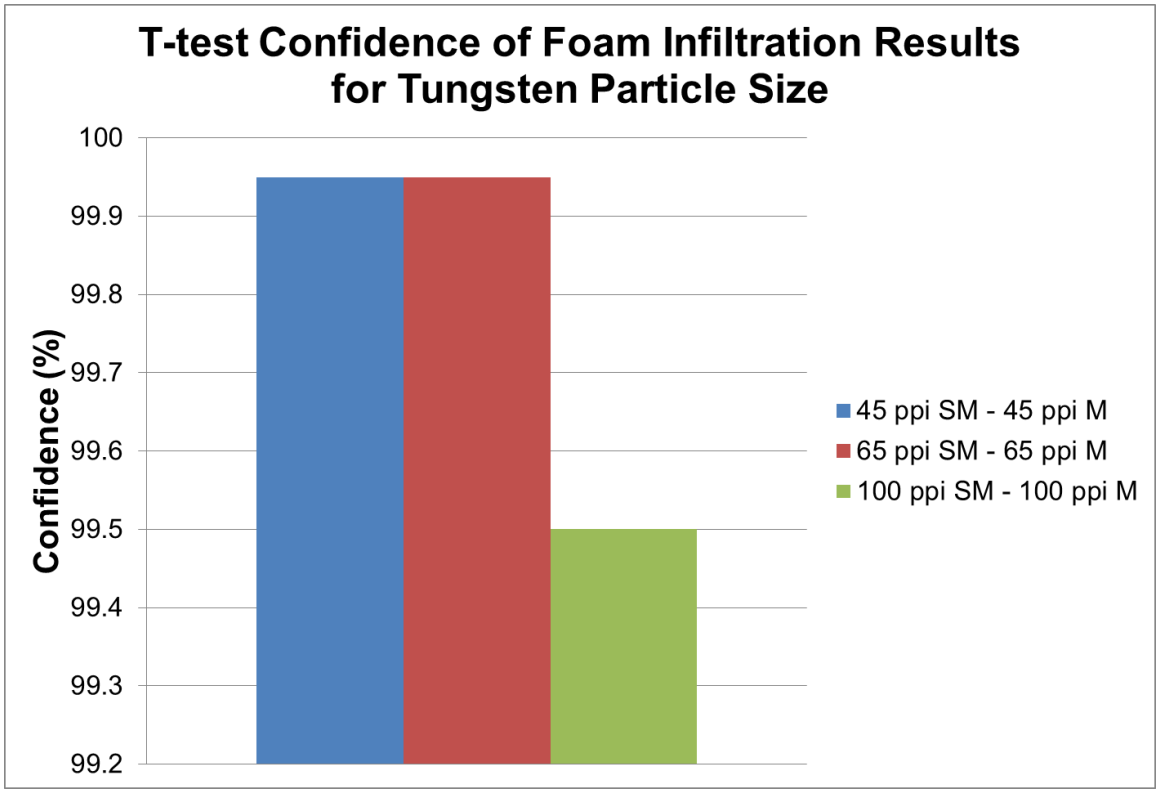

Figure 103. T-test confidence of foam infiltration results for tungsten particle size.

The statistical analysis shown in Table XXXIV and Figure 103 indicate at least a 99.5% probability that tungsten particle size influences infiltrated density for all foam pore densities.

An image of a 45 ppi RVC foam infiltrated with tungsten powder, prior to sintering, is shown in Figure 104.

Figure 104. Infiltrated 45 ppi RVC foam prior to sintering

Consolidation of the Composite

Optical microscopy was conducted on RVC foams infiltrated with tungsten powder prior to and after sintering. Figure 105-Figure 110 are optical micrographs of the surfaces of 45 ppi, 65 ppi, and 100 ppi RVC foams infiltrated with sub-micron tungsten powder and sintered. Abundant macroscopic voids are present in micrographs for all pore densities. The voids were not present prior to sintering and are the result of consolidation of the sub-micron particles.

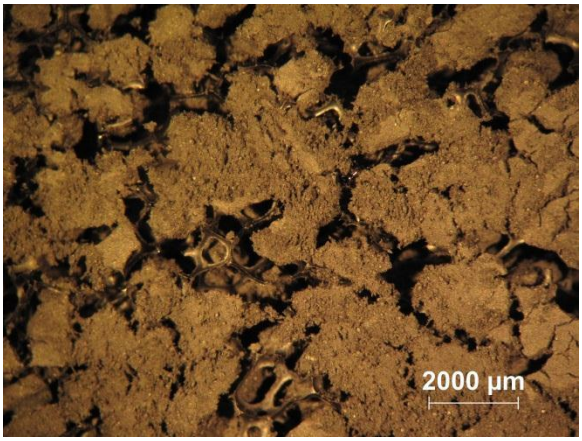

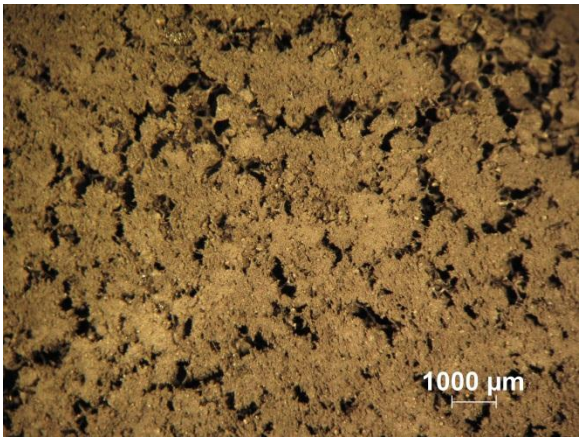

Figure 105.(left) Optical micrograph of 45 ppi RVC foam infiltrated with sub-micron tungsten and sintered.
Figure 106.(right) Optical micrograph of 65 ppi RVC foam infiltrated with sub-micron tungsten and sintered.

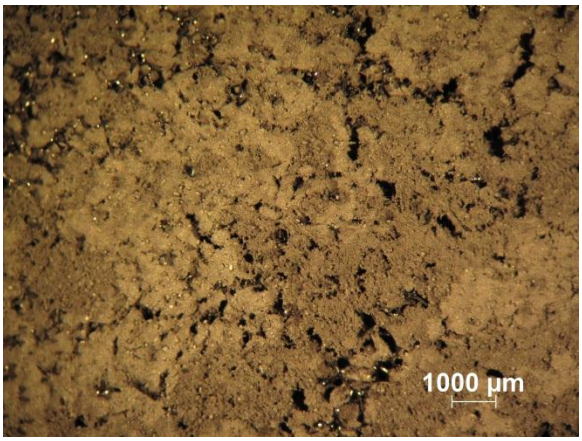

Figure 107. Optical micrograph of 100 ppi RVC foam infiltrated with sub-micron tungsten and sintered.

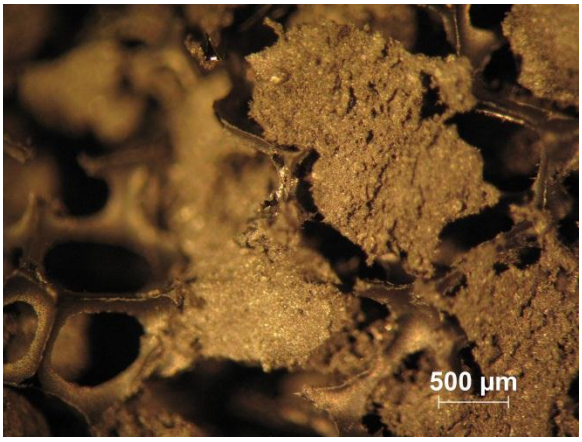

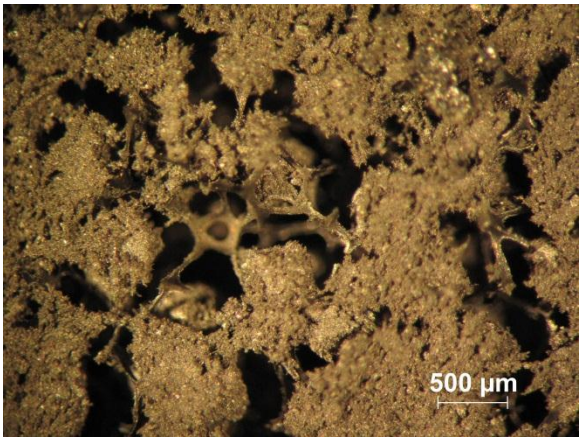

Figure 108.(left) Optical micrograph of 45 ppi RVC foam infiltrated with sub-micron tungsten and sintered.
Figure 109.(right) Optical micrograph of 65 ppi RVC foam infiltrated with sub-micron tungsten and sintered.

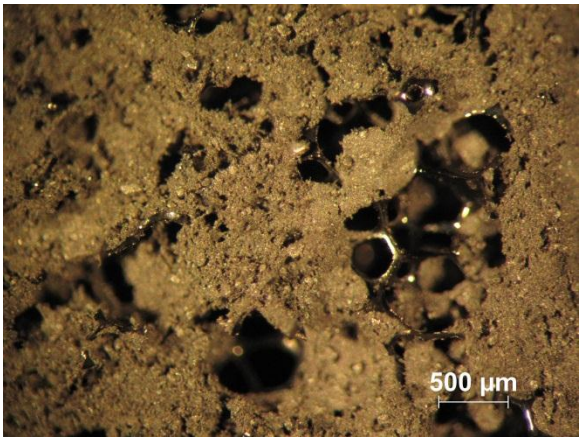

Figure 110. Optical micrograph of 100 ppi RVC foam infiltrated with sub-micron tungsten and sintered.

During sintering, sub-micron tungsten consolidated into spheres within the porosity of the foams. The spheres were not interconnected through the foam pore space. The consolidation left more volume available for infiltration of more tungsten. However, the foams were substantially more fragile after sintering, and the struts appeared to have decreased in thickness. The foams infiltrated with sub-micron powder would not withstand vibrational infiltration after sintering. An attempted infiltration caused the foam to fracture into multiple pieces. It is likely that a vapor phase carbide of tungsten was formed, facilitated by the high surface area of both the tungsten powder and foam, and the low furnace pressures. A silver deposit was observed on the pyrometer window after each sintering run, and was likely a carbide of tungsten.

Evidence of densification within the sub-micron tungsten infiltrated RVC foams was macroscopically observed by the consolidation of a uniformly distributed powder throughout the pore space in RVC foam into non-interconnected spheres within the RVC foam cells. Figure 111-Figure 113 show spherical tungsten particles that consolidated within the pore space of sub-micron tungsten infiltrated 45 ppi, 65 ppi, and 100 ppi foams, respectively.

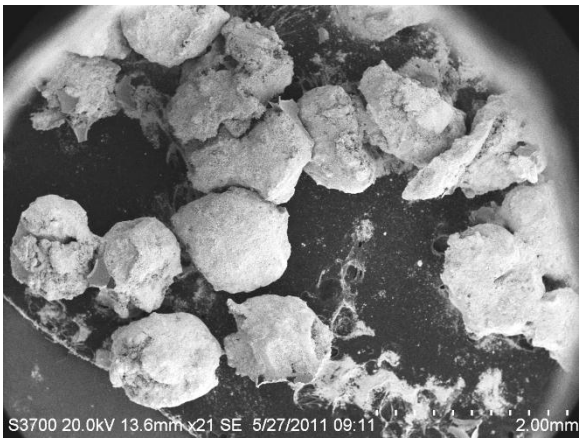

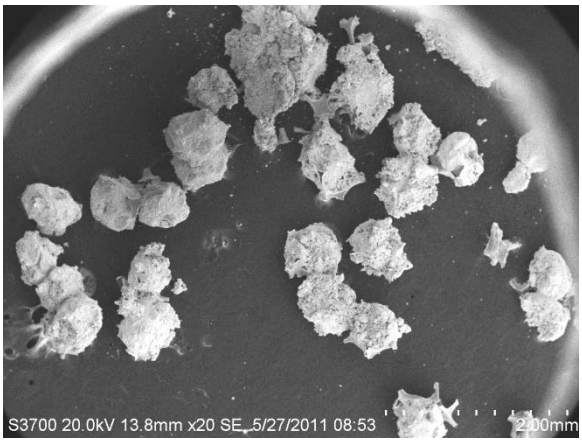

Figure 111.(left) Sub-micron tungsten that consolidated into spheres within the pore space of a 45 ppi RVC foam during sintering
Figure 112.(right) Sub-micron tungsten that consolidated into spheres within the pore space of a 65 ppi RVC foam during sintering

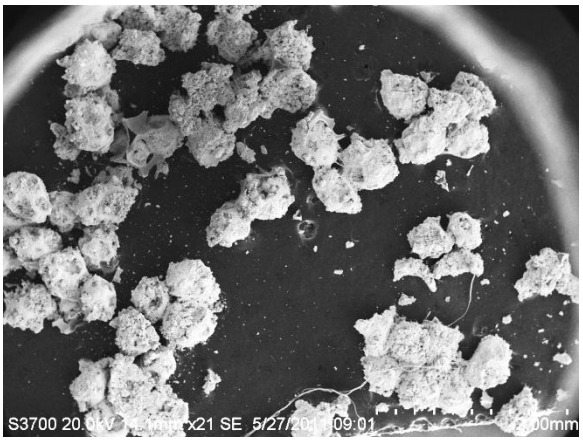

Figure 113. Sub-micron tungsten that consolidated into spheres within the pore space of a 100 ppi RVC foam during sintering

Figure 114-Figure 116 show the microstructure of the sintered tungsten spheres from 45 ppi, 65 ppi, and 100 ppi RVC foams, respectively. The unsintered particles present in Figure 114 are a result of a failed post-sintering second infiltration attempt. The attempted infiltration resulted in the infiltrated/sintered round breaking into multiple pieces.

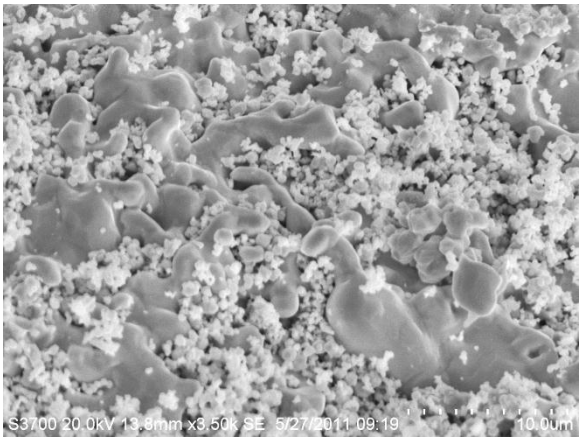

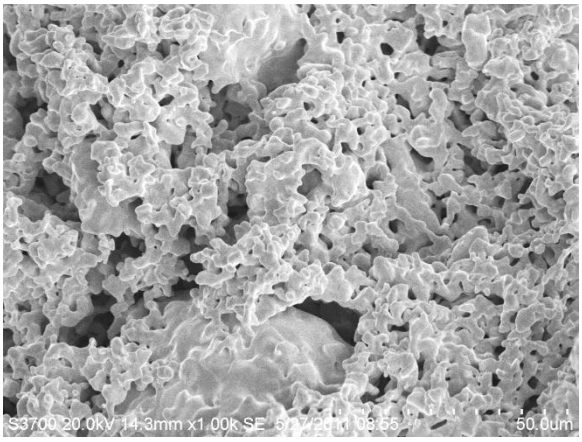

Figure 114.(left) Microstructure of tungsten sphere that consolidated during sintering within the pore space of a 45 ppi RVC foam
Figure 115.(right) Microstructure of tungsten sphere that consolidated during sintering within the pore space of a 65 ppi RVC foam

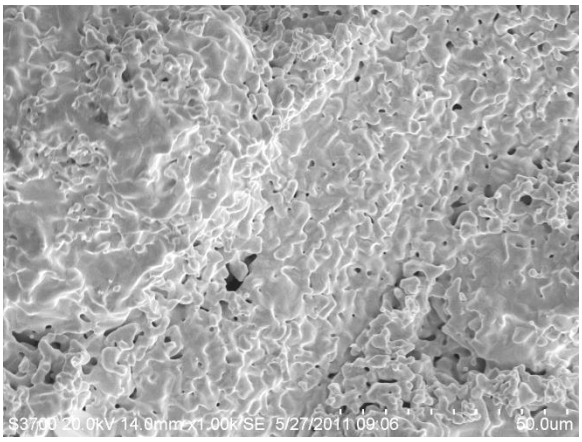

Figure 116. Microstructure of tungsten sphere that consolidated during sintering within the pore space of a 100 ppi RVC foam

The micrographs shown in Figure 114-Figure 116 indicated that a late intermediate stage to final stage of sintering was achieved in the tungsten powder. Densification was microscopically observed within the tungsten spheres through the elimination of much of the porosity between tungsten particles. The remaining smooth and spherical pores, particularly evident in Figure 116, indicate the final stage of sintering was reached.

The average diameters and standard deviations of the sintered tungsten spheres were measured and are shown in Table XXXV. The measured diameters of the tungsten spheres are approximately twice as large as the pore sizes measured for each of the respective RVC foam sizes. RVC pore sizes were measured from faces of cells within the foam. The internal diameter of a tetrakaidecahedron cell is substantially larger than the sizes of the cell faces. Since the tungsten powder consolidated into spheres within the volume of each cell, the sintered tungsten spheres have larger diameters than the measured pore sizes of the RVC foams.

Table XXXV. Average Diameter and Standard Deviation of Sintered Sub-micron Tungsten Spheres

Tungsten Spheres	Average Diameter (μm)	Standard Deviation (μm)
45 ppi RVC	985	72
65 ppi RVC	528	62
100 ppi RVC	446	25

Sintered foams infiltrated with 5-10 micron tungsten exhibited a different microstructure than the foams infiltrated with sub-micron tungsten. The sintered foams infiltrated with 5-10 micron

tungsten had an interpenetrating tungsten network through the foam pore space. They were substantially stronger than the sintered and infiltrated sub-micron tungsten foams. The 5-10 micron tungsten infiltrated foams could withstand vibrational infiltrations after the first sintering. However, unlike the sub-micron infiltrated foams, there was negligible macroscopic volume available for penetration of additional particles into the foam pore space after the first sintering. Therefore, no additional vibrational infiltration runs were performed after sintering.

Figure 117-Figure 122 are optical micrographs of cross-sections of 45 ppi, 65 ppi, and 100 ppi RVC foams infiltrated with 5-10 micron tungsten powder and sintered. The black areas are RVC struts and the grey areas are sintered tungsten. The micrographs show a fairly uniform sub-macroscopic infiltration of tungsten powder throughout the porosity of the foam.

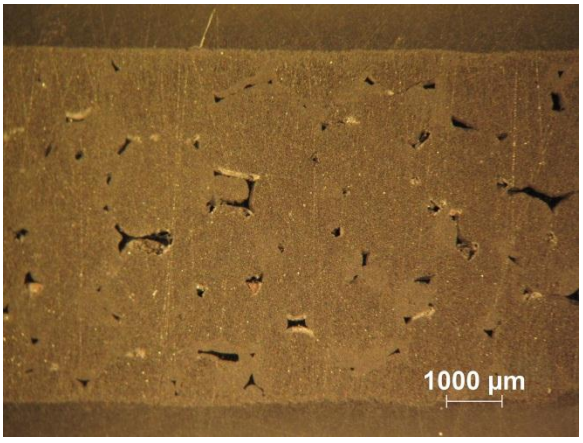

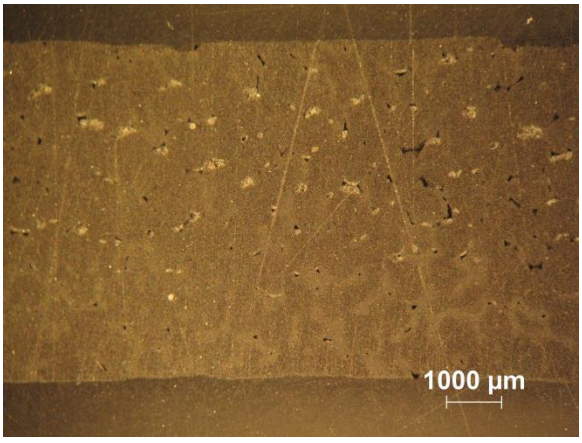

Figure 117.(left) Optical micrograph of 45 ppi RVC foam infiltrated with 5-10 micron tungsten and sintered.
Figure 118.(right) Optical micrograph of 65 ppi RVC foam infiltrated with 5-10 micron tungsten and sintered.

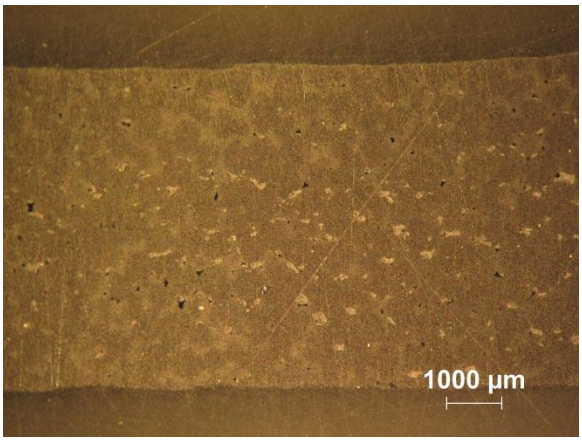

Figure 119. Optical micrograph of 100 ppi RVC foam infiltrated with 5-10 micron tungsten and sintered.

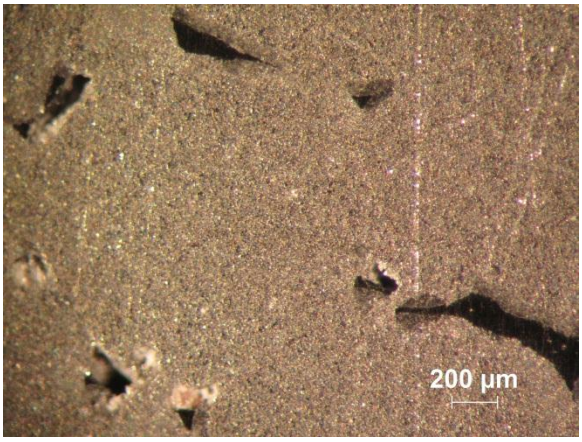

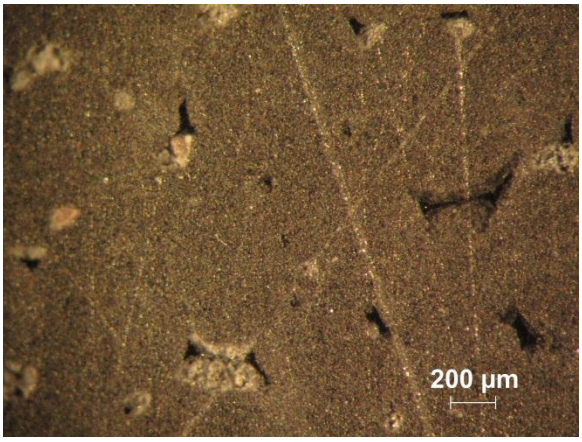

Figure 120.(left) Optical micrograph of 45 ppi RVC foam infiltrated with 5-10 micron tungsten and sintered.
Figure 121.(right) Optical micrograph of 65 ppi RVC foam infiltrated with 5-10 micron tungsten and sintered.

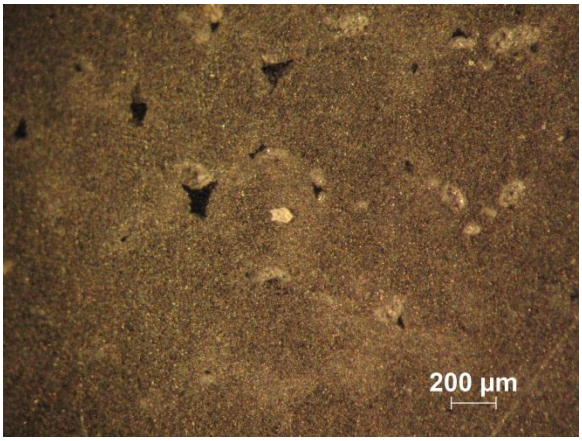

Figure 122. Optical micrograph of 100 ppi RVC foam infiltrated with 5-10 micron tungsten and sintered.

Figure 123-Figure 125 are SEM micrographs of the microstructure of a 45 ppi RVC foam infiltrated with 5-10 micron tungsten after sintering. The black areas are struts of the RVC foam, surrounded by the grey areas of sintered tungsten. The images were obtained from the outer surface of the round. Figure 126 and Figure 127 show neck formation between tungsten particles that occurred during the sintering process.

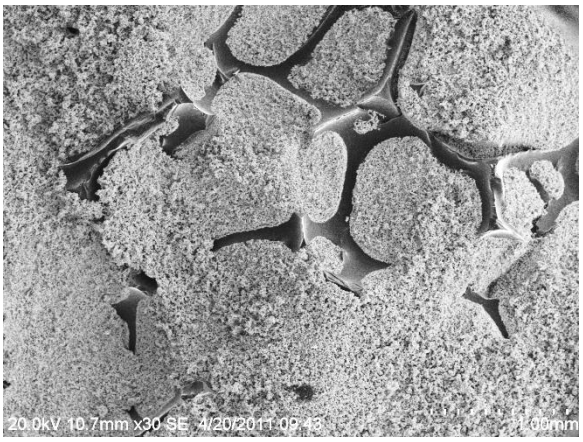

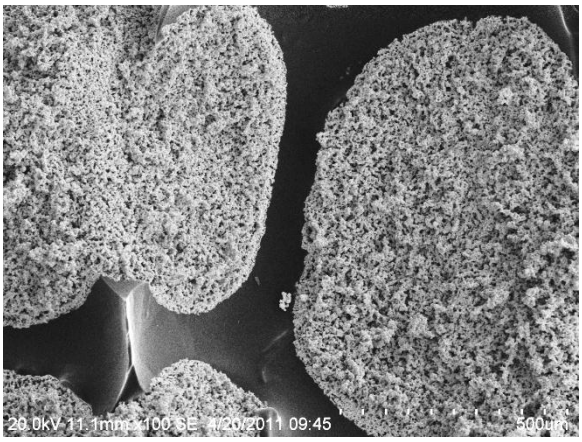

Figure 123.(left) 45 ppi RVC foam infiltrated with 5-10 micron tungsten and sintered.
Figure 124.(right) 45 ppi RVC foam infiltrated with 5-10 micron tungsten and sintered.

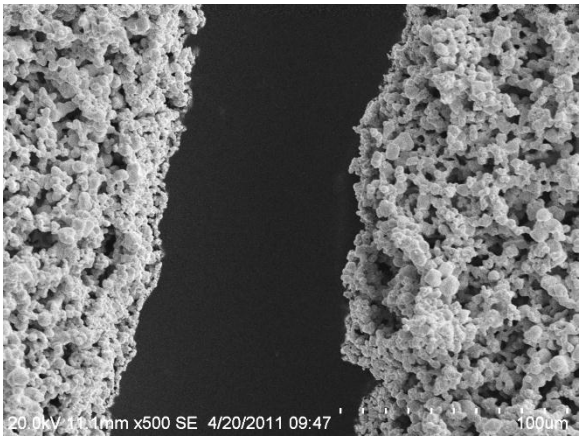

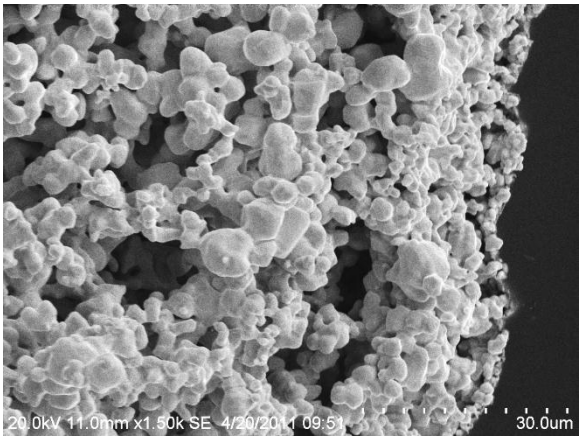

Figure 125.(left) 45 ppi RVC foam infiltrated with 5-10 micron tungsten and sintered.
Figure 126.(right) 45 ppi RVC foam infiltrated with 5-10 micron tungsten and sintered.

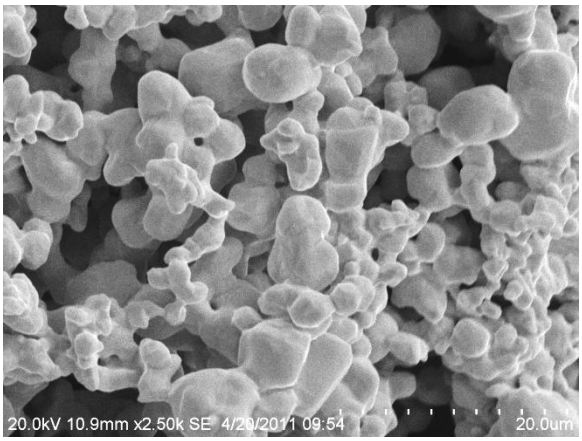

Figure 127. 45 ppi RVC foam infiltrated with 5-10 micron tungsten and sintered.

Figure 128-Figure 130 are SEM micrographs of a cross-section of a 45 ppi RVC foam infiltrated with 5-10 μm tungsten and sintered. Figure 128 shows an RVC strut surrounded by sintered tungsten. Figure 129 and Figure 130 show neck growth between tungsten particles induced by the sintering process.

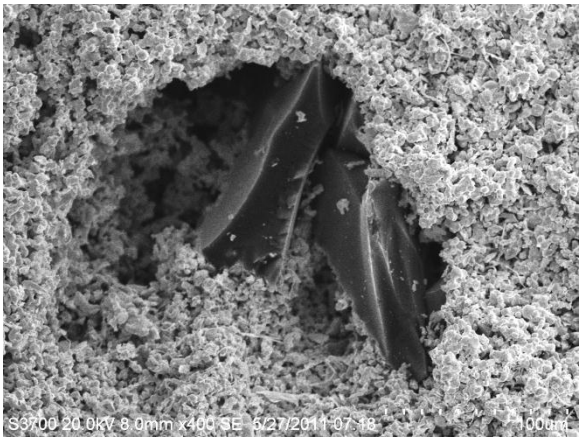

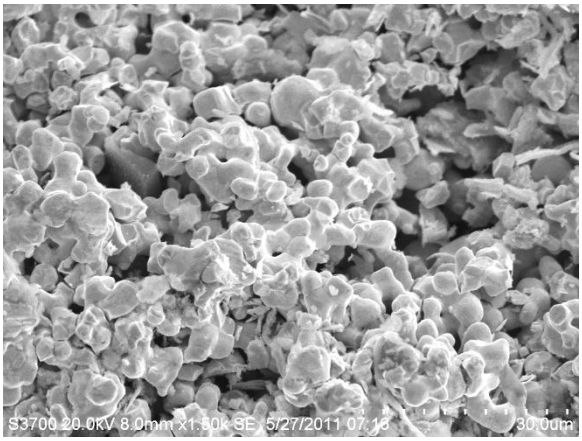

Figure 128.(left) Micrograph of a 45 ppi RVC foam strut surrounded by sintered 5-10 micron tungsten.
Figure 129.(right) Micrograph of sintered 5-10 micron tungsten in an infiltrated 45 ppi RVC foam.

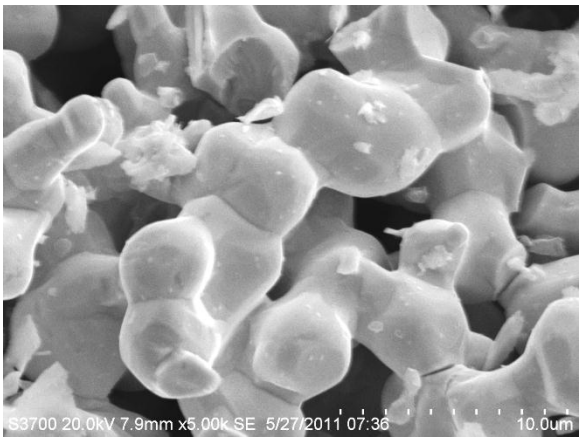

Figure 130. Micrograph of neck growth between sintered 5-10 micron tungsten particles in an infiltrated 45 ppi RVC foam.

Figure 131-Figure 134 are SEM micrographs of a cross-section of a 65 ppi RVC foam infiltrated with 5-10 μm tungsten and sintered. Figure 131 shows an RVC strut surrounded by sintered tungsten. Figure 132-Figure 134 show neck growth between tungsten particles induced by the sintering process.

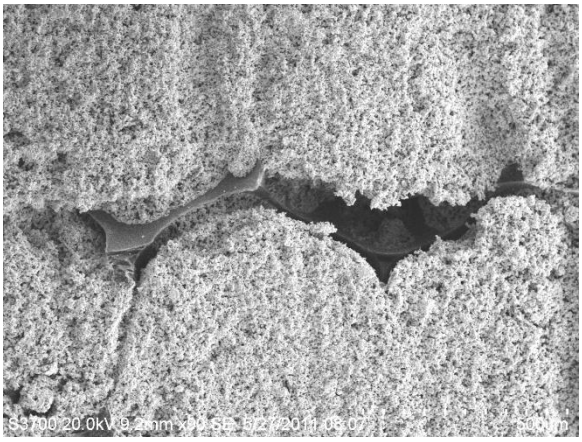

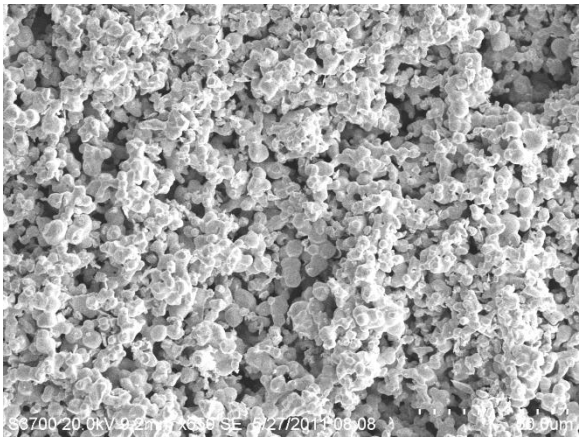

Figure 131.(left) Micrograph of a 65 ppi RVC foam strut surrounded by sintered 5-10 micron tungsten.
Figure 132.(right) Micrograph of sintered 5-10 micron tungsten in an infiltrated 65 ppi RVC foam.

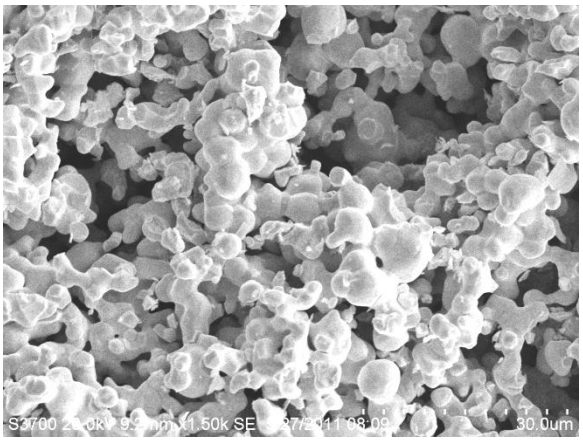

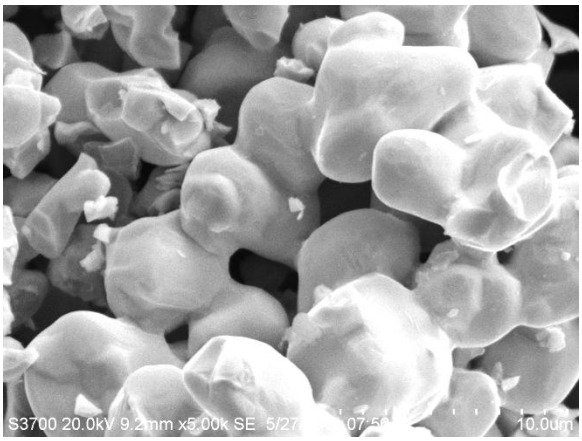

Figure 133.(left) Micrograph of sintered 5-10 micron tungsten particles in an infiltrated 65 ppi RVC foam. Figure 134.(right) Micrograph of neck growth between sintered 5-10 micron tungsten particles in an infiltrated 65 ppi RVC foam.

Figure 135-Figure 139 are SEM micrographs of a cross-section of a 100 ppi RVC foam infiltrated with 5-10 μm tungsten and sintered. Figure 135 and Figure 137 show an RVC strut surrounded by sintered tungsten. Figure 136, Figure 138, and Figure 139 show neck growth between tungsten particles induced by the sintering process.

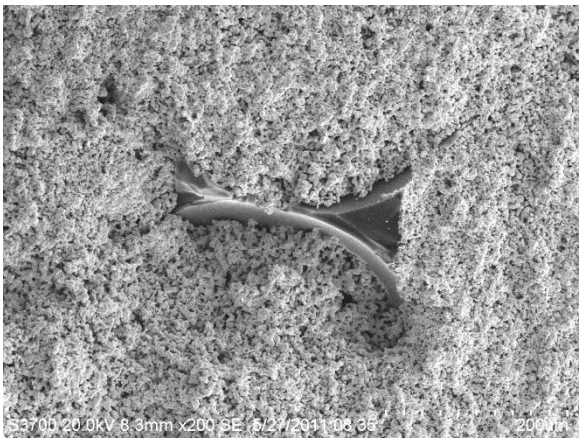

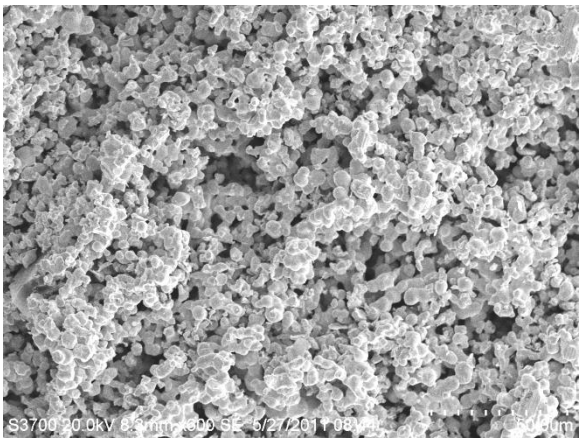

Figure 135.(left) Micrograph of a 100 ppi RVC foam strut surrounded by sintered 5-10 micron tungsten. Figure 136.(right) Micrograph of sintered 5-10 micron tungsten particles in an infiltrated 100 ppi RVC foam.

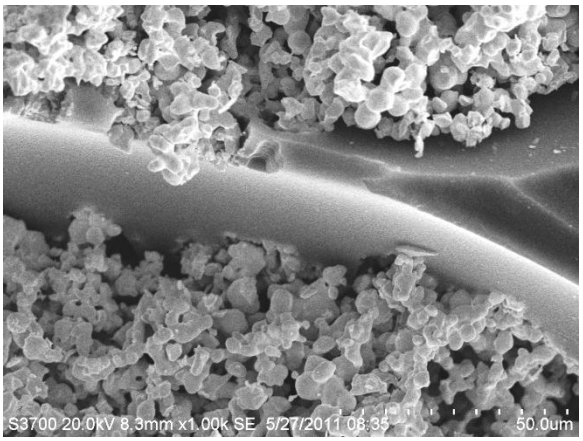

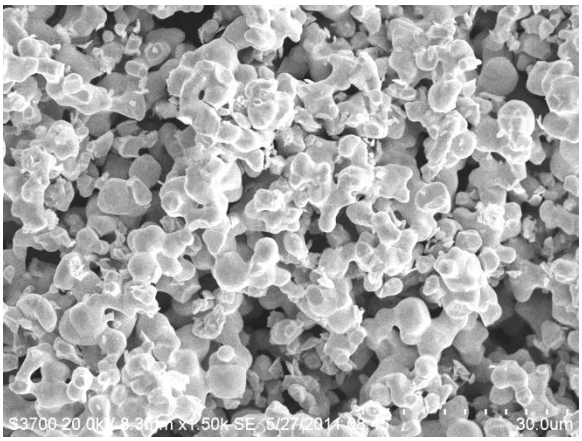

Figure 137.(left) Micrograph of a 100 ppi RVC foam strut surrounded by sintered 5-10 micron tungsten.
Figure 138.(right) Micrograph of sintered 5-10 micron tungsten particles in an infiltrated 100 ppi RVC foam.

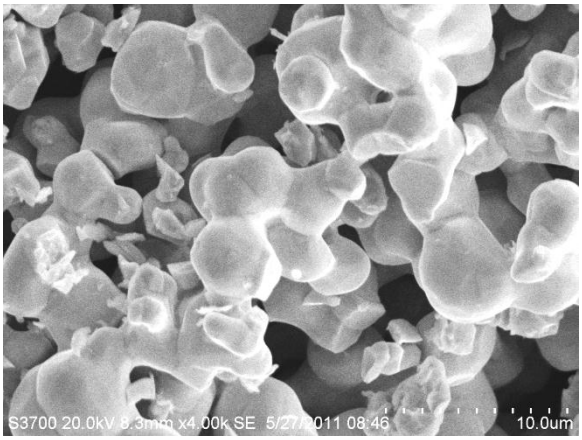

Figure 139. Micrograph of neck growth between sintered 5-10 micron tungsten particles in an infiltrated 100 ppi RVC foam.

Greater than 10 measurements of the ratio of tungsten particle diameter to neck diameter were made for each RVC foam pore density. The average and standard deviation of the measurements are shown in Table XXXVI for 5-10 micron tungsten infiltrated and sintered RVC foams.

Table XXXVI. Average Neck Diameter to Particle Diameter Ratio for Infiltrated and Sintered RVC Foams

Foam Type	Average Ratio	Standard Deviation
45 ppi	0.71	0.10
65 ppi	0.71	0.09
100 ppi	0.68	0.09

No measurable difference was observed in the neck to particle diameter ratio for different foam pore densities. The large ratio indicated that the tungsten sintering progressed well beyond the initial stage of sintering, which typically culminates at a neck to particle diameter ratio of ~ 0.3. However, the presence of the RVC foam throughout the tungsten compact constrained densification during the sintering process. The result was extensive neck growth between tungsten particles with little densification, creating an open-pore tungsten foam within the RVC foam.

Although the foams infiltrated with sub-micron tungsten did not consolidate into a coherent specimen, the individual tungsten spheres exhibited a more advanced stage of sintering than the 5-10 micron tungsten particles. The more extensive sintering observed in the sub-micron tungsten supports the importance of particle size as a sintering parameter as described in Equation 19.

Evidence of a reaction between the tungsten particles and an RVC foam strut can be observed in Figure 140 and Figure 141. Some of the areas of RVC struts that were in contact with 5-10 micron tungsten particles during sintered have been vaporized, likely through formation of a tungsten carbide.

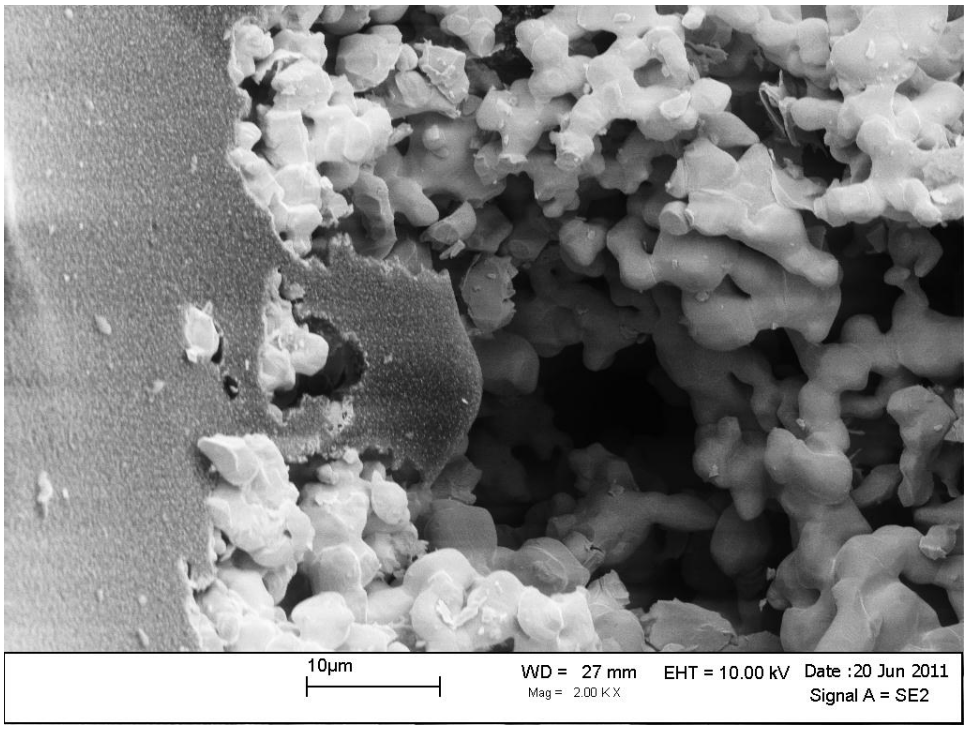

Figure 140. Micrograph of vaporized area on foam strut in 100 ppi RVC foam infiltrated with 5-10 micron tungsten and sintered.

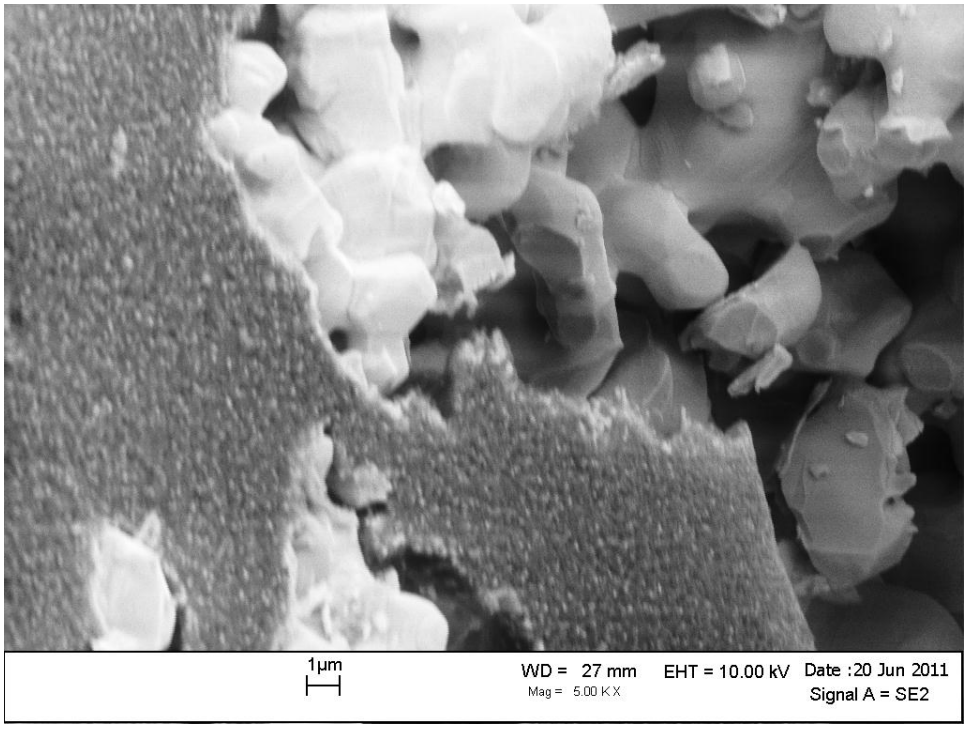

Figure 141. Micrograph of vaporized area on foam strut in 100 ppi RVC foam infiltrated with 5-10 micron tungsten and sintered.

The volumes of infiltrated foams were measured using pycnometry after sintering. A total of 12 volumetric measurements were performed on each foam specimen. The average volume and standard deviation were calculated from the final 3 measurements. Table XXXVII and

Table XXXVIII show average volumes of foams infiltrated with 5-10 micron tungsten powder, and sub-micron tungsten powder, respectively.

Table XXXVII. Average Post-sintering Volume and Standard Deviation for RVC foams Infiltrated with 5-10 Micron Tungsten Powder

Sample	Average Volume (cm^3)	Standard Deviation (cm^3)
45RVCR1	1.5193	0.0007
45RVCR5	1.5895	0.0057
65RVCR1	1.5767	0.0078
65RVCR2	1.5997	0.0043
100RVCR2	1.5877	0.0070
100RVCR6	1.4925	0.0004

Table XXXVIII. Average Post-sintering Volume and Standard Deviation for RVC foams Infiltrated with Sub-micron Tungsten Powder

Sample	Average Volume (cm^3)	Standard Deviation (cm^3)
45RVCR2	1.1127	0.0025
45RVCR4	1.0089	0.0130
65RVCR5	0.9256	0.0010
65RVCR6	0.9209	0.0027
100RVCR3	0.8090	0.0056
100RVCR4	0.6801	0.0047

The data in Table XXXVII and Table XXXVIII largely follow the graphs of infiltrated foam density for sub-micron and 5-10 micron powders for the various foam pore densities.

The specimen of sub-micron tungsten powder that was sintered without RVC foam had a post-sinter mass of 34.733 g. The volume was determined through pycnometry and was 1.8692 cm^3 +/-0.0050. The density of the specimen was 18.603 g/cm^3, which is 96.6% theoretical tungsten density. The significantly higher degree of densification that was obtained in tungsten through loose powder sintering than obtained during consolidation of the tungsten infiltrated RVC foams indicated that the presence of the foams struts significantly inhibited densification within the tungsten. The presence of the foam constrained tungsten densification throughout the bulk infiltrated foam specimen. However, densification did occur within the sub-micron tungsten powder in each pore of the foam. When foams infiltrated with 5-10 micron tungsten powder were sintered, densification was again constrained, but neck growth proceeded throughout the infiltrated foam to form a continuous low-density network of sintered tungsten.

Modulus Measurement Using Impulse Excitation

A graph of the waveform generated through impulse excitation of an infiltrated and sintered foam round is shown in Figure 142. The graph of the fast Fourier transform of the waveform in Figure 142 is shown in Figure 143. The units on the x-axis are Hertz and the amplitude is measured on the y-axis. Graphs of waveforms and fast Fourier transforms for all impulse excitation measurements are shown in Appendix H. Multiple resonant frequency peaks were observed in the fast fourier transform graphs generated from impulse excitation. The multiple peaks are likely due to the material under investigation being a composite and a having a high porosity.

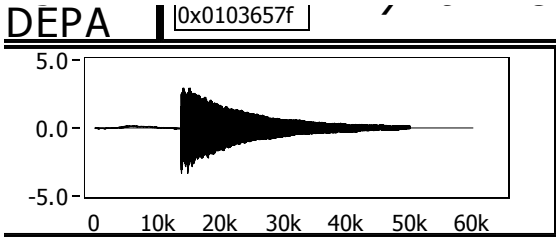

Figure 142. Graph of waveform for vibration induced in sample 45RVCR1.

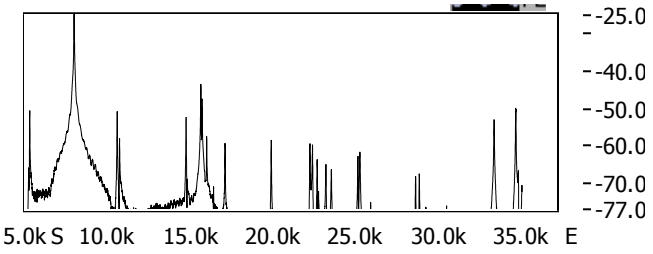

Figure 143. Graph of fast Fourier transform for the above waveform.

Average measurements from impulse excitation of sintered RVC foam rounds that were infiltrated with 5-10 micron tungsten powder are shown in Table XXXIX.

Table XXXIX. Average Impulse Excitation Measurements for RVC Foam Rounds Infiltrated with 5-10 Micron Tungsten Powder and Sintered

		Flexural frequency (Hz)	Anti-flexural frequency (Hz)	Young's modulus (Gpa)	Shear modulus (Gpa)	Poisson's ratio
45RVCR1	Average	5160.34	7907.05	4.57	1.87	0.22
	Std. Dev.	1.34	1.13			
45RVCR5	Average	7222.69	10785.52	9.70	4.11	0.18
	Std. Dev.	0.63	1.85			
65RVCR1	Average	6515.82	9736.79	7.67	3.25	0.18
	Std. Dev.	0.29	0.94			
65RVCR2	Average	6533.21	9839.85	8.35	3.47	0.20
	Std. Dev.	0.32	0.37			
100RVCR2	Average	6760.44	10135.62	8.29	3.51	0.18
	Std. Dev.	0.35	0.53			
100RVCR6	Average	5542.36	8366.07	5.28	2.19	0.20
	Std. Dev.	0.17	0.95			

The results of impulse excitation measurements were found to be quite repeatable within a given specimen, as evidenced by the low standard deviation in the measured flexural and anti-flexural

frequencies. Young's moduli from 4.57-9.7 GPa were measured for consolidated infiltrated foams. The data in Table XXXIX indicate significant differences in the moduli for the two consolidated samples of 45 ppi and 100 ppi tungsten-infiltrated foams. Sample 45RVCR5 had significantly larger moduli than 45RVCR1, and also had a higher measured volume and infiltrated mass. The same phenomenon was observed between sample 100RVCR2 and 100RVCR6. It is believed that larger volume and larger mass within the samples were the reasons for the differences in moduli between infiltrated foams of equivalent pore density. The measured volumes and masses of the infiltrated 65 ppi foams were considerably more similar than those of the 45 ppi and 100 ppi, as were the predicted moduli.

V. Conclusions

This section describes the conclusions drawn for the objectives of this study, which included: Understanding the influence of strut/pore size, foam composition, and foam density on the neutron transmission in TaC foams, understanding the influence of strut/pore size, foam composition, foam density, thermal fatigue, and thermal shock on mechanical behavior of TaC foams, and understanding the influence of foam pore size and tungsten particle size/surface area on vibration-induced tungsten particle infiltration and densification within RVC foams, with the goal of forming an IPC.

The morphology of TaC foams typically consisted of cell faces with square, pentagonal, and hexagonal geometries. Average foam strut thicknesses ranged from 318-142 microns for 45-100 ppi TaC/PyC/RVC foams. The average strut thicknesses for 45-100 ppi TaC/RVC foams ranged from 256-74 microns. Average pore sizes ranged from 546-198 microns for 45-100 ppi TaC/PyC/RVC foams. The average pore sizes for 45-100 ppi TaC/RVC foams ranged from 654-164 microns.

The average thickness of the TaC coating on TaC/RVC foams ranged from 39-10 microns for 45-100 ppi foams. The average RVC core strut thickness ranged from 118-47 microns for 45-100 ppi TaC/RVC foams. TaC/PyC/RVC foams had an average TaC coating thickness that ranged from 40-14 microns for 45-100 ppi foams. The average pyrolytic carbon thickness ranged from 44-7 microns for 45-100 ppi TaC/PyC/RVC foams. The average RVC core strut thickness ranged from 130-45 microns for 45-100 ppi TaC/PyC/RVC foams. Open porosity ranged from 88.3%-90.7% for TaC/RVC foams, whereas for TaC/PyC/RVC foams it ranged from 80.3-86.2%.

Influence of Strut/Pore Size, Foam Composition, and Foam Density on the Neutronic Properties of the Foam

Strut and/or pore size was found to have no measurable influence on experimental neutron transmission measurements using an AmBe neutron source. A small decrease in neutron transmission was observed in foams containing a PyC layer. A larger decrease in neutron transmission was observed as mass of the PyC layer increased. Foam density was found to have the most profound impact on neutron transmission. Neutron transmission decreased linearly

within TaC/RVC foams as areal TaC density increased. Experimental neutron transmission measurements followed the equation y=-0.0605x+0.9594. Neutron transmission decreased in TaC/RVC foams modeled in MCNP following the equation y=-0.0702x+0.9851, where *y* is neutron transmission relative to baseline and *x* is areal density of TaC. MCNP modeling results were typically within one standard deviation of experimental neutron transmission measurements. MCNP modeling results indicate that neutron transmission through the TaC foam was reduced the most at neutron energies between 1E-08 - 1E-07 MeV and 3-10 MeV. There was also reduction of neutron transmission in the vicinity of 1E-05 MeV. All MCNP modeling runs predicted slightly higher neutron transmission than what was experimentally measured, possibly indicating that the foam structure has a small influence on neutron transmission.

Influence of Strut/Pore Size, Foam Composition, Foam Density, Thermal Fatigue, and Thermal Shock on the Mechanical Properties of the Foam

Prior to thermal cycling, only the 45 ppi TaC/PyC/RVC foams were observed to have significant quantities of micro-cracks in the struts. Extensive micro-cracking was observed in the TaC coating of all foam specimens after 18 thermal cycles. Debonding was observed in several areas along the TaC/PyC interface in TaC/PyC/RVC foams. However, no debonding was observed along the PyC/RVC interface in TaC/PyC/RVC foams. Debonding was also observed in several areas at the TaC/RVC interface in TaC/RVC foams. TaC/RVC foams tended to exhibit less extensive micro-cracking than the TaC/PyC/RVC foams. In addition, the 100 ppi foams tended to have less extensive micro-cracking than 45 ppi and 65 ppi foams. No observable micro-cracking or other microstructural effects were observed upon examination of foams after thermal shock in liquid nitrogen.

A significant decrease in compressive strength was observed in thermally cycled foams with respect to baseline compressive strength, as a result of micro-cracking. The compressive strength of thermally cycled foams tended to be 1/3-1/2 of baseline specimens. The average strengths of baseline TaC/RVC foams were 1.970 MPa, 3.824 MPa, and 3.531 MPa for 45 ppi, 65 ppi, and 100 ppi foams, respectively. The average strengths dropped to 0.609 MPa, 0.764 MPa, and 1.421 MPa for the respective foam pore densities after 18 thermal cycles. The baseline

TaC/PyC/RVC foams exhibited average strengths of 5.560 MPa, 4.566 MPa, 8.724 MPa, and 12.599 MPa for 45 ppi, 65 ppi, 100 ppi Type A, and 100 ppi Type B TaC/PyC/RVC foams, respectively. After 18 thermal cycles the average strength was reduced to 2.766 MPa, 1.964 MPa, 3.394 MPa, and 7.510 MPa for the respective foam pore densities. Thermally shocked TaC/RVC and TaC/PyC/RVC foams had significantly higher compressive strengths than thermally cycled foams. Typically the strength of thermally shocked foams was within one standard deviation of the mean baseline foam strength.

T-tests conducted on the compressive strength datasets yielded the following results: There was at least a 90% probability in 9 of 12 datasets that the presence of PyC increased the strength of TaC foams. In 4 of 9 datasets there was at least a 90% probability that strut size influenced the strength within TaC/RVC foams. There was at least an 85% probability in 12 of 15 datasets that strut size influenced strength within TaC/PyC/RVC foams. In 6 of 9 datasets there was at least a 90% probability that thermal cycling decreased foam strength relative to baseline and thermally shocked TaC/RVC foams. There was at least a 90% probability in 11 of 12 datasets that thermal cycling decreased foam strength relative to baseline and thermally shocked TaC/PyC/RVC foams.

The TaC/PyC/RVC foams exhibited higher strengths than the TaC/RVC foams. Upon foam strut failure, the PyC layer exhibited laminar cleavage, whereas the RVC core exhibited conchoidal fracture. It was hypothesized that the increase in strength was due to crack deflection and delamination within the PyC interlayer, which increased the energy needed for crack propagation through the foam struts, thus increasing foam strength. TaC foams tended to exhibit a trend of increasing strength with increasing TaC relative density. The trend was most pronounced in the TaC/RVC foams. It was observed that TaC coating thicknesses of ~25 microns, and PyC coating thicknesses between 25-30 microns produced the highest compressive strengths within foams. As thicknesses increased or decreased from those values, the compressive strength decreased.

The assumptions used in predicting the mechanical strength of TaC foams resulted in a broad range of predicted strengths. Experimental measurements typically fell within the range of predicted values. However for 100 ppi foams, the strength predictions were lower than

experimental measurements. The results indicate that strut cross-sectional area fractions can be used to calculate a composite strut modulus of rupture, which in turn can be used in Equation 7 to estimate the compressive strength of the foam. The correlation between prediction and measurement of Young's modulus was not as good as that observed with compressive strength. However, all experimental Young's modulus measurements were within or above the predicted Young's modulus range except for 45 TaC/PyC/RVC foams. The low measurements of Young's modulus in 45 TaC/PyC/RVC foams are thought to be the result of the presence of micro-cracks in the specimens.

Formation of a Tungsten- Ceramic Foam Composite

Particle size of the tungsten powder was found to play a more significant role than the pore size of the foams during the infiltration process. Particle size analysis conducted on the sub-micron powder using a dry analysis method coupled with SEM analysis indicated that the powder had a substantially larger apparent particle size due to particle agglomeration. The agglomeration of sub-micron tungsten particles is also likely to have reduced densities achieved within vibrationally infiltrated RVC foams.

There was a small decrease in tungsten infiltration with decreasing pore size observed with the 5-10 micron tungsten powder. The decrease in tungsten infiltration was more pronounced with the sub-micron powder. Infiltrated 5-10 micron tungsten achieved theoretical densities ranging from 23-25% theoretical within RVC foams, whereas sub-micron tungsten densities ranged from 11-16% theoretical. The tap density of 5-10 micron tungsten (with no foam present) was measured to be 28% of the theoretical tungsten density, whereas the sub-micron tungsten was found to be 19% of the theoretical tungsten density.

The significantly higher density (96.6% theoretical) achieved in the sintering of plain sub-micron tungsten powder when compared with the tungsten infiltrated foams, indicated that the presence of the foam constrained the densification of tungsten. While densification was constrained, neck growth was extensive in both sub-micron and 5-10 micron tungsten powders.

T-tests conducted on the foam infiltration datasets yielded the following results: There was at least an 85% probability that 65 ppi RVC foams infiltrated to higher densities with 5-10 micron tungsten than 45 ppi and 100 ppi RVC foams. At least a 99% probability existed that the infiltration of sub-micron tungsten particles decreased as RVC foam pore density increased. There was at least a 99.5% probability that 5-10 micron tungsten powder produced higher infiltrated densities within RVC foams than sub-micron tungsten powder.

Sintering of the RVC rounds infiltrated with sub-micron tungsten resulted in consolidation of the tungsten into spherical particles within the foam pore space. The spherical particles were not connected throughout the pore structure of the foam. However, microstructural analysis of consolidated spherical particles indicated that they had progressed to the final stage of sintering. The RVC foam infiltrated with 5-10 micron tungsten exhibited an interpenetrating tungsten network after sintering. Cross-sections of sintered 5-10 micron tungsten infiltrated foams exhibited uniform infiltration throughout the foam thickness. The neck diameter to particle diameter ratio for infiltrated and sintered 5-10 micron tungsten foams was approximately 0.7 for all RVC foam pore densities, indicating that sintering had progressed well beyond the initial sintering stage. The combination of neck growth and constrained densification allowed formation of a tungsten foam within the RVC foam. Impulse excitation measurements of the tungsten-foam composite resulted in Young's moduli between 4.57-9.7 GPa, shear moduli from 1.87-4.11 GPa and Poisson's ratios between 0.18-0.22.

Future Work

Results from the infiltration and sintering of RVC foams provide further avenues for future research. One concept could include heat-treating consolidated, tungsten- infiltrated RVC foams in a hydrogen environment to eliminate the RVC, leaving only porous tungsten. Melt-infiltration or CVI could be used to deposit nuclear fuel within the porosity of the tungsten. A coating of tungsten-rhenium could then be deposited for further encapsulation of the nuclear fuel. Another possibility would be to vibrationally infiltrate RVC foam with a nuclear fuel. The infiltrated foam could be sintered and then heat-treated in hydrogen to remove the RVC. The porous nuclear fuel could be used as-is, or a coating of tungsten-rhenium could be applied for further encapsulation.

Further research could also involve infiltrating RVC foams with a larger size of tungsten particles in order to determine the maximum particle size that can be used without decreasing the infiltrated density. Thicker foams could be utilized in order to determine the efficiency of particle infiltration throughout the foam thickness.

References

1. Youchison, D.L., et al., *A Tricarbide Foam Fuel Matrix for Nuclear Thermal Propulsion*, in *42nd AIAA/ASME/SAE/ASEE Joint Propulsion Conference & Exhibit*2006: Sacramento, CA.
2. DelaRosa, M.J. and Tuffias, R.H., *Materials Characterization and Design for Solar-Thermal Propulsion*, 1993.
3. Teague, M.C., Hilmas, G.E., and Fahrenholtz, W.G., *Reaction Processing of Ultra-High Temperature W/Ta_2C-Based Cermets.* J. Am. Ceram. Soc., 2009. 92(9): p. 1966-1971.
4. López-de-laTorre, L., et al., *Elastic Properties of Tantalum Carbide (TaC).* Solid State Communications, 2005. 134: p. 245-250.
5. Hust, J.G. and Giarratano, P.J., *Thermal Conductivity and Electrical Resistivity Standard Reference Materials: Tungsten SRM's 730 and 799 From 4 to 3000 K*, 1975, US Department of Commerce-National Bureau of Standards: Boulder.
6. Ross, S.D., *Nuclear Thermal Rockets: The Physics of the Fission Reactor*, 2001, Control and Dynamical Systems-Caltech: Pasadena.
7. Araj, K.J., et al., *Ultra-high Temperature Direct Propulsion*, Brookhaven National Laboratory.
8. Lawrence, T.J., *Nuclear Thermal Rocket Propulsion Systems*, 2005, IAA, USAF: Paris, .
9. Clark, R.A. and Sheldon, R.B., *Dusty Plasma Based Fission Fragment Nuclear Reactor*, in *41st AIAA/ASME/SAE/ASEE Joint Propulsion Conference & Exhibit*2005, AIAA: Tucson, AZ.
10. Bess, J.D., *Tungsten Cermet Reactors*, 2006, CSNR-INL.
11. Kruger, G. *A CERMET Fuel Reactor for Nuclear Thermal Propulsion*. in *Nuclear Thermal Propulsion: A Joint NASA/DOE/DOD Workshop*. 1990. Cleveland, OH: NASA.
12. Ma, B.M., *Nuclear Reactor Materials and Applications*1983, New York: Van Nostrand Reinhold Company. 610.
13. Anghaie, S., *Fuels Applicable to Nuclear Thermal Propulsion Reactor Cores*, 2009, Innovative Nuclear Space Power & Propulsion Institute-University of Florida: Atlanta.
14. Panda, B., Hickman, R.R., and Shah, S., *Solid Solution Carbides are the Key Fuels for Future Nuclear Thermal Propulsion*, NASA Marshall Space Flight Center.
15. Lundberg, L.B. and Hobbins, R.R., *Nuclear Fuels for Very High Temperature Applications*, in *Intersociety Energy Conversion Engineering Conference,*1992: San Diego, CA.
16. Anghaie, S. *Droplet Core Nuclear Reactor (DCNR)*. in *Nuclear Thermal Propulsion: A Joint NASA/DOE/DOD Workshop*. 1990. Cleveland, OH: NASA.
17. Bhaduri, S.B., *Science and Technology of Ceramic Foams.* Advanced Performance Materials, 1994. 1: p. 205-220.
18. Colombo, P. and Hellman, J.R., *Ceramic foams from preceramic polymers.* Mat Res Innovat, 2002. 6: p. 260-272.
19. Sharafat, S., et al., *Micro-engineered first wall tungsten armor for high average power laser fusion energy systems.* Journal of Nuclear Materials, 2005. 347: p. 217-243.
20. Twigg, M.V. and Richardson, J.T., *Fundamentals and Applications of Structured Ceramic Foam Catalysts.* Ind. Eng. Chem. Res., 2007. 46: p. 4166-4177.
21. Ashby, M.F., *The Properties of Foams and Lattices.* Phil. Trans. R. Soc. A, 2006. 364: p. 15-30.
22. Colombo, P., Hellman, J.R., and Shelleman, D.L., *Mechanical Properties of Silicon Oxycarbide Ceramic Foams.* J. Am. Ceram. Soc., 2001. 84(10): p. 2245-2251.
23. Gibson, L.J. and Ashby, M.F., *Cellular Solids: Structure and Properties*. 2 ed1997, Cambridge: Cambridge University Press. 510.
24. Callister, W.D., *Fundamentals of Materials Science and Engineering*. 2 ed2005: John Wiley & Sons. 712.
25. Vedula, V.R., Green, D.J., and Hellman, J.R., *Thermal Fatigue Resistance of Open Cell Ceramic Foams.* Journal of the European Ceramic Society, 1998. 18(14): p. 2073-2080.
26. Ultramet. *Ultramet Refractory Open Cell Foams*. 2010 July 21, 2010]; Available from: http://www.ultramet.com.
27. Friedrich, J.M., et al., *Reticulated vitreous carbon as an electrode material.* Journal of Electroanalytical Chemistry, 2004. 561: p. 203-217.

28. **Wang, J., *Reticulated Vitreous Carbon-A New Versatile Electrode Material.* Electrochimica Acta, 1981. 26(12): p. 1721-1726.**
29. **Kinoshita, K., *Carbon-Electrochemical and Physicochemical Properties*1988, New York: John Wiley & Sons. 533.**
30. **Morgan, P., *Carbon Fibers and their Composites*2005, Boca Raton: Taylor & Francis. 1153.**
31. **Bhat, S.V., *Biomaterials*2005: Alpha Science International. 294.**
32. **Nozawa, T., et al., *Shear properties at the PyC/SiC interface of a TRISO-coating.* Journal of Nuclear Materials, 2007. 371(1-3): p. 304-313.**
33. **Hou, X., et al., *Interface-like fracture mechanism in pyrolytic carbon matrix-based carbon-carbon composites.* Materials Letters, 2001. 48: p. 117-120.**
34. **Lowenthal, G.C. and Airey, P.L., *Practical Applications of Radioactivity and Nuclear Radiations*2001, Cambridge: Cambridge University Press. 337.**
35. **Rinard, P., *Neutron Interactions with Matter*, in *Passive Nondestructive Assay of Nuclear Materials*, D. Reilly, N. Ensslin, and H. Smith, Editors. 1991.**
36. ***Radiation Source Use and Replacement*2008: National Academies Press. 232.**
37. **Tuli, J.K., *Nuclear Wallet Cards*, 2005, National Nuclear Data Center-Brookhaven National Lab: Upton. p. 115.**
38. **Briesmeister, J.F., ed. *MCNP-A General Monte Carlo N-Particle Transport Code*. 1997, Los Alamos National Lab.**
39. **Wegner, L.D. and Gibson, L.J., *The Fracture Toughness Behaviour of Interpenetrating Phase Composites.* International Journal of Mechanical Sciences, 2001. 43: p. 1771-1791.**
40. **Mattern, A., et al., *Preparation of Interpenetrating Ceramic-metal Composites.* Journal of the European Ceramic Society, 2004. 24: p. 3399-3408.**
41. **Clarke, D.R., *Interpenetrating Phase Composites.* J. Am. Ceram. Soc., 1992. 75(4): p. 739-759.**
42. **Peng, H.X., Fan, Z., and Evans, J.G., *Bi-continuous Metal Matrix Composites.* Materials Science and Engineering A, 2001. 303: p. 37-45.**
43. **Zhou, W., Hu, W., and Zhang, D., *Metal-matrix Interpenetrating Phase Composite and its In Situ Fracture Observation.* Materials Letters, 1999. 40: p. 156-160.**
44. **Cree, D. and Pugh, M., *Production and characterization of a three-dimensional cellular metal-filled ceramic composite.* Journal of Materials Processing Technology, 2010. 210: p. 1905-1917.**
45. **Moraga, N.O., Jacobson, D.L., and Morris, J.F., *Fracture-Resistant Ultralloys for Space-Power Systems: Nuclear-Thermionic-Conversion Implications of W,27 Re.* Engineering Fracture Mechanics, 1989. 34(3): p. 553-565.**
46. **Luo, A., Shin, K.S., and Jacobson, D.L., *Hafnium Carbide Strengthening in a Tungsten-Rhenium Matrix at Ultrahigh Temperatures.* Acta metall. mater., 1992. 40(9): p. 2225-2232.**
47. **Kieffer, R., Sedlatschek, K., and Braun, H., *Tungsten Alloys of High Melting Point.* Journal of the Less-Common Metals, 1959. 1: p. 19-33.**
48. **Makarov, P. and Povarova, K., *Development of Tungsten-based Vacuum Melted and Powder Structural Alloys.* International Journal of Refractory Metals & Hard Materials, 2002. 20: p. 277-285.**
49. **Raffo, P.L., *Yielding and Fracture in Tungsten and Tungsten-Rhenium Alloys.* J. Less-Common Metals, 1969. 17: p. 133-149.**
50. **Blaschko, O., Prem, M., and Leichtfried, G., *Porosity Evolution During SIntering In Tungsten Powders of Different Grain Size.* Scripta Materialia, 1996. 34(7): p. 1045-1049.**
51. **Wang, H., et al., *Sinter-ability of Nanocrystalline Tungsten Powder.* Int. Journal of Refractory Metals & Hard Materials, 2010. 28: p. 312-316.**
52. **Kitsunai, Y., et al., *Microstructure and impact properties of ultra-fine grained tungsten alloys dispersed with TiC.* Journal of Nuclear Materials, 1999. 271-272: p. 423-428.**
53. **German, R.M., *Powder Metallurgy Science*1994, Princeton: Metal Powder Industries Federation. 472.**
54. **Nowak, E.R., et al., *Reversibility and irreversibility in the packing of vibrated granular material.* Powder Technology, 1997. 94: p. 79-83.**
55. **Edwards, S.F. and Grinev, D.V., *Statistical Mechanics of Vibration-Induced Compaction of Powders.* Phys. Rev. E, 1998. 58(4): p. 4758-4762.**
56. **Ashby, M.F., *A First Report on Sintering Diagrams.* Acta Metallurgica, 1974. 22: p. 275-289.**
57. **Hanwei, H., Kechao, Z., and Xiang, X., *A Novel Method for Preparation of TaC Coating on C/C Composite Material.* J. Mater. Sci. Technol., 2005. 21(3): p. 381-385.**

58. **Pierson, H.O.,** ***Handbook of Chemical Vapor Deposition: Principles, Technology, and Applications*** **1999: William Andrew. 506.**

59. **Kim, C., Grummon, D.S., and Gottstein, G.,** ***Processing and Interface Characteristics of Graphite Fiber Reinforced Tantalum Carbide Matrix Composites.*** **Scripta Metallurgica et Materialia, 1991. 25: p. 2351-2356.**

60. **Santoro, G.,** ***Variation of Some Properties of Tantalum Carbide with Carbon Content.*** **Transactions of the Metallurgical Society of AIME, 1963: p. 1361-1368.**

61. **Honeycutt, L., III., Jennings, W.H., and Manning, C.R., Jr.,** ***High Temperature Erosion of Tantalum Carbide Composites.*** **Wear, 1976. 37: p. 209-216.**

62. **ASTM,** ***Standard Test Method for Dynamic Young's Modulus, Shear Modulus, and Poisson's Ratio by Impulse Excitation of Vibration,*** **2009, ASTM.**

63. **ASTM,** ***Standard Test Method for Dynamic Young's Modulus, Shear Modulus, and Poisson's Ratio for Advanced Ceramics by Impulse Excitation of VIbration,*** **2008.**

64. **Keppel, G., Saufley, W.H., and Tokunaga, H.,** ***Introduction to design and analysis: a student's handbook*****. 2 ed1992: Macmillan. 626.**

65. **Price, R.J. and Bokros, J.C.,** ***Mechanical Properties of Neutron-Irradiated Pyrolytic Carbons.*** **Journal of Nuclear Materials, 1967. 21: p. 158-174.**

66. **Bakshi, S.R., et al.,** ***Spark plasma sintered tantalum carbide: Effect of pressure and nano-boron carbide addition on microstructure and mechanical properties.*** **Materials Science and Engineering A, 2011. 528: p. 1287-1295.**

Appendix A. Tantalum Carbide Foam Specifications Produced from Data Provided by Ultramet®

Table XL. Tantalum Carbide Foam Specifications Produced from Data Provided by Ultramet®

Foam Composition	PPI	Sample #	Geometric Volume (cm^3)	Mass (g)	TaC Mass Gain (g)	Foam Core Mass (g) RVC or PyC/RVC	TaC Theoretical Density	TaC Density (g)	Carbon Density (g)
TaC/PyC/RVC	45	1	6.246	7.7348	6.5108	1.224	7.19%	1.042	0.196
		3	6.242	7.8124	6.5884	1.224	7.28%	1.055	0.196
		4	6.332	7.4724	6.2314	1.241	6.79%	0.984	0.196
		5	6.336	7.5262	6.2832	1.243	6.84%	0.992	0.196
		6	6.218	7.5672	6.3472	1.220	7.04%	1.021	0.196
		7	6.242	7.0794	5.8544	1.225	6.47%	0.938	0.196
TaC/PyC/RVC	65	1	6.178	6.3751	5.8581	0.517	6.54%	0.948	0.084
		2	6.178	7.9101	7.3931	0.517	8.25%	1.197	0.084
		3	6.178	6.3849	5.8679	0.517	6.55%	0.950	0.084
		4	6.178	7.9667	7.4497	0.517	8.32%	1.206	0.084
		5	6.178	8.6333	8.1163	0.517	9.06%	1.314	0.084
		6	6.178	6.1974	5.6804	0.517	6.34%	0.919	0.084
TaC/PyC/RVC	100	1	6.143	7.3830	5.7740	1.609	6.48%	0.940	0.262
		2	6.056	8.4113	6.8263	1.585	7.77%	1.127	0.262
		6	6.212	8.9401	7.3161	1.624	8.12%	1.178	0.261
TaC/PyC/RVC	100	1n	6.155	7.6621	7.1511	0.511	8.01%	1.162	0.083
		2n	6.108	7.4491	6.9421	0.507	7.84%	1.137	0.083
		3n	6.108	7.7135	7.2065	0.507	8.14%	1.180	0.083
TaC/RVC	45	1	6.204	7.5863	7.3320	0.254	8.15%	1.182	0.041
		2	6.204	7.7885	7.5290	0.260	8.37%	1.214	0.042
		3	6.195	7.2914	7.0330	0.258	7.83%	1.135	0.042
		4	6.180	7.6525	7.4020	0.251	8.26%	1.198	0.041
		5	6.175	6.0074	5.7570	0.250	6.43%	0.932	0.041
		6	6.227	7.8116	7.6100	0.202	8.43%	1.222	0.032
		7	6.181	7.5660	7.3130	0.253	8.16%	1.183	0.041

TaC/RVC	65	2a	6.062	7.1701	6.8910	0.279	7.84%	1.137	0.046
		3a	6.175	8.9045	8.6220	0.283	9.63%	1.396	0.046
		4a	5.982	7.1907	6.9130	0.278	7.97%	1.156	0.046
		5a	6.081	8.1556	7.8830	0.273	8.94%	1.296	0.045
TaC/RVC	100	1	6.102	5.2348	4.9900	0.245	5.64%	0.818	0.040
		2	5.957	6.1270	5.8910	0.236	6.82%	0.989	0.040
		3	6.022	5.1326	4.8900	0.243	5.60%	0.812	0.040
		4	5.921	5.2695	5.0310	0.239	5.86%	0.850	0.040

Appendix B. Example of an Input File that was Used in MCNP Neutron Transport Modeling

```
c LaRC 1C Am-Be Neutron Source, FA-045-071906-03 Disc 1 Round 6 TaC/RVC
c
c Cells
c
1000  0             -010     -100 +120     IMP:N=1  $ AmBe neutron source insertion hole
1010  0             -010     -120 +130     IMP:N=1  $ AmBe neutron source
1020  1  -0.92      -010     -130 +110     IMP:N=1  $ Polyethylene below neutron source
c
2000  1  -0.92      -020 +010 -100 +110     IMP:N=1  $ Remaining polyethylene
c
3000  2  -1.259     -200     +020 -210 +230 IMP:N=1 VOL=6.207  $ Test specimen
3010  3  -7.31      -205     +210 -220 +230 IMP:N=1 VOL=0.310  $ Indium foil
3020  0             +020 -210 -100 +110 +200 IMP:N=0  $ Region outside polyethylene except
test specimen
c
3030  0             +210 -220 -100 +110 +205 IMP:N=0  $ Region outside polyethylene except
indium foil
c
3040  0             -200     +020 -210 -230 IMP:N=0  $ Region opposite of test specimen
3050  0             -205     +210 -220 -230 IMP:N=0  $ Region opposite of indium foil
c
9999  0             +220:+100:-110         IMP:N=0  $ Universe

c
c Surfaces
c
010   CZ   2.506  $ Diameter of neutron source hole: 5.012 cm, Radius: 2.506 cm
020   CZ   7.290  $ Diameter of polyethylene cylinder: 14.58 cm, Radius: 7.290 cm
c
100   PZ   9.6045  $ Height of polyethylene: 19.209 cm
110   PZ  -9.6045
120   PZ   1.253   $ Height of source: 2.506 cm (guess)
130   PZ  -1.253
c
200   CX   1.724  $ Radius of test specimen: 1.724 cm
205   CX   1.340  $ Indium foil radius is 1.340 cm
210   CZ   7.957  $ Thickness of test specimen: 0.667 cm
220   CZ   8.012  $ Thickness of indium foil: 0.055 cm
230   PX   0.0    $ marker for left and right half test places
c
c Mode and number of particles
c
nps 1000000000
```

```
mode n
c
prdmp 2j 1      $ print an mctal file
c
c Materials
c
c
m1   01001  2       06000 1         $ Polyethylene CH2
m2   73181 -0.914   06000 -0.086    $ Foam specimen
m3   49113 -0.0429  49115 -0.9571   $ Indium foil
c
c Am/Be Source (1Curie source - 3.7e10 disintegrations/sec)
c
sdef POS=0 0 0  ERG=D1 WGT=1.85e6
si1 H 4.14E-7 1.10E-1 3.30E-1 5.40E-1 7.50E-1 9.70E-1 1.18
     1.4 1.61 1.82 2.04 2.25 2.47 2.68 2.90 3.11 3.32 3.54
     3.75 3.97 4.18 4.39 4.61 4.82 5.04 5.25 5.47 5.68 5.89
     6.11 6.32 6.54 6.75 6.96 7.18 7.39 7.61 7.82 8.03 8.25
     8.46 8.68 8.89 9.11 9.32 9.53 9.75 9.96 10.2 10.4 10.6
     10.8 11.0
sp1 D 0 1.44E-2 3.34E-2 3.13E-2 2.81E-2 2.50E-2 2.14E-2
     1.98e-2 1.75E-2 1.92E-2 2.23E-2 2.15E-2 2.25E-2
     2.28e-2 2.95E-2 3.56E-2 3.69E-2 3.46E-2 3.07E-2
     3.00e-2 2.69E-2 2.86E-2 3.18E-2 3.07E-2 3.33E-2
     3.04e-2 2.74E-2 2.33E-2 2.06E-2 1.82E-2 1.77E-2
     2.04e-2 1.83E-2 1.63E-2 1.68E-2 1.88E-2 1.84E-2
     1.69e-2 1.44E-2 9.68E-3 6.52E-3 4.26E-3 3.67E-3
     3.81e-3 5.06E-3 6.25E-3 5.52E-3 4.68E-3 3.7E-3
     2.78e-3 1.51E-3 3.63E-4 0
c
c Tallies
c
e0 1.0e-8 99log 1.0e+2 T
c0 0.0 1.0 T
c
fc01 Neutron flux at polyethylene surface in particles/time
f001:n 020
c
fc21 Neutron source flux in particles/time
f021:n 010
c
fc011 Neutron flux at specimen/indium surface in particles/time
f011:n 210
c
fc14 Neutron flux going through test in particles/cm^2/time
f014:n 3000 3010
```

```
c
c 100% efficient detector used below
fc24 In Foil Reaction rate for beta decay in betas/cm^3/time
f024:n 3010
fm24 -0.2343 3 -2
```

Appendix C. Graphs of Experimental Neutron Transmission Measurements and MCNP Modeled Neutron Transmission Spectrums

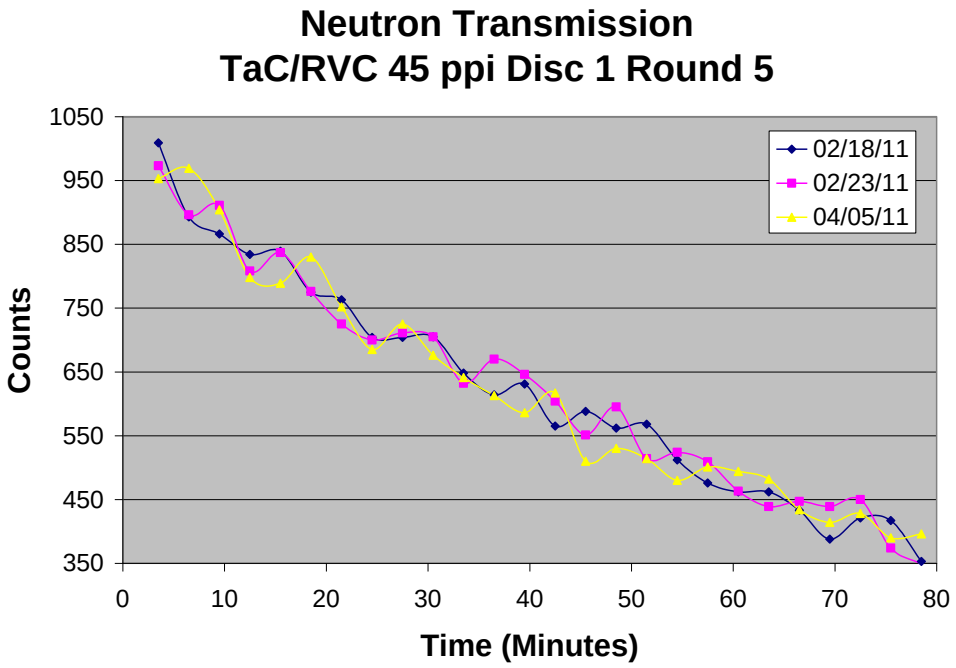

Figure 144. Graph of indium decay measurements for TaC/RVC 45 ppi foam Disc 1 Round 5

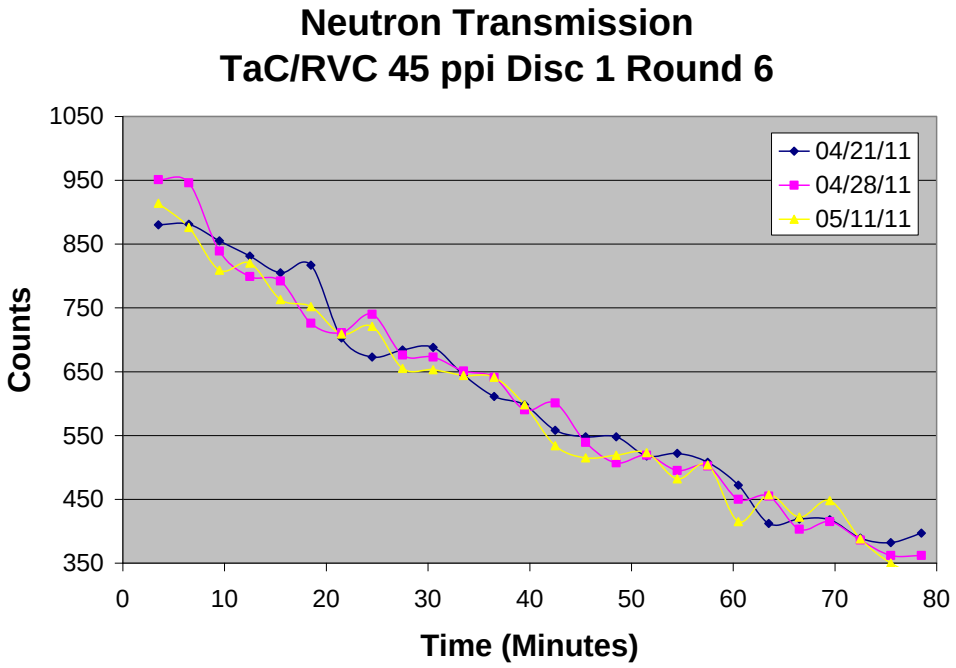

Figure 145. Graph of indium decay measurements for TaC/RVC 45 ppi foam Disc 1 Round 6.

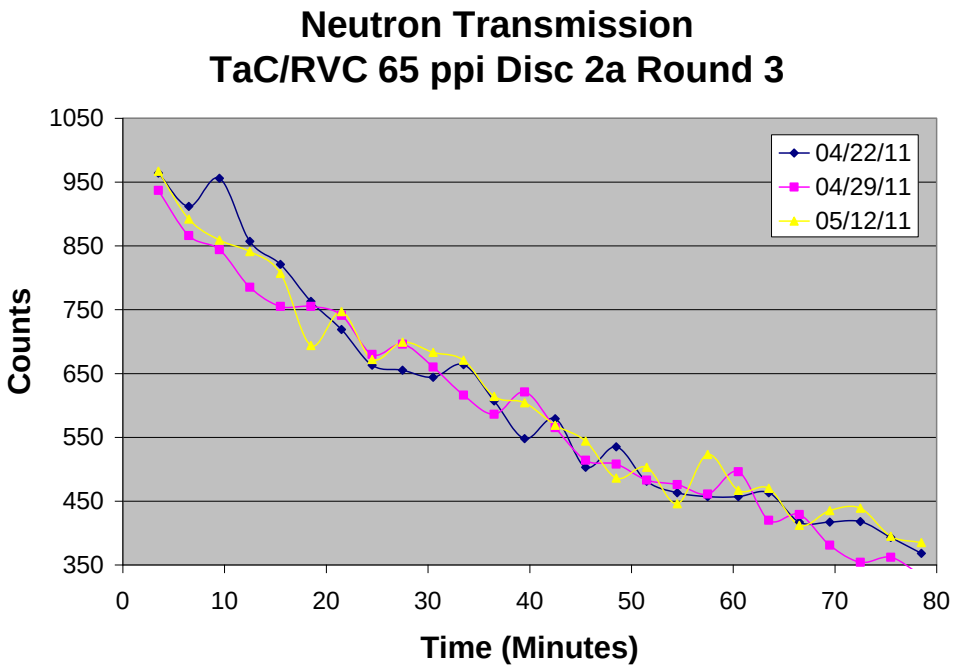

Figure 146. Graph of indium decay measurements for TaC/RVC 65 ppi foam Disc 2a Round 3.

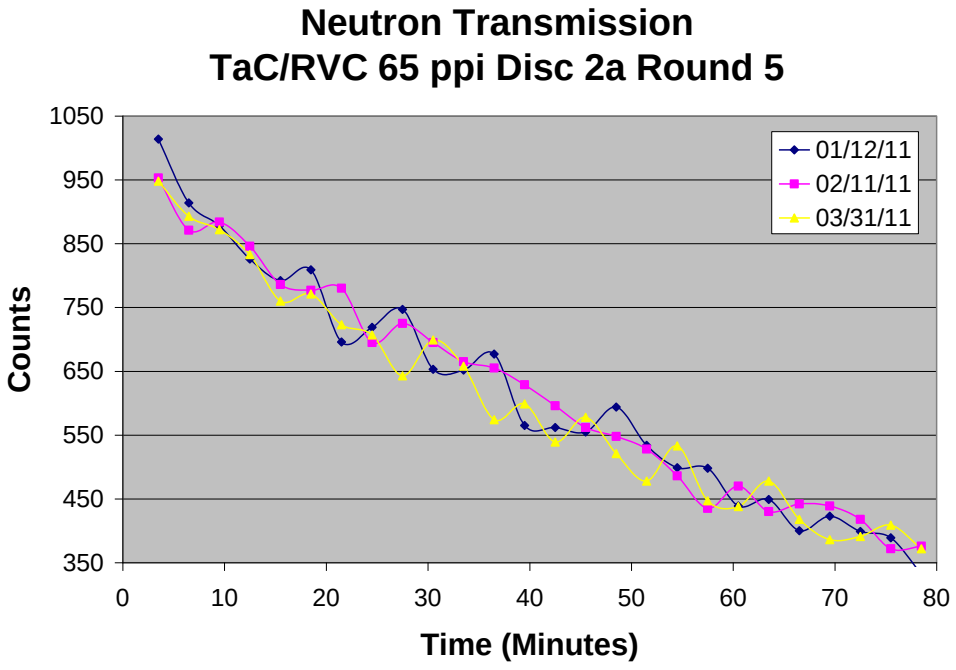

Figure 147. Graph of indium decay measurements for TaC/RVC 65 ppi foam Disc 2a Round 5.

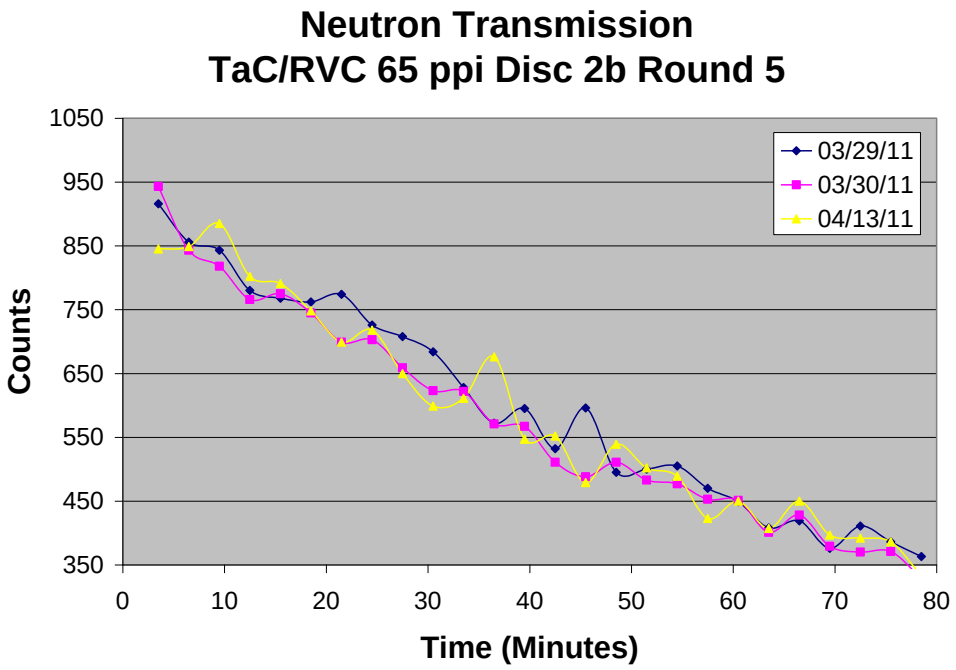

Figure 148. Graph of indium decay measurements for TaC/RVC 65 ppi Disc 2b Round 5.

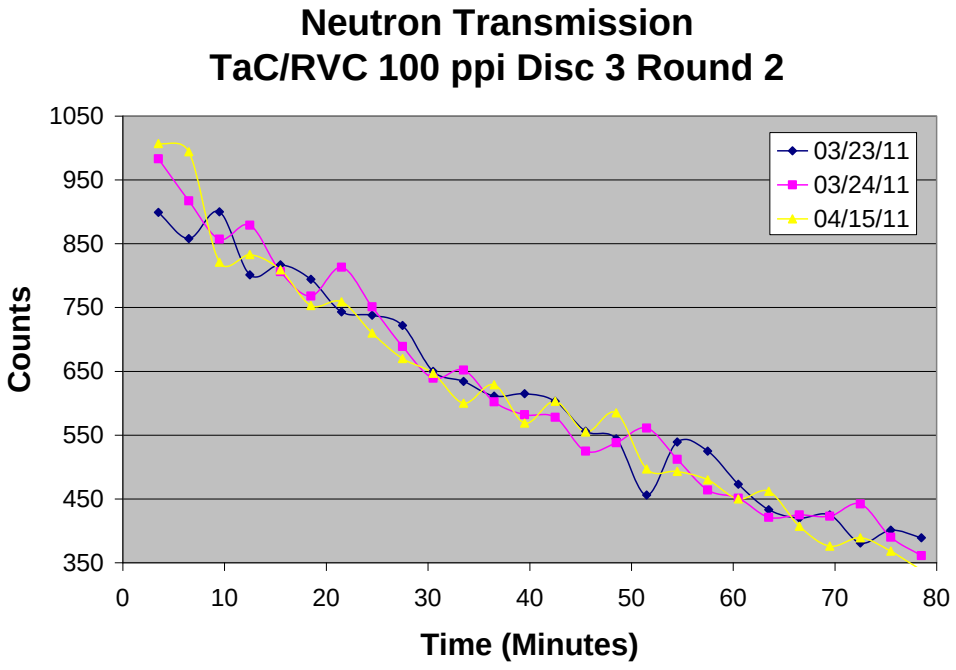

Figure 149. Graph of indium decay measurements for TaC/RVC 100 ppi foam Disc 3 Round 2.

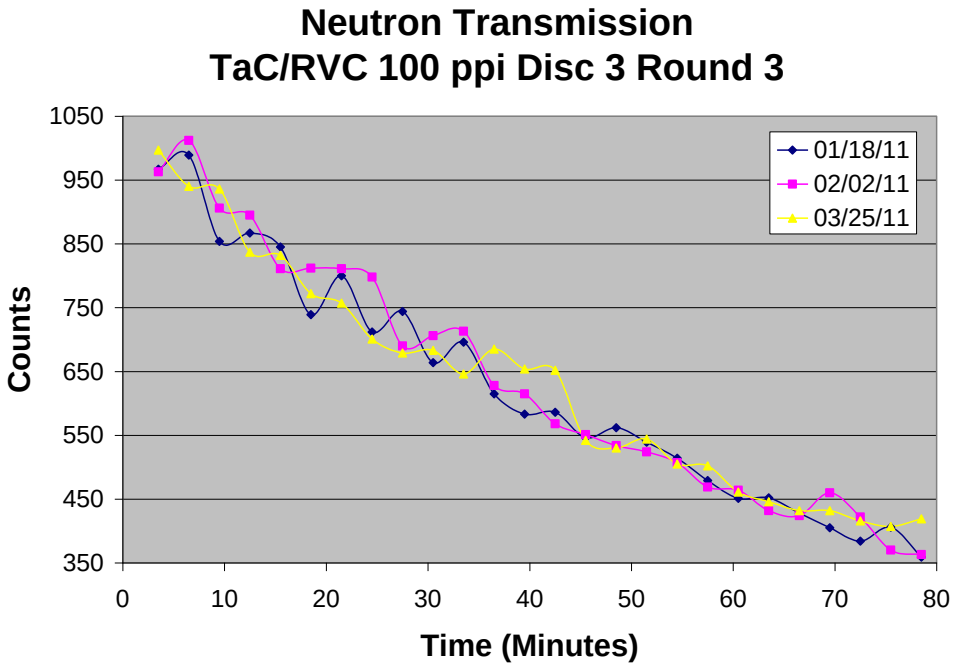

Figure 150. Graph of indium decay measurements for TaC/RVC 100 ppi foam Disc 3 Round 3.

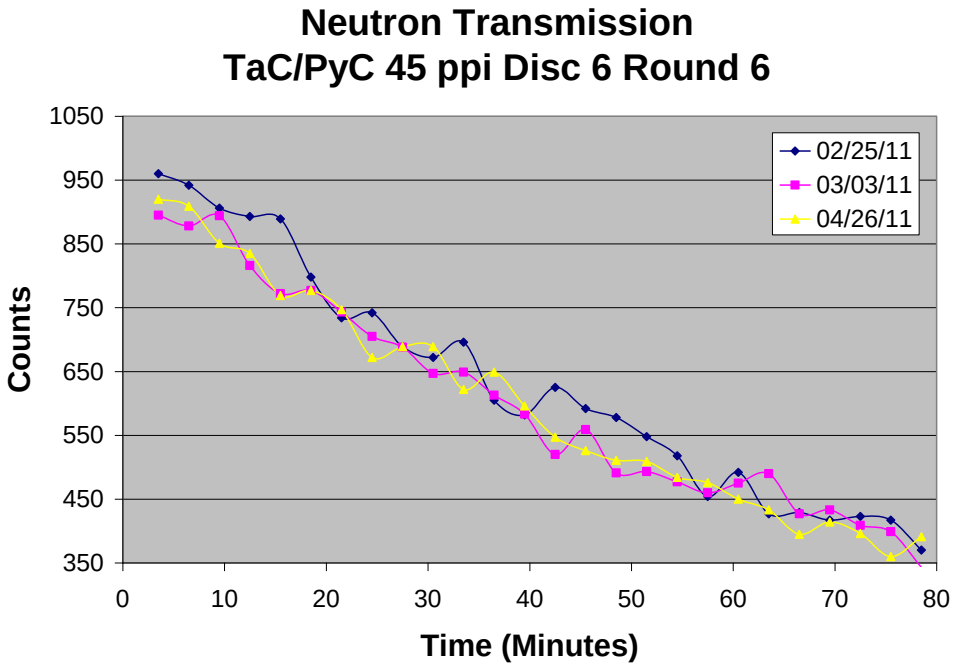

Figure 151. Graph of indium decay measurements for TaC/PyC/RVC 45 ppi foam Disc 6 Round 6.

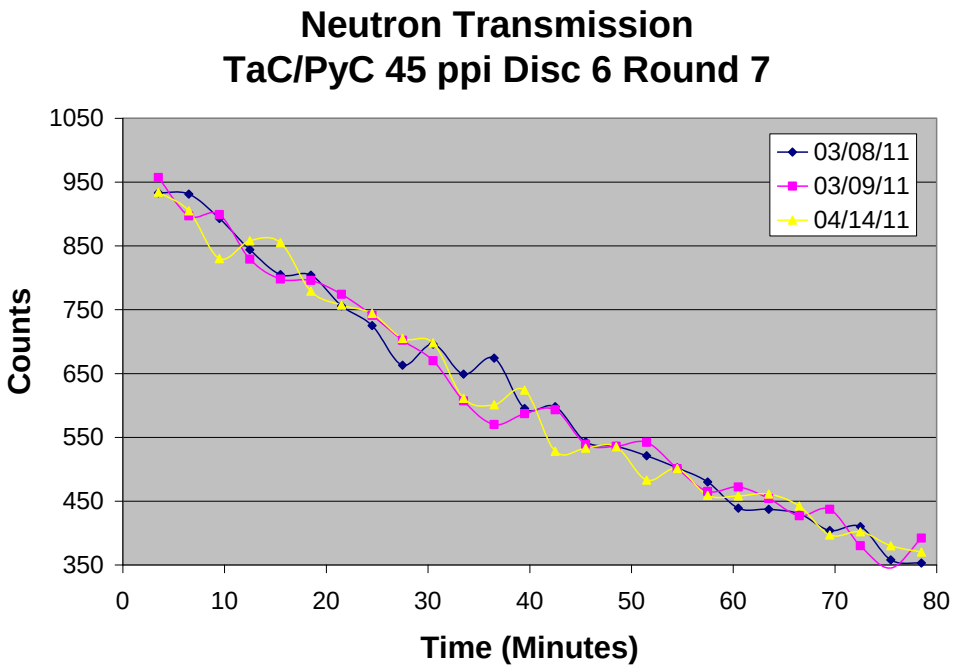

Figure 152. Graph of indium decay measurements for TaC/PyC/RVC 45 ppi foam Disc 6 Round 7.

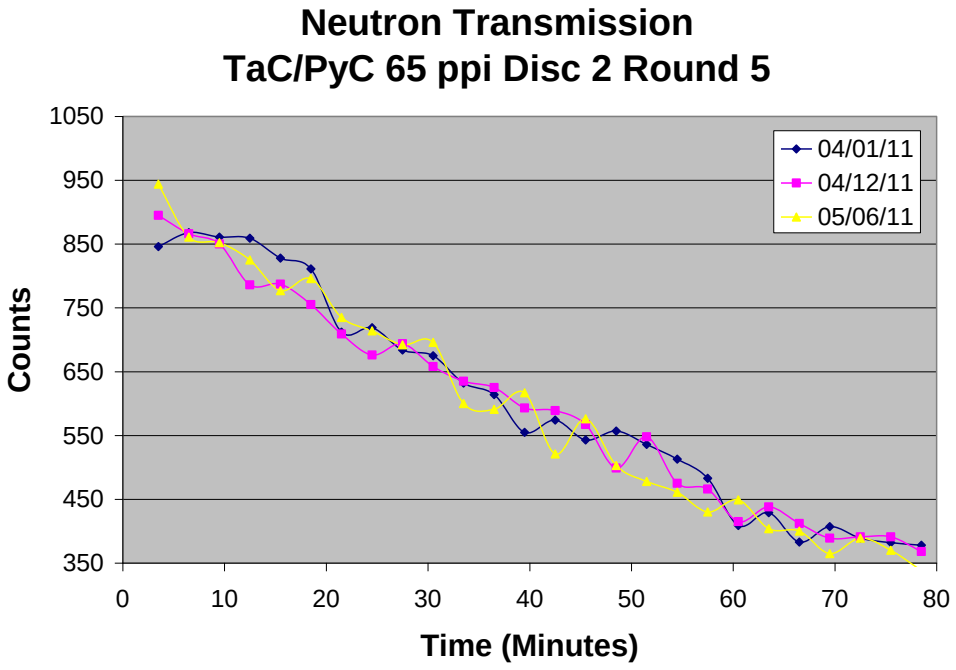

Figure 153. Graph of indium decay measurements for TaC/PyC/RVC 65 ppi foam Disc 2 Round 5.

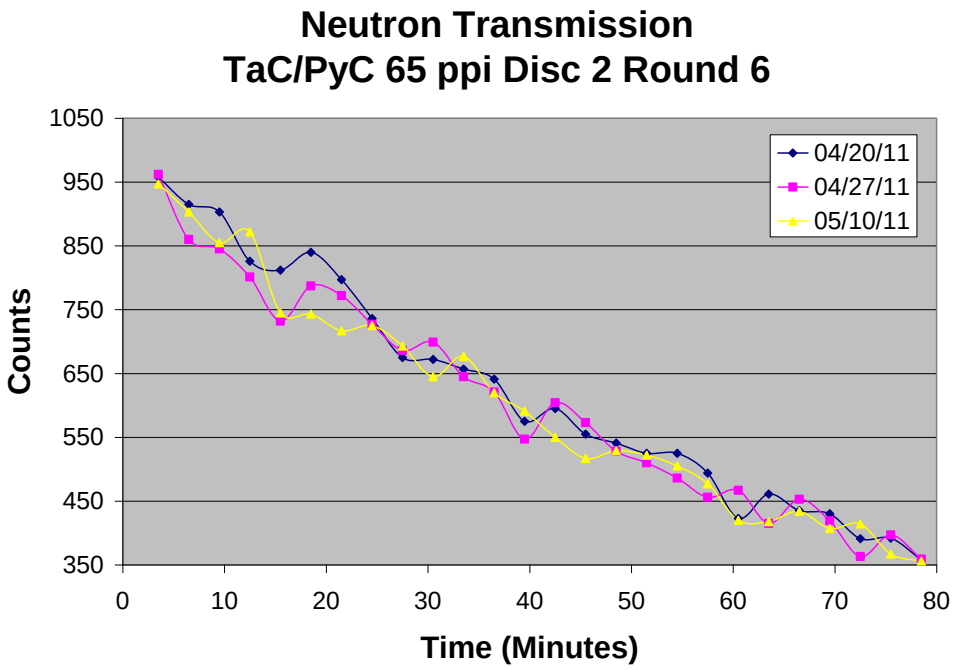

Figure 154. Graph of indium decay measurements for TaC/PyC/RVC 65 ppi foam Disc 2 Round 6.

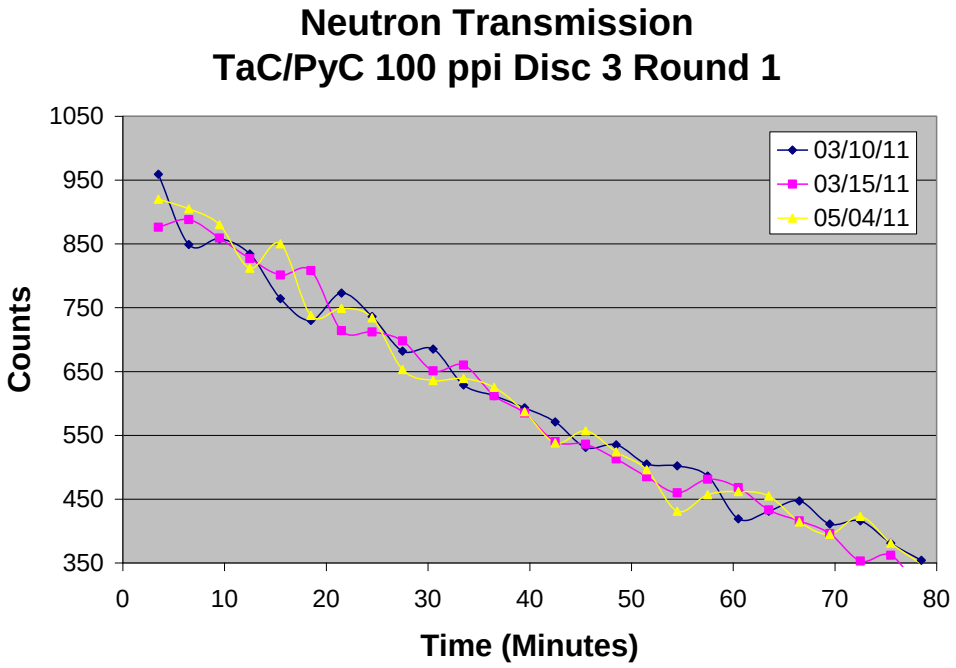

Figure 155. Graph of indium decay measurements for TaC/PyC/RVC 100 ppi foam Disc 3 Round 1.

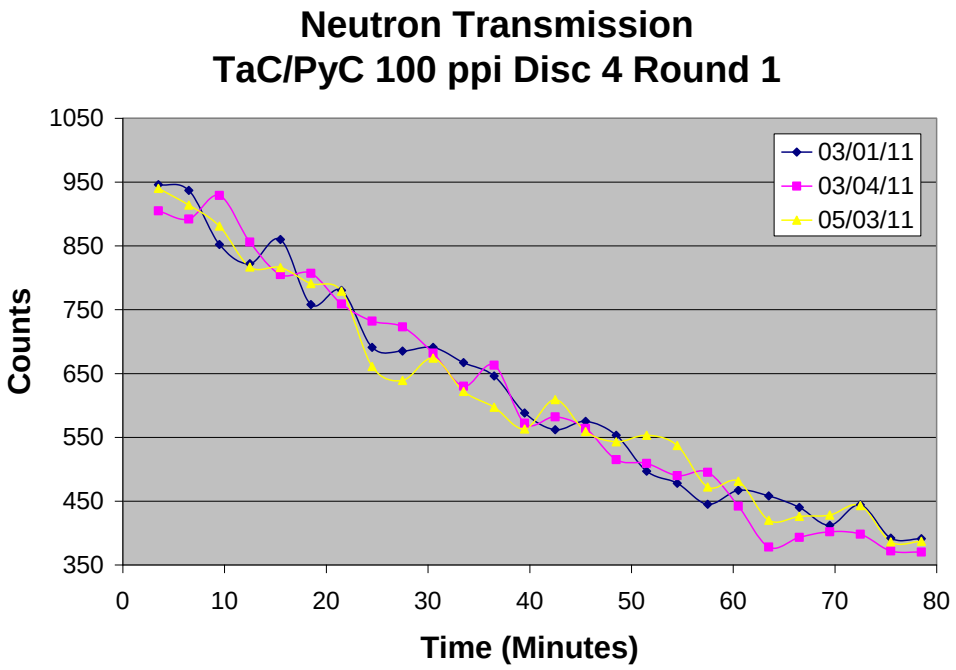

Figure 156. Graph of indium decay measurements for TaC/PyC/RVC 100 ppi foam Disc 4 Round 1.

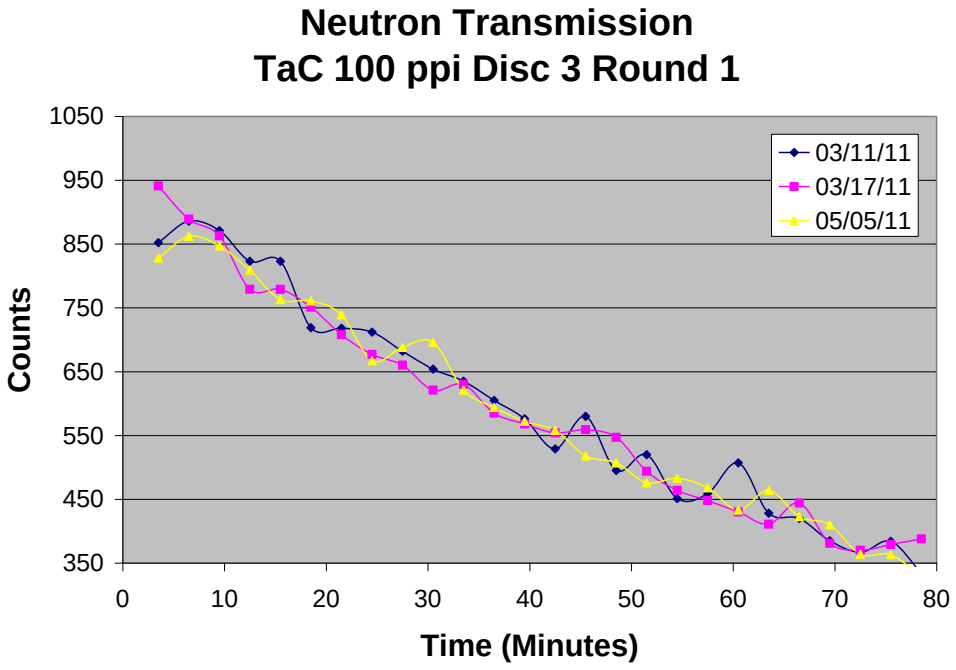

Figure 157. Graph of indium decay measurements for TaC 100 ppi foam Disc 3 Round 1.

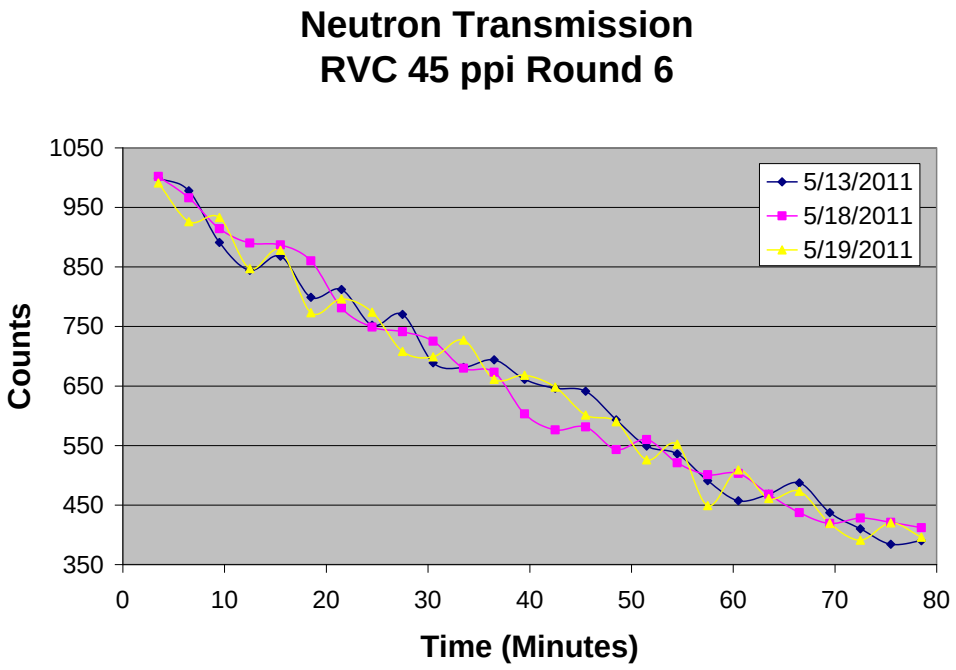

Figure 158. Graph of indium decay measurements for RVC 45 ppi foam Round 6.

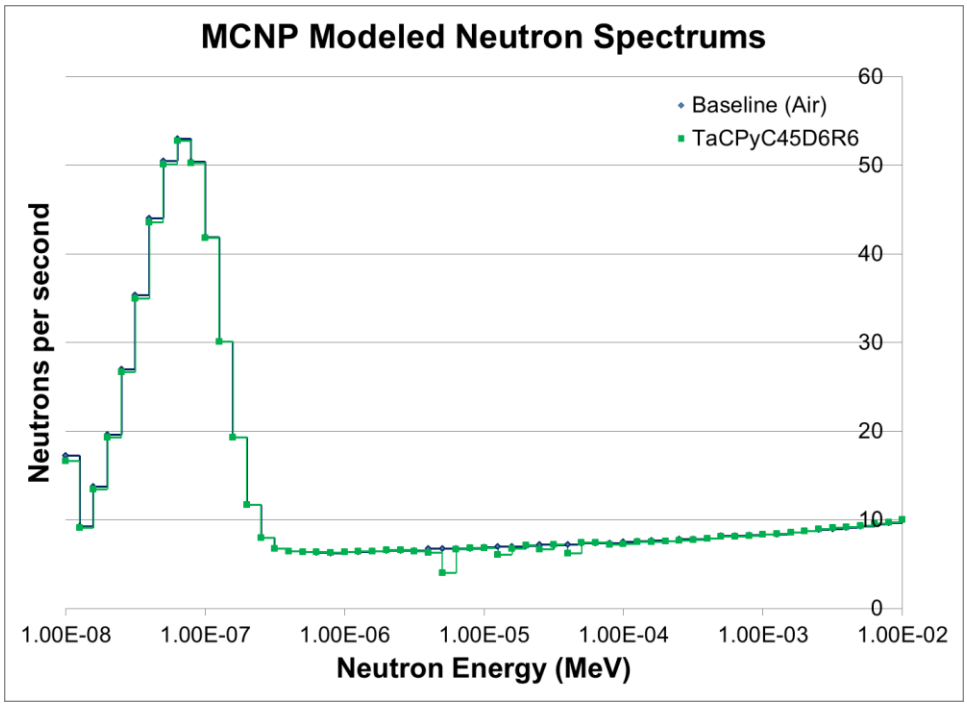

Figure 159. Graph of MCNP modeled low energy neutron transmission spectrum for TaCPyC45D6R6.

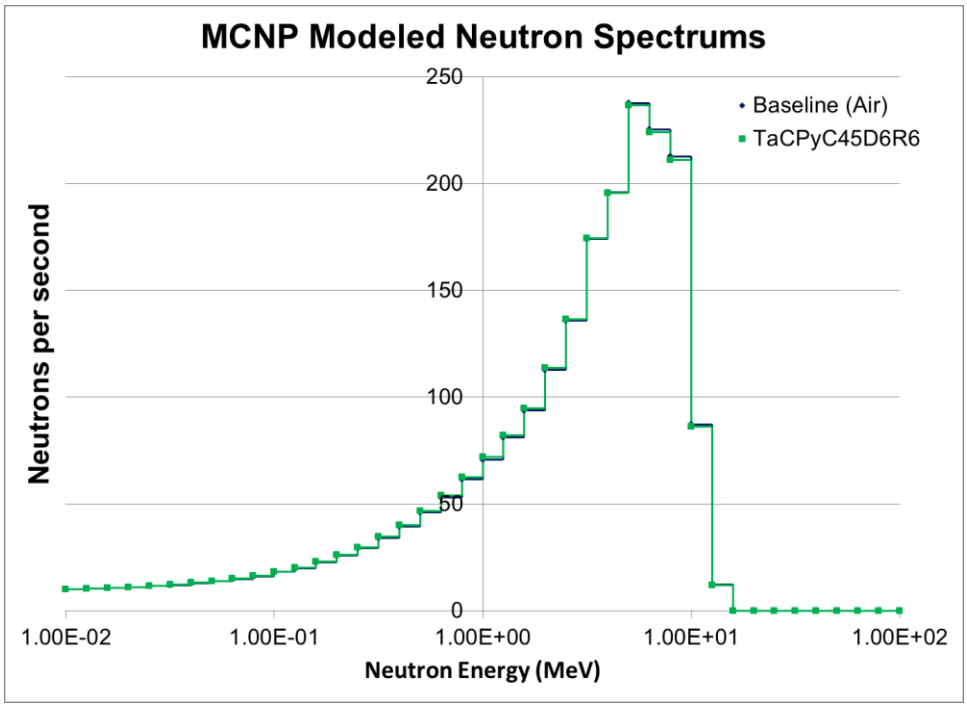

Figure 160. Graph of MCNP modeled high energy neutron transmission spectrum for TaCPyC45D6R6.

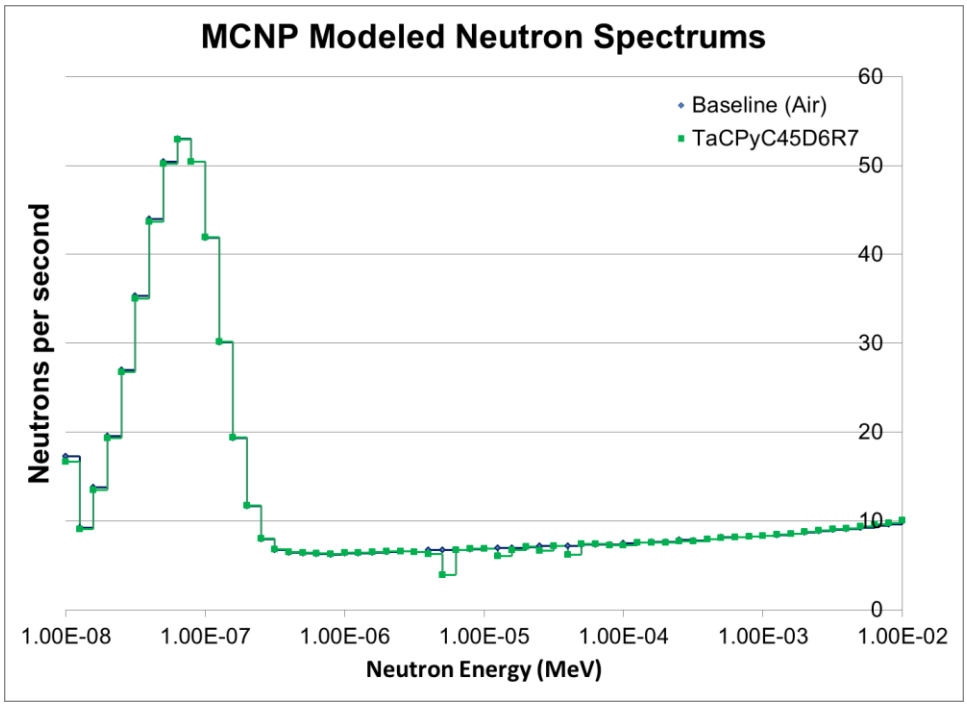

Figure 161. Graph of MCNP modeled low energy neutron transmission spectrum for TaCPyC45D6R7.

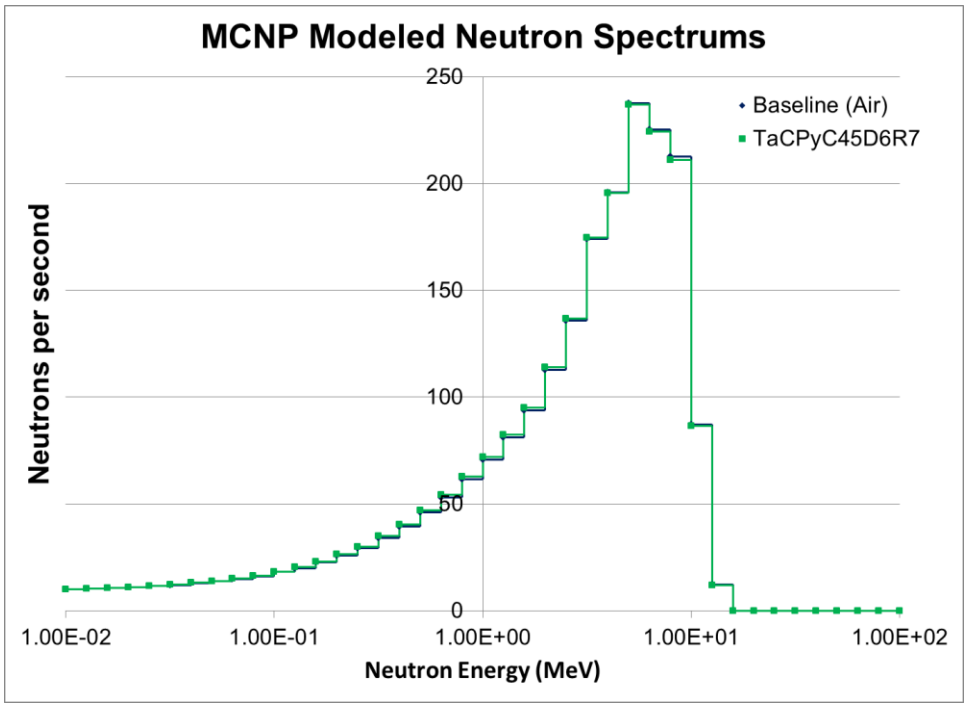

Figure 162. Graph of MCNP modeled high energy neutron transmission spectrum for TaCPyC45D6R7.

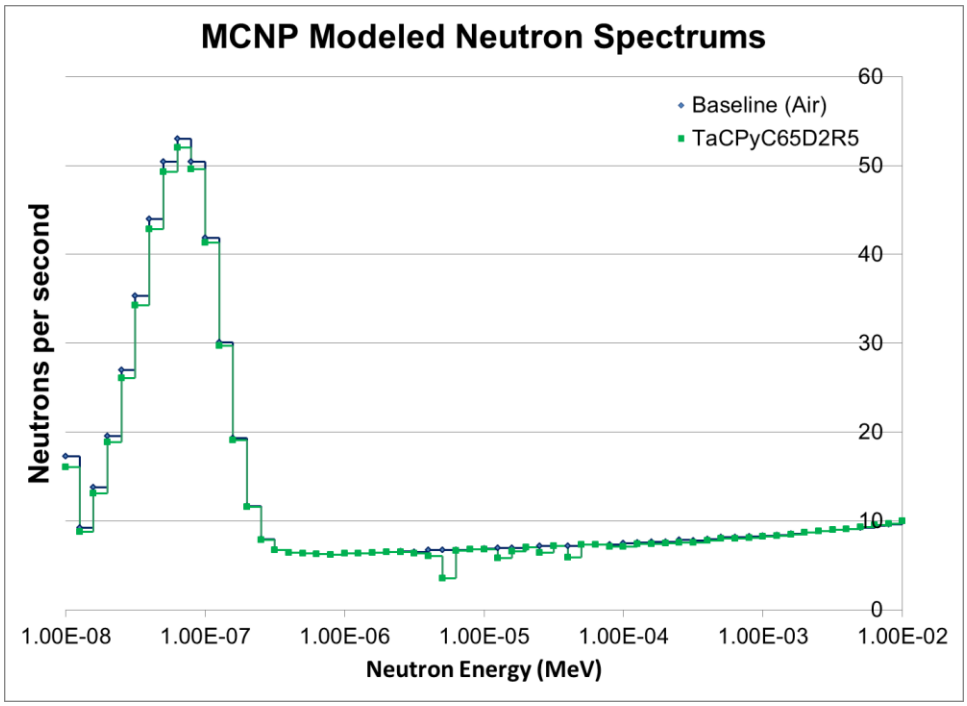

Figure 163. Graph of MCNP modeled low energy neutron transmission spectrum for TaCPyC65D2R5.

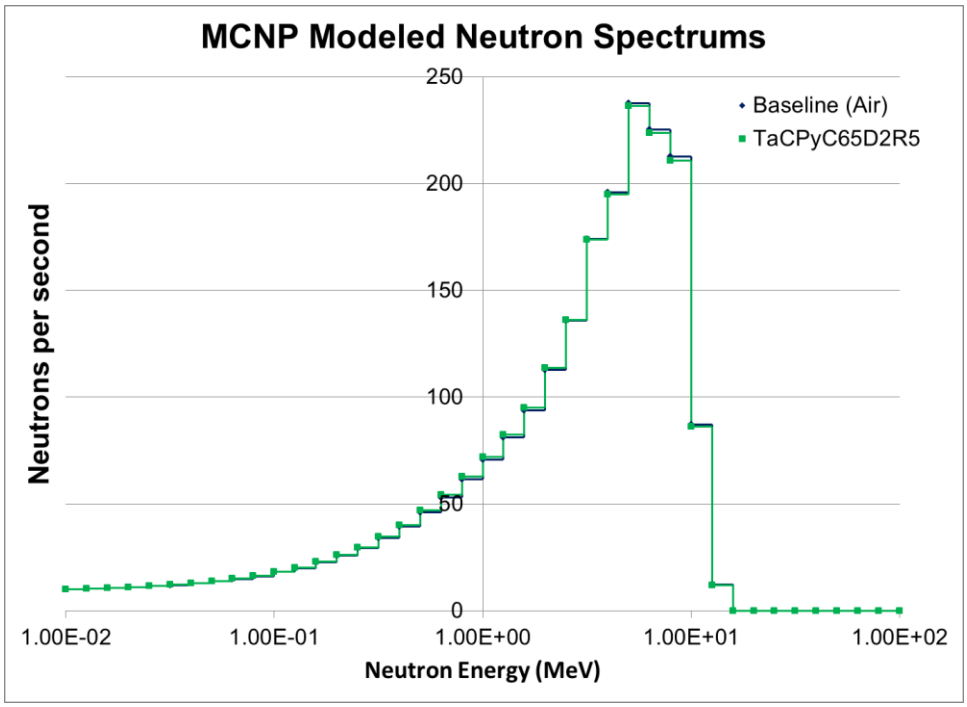

Figure 164. Graph of MCNP modeled high energy neutron transmission spectrum for TaCPyC65D2R5.

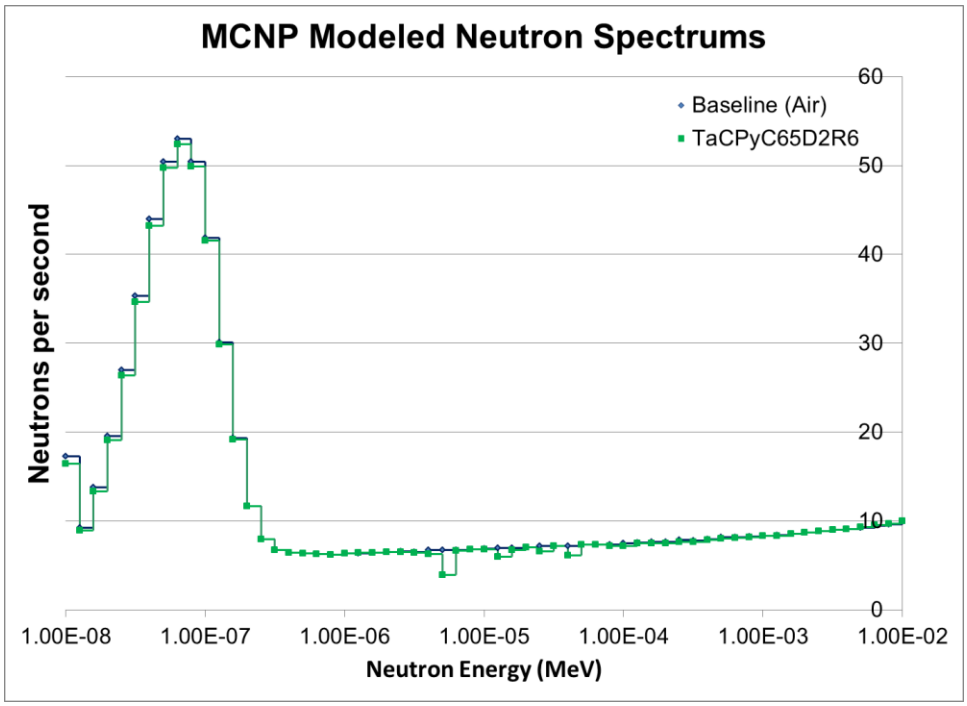

Figure 165. Graph of MCNP modeled low energy neutron transmission spectrum for TaCPyC65D2R6.

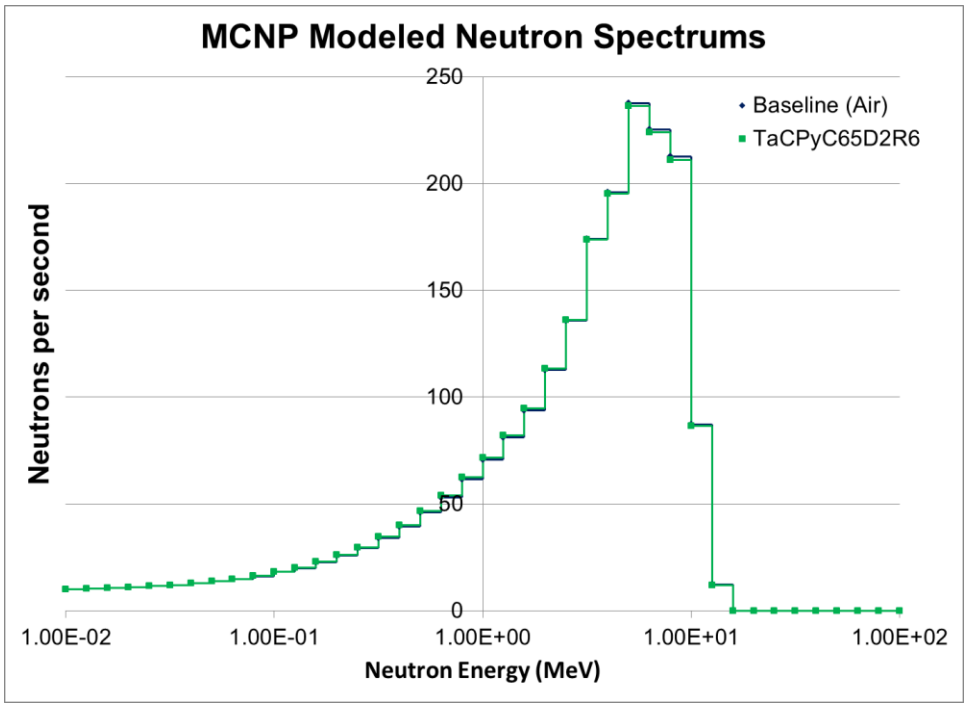

Figure 166. Graph of MCNP modeled high energy neutron transmission spectrum for TaCPyC65D2R6.

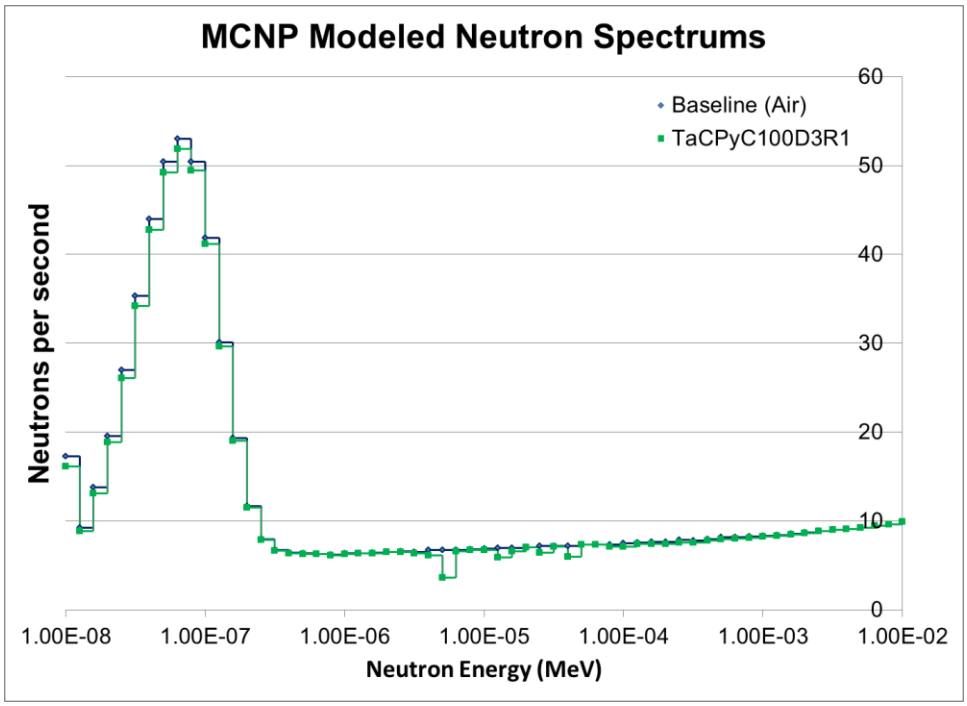

Figure 167. Graph of MCNP modeled low energy neutron transmission spectrum for TaCPyC100D3R1.

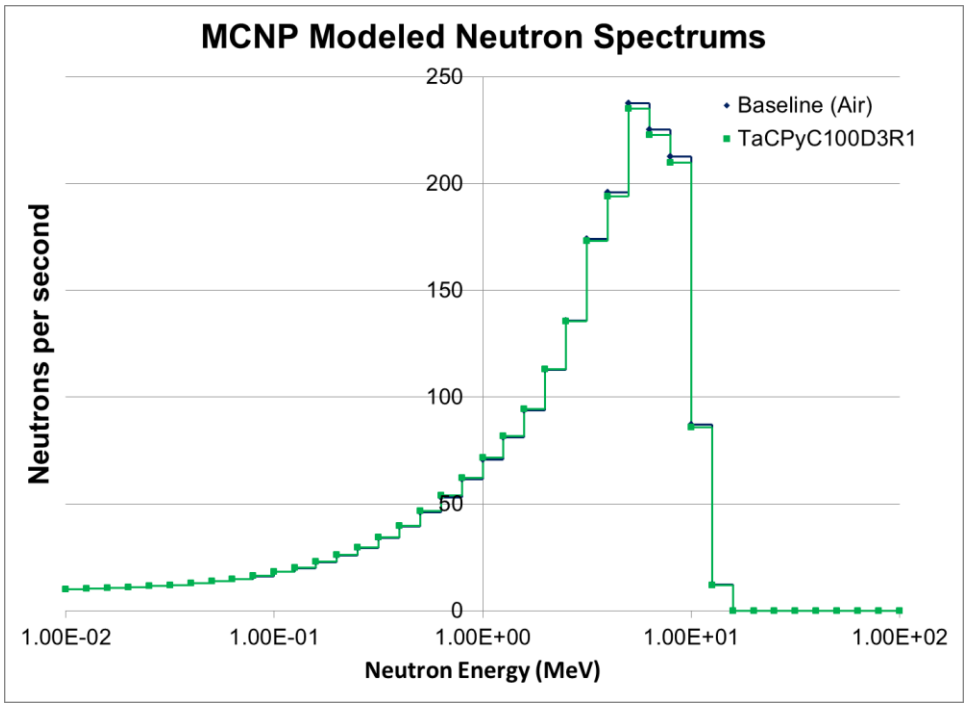

Figure 168. Graph of MCNP modeled high energy neutron transmission spectrum for TaCPyC100D3R1.

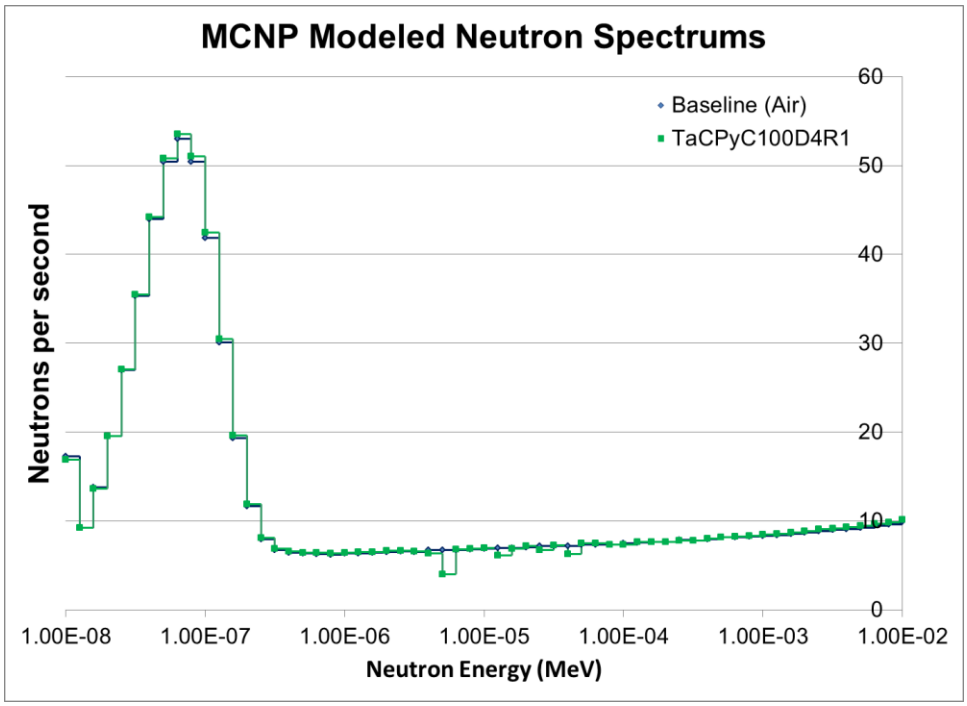

Figure 169. Graph of MCNP modeled low energy neutron transmission spectrum for TaCPyC100D4R1.

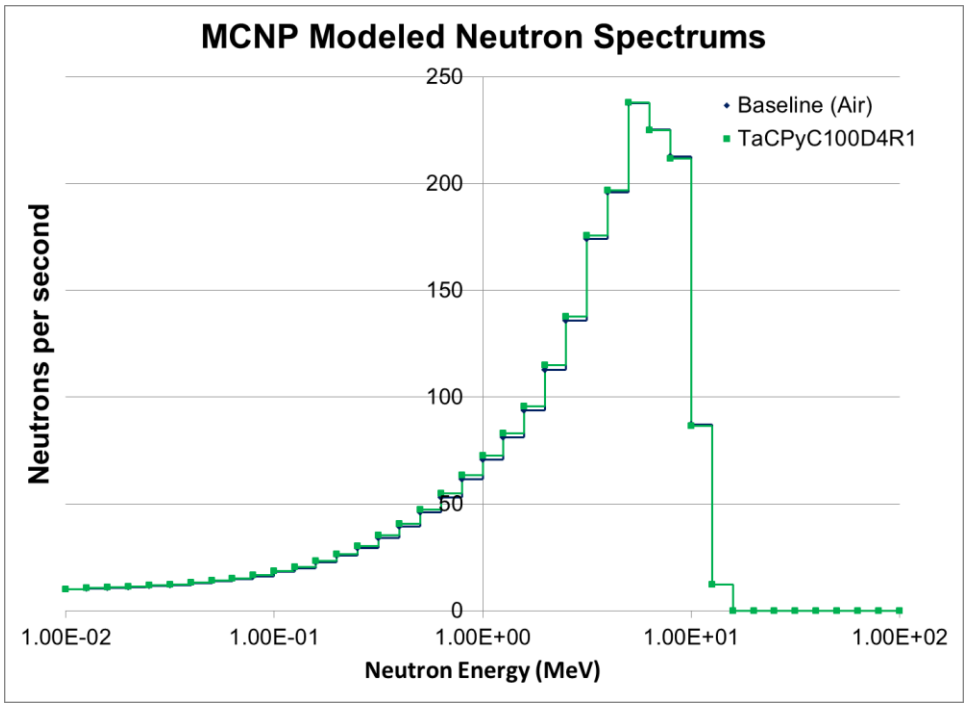

Figure 170. Graph of MCNP modeled high energy neutron transmission spectrum for TaCPyC100D4R1.

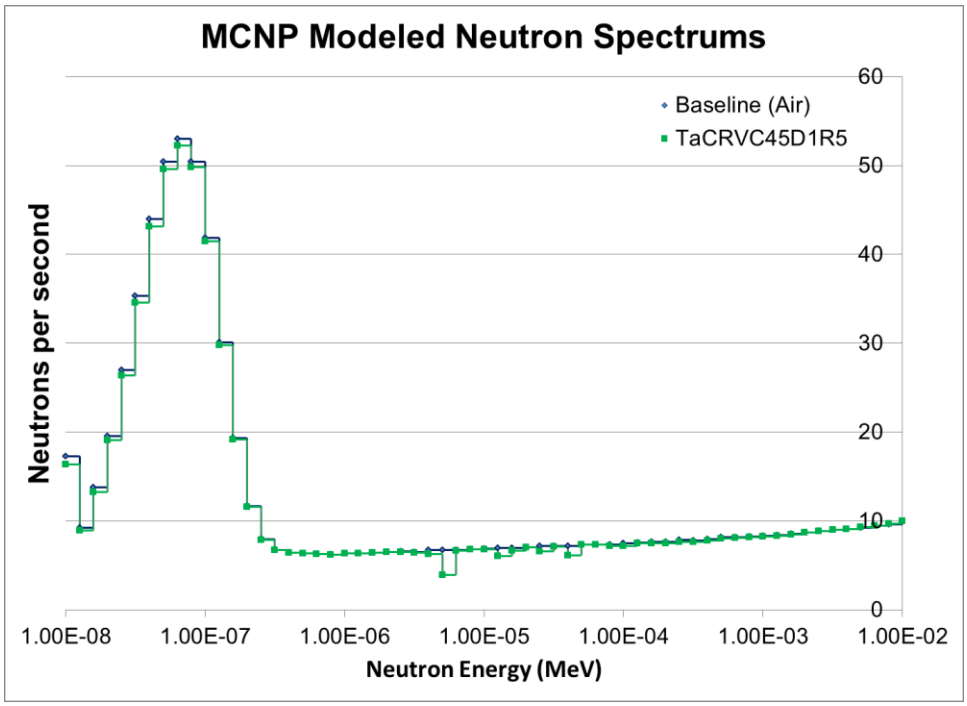

Figure 171. Graph of MCNP modeled low energy neutron transmission spectrum for TaCRVC45D1R5.

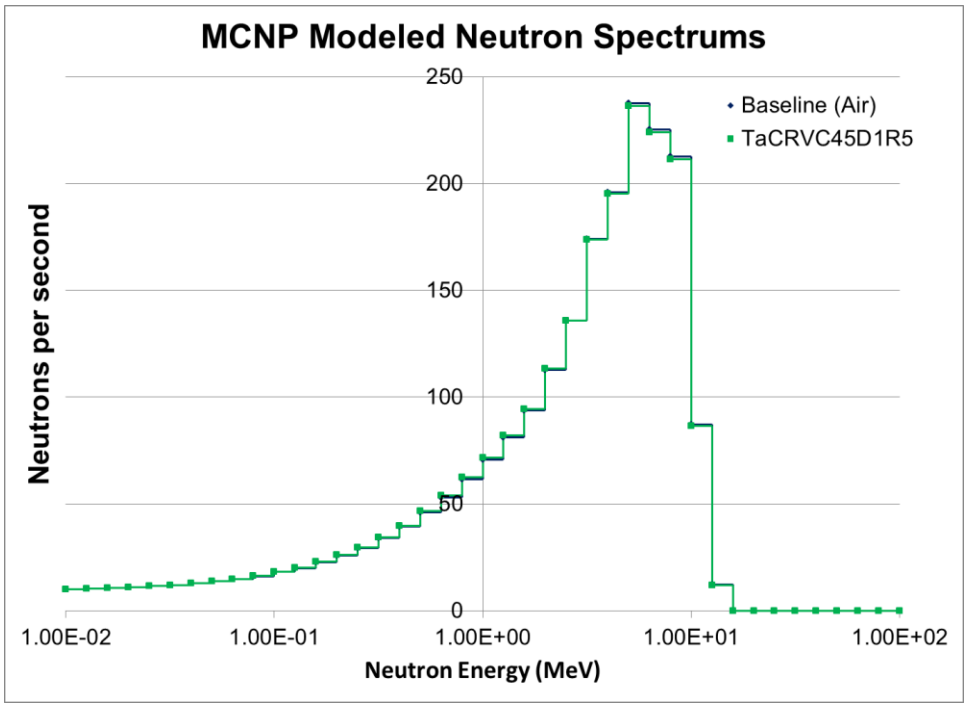

Figure 172. Graph of MCNP modeled high energy neutron transmission spectrum for TaCRVC45D1R5.

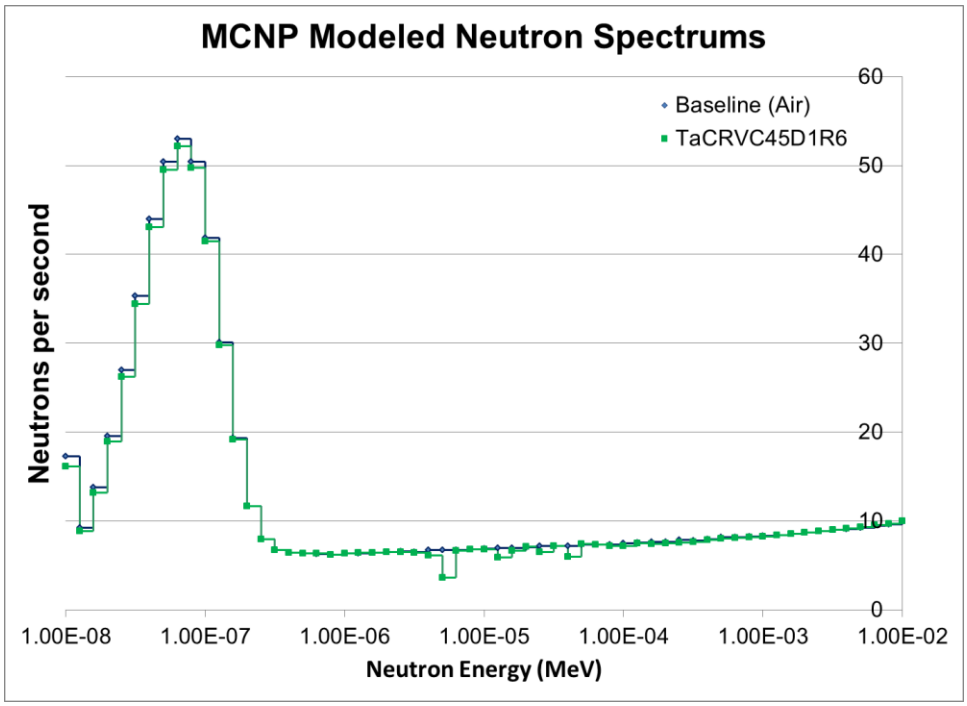

Figure 173. Graph of MCNP modeled low energy neutron transmission spectrum for TaCRVC45D1R6.

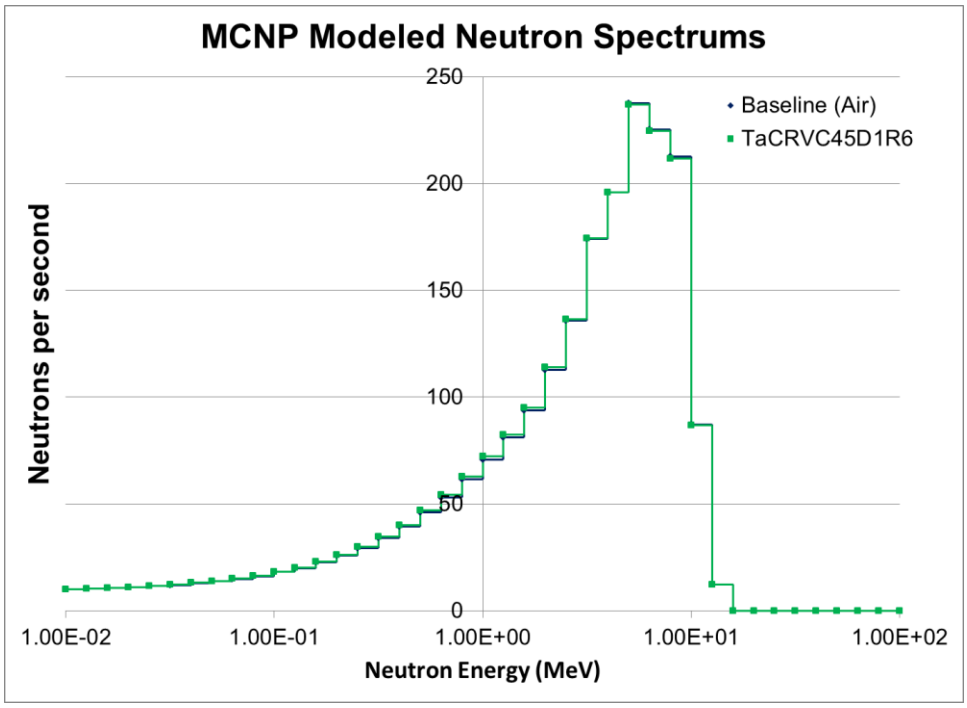

Figure 174. Graph of MCNP modeled high energy neutron transmission spectrum for TaCRVC45D1R6.

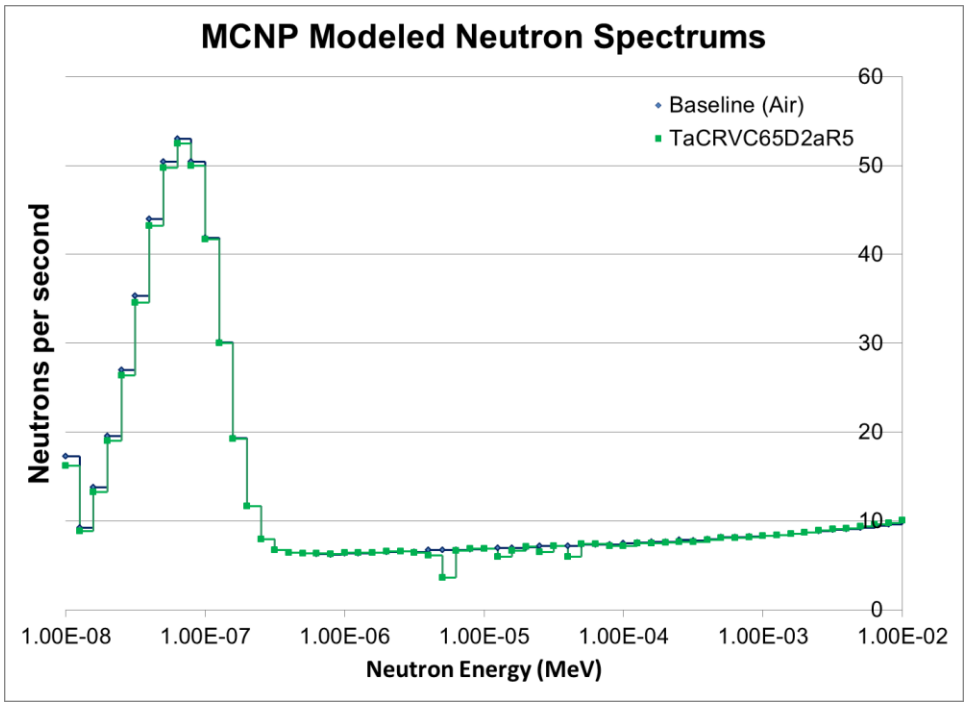

Figure 175. Graph of MCNP modeled low energy neutron transmission spectrum for TaCRVC65D2aR5.

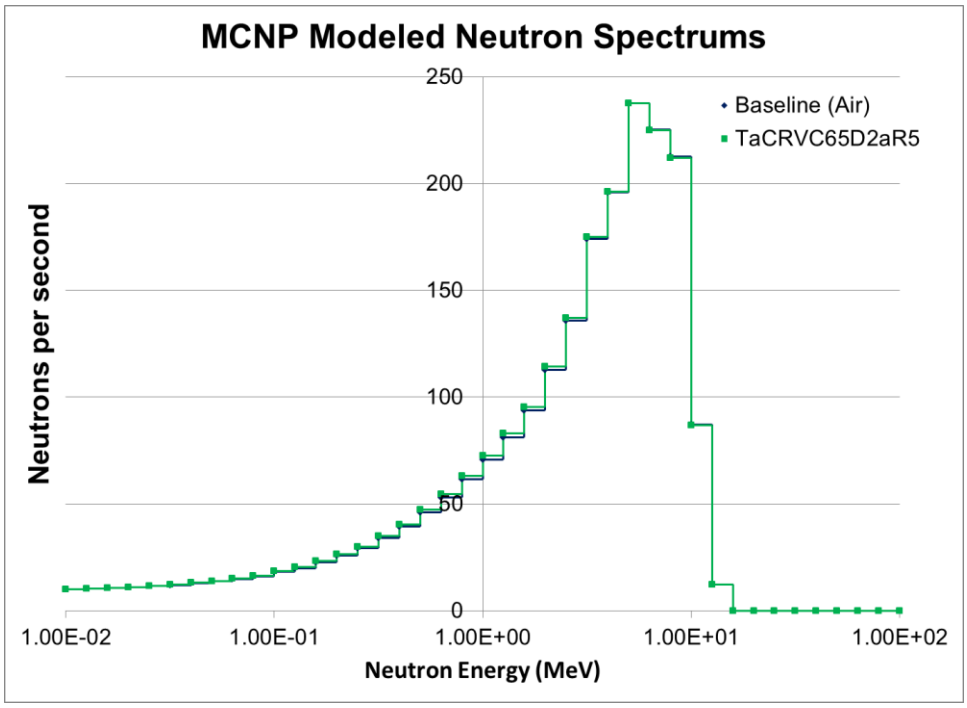

Figure 176. Graph of MCNP modeled high energy neutron transmission spectrum for TaCRVC65D2aR5.

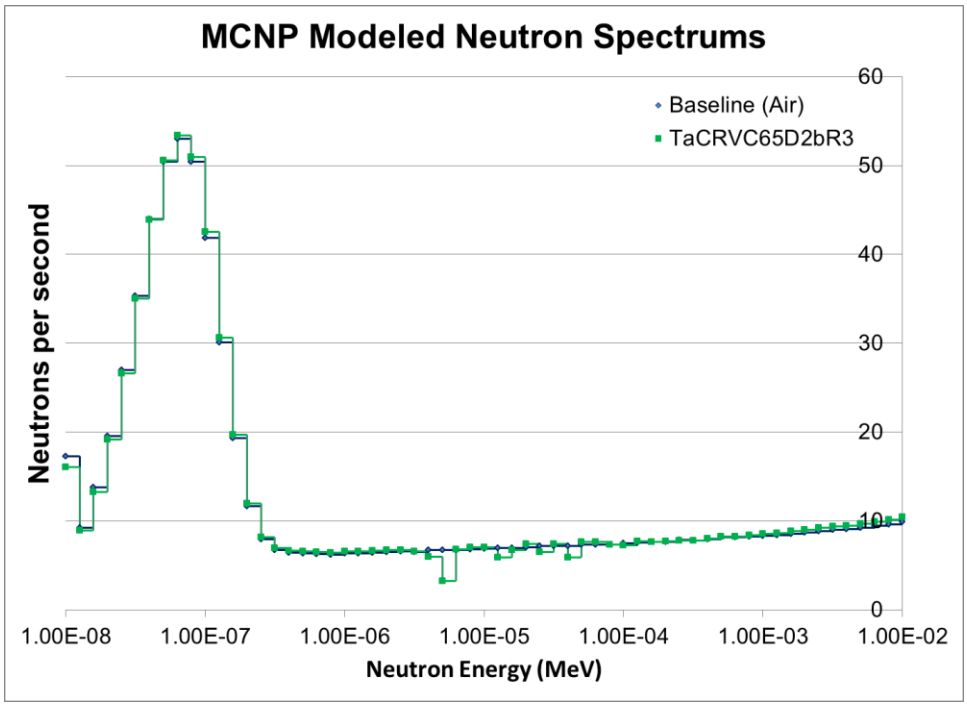

Figure 177. Graph of MCNP modeled low energy neutron transmission spectrum for TaCRVC65D2bR3.

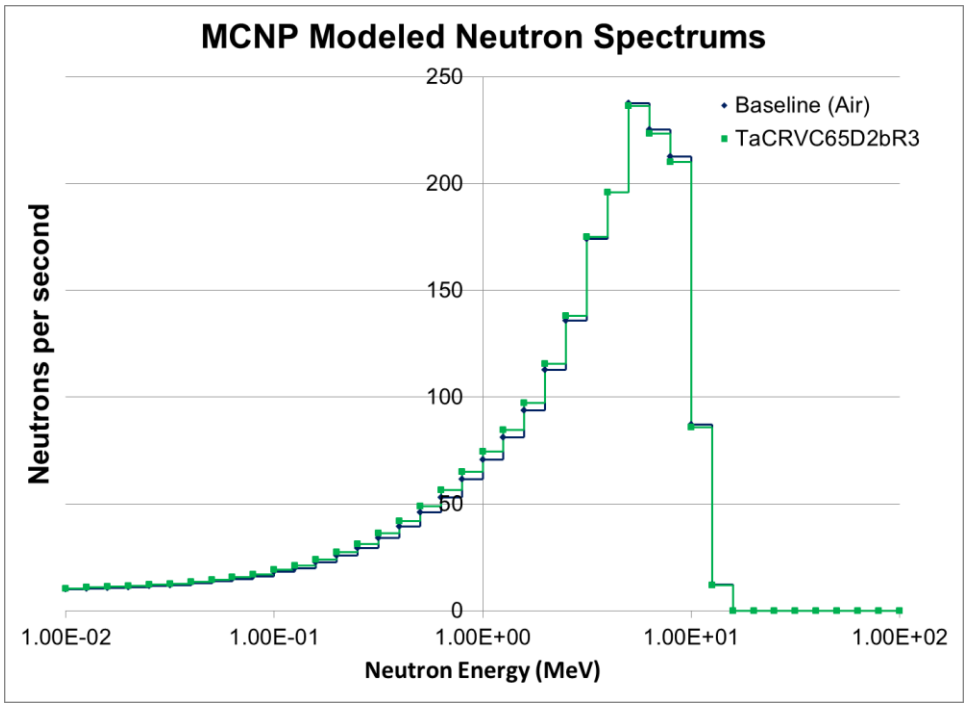

Figure 178. Graph of MCNP modeled high energy neutron transmission spectrum for TaCRVC65D2bR3.

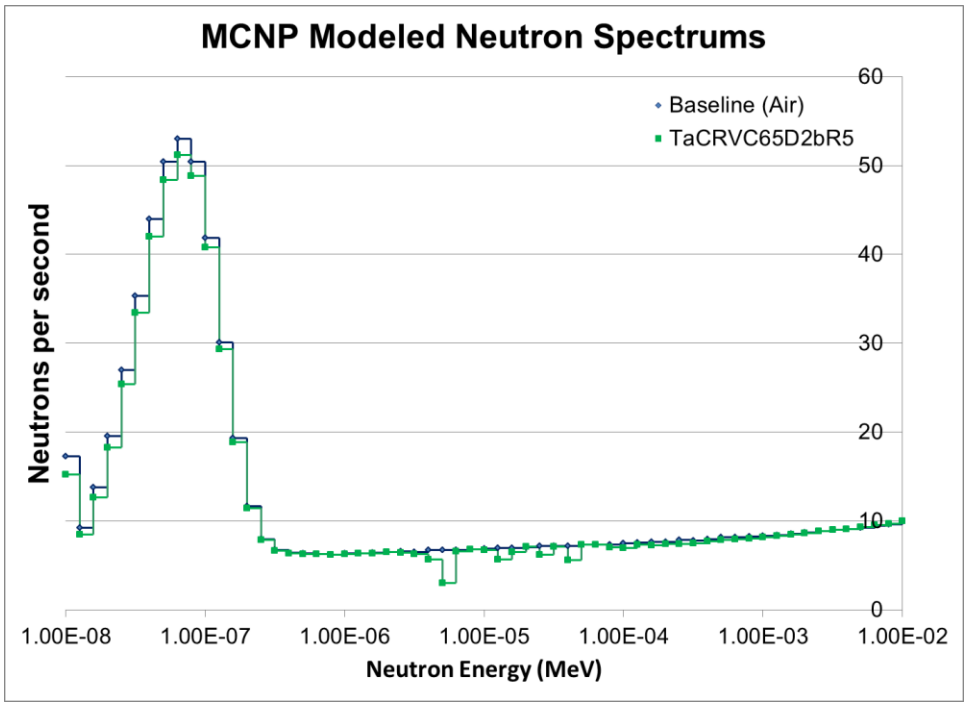

Figure 179. Graph of MCNP modeled low energy neutron transmission spectrum for TaCRVC65D2bR5.

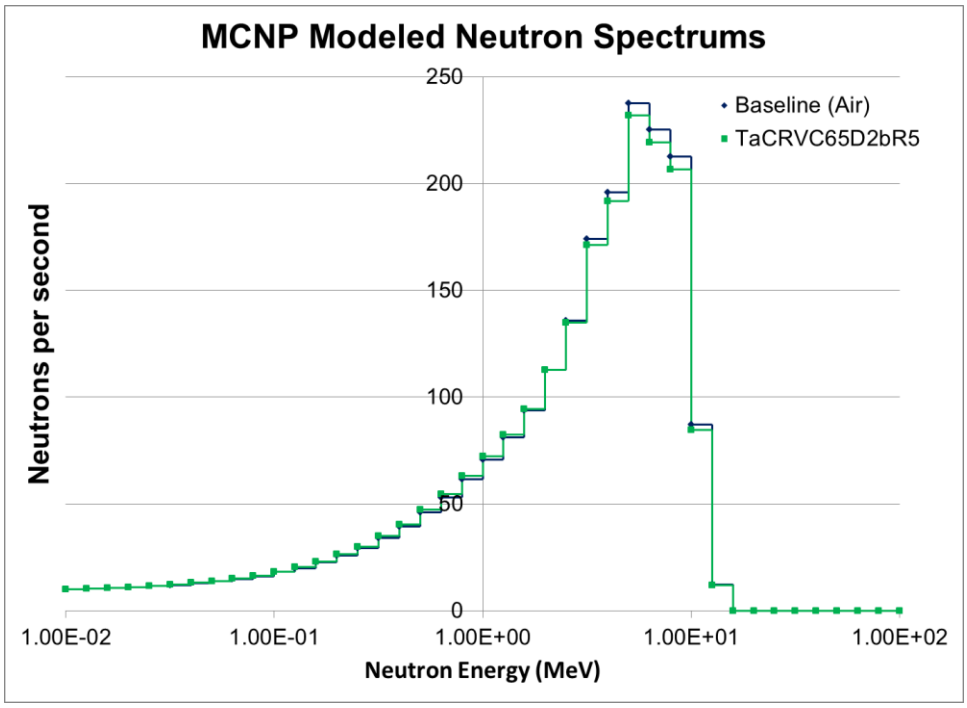

Figure 180. Graph of MCNP modeled high energy neutron transmission spectrum for TaCRVC65D2bR5.

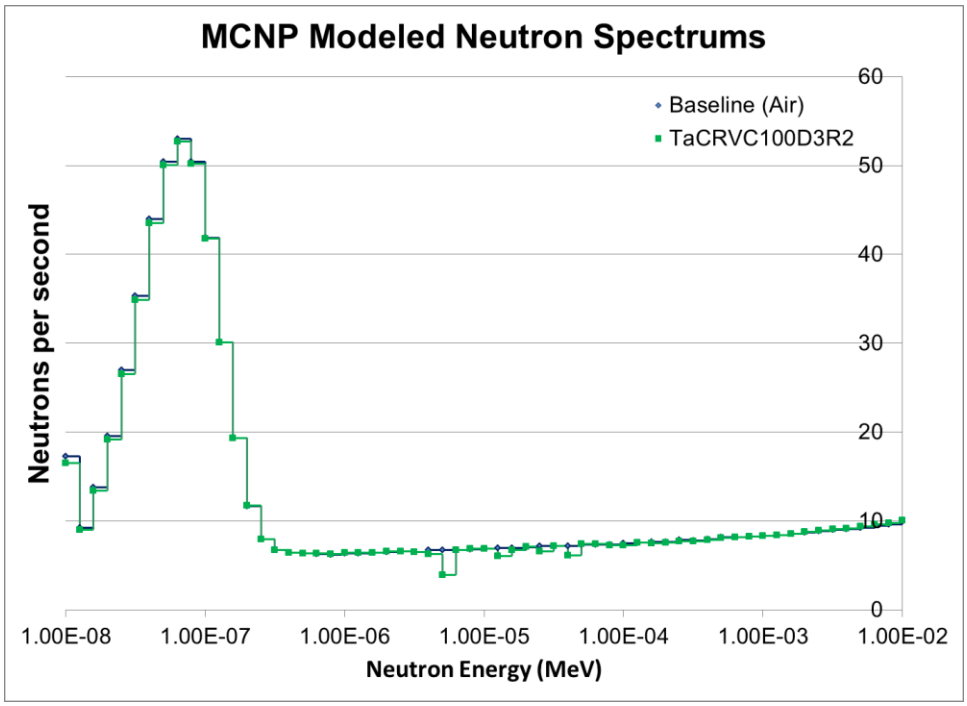

Figure 181. Graph of MCNP modeled low energy neutron transmission spectrum for TaCRVC100D3R2.

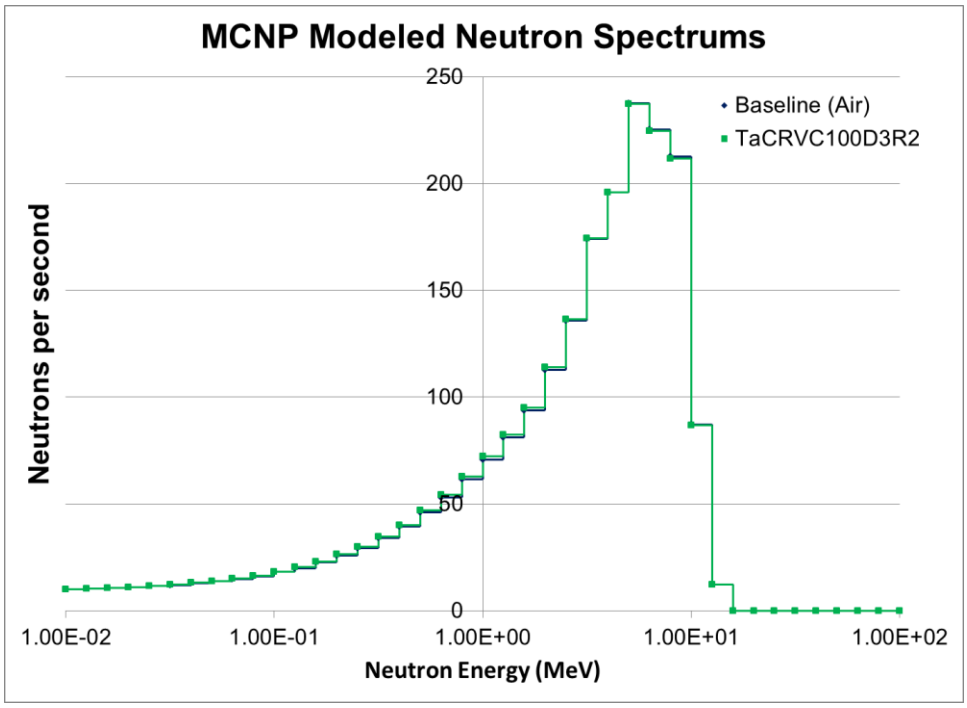

Figure 182. Graph of MCNP modeled high energy neutron transmission spectrum for TaCRVC100D3R2.

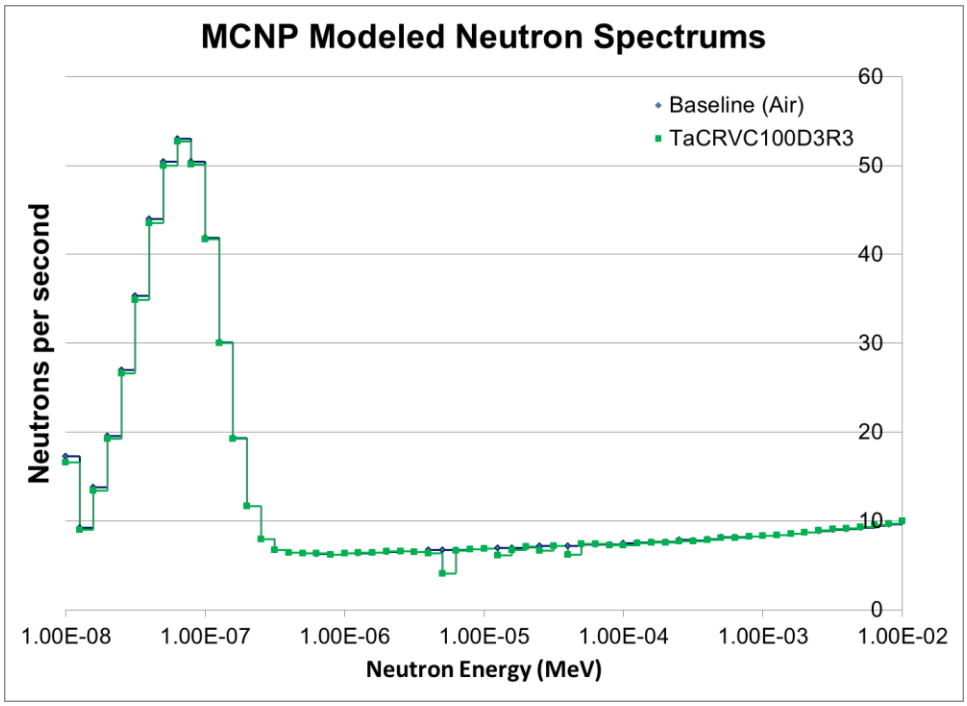

Figure 183. Graph of MCNP modeled low energy neutron transmission spectrum for TaCRVC100D3R3.

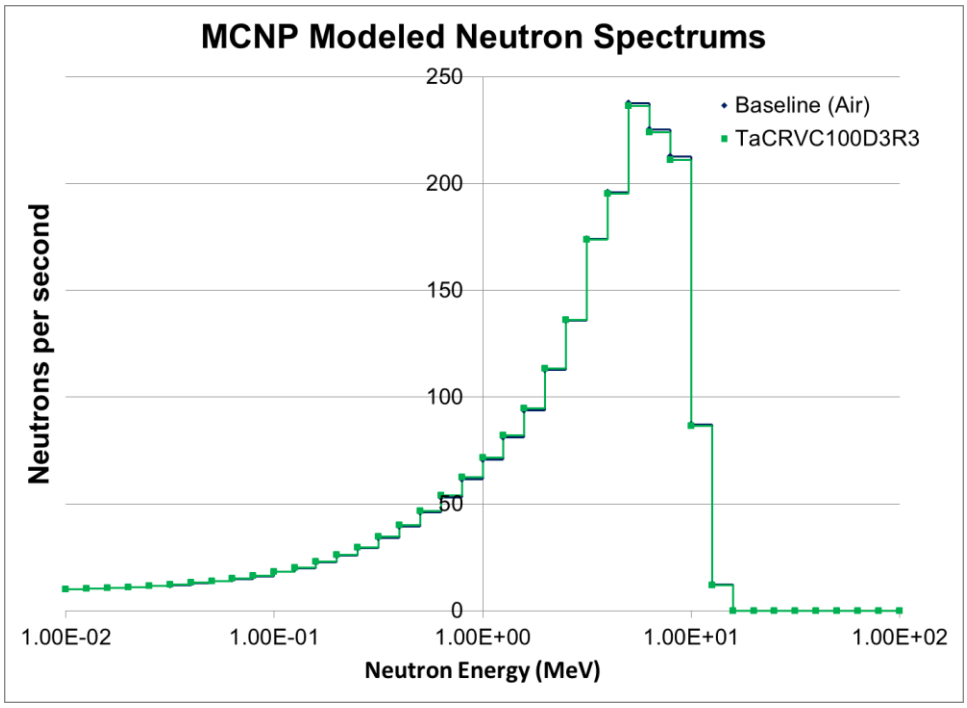

Figure 184. Graph of MCNP modeled high energy neutron transmission spectrum for TaCRVC100D3R3.

Appendix D: Microstructural Analysis of Thermally Cycled and Baseline TaC Foams

45 TaC/PyC/RVC

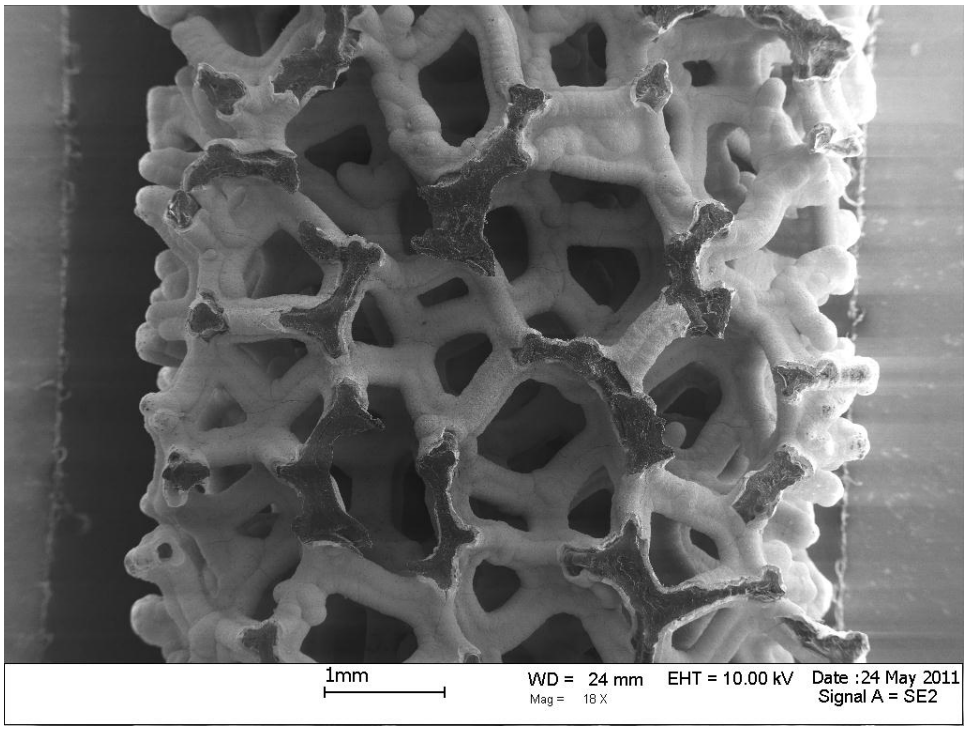

Figure 185. SEM micrograph of the baseline microstructure of a 45 ppi TaC/PyC/RVC foam specimen.

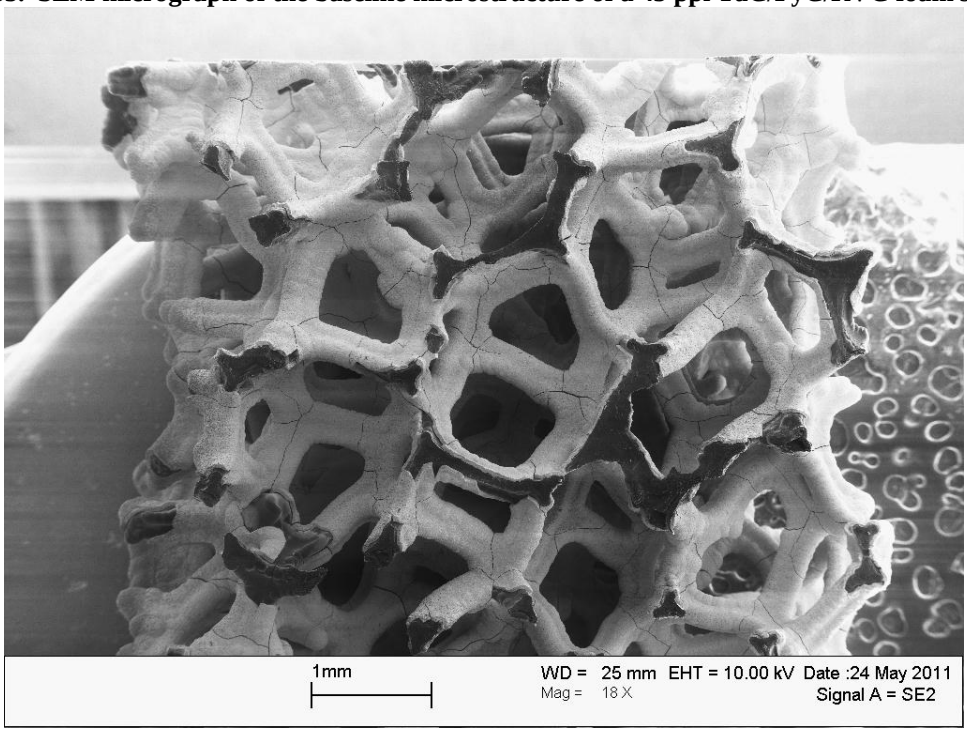

Figure 186. SEM micrograph of the microstructure of a 45 ppi TaC/PyC/RVC foam specimen after thermal cycling.

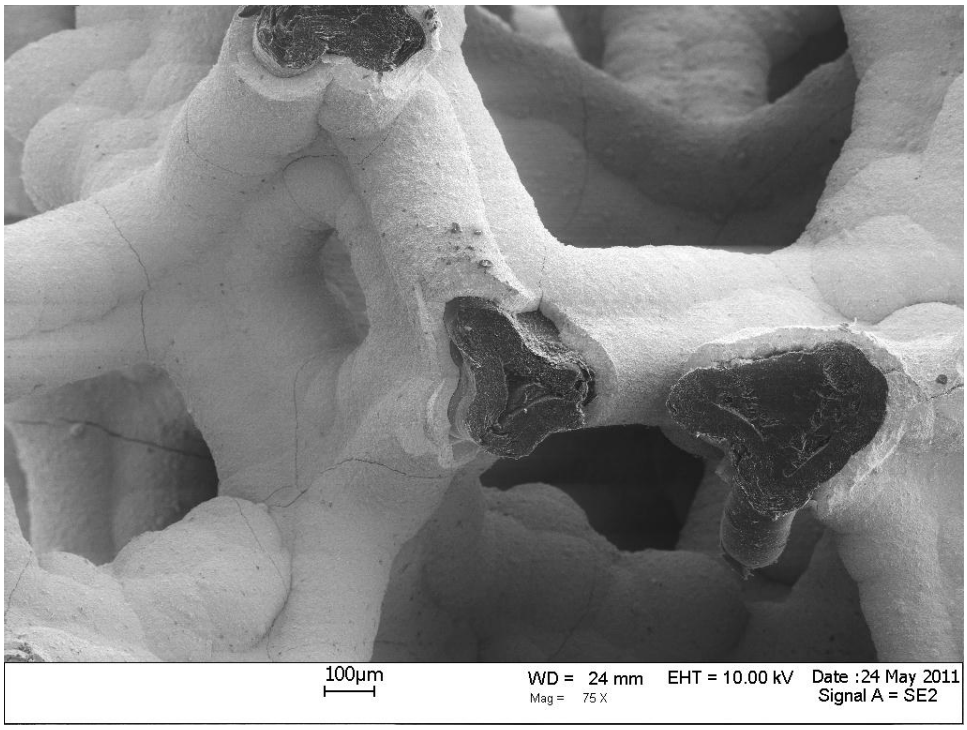

Figure 187. SEM micrograph of the baseline microstructure of a 45 ppi TaC/PyC/RVC foam specimen.

Figure 188. SEM micrograph of the microstructure of a 45 ppi TaC/PyC/RVC foam specimen after thermal cycling.

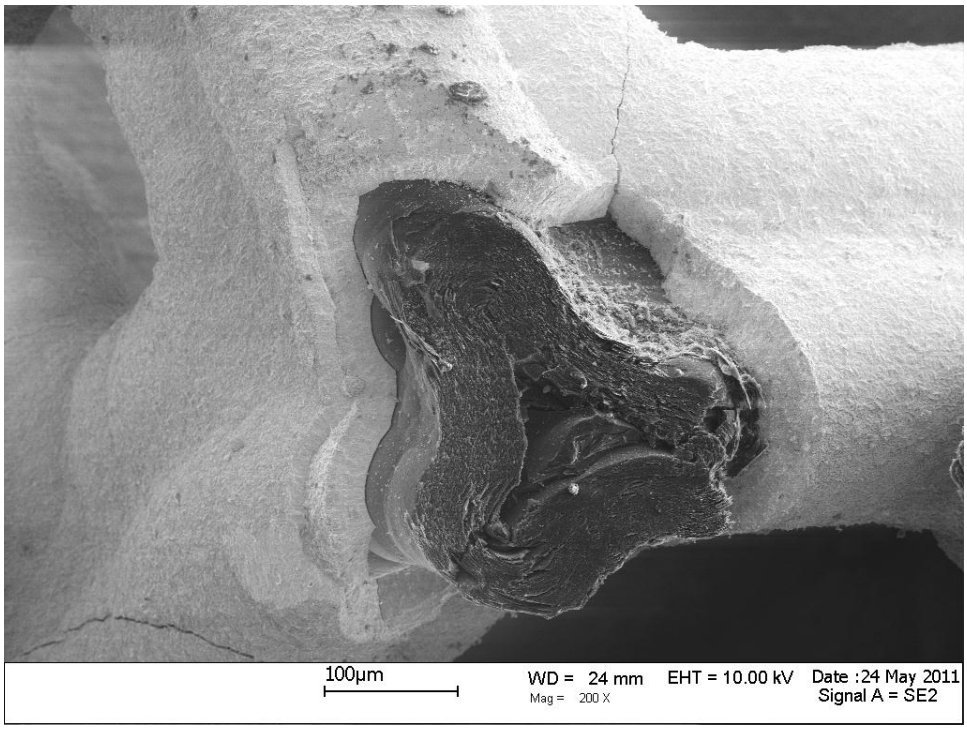

Figure 189. SEM micrograph of the baseline microstructure of a 45 ppi TaC/PyC/RVC foam specimen.

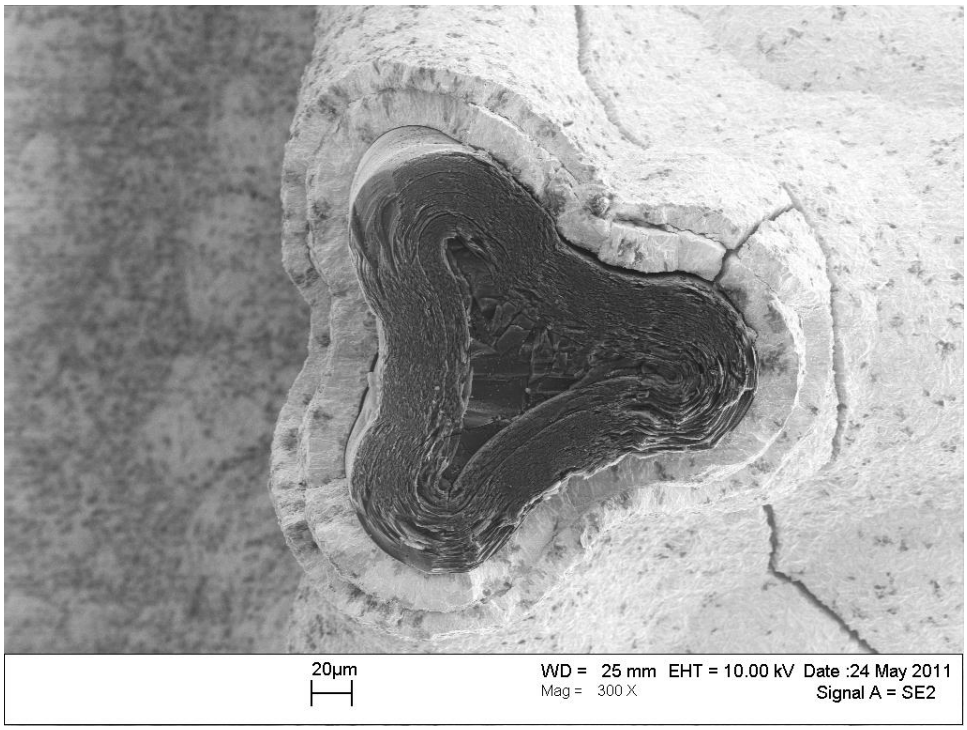

Figure 190. SEM micrograph of the microstructure of a 45 ppi TaC/PyC/RVC foam specimen after thermal cycling.

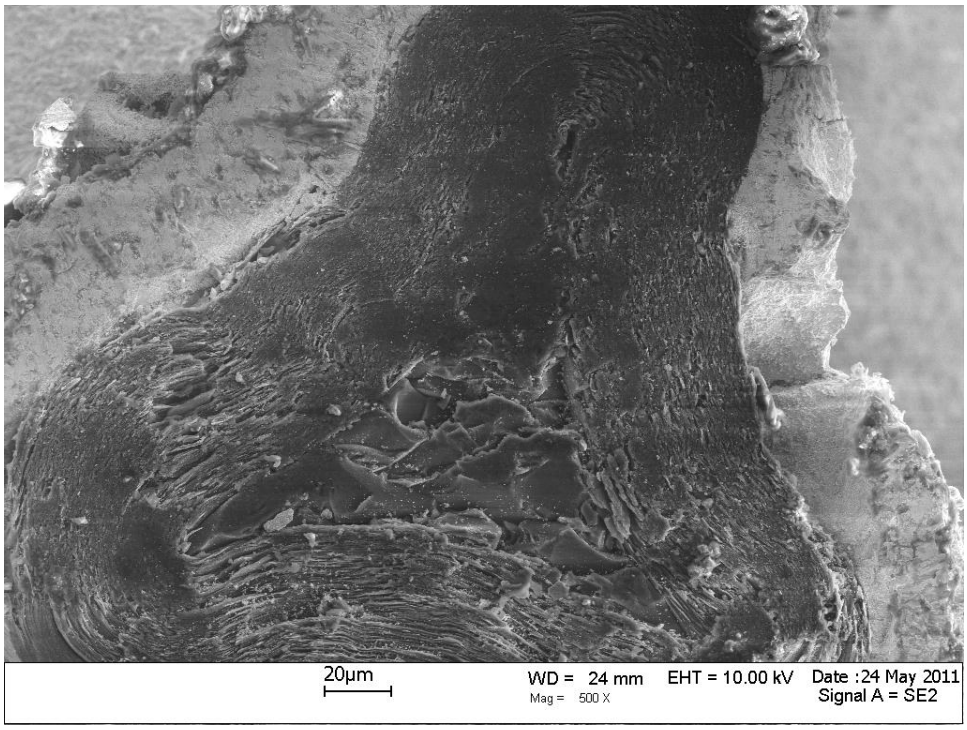

Figure 191. SEM micrograph of the baseline microstructure of a 45 ppi TaC/PyC/RVC foam specimen.

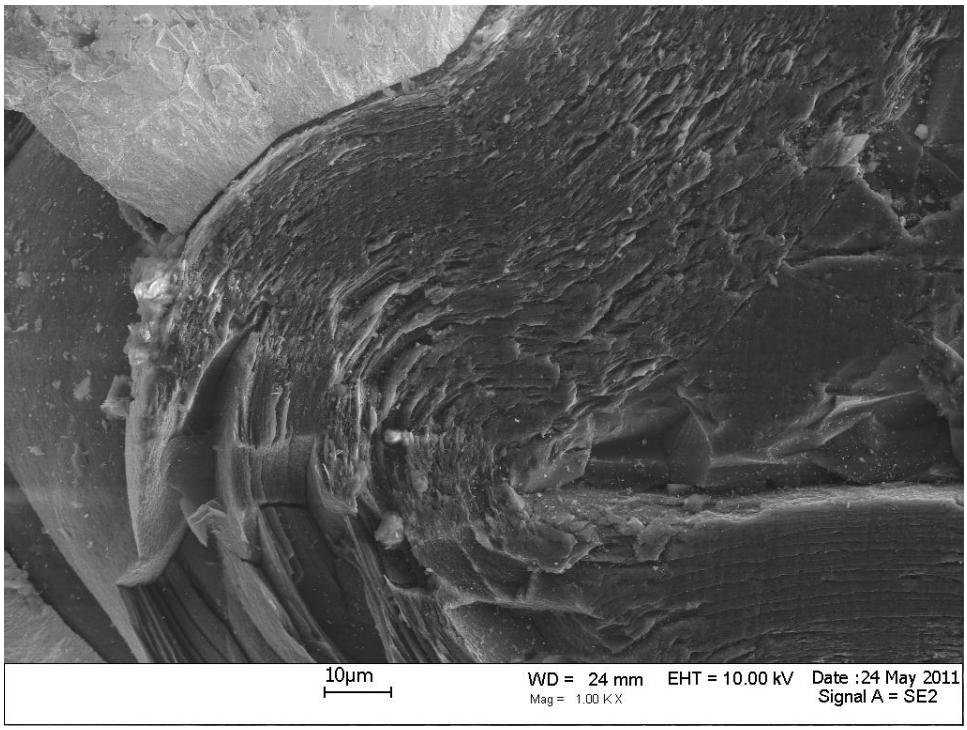

Figure 192. SEM micrograph of the baseline microstructure of a 45 ppi TaC/PyC/RVC foam specimen.

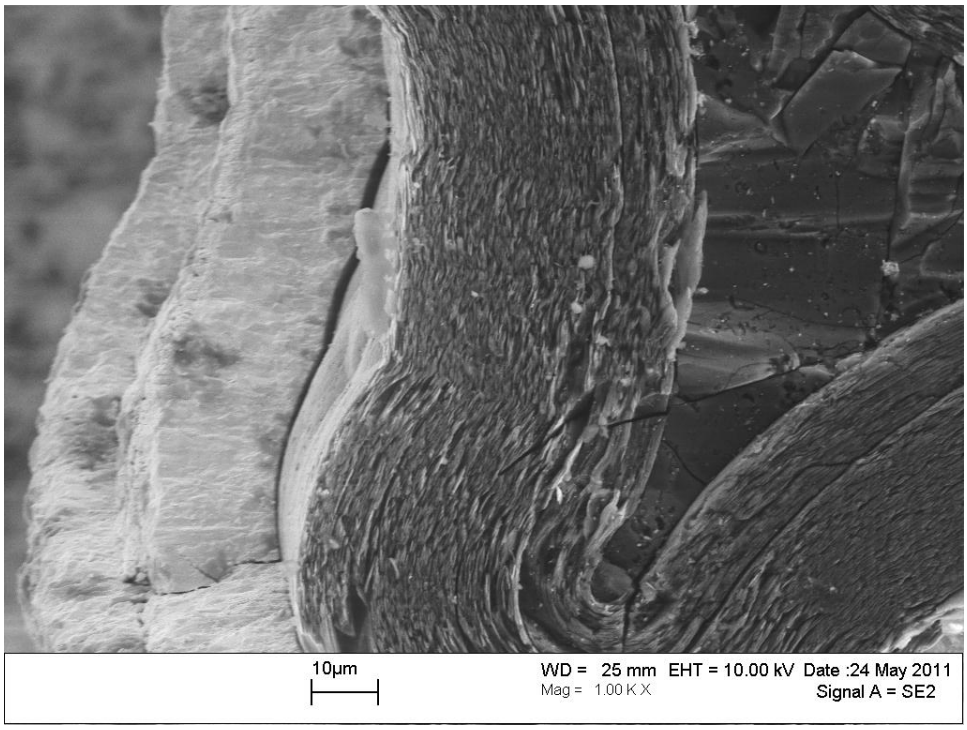

Figure 193. SEM micrograph of the microstructure of a 45 ppi TaC/PyC/RVC foam specimen after thermal cycling.

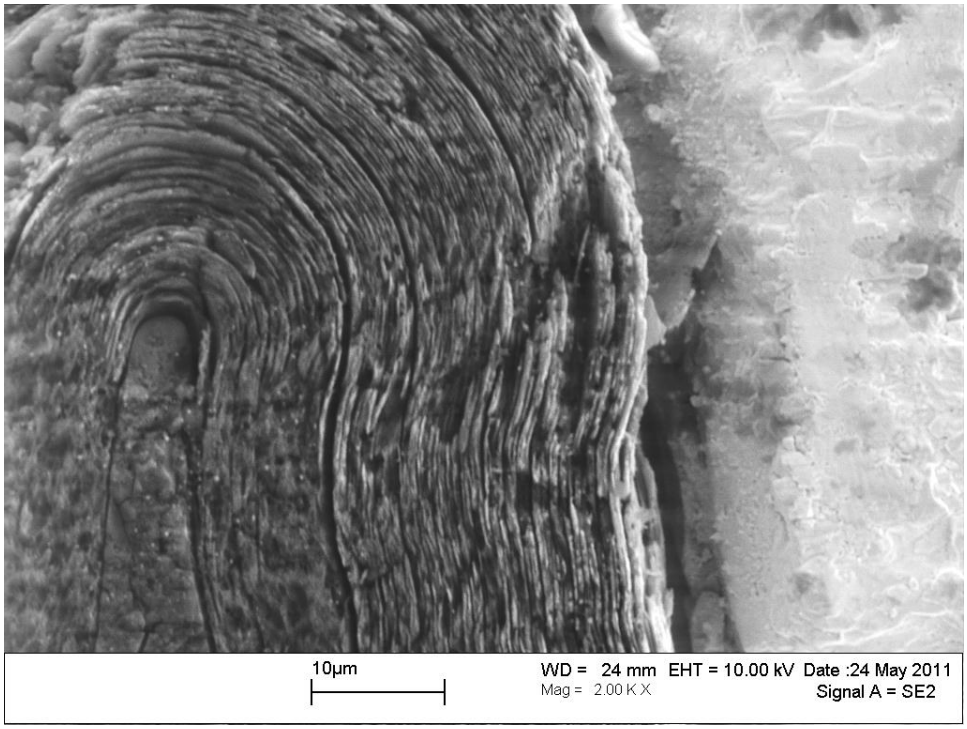

Figure 194. SEM micrograph of the microstructure of a 45 ppi TaC/PyC/RVC foam specimen after thermal cycling.

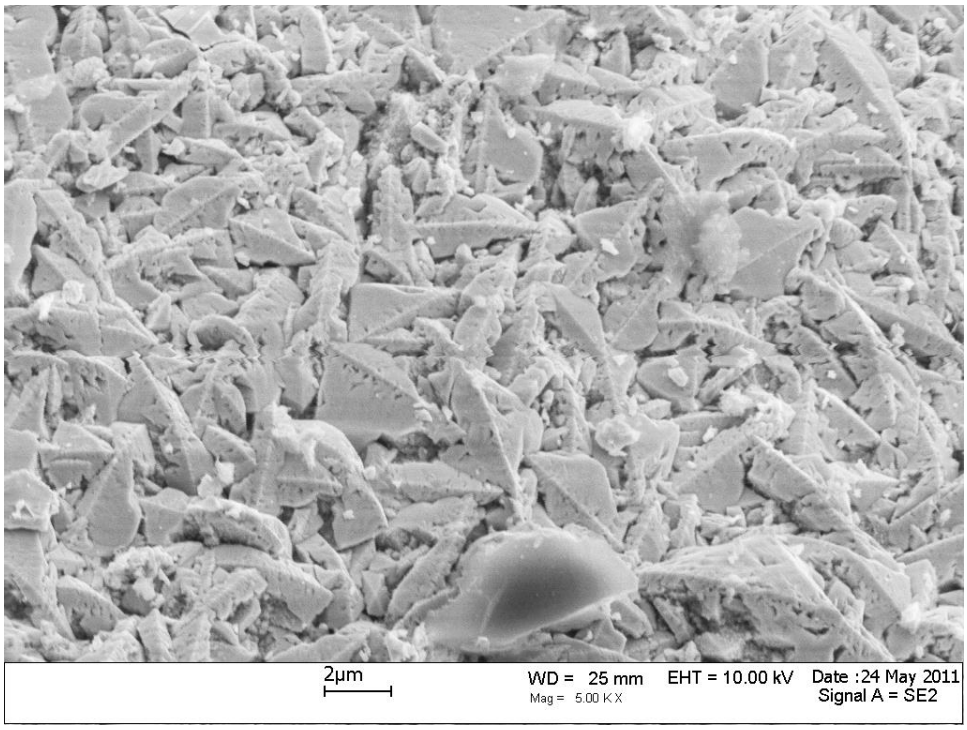

Figure 195. SEM micrograph of the baseline microstructure of a 45 ppi TaC/PyC/RVC foam specimen.

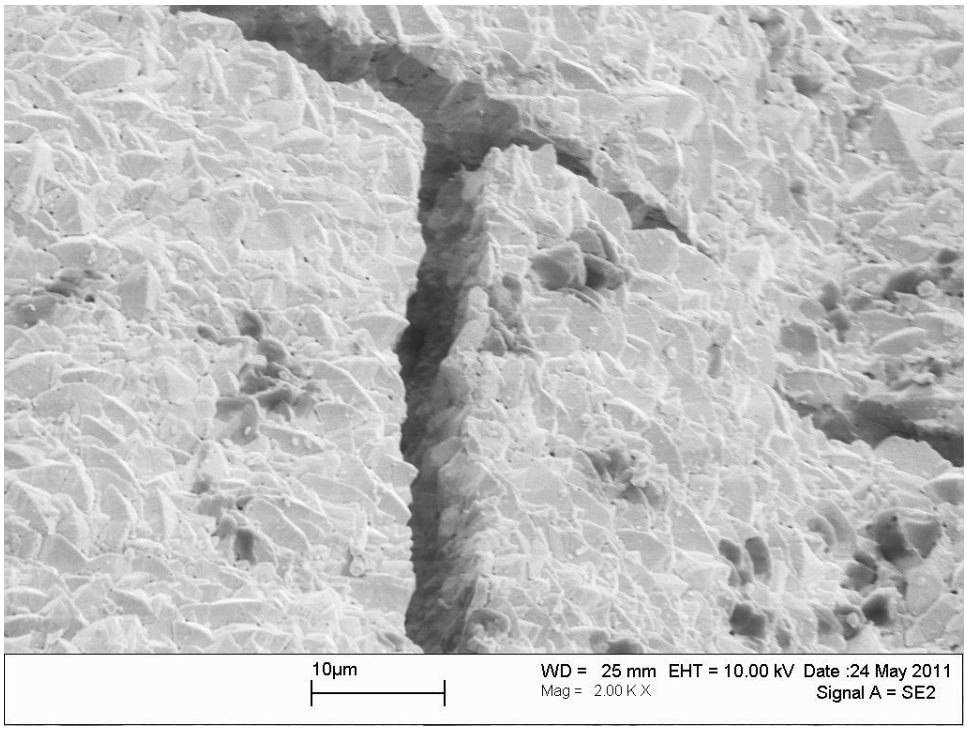

Figure 196. SEM micrograph of the microstructure of a 45 ppi TaC/PyC/RVC foam specimen after thermal cycling.

45 TaC/RVC

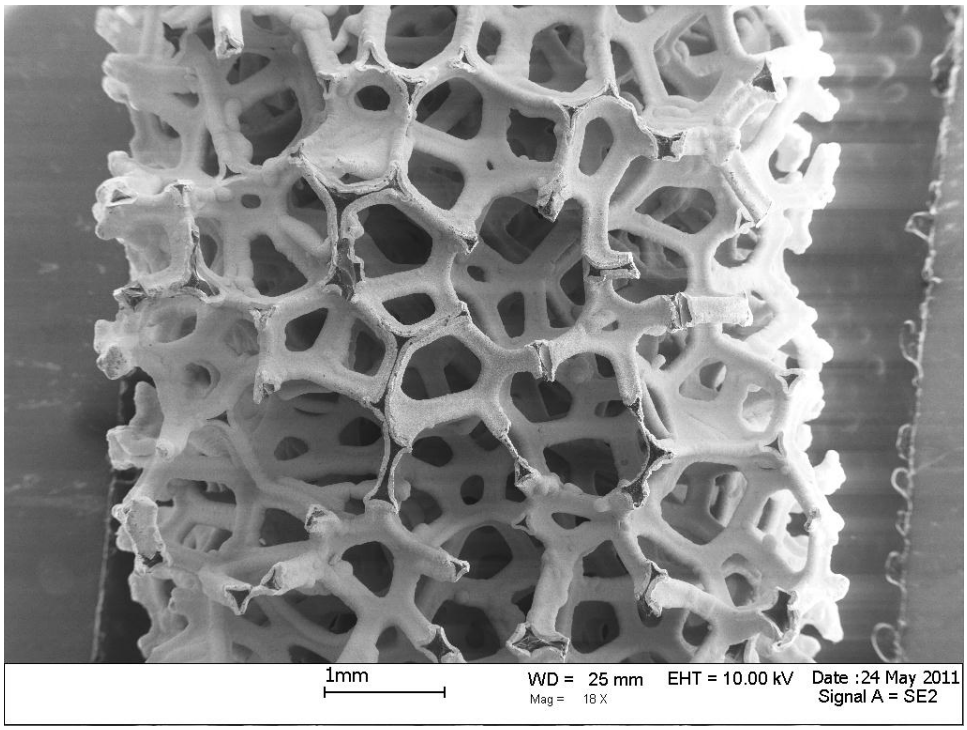

Figure 197. SEM micrograph of the baseline microstructure of a 45 ppi TaC/RVC foam specimen.

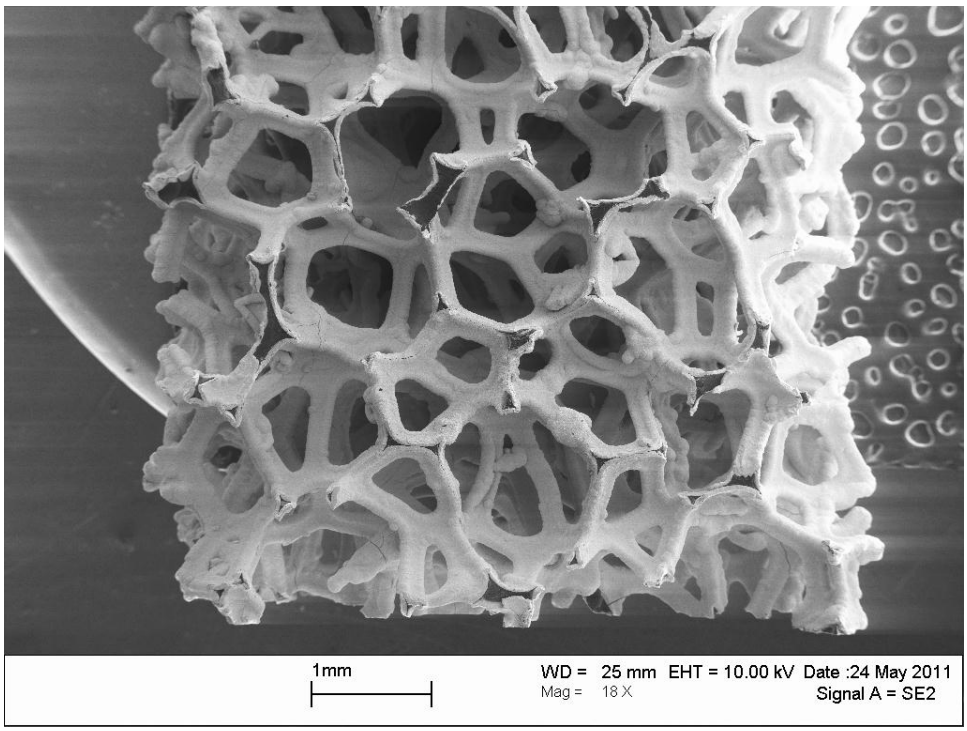

Figure 198. SEM micrograph of the baseline microstructure of a 45 ppi TaC/RVC foam specimen.

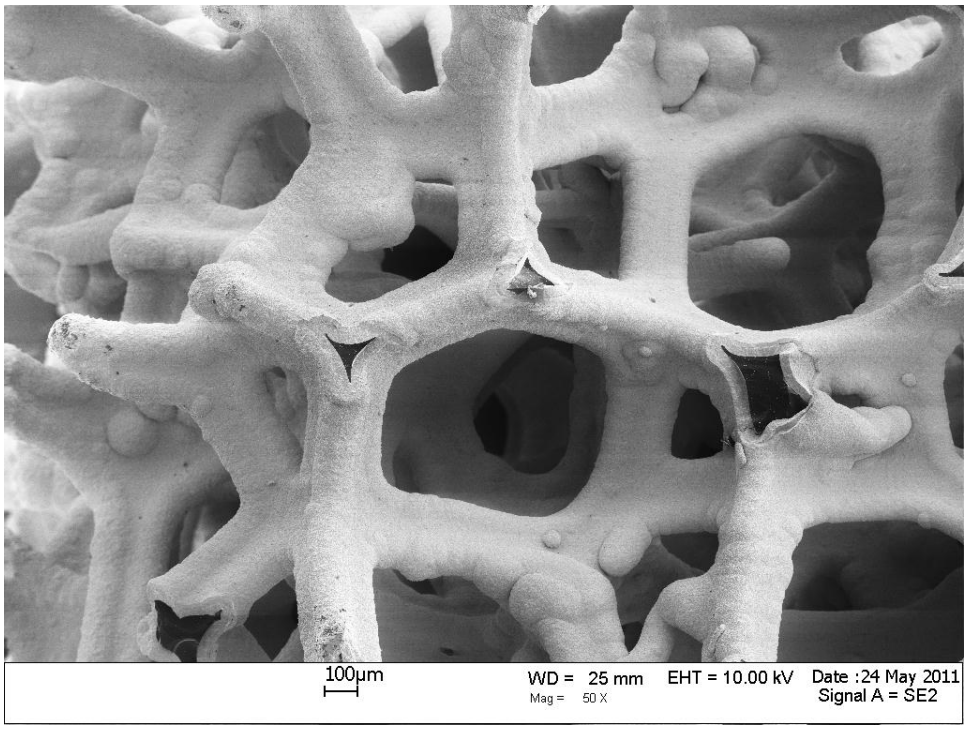

Figure 199. SEM micrograph of the baseline microstructure of a 45 ppi TaC/RVC foam specimen.

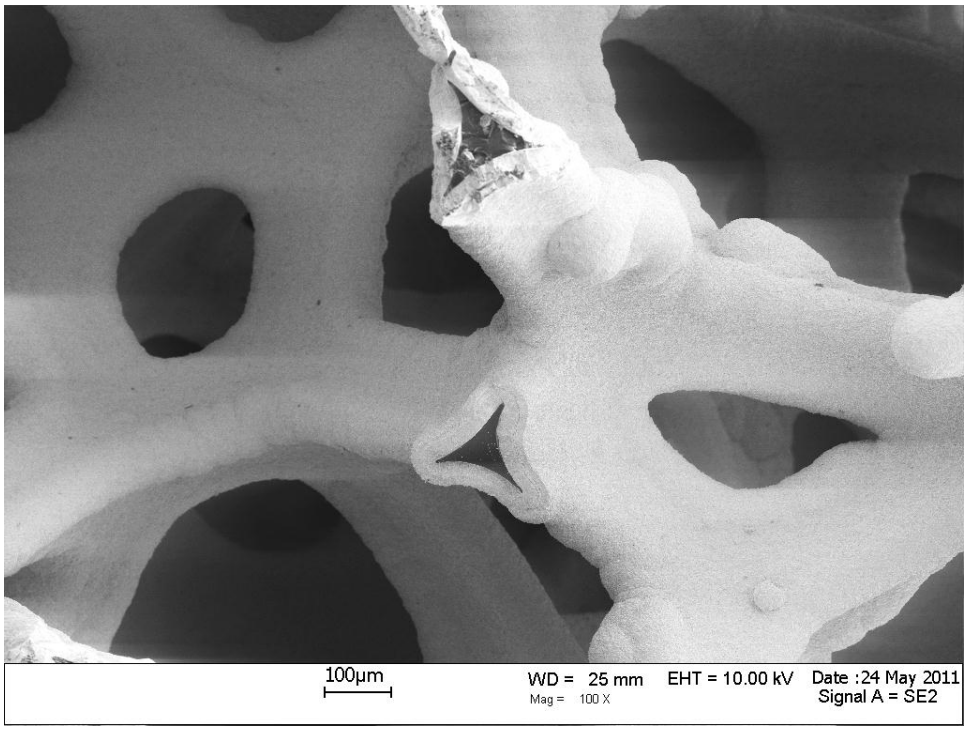

Figure 200. SEM micrograph of the baseline microstructure of a 45 ppi TaC/RVC foam specimen.

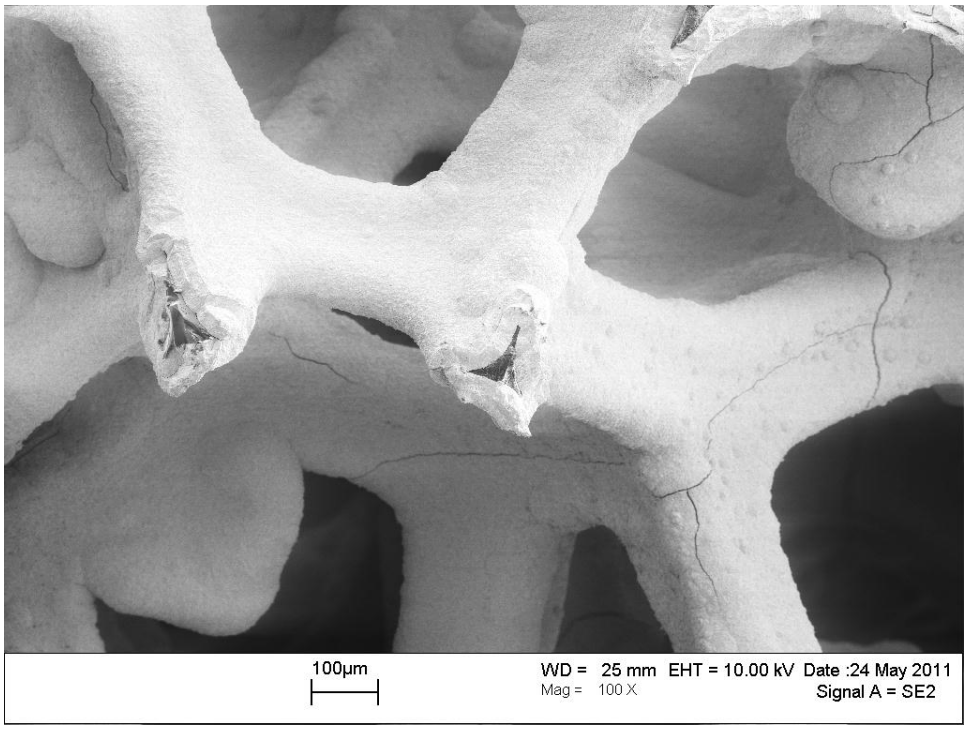

Figure 201. SEM micrograph of the microstructure of a 45 ppi TaC/RVC foam specimen after thermal cycling.

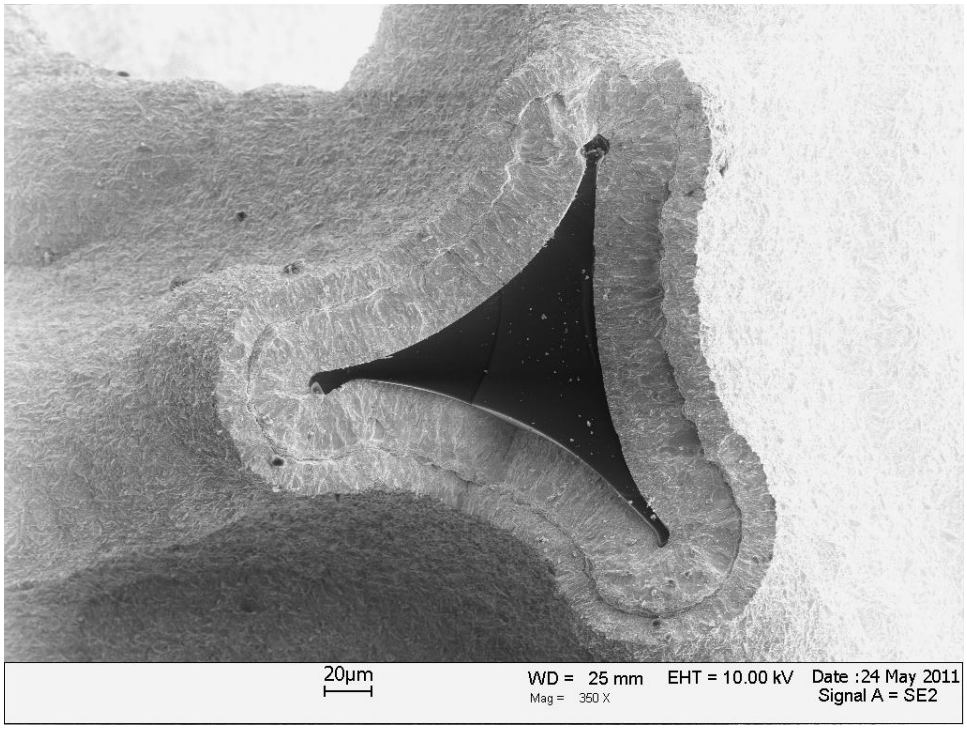

Figure 202. SEM micrograph of the baseline microstructure of a 45 ppi TaC/RVC foam specimen.

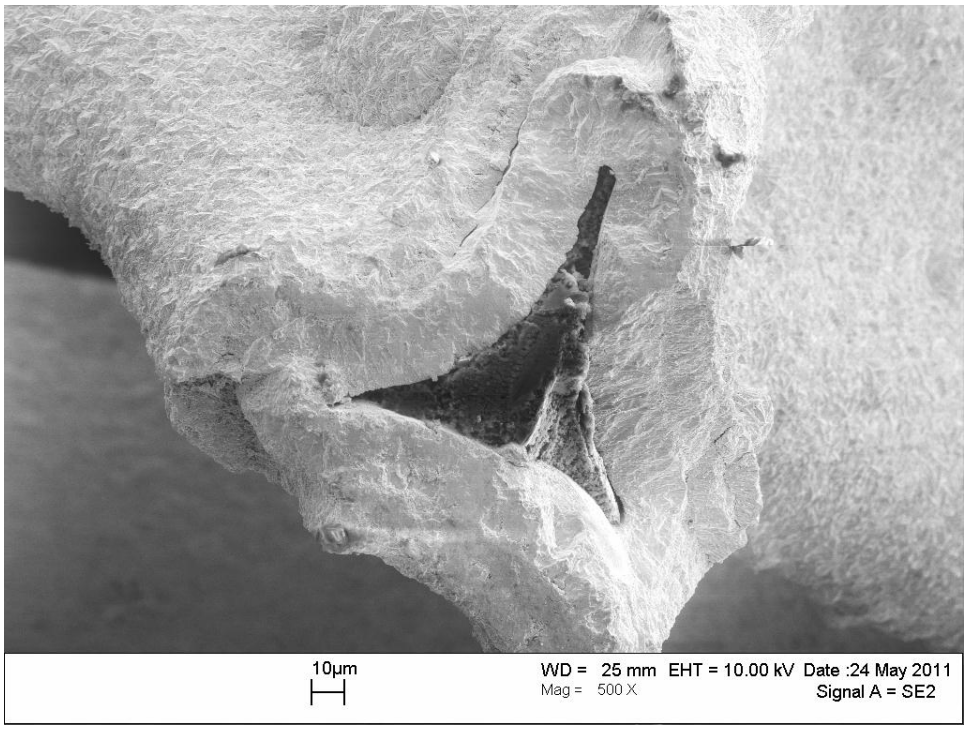

Figure 203. SEM micrograph of the microstructure of a 45 ppi TaC/RVC foam specimen after thermal cycling.

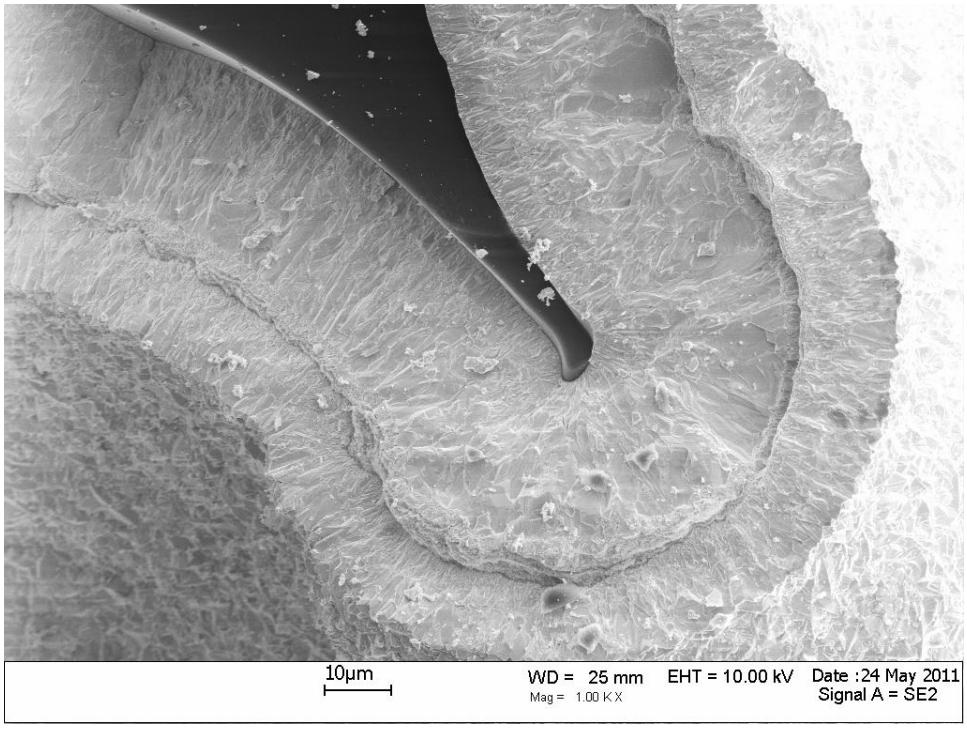

Figure 204. SEM micrograph of the baseline microstructure of a 45 ppi TaC/RVC foam specimen.

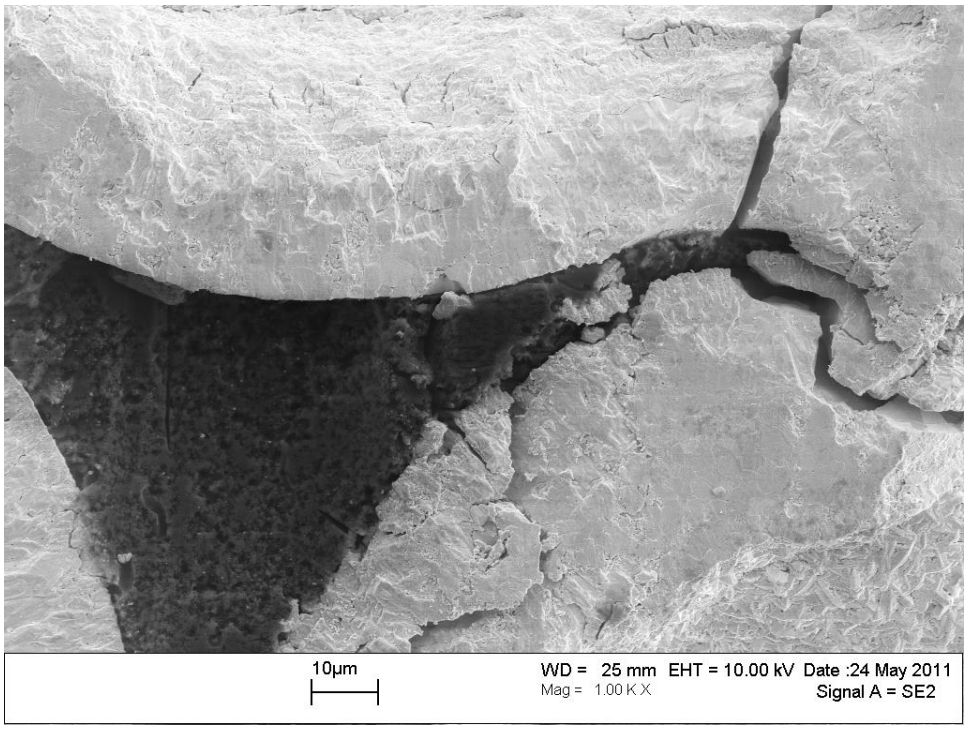

Figure 205. SEM micrograph of the microstructure of a 45 ppi TaC/RVC foam specimen after thermal cycling.

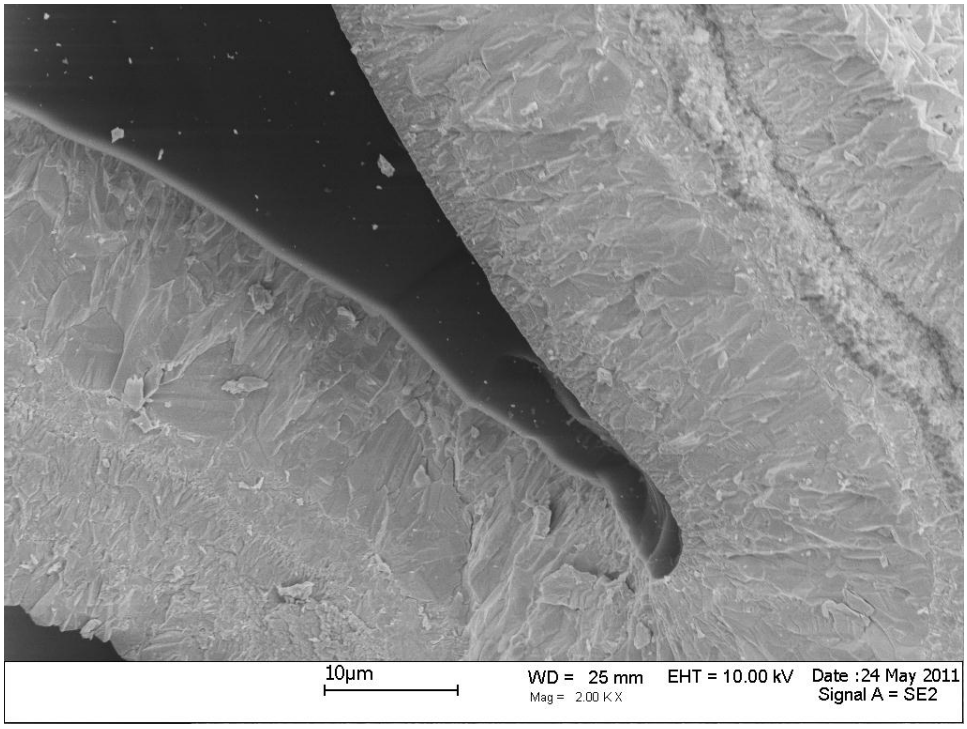

Figure 206. SEM micrograph of the baseline microstructure of a 45 ppi TaC/RVC foam specimen.

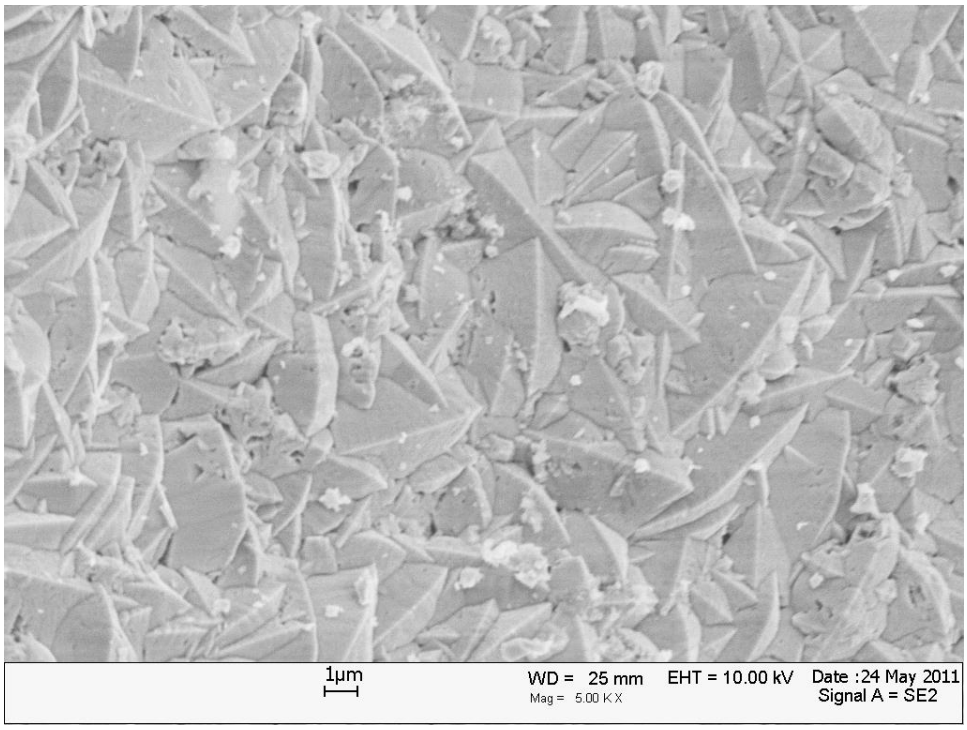

Figure 207. SEM micrograph of the baseline microstructure of a 45 ppi TaC/RVC foam specimen.

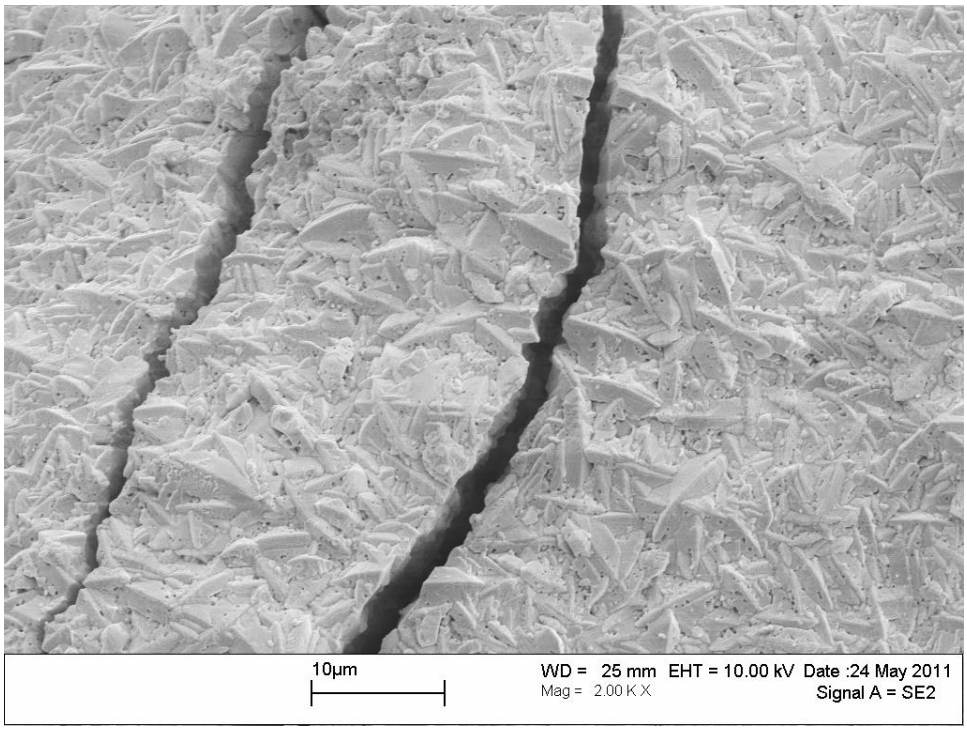

Figure 208. SEM micrograph of the microstructure of a 45 ppi TaC/RVC foam specimen after thermal cycling.

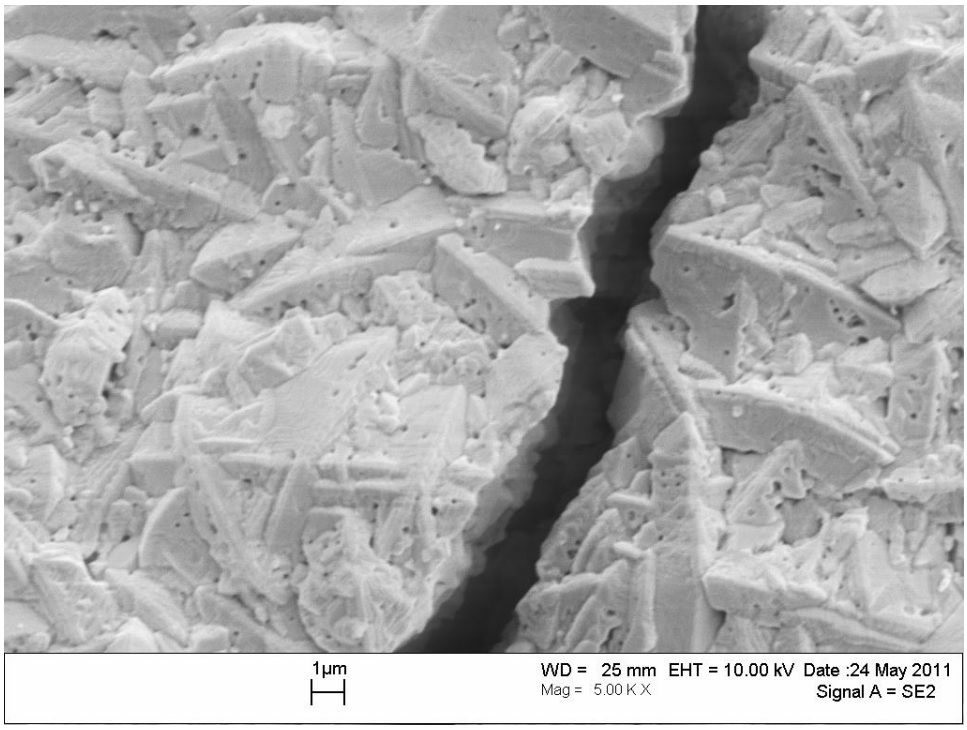

Figure 209. SEM micrograph of the microstructure of a 45 ppi TaC/RVC foam specimen after thermal cycling.

65 TaC/PyC/RVC

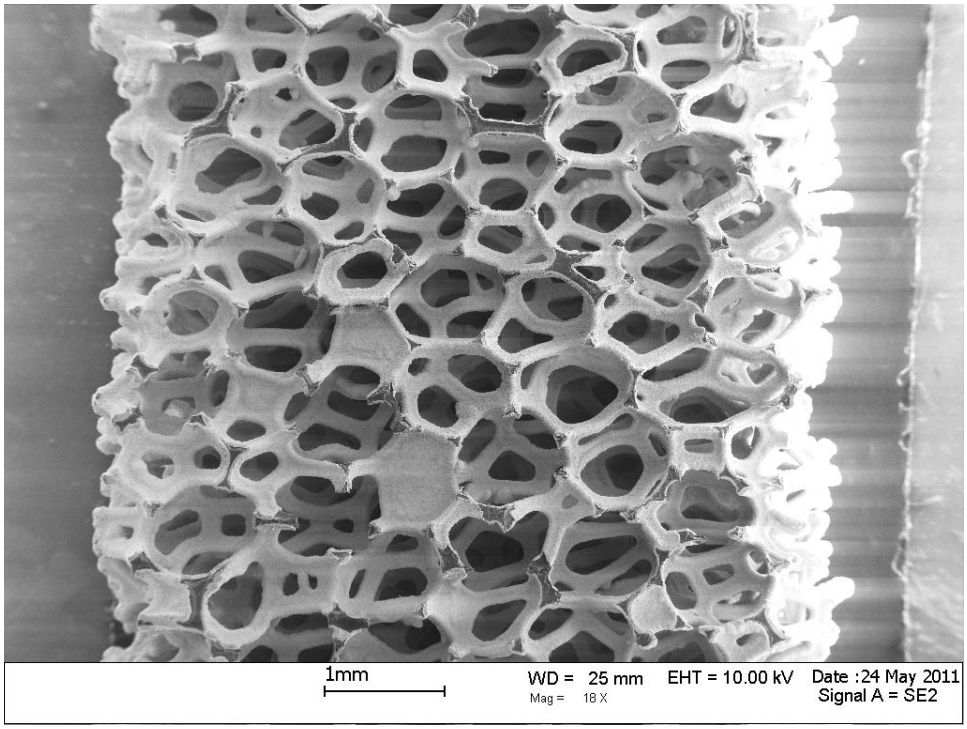

Figure 210. SEM micrograph of the baseline microstructure of a 65 ppi TaC/PyC/RVC foam specimen.

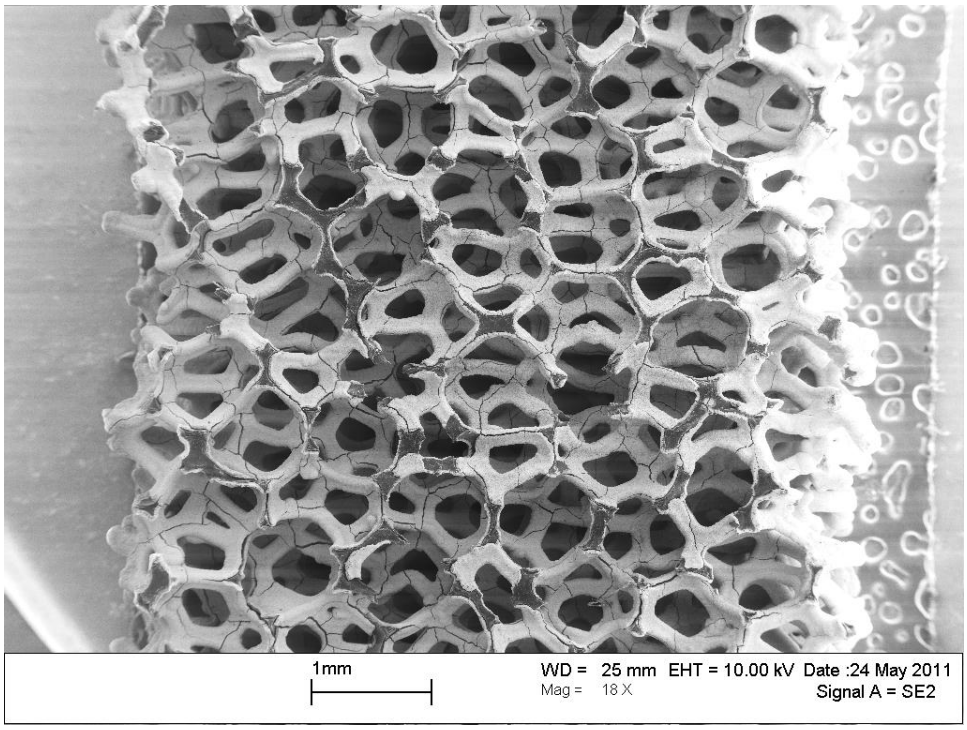

Figure 211. SEM micrograph of the microstructure of a 65 ppi TaC/PyC/RVC foam specimen after thermal cycling.

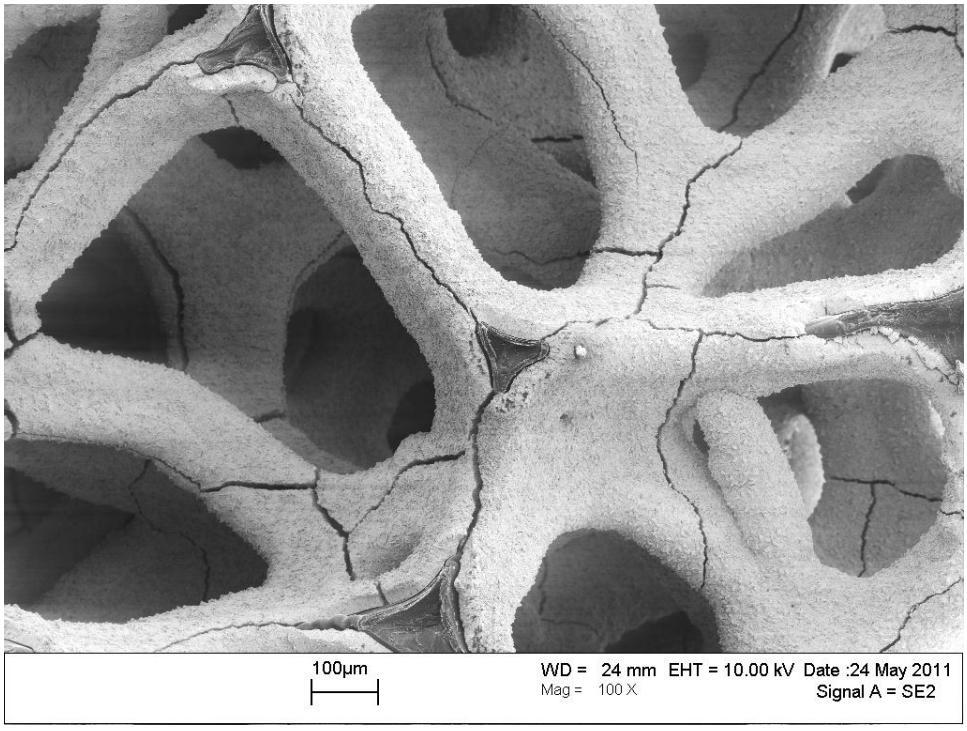

Figure 212. SEM micrograph of the microstructure of a 65 ppi TaC/PyC/RVC foam specimen after thermal cycling.

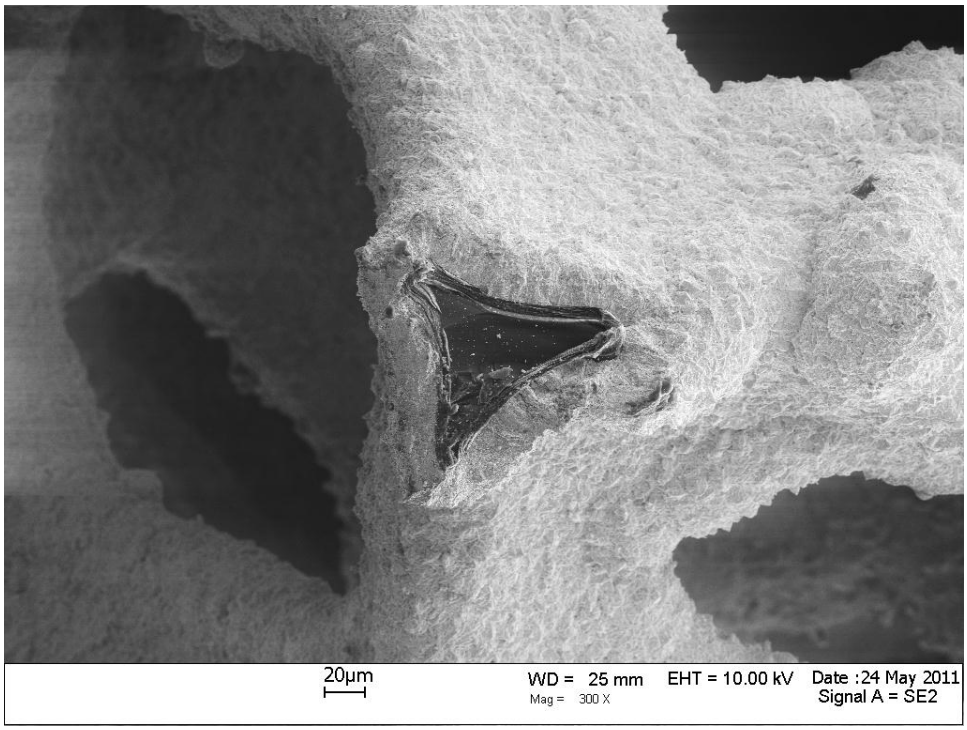

Figure 213. SEM micrograph of the baseline microstructure of a 65 ppi TaC/PyC/RVC foam specimen.

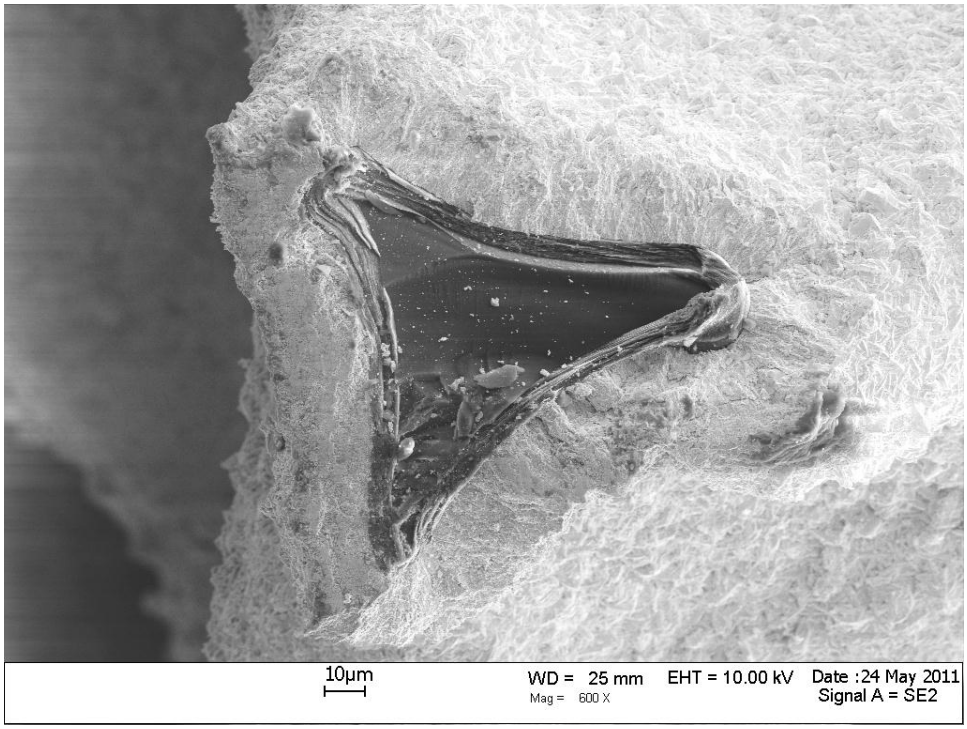

Figure 214. SEM micrograph of the baseline microstructure of a 65 ppi TaC/PyC/RVC foam specimen.

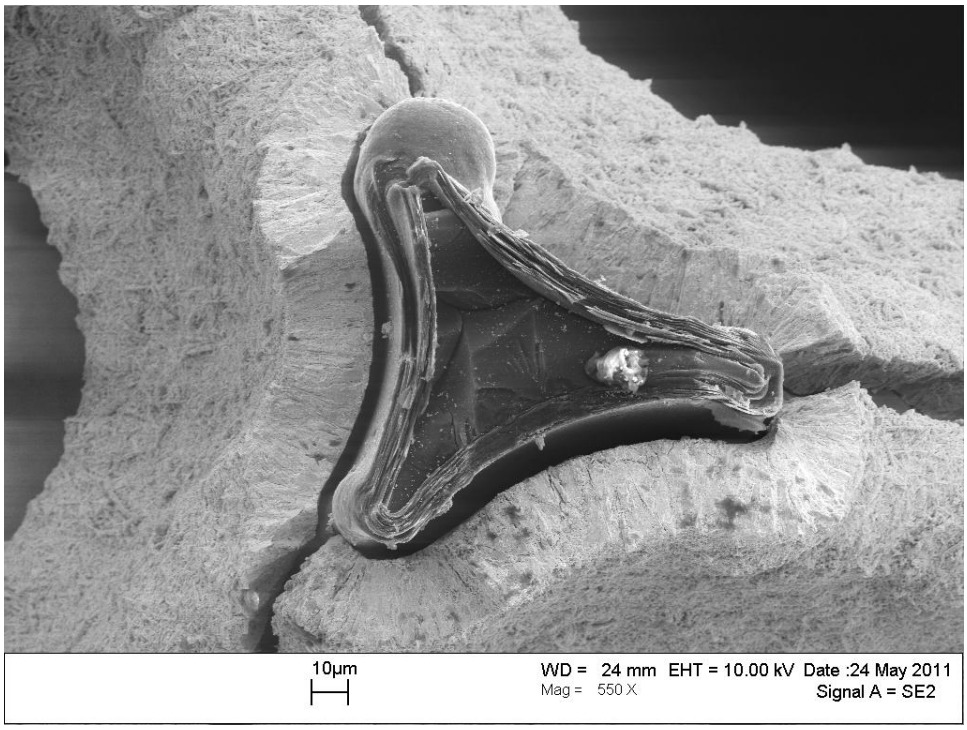

Figure 215. SEM micrograph of the microstructure of a 65 ppi TaC/PyC/RVC foam specimen after thermal cycling.

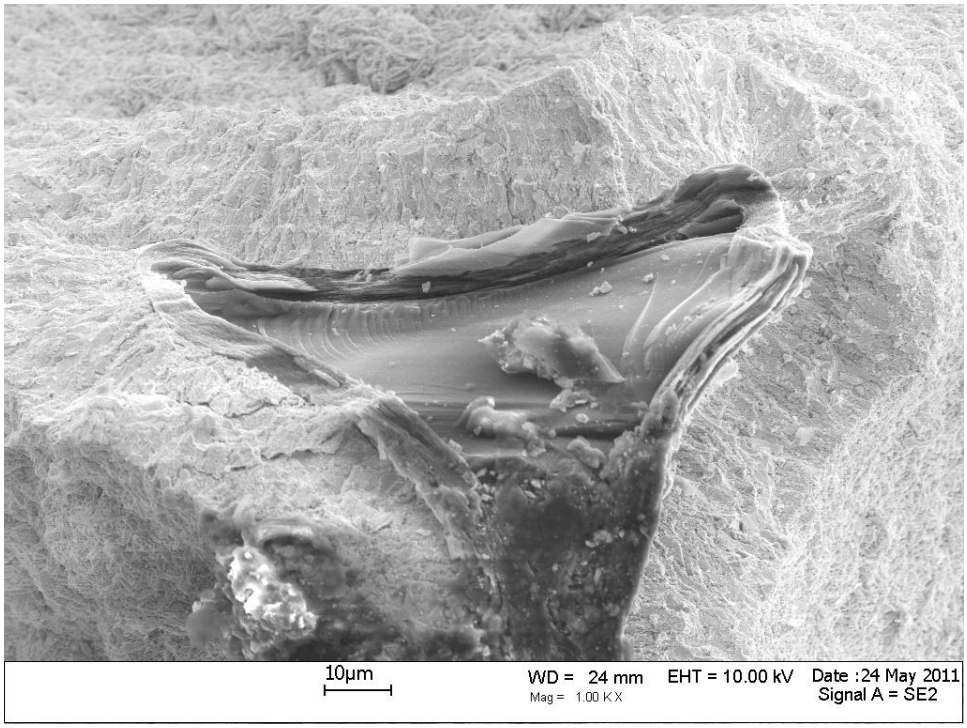

Figure 216. SEM micrograph of the baseline microstructure of a 65 ppi TaC/PyC/RVC foam specimen.

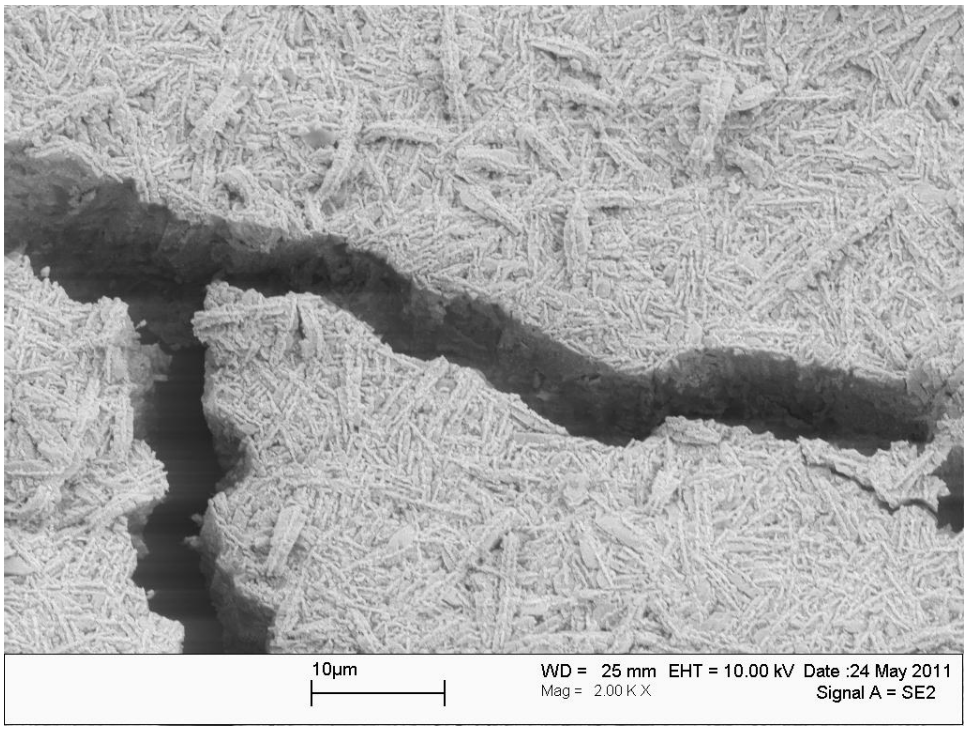

Figure 217. SEM micrograph of the microstructure of a 65 ppi TaC/PyC/RVC foam specimen after thermal cycling.

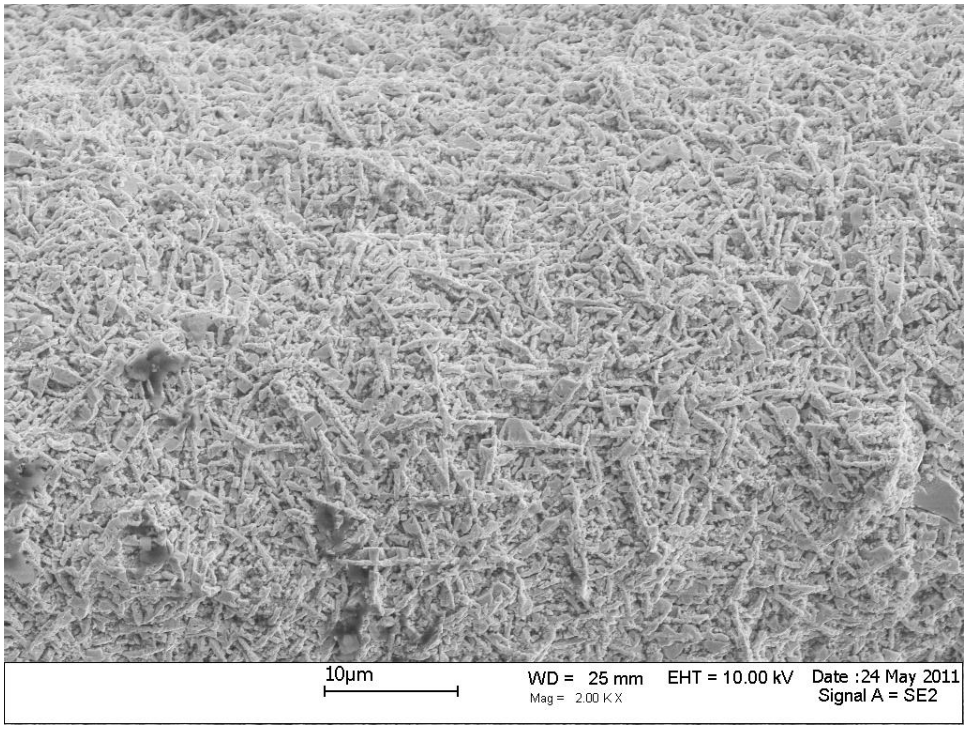

Figure 218. SEM micrograph of the baseline microstructure of a 65 ppi TaC/PyC/RVC foam specimen.

65 TaC/RVC

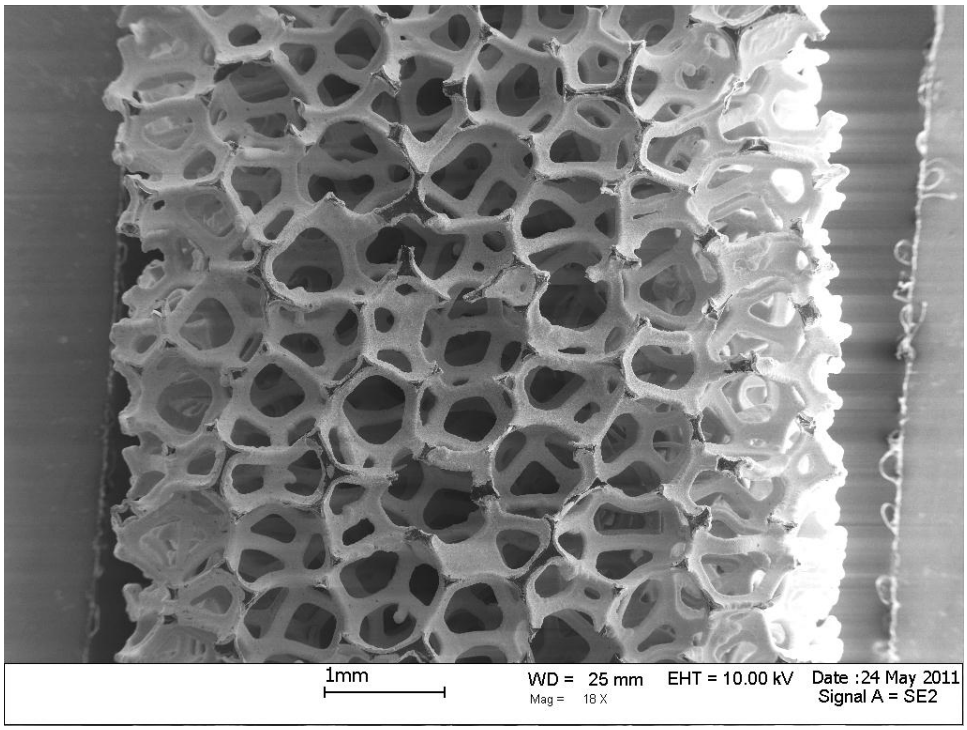

Figure 219. SEM micrograph of the baseline microstructure of a 65 ppi TaC/RVC foam specimen.

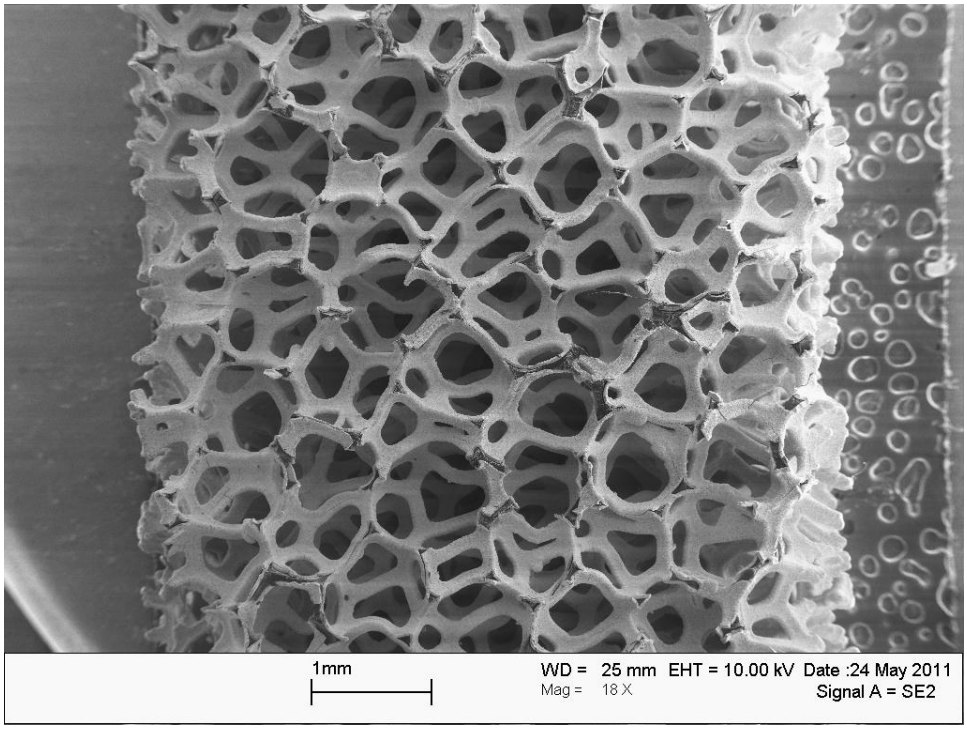

Figure 220. SEM micrograph of the microstructure of a 65 ppi TaC/RVC foam specimen after thermal cycling.

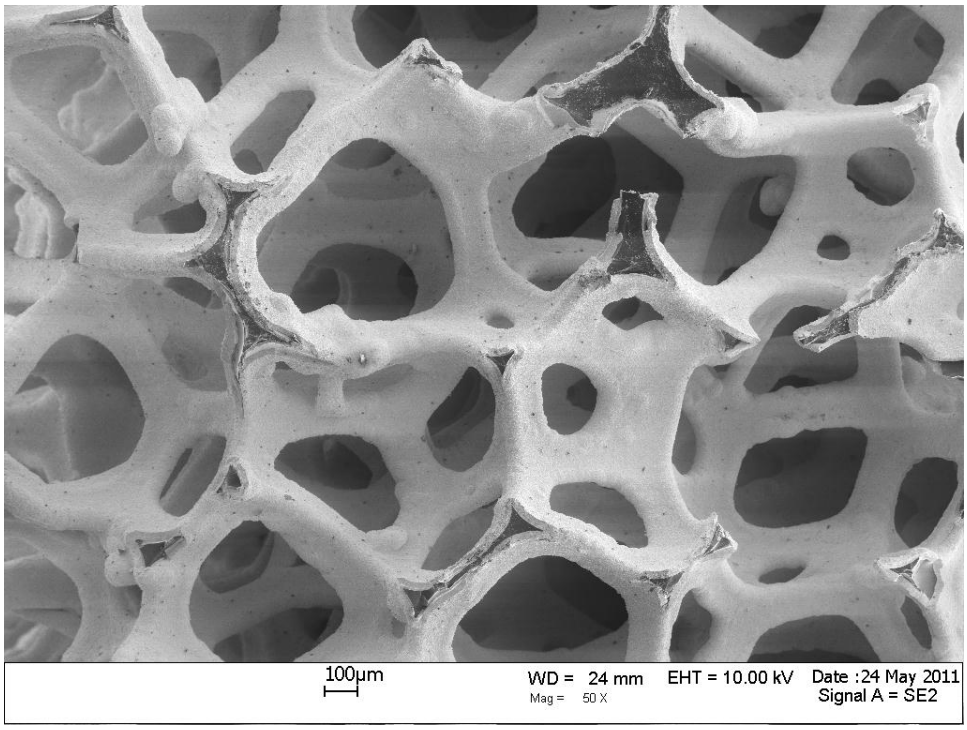

Figure 221. SEM micrograph of the baseline microstructure of a 65 ppi TaC/RVC foam specimen.

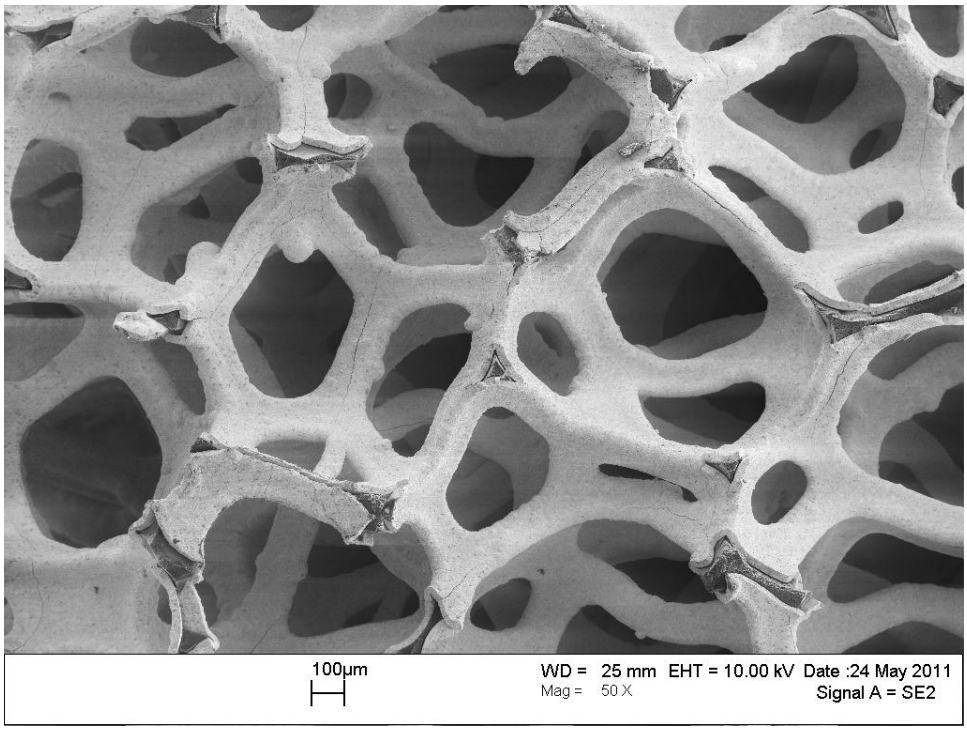

Figure 222. SEM micrograph of the microstructure of a 65 ppi TaC/RVC foam specimen after thermal cycling.

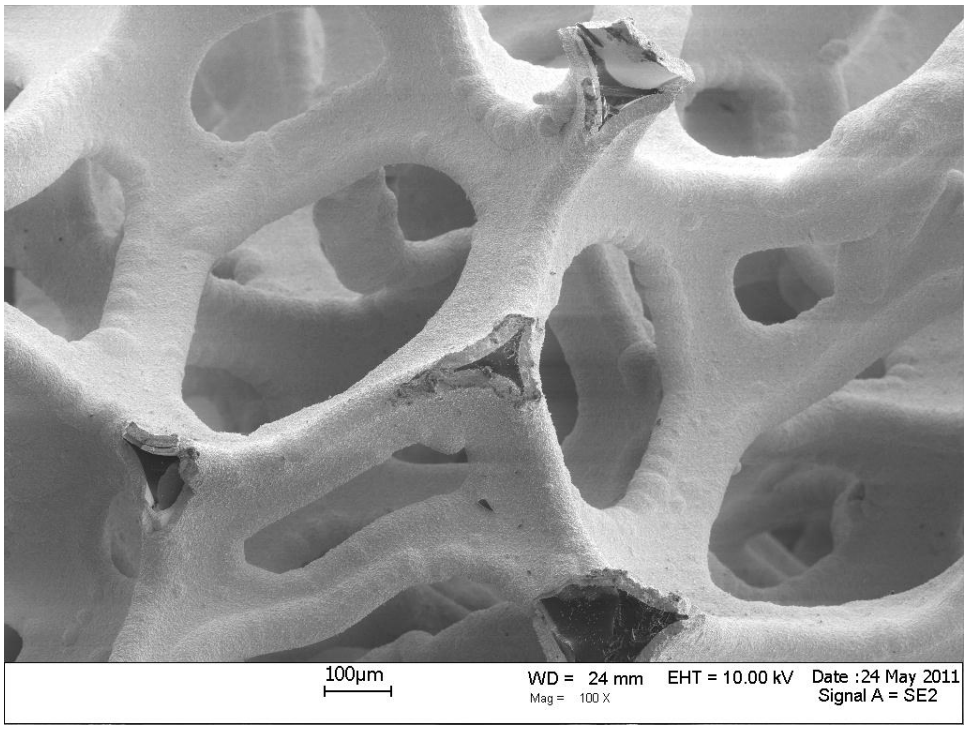

Figure 223. SEM micrograph of the baseline microstructure of a 65 ppi TaC/RVC foam specimen.

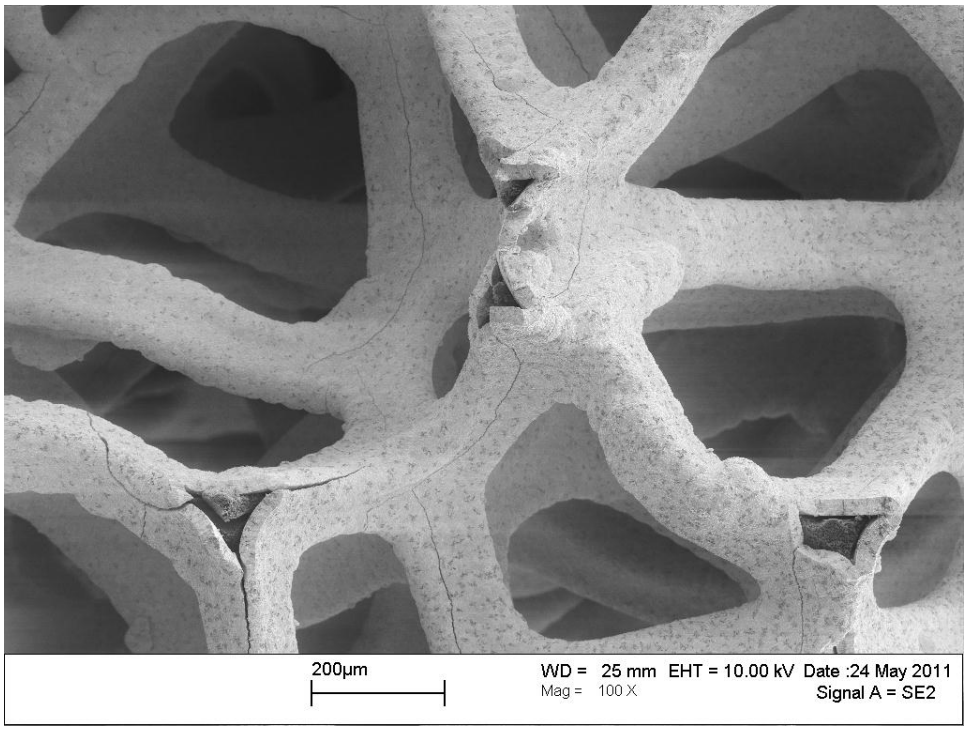

Figure 224. SEM micrograph of the microstructure of a 65 ppi TaC/RVC foam specimen after thermal cycling.

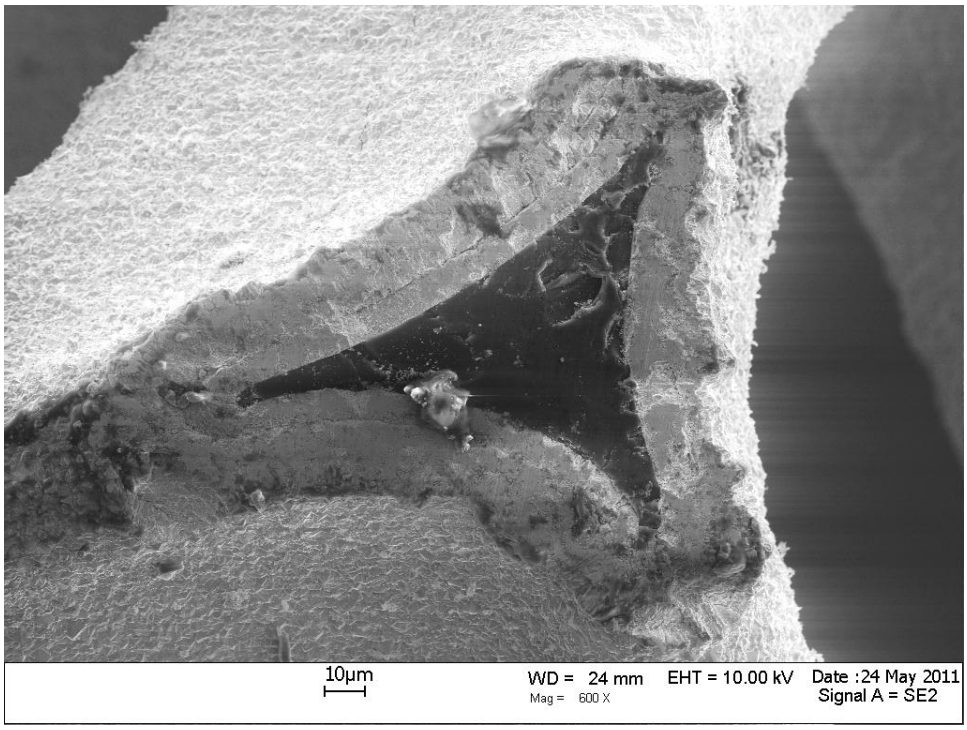

Figure 225. SEM micrograph of the baseline microstructure of a 65 ppi TaC/RVC foam specimen.

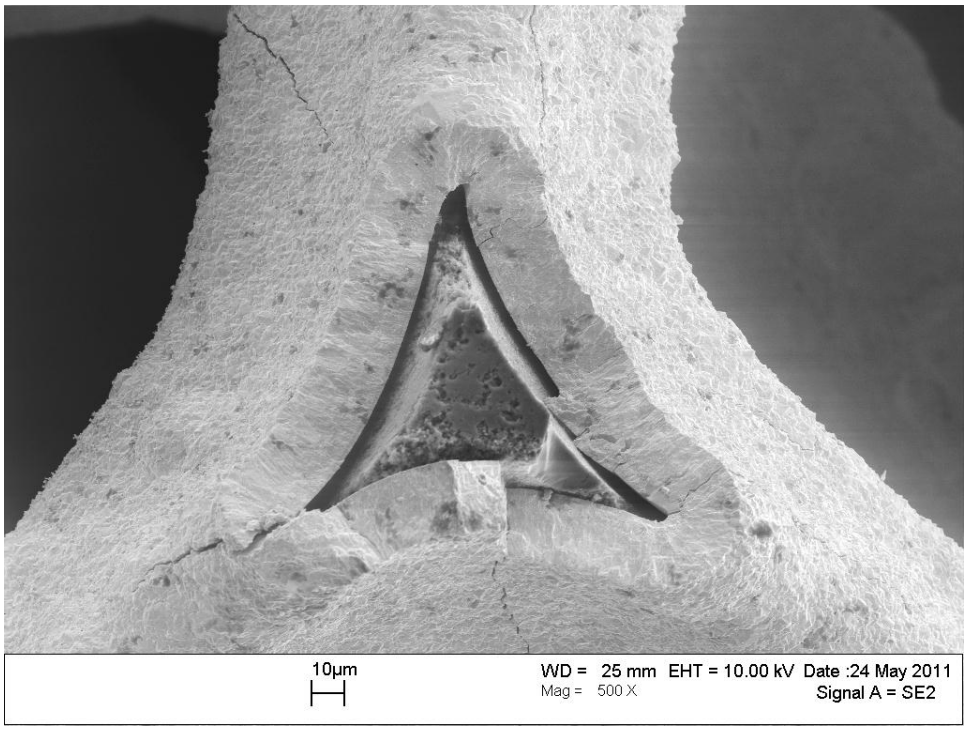

Figure 226. SEM micrograph of the microstructure of a 65 ppi TaC/RVC foam specimen after thermal cycling.

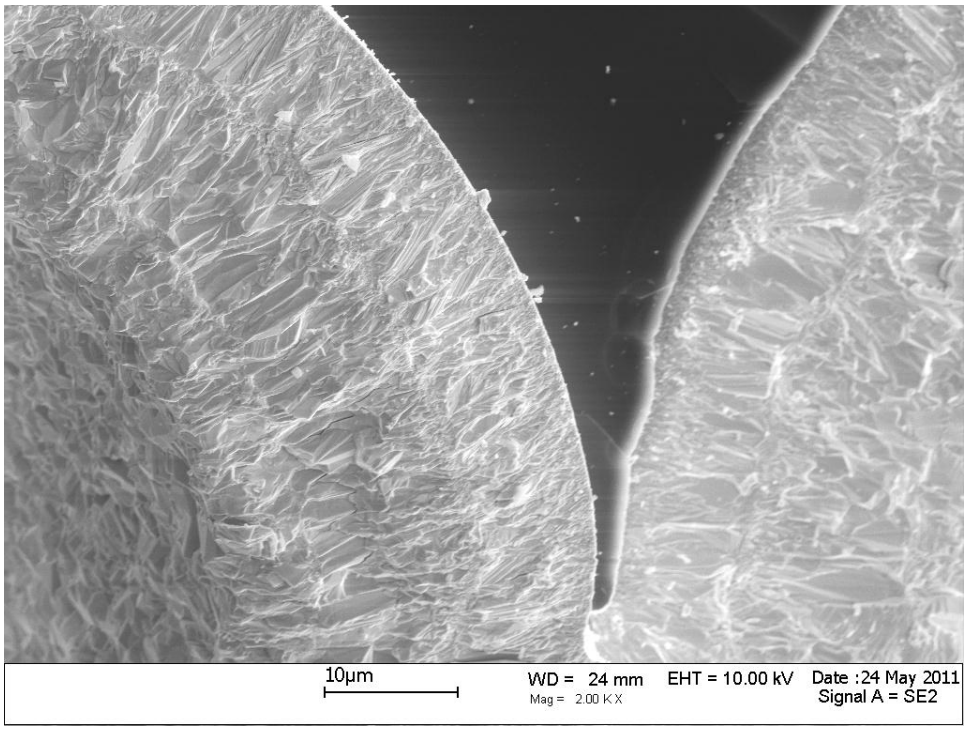

Figure 227. SEM micrograph of the baseline microstructure of a 65 ppi TaC/RVC foam specimen.

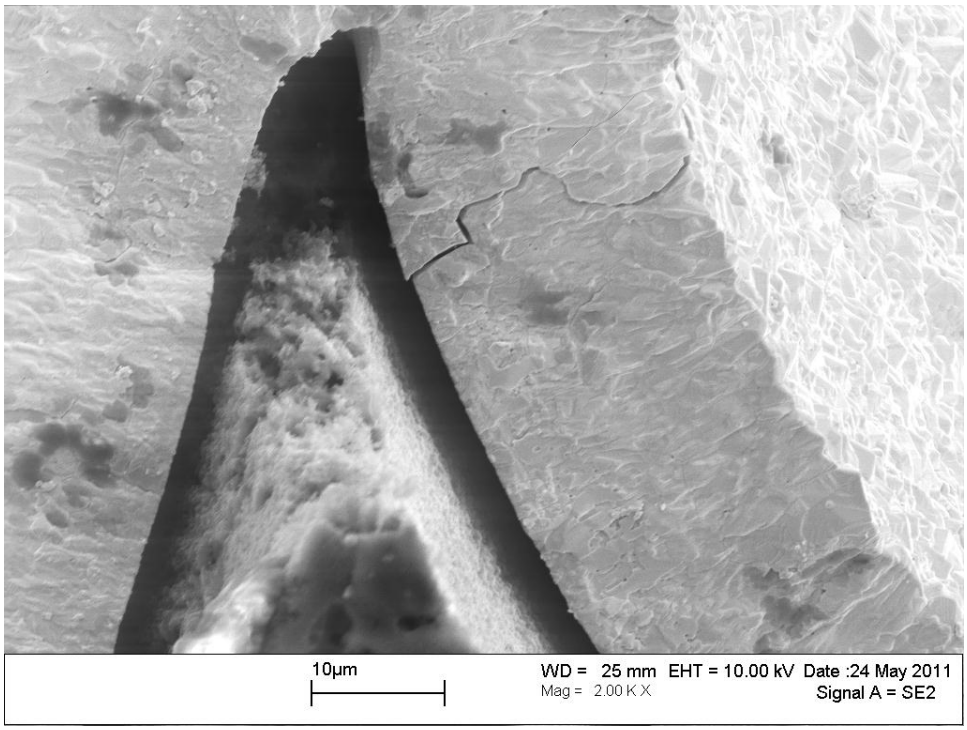

Figure 228. SEM micrograph of the microstructure of a 65 ppi TaC/RVC foam specimen after thermal cycling.

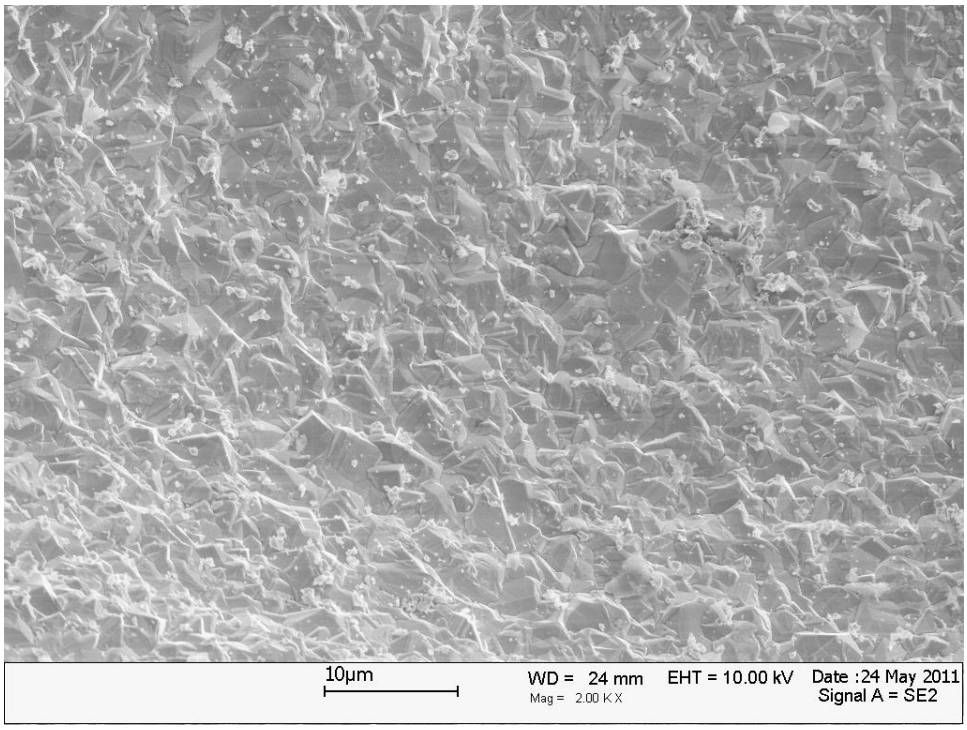

Figure 229. SEM micrograph of the baseline microstructure of a 65 ppi TaC/RVC foam specimen.

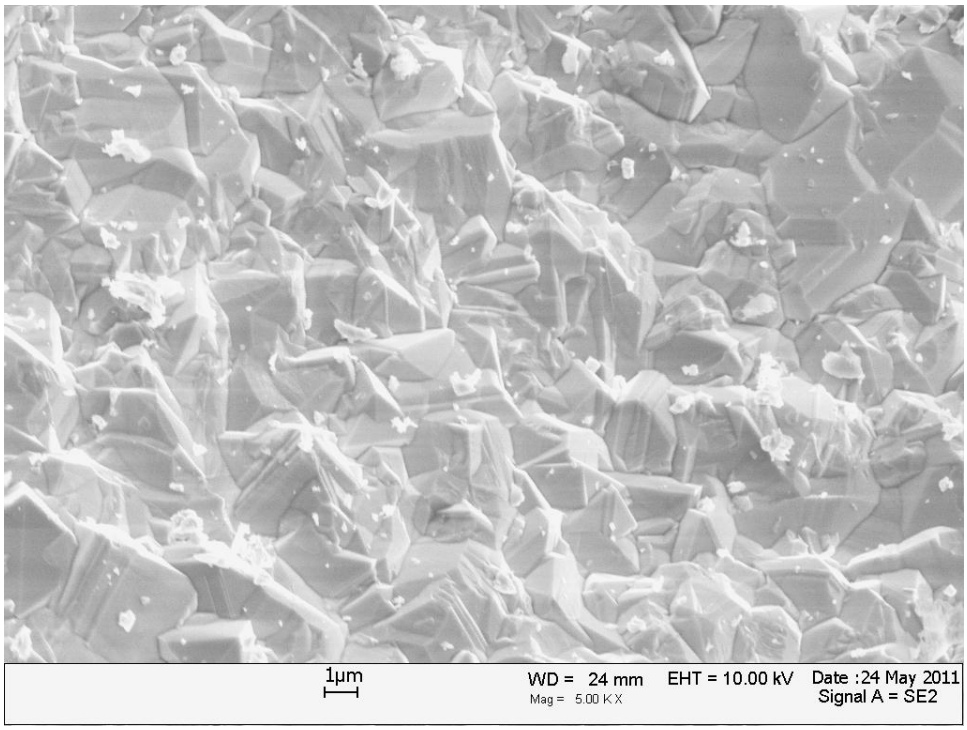

Figure 230. SEM micrograph of the baseline microstructure of a 65 ppi TaC/RVC foam specimen.

100 TaC/PyC/RVC

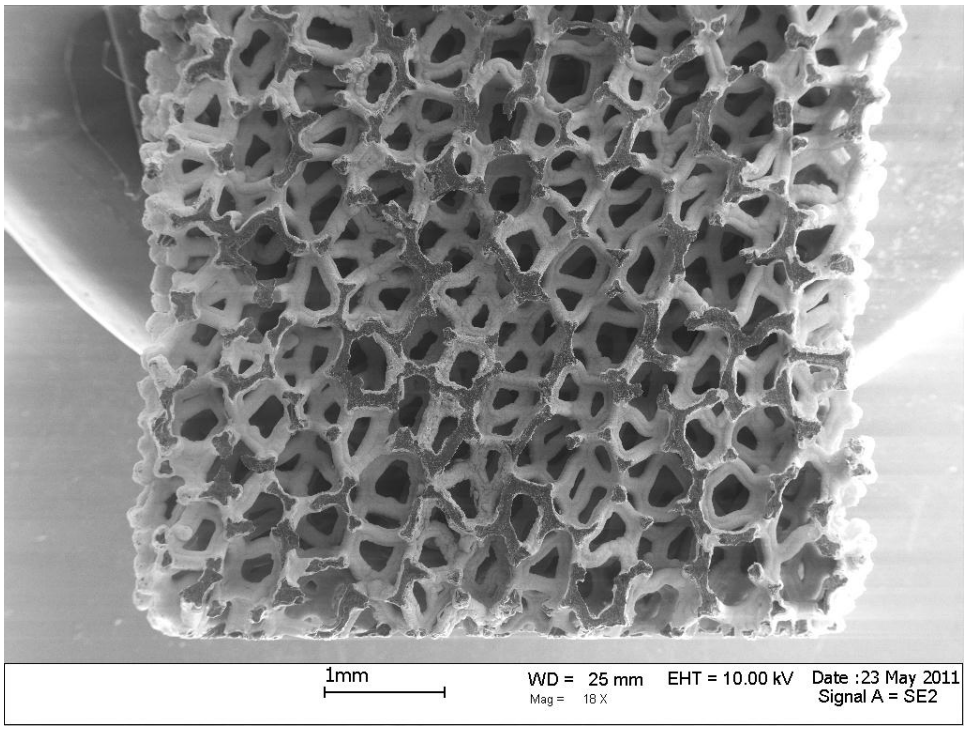

Figure 231. SEM micrograph of the baseline microstructure of a 100 ppi TaC/PyC/RVC Type B foam specimen.

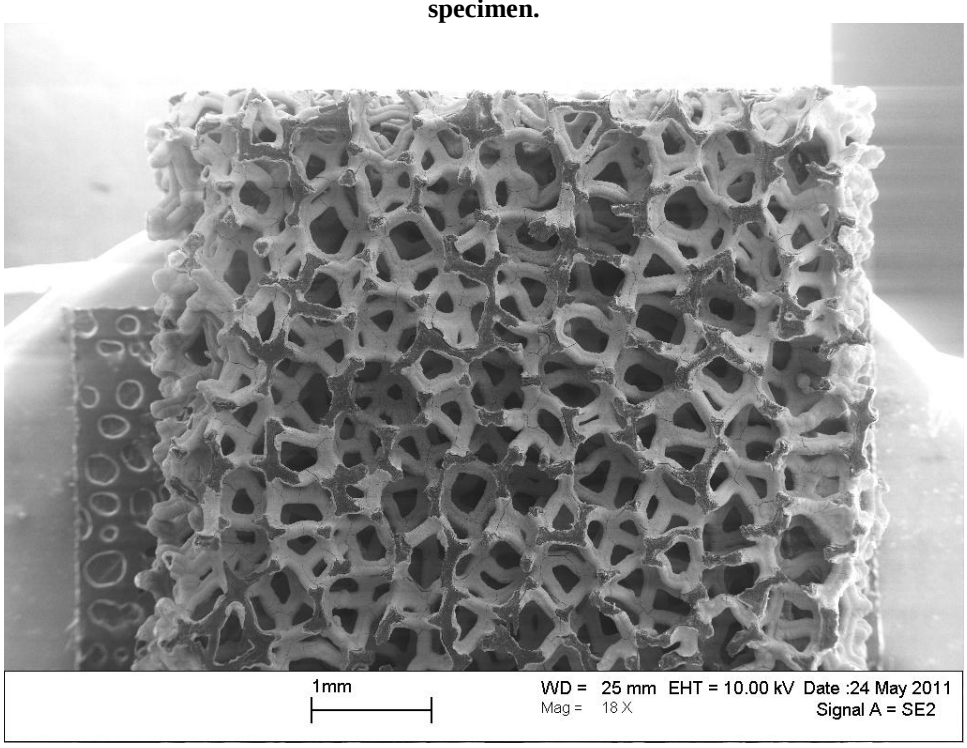

Figure 232. SEM micrograph of the microstructure of a 100 ppi TaC/PyC/RVC Type B foam specimen after thermal cycling.

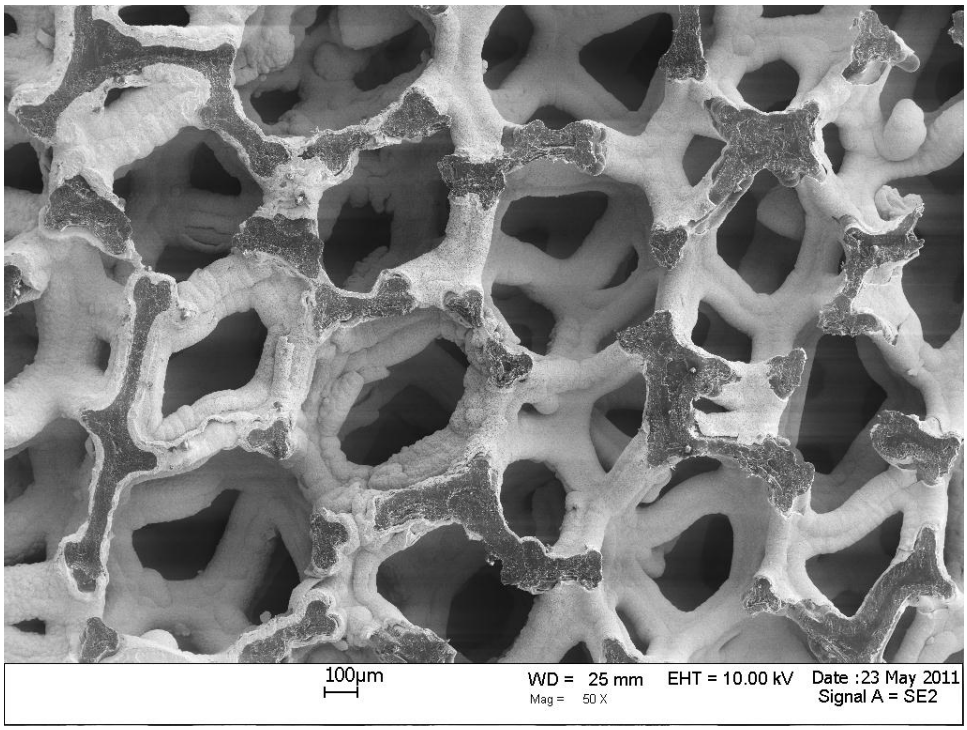

Figure 233. SEM micrograph of the baseline microstructure of a 100 ppi TaC/PyC/RVC Type B foam specimen.

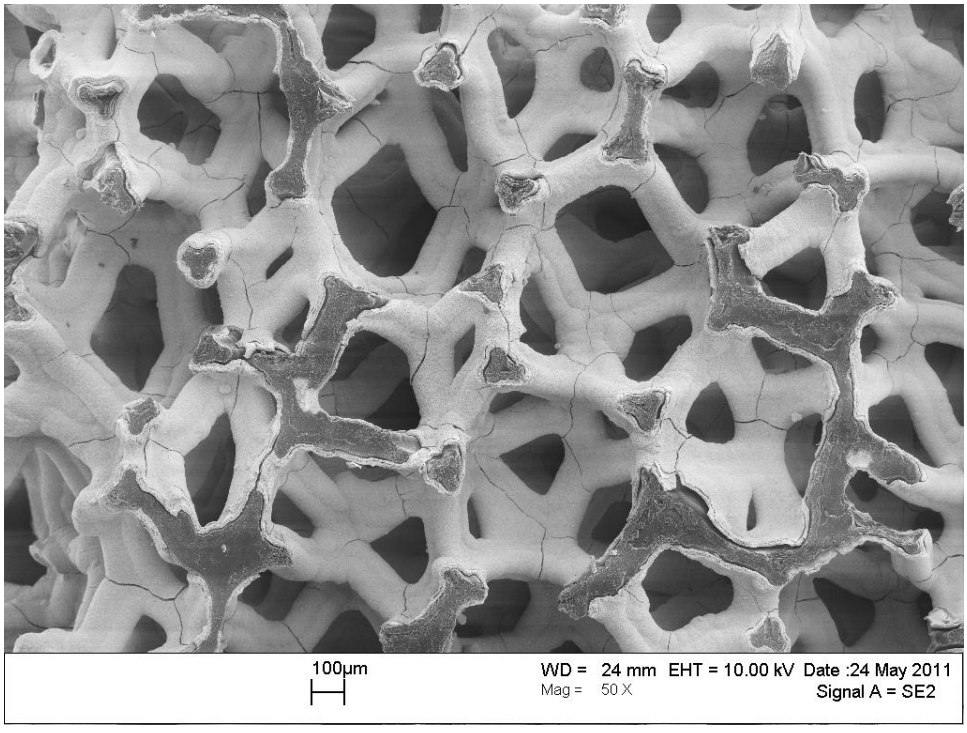

Figure 234. SEM micrograph of the microstructure of a 100 ppi TaC/PyC/RVC Type B foam specimen after thermal cycling.

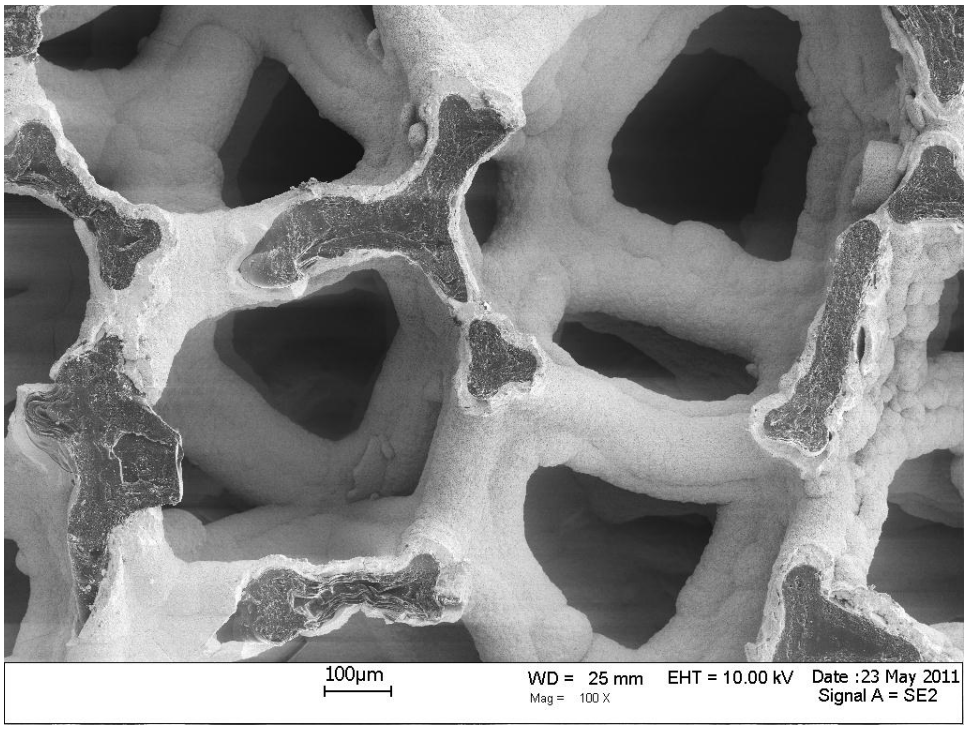

Figure 235. SEM micrograph of the baseline microstructure of a 100 ppi TaC/PyC/RVC Type B foam specimen.

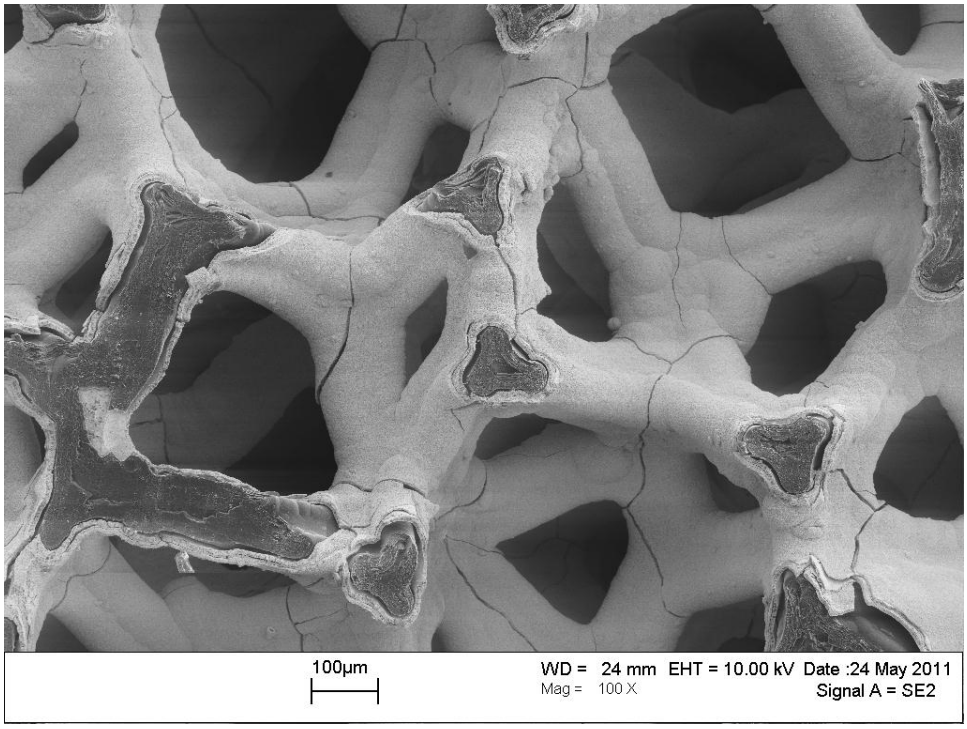

Figure 236. SEM micrograph of the microstructure of a 100 ppi TaC/PyC/RVC Type B foam specimen after thermal cycling.

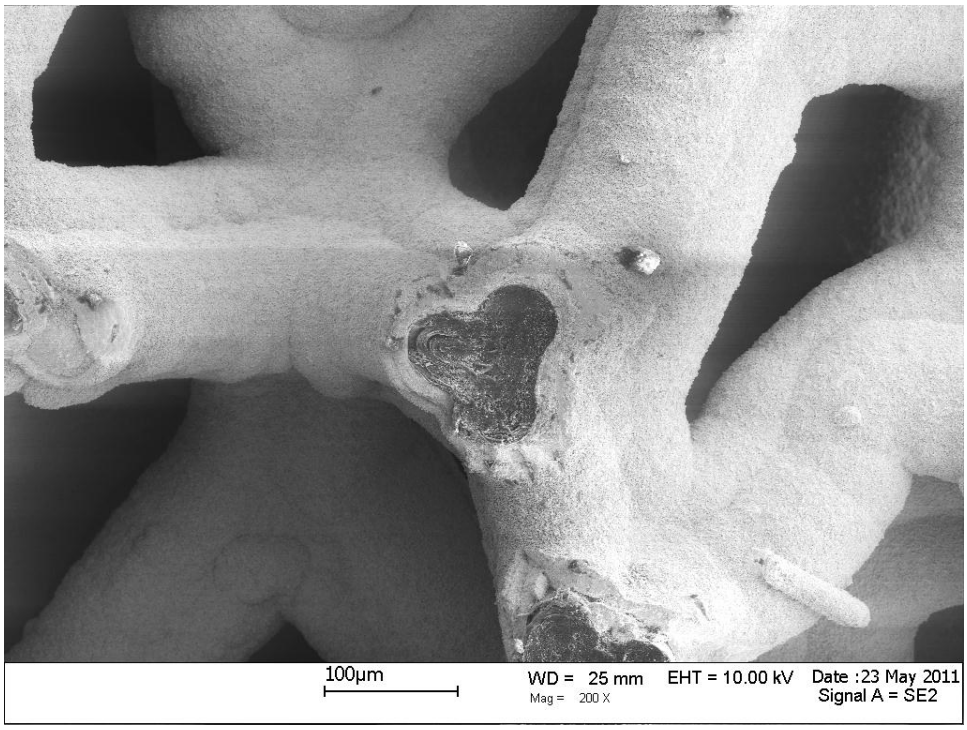

Figure 237. SEM micrograph of the baseline microstructure of a 100 ppi TaC/PyC/RVC Type B foam specimen.

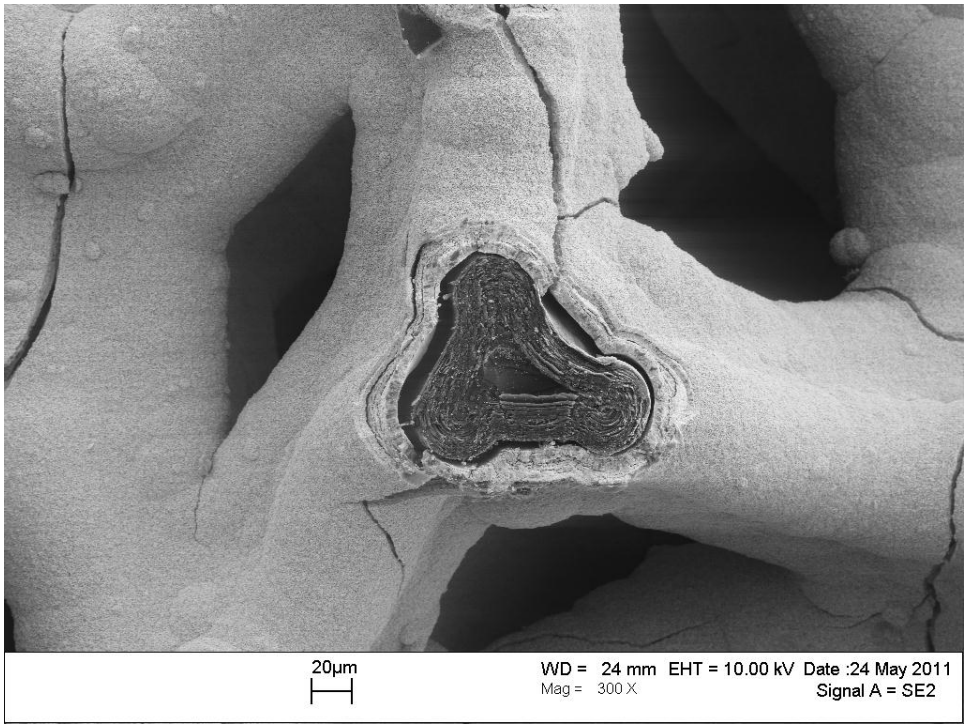

Figure 238. SEM micrograph of the microstructure of a 100 ppi TaC/PyC/RVC Type B foam specimen after thermal cycling.

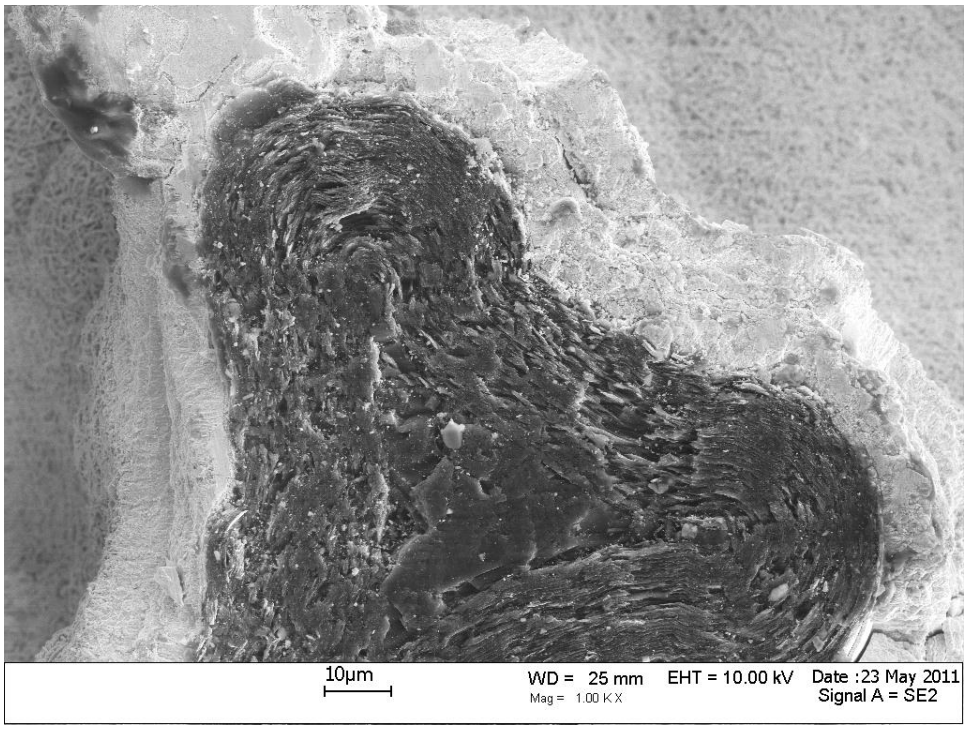

Figure 239. SEM micrograph of the baseline microstructure of a 100 ppi TaC/PyC/RVC Type B foam specimen.

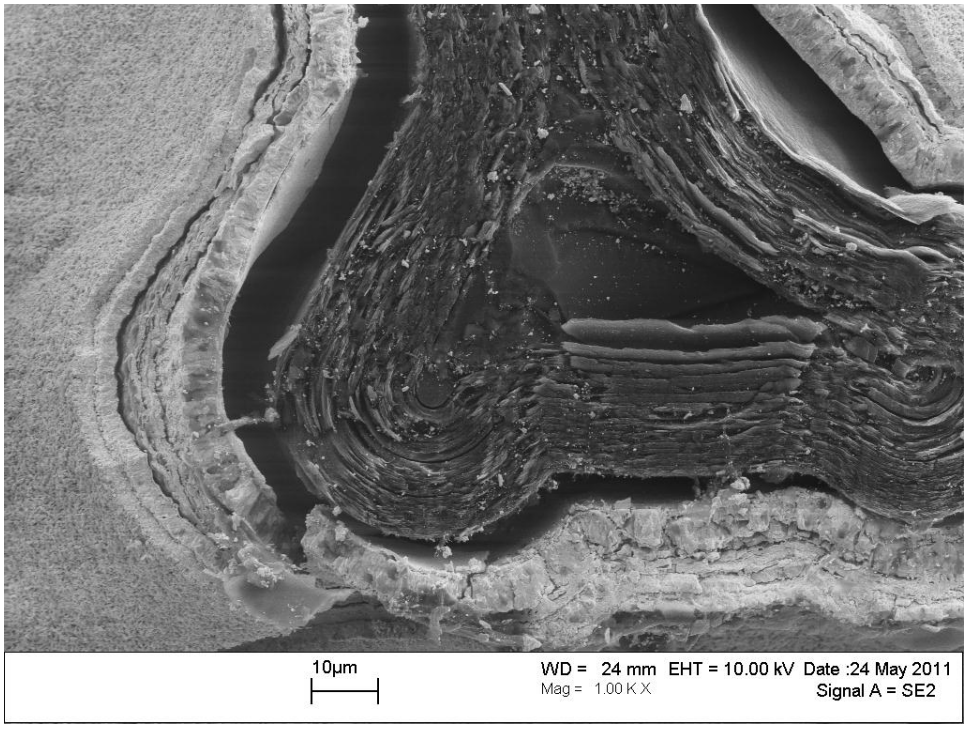

Figure 240. SEM micrograph of the microstructure of a 100 ppi TaC/PyC/RVC Type B foam specimen after thermal cycling.

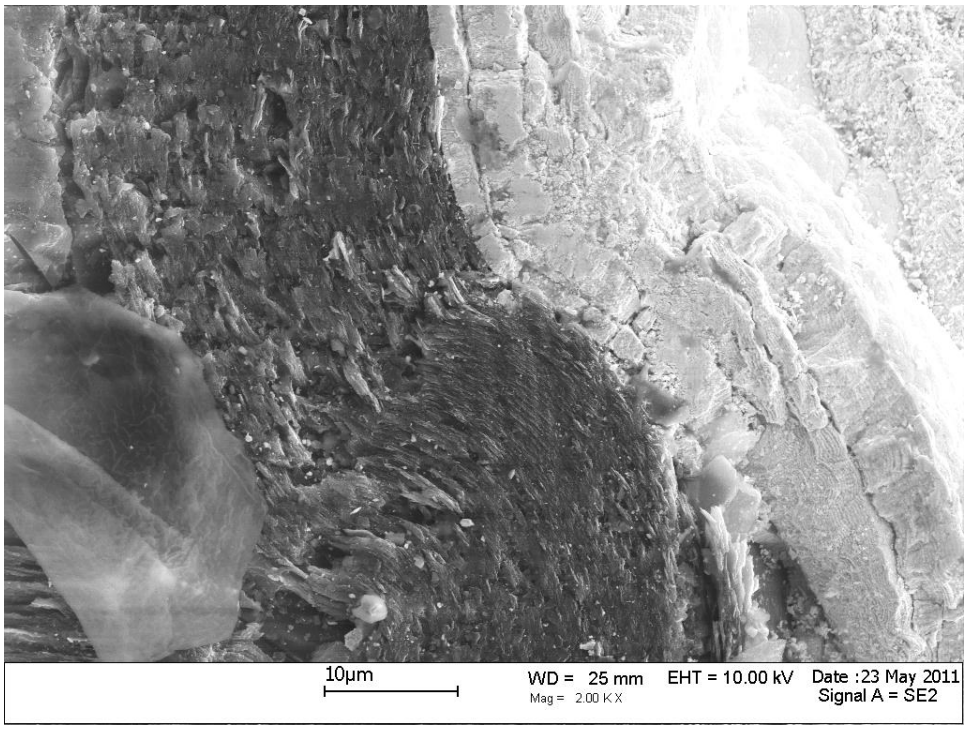

Figure 241. SEM micrograph of the baseline microstructure of a 100 ppi TaC/PyC/RVC Type B foam specimen.

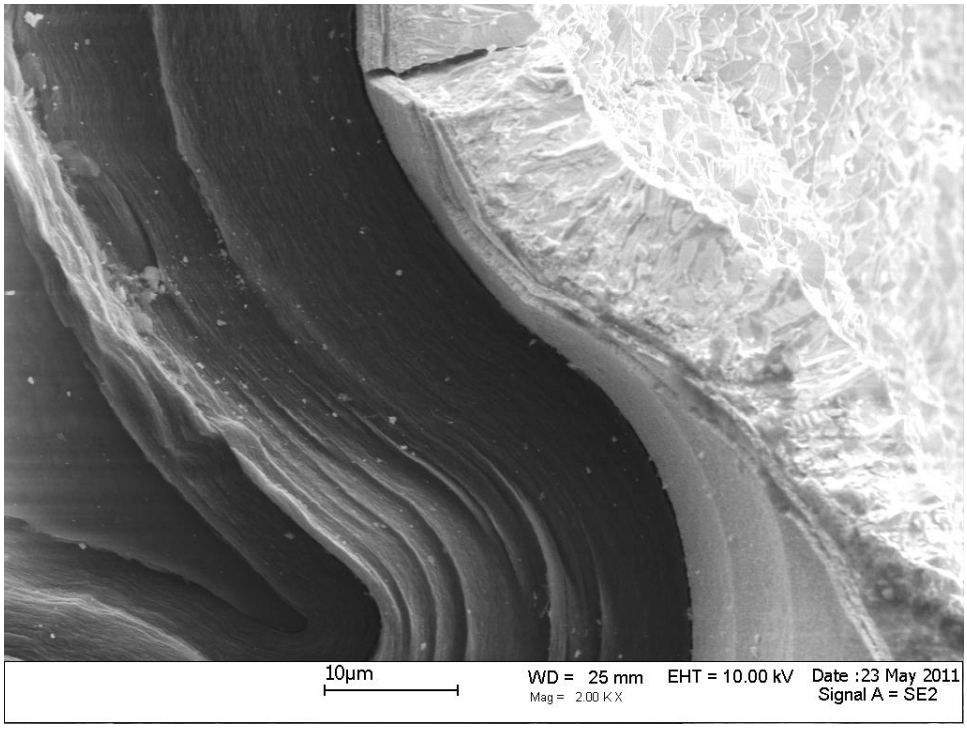

Figure 242. SEM micrograph of the baseline microstructure of a 100 ppi TaC/PyC/RVC Type B foam specimen.

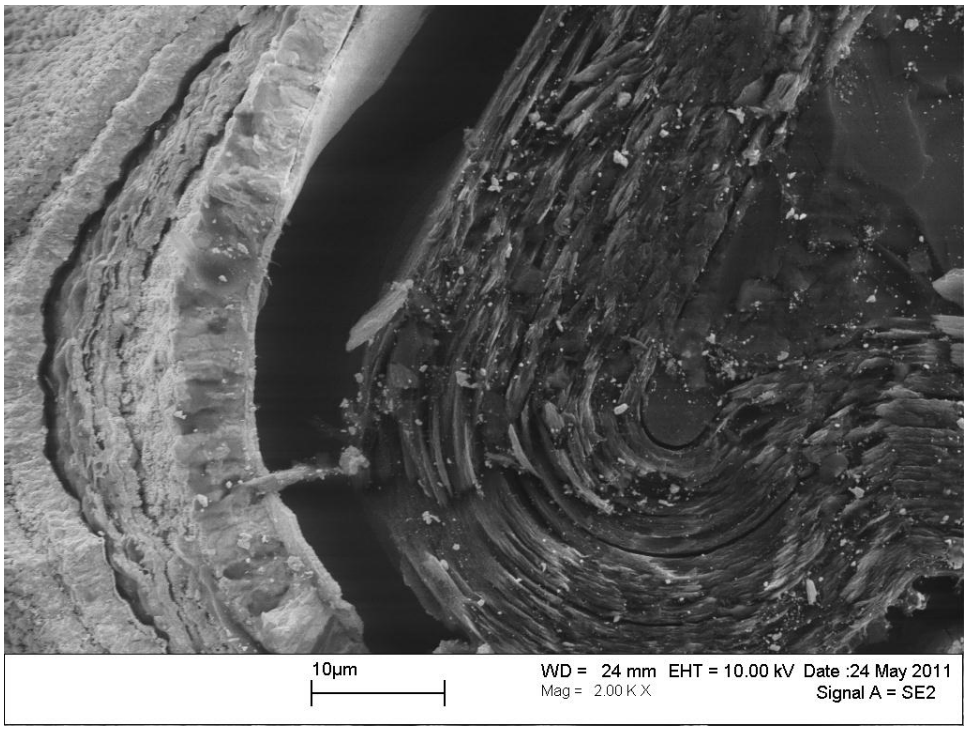

Figure 243. SEM micrograph of the microstructure of a 100 ppi TaC/PyC/RVC Type B foam specimen after thermal cycling.

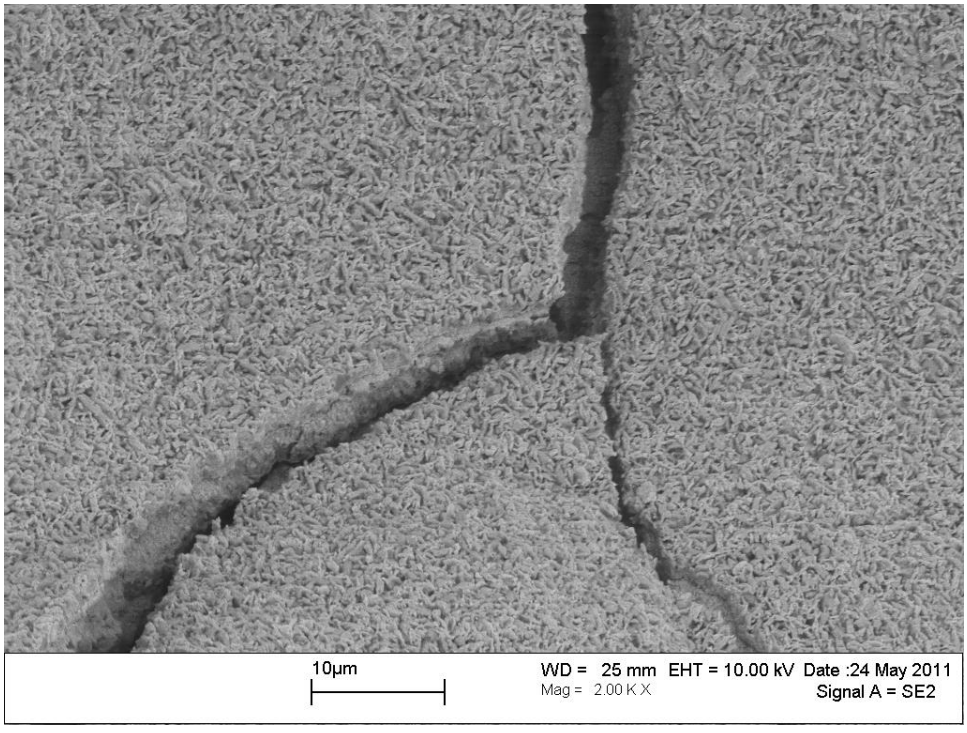

Figure 244. SEM micrograph of the microstructure of a 100 ppi TaC/PyC/RVC Type B foam specimen after thermal cycling.

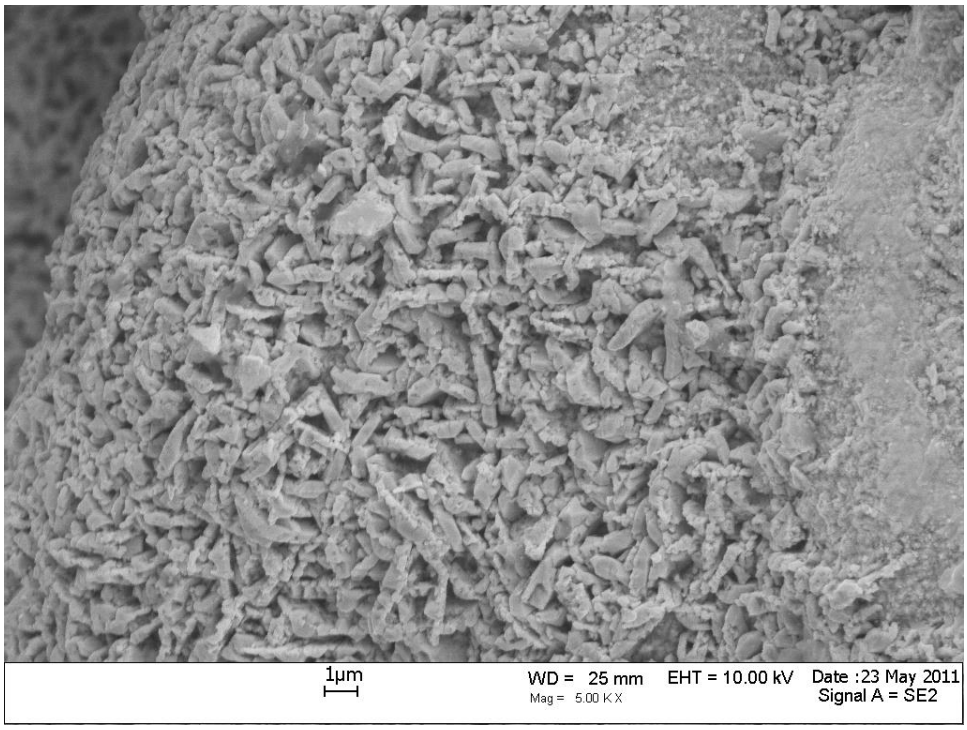

Figure 245. SEM micrograph of the baseline microstructure of a 100 ppi TaC/PyC/RVC Type B foam specimen.

100 TaC/RVC

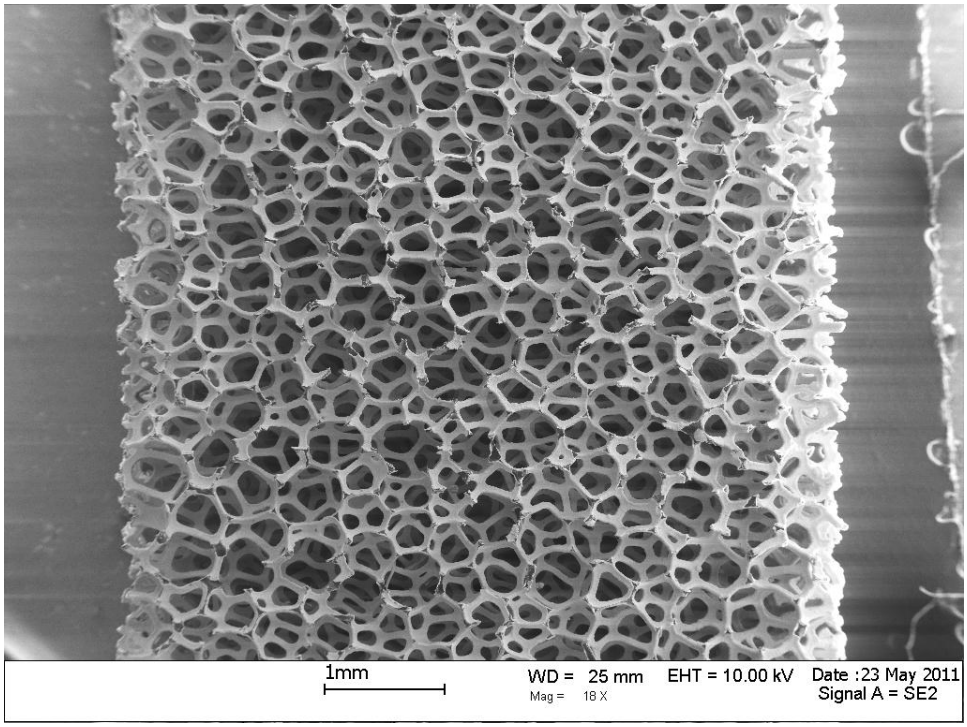

Figure 246. SEM micrograph of the baseline microstructure of a 100 ppi TaC/RVC foam specimen.

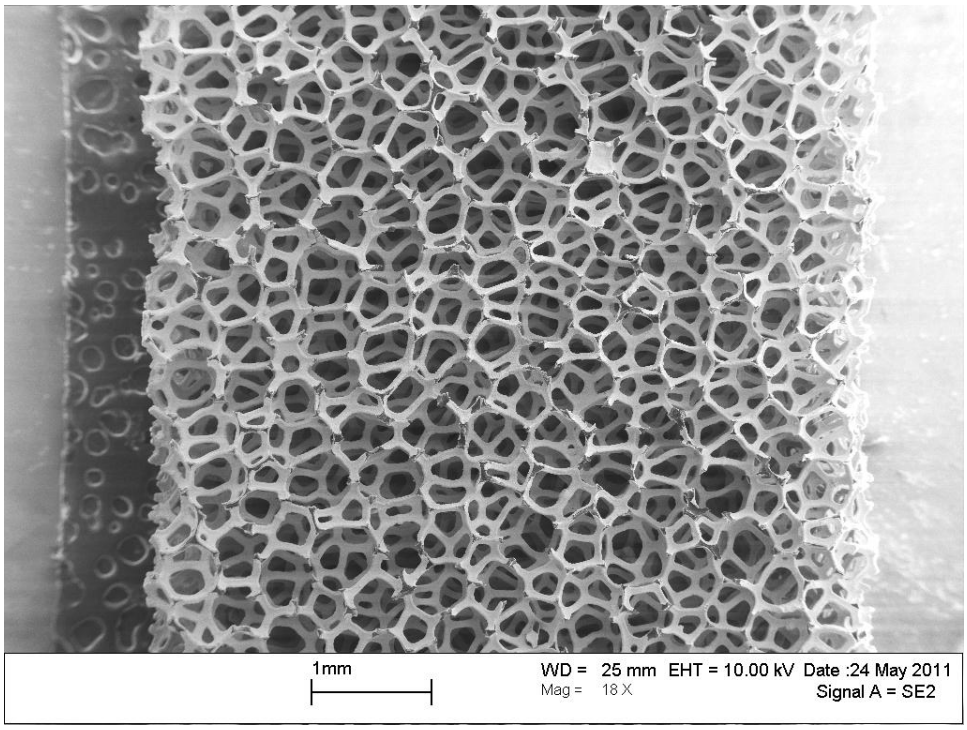

Figure 247. SEM micrograph of the microstructure of a 100 ppi TaC/RVC foam specimen after thermal cycling.

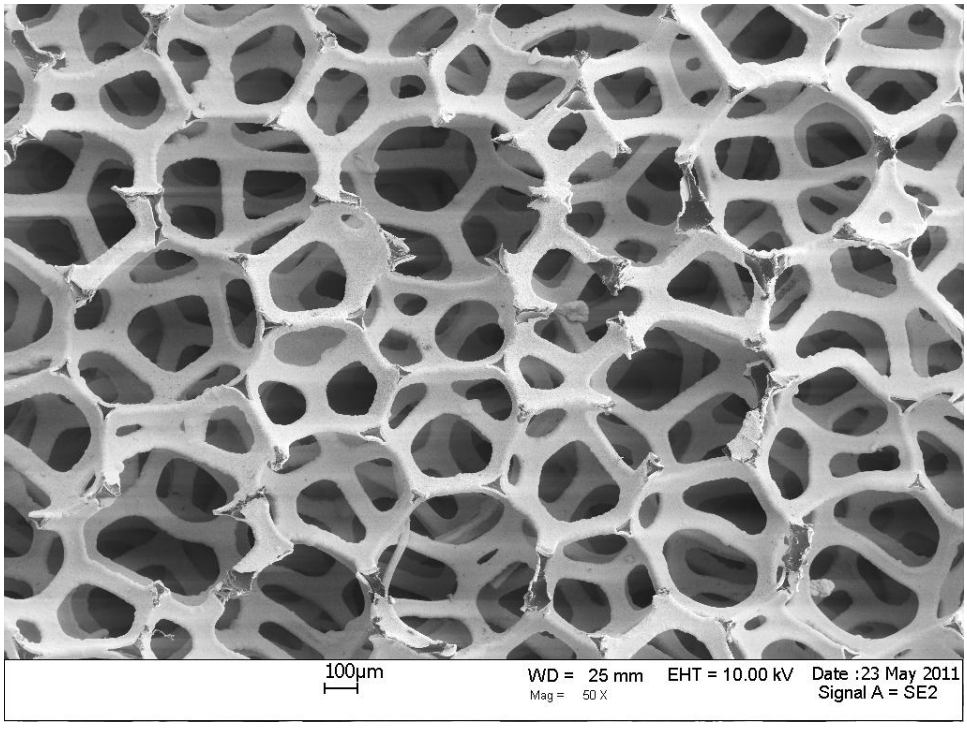

Figure 248. SEM micrograph of the baseline microstructure of a 100 ppi TaC/RVC foam specimen.

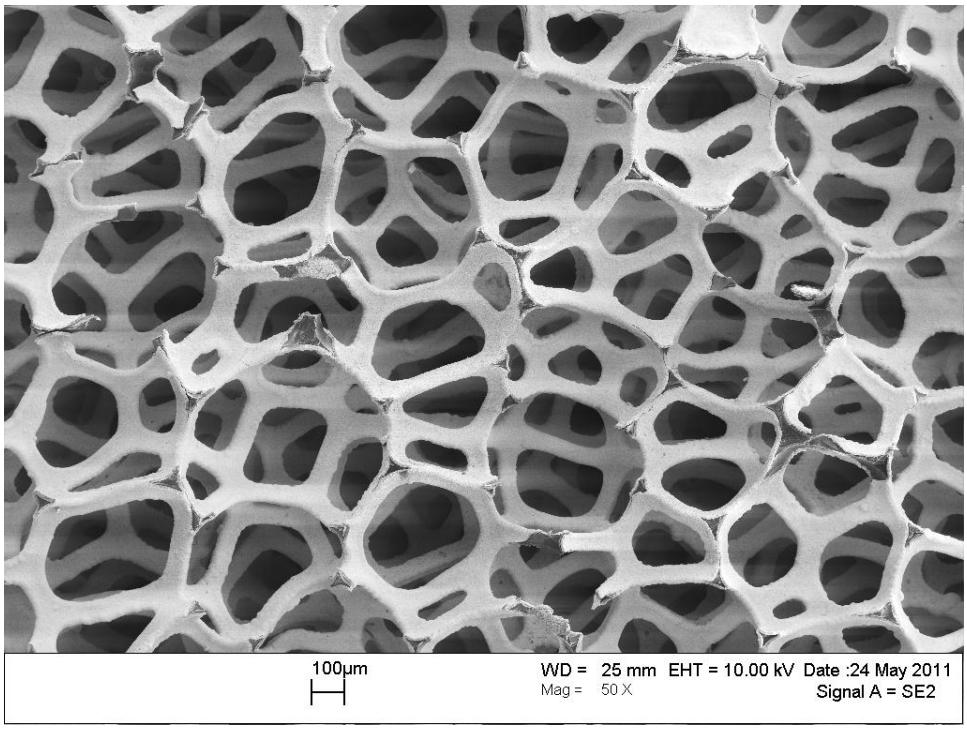

Figure 249. SEM micrograph of the microstructure of a 100 ppi TaC/RVC foam specimen after thermal cycling.

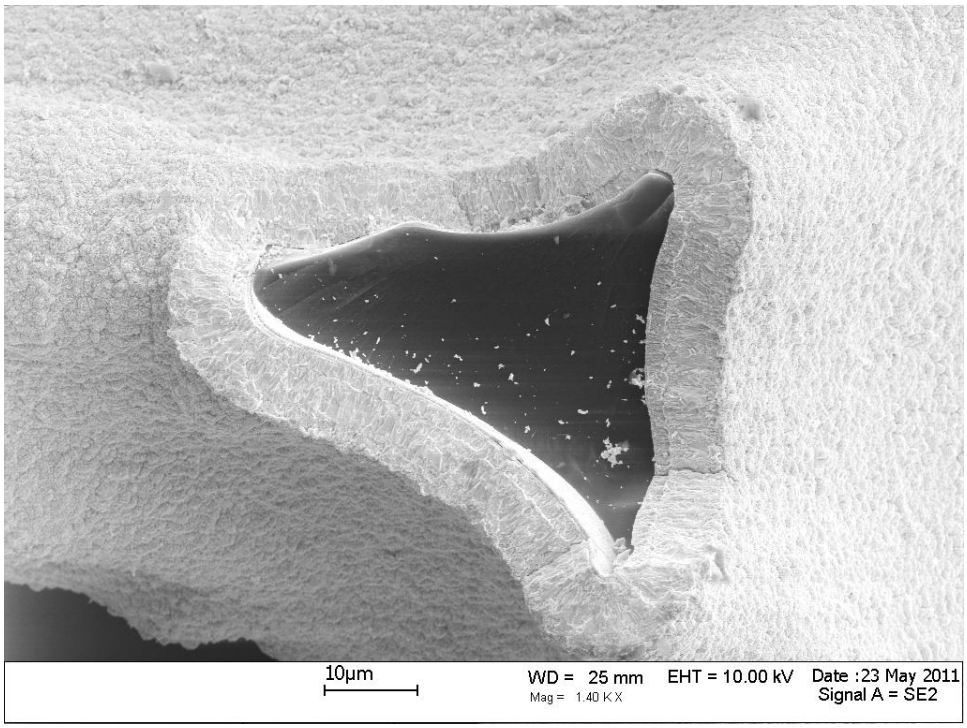

Figure 250. SEM micrograph of the baseline microstructure of a 100 ppi TaC/RVC foam specimen.

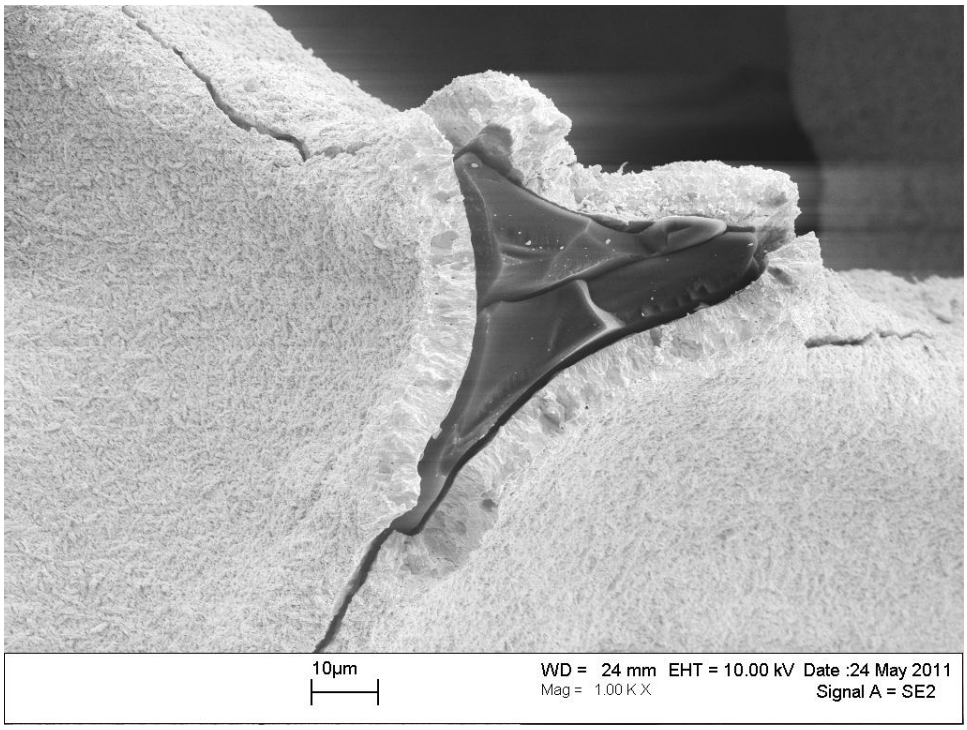

Figure 251. SEM micrograph of the microstructure of a 100 ppi TaC/RVC foam specimen after thermal cycling.

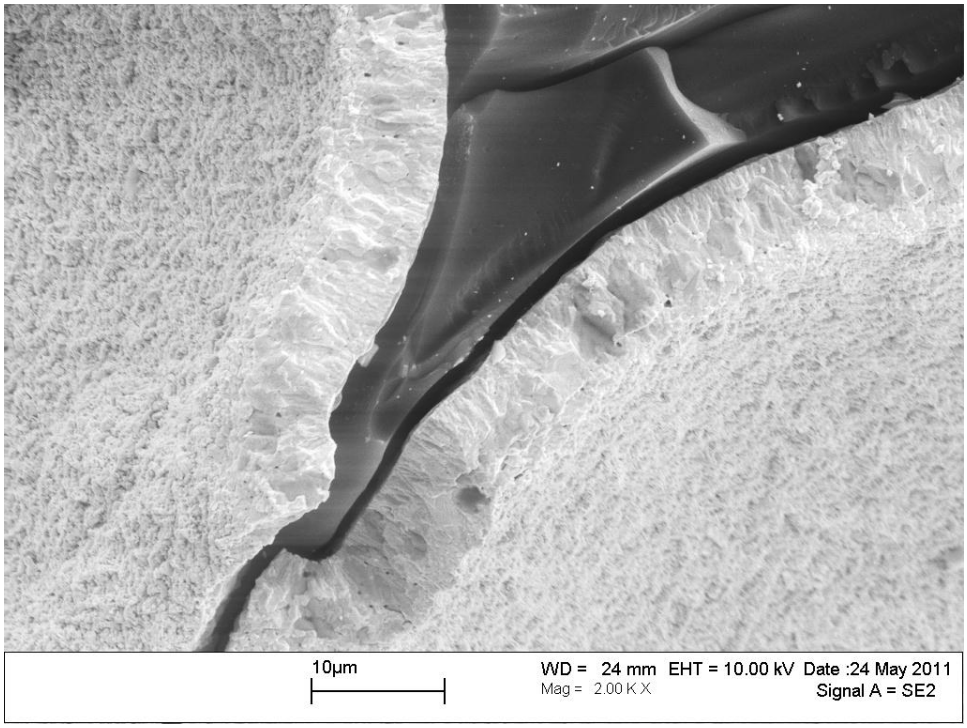

Figure 252. SEM micrograph of the microstructure of a 100 ppi TaC/RVC foam specimen after thermal cycling.

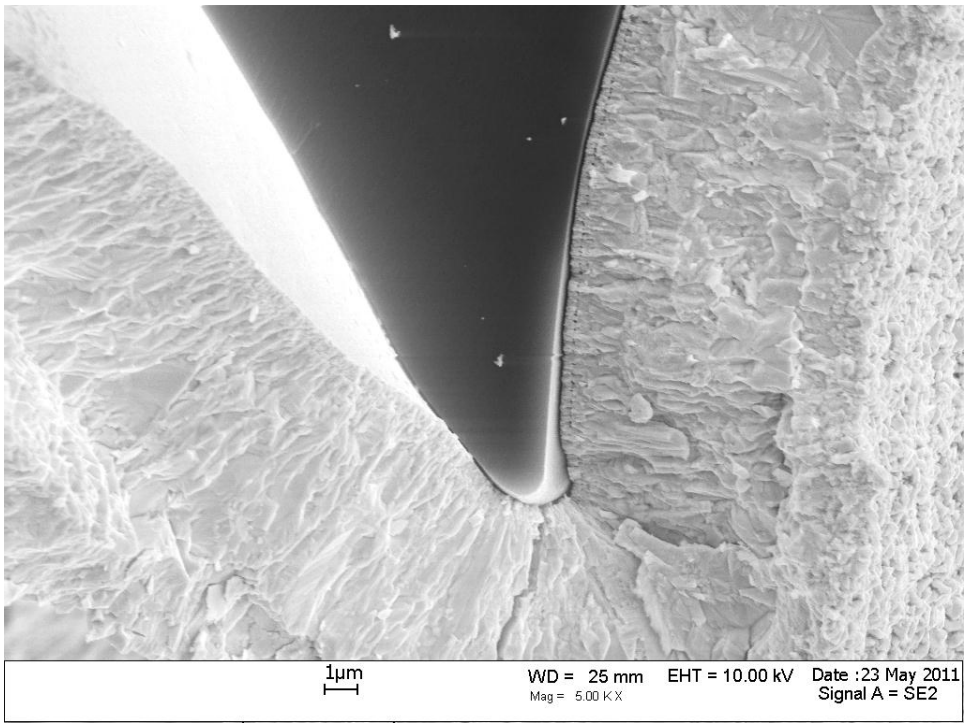

Figure 253. SEM micrograph of the baseline microstructure of a 100 ppi TaC/RVC foam specimen.

Appendix E. TaC Specimen Masses After Selected Thermal Cycles

Table XLI. TaC Specimen Masses After Selected Thermal Cycles

Sample	Pre-Cycling (g)	Post-1 Cycle (g)	Post-8 Cycles (g)	Post-18 Cycles (g)	Net Mass Change (g)
1	0.727	0.726	0.725	0.726	0.001
2	0.459	0.456	0.455	0.457	0.002
3	0.535	0.534	0.532	0.533	0.002
4	0.641	0.641	0.639	0.641	0.000
5	0.605	0.605	0.604	0.605	0.000
6	0.606	0.607	0.606	0.606	0.000
7	0.582	0.581	0.580	0.578	0.004
8	0.665	0.666	0.664	0.663	0.002
9	0.597	0.595	0.594	0.593	0.004
10	-	-	-	-	-
11	-	-	-	-	-
12	0.545	0.544	0.541	0.542	0.003
13	0.684	0.684	0.682	0.682	0.002
14	0.592	0.591	0.589	0.588	0.004
15	0.672	0.671	0.668	0.669	0.003
16	0.441	0.441	0.439	0.440	0.001
17	0.668	0.669	0.667	0.668	0.000
18	0.358	0.358	0.356	0.357	0.001
19	0.551	0.553	0.550	0.550	0.001
20	0.446	0.446	0.444	0.443	0.003
21	0.708	0.709	0.707	0.706	0.002
22	0.731	0.731	0.728	0.727	0.004
23	0.708	0.707	0.707	0.705	0.003
24	0.696	0.695	0.694	0.692	0.004

Appendix F. Stress-Strain Curves for TaC Foam Specimens

Baseline Specimens

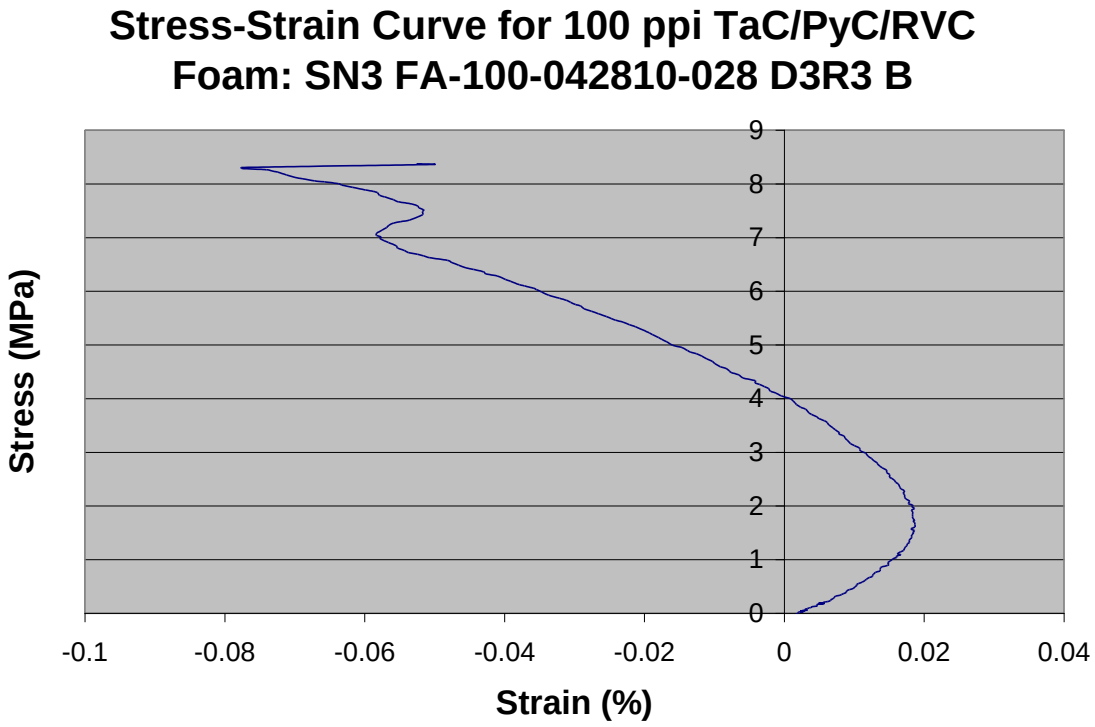

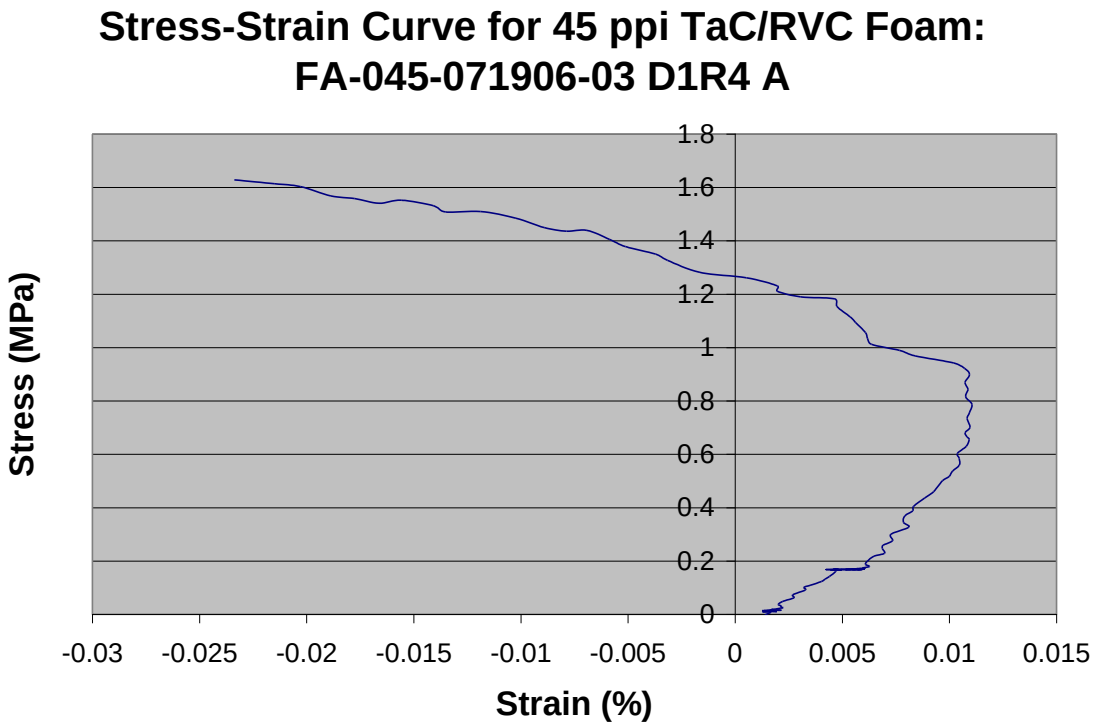

Stress-Strain Curve for 100 ppi TaC/RVC
Foam: FA-100-070809-03 D3R1 F

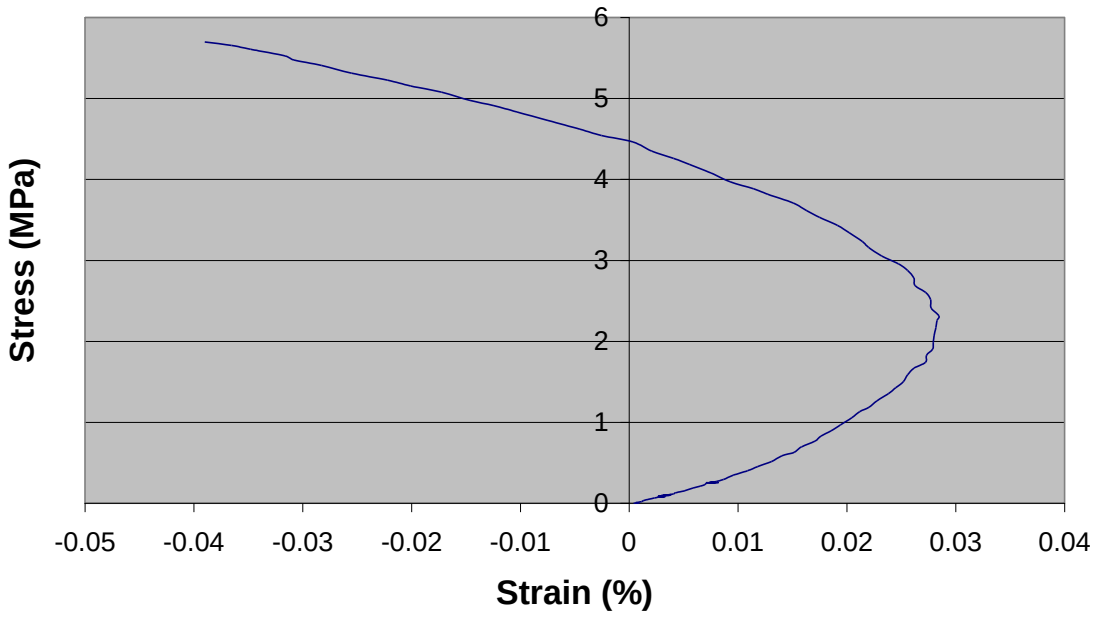

Stress-Strain Curve for 45 ppi TaC/PyC/RVC
Foam: FA-045-071706-02 D6R1 E

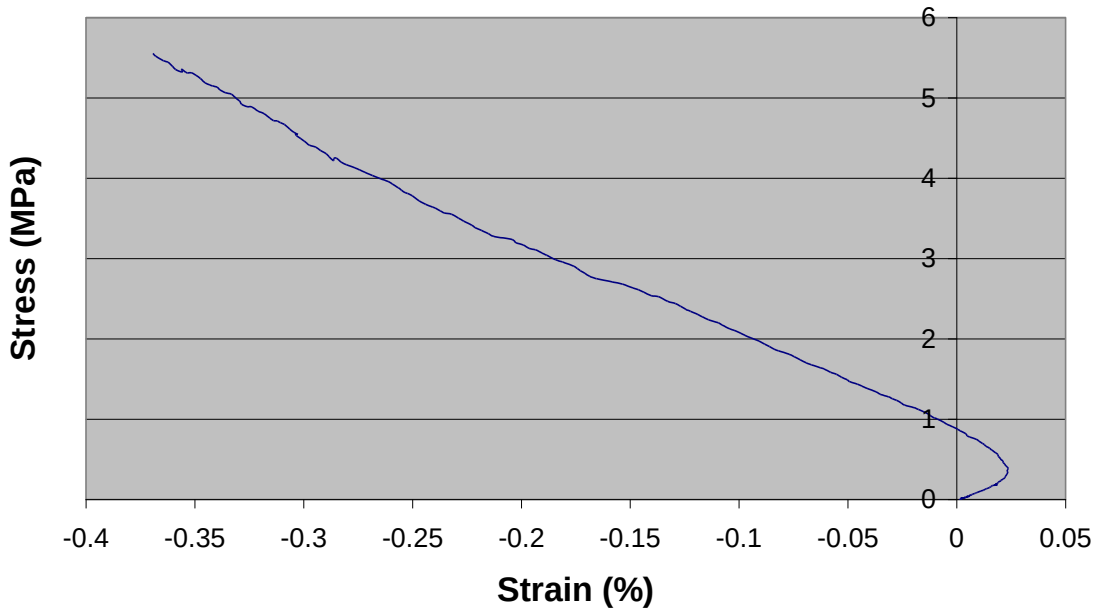

Stress-Strain Curve for 45 ppi TaC/PyC/RVC Foam: FA-045-071706-02 D6R1 D

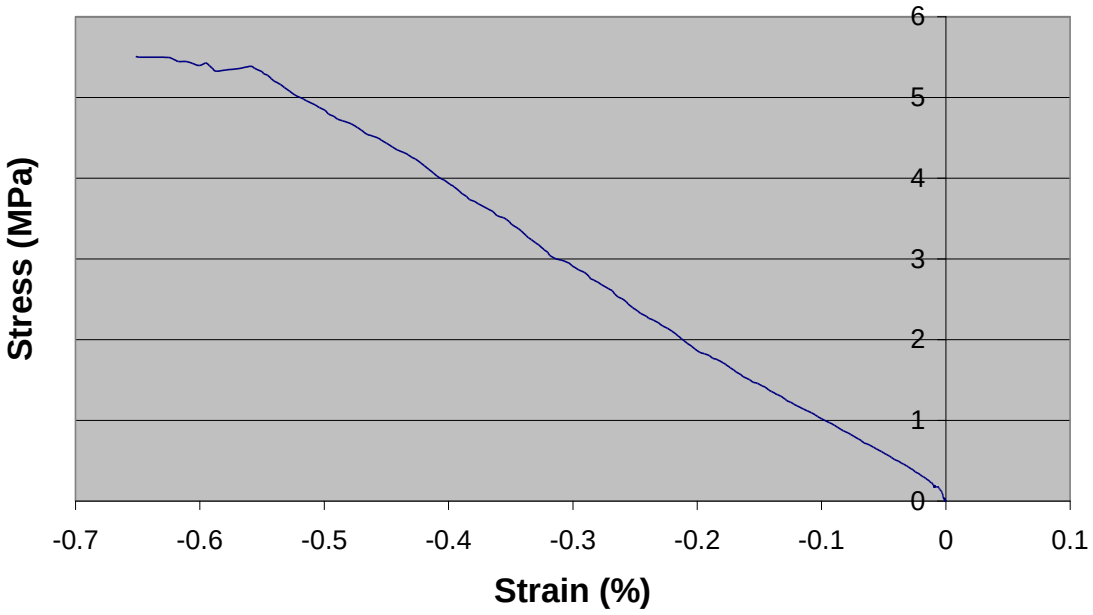

Stress-Strain Curve for 45 ppi TaC/PyC/RVC Foam: FA-045-071706-02 D6R1 B

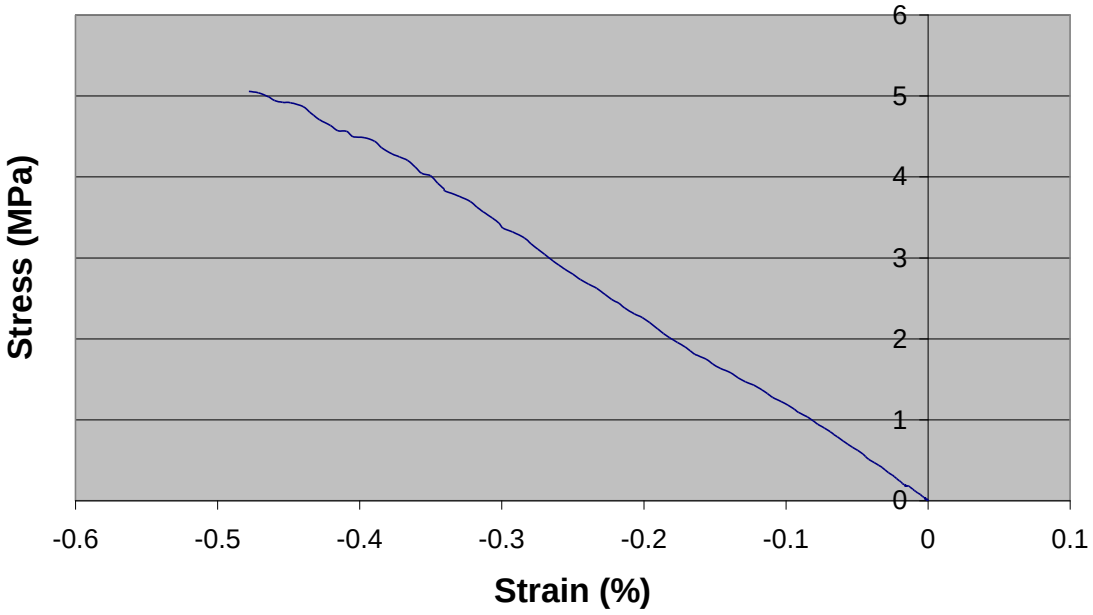

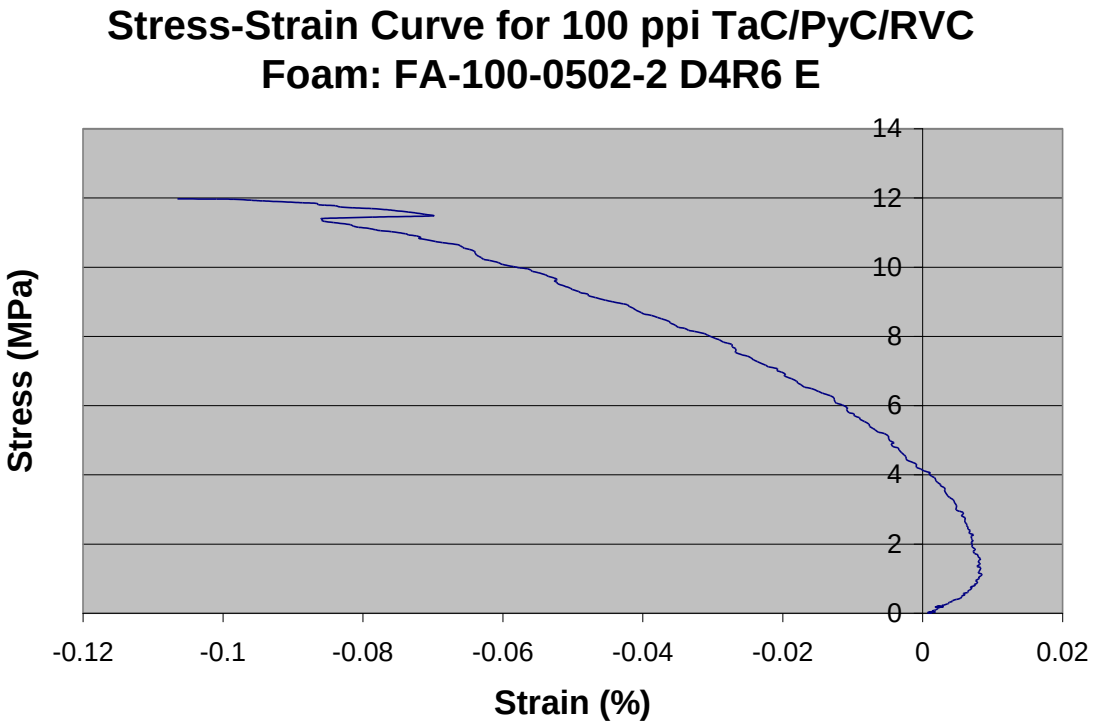
Stress-Strain Curve for 100 ppi TaC/PyC/RVC
Foam: FA-100-0502-2 D4R6 E
Stress (MPa)
14
12
10
8
6
4
2
0
-0.12
-0.1
-0.08
-0.06
-0.04
-0.02
0
0.02
Strain (%)

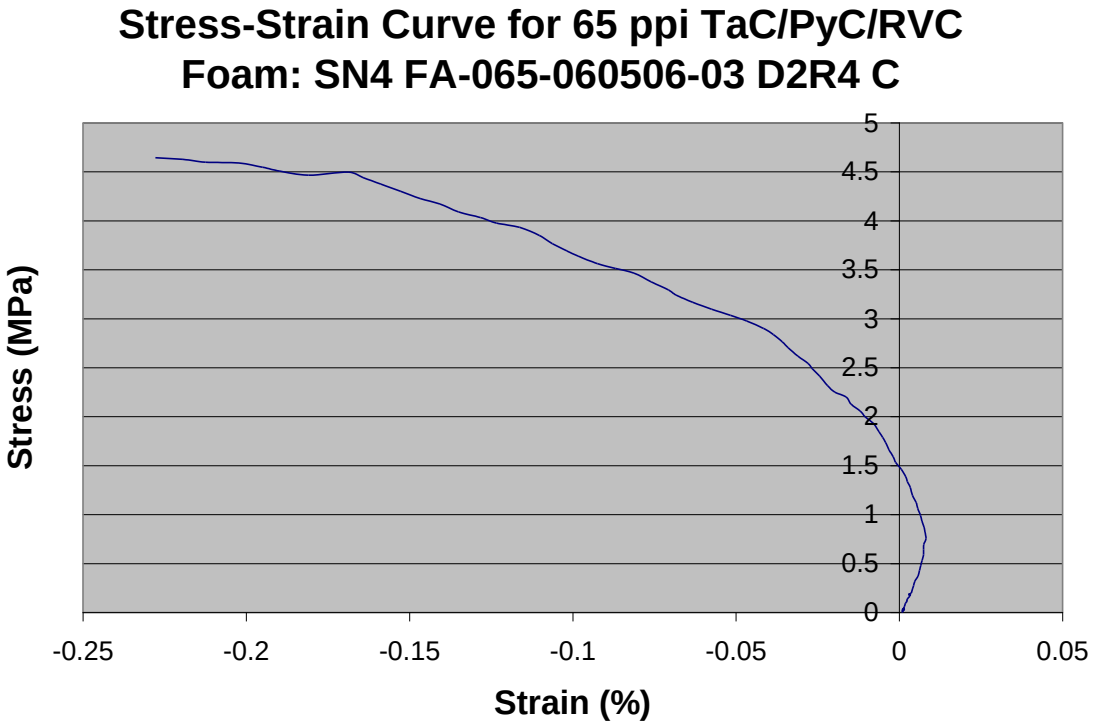
Stress-Strain Curve for 65 ppi TaC/PyC/RVC
Foam: SN4 FA-065-060506-03 D2R4 C
Stress (MPa)
5
4.5
4
3.5
3
2.5
2
1.5
1
0.5
0
-0.25
-0.2
-0.15
-0.1
-0.05
0
0.05
Strain (%)

Stress-Strain Curve for 65 ppi TaC/PyC/RVC Foam: SN4 FA-065-060506-03 D2R4 B

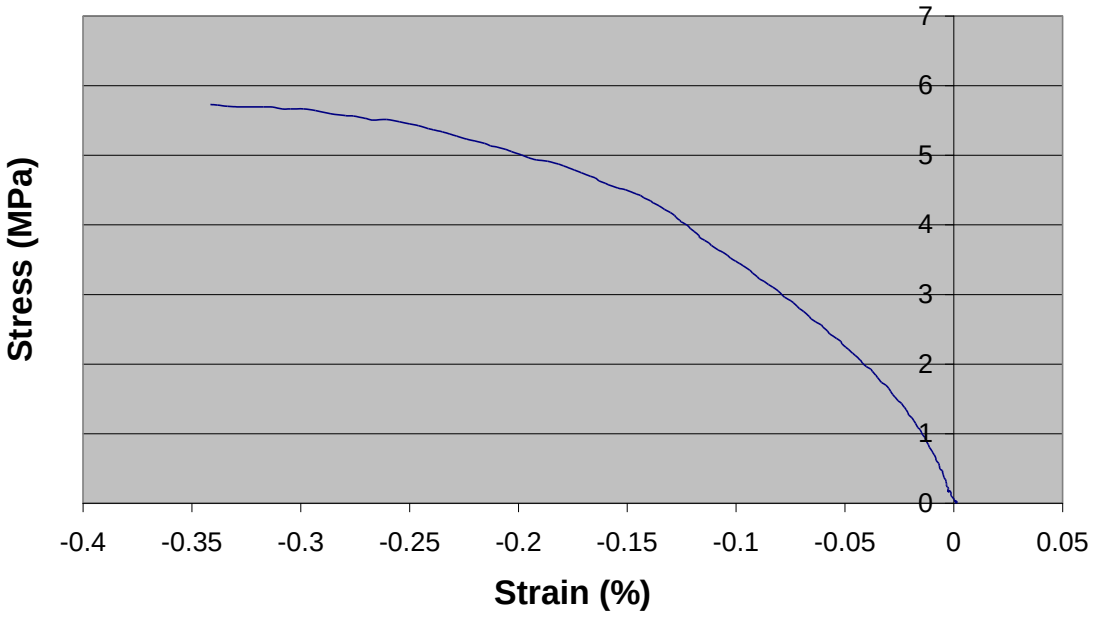

Stress-Strain Curve for 100 ppi TaC/PyC/RVC Foam: FA-100-0502-2 D4R6 B

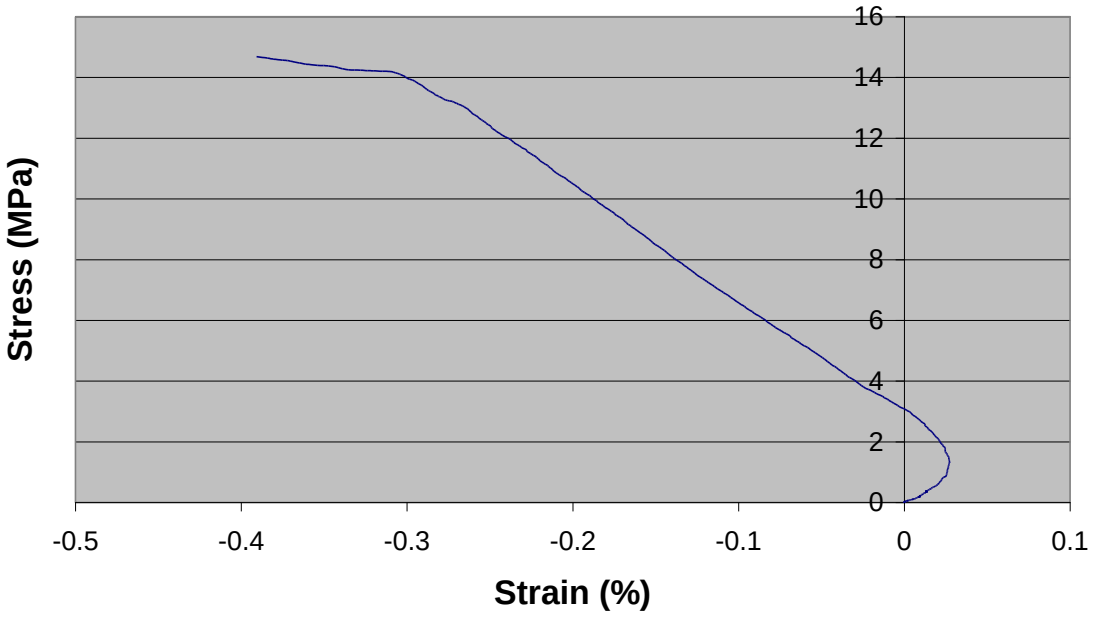

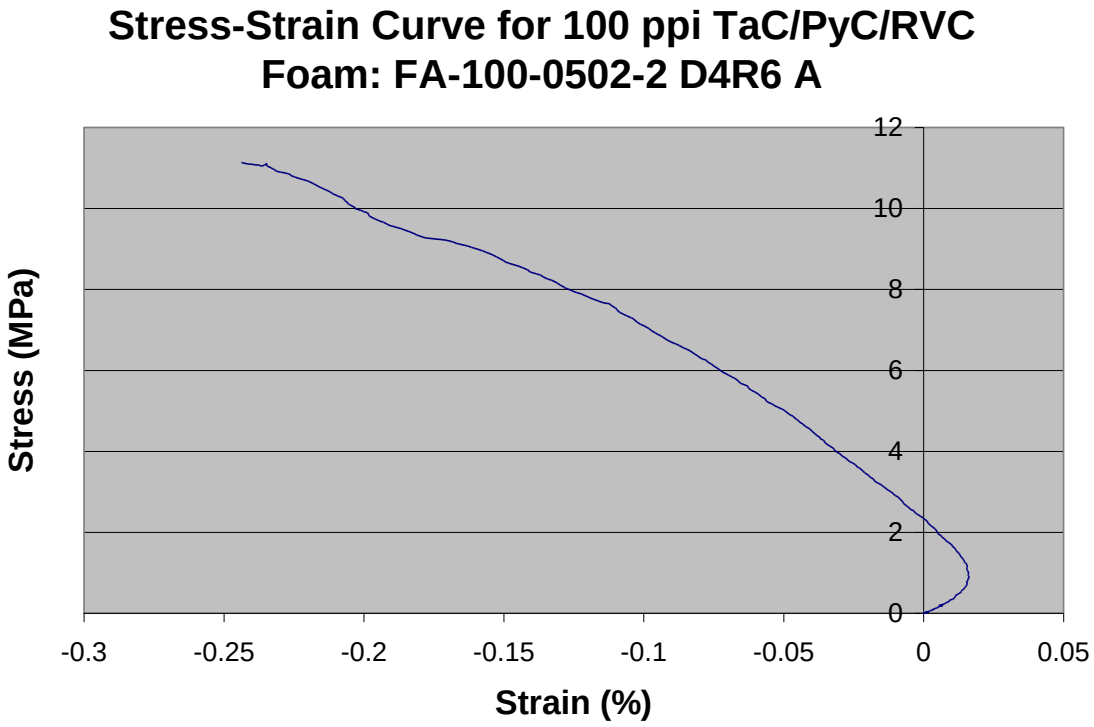
Stress-Strain Curve for 100 ppi TaC/PyC/RVC
Foam: FA-100-0502-2 D4R6 A
Stress (MPa)
12
10
8
6
4
2
0
-0.3
-0.25
-0.2
-0.15
-0.1
-0.05
0
0.05
Strain (%)

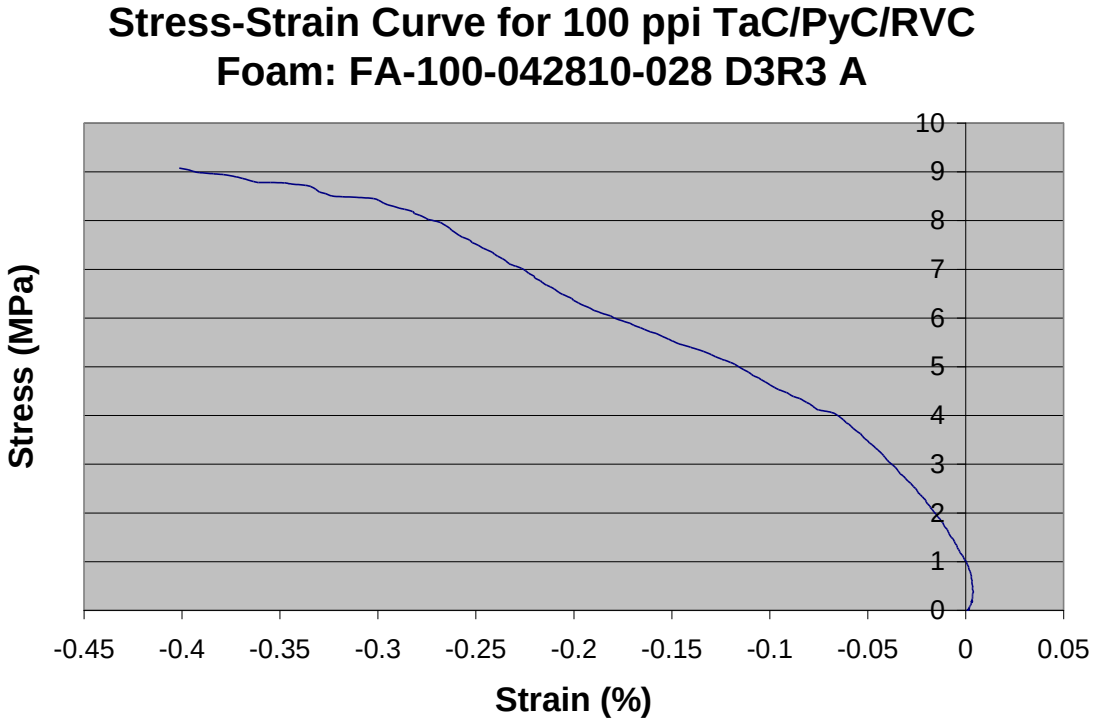
Stress-Strain Curve for 100 ppi TaC/PyC/RVC
Foam: FA-100-042810-028 D3R3 A
Stress (MPa)
10
9
8
7
6
5
4
3
2
1
0
-0.45
-0.4
-0.35
-0.3
-0.25
-0.2
-0.15
-0.1
-0.05
0
0.05
Strain (%)

Thermally Cycled Specimens

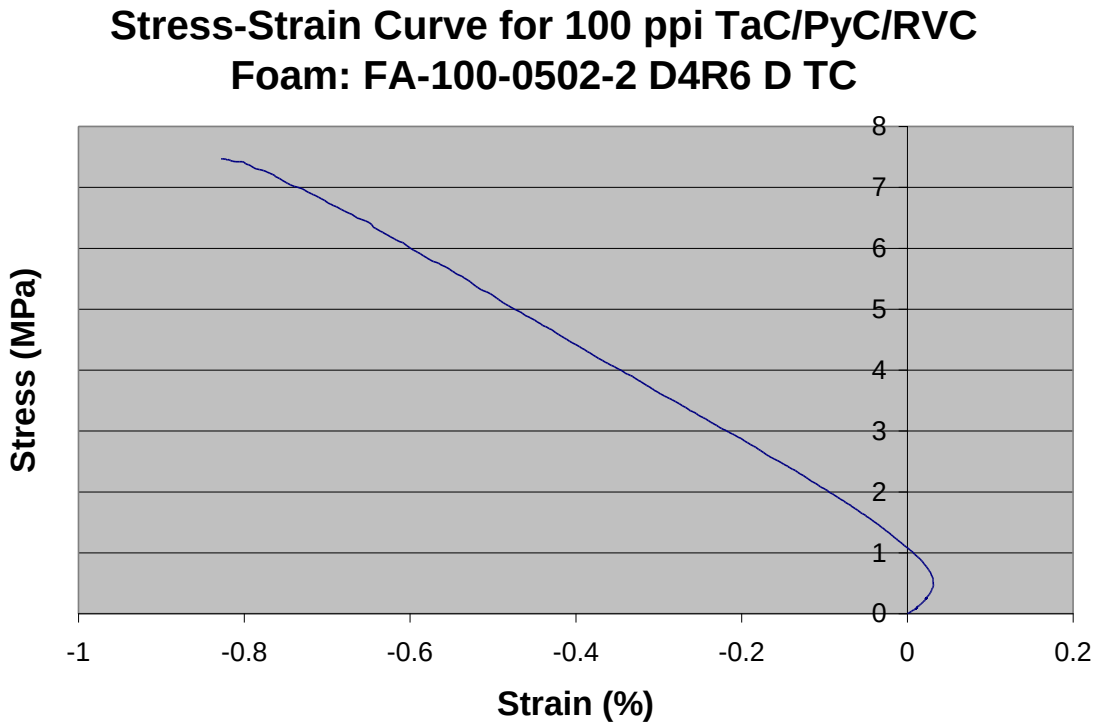

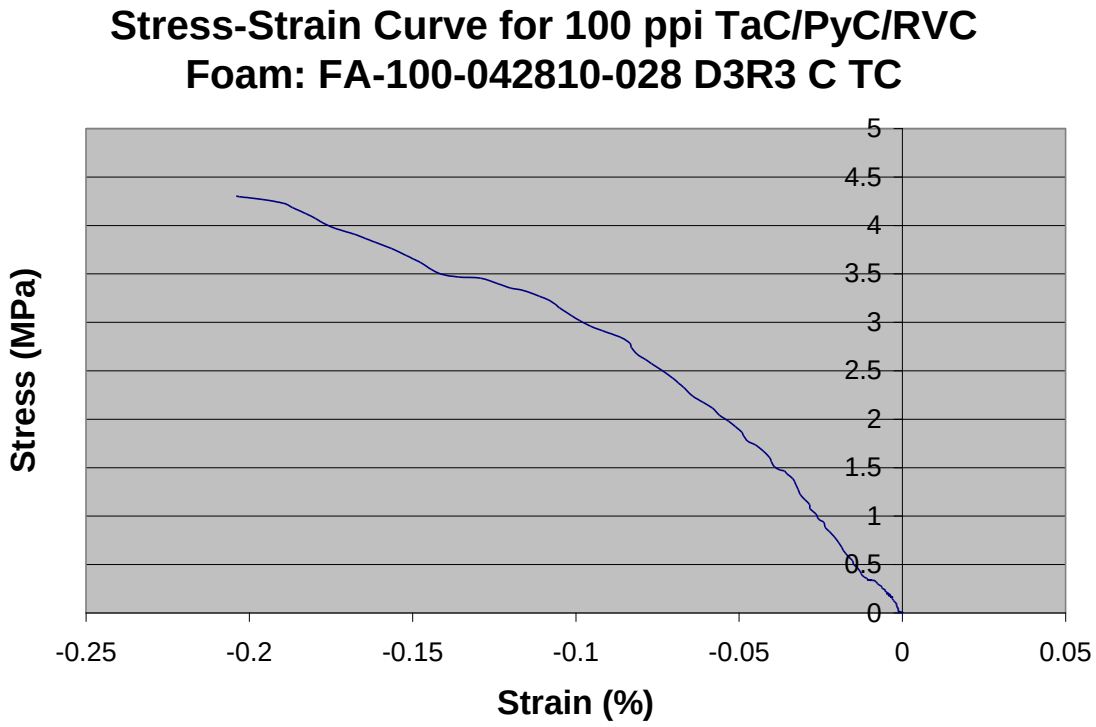

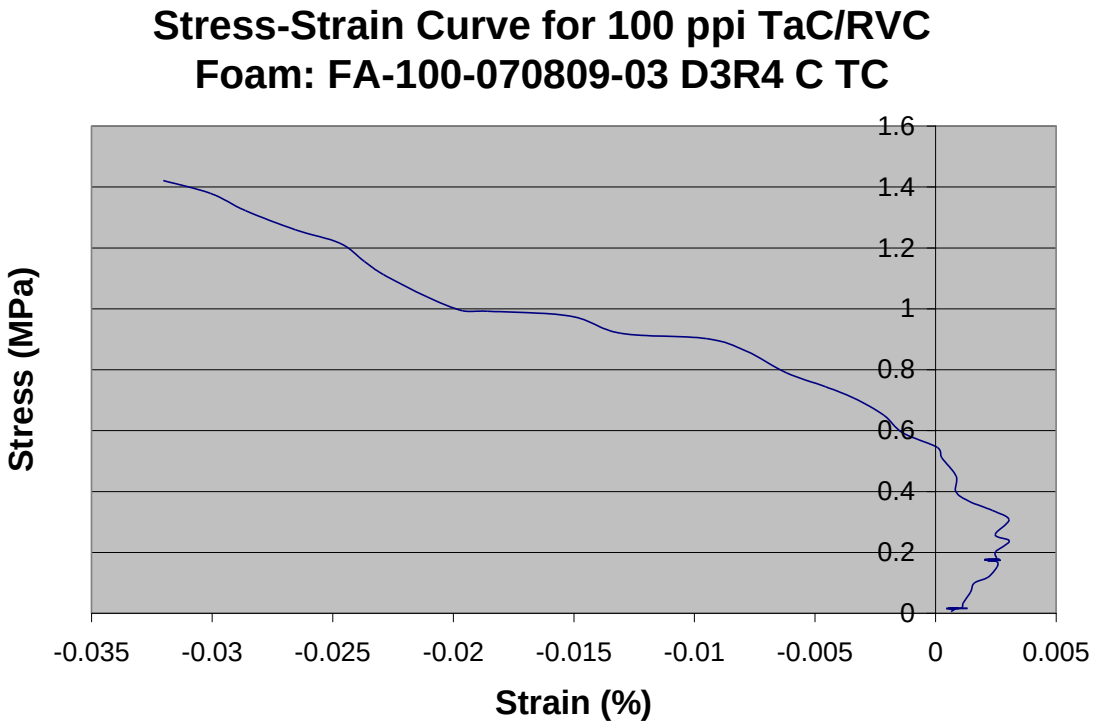
Stress-Strain Curve for 100 ppi TaC/RVC
Foam: FA-100-070809-03 D3R4 C TC
Stress (MPa)
1.6
1.4
1.2
1
0.8
0.6
0.4
0.2
0
-0.035
-0.03
-0.025
-0.02
-0.015
-0.01
-0.005
0
0.005
Strain (%)

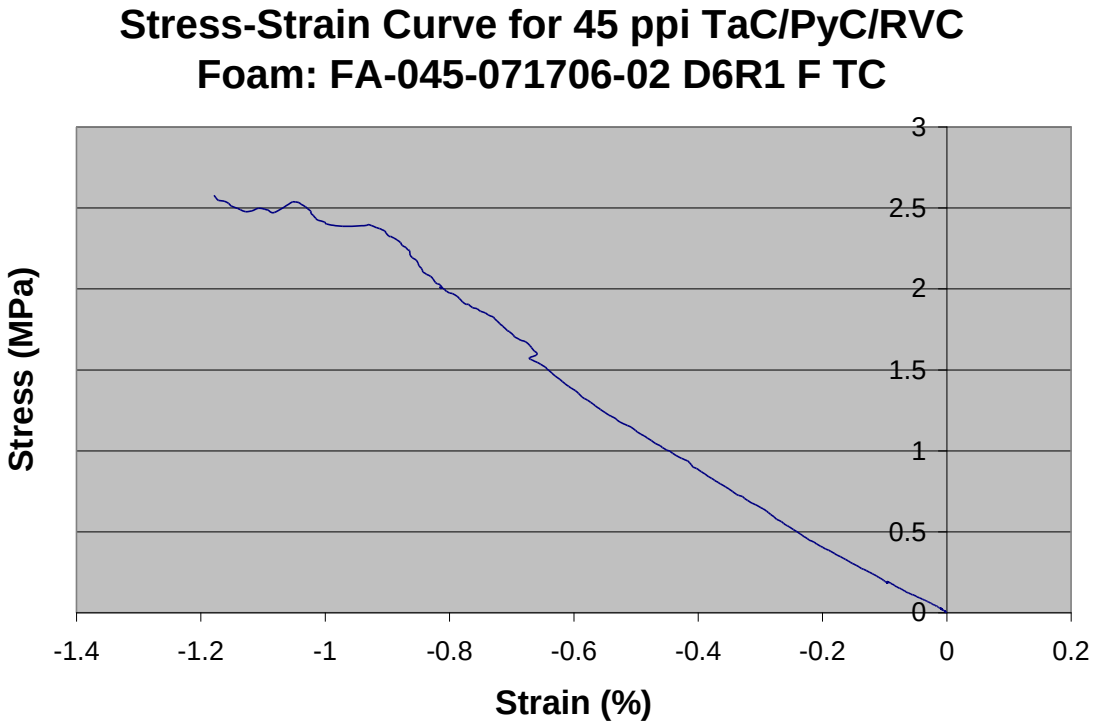
Stress-Strain Curve for 45 ppi TaC/PyC/RVC
Foam: FA-045-071706-02 D6R1 F TC
Stress (MPa)
3
2.5
2
1.5
1
0.5
0
-1.4
-1.2
-1
-0.8
-0.6
-0.4
-0.2
0
0.2
Strain (%)

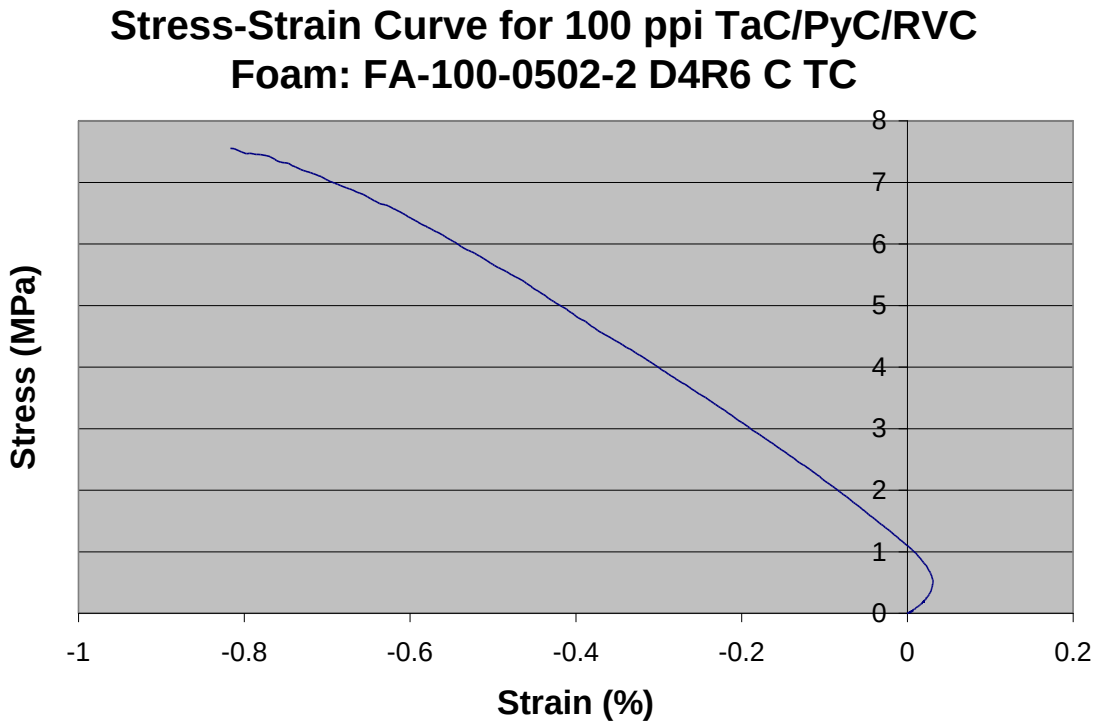
Stress-Strain Curve for 100 ppi TaC/PyC/RVC
Foam: FA-100-0502-2 D4R6 C TC
Stress (MPa)
8
7
6
5
4
3
2
1
0
-1
-0.8
-0.6
-0.4
-0.2
0
0.2
Strain (%)

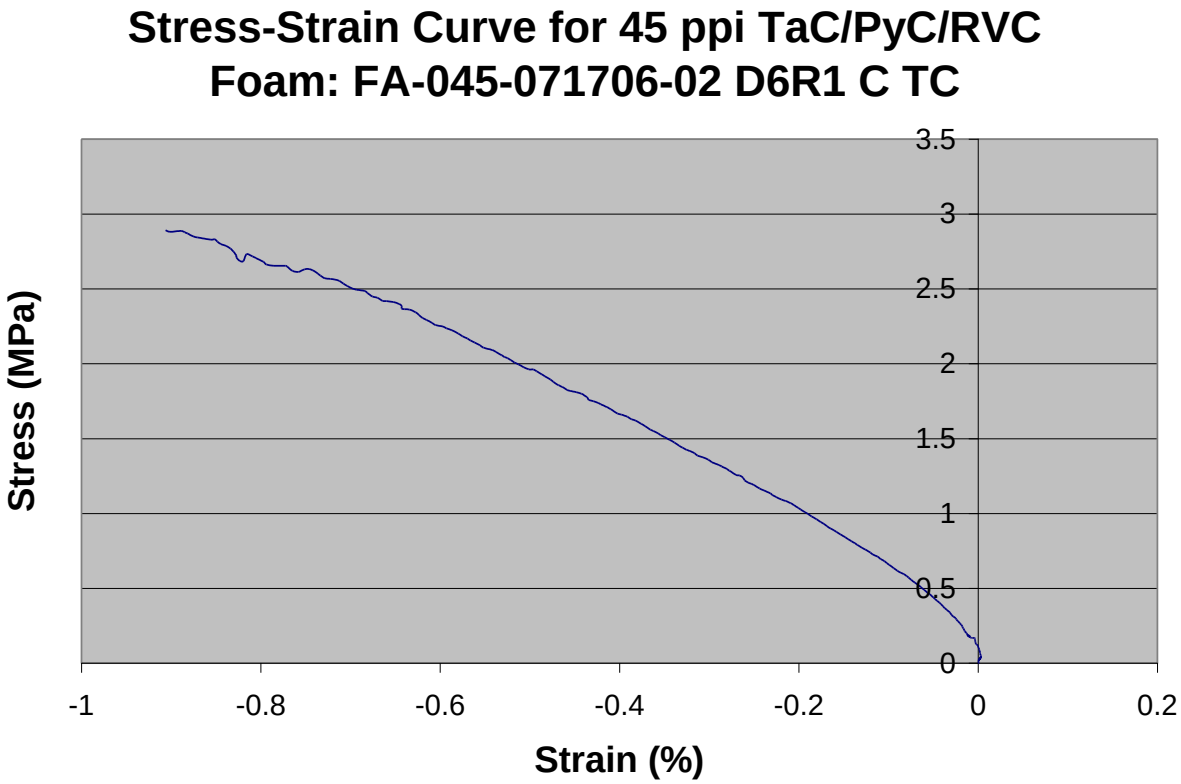
Stress-Strain Curve for 45 ppi TaC/PyC/RVC
Foam: FA-045-071706-02 D6R1 C TC
Stress (MPa)
3.5
3
2.5
2
1.5
1
0.5
0
-1
-0.8
-0.6
-0.4
-0.2
0
0.2
Strain (%)

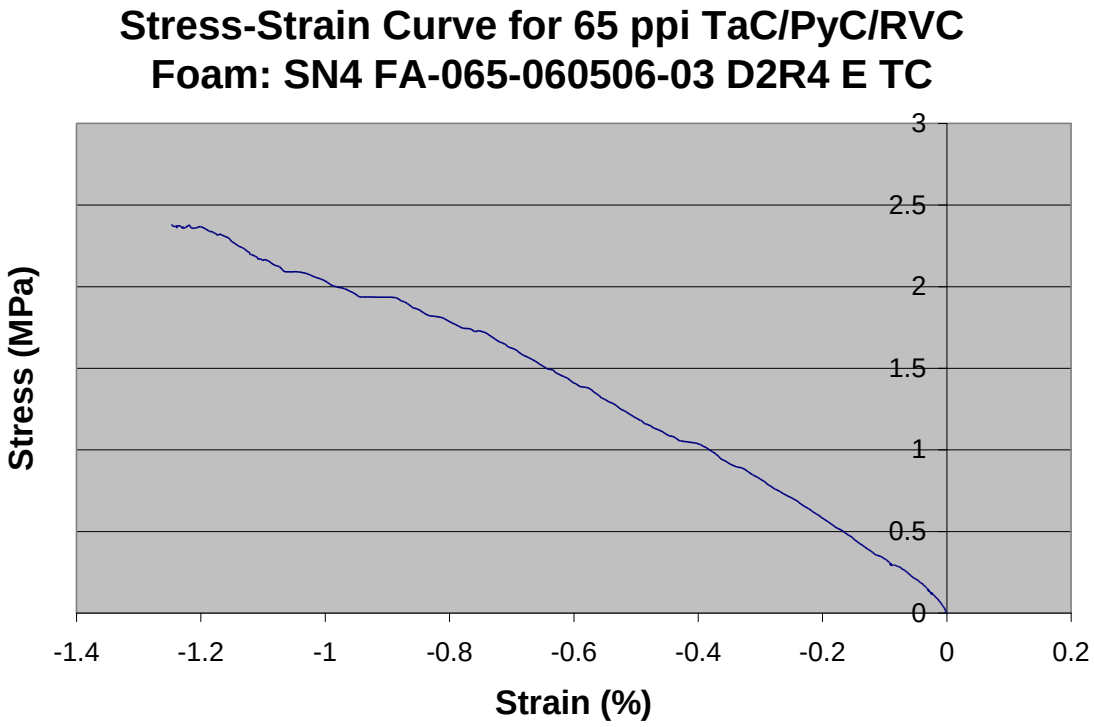
Stress-Strain Curve for 65 ppi TaC/PyC/RVC
Foam: SN4 FA-065-060506-03 D2R4 E TC
Stress (MPa)
3
2.5
2
1.5
1
0.5
0
-1.4
-1.2
-1
-0.8
-0.6
-0.4
-0.2
0
0.2
Strain (%)

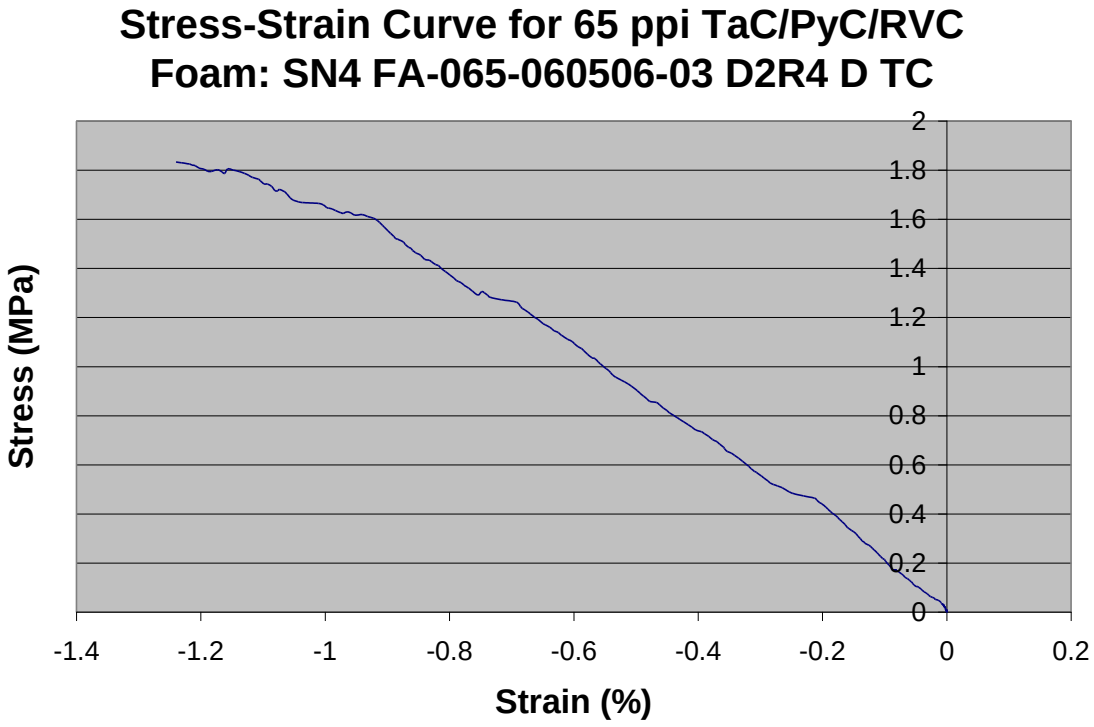
Stress-Strain Curve for 65 ppi TaC/PyC/RVC
Foam: SN4 FA-065-060506-03 D2R4 D TC
Stress (MPa)
2
1.8
1.6
1.4
1.2
1
0.8
0.6
0.4
0.2
0
-1.4
-1.2
-1
-0.8
-0.6
-0.4
-0.2
0
0.2
Strain (%)

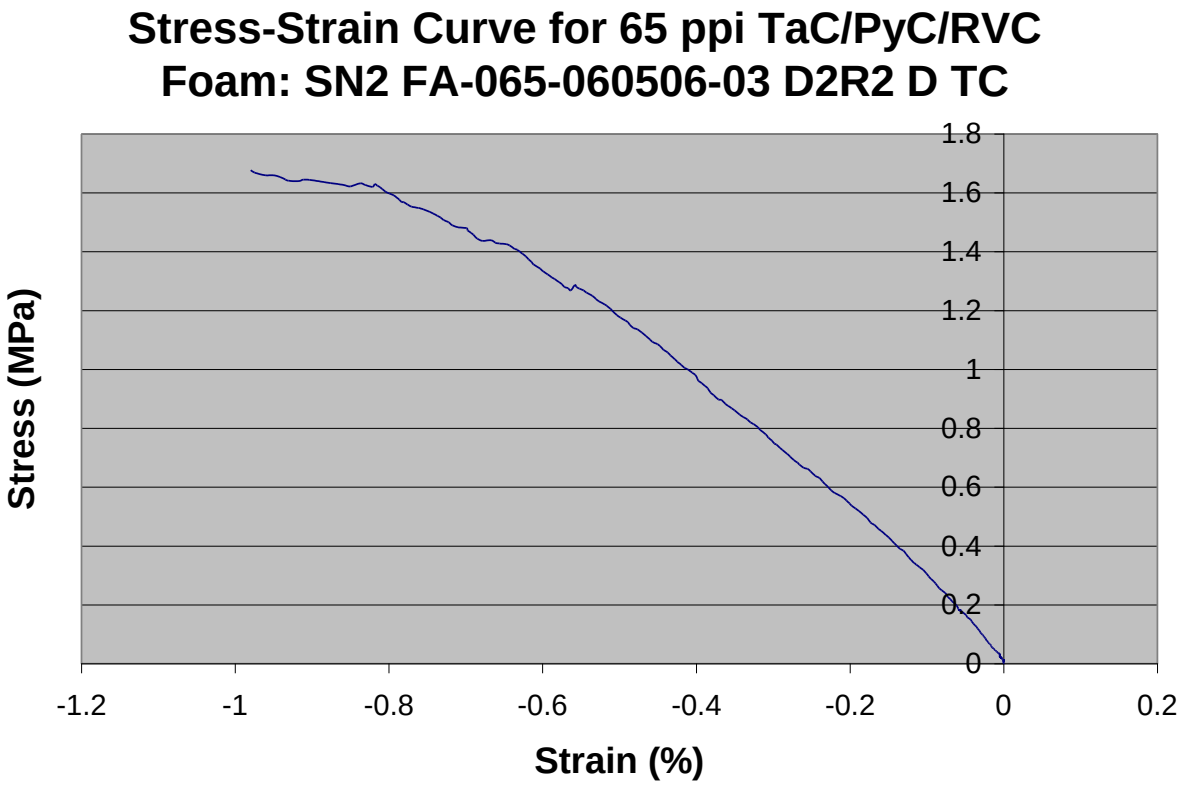
Stress-Strain Curve for 65 ppi TaC/PyC/RVC
Foam: SN2 FA-065-060506-03 D2R2 D TC
Stress (MPa)
1.8
1.6
1.4
1.2
1
0.8
0.6
0.4
0.2
0
-1.2
-1
-0.8
-0.6
-0.4
-0.2
0
0.2
Strain (%)

Thermally Shocked Specimens

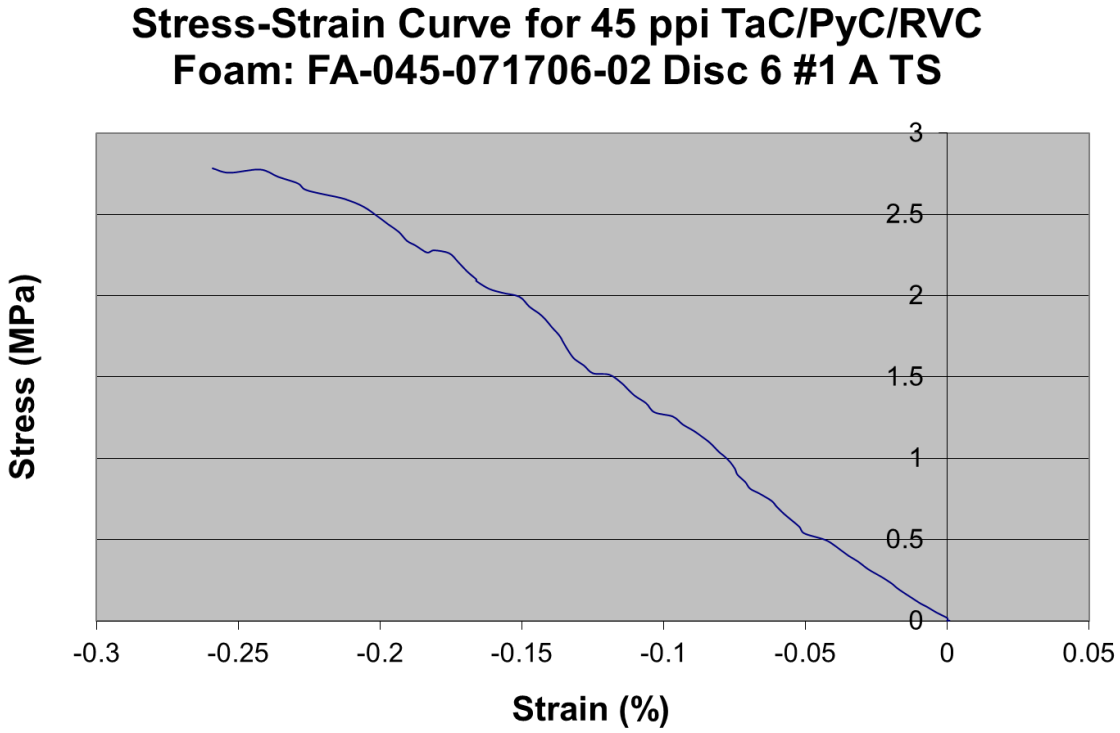

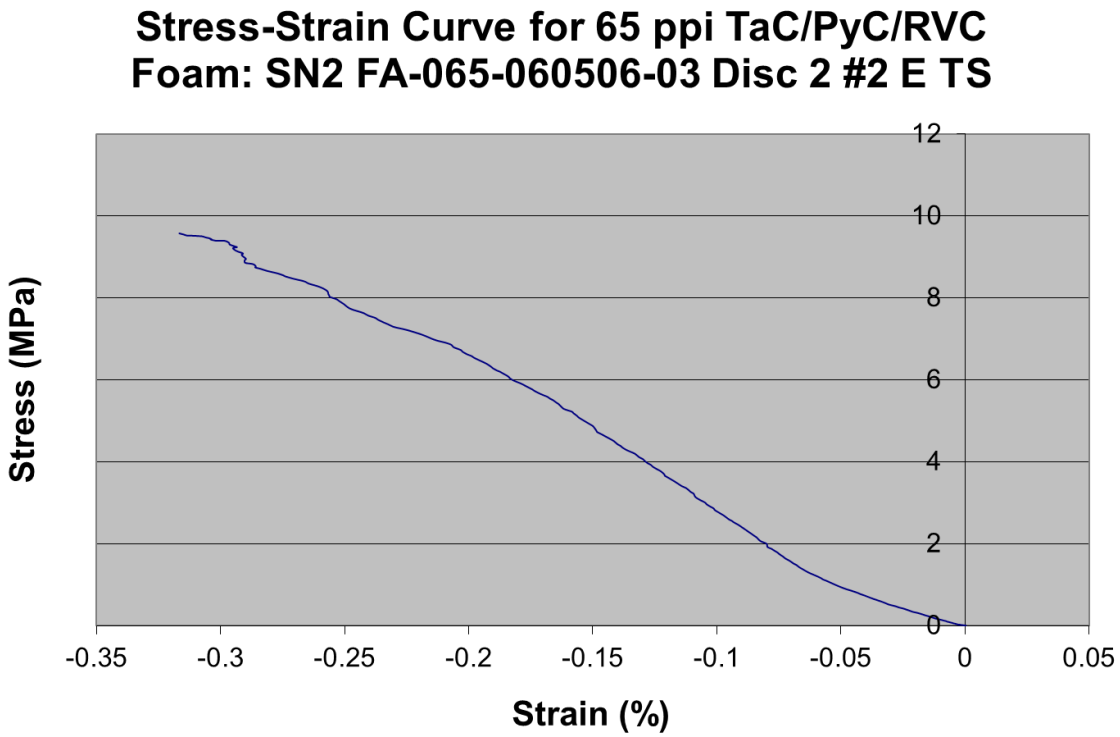

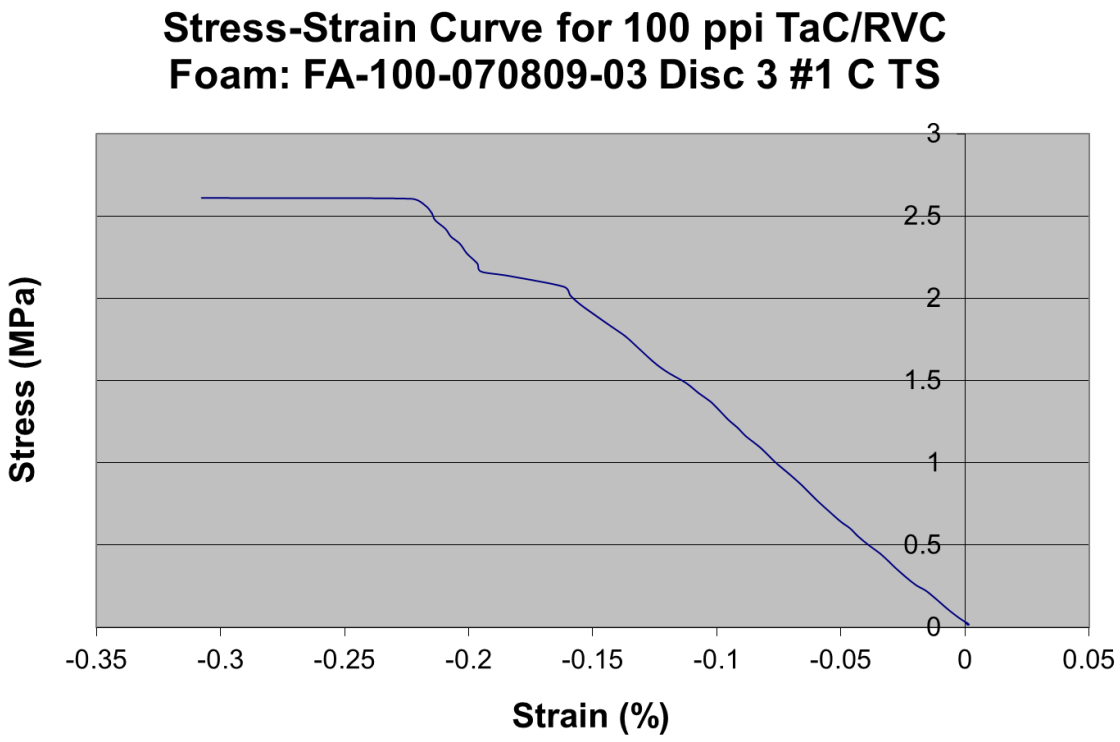
Stress-Strain Curve for 100 ppi TaC/RVC
Foam: FA-100-070809-03 Disc 3 #1 C TS
Stress (MPa)
3
2.5
2
1.5
1
0.5
0
-0.35
-0.3
-0.25
-0.2
-0.15
-0.1
-0.05
0
0.05
Strain (%)

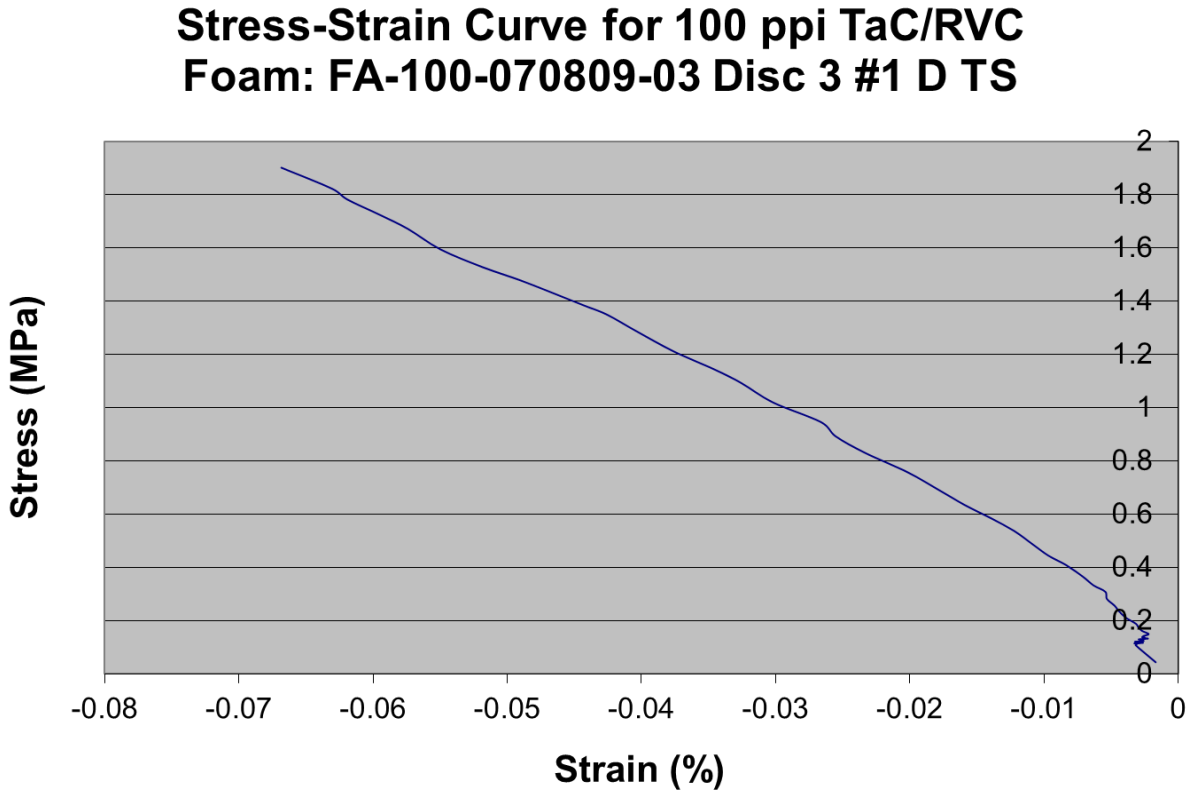
Stress-Strain Curve for 100 ppi TaC/RVC
Foam: FA-100-070809-03 Disc 3 #1 D TS
Stress (MPa)
2
1.8
1.6
1.4
1.2
1
0.8
0.6
0.4
0.2
0
-0.08
-0.07
-0.06
-0.05
-0.04
-0.03
-0.02
-0.01
0
Strain (%)

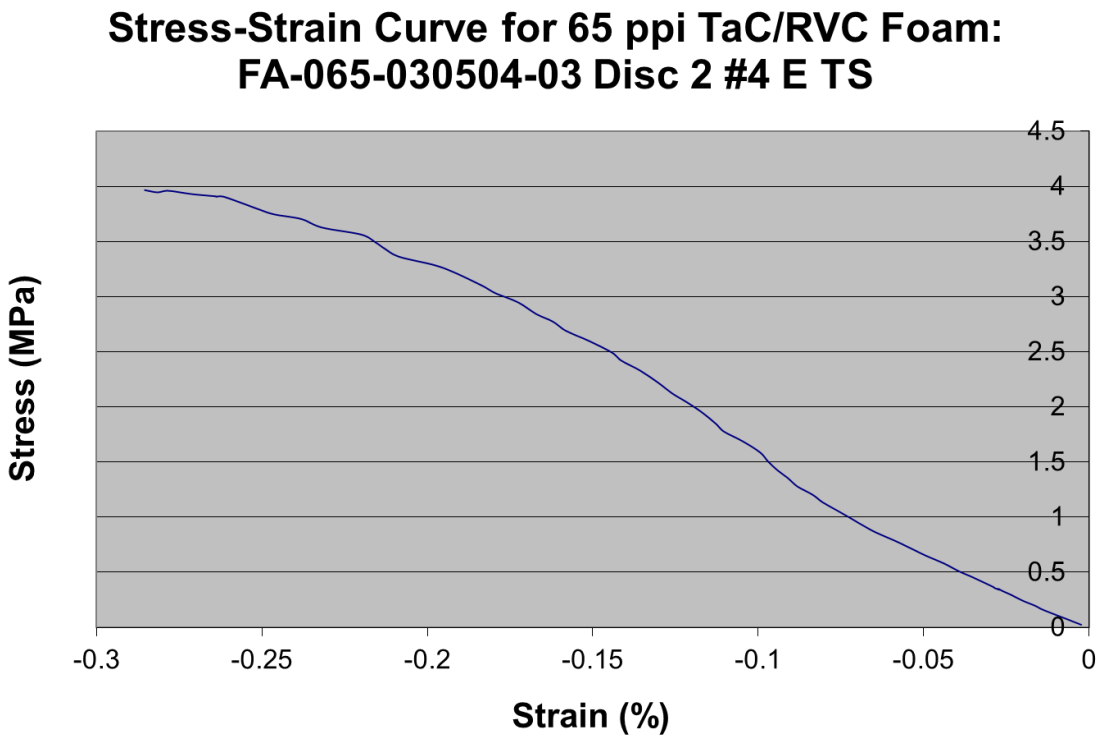
Stress-Strain Curve for 65 ppi TaC/RVC Foam: FA-065-030504-03 Disc 2 #4 E TS
Stress (MPa)
4.5
4
3.5
3
2.5
2
1.5
1
0.5
0
-0.3
-0.25
-0.2
-0.15
-0.1
-0.05
0
Strain (%)

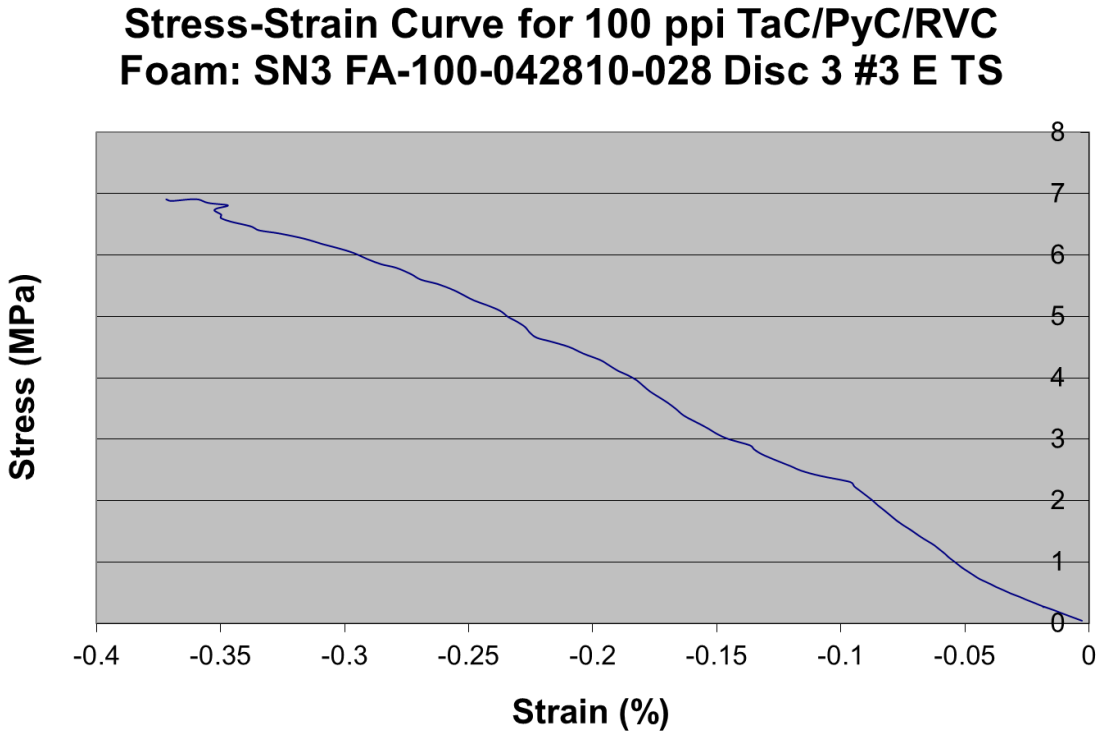
Stress-Strain Curve for 100 ppi TaC/PyC/RVC Foam: SN3 FA-100-042810-028 Disc 3 #3 E TS
Stress (MPa)
8
7
6
5
4
3
2
1
0
-0.4
-0.35
-0.3
-0.25
-0.2
-0.15
-0.1
-0.05
0
Strain (%)

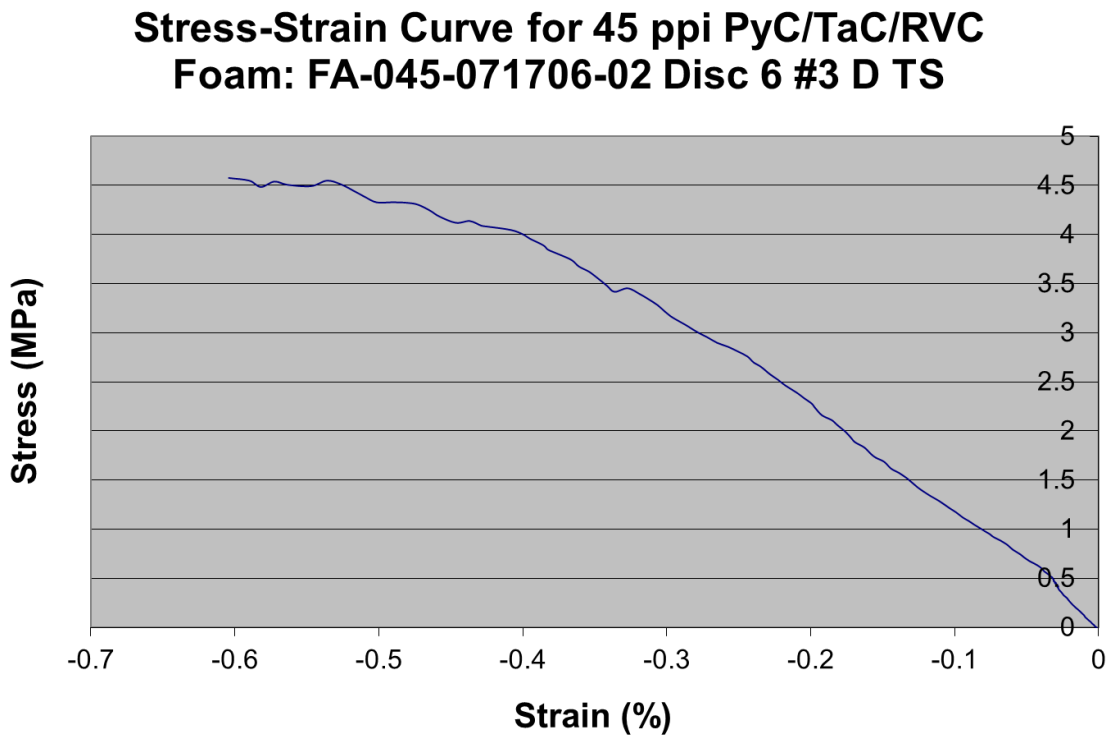
Stress-Strain Curve for 45 ppi PyC/TaC/RVC Foam: FA-045-071706-02 Disc 6 #3 D TS
Stress (MPa)
5
4.5
4
3.5
3
2.5
2
1.5
1
0.5
0
-0.7
-0.6
-0.5
-0.4
-0.3
-0.2
-0.1
0
Strain (%)

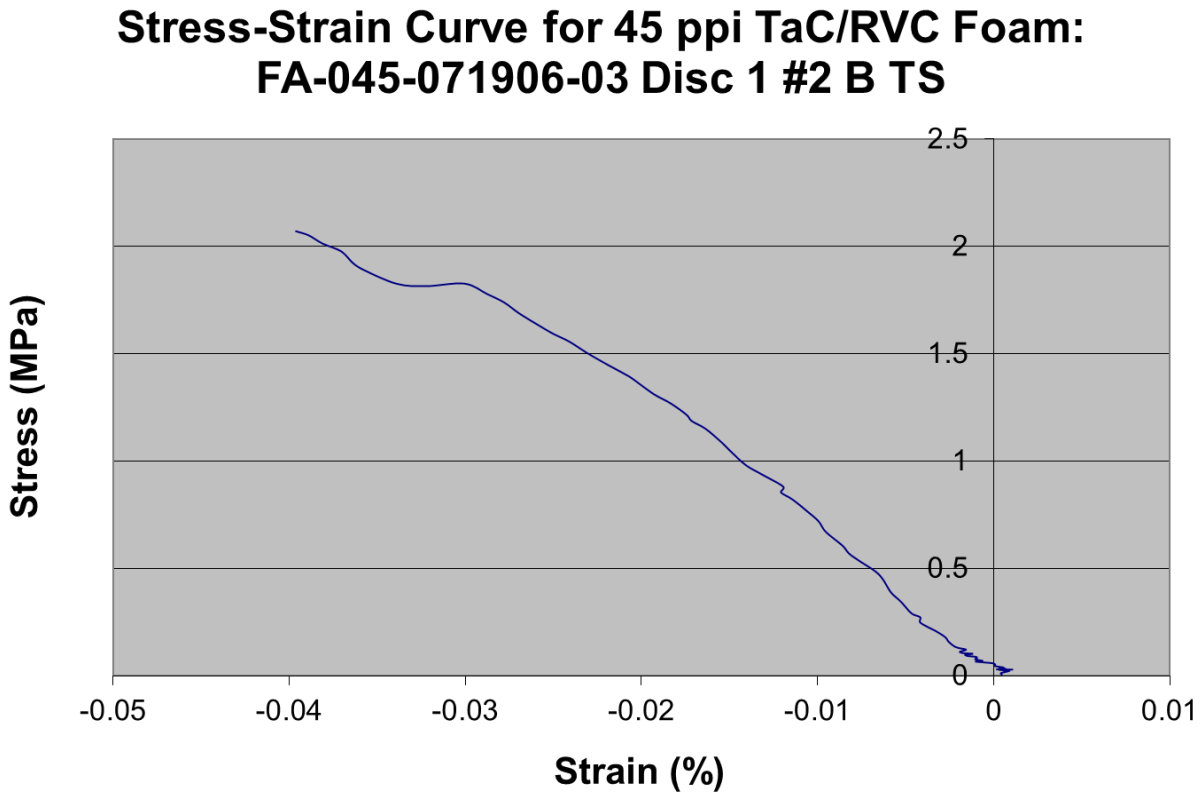
Stress-Strain Curve for 45 ppi TaC/RVC Foam: FA-045-071906-03 Disc 1 #2 B TS
Stress (MPa)
2.5
2
1.5
1
0.5
0
-0.05
-0.04
-0.03
-0.02
-0.01
0
0.01
Strain (%)

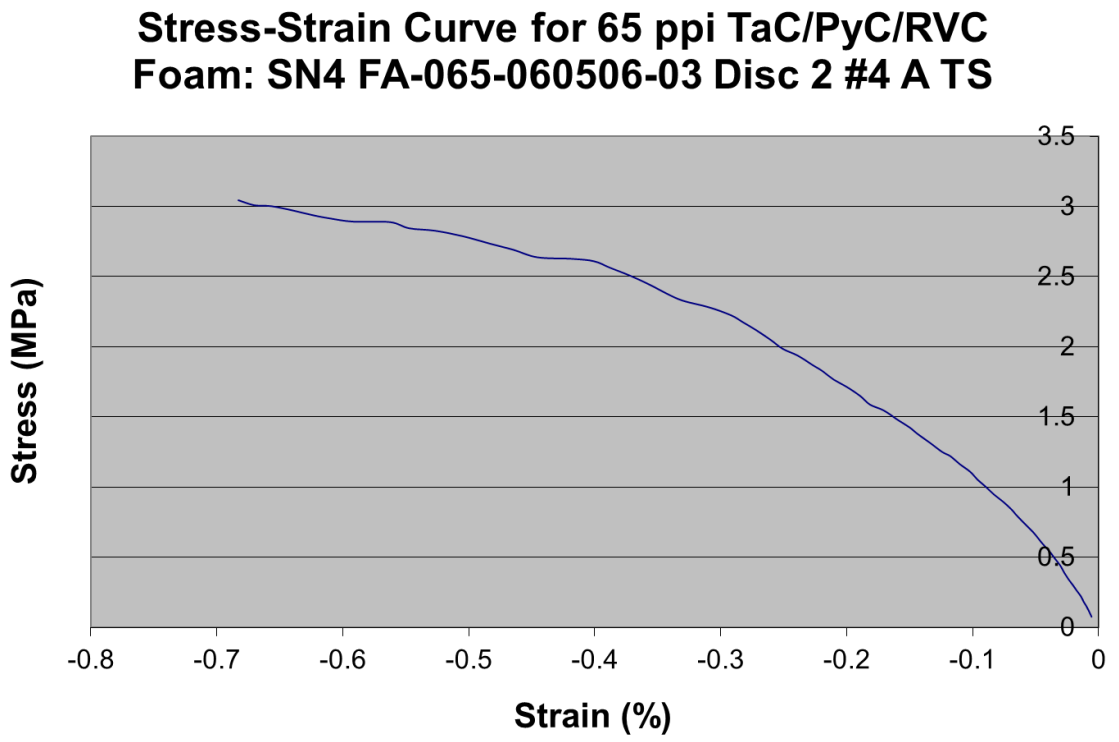
Stress-Strain Curve for 65 ppi TaC/PyC/RVC Foam: SN4 FA-065-060506-03 Disc 2 #4 A TS
Stress (MPa)
3.5
3
2.5
2
1.5
1
0.5
0
-0.8
-0.7
-0.6
-0.5
-0.4
-0.3
-0.2
-0.1
0
Strain (%)

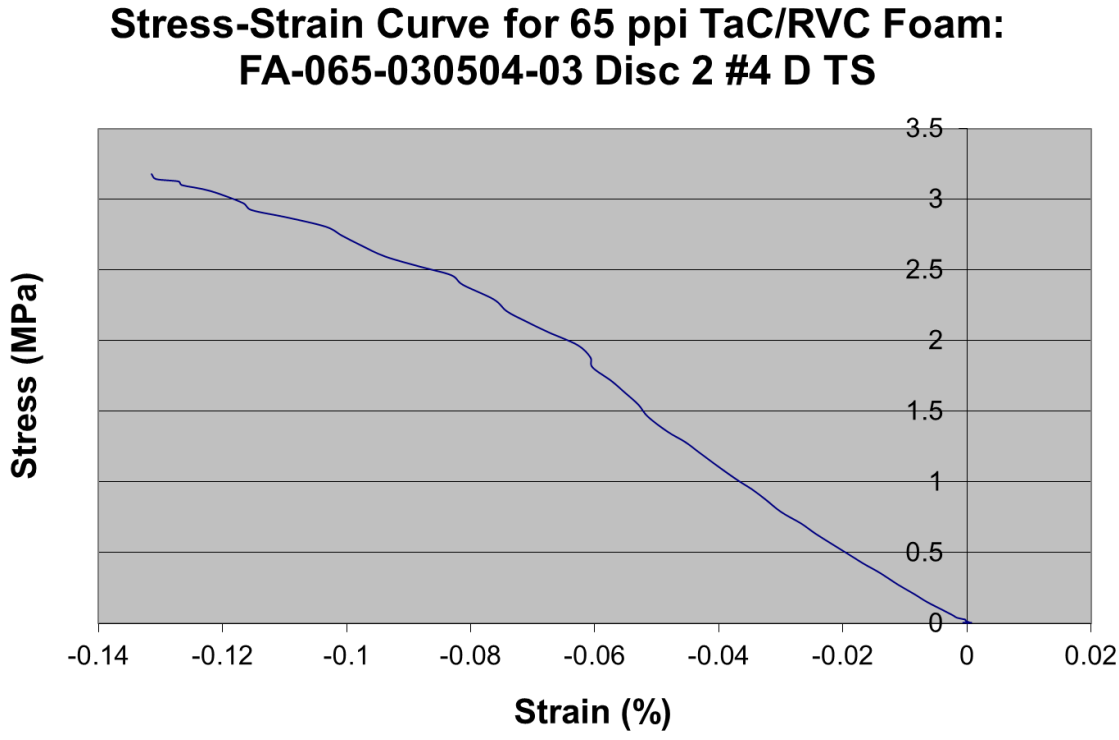
Stress-Strain Curve for 65 ppi TaC/RVC Foam: FA-065-030504-03 Disc 2 #4 D TS
Stress (MPa)
3.5
3
2.5
2
1.5
1
0.5
0
-0.14
-0.12
-0.1
-0.08
-0.06
-0.04
-0.02
0
0.02
Strain (%)

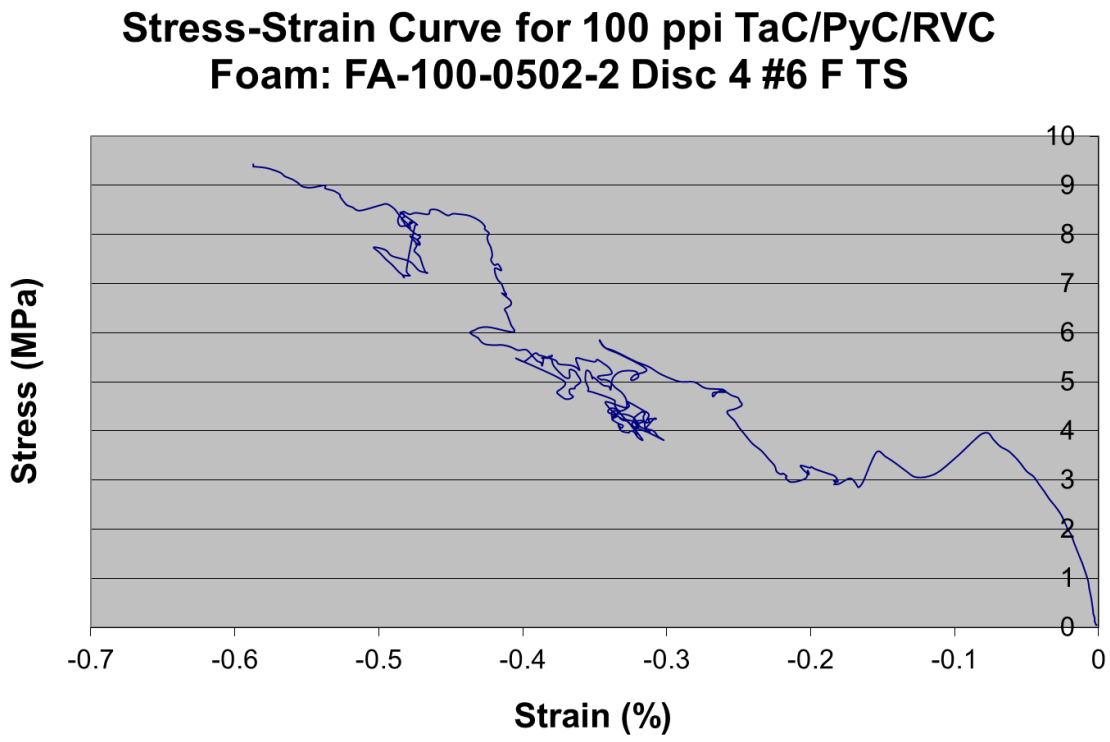
Stress-Strain Curve for 100 ppi TaC/PyC/RVC
Foam: FA-100-0502-2 Disc 4 #6 F TS
Stress (MPa)
10
9
8
7
6
5
4
3
2
1
0
-0.7
-0.6
-0.5
-0.4
-0.3
-0.2
-0.1
0
Strain (%)

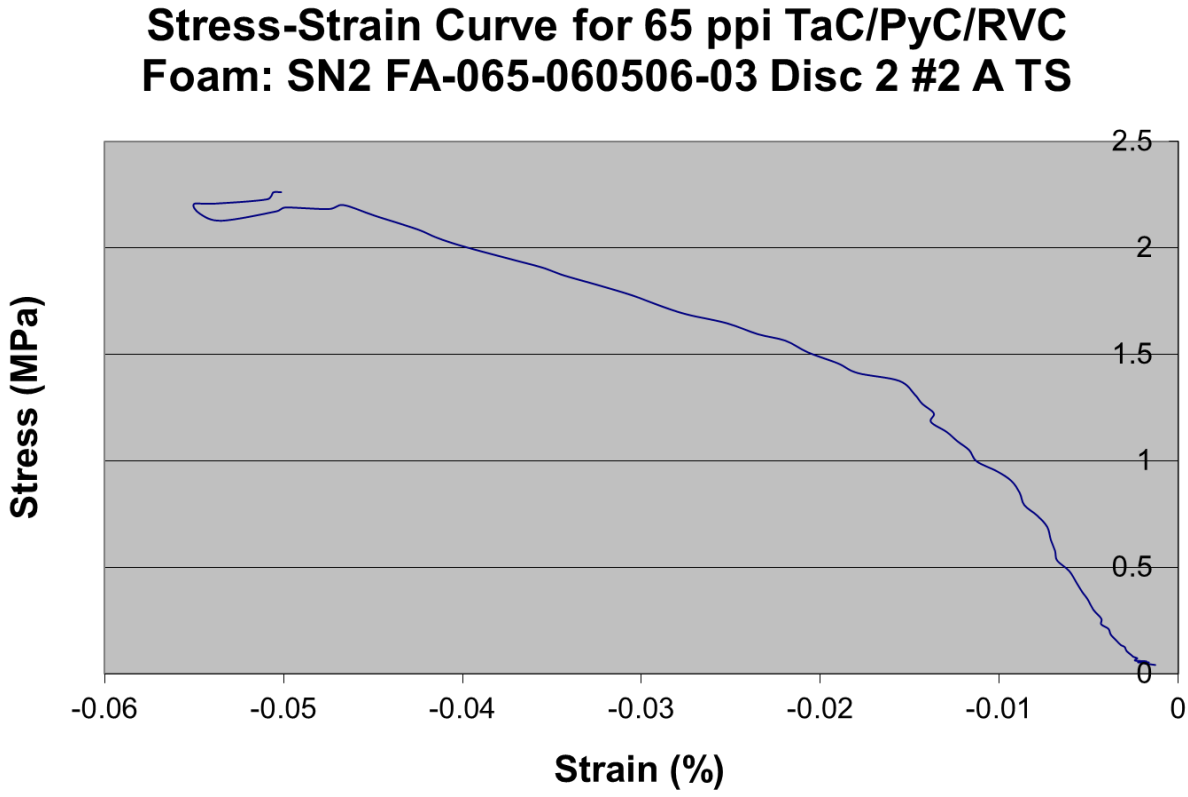
Stress-Strain Curve for 65 ppi TaC/PyC/RVC
Foam: SN2 FA-065-060506-03 Disc 2 #2 A TS
Stress (MPa)
2.5
2
1.5
1
0.5
0
-0.06
-0.05
-0.04
-0.03
-0.02
-0.01
0
Strain (%)

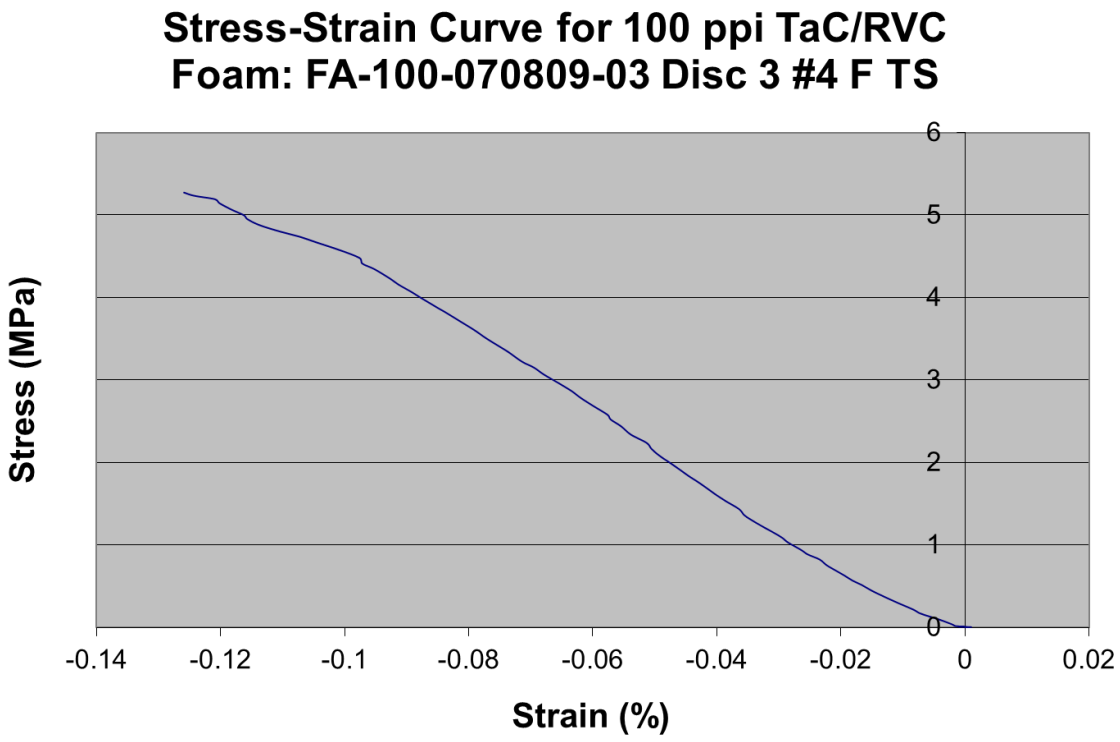
Stress-Strain Curve for 100 ppi TaC/RVC Foam: FA-100-070809-03 Disc 3 #4 F TS
Stress (MPa)
6
5
4
3
2
1
0
-0.14
-0.12
-0.1
-0.08
-0.06
-0.04
-0.02
0
0.02
Strain (%)

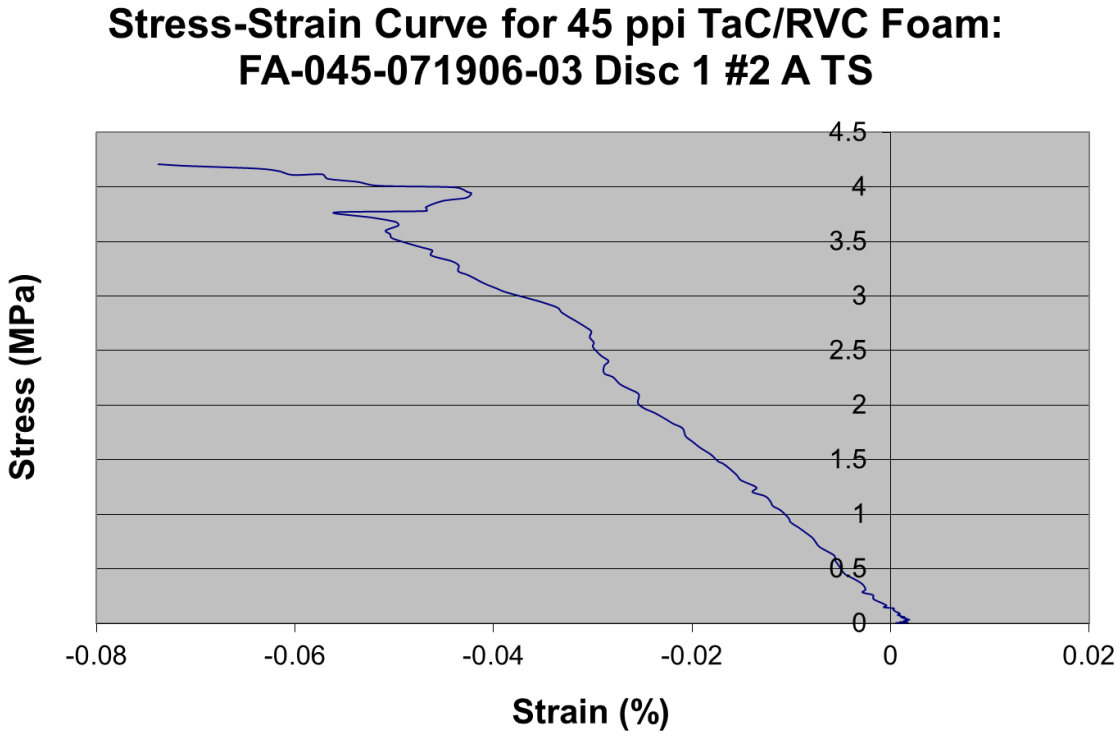
Stress-Strain Curve for 45 ppi TaC/RVC Foam: FA-045-071906-03 Disc 1 #2 A TS
Stress (MPa)
4.5
4
3.5
3
2.5
2
1.5
1
0.5
0
-0.08
-0.06
-0.04
-0.02
0
0.02
Strain (%)

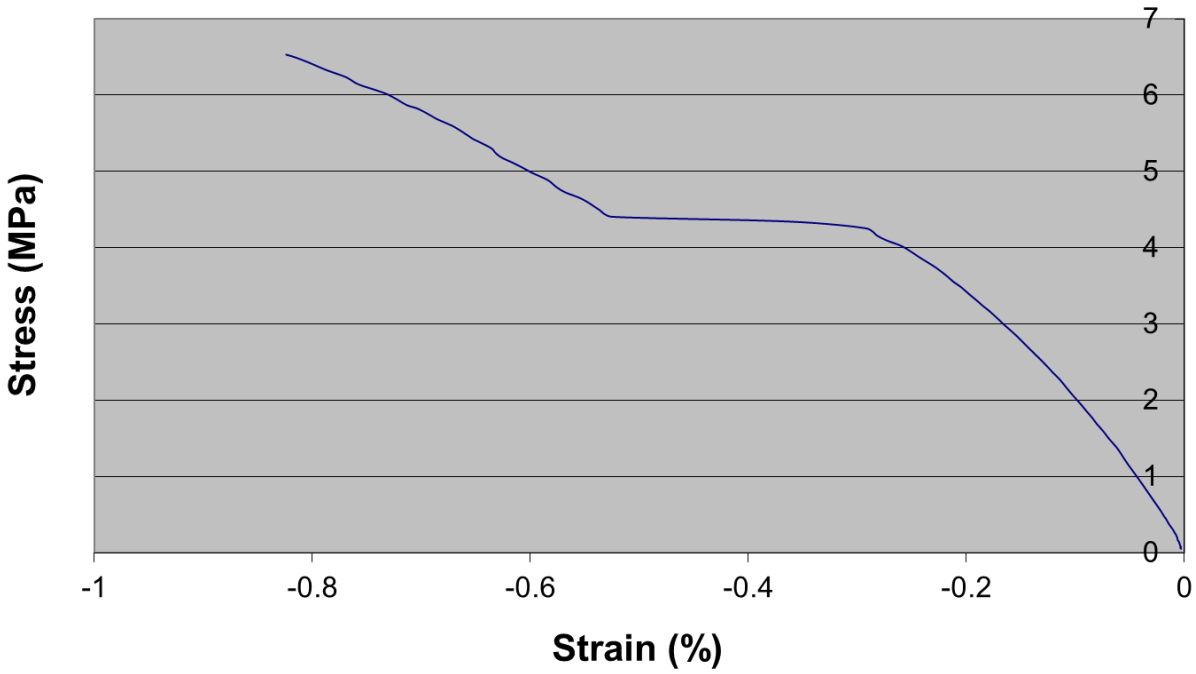
Stress-Strain Curve for 100 ppi TaC/PyC/RVC
Foam: SN3 FA-100-042810-028 Disc 3 #3 D TS
Stress (MPa)
7
6
5
4
3
2
1
0
-1
-0.8
-0.6
-0.4
-0.2
0
Strain (%)

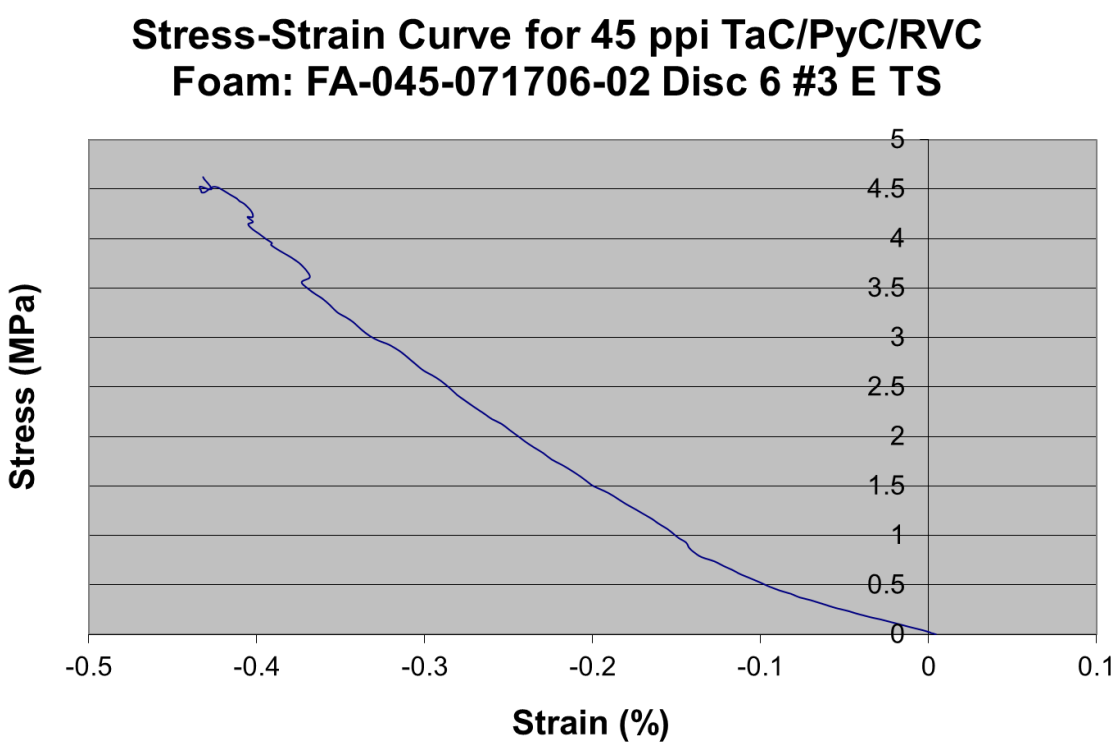
Stress-Strain Curve for 45 ppi TaC/PyC/RVC
Foam: FA-045-071706-02 Disc 6 #3 E TS
Stress (MPa)
5
4.5
4
3.5
3
2.5
2
1.5
1
0.5
0
-0.5
-0.4
-0.3
-0.2
-0.1
0
0.1
Strain (%)

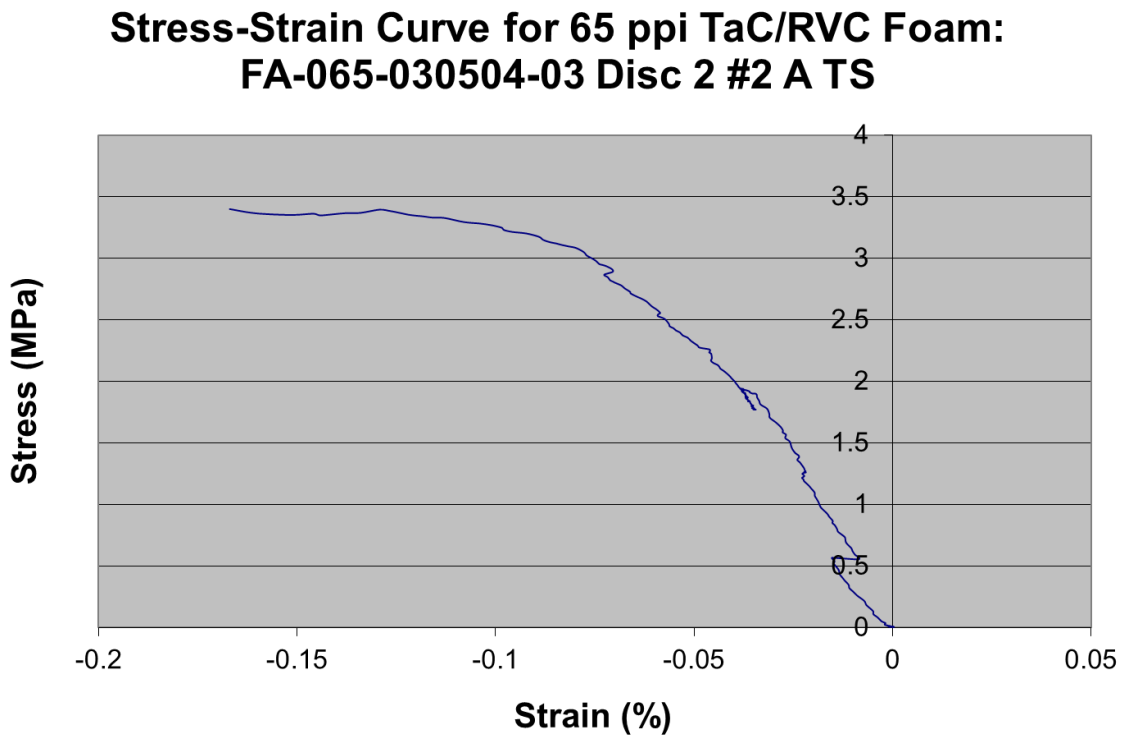
Stress-Strain Curve for 65 ppi TaC/RVC Foam:
FA-065-030504-03 Disc 2 #2 A TS
Stress (MPa)
4
3.5
3
2.5
2
1.5
1
0.5
0
-0.2
-0.15
-0.1
-0.05
0
0.05
Strain (%)

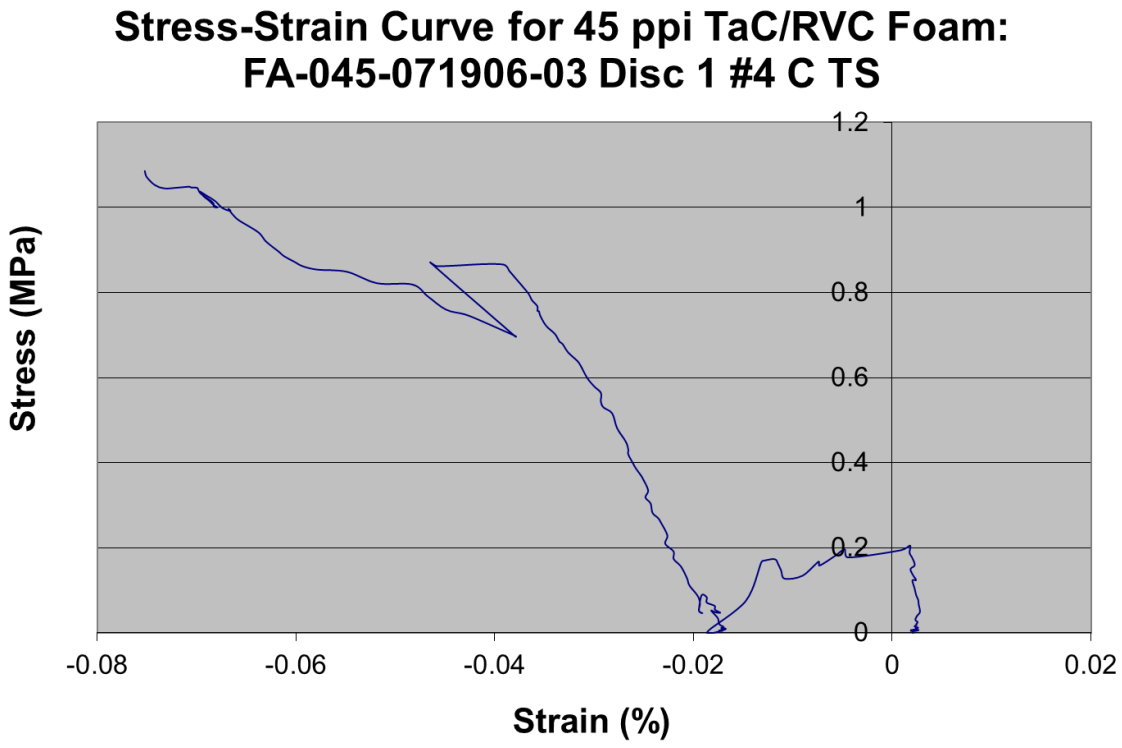
Stress-Strain Curve for 45 ppi TaC/RVC Foam:
FA-045-071906-03 Disc 1 #4 C TS
Stress (MPa)
1.2
1
0.8
0.6
0.4
0.2
0
-0.08
-0.06
-0.04
-0.02
0
0.02
Strain (%)

Appendix G. Graphs of Infiltrated Foam Mass vs Time for Tungsten Infiltration of RVC Foams

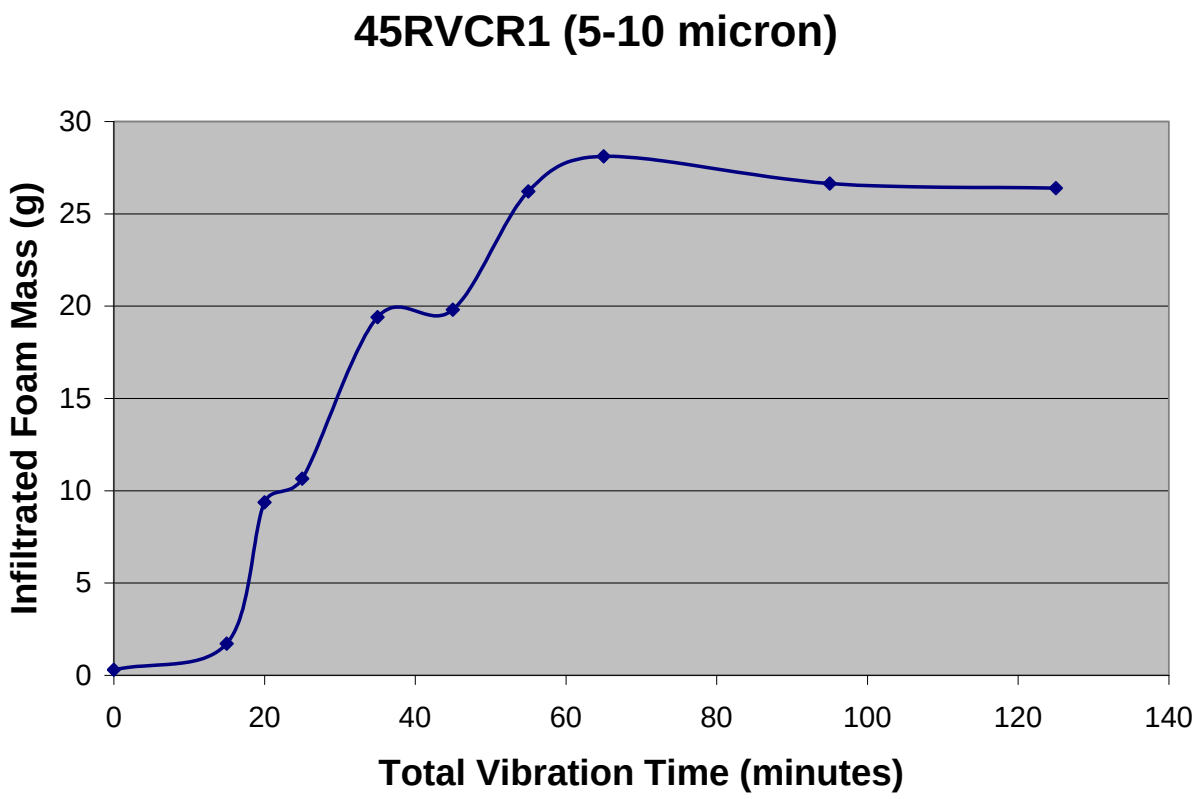

Figure 254. Graph of 5-10 micron tungsten infiltration within RVC 45 ppi foam round 1.

Table XLII. Table of 5-10 Micron Tungsten Infiltration Parameters and Measurements for RVC 45 ppi Foam Round 1

Net vibration time (min)	Vibration run time (min)	Acceleration min (m/s^2)	Acceleration max (m/s^2)	Tungsten mass (g)	Infiltrated mass (g)	Infiltration rate (g/min)
0					0.292	
15	15	25	28	15.001	1.715	0.095
20	5	12.3	12.5	20.024	9.372	1.531
25	5	12	12.1	25.015	10.648	0.255
35	10	12.4	12.5	25.003	19.398	0.875
45	10	12.4	12.6	25.083	19.796	0.040
55	10	18	20	24.596	26.213	0.642
65	10	24	27	25.124	28.105	0.189
95	30	12.4	12.7	25.127	26.631	-0.049
125	30	12.5	12.8	26.36	26.387	-0.008

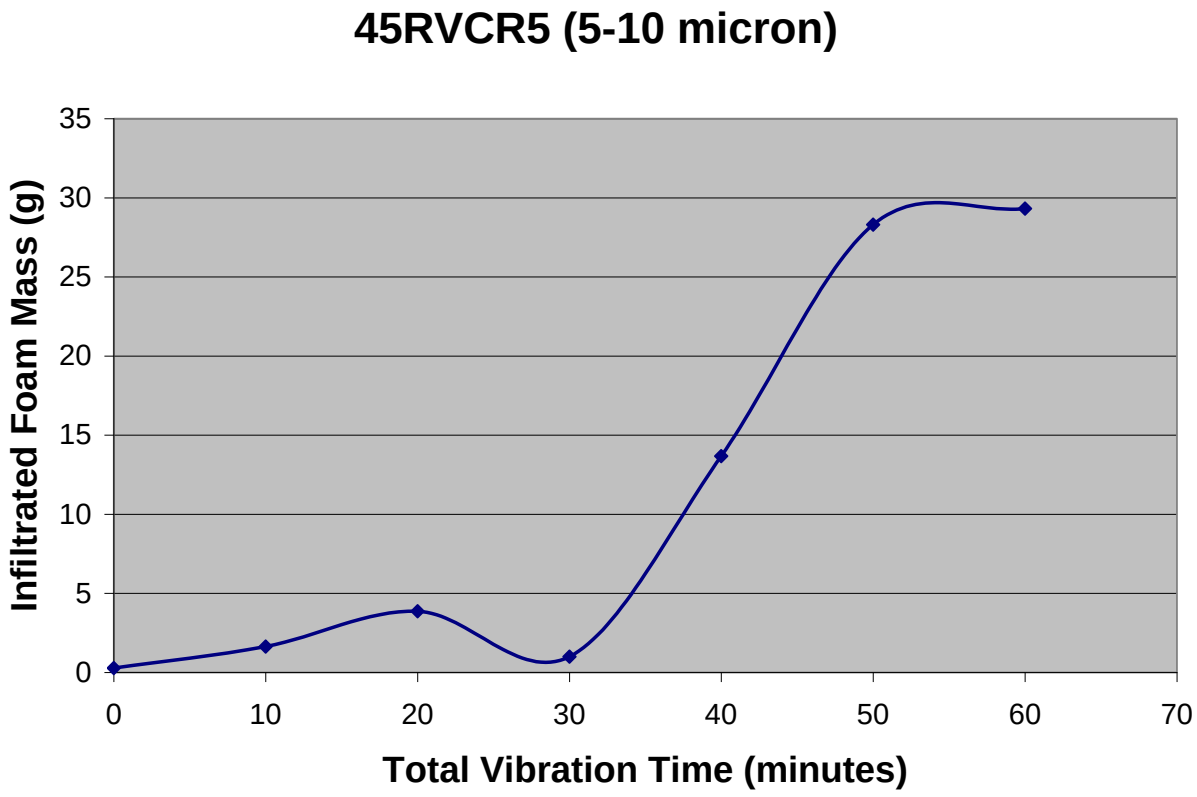

Figure 255. Graph of 5-10 micron tungsten infiltration within RVC 45 ppi foam round 5.

Table XLIII. Table of 5-10 Micron Tungsten Infiltration Parameters and Measurements for RVC 45 ppi Foam Round 5

Net vibration time (min)	Vibration run time (min)	Acceleration min (m/s^2)	Acceleration max (m/s^2)	Tungsten mass (g)	Infiltrated mass (g)	Infiltration rate (g/min)
0					0.273	
10	10	12.3	12.4	25.015	1.638	0.137
20	10	12.3	12.4	25.066	3.863	0.223
30	10	12.3	12.4	25.036	0.996	-0.287
40	10	13.3	13.6	25.008	13.673	1.268
50	10	23	25	25.015	28.297	1.462
60	10	23	25	25.018	29.319	0.102

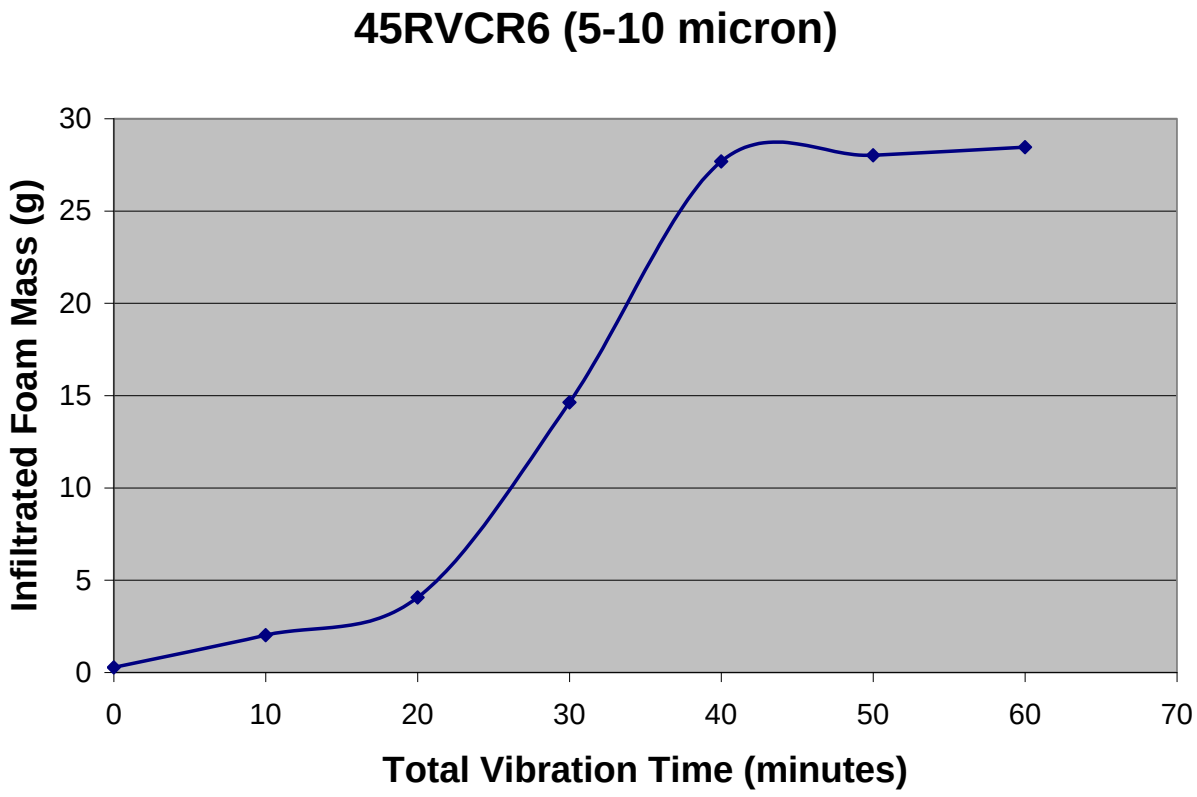

Figure 256. Graph of 5-10 micron tungsten infiltration within RVC 45 ppi foam round 6.

Table XLIV. Table of 5-10 Micron Tungsten Infiltration Parameters and Measurements for RVC 45 ppi Foam Round 6

Net vibration time (min)	Vibration run time (min)	Acceleration min (m/s^2)	Acceleration max (m/s^2)	Tungsten mass (g)	Infiltrated mass (g)	Infiltration rate (g/min)
0					0.271	
10	10	13.4	13.7	25.114	2.025	0.175
20	10	13.5	13.9	25.038	4.062	0.204
30	10	23	25	25.042	14.636	1.057
40	10	23	25	25.063	27.686	1.305
50	10	23	25	25.045	28.016	0.033
60	10	23	25	25.027	28.453	0.044

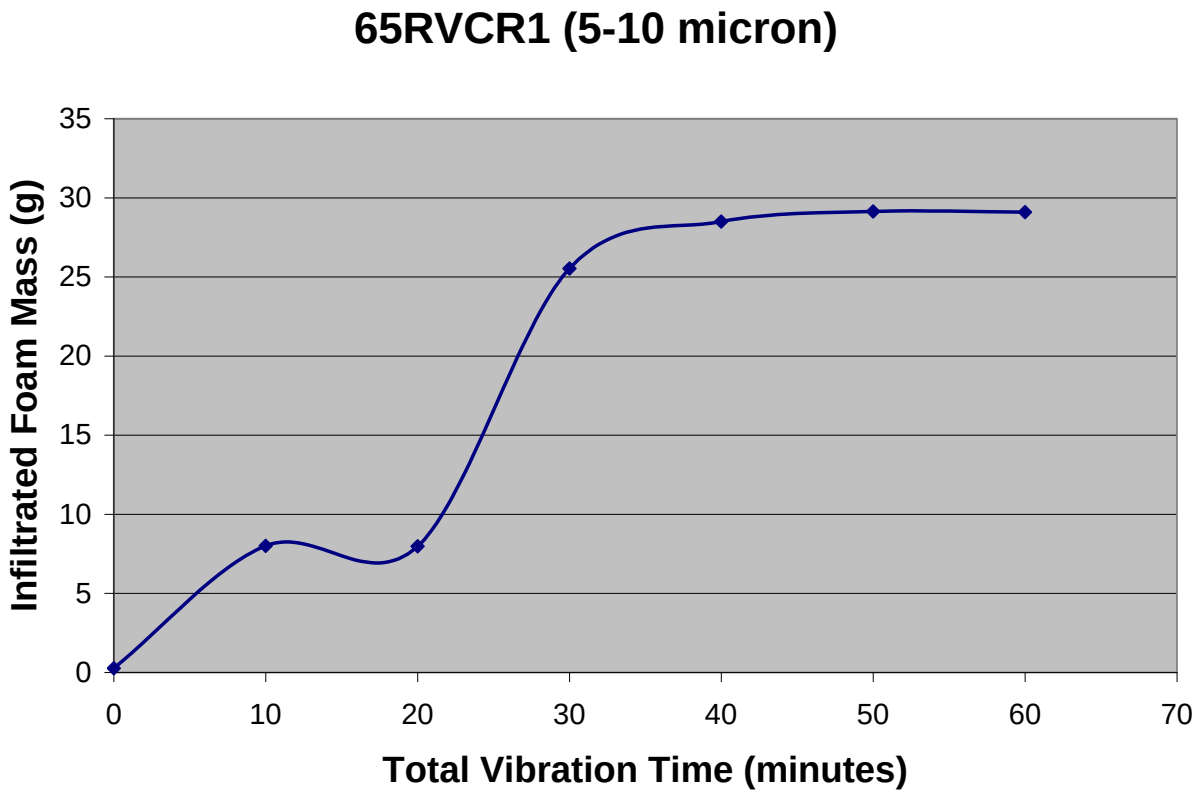

Figure 257. Graph of 5-10 micron tungsten infiltration within RVC 65 ppi foam round 1.

Table XLV. Table of 5-10 Micron Tungsten Infiltration Parameters and Measurements for RVC 65 ppi Foam Round 1

Net vibration time (min)	Vibration run time (min)	Acceleration min (m/s^2)	Acceleration max (m/s^2)	Tungsten mass (g)	Infiltrated mass (g)	Infiltration rate (g/min)
0					0.261	
10	10	13.2	13.4	25.048	8.001	0.774
20	10	13.2	13.5	25.067	7.97	-0.003
30	10	23	25	25.085	25.535	1.757
40	10	23	25	25.092	28.492	0.296
50	10	23	25	25.046	29.136	0.064
60	10	23	25	25.038	29.096	-0.004

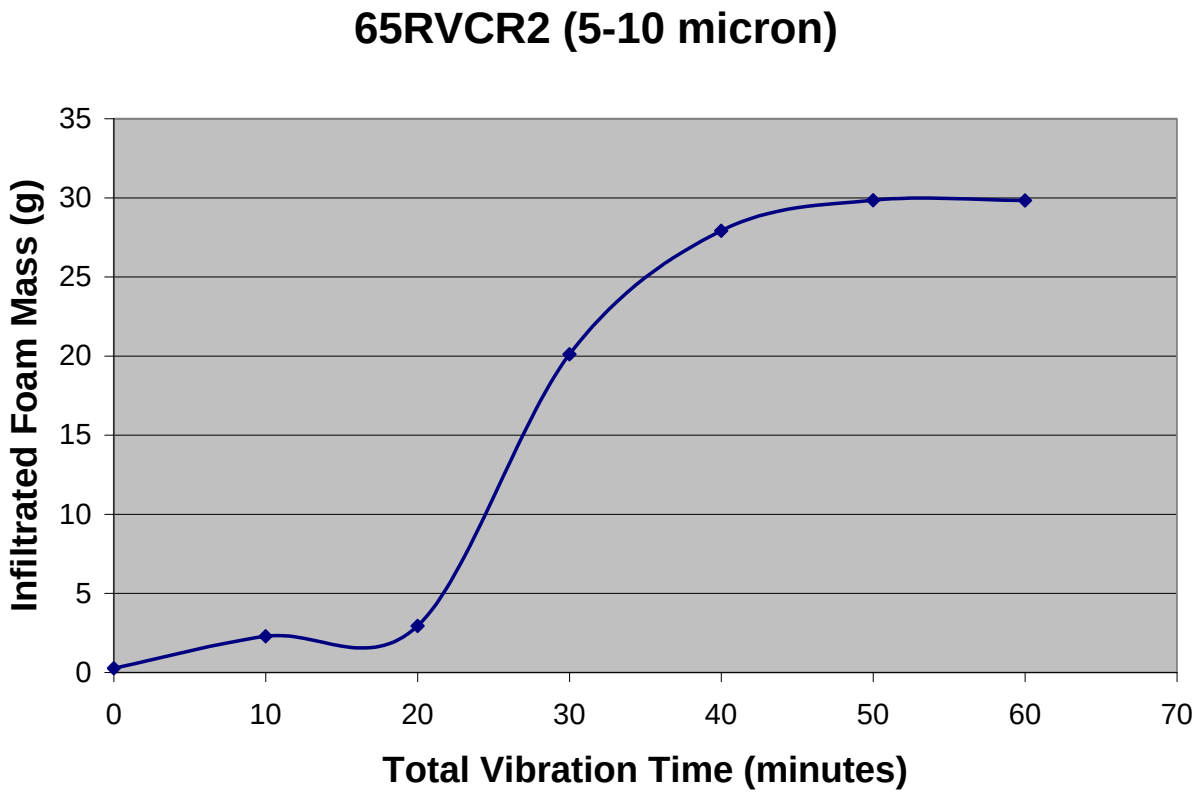

Figure 258. Graph of 5-10 micron tungsten infiltration within RVC 65 ppi foam round 2.

Table XLVI. Table of 5-10 Micron Tungsten Infiltration Parameters and Measurements for RVC 65 ppi Foam Round 2

Net vibration time (min)	Vibration run time (min)	Acceleration min (m/s^2)	Acceleration max (m/s^2)	Tungsten mass (g)	Infiltrated mass (g)	Infiltration rate (g/min)
0					0.267	
10	10	13.4	13.6	25.068	2.293	0.203
20	10	13.4	13.6	25.005	2.939	0.065
30	10	23	25	25.036	20.113	1.717
40	10	23	25	25.03	27.917	0.780
50	10	23	25	25.057	29.841	0.192
60	10	23	25	25.035	29.824	-0.002

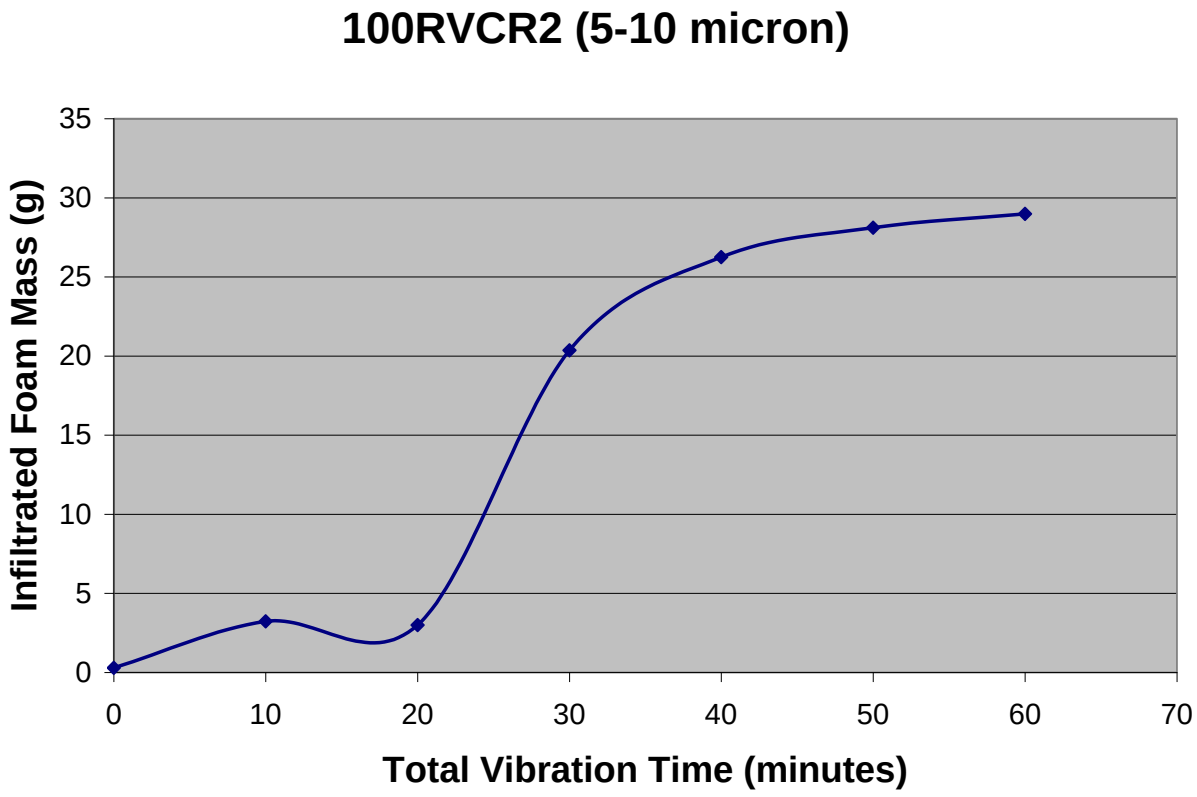

Figure 259. Graph of 5-10 micron tungsten infiltration within RVC 45 ppi foam round 2.

Table XLVII. Table of 5-10 Micron Tungsten Infiltration Parameters and Measurements for RVC 45 ppi Foam Round 2

Net vibration time (min)	Vibration run time (min)	Acceleration min (m/s^2)	Acceleration max (m/s^2)	Tungsten mass (g)	Infiltrated mass (g)	Infiltration rate (g/min)
0					0.291	
10	10	13.4	13.6	25.036	3.229	0.294
20	10	13.4	13.6	25.032	3.001	-0.023
30	10	23	25	25.042	20.351	1.735
40	10	23	25	25.056	26.246	0.590
50	10	23	25	25.077	28.112	0.187
60	10	23	25	25.02	28.975	0.086

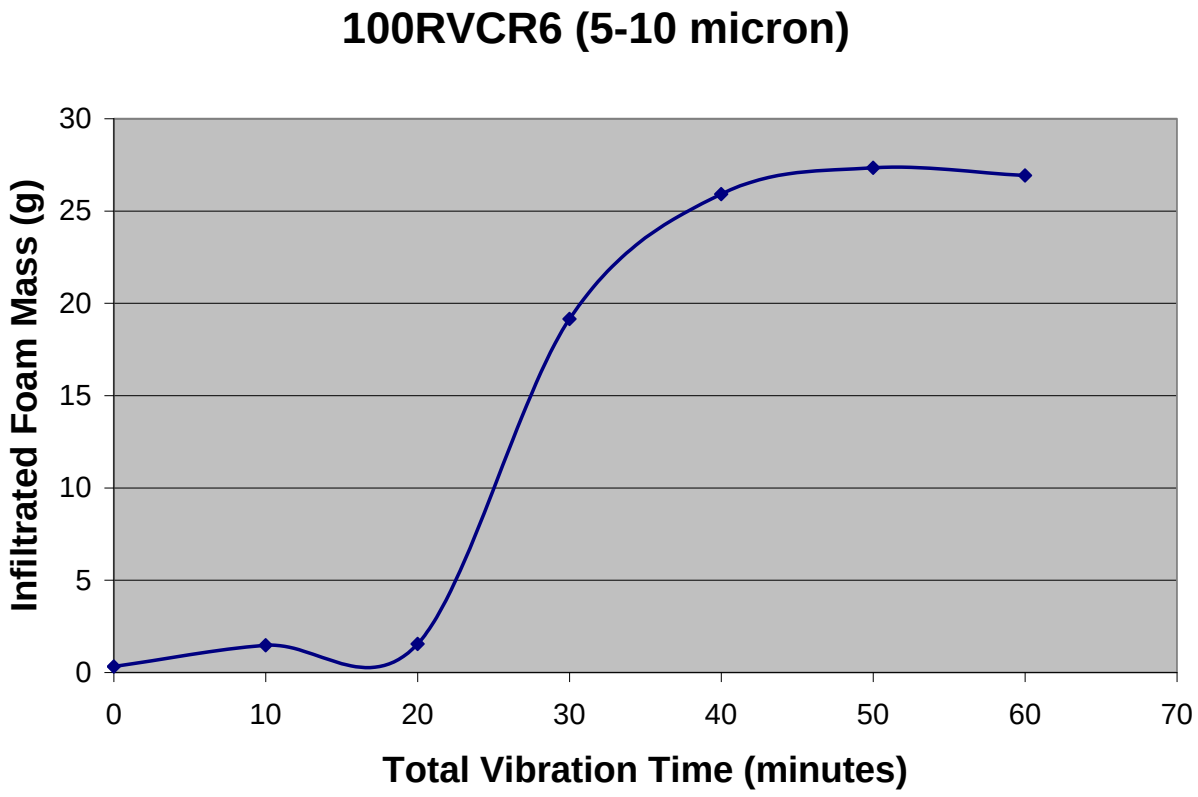

Figure 260. Graph of 5-10 micron tungsten infiltration within RVC 100 ppi foam round 6.

Table XLVIII. Table of 5-10 Micron Tungsten Infiltration Parameters and Measurements for RVC 100 ppi Foam Round 6

Net vibration time (min)	Vibration run time (min)	Acceleration min (m/s^2)	Acceleration max (m/s^2)	Tungsten mass (g)	Infiltrated mass (g)	Infiltration rate (g/min)
0					0.326	
10	10	13.4	13.6	25.085	1.479	0.115
20	10	13.4	13.6	25.057	1.543	0.006
30	10	23	25	25.002	19.149	1.761
40	10	23	25	25.08	25.914	0.677
50	10	23	25	25.013	27.335	0.142
60	10	23	25	25.085	26.917	-0.042

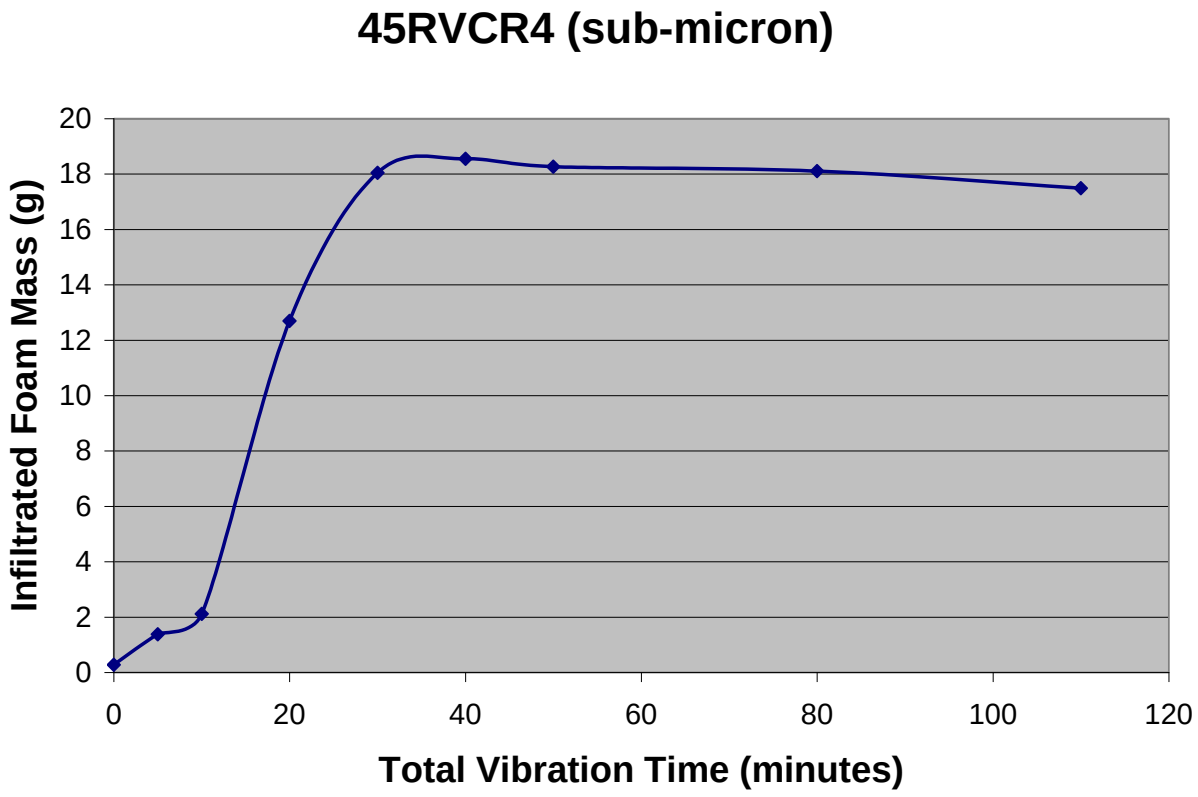

Figure 261. Graph of sub-micron tungsten infiltration within RVC 45 ppi foam round 4.

Table XLIX. Table of Sub-micron Tungsten Infiltration Parameters and Measurements for RVC 45 ppi Foam Round 4

Net vibration time (min)	Vibration run time (min)	Acceleration min (m/s^2)	Acceleration max (m/s^2)	Tungsten mass (g)	Infiltrated mass (g)	Infiltration rate (g/min)
0					0.277	
5	5	12.3	12.4	25.008	1.379	0.220
10	5	12.3	12.5	25.013	2.112	0.147
20	10	23	25	15.066	12.692	1.058
30	10	23	25	15.007	18.044	0.535
40	10	23	25	14.997	18.546	0.050
50	10	23	25	15.031	18.266	-0.028
80	30	12.4	12.5	15.015	18.108	-0.005
110	30	12.4	12.5	15.165	17.491	-0.021

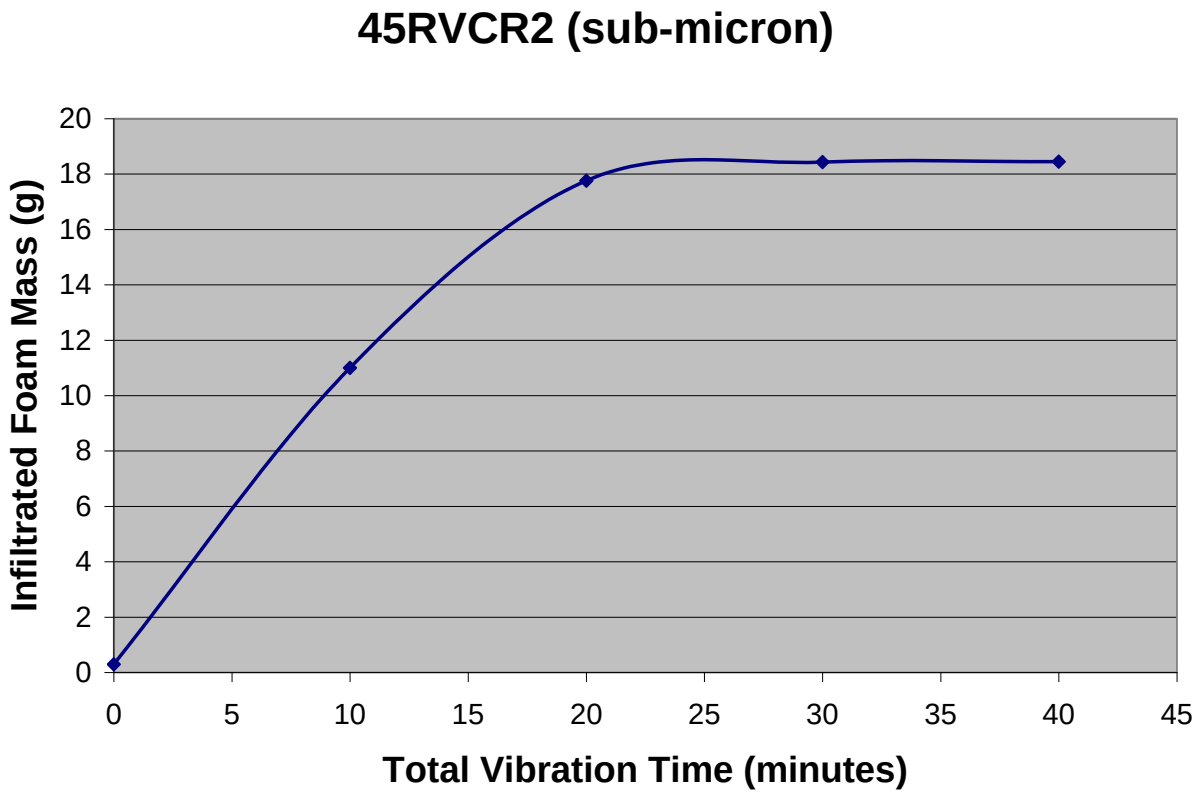

Figure 262. Graph of sub-micron tungsten infiltration within RVC 45 ppi foam round 2.

Table L. Table of Sub-micron Tungsten Infiltration Parameters and Measurements for RVC 45 ppi Foam Round 2

Net vibration time (min)	Vibration run time (min)	Acceleration min (m/s^2)	Acceleration max (m/s^2)	Tungsten mass (g)	Infiltrated mass (g)	Infiltration rate (g/min)
0					0.294	
10	10	23	25	15.017	10.995	1.070
20	10	23	25	15.082	17.76	0.677
30	10	23	25	15	18.43	0.067
40	10	23	25	15.038	18.447	0.002

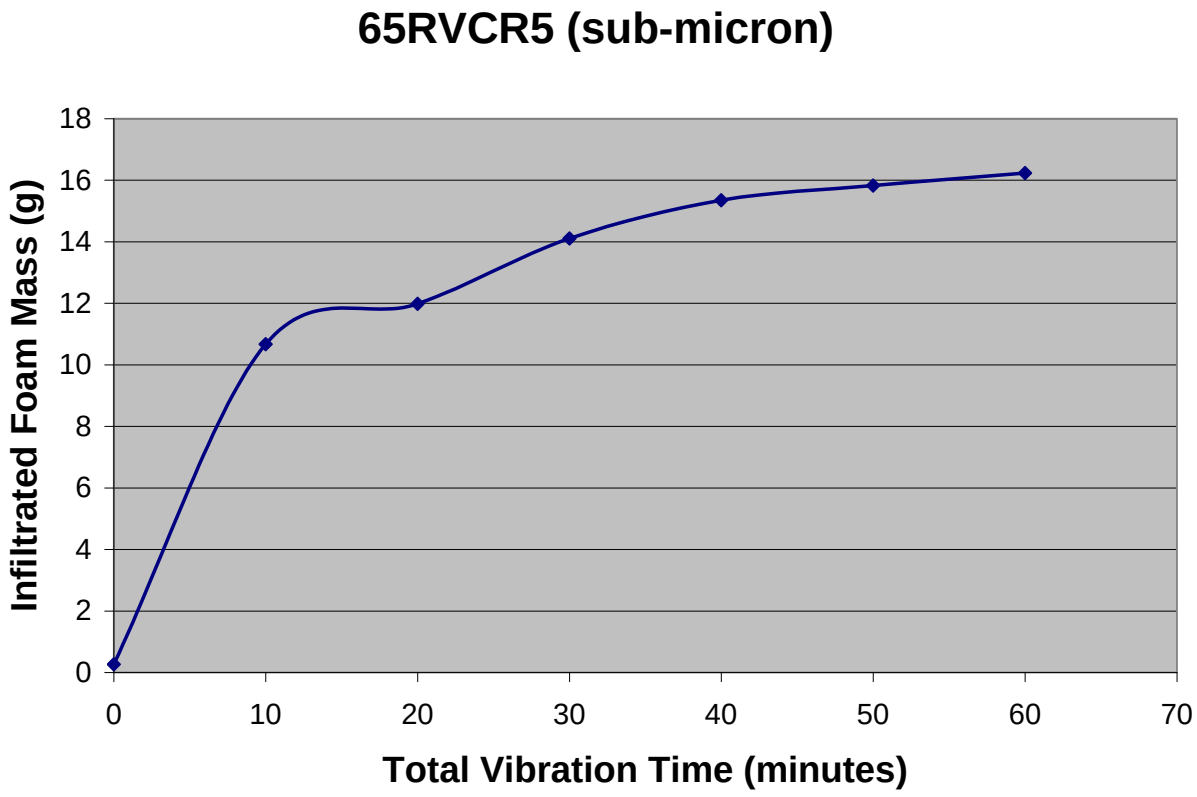

Figure 263. Graph of sub-micron tungsten infiltration within RVC 65 ppi foam round 5.

Table LI. Table of Sub-micron Tungsten Infiltration Parameters and Measurements for RVC 65 ppi Foam Round 5

Net vibration time (min)	Vibration run time (min)	Acceleration min (m/s^2)	Acceleration max (m/s^2)	Tungsten mass (g)	Infiltrated mass (g)	Infiltration rate (g/min)
0					0.263	
10	10	23	25	15.017	10.667	1.040
20	10	23	25	15.063	11.983	0.132
30	10	23	25	15.09	14.107	0.212
40	10	23	25	15.099	15.347	0.124
50	10	23	25	15.086	15.828	0.048
60	10	23	25	15.019	16.232	0.040

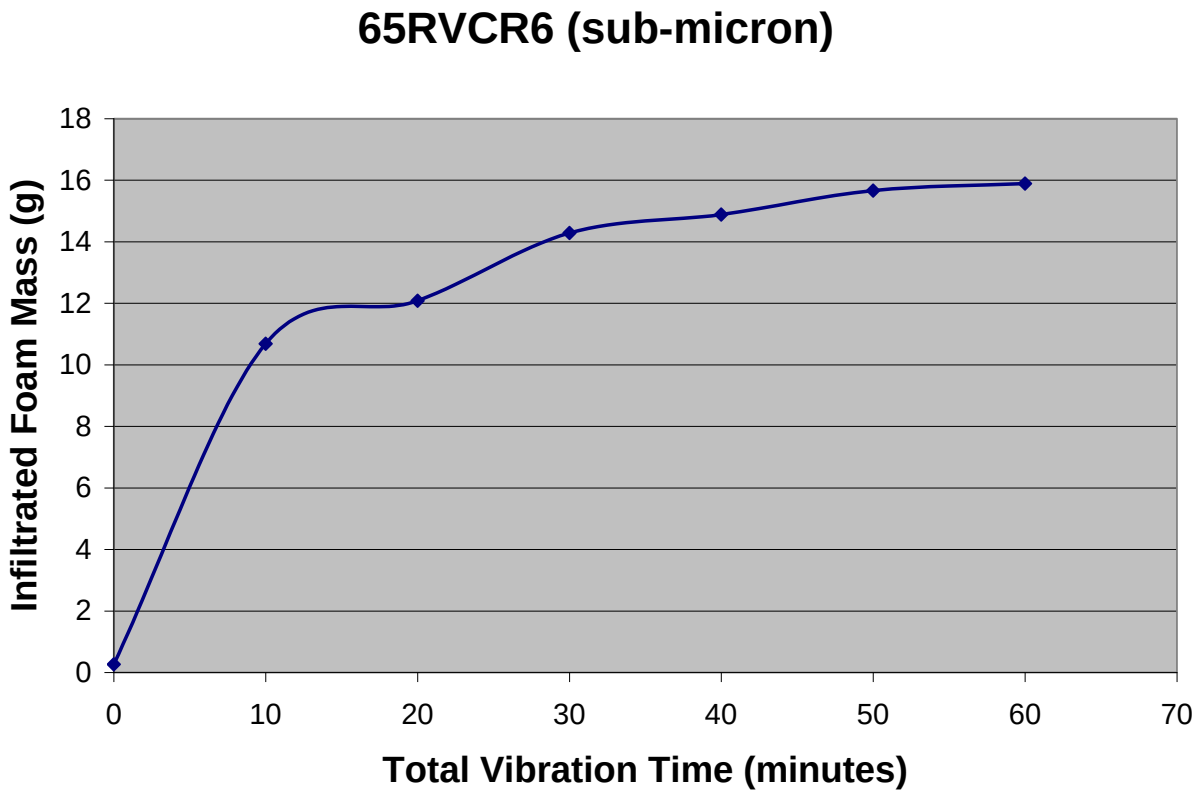

Figure 264. Graph of sub-micron tungsten infiltration within RVC 65 ppi foam round 6.

Table LII. Table of Sub-micron Tungsten Infiltration Parameters and Measurements for RVC 65 ppi Foam Round 6

Net vibration time (min)	Vibration run time (min)	Acceleration min (m/s^2)	Acceleration max (m/s^2)	Tungsten mass (g)	Infiltrated mass (g)	Infiltration rate (g/min)
0					0.261	
10	10	23	25	15.022	10.685	1.042
20	10	23	25	15.015	12.079	0.139
30	10	23	25	15.008	14.284	0.221
40	10	23	25	15.031	14.881	0.060
50	10	23	25	15.069	15.663	0.078
60	10	23	25	15.035	15.888	0.023

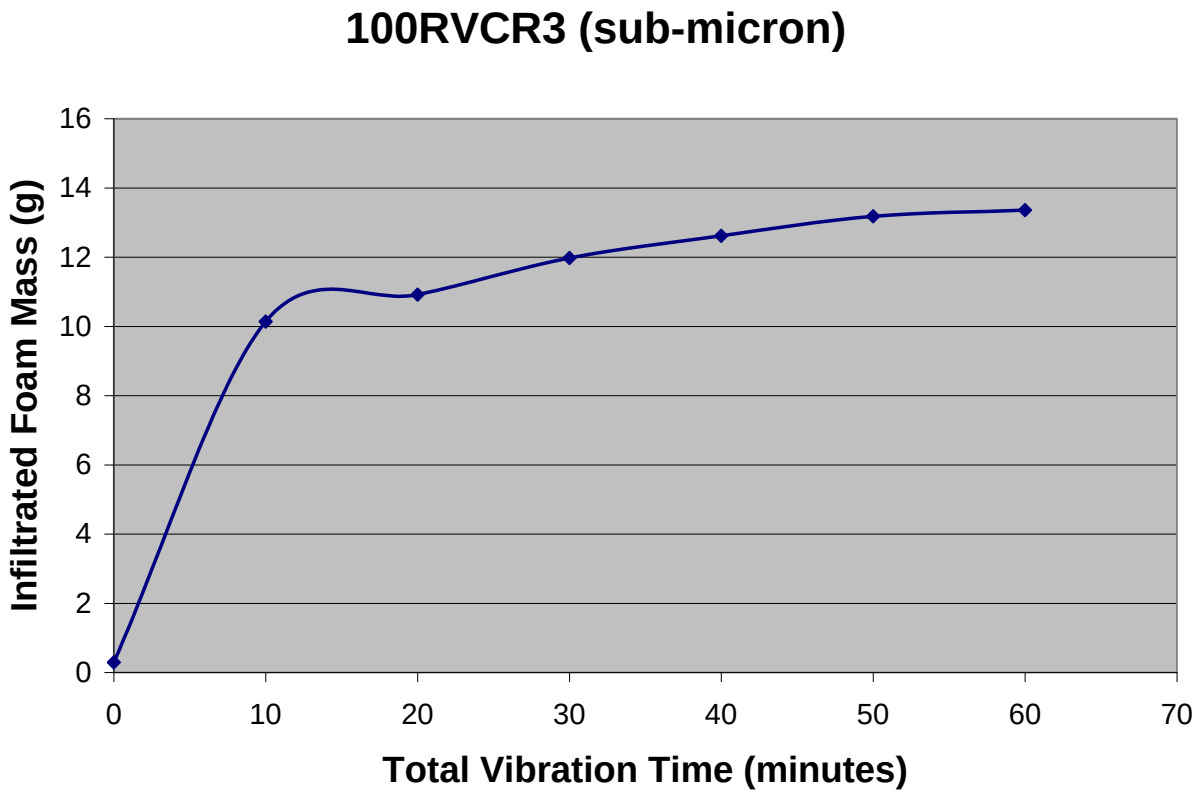

Figure 265. Graph of sub-micron tungsten infiltration within RVC 100 ppi foam round 3.

Table LIII. Table of Sub-micron Tungsten Infiltration Parameters and Measurements for RVC 100 ppi Foam Round 3

Net vibration time (min)	Vibration run time (min)	Acceleration min (m/s^2)	Acceleration max (m/s^2)	Tungsten mass (g)	Infiltrated mass (g)	Infiltration rate (g/min)
0					0.292	
10	10	23	25	15.036	10.134	0.984
20	10	23	25	15.055	10.915	0.078
30	10	23	25	15.03	11.976	0.106
40	10	23	25	15.019	12.612	0.064
50	10	23	25	15.036	13.178	0.057
60	10	23	25	15.053	13.354	0.018

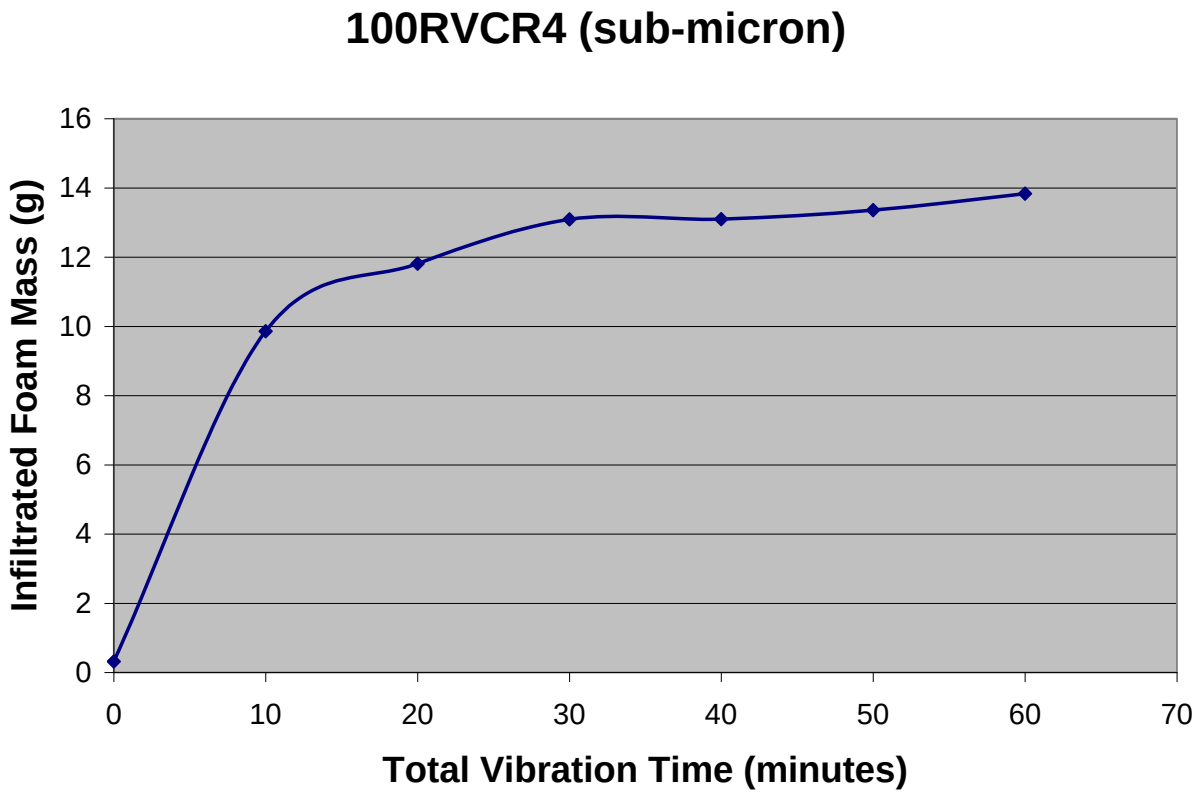

Figure 266. Graph of sub-micron tungsten infiltration within RVC 100 ppi foam round 4.

Table LIV. Table of Sub-micron Tungsten Infiltration Parameters and Measurements for RVC 100 ppi Foam Round 4

Net vibration time (min)	Vibration run time (min)	Acceleration min (m/s^2)	Acceleration max (m/s^2)	Tungsten mass (g)	Infiltrated mass (g)	Infiltration rate (g/min)
0					0.316	
10	10	23	25	15.085	9.858	0.954
20	10	23	25	15.003	11.807	0.195
30	10	23	25	15.09	13.093	0.129
40	10	23	25	15.015	13.095	0.000
50	10	23	25	15.017	13.356	0.026
60	10	23	25	15.04	13.831	0.048

Appendix H. Graphs of Waveforms Produced from Impulse Excitation and the Fast Fourier Transform (FFT) Used to Determine the Resonant Frequency

Graphs of waveform produced during impulse excitation of samples are on the left. The fast Fourier transform of each waveform is on the right.

45RVCR1 Flexure

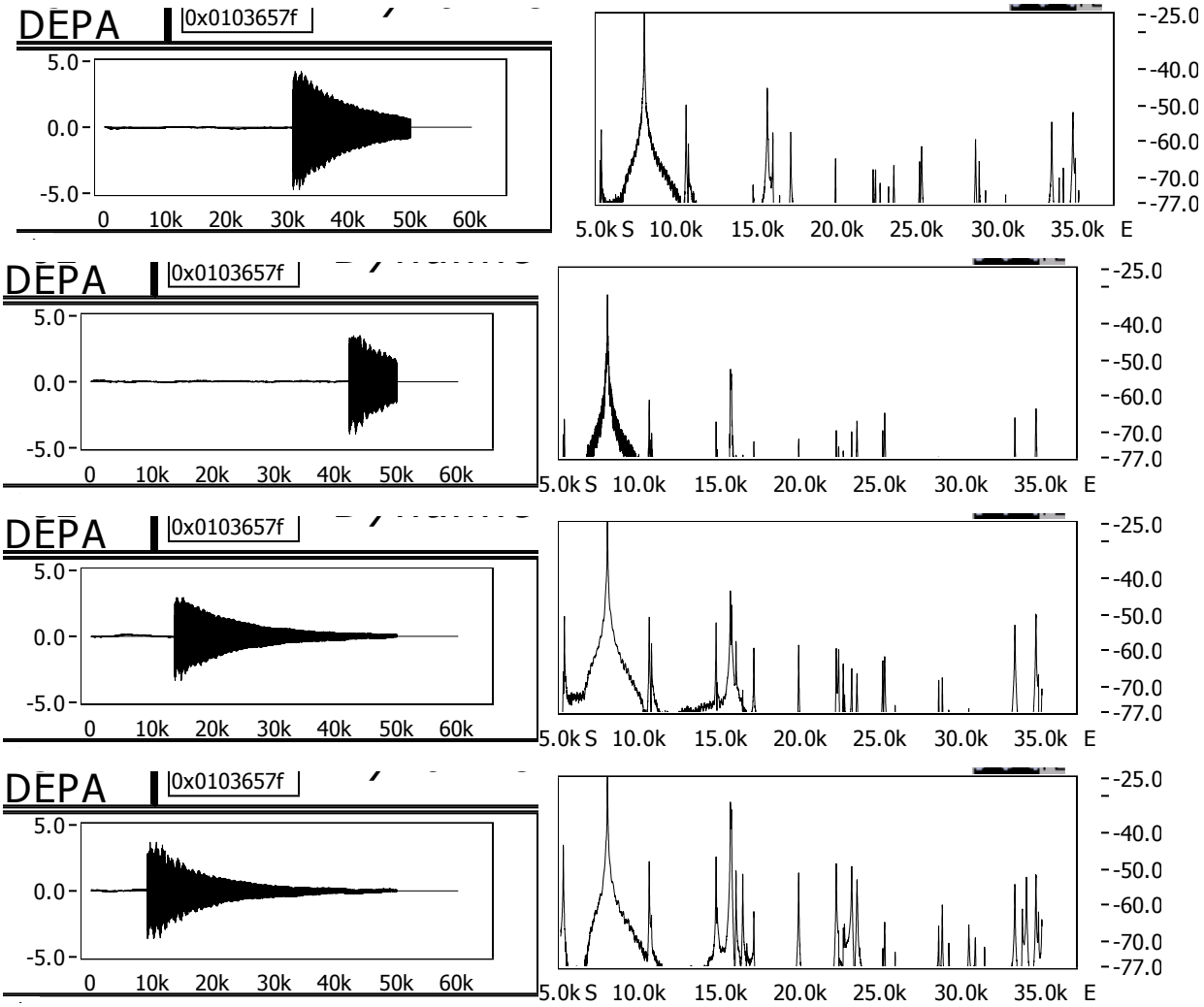

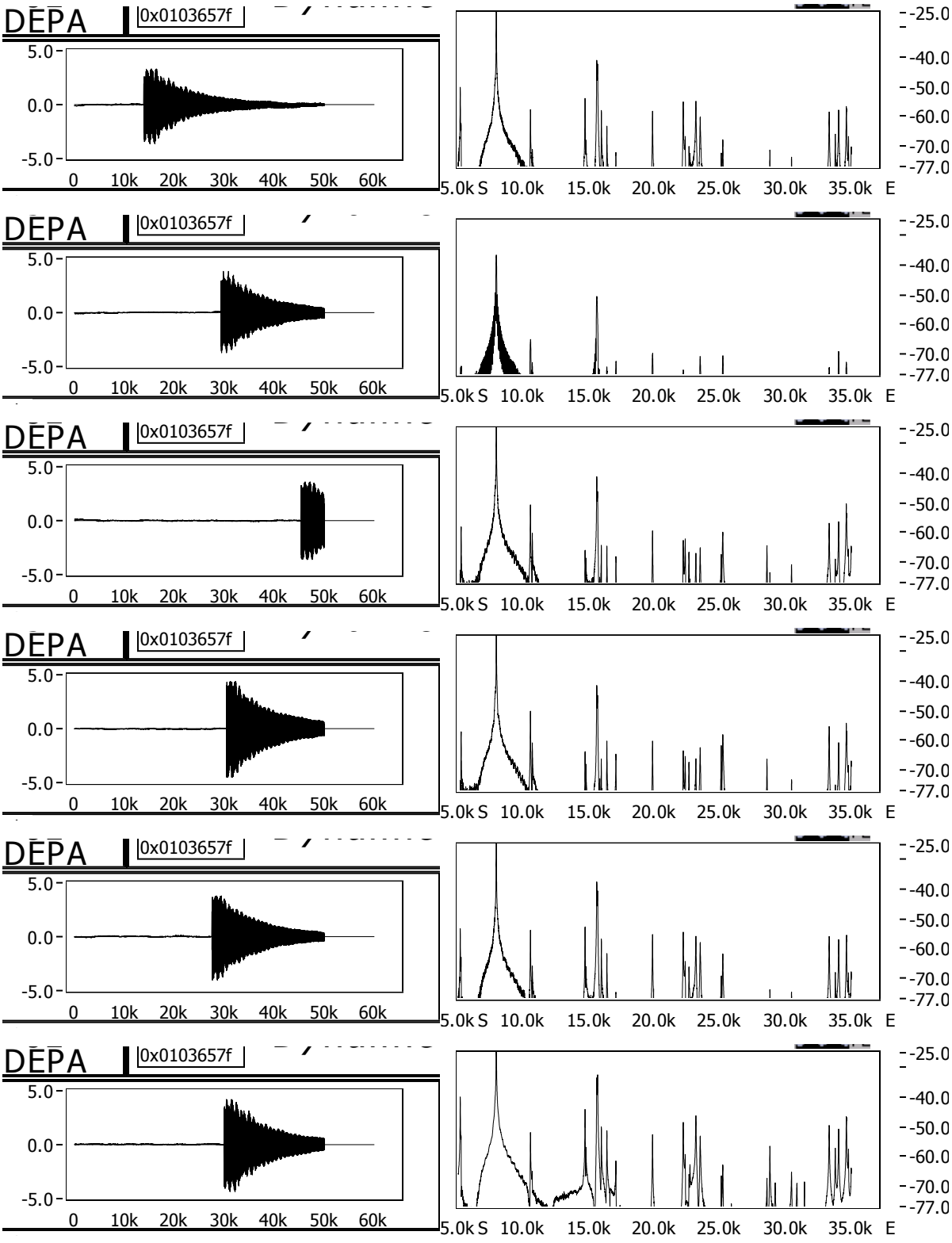
DEPA
0x0103657f
5.0
0.0
-5.0
0 10k 20k 30k 40k 50k 60k
-25.0
-40.0
-50.0
-60.0
-70.0
-77.0
5.0k S 10.0k 15.0k 20.0k 25.0k 30.0k 35.0k E

45RVCR1 anti-flexure

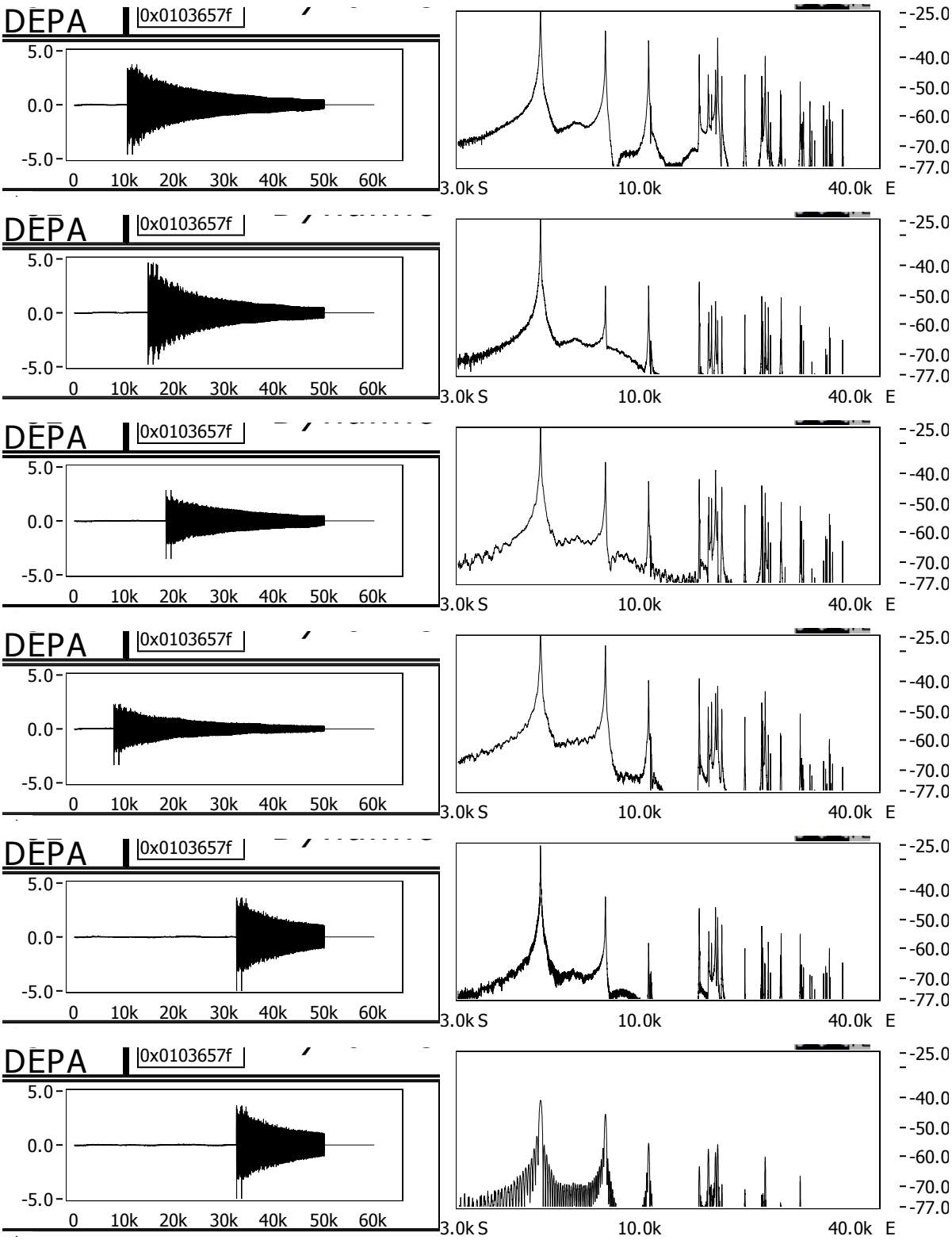

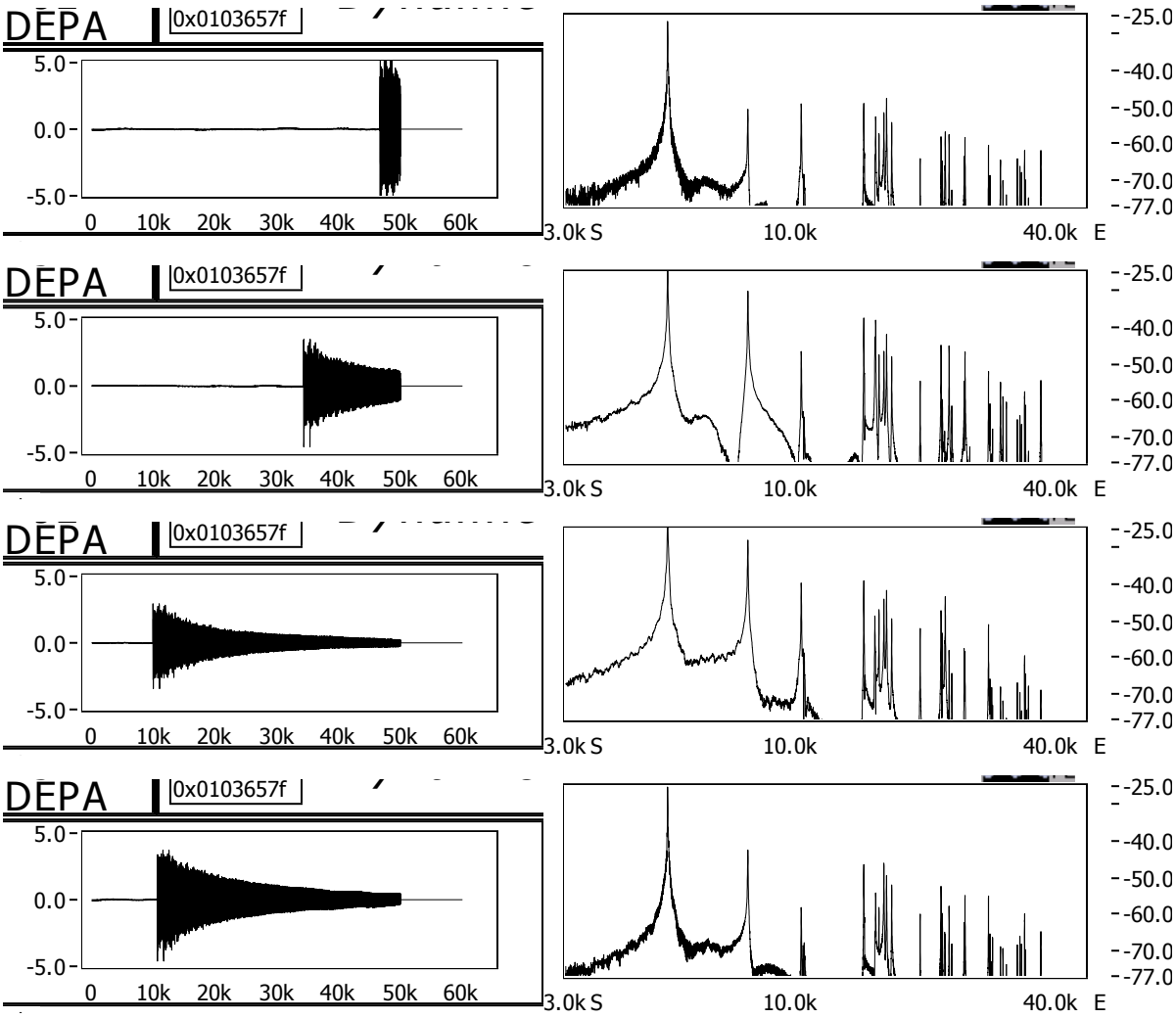

45RVCR5 Flexure

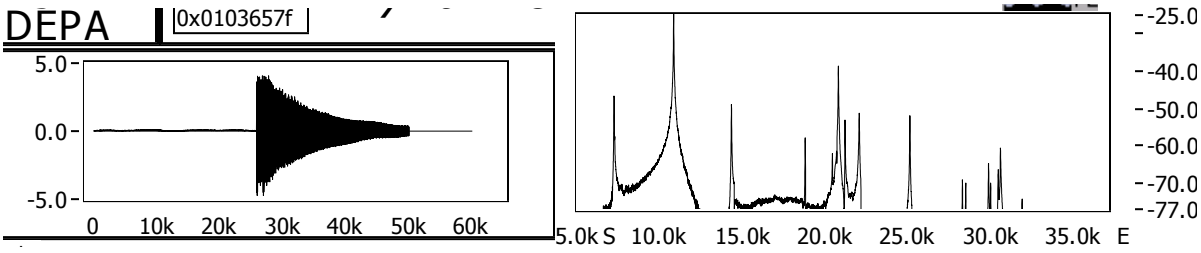

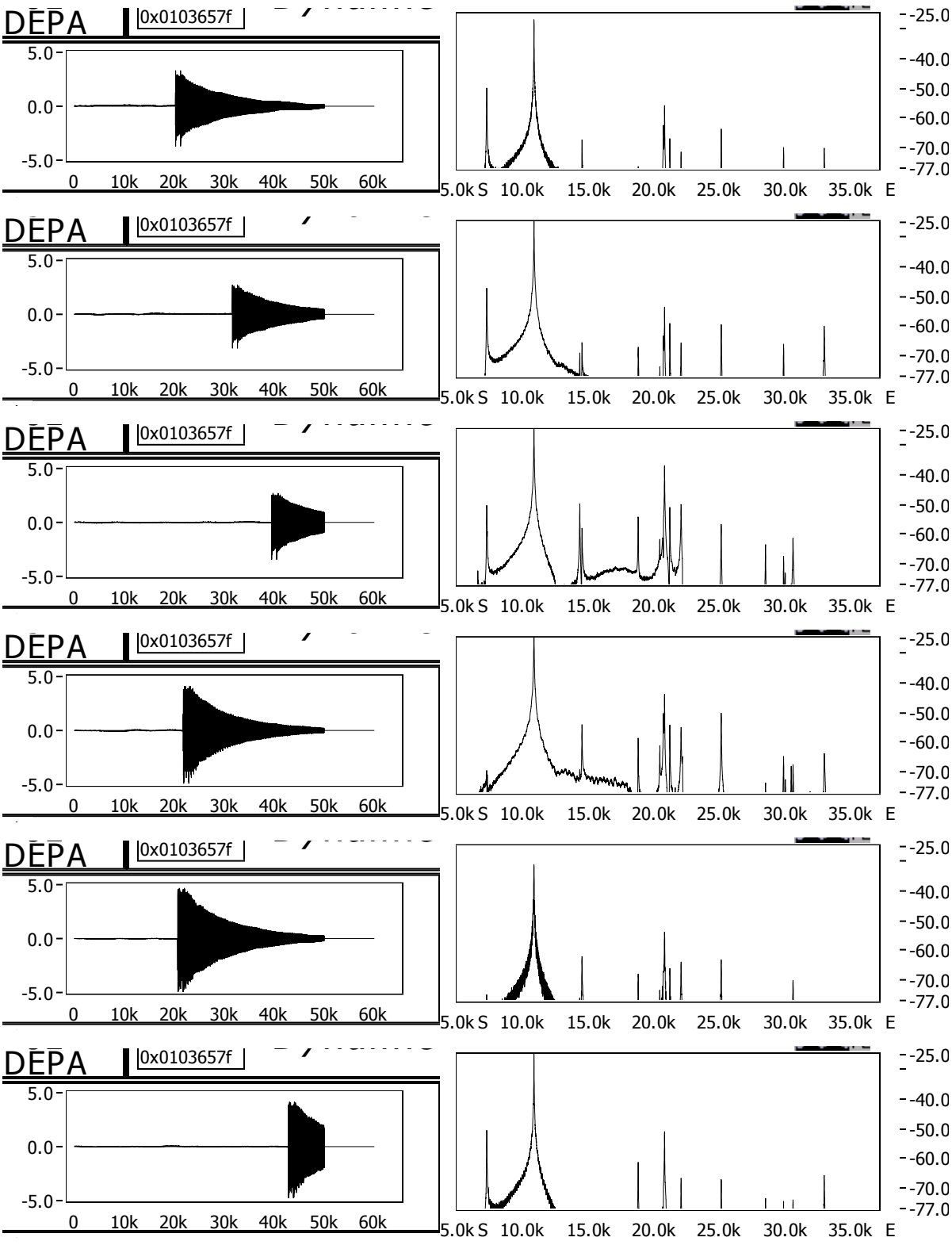
DEPA
0x0103657f
5.0
0.0
-5.0
0 10k 20k 30k 40k 50k 60k
-25.0
-40.0
-50.0
-60.0
-70.0
-77.0
5.0k S 10.0k 15.0k 20.0k 25.0k 30.0k 35.0k E

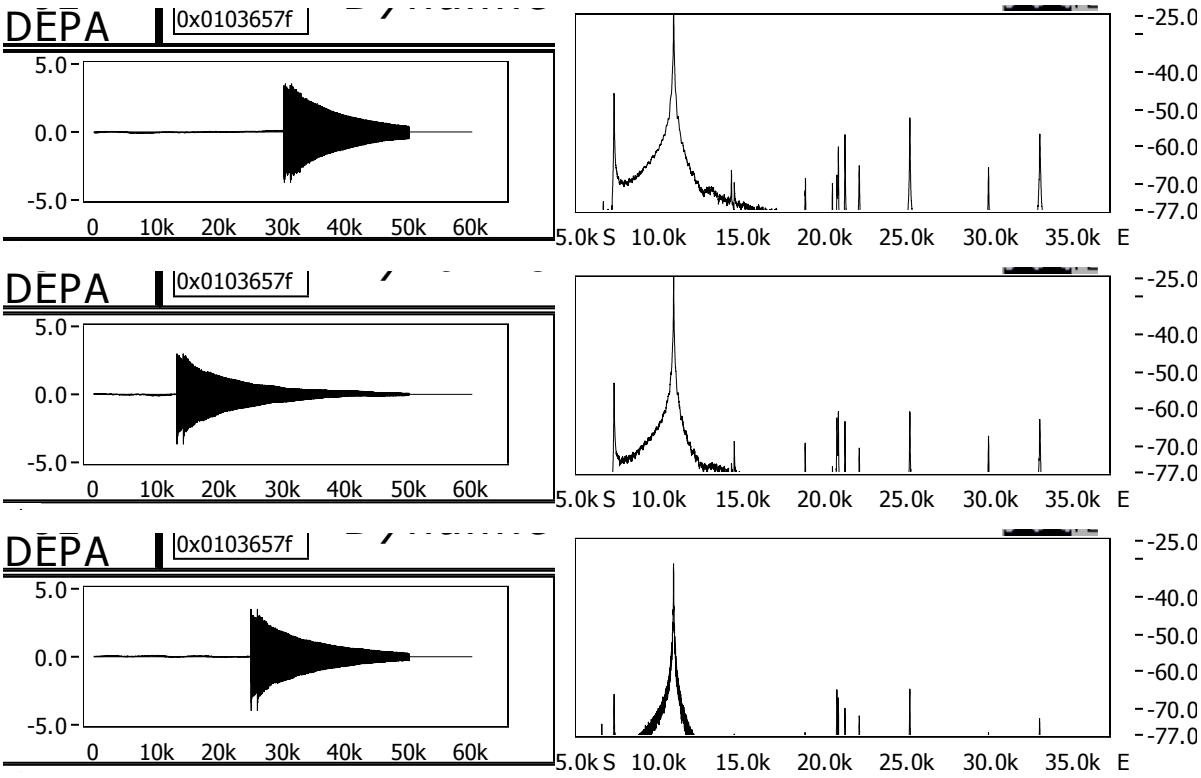

45RVCR5 Anti-Flexure

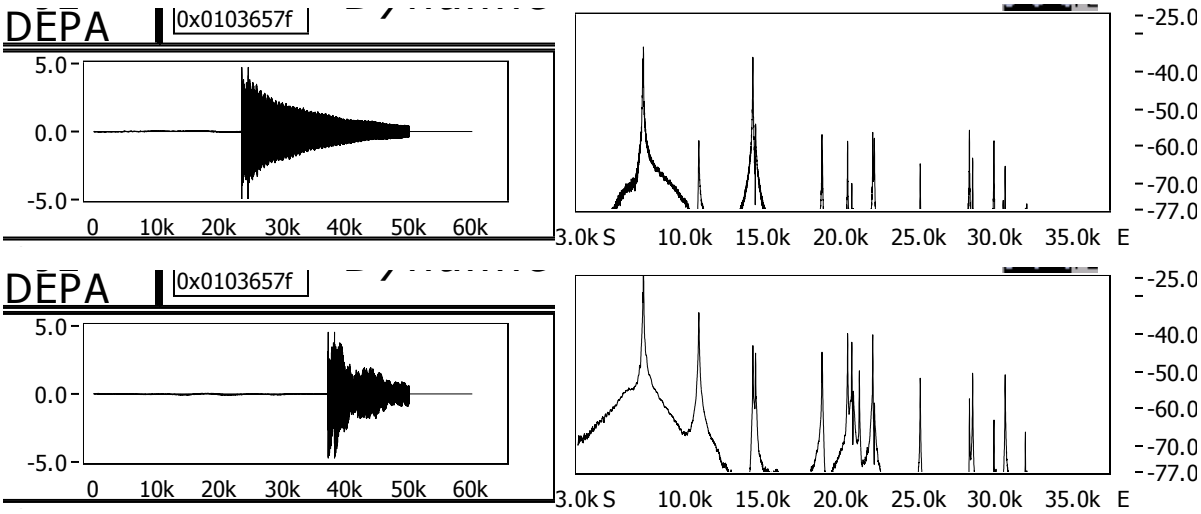

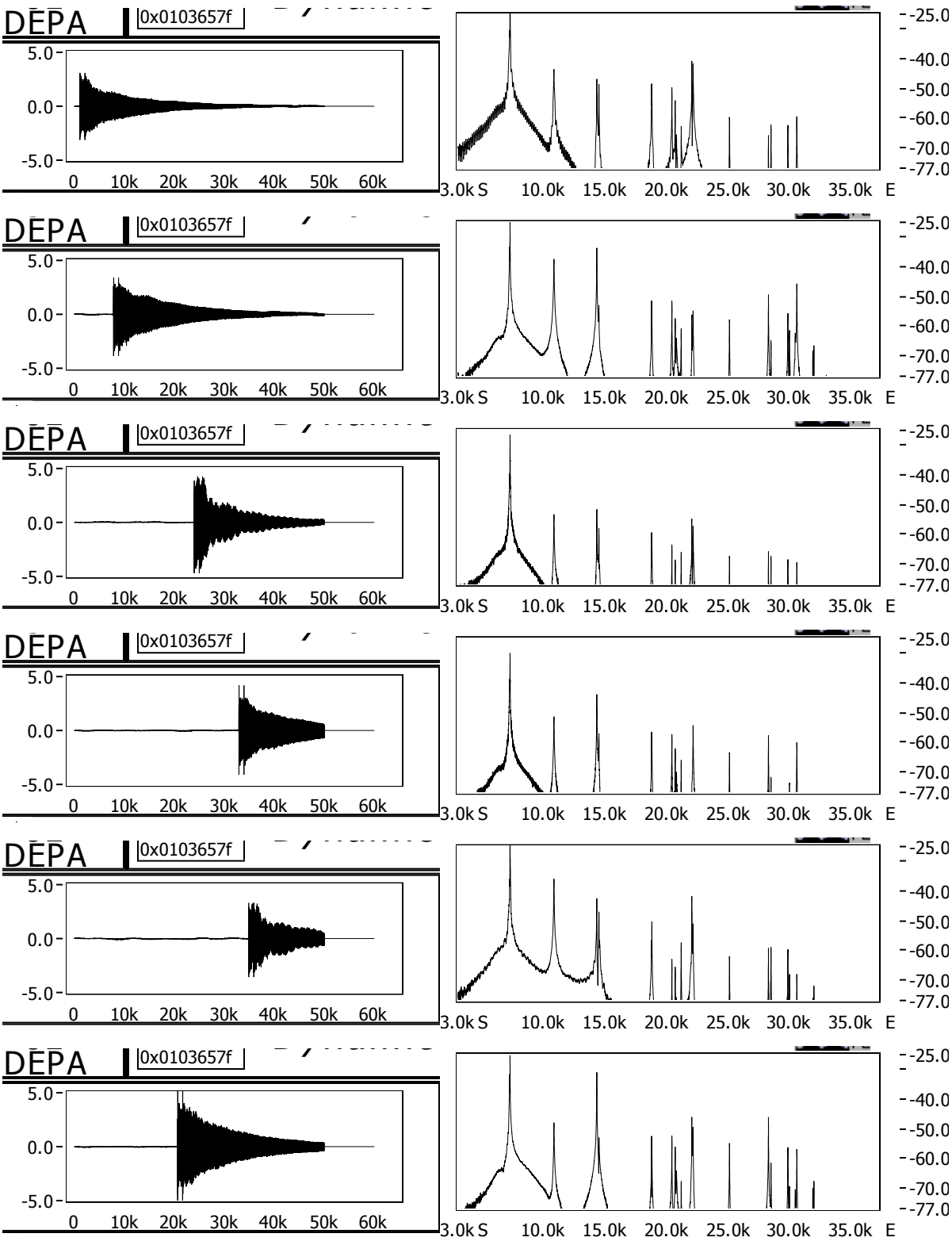
DEPA
0x0103657f
5.0
0.0
-5.0
0 10k 20k 30k 40k 50k 60k
3.0k S 10.0k 15.0k 20.0k 25.0k 30.0k 35.0k E
-25.0
-40.0
-50.0
-60.0
-70.0
-77.0

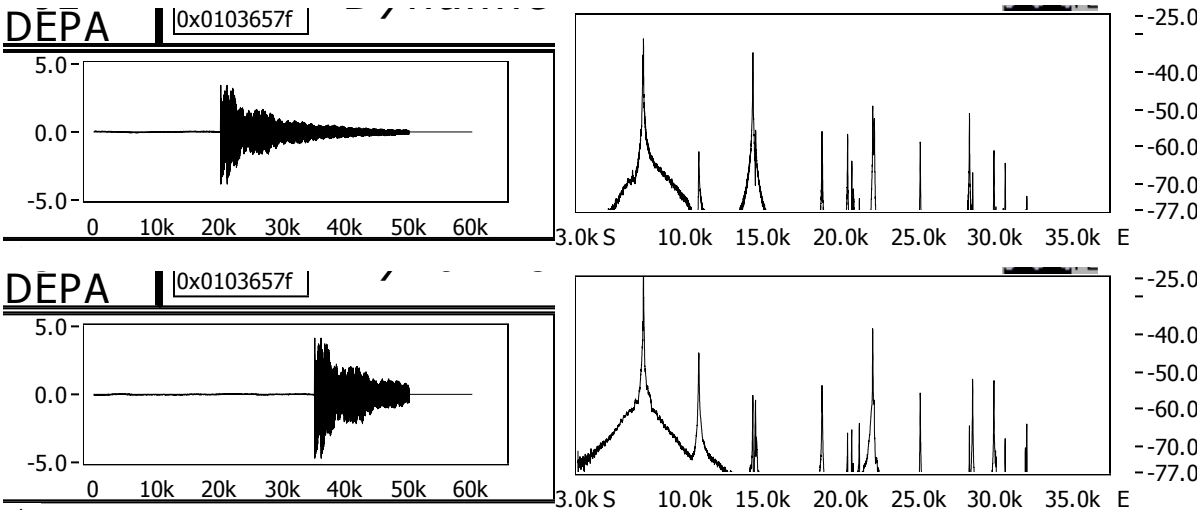

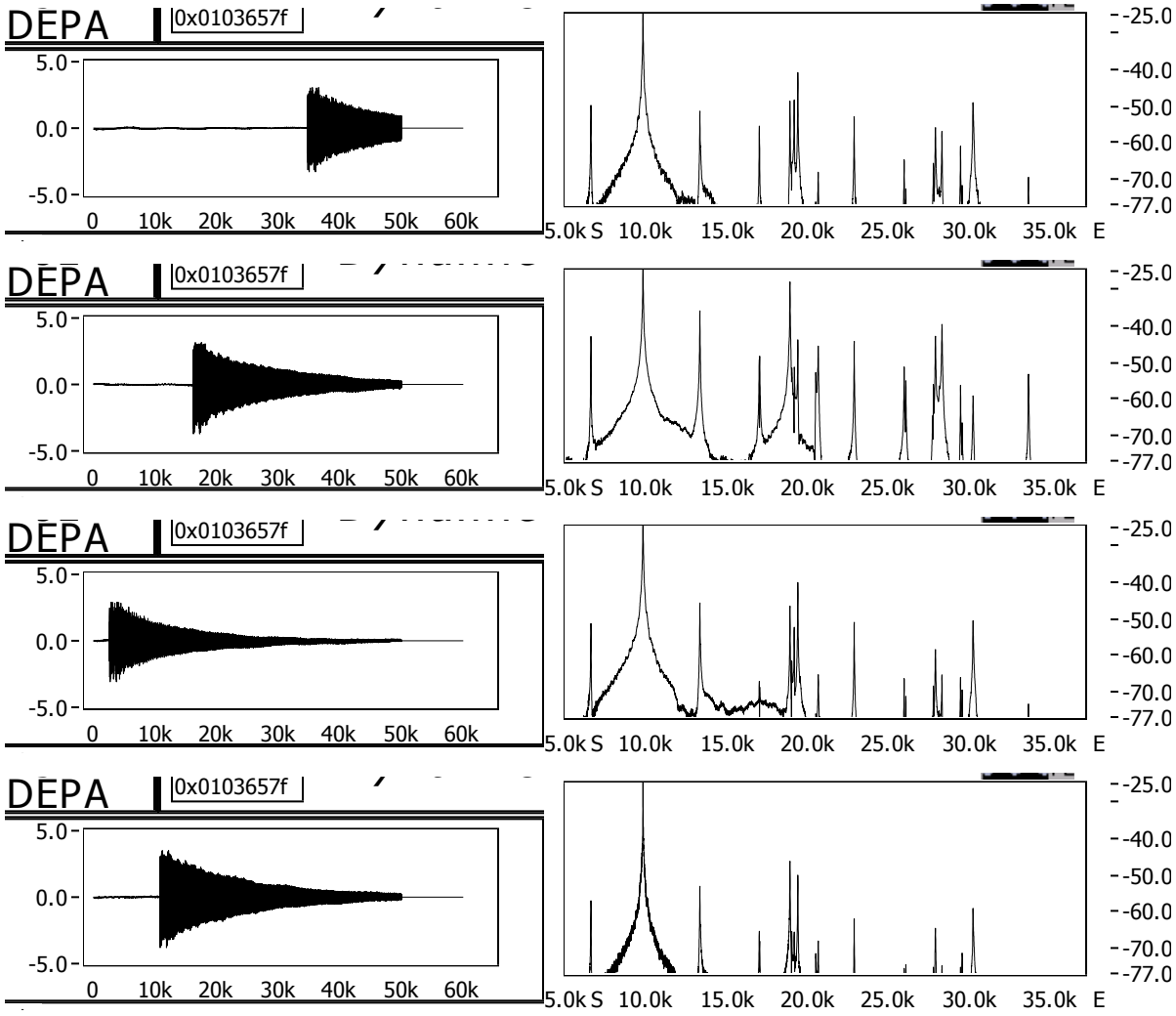

65RVCR1 Flexure

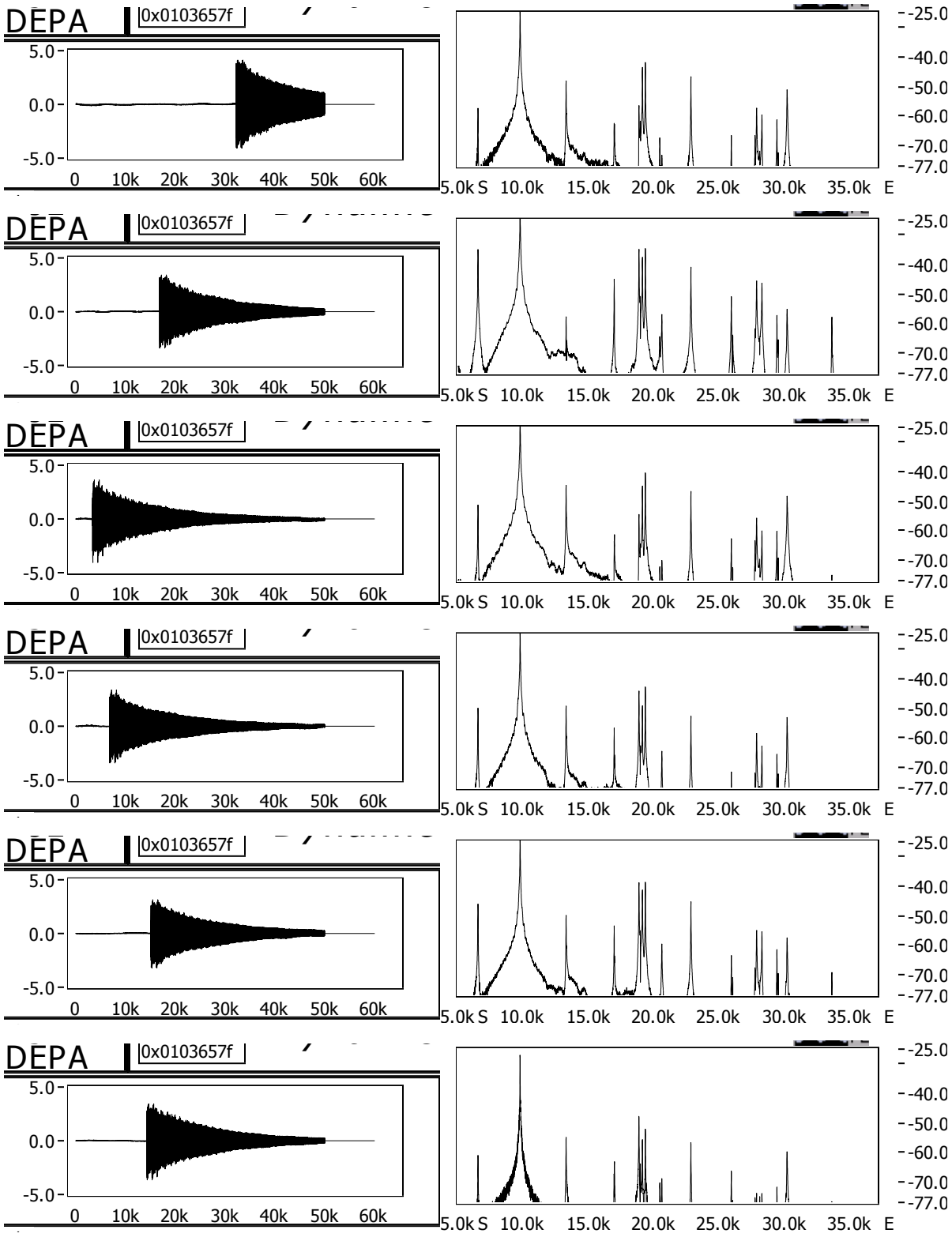
DEPA
0x0103657f
5.0
0.0
-5.0
0 10k 20k 30k 40k 50k 60k
-25.0
-40.0
-50.0
-60.0
-70.0
-77.0
5.0k S 10.0k 15.0k 20.0k 25.0k 30.0k 35.0k E

65RVCR1 Anti-Flexure

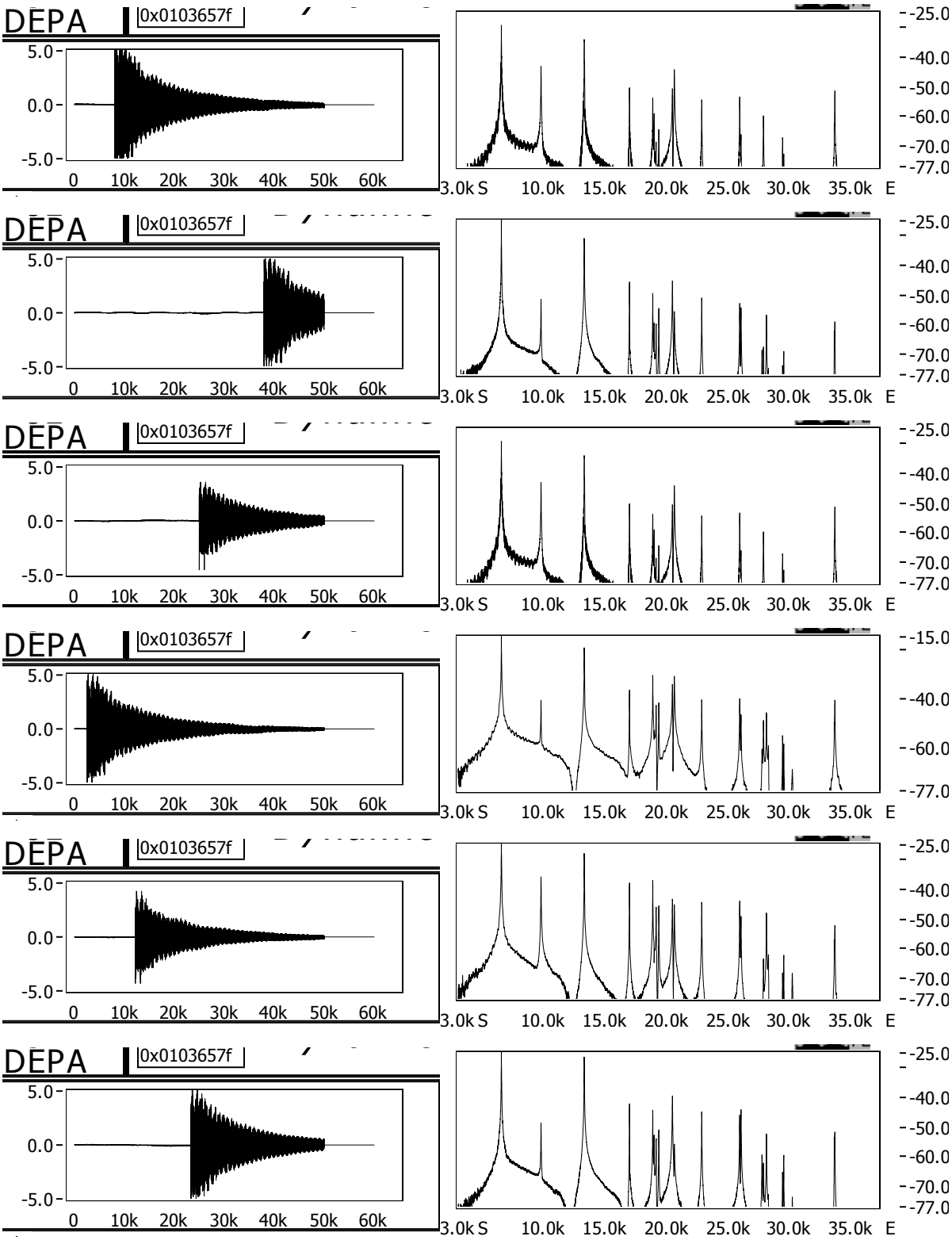

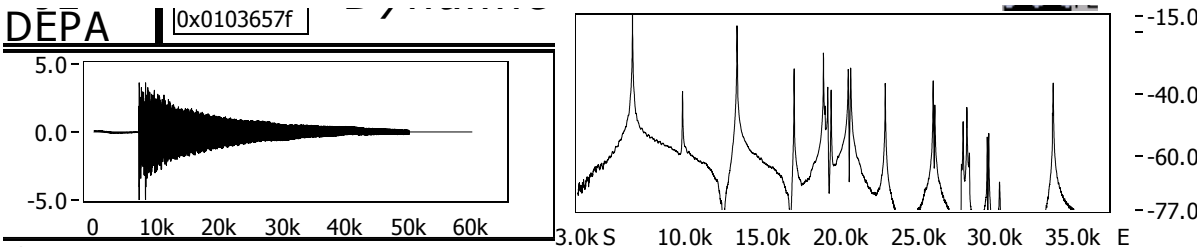

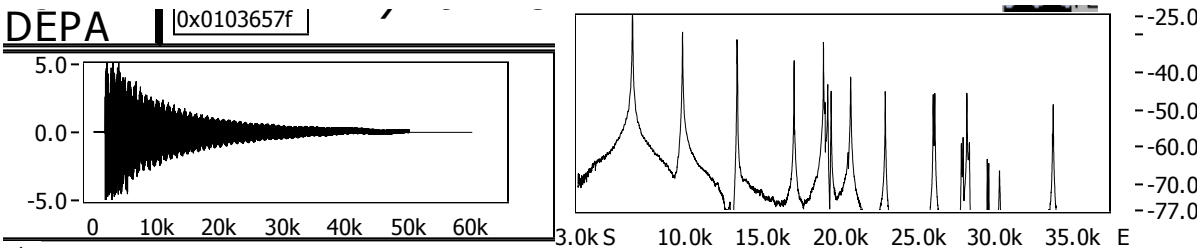

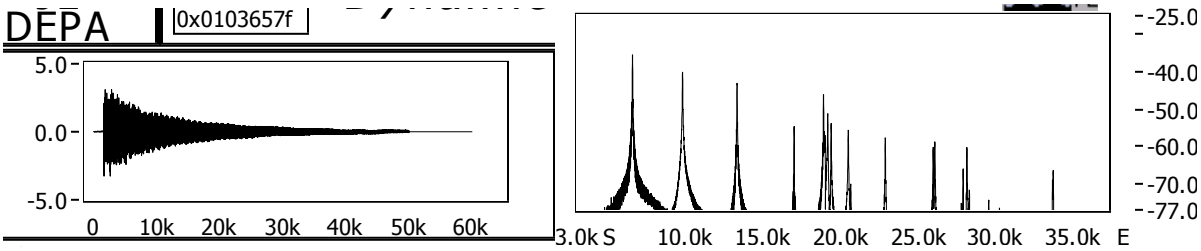

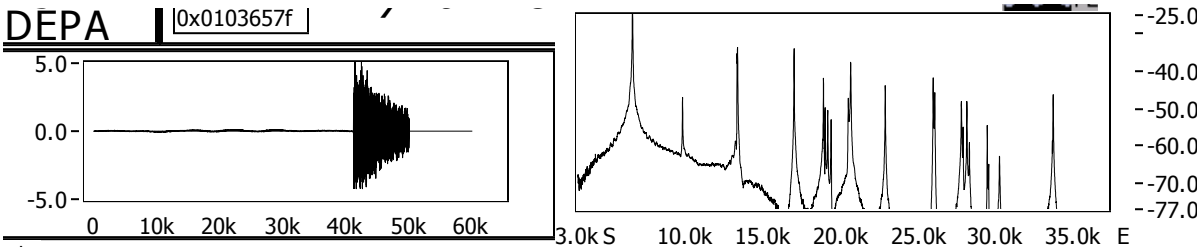

65RVCR2 Flexure

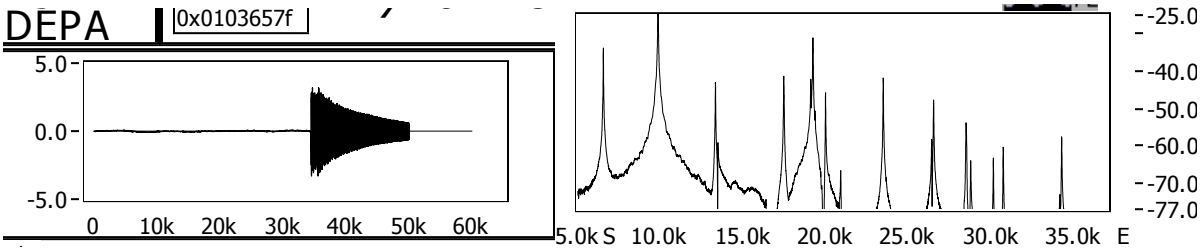

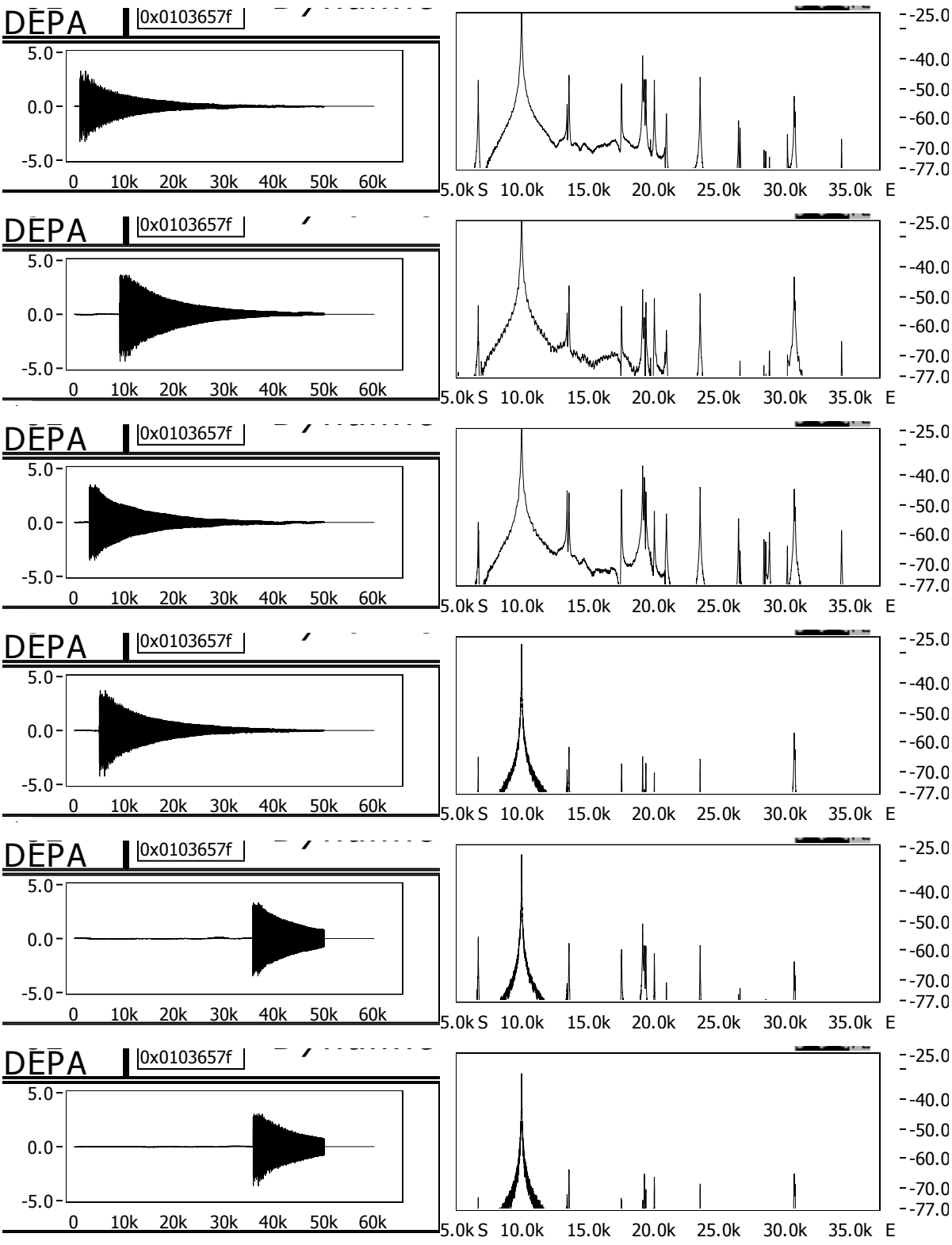
DEPA
0x0103657f
5.0
0.0
-5.0
0 10k 20k 30k 40k 50k 60k
-25.0
-40.0
-50.0
-60.0
-70.0
-77.0
5.0k S 10.0k 15.0k 20.0k 25.0k 30.0k 35.0k E

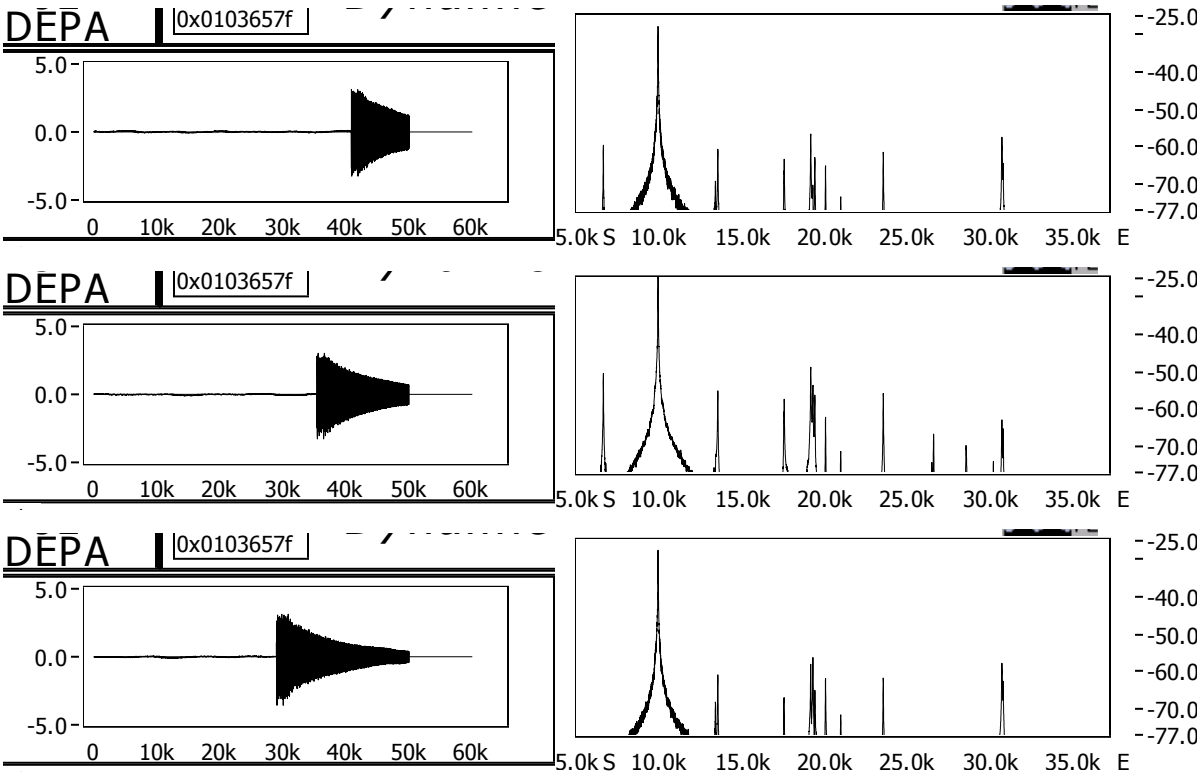

65RVCR2 Anti-flexure

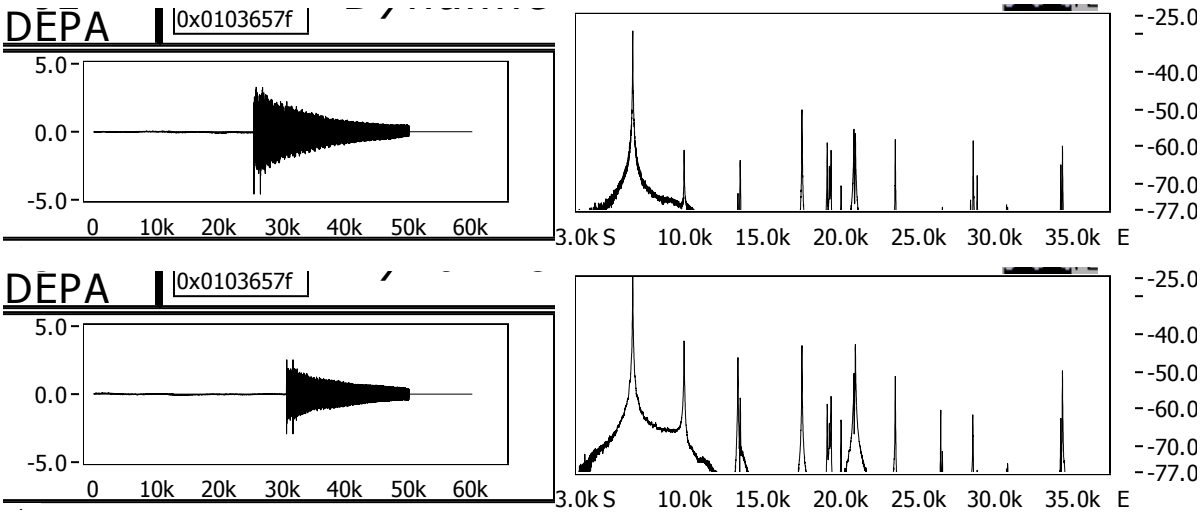

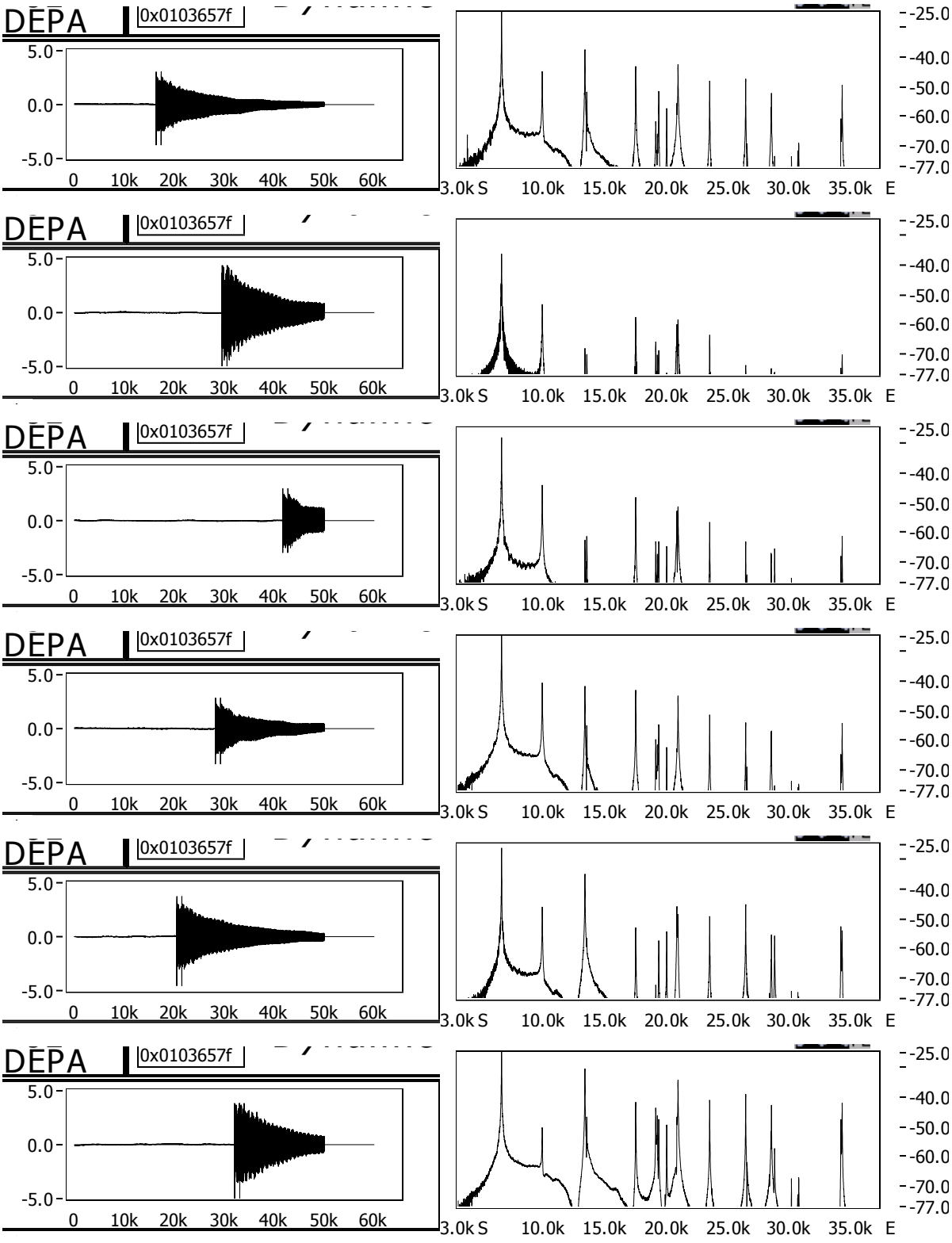
DEPA
0x0103657f
5.0
0.0
-5.0
0 10k 20k 30k 40k 50k 60k
-25.0
-40.0
-50.0
-60.0
-70.0
-77.0
3.0k S 10.0k 15.0k 20.0k 25.0k 30.0k 35.0k E

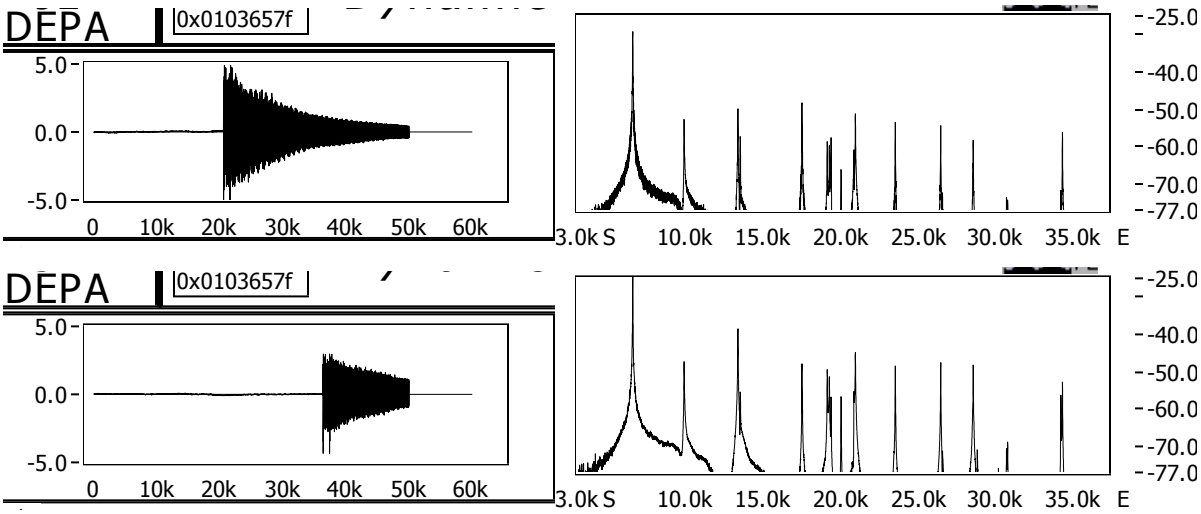

100RVCR2 flexure

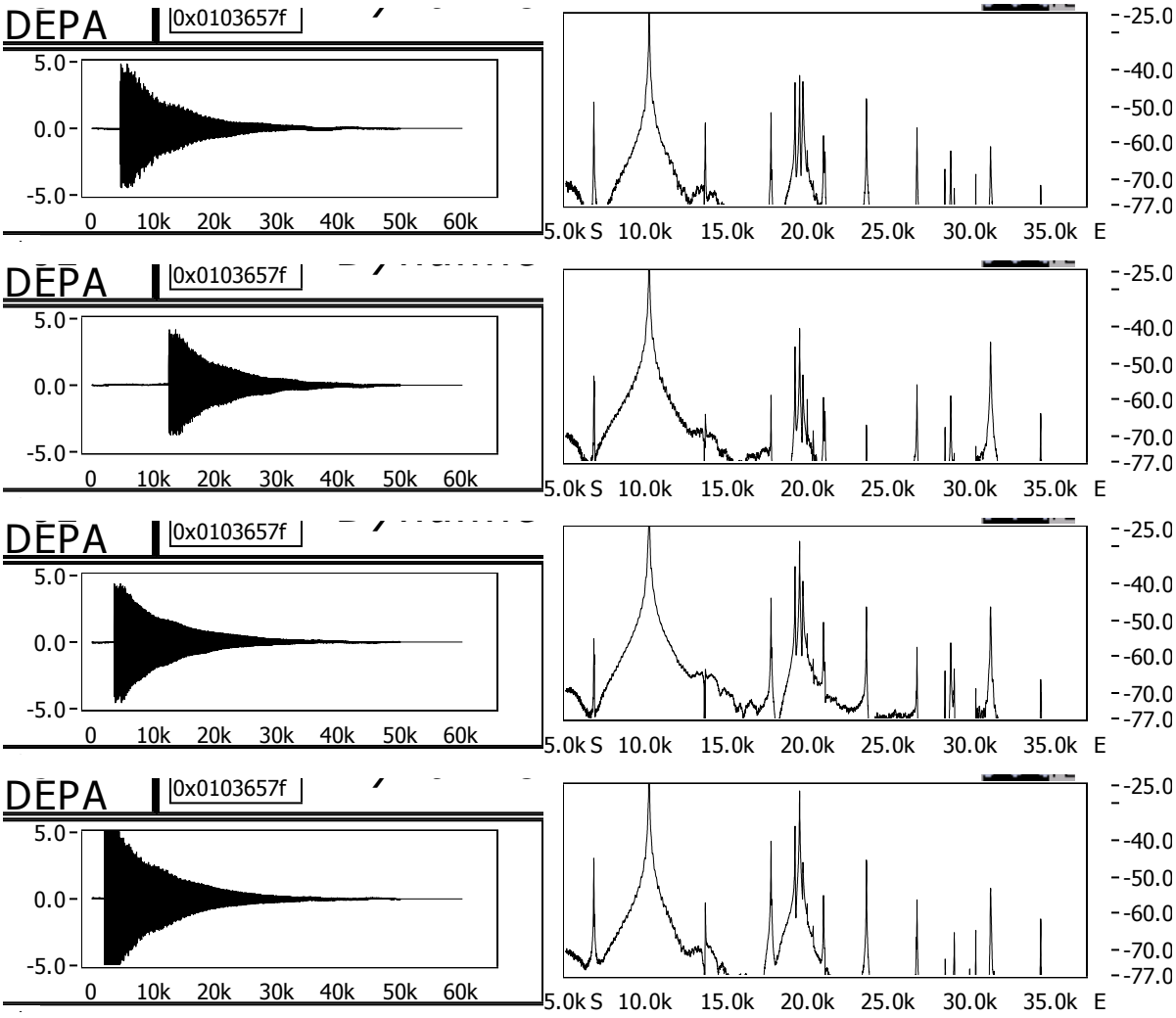

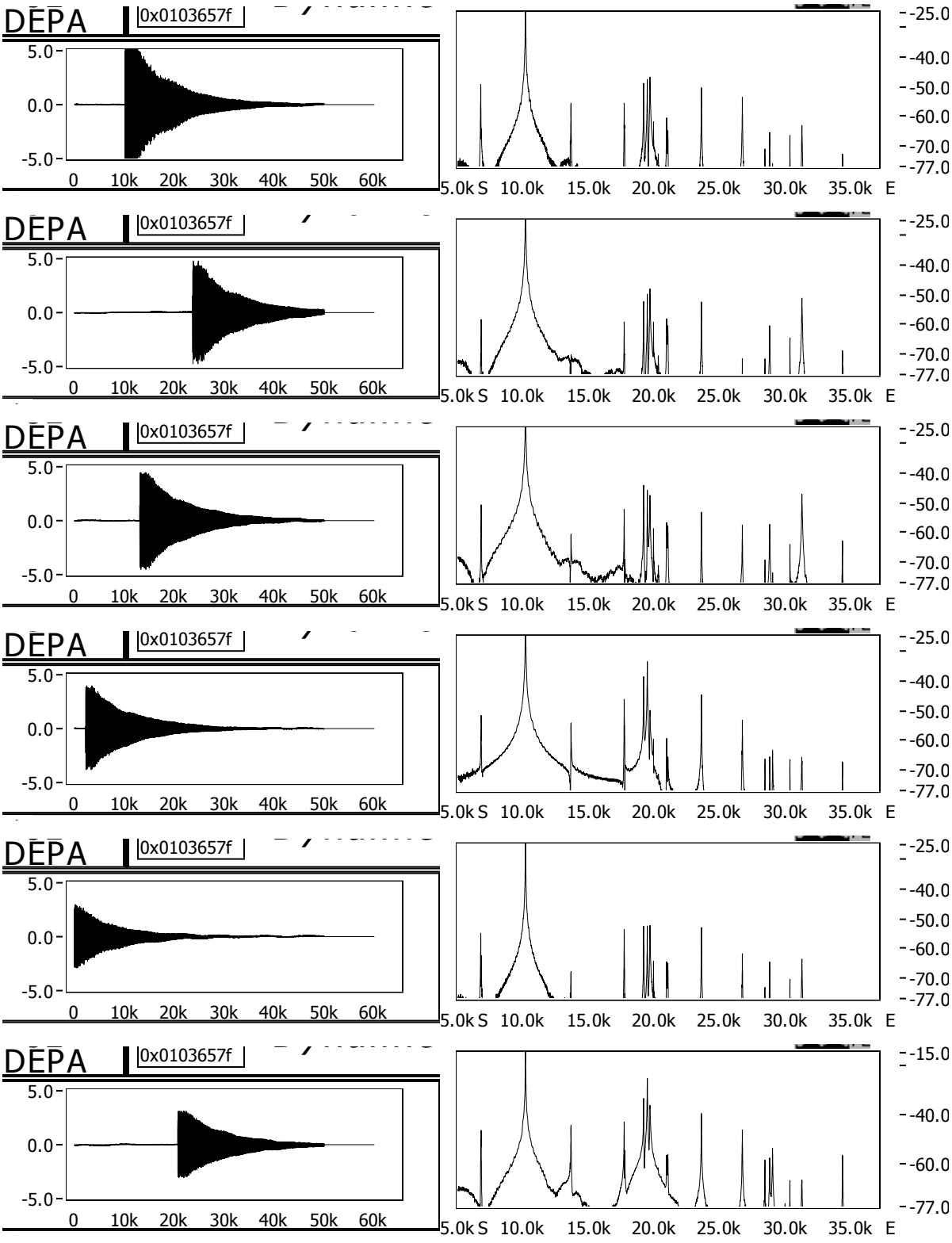

DEPA
0x0103657f
5.0
0.0
-5.0
0
10k
20k
30k
40k
50k
60k
5.0k S
10.0k
15.0k
20.0k
25.0k
30.0k
35.0k
E
-25.0
-40.0
-50.0
-60.0
-70.0
-77.0

DEPA
0x0103657f
5.0
0.0
-5.0
0
10k
20k
30k
40k
50k
60k
5.0k S
10.0k
15.0k
20.0k
25.0k
30.0k
35.0k
E
-25.0
-40.0
-50.0
-60.0
-70.0
-77.0

DEPA
0x0103657f
5.0
0.0
-5.0
0
10k
20k
30k
40k
50k
60k
5.0k S
10.0k
15.0k
20.0k
25.0k
30.0k
35.0k
E
-25.0
-40.0
-50.0
-60.0
-70.0
-77.0

DEPA
0x0103657f
5.0
0.0
-5.0
0
10k
20k
30k
40k
50k
60k
5.0k S
10.0k
15.0k
20.0k
25.0k
30.0k
35.0k
E
-25.0
-40.0
-50.0
-60.0
-70.0
-77.0

DEPA
0x0103657f
5.0
0.0
-5.0
0
10k
20k
30k
40k
50k
60k
5.0k S
10.0k
15.0k
20.0k
25.0k
30.0k
35.0k
E
-25.0
-40.0
-50.0
-60.0
-70.0
-77.0

DEPA
0x0103657f
5.0
0.0
-5.0
0
10k
20k
30k
40k
50k
60k
5.0k S
10.0k
15.0k
20.0k
25.0k
30.0k
35.0k
E
-15.0
-40.0
-60.0
-77.0

100RVCR2 anti-flexure

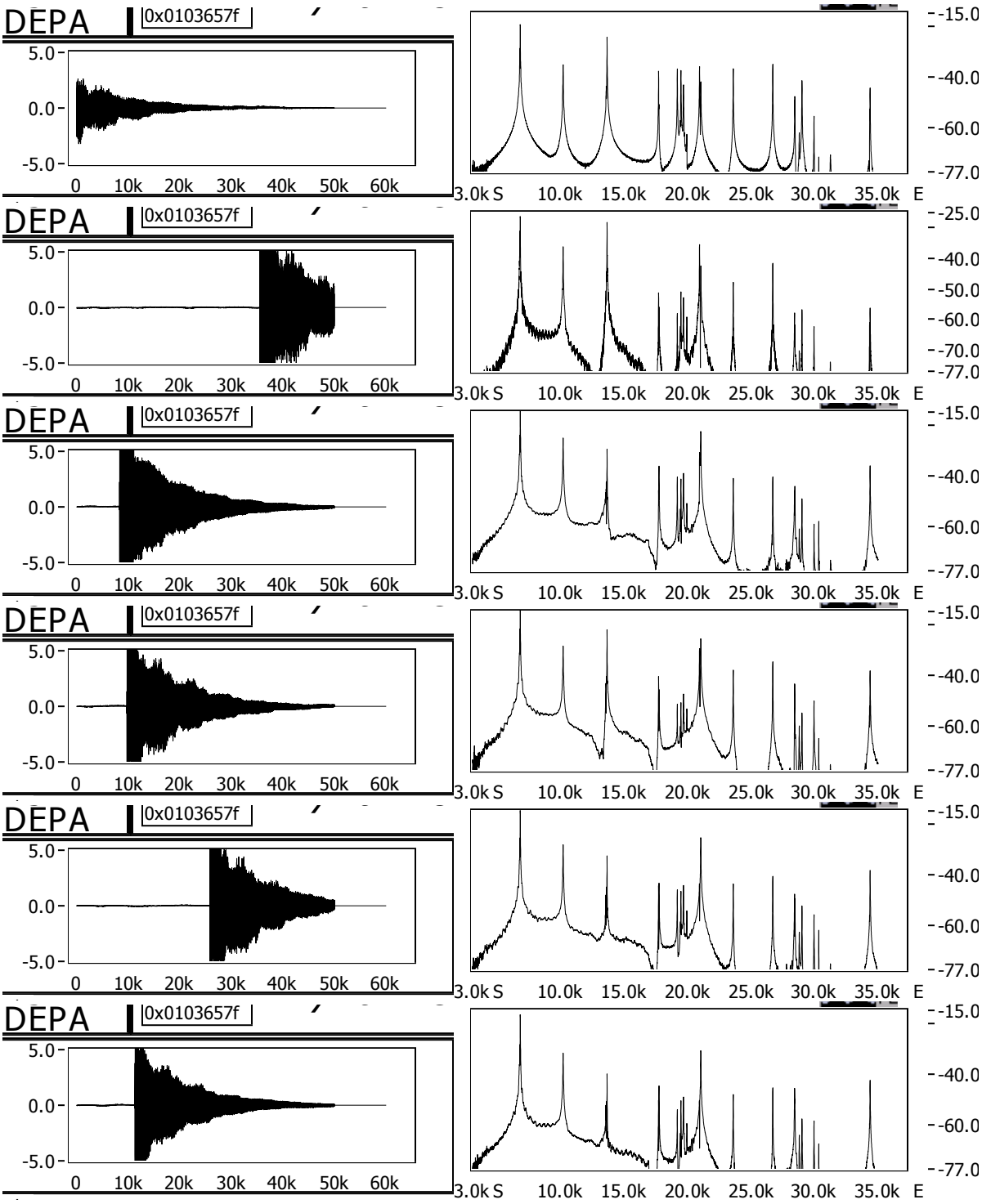

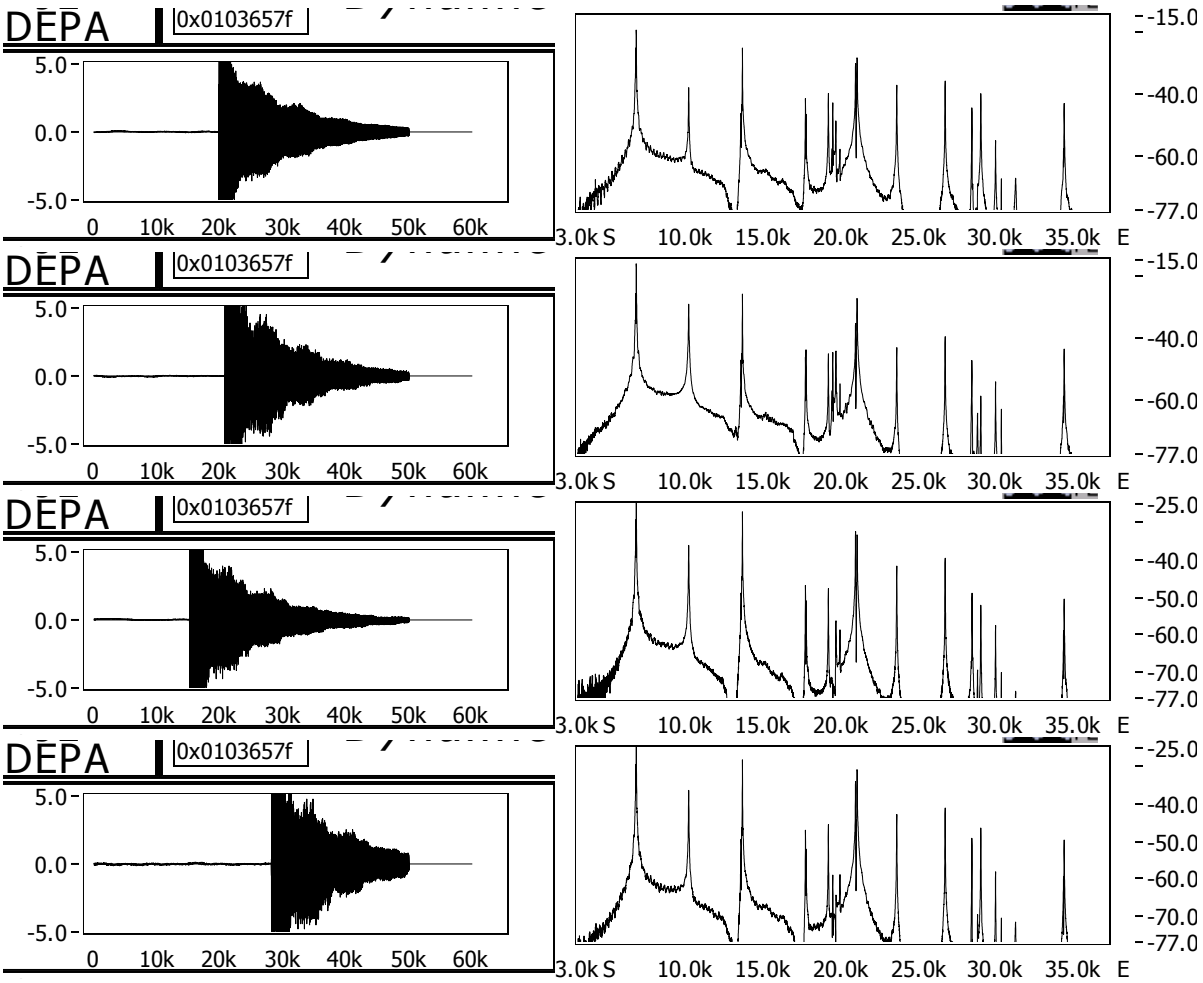

100RVCR6 flexure

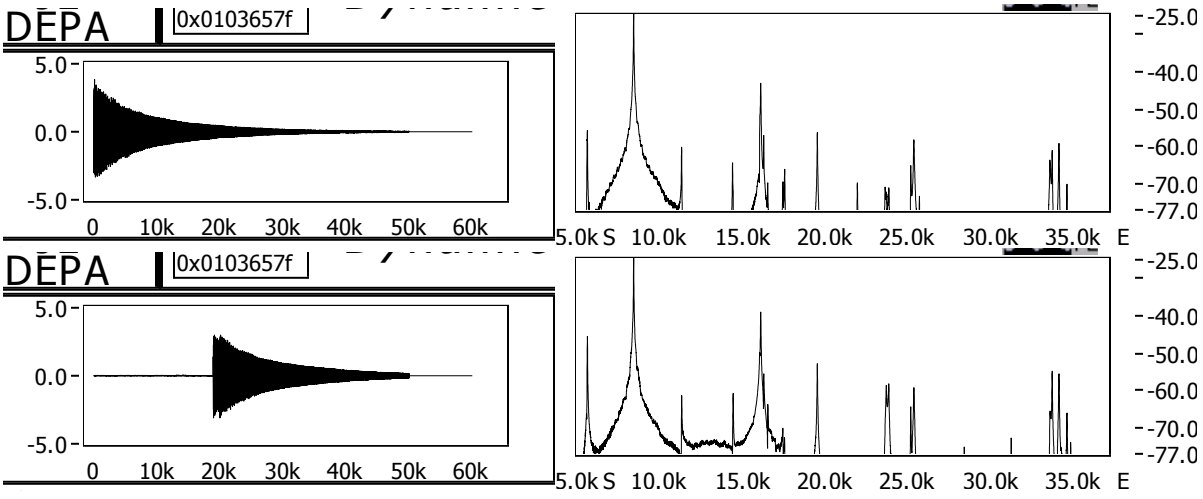

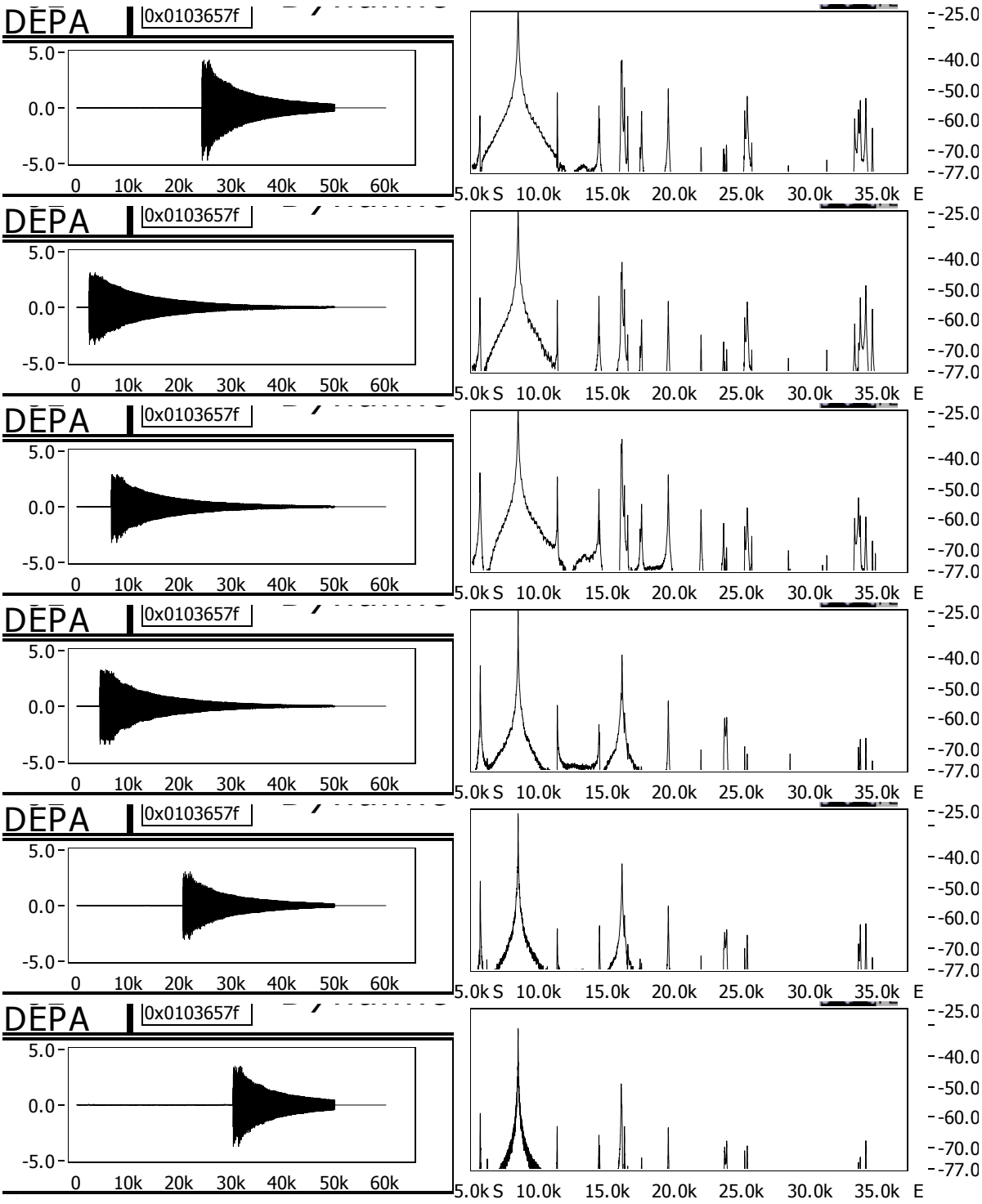
DEPA
0x0103657f
5.0
0.0
-5.0
0 10k 20k 30k 40k 50k 60k
-25.0
-40.0
-50.0
-60.0
-70.0
-77.0
5.0k S 10.0k 15.0k 20.0k 25.0k 30.0k 35.0k E

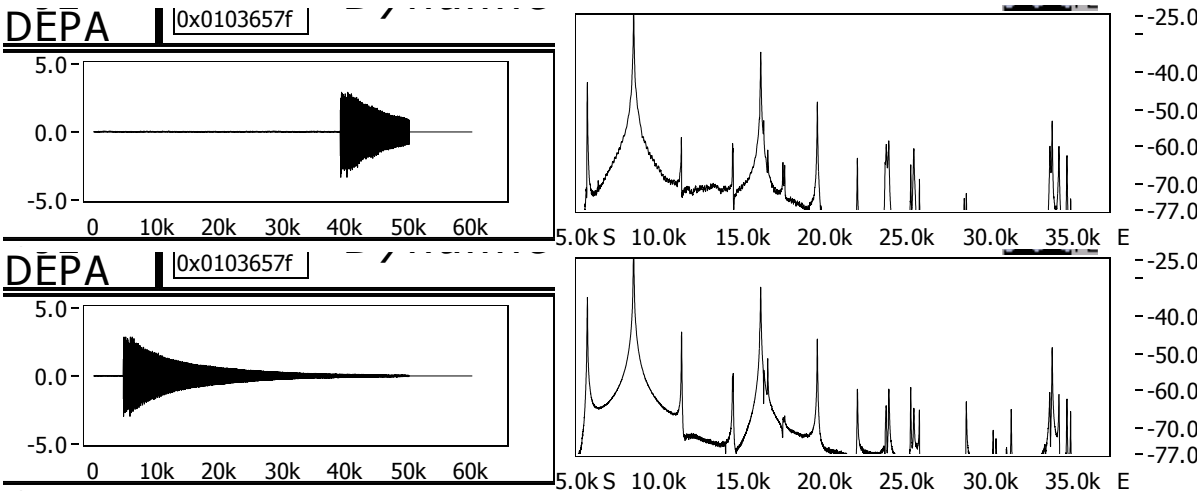

100RVCR6 anti-flexure

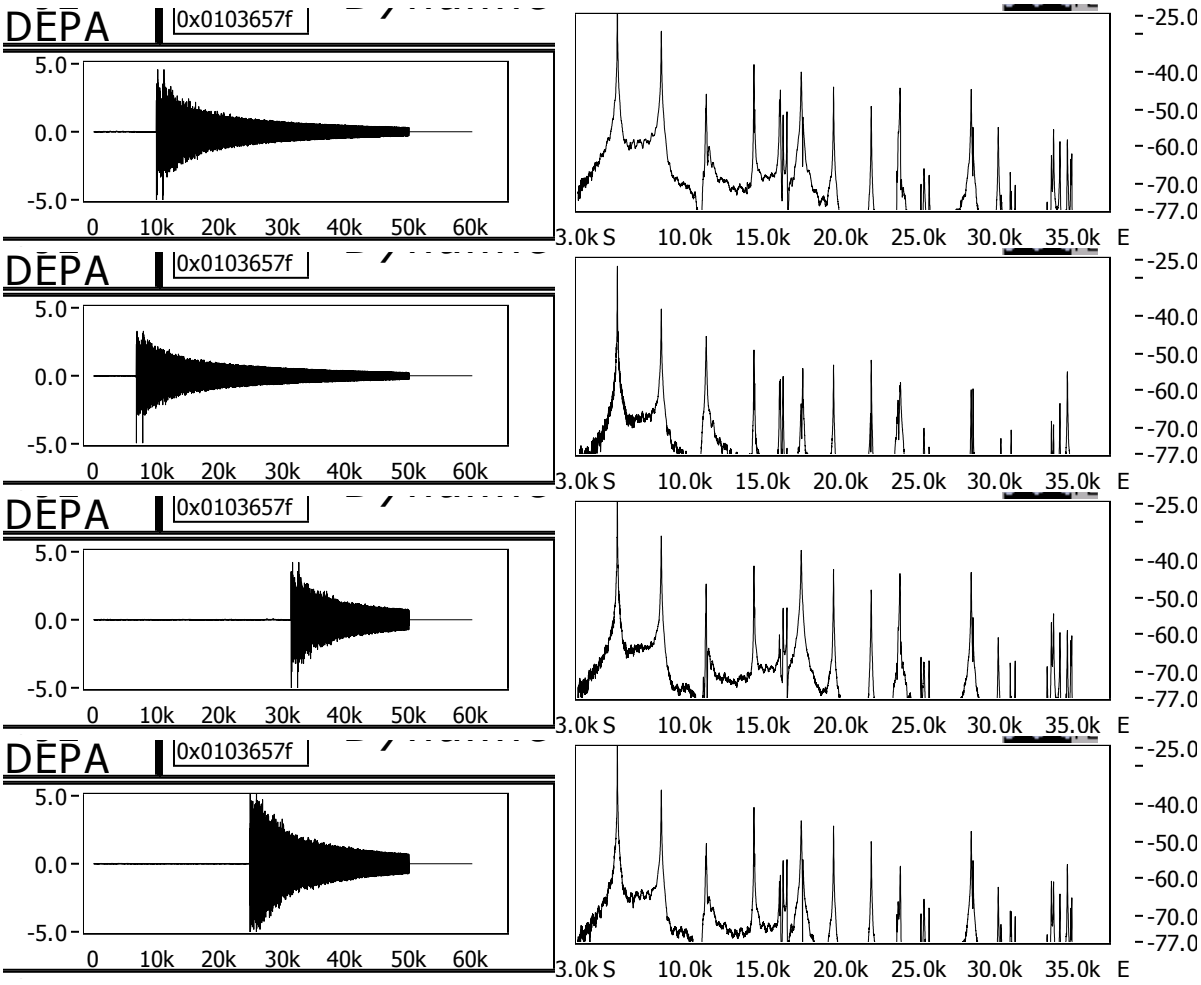

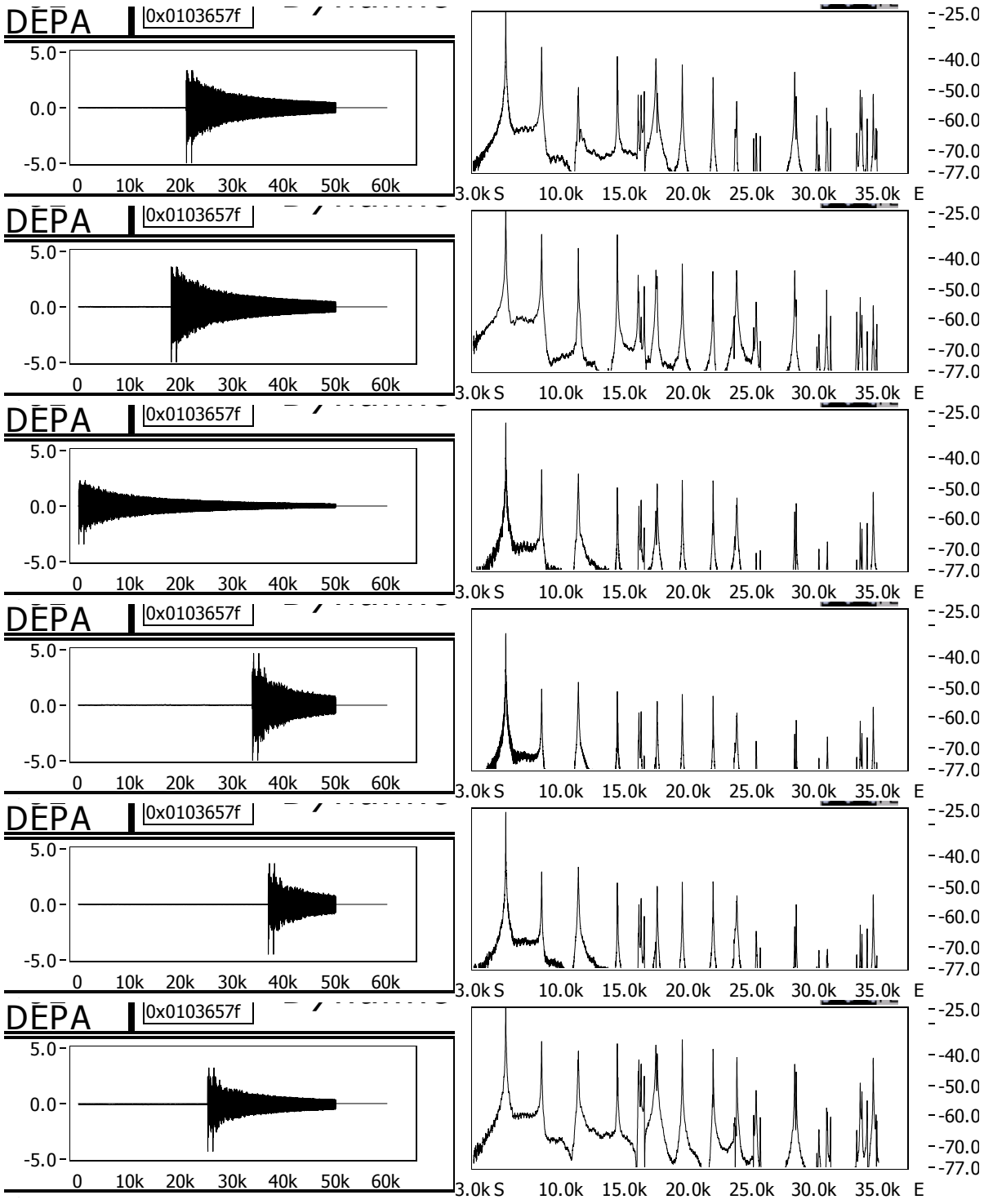
DEPA
0x0103657f
5.0
0.0
-5.0
0
10k
20k
30k
40k
50k
60k
3.0k S
10.0k
15.0k
20.0k
25.0k
30.0k
35.0k
E
-25.0
-40.0
-50.0
-60.0
-70.0
-77.0